https://ntrs.nasa.gov/search.jsp?R=19760004979 2020-03-22T17:44:44+00:00Z

General Disclaimer

One or more of the Following Statements may affect this Document

- This document has been reproduced from the best copy furnished by the organizational source. It is being released in the interest of making available as much information as possible.

- This document may contain data, which exceeds the sheet parameters. It was furnished in this condition by the organizational source and is the best copy available.

- This document may contain tone-on-tone or color graphs, charts and/or pictures, which have been reproduced in black and white.

- This document is paginated as submitted by the original source.

- Portions of this document are not fully legible due to the historical nature of some of the material. However, it is the best reproduction available from the original submission.

Produced by the NASA Center for Aerospace Information (CASI)

NASA CR-134876
PWA-5299

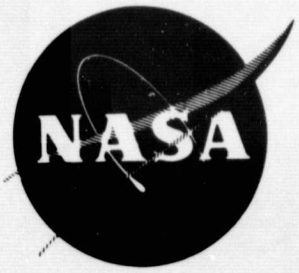

FINAL REPORT ON PHASE II
PROGRAM FOR REFAN JT8D ENGINE DESIGN, FABRICATION AND TEST

By

J. A. Glass, E. S. Zimmerman, V. M. Scaramella

PRATT & WHITNEY AIRCRAFT
DIVISION OF UNITED TECHNOLOGIES CORPORATION

November 1975

Prepared for

NATIONAL AERONAUTICS AND SPACE ADMINISTRATION

NASA LEWIS RESEARCH CENTER
CONTRACT NAS3-17840

(NASA-CR-134876) PROGRAM FOR REFAN JT8D ENGINE DESIGN, FABRICATION AND TEST, PHASE 2 Final Report (Pratt and Whitney Aircraft) 367 p HC $10.50 CSCI 21E

N76-12067

Unclas
G3/07 04122

DEC 1975
RECEIVED
NASA STI FACILITY
INPUT BRANCH

1. Report No.	2. Government Accession No.	3. Recipient's Catalog No.
NASA CR- CR-134876		

4. Title and Subtitle	5. Report Date
FINAL REPORT ON PHASE II PROGRAM FOR REFAN JT8D ENGINE	November 1975
	6. Performing Organization Code
7. Author(s)	8. Performing Organization Report No.
J. A. Glass, E. S. Zimmerman, V. M. Scaramella	PWA-5299
	10. Work Unit No.
9. Performing Organization Name and Address	11. Contract or Grant No.
PRATT & WHITNEY AIRCRAFT DIVISION OF UNITED TECHNOLOGIES CORPORATION EAST HARTFORD, CT. 06033	NAS3-17840
	13. Type of Report and Period Covered
12. Sponsoring Agency Name and Address	CONTRACTOR'S REPORT
NATIONAL AERONAUTICS AND SPACE ADMINISTRATION WASHINGTON, D. C.	14. Sponsoring Agency Code

15. Supplementary Notes

PROJECT MANAGER, ROBERT W. SCHROEDER, V/STOL AND NOISE DIVISION, NASA LEWIS RESEARCH CENTER, CLEVELAND, OHIO

16. Abstract

The objective of the JT8D refan program was to design, fabricate and test certifiable modifications of the JT8D engine which would reduce noise generated by JT8D powered aircraft. This was to be accomplished without affecting reliability and maintainability, at minimum retrofit cost, and with no performance penalty. This report documents the mechanical design, engine performance and stability characteristics at sea-level and altitude and the engine noise characteristics of the test engines. Results confirmed the structural integrity of the JT8D-109. Engine operation was stable throughout the airplane flight envelope. Fuel consumption of the test engines was higher than that required to meet the goal of no airplane performance penalty, but the causes were identified and could be corrected during a normal pre-certification engine development program. Compared to the baseline JT8D-109 engine, the acoustically treated JT8D-109 engine showed noise reductions of 6 PNdB at takeoff and 11 PNdB at a typical approach power setting.

17. Key Words (Suggested by Author(s))	18. Distribution Statement
JT8D REFAN ENGINE QUIET ENGINE JT8D-109 TURBOFAN	UNCLASSIFIED - UNLIMITED

19. Security Classif. (of this report)	20. Security Classif. (of this page)	21. No. of Pages	22. Price*
UNLIMITED	UNCLASSIFIED	367	

* For sale by the National Technical Information Service, Springfield, Virginia 22151

TABLE OF CONTENTS

TABLE OF CONTENTS (Cont'd)

LIST OF ILLUSTRATIONS

LIST OF ILLUSTRATIONS (Cont'd)

LIST OF ILLUSTRATIONS (Cont'd)

LIST OF ILLUSTRATIONS (Cont'd)

LIST OF ILLUSTRATIONS (Cont'd)

LIST OF ILLUSTRATIONS (Cont'd)

INDEX OF FIGURES

INDEX OF FIGURES (Cont'd)

INDEX OF FIGURES (Cont'd)

INDEX OF FIGURES (Cont'd)

INDEX OF FIGURES (Cont'd)

INDEX OF FIGURES (Cont'd)

INDEX OF FIGURES (Cont'd)

INDEX OF FIGURES (Cont'd)

INDEX OF FIGURES (Cont'd)

INDEX OF FIGURES (Cont'd)

LIST OF TABLES

LIST OF TABLES (Cont'd)

LIST OF TABLES (Cont'd)

LIST OF TABLES (Cont'd)

I. SUMMARY

The objective of the JT8D refan program was to design, fabricate and test certifiable modifications of the JT8D engine which would reduce the noise generated by JT8D-powered aircraft. This noise reduction objective was to be accomplished without affecting the demonstrated reliability and maintainability of the JT8D engine, at minimum retrofit cost, with no degradation of current JT8D powered aircraft performance.

The refan program was conducted by Pratt & Whitney Aircraft under NASA Contracts NAS3-16808 and NAS3-17840. The program was divided into two phases: Phase I, Contract NAS3-16808, which covered the preliminary definition and design of the refan engine modifications, and Phase II, Contract NAS3-17840, which covered the installation design effort and the development testing of the engine modifications. The development testing was to ensure the structural integrity of the engine modifications and to determine whether the program objective of engine noise reduction had been achieved, while maintaining or improving the engine stability and performance.

This report, as required under Task VIII of the Phase II contract, documents the following:

- The final mechanical design of the JT8D-100 engine including the engine condition and durability results of development testing
- Engine performance characteristics including discussions of sea-level and altitude performance testing and a list of potential performance improvement modifications based on development test results
- Engine stability characteristics as determined from sea level and altitude development testing
- Engine noise characteristics including discussions of component and overall noise results determined during sea level development testing.

II. INTRODUCTION

The JT8D engine was first introduced into commercial service in 1964 and is used primarily to power the 727, 737 and DC-9 aircraft. Since its introduction, over 7000 JT8D engines have been produced. Approximately 55% of the jet transport airplanes in the US commercial fleet are powered by JT8D engines and these airplanes are used primarily on short and intermediate range domestic routes.

Since these aircraft comprise a significant part of the domestic airline fleet, a reduction in their noise level would have a favorable effect on the airport community noise environment. Thus, the JT8D-100 series engines were designed as low-noise, retrofit configurations obtainable from any of the current JT8D engine models. The fundamental design concept of the JT8D refan program was to provide a higher-bypass-ratio engine to reduce the jet exhaust velocity and, thereby, the jet noise. Fan and compressor noise levels were minimized by the strict application of acoustic design principles and designed-in noise reduction features.

To demonstrate that the JT8D engine could be modified to significantly reduce noise generation without sacrificing engine performance or durability characteristics, a coordinated program involving P&WA, McDonnell-Douglas and The Boeing Company was undertaken. Pratt & Whitney Aircraft designed, fabricated and installed the modifications to the basic engine and conducted performance and static noise tests; McDonnell-Douglas conducted flight tests with a DC-9-30 aircraft and Boeing conducted static ground tests to determine 727 compatibility. The results of the McDonnell-Douglas Program are summarized in Ref. 1 (CR-134857) and the Boeing studies are summarized in Ref. 2 (CR-134797).

Design studies were initiated at Pratt & Whitney Aircraft in August 1972 to establish the extent to which advanced noise technology could be applied to the JT8D engine.

The resulting modified engine cycle, selected during Phase I, Contract NAS3-16808, of the refan program, was based upon an increased-diameter, single-stage fan and two additional core engine compressor stages, which replace the existing two-stage fan. Modifications were also made to the low-pressure turbine to provide the increased torque required by the larger-diameter fan. These modifications are documented in the Phase I Final Report, Ref. 3 (CR-134654).

The resultant JT8D-100 engine models have the following characteristics at takeoff thrust, compared to the current JT8D engine; (1) the airflow and the bypass ratio are increased, and (2) the fan pressure ratio and the engine speed are reduced. The resultant engine is also longer, larger in diameter, and heavier than the JT8D base model, but these latter changes are compensated by the increased thrust and decreased fuel consumption of the modified engine, thus providing the capability for maintaining the performance of the current JT8D-powered aircraft.

Phase II of the JT8D refan program, Contract NAS3-17840, was comprised of (1) completion of the Phase I mechanical design effort and (2) evaluation of the JT8D-100 component designs through additional design analysis and rig and engine testing. In compliance with this task, a system development program was conducted by Pratt & Whitney Aircraft on three experimental engines and a fan/low-pressure compressor rig. This development testing was to ensure the structural integrity of the engine modifications and to determine whether the program objective of engine noise reduction had been achieved, while maintaining or improving the engine performance and stability.

Two of the engines were obtained from the P&WA JT8D experimental engine program and were designated Experimental Engine Number 1 (EE-1) and Experimental Engine Number 2 (EE-2). These engines were updated to JT8D-9 specifications and calibrated to establish their base performance levels and transient performance characteristics prior to their conversion to the JT8D-109 configuration. Subsequent to the conversions, a systems development program was conducted which included the following programs:

- Sea level performance calibrations
- Two 1000-cycle LCF tests
- 150-hour FAA-type endurance test
- Stress measurements on the unique JT8D-100 parts
- Stability tests with inlet distortion
- Low-pressure and high-pressure compressor sea level static surge margin tests
- Douglas DC-9 inlet and exhaust system engine matching and compatibility tests
- Acoustic evaluation of the fully treated JT8D-109 engine with the P&WA reference hardware (hardwall) and with treated inlet and exhaust hardware designed to simulate the DC-9 flight inlet and exhaust systems.

The third engine utilized in the experimental engine program, designated Experimental Engine Number 3 (EE-3), was acquired from Pratt & Whitney Aircraft Sales as a new JT8D-9 zero time production engine. The engine was tested as a JT8D-9 engine to establish base levels of steady-state and transient performance prior to conversion to the JT8D-109 configuration. Subsequent to this conversion, steady state and transient performance testing was conducted to determine JT8D-109 characteristics. Following this testing a systems development program was conducted at the NASA Lewis Research Center (NASA LeRC) in Cleveland, Ohio. The following programs were conducted:

- Engine transient performance characteristics with and without inlet distortion at altitude conditions
- Determination of altitude starting envelope
- Altitude steady state performance calibrations

A fan/low pressure compressor (LPC) test unit, consisting of a full-scale fan/LPC section of the JT8D-109 engine was assembled into a rig configuration. The following tests were conducted:

- Stress measurements on selected disks, blades and stators

- Uniform inlet flow performance for various fan and LPC operating lines
- Distorted inlet flow for various fan and LPC operating lines

In addition to the three refan experimental engines, two JT8D-109 refanned production engines were provided for DC-9 flight testing by Douglas Aircraft and one JT8D-115 refanned production engine was supplied to The Boeing Company for ground testing to determine 727 compatibility.

The stability characteristics presented in this report are based on test results obtained from sea level testing at Pratt & Whitney Aircraft, altitude testing at NASA, LeRC, and DC-9 flight testing as conducted by Douglas Aircraft Company. Additional information is summarized in Ref. 4 (CR-134874).

The performance characteristics presented later in this report utilize the data obtained from the production quality engine EE-3, in both the JT8D-9 and the refan JT8D-109 configurations. Additional information from the DC-9 flight test program and from the sea level testing of engines EE-1 and EE-2 is presented as required. Additional information is summarized in Ref. 4

The acoustic characteristics presented utilize the data obtained from testing conducted on EE-1 and EE-2 in the refan configuration as conducted on an outdoor noise test facility at P&WA. Additional information is summarized in Ref. 5 (CR-134875).

III. RESULTS AND DISCUSSION OF RESULTS

A. ENGINE DESIGN

1. Design Summary

a. Cycle Selection

The JT8D engine is a relatively low-bypass fan engine with a relatively high primary jet velocity. Means for attenuating fan generated engine noise using nacelle treatment have been developed, but no practical method for reducing the noise generated by the interaction of the primary jet stream with the ambient air, by means external to the engine, has been developed. For the JT8D engine, jet noise is predominant at takeoff power and also at lower power conditions when fan duct acoustic treatment is incorporated. Thus, a significant reduction in the overall flyover noise level can only be achieved by reducing the primary jet velocity and its accompanying jet noise. A cycle selection study was undertaken to evaluate the feasibility of reducing jet noise by varying the basic engine cycle to avoid producing the acoustic energy in the exhaust jet.

Several means are theoretically available to reduce the jet velocity of a less-than-perfectly mixed common-flow exhaust turbofan engine. These may be illustrated by considering the total thrust as the sum of theoretical bypass stream thrust and core stream thrust. (This simplification ignores the partial mixing which produces a gradient layer of air between the higher velocity core stream and the lower velocity bypass stream, for which the total thrust equation is modified when performing actual mixed stream thrust calculations.) At constant thrust, the three general paths that result in decreased primary stream jet velocities, indicated by this simplified illustration, are: increasing core stream airflow, increasing bypass stream jet velocity, or increasing bypass stream airflow.

The retrofit concept involved selecting a path which would require the least total number of parts to be changed. Due to the complexity of the core engine, it was apparent that the configuration changes required to reduce core jet velocity should be restricted to the fan section and bypass ducts. Thus, increasing core stream airflow was ruled out because core compressor modifications would be required. It would also have required reduced turbine temperature to achieve the core jet velocity reduction. This is inconsistent with the fact that the maximum capability of the core engine with respect to pressure, flow, and temperature levels must be used to maintain an efficient, competitive engine.

The selection of increased bypass stream airflow over increased bypass stream jet velocity involved evaluating the characteristics of the various types of noise produced by the engine components and the available means of reducing these noise levels. Increasing bypass stream jet velocity can only be accomplished by increasing the fan pressure ratio which would then increase fan generated turbomachinery noise. While fan noise could be minimized by the proper blade and vane spacing and by the proper choice of the number of blades and vanes in each row, increasing bypass stream jet velocity was not feasible because the single stage fan would not have the necessary pressure rise capability. The addition of a two stage fan for the modified engine would result in an unacceptable increase in engine length due to the large axial spacing required.

A single stage fan with a larger diameter to increase bypass stream air flow was selected. To minimize the diameter increase and tip speed, the fan was designed for the highest levels of flow per unit area consistent with maintaining high efficiency levels in the range of cruise operation. The design pressure ratio was selected to maintain current stability levels. Bypass airflow was limited by engine low rotor shaft torque carrying capabilities and the work extraction capability of the current JT8D three stage low pressure turbine.

The fan rotor diameter consistent with the airflow limits would have produced unacceptable stress levels in the rotor if operated at the current JT8D low rotor speed levels. Thus, it was necessary to slow the low rotor down to a speed consistent with acceptable fan stress levels. Although the lower rotor speeds could be accommodated within the new fan rotor design, compensation for the reduced core engine airflow pumping capability was required. Two new core low pressure compressor stages were required to maintain the current JT8D core airflow levels. The torque levels were within the capability of an improved low shaft, and the low pressure turbine efficiency levels were acceptable if the available JT8D-1, -7 fourth turbine blade, 4° open relative to the JT8D-9 blade, was used.

An extensive evaluation was undertaken to determine the feasibility of eliminating the inlet guide vanes, since this concept could be advantageous in reducing fan generated noise and the overall weight of the modified engine. It was concluded that, even though the inlet guide vanes may generate additional aft radiated fan noise, the full length fan duct of the JT8D engine provides sufficient area for peripheral acoustic treatment to attenuate the noise generated in the fan. The subsequent weight advantage of a non-inlet guide vane configuration had an insignificant effect on overall aircraft performance. Because of these conclusions, the inlet guide vane was retained, reducing the fan rotor tip relative Mach number and providing increased core engine airflow pumping capability by adding preswirl at the root of the fan rotor.

The selected cycle, obtained by a combination of an increased diameter single stage fan with inlet guide vanes, a full length bypass duct, a single common flow exhaust nozzle, and two new core low compressor stages, doubled the amount of bypass air while maintaining current JT8D levels of core engine airflow, pressure rise, and turbine inlet temperature. This cycle provided increased takeoff thrust and reduced cruise fuel consumption for high cruise power requirements. The effectiveness of the higher bypass ratio in reducing cruise fuel consumption was partially counteracted by a reduction in low turbine efficiency caused by increased work extraction at lower rotor speed, an increased level of turbine exit strut loss caused by high incidence angles and increased local Mach number, and an increased fan exit guide vane pressure loss caused by the lower cruise fan operating line that results from a high bypass ratio, low exhaust pressure ratio cycle.

With both lower bypass and core stream jet velocities, the relative velocity between the two streams is similar to the current JT8D cycle. The predicted jet noise reductions assume that the amount of bypass/primary stream mixing is also similar to the current JT8D. Should an effective exhaust stream mixer be included in the design, further exhaust noise reductions would be possible..

b. Engine Configuration

The JT8D-100 engine is a two-spool turbofan engine with a mechanically coupled fan and low-pressure compressor. It has a single-stage fan, six low-compressor stages and seven high-compressor stages. The compressor system generates a takeoff compressor pressure ratio of approximately 15.8 and a 2.00 bypass ratio. The burner section consists of nine separate combustion chambers in an annular array. The JT8D-100 derivative of a particular engine model uses the air-cooled or uncooled single-stage high-pressure turbine applicable for the rating of the particular current engine model, and a three-stage low-pressure turbine. Figure A-1 is a cross section view of the JT8D-109 turbofan engine. Also shown in the figure are the instrumentation stations.

The JT8D-100 series engines were designed as low-noise retrofit configurations, obtainable from any of the current JT8D engine models. The fundamental design concept was to provide a higher bypass ratio engine which would lead to a lower jet exhaust velocity and, therefore, lower jet noise. Fan and compressor noise levels were reduced through the elimination of a fan stage, increased fan rotor/exit guide vane spacing and the proper selection of blade and vane numbers. The fan noise was further reduced through the use of acoustical treatment forward of the fan rotor and downstream in the fan ducts.

1) Fan/Low Pressure Compressor

The JT8D-100 series fan is a single stage unit with increased diameter compared to current JT8D parts to increase the fan bypass ratio. The blade design configuration is based upon current production engine design technology to minimize development risk. A wide chord fan blade with a single part-span shroud was selected to reduce cost and achieve the aerodynamic requirements. This single stage unit produces increased fan duct air flow at lower pressure and velocity than the two stage JT8D fan configuration.

The new low pressure compressor has six stages compared to four stages for the current JT8D engine. The compressor operates at a lower speed than the current engine to reduce noise and decrease the blade tip speed of the larger diameter fan. Two new stages were required to maintain the core engine pressure ratio and air flow rate at this lower speed with the single stage fan assembly. These core engine characteristics are required to achieve the thrust level requirements at the reduced low rotor operating speed. Since the D-100 fan/LPC assembly has seven stages, compared to six in the current JT8D engine, the two new core stages were identified as stages 1 and 1.5 to avoid changing the designations of the unmodified following stages.

Noise reduction was a major requirement governing various aspects of the fan-low compressor design. The numbers of blades and vanes in the fan and new low compressor stages were selected tominimize noise generation. The axial spacing of these new stages was also selected to reduce noise generation. Acoustic treatment was incorporated into the fan duct walls fore and aft of the fan blade to reduce radiated noise.

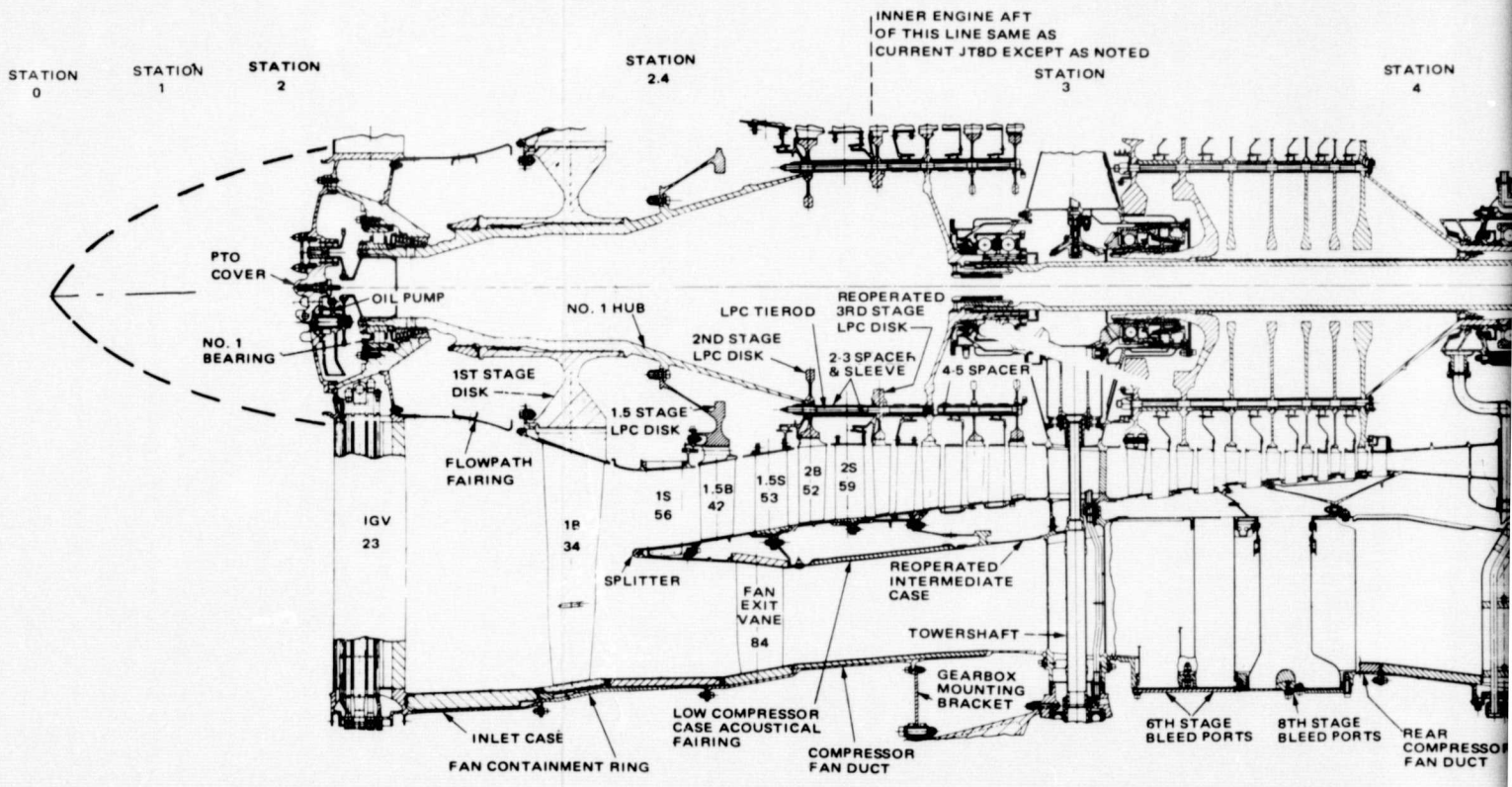

Figure A-1 JT8D-109 Engine Cross Section

ORIGINAL PAGE IS
OF POOR QUALITY

FOLDOUT FRAME

NOTED
ON

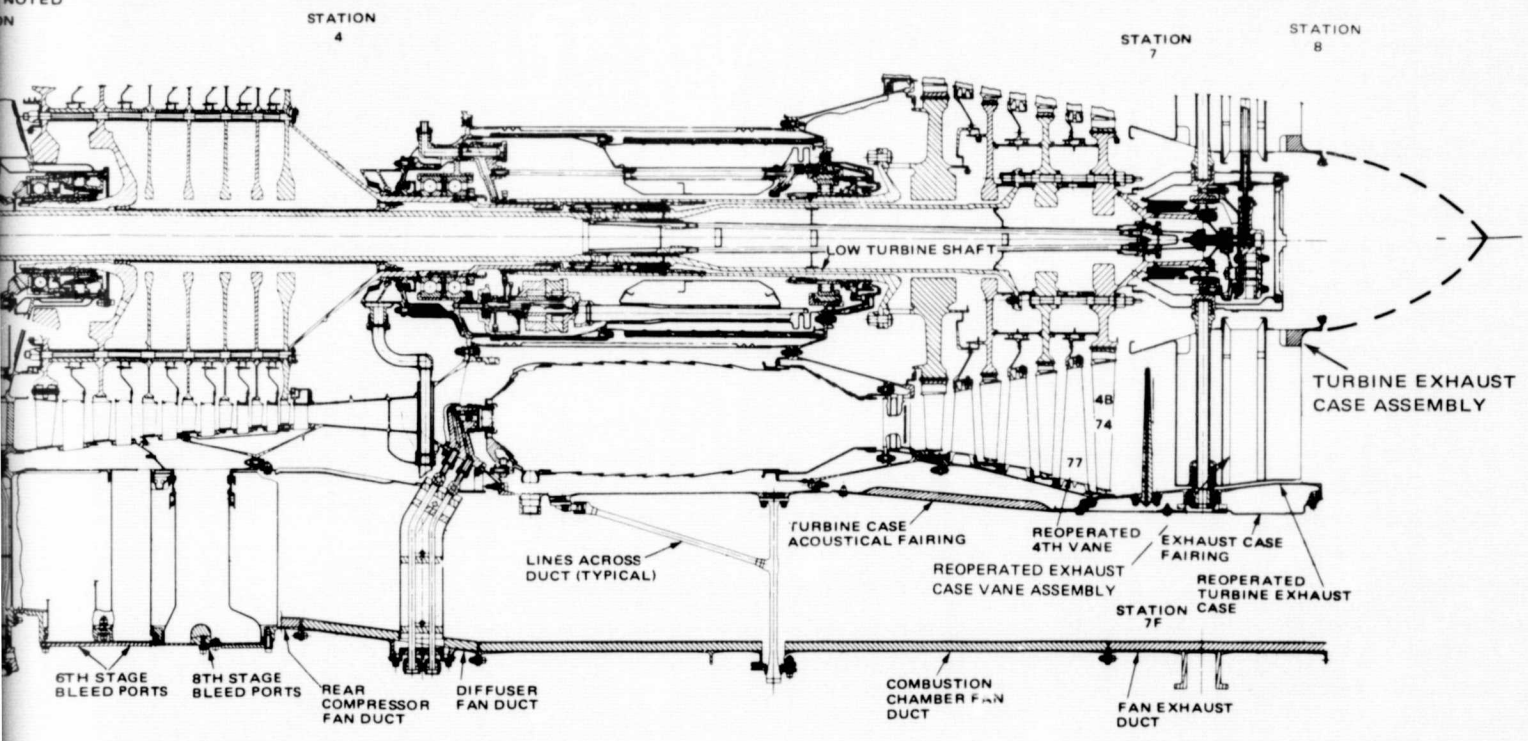

FOLDOUT FRAME 3

2) High Pressure Compressor, Burner and Turbines

The seven stage high pressure compressor, the can-annular burner, and the air-cooled or uncooled single stage high turbine of the various current JT8D models were retained. The three stage low pressure turbine was retained but the fourth stage blade of the D-9, -11, -15 models was replaced to reduce the turbine rotor exit Mach number. The fourth-stage vane area has been increased to reduce the fourth rotor air flow incidence angle. The present four exhaust case struts were recambered and four additional exhaust struts have been added to further reduce exit swirl to the level being experienced on the current JT8D engine models. A revised low turbine shaft material was required to maintain adequate strength at the increased torque. The maximum turbine temperature levels of the JT8D-100 derivative of a particular JT8D engine model are comparable to the levels for that particular current JT8D engine model.

3) Bearings and Support Structure

The number one bearing and support structure have been redesigned for compatibility with the increased rotor length and larger diameter fan. All other bearings and their support structure remain unchanged.

4) Fan and Primary Engine Cases

Increased diameter fan cases were required for the increased diameter fan rotor. The current JT8D engine core engine cases were retained except in those instances where the core and fan cases are an integral assembly or the fan flow path requirement necessitated the redesign of the core engine case.

Acoustic treatment has been provided on the inner walls of the fan cases and the outer walls of certain engine core cases to reduce fan radiated noise.

5) Accessories

The high rotor accessory gearbox, oil tank, oil pumps and oil system filters are the same as current JT8D engine models. The JT8D fuel control, fuel pump, fuel-oil cooler, fuel filters, bleed control and pressurizing valve were retained. The ignition system and the anti-icing and fuel de-icing valves from the current JT8D engine have also been retained. In conjunction with the increased diameter fan, the engine airbleed service pads located on the fan ducts were spaced radially outward at the same axial locations relative to the forward and rear mounts. Two additional fan bleed ports were required to satisfy airframe requirements.

6) Acoustical Treatment

Design of acoustical treatment was based on an analytical procedure developed by Pratt & Whitney Aircraft. A target attenuation spectrum, duct geometry, length and location of treatment, and flow Mach number were used as input to the lining design program.

This target attenuation spectrum for the JT8D-109 engine was obtained from noise predictions and is shown in Figure A-2a. This target concept defines the frequency range to which the treatment should be tuned for maximum PNdB reduction. The computer program first calculated the effective treatment length to duct height ratio from the input geometry. A peak attenuation was then computed as a function of the effective length to height ratio and duct Mach number, assuming optimum backing depths and facing sheet impedance. The optimum backing depth was then selected based on the frequency of peak attenuation, length to height ratio and annular distance between treatments (effective duct height). The attenuation spectrum was then calculated and compared with the design target attenuation spectrum. Iterations were than carried out until a satisfactory solution was obtained. Figure A-2b shows the resulting predicted attenuation spectrum.

The aluminum acoustic treatment for areas 1 through 5 (Figure A-2c) consists of perforated face sheet over honeycomb core. The core is bonded directly to the ducts or to a solid backing sheet, and the perforated face sheet is bonded to the core. The ducts and perforated sheet are anodized, dichromate sealed and their adhesive joining surfaces primed with American Cyanamic BR-400 modified epoxy primer. American Cyanamid FM-400-6 reticulating modified epoxy sheet adhesive is heat shrunk to the cell edges of the honeycomb core. (A reticulating adhesive is one that will shrink and bead up on the edge of the honeycomb-face sheet interface, thus producing stronger joints. A reticulating adhesive must be used when bonding the perforated sheet to the honeycomb, as a continuous adhesive layer would block the perforations.) The core is then laid up to the case. The perimeter of each core segment is filled with epoxy foam (Minnesota Mining and Manufacturing Scotch Weld® Core Splice Adhesive EC 3500 B/A), the perforated sheet positioned, and the entire layup is cured. The perforated sheet is AMS 4027, 0.041 cm (.016 in.) thick, with 0.140 cm (.055 in.) diameter holes, and with 12% open area everywhere except in area 1, where 20% open area is used. The honeycomb core is American Cyanamid Duracore®, 0.953 cm (0.375 in.) cell, 0.010 cm (0.004 in.) foil, corrosion inhibited, AMS 4004. Penetration holes through the acoustic treatment are ringed with epoxy foam. See Figure A-3.

In area 1, (between the inlet case and fan rotor) and in area 2 (between the fan rotor and fan exit guide vanes), the acoustic treatment is in the form of mechanically-retained replaceable panels. These panels are made to be removable since foreign object damage may necessitate replacement. In area 3, the region between exit guide vanes and the intermediate case at the outer wall of the fan flowpath, the treatment is bonded directly to the case. Foreign object damage is expected to be minimal in this area. This treatment was designed to attenuate the noise associated with the forward propagation out the inlet duct of shock waves of a transonic rotor. This noise is known as combination tone noise or multiple pure tone noise. The engine treatment downstream of the fan is comprised of perforated sheet, exposed to the flow path and bonded to a cellular honeycomb structure, which is in turn bonded to an impervious septum that serves as the duct pressure vessel wall.

The acoustic treatment in area 4, the region between the fan exit guide vanes and the intermediate case at the inner wall of the fan flowpath, is in the form of two removable non-structural fairing segments fabricated by bonding aluminum honeycomb core to a solid backing sheet and a perforated flowpath sheet. These panels form the required flowpath.

From the aft outer flange of the intermediate case to the fan exhaust duct (area 5), the acoustical treatment is bonded directly to the ducts. Area 5 includes the compressor fan duct, the diffuser fan duct and the combustion chamber fan duct.

The acoustic treatment in area 6 is a two-piece, removable steel fairing attached to the turbine cases. The honeycomb foil is welded to the solid backing sheet and perforated top sheet because the higher temperature precludes the use of a bonded assembly.

The acoustic treatment in area 7 is located aft of the combustion chamber fan duct and is mechanically attached to the fan exhaust duct. The panels are constructed of aluminum honeycomb core with a perforated aluminum top sheet and a backing of glass fabric in two layers. This treatment was not bonded directly to the duct because duct deflections during maneuver loading might cause some bond delamination.

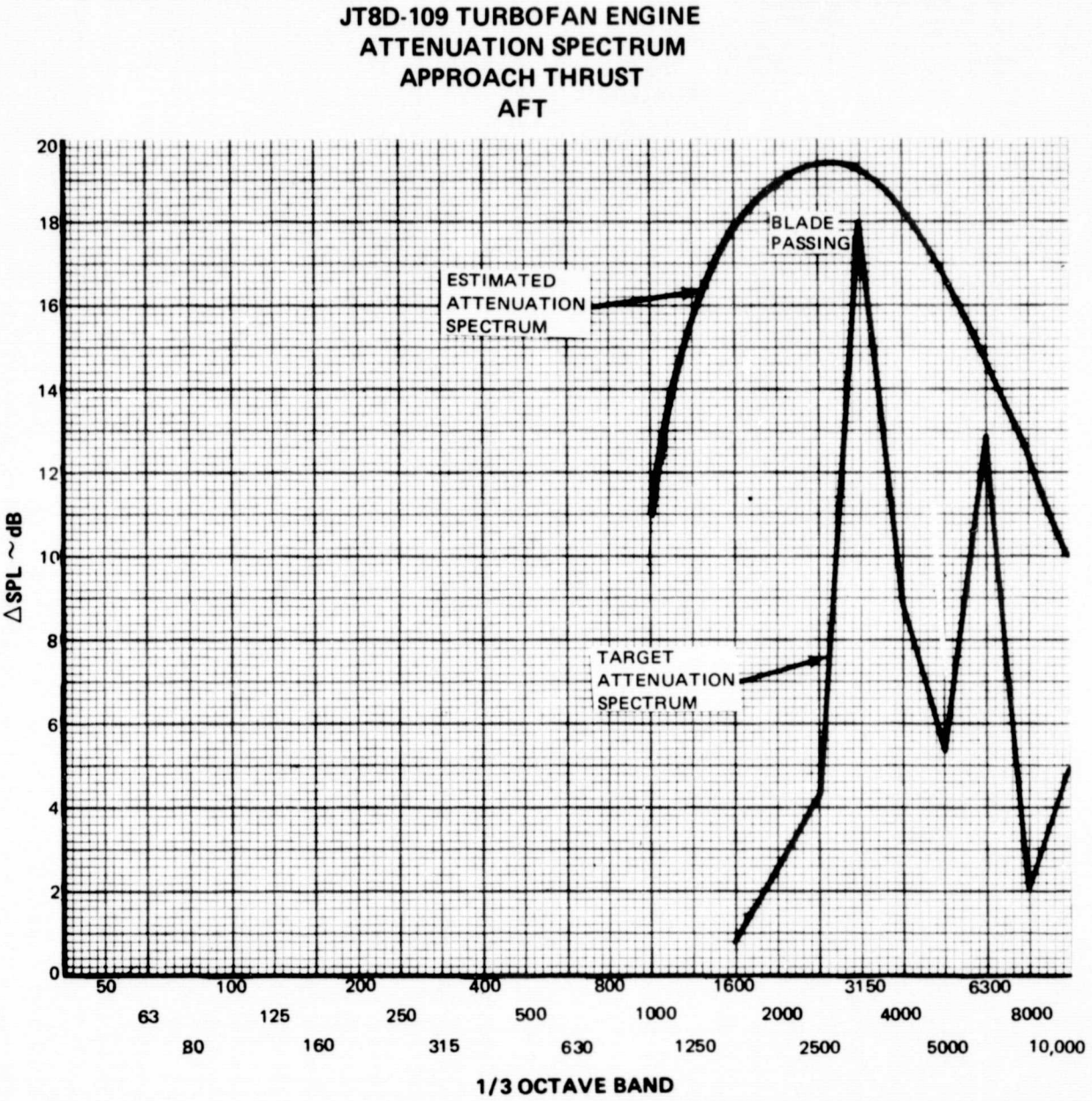

Figure A-2a JT8D-109 Turbofan Engine Estimated Attenuation Approach Thrust AFT

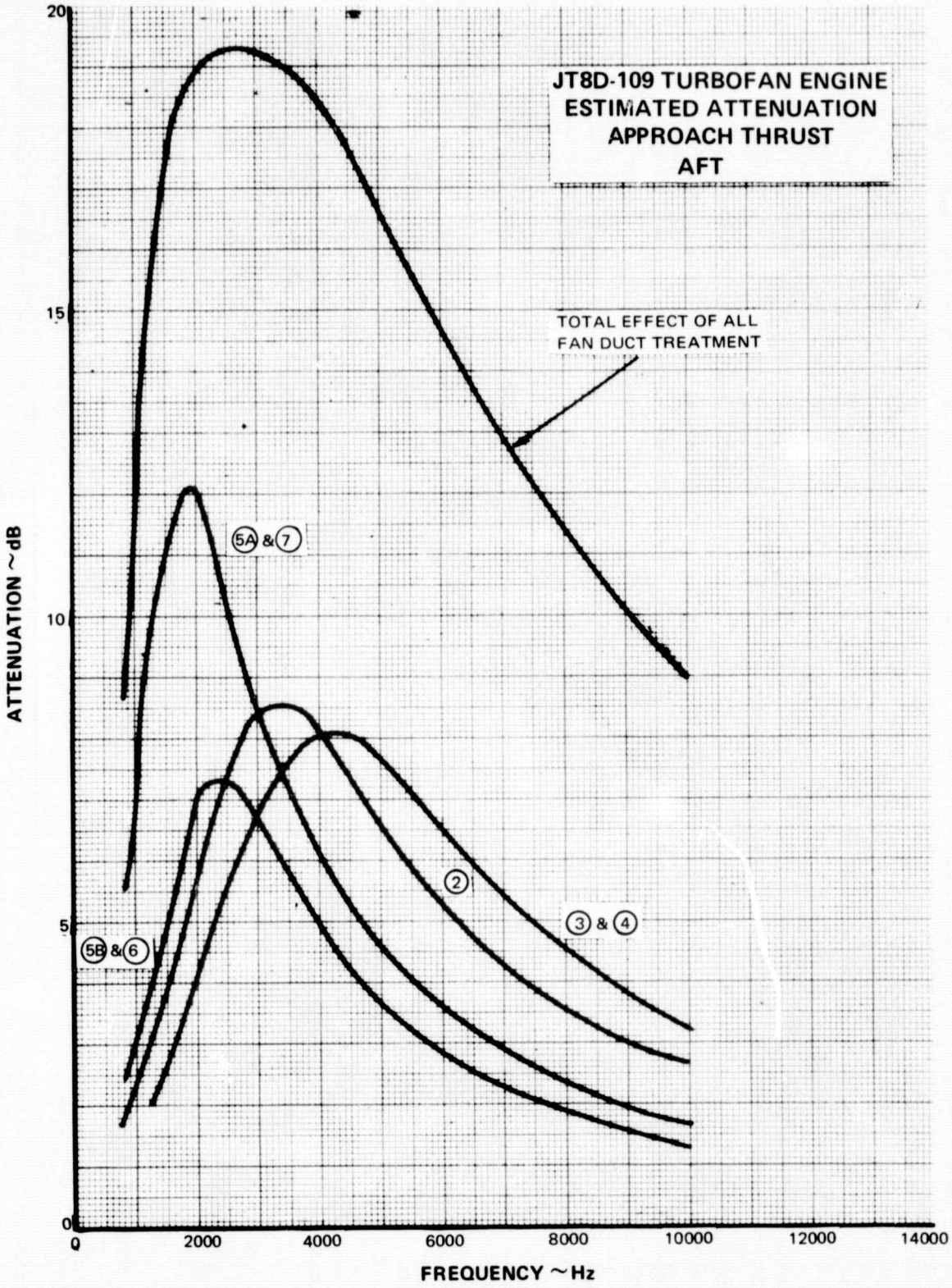

Figure A-2b JT8D-109 Turbofan Engine Attenuation Spectrum Approach Thrust AFT

ORIGINAL PAGE IS
OF POOR QUALITY

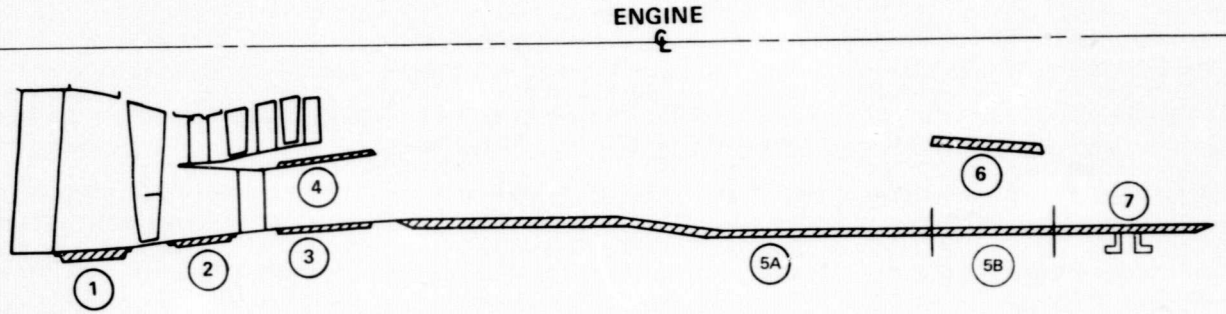

FAN DUCT LOCATION	TREATMENT LENGTH M (IN)	PASSAGE HEIGHT M (IN)	LENGTH/HEIGHT L/H	FACE SHEET MATERIAL	TOP SHEET HOLE DIA. CM (IN)	TOP SHEET THICKNESS CM (IN)	PEAK TUNING FREQ. ~HZ
1	0.177 (7.0)	N.A.	N.A.	AMS 4027 (AL)	0.114 – 0.152 (0.045 – 0.060)	0.0405 (0.016)	1600
2	0.152 (6.0)	0.221 (8.7)*	1.5	AMS 4027 (AL)	0.114 – 0.152 (0.045 – 0.060)	0.0405 (0.016)	2100
3	0.286 (11.25)	0.155 (6.1)	–	AMS 4027 (AL)	0.114 – 0.152 (0.045 – 0.060)	0.0405 (0.016)	4200
4	0.213 (8.4)	0.155 (6.1)	1.6	AMS 4027 (AL)	0.114 – 0.152 (0.045 – 0.060)	0.0405 (0.016)	4200
5A & 5B	1.42 (56.0)	0.226 (8.9)	2.5	AMS 4027 (AL)	0.114 – 0.152 (0.045 – 0.060)	0.0405 (0.016)	2100
6	0.279 (11.0)	0.213 (8.4)	1.3	AMS 5520 (SST)	0.114 – 0.152 (0.045 – 0.060)	0.0405 (0.016)	2650
7	0.395 (15.6)	0.201 (7.9)	1.0	AMS 4027 (AL)	0.114 – 0.152 (0.045 – 0.060)	0.0405 (0.016)	2100

FAN DUCT LOCATION	% OPENING FACE SHEET	CORE HONEYCOMB CELL SIZE cm (IN)	APPROX. DEPTH OF HONEYCOMB cm (IN)	HONEYCOMB FOIL MAT'L	BACK SHEET MAT'L	CASE MAT'L	BONDED (INTEGRAL TO STRUCT)	REMOVABLE (PANEL SEGMENTS)
1	20	0.95 (0.375) HEX	2.54 (1.0)	PWA 122**	AMS 4027 (AL)	N.A.	NO	YES
2	12	0.95 (0.375) HEX	1.27 (0.5)	PWA 122	AMS 4027 (AL)	N.A.	NO	YES
3	12	0.95 (0.375) HEX	0.64 (0.25)	PWA 122	N.A.	AMS 4153 (AL)	YES	NO
4	12	0.95 (0.375) HEX	0.64 (0.25)	PWA 122	AMS 4027 (AL)	N.A.	NO	YES
5A & 5B	12	0.95 (0.375) HEX	1.27 (0.5)	PWA 122	N.A.	SEE Δ BELOW	YES	NO
6	12	0.95 (0.375) SQ.	1.27 (0.5)	AMS 5520 (SST)	AMS 5520 (SST)	N.A.	NO	YES
7	12	0.95 (0.375) HEX	1.27 (0.5)	PWA 122	PWA 411 FIBERGLASS	N.A.	NO	YES

N.A. = NOT APPLICABLE ** PWA 122 IS CORROSION RESISTANT AMS4004 Δ THREE FAN DUCTS, 2 AMS 4135 (AL), 1 AMS 4027 (AL)

*H_{EFF} = 0.1016 (4.0)

Figure A-2c JT8D-100 Fan Duct Acoustic Treatment

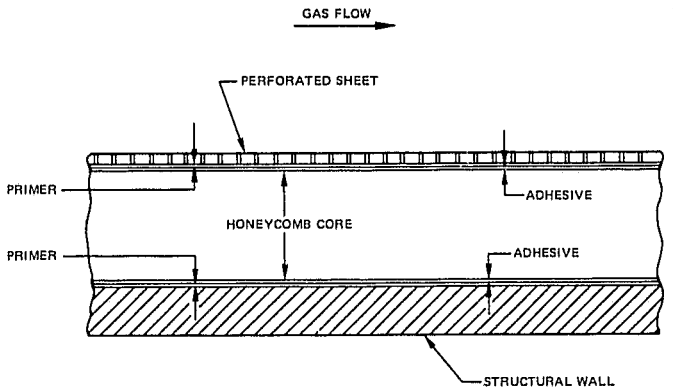

Figure A-3 JT8D-100 Typical Section Through Bonded Structure of Honeycomb Acoustically Treated Case

At the request of the NASA, an alternate scheme was designed to provide mechanical retention of the bonded honeycomb areas, which could be utilized if engine development testing resulted in bond failure that might result in extensive delamination of the sound absorbing material from the structural ducts. Engine development testing was successful and there was no need to incorporate this design.

c. Structural Considerations

The loads used for structural analysis of JT8D-100 engine components are cyclic LCF loads, limit and ultimate maneuver loads, cowl gust loads, thrust reverser loads, single airfoil impact load, and blade loss unbalance loads. See Figures A-4 and A-5.

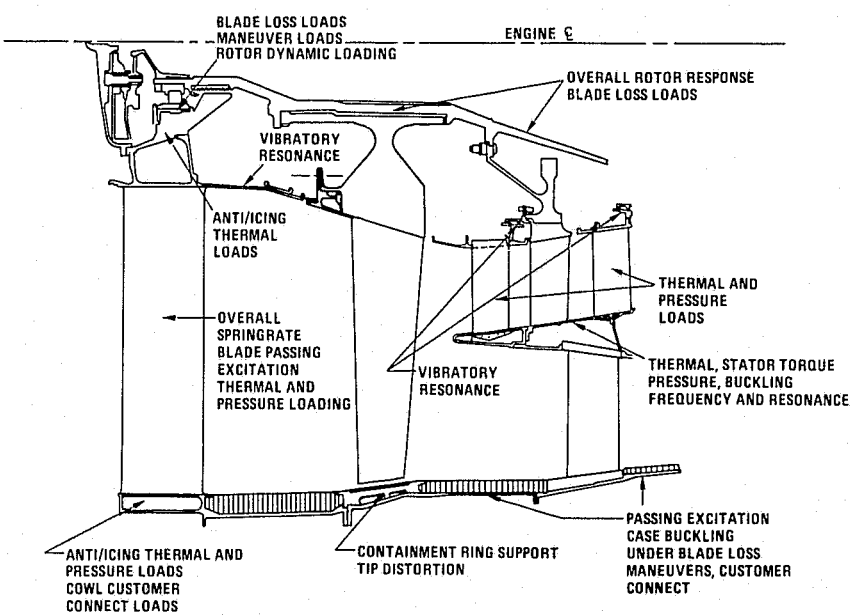

Figure A-4 JT8D-100 Basic Engine Structural Design Considerations

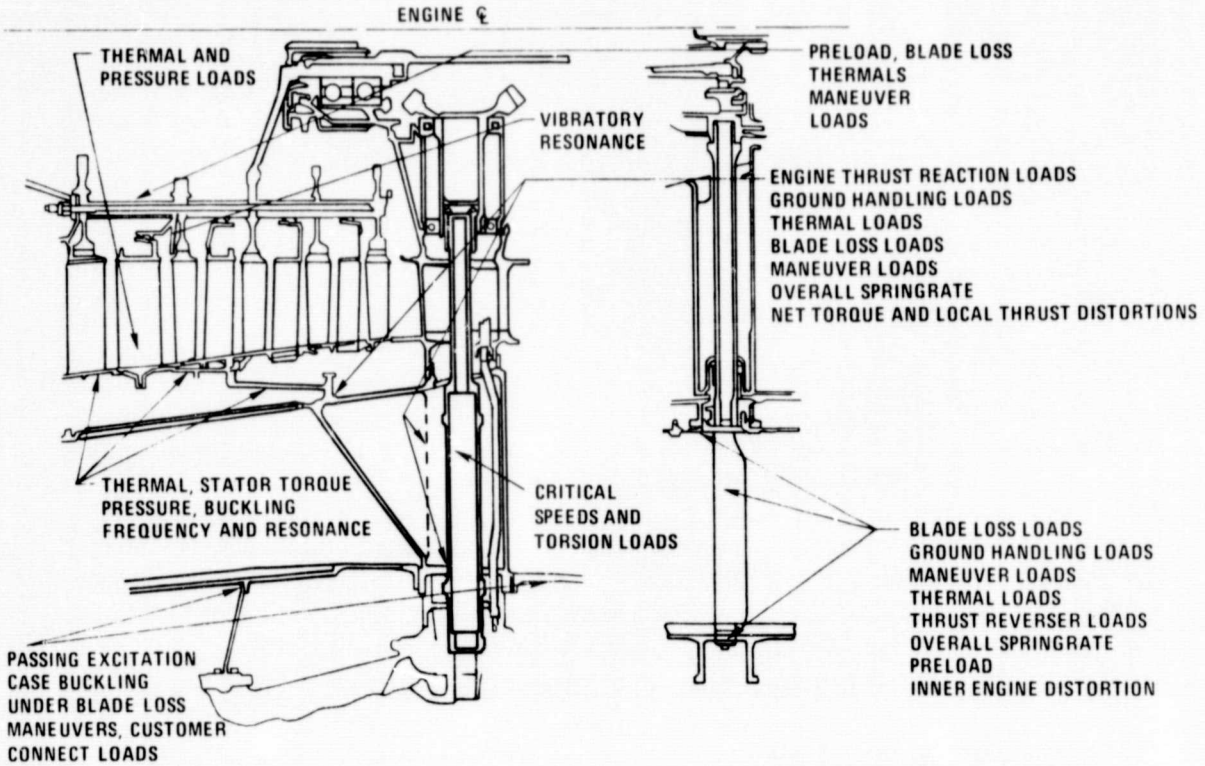

Figure A-5 JT8D-100 Basic Engine Structural Design Considerations

In the event of a fan blade failure, the cases forward of the intermediate case will be subjected to simultaneous application of equal tangential and radial shear loads as a result of the single airfoil impacting the case structure at the containment case. This impact produces transverse shear loading on the flange snaps, shear loading on the flange bolts, and both transverse shear and torque loading on the cases. The applied load dies out over the length of the ducts.

d. Aerodynamic Considerations

The aerodynamic design of the JT8D-100 was optimized by analysis of each engine component within the primary and fan flow paths. The components considered were as follows:

1) Compressor Section

a) Inlet Guide Vane (IGV)

An IGV was considered necessary to increase the fan root work while maintaining low loading levels required for adequate surge margin and acceptable stress level, particularly the untwist stress. Design studies without an IGV resulted in a speed increase of about 7% to avoid an additional supercharging stage. The increase in speed (U_{TIP} = 560.83 m/sec [1840 ft/sec] at red line speed) was rejected as being excessive. The additional supercharging stage design was rejected because of the added complexity, cost, weight, and design effort required to get an acceptable shaft configuration.

b) Fan

A multi-circular-arc airfoil design was selected for the fan rotor. Multi-circular-arc fans have demonstrated better performance than double circular arc airfoils used in the present JT8D fan at the higher Mach numbers required for this design. The principle design considerations were to keep the design loading low enough to obtain 25% surge margin and to efficiently pass the flow required at the maximum cruise condition.

c) Fan Exit Guide Vane (FEGV)

The fan exit guide vane design was a compromise between the large incidence swing required by the surge margin requirement, choking at the minimum cruise condition and structural requirements of the aluminum strip stock vane. The vane was designed as thin as could be structurally justified and with the incidence as large as could be justified at the surge condition. The resulting choke margin at the minimum cruise flight condition is less than desirable, but should not impose a large penalty in the normal cruise range.

d) Fan Duct

The duct area was opened downstream of the FEGV so that the local corrected specific flow would be the same as in the JT8D-9 duct to keep the duct losses at least as low as in the present engine. The flowpath was contoured at the intermediate case to minimize the blockage effects caused by the fairings and struts.

e) LPC Supercharging Stages

Two supercharging stages were added to the existing 4 stage LPC to achieve the required performance. The primary aerodynamic considerations were to ensure sufficient choke margin to efficiently pass the required flow at the maximum cruise condition while keeping the incidence and loading low enough so that the supercharging stages would not initiate surge before the existing 4 stage LPC presently surges in the part speed flight regime.

2) Turbine Section

The low pressure turbine and exhaust case were modified for the refan engine cycle. The major considerations were the requirement to increase low-pressure turbine work by increasing the by-pass ratio without increasing either the gas generator flowrate, turbine inlet total temperature or pressure; and the requirement to reduce low rotor shaft speed.

The increased work requirement, at constant turbine inlet temperature, resulted in an increase in low pressure turbine expansion ratio. This increase in turbine expansion ratio resulted in an increase in turbine exit flow parameter. The combined effects of increased exit flow parameter and reduced shaft speed resulted in increased Mach number and swirl levels entering the turbine exhaust case. To minimize turbine and exhaust case performance penalties resulting from the increased loading and Mach number levels, the low turbine and exhaust case were modified as follows:

a) Low Pressure Turbine Modifications

1st LPT (2nd stage turbine) Vane Area Reduction – The flow area was reduced 3.68%. The reduction in flow area maintains the turbine inlet flow parameter when operating at increased pressure ratio and reduced shaft speed. The area change was accomplished by a class change. (Each vane platform is machined so that a particular flow area, as measured between two adjacent vanes, is produced. The resulting area corresponds to a vane "class".)

3rd LPT (4th stage turbine) Rotor Area Increase – The flow area was increased 9.8% to redistribute the work and reduce the rotor exit absolute Mach number to a level that would provide acceptable exhaust case performance. The increase in area was accomplished by replacing the current D-9 blade with the D-7 blade (identical design rotated 4° open).

3rd LPT (4th stage turbine) Vane Area Increase – The flow area of the vane was increased 5% to eliminate a potential aerodynamic problem in the root region of the 3rd blade, imposed by the increase in rotor inlet relative Mach number and incidence associated with increased stage pressure ratio and reduced shaft speed. The increase in area was accomplished by cutting back the trailing edge of the current D-9 vanes.

b) Exhaust Case Modifications

The JT8D-9 turbine exit guide vane assembly consists of four vanes which house the bearing support rods. One of the four also contains the No. 6 bearing oil supply line. The pitch/chord ratio of these guide vanes varies from 1.6 at the root to 4.0 at the tip, hence their performance characteristics are essentially those of an isolated airfoil. Analyses have shown that these airfoils would leave an unacceptable level of residual swirl in the primary stream when operating at the refan engine conditions. A redesigned assembly was required to minimize the total pressure loss and residual swirl.

The four existing vanes were recambered to match the Mach number and gas angle profile leaving the modified 3rd LPT rotor. Four additional vanes having a reduced thickness/chord ratio were added to impose cascade rather than isolated airfoil characteristics. The reduction in thickness/chord ratio of the additional vanes was required to provide adequace choke margin.

2. Design Details

Subsequent paragraphs in this section of the report provide detailed design descriptions of major subassembly components which were redesigned relative to the basic JT8D turbofan engine. In addition, modifications to the preliminary design configuration completed during Phase I of this program (Ref. 3) and the factors which gave rise to the modifications are also presented, as well as alternative methods by which the modifications can be achieved.

a. Fan, Low Pressure Compressor

The JT8D-100 series engine fan is a single-stage unit which has an increased diameter compared to current JT8D parts to increase the fan bypass ratio. The blade design configuration was based upon current production engine design technology to minimize development risk. A wide-chord fan blade with a single, part-span shroud was selected rather than a narrow-chord, double part-span shroud blade to reduce cost and achieve the aerodynamic requirements. This single-stage unit of increased diameter produces an increased fan duct air flow at lower pressure and velocity compared to the two-stage JT8D fan configuration.

The low-pressure compressor has six stages compared to the four-stage unit for the current JT8D engine. The compressor operates at a lower speed (approximately 7%) compared to the current JT8D to reduce noise and limit the blade tip speed of the larger diameter fan stage so as to reduce blade stresses to an acceptable level. Thus, to maintain the core engine pressure ratio and air flow rate at this lower speed with the single-rather than two-stage fan assembly, two new stages were added to the current four-stage low compressor. These core engine characteristics are required in order to achieve the thrust level requirements at the reduced low-rotor operating speed. Table A-I presents the design point performance characteristics for both the basic JT8D-9 turbofan engine low pressure compressor and the derivative JT8D-109 turbofan quiet engine low pressure compressor.

Noise reduction was a major parameter which governed various aspects of the fan low-compressor design. The numbers of blades and vanes in the fan and new low compressor stages were selected to minimize noise generation. The axial spacing of these new stages was also selected to reduce noise generation. Acoustic treatment was incorporated in the fan duct walls fore and aft of the fan blade to reduce radiated noise.

1) Fan Inlet Case Structure

The primary fan inlet case structure consists of the inlet guide vanes (IGV), a titanium outer case structure, an inner ring to support the No. 1 bearing structure and N_1 gearbox, and an inner flow path extension. Figure A-6 is a cross section view of this structure. The structure is similar to current JT8D inlet cases except for the integral attachment of one of the fan cases to the inlet guide vane structure and the addition of external attachment flanges.

The welding of one of the titanium fan ducts to the inlet case structure resulted in a weight saving because it eliminated two flanges and a set of bolts at this location. The integral external front flange was designed to support the airframe-supplied inlet duct. The other external flanges were designed to support engine airframe accessories. The inner ring was designed to support the airframe-supplied nose cone.

The basic design of the fan inlet case structure as presented in Reference 3 was evaluated and found to be acceptable. However, a potential assembly problem did arise in Paragraph (d), page 25 of this document.

TABLE A-I

JT8D-109, JT8D-9 FAN, LOW PRESSURE COMPRESSOR DESIGN PERFORMANCE AT SEA LEVEL TAKE OFF

	JT8D-109	JT8D-9
Corrected Total Flow	211.83 kg/s (467 lb/sec)	144.7 kg/s (319 lb/sec)
Corrected Total Flow/Area	205.06 kg/s/m^2 (42.0 lb/sec/ft^2)	199.2 kg/s/m^2 (40.8 lb/sec/ft^2)
Duct Flow/Engine Flow	2.0	1.045
Corrected N_1 - RPM	7450	8045
Fan Tip Diameter	1.25m (49.2 in.)	1.03 m (40.5 in.)
$U_{TIP}/\sqrt{\theta_{T2}}$	488 m/s (1600 ft/sec)	435 m/s (1425 ft/sec)
Relative Mach No.	1.5	1.23
No. Fan Stages	1	2
No. Low Pressure Compressor Stages	6	4
Duct Pressure Ratio	1.672	1.966
Fan Efficiency (Aft. of Fan Exit Guide Vane)	0.793	0.788
Pressure Ratio (Station 3/ Station 2)	4.199	4.135
Efficiency (Station 3/Station 2)	0.866	0.867

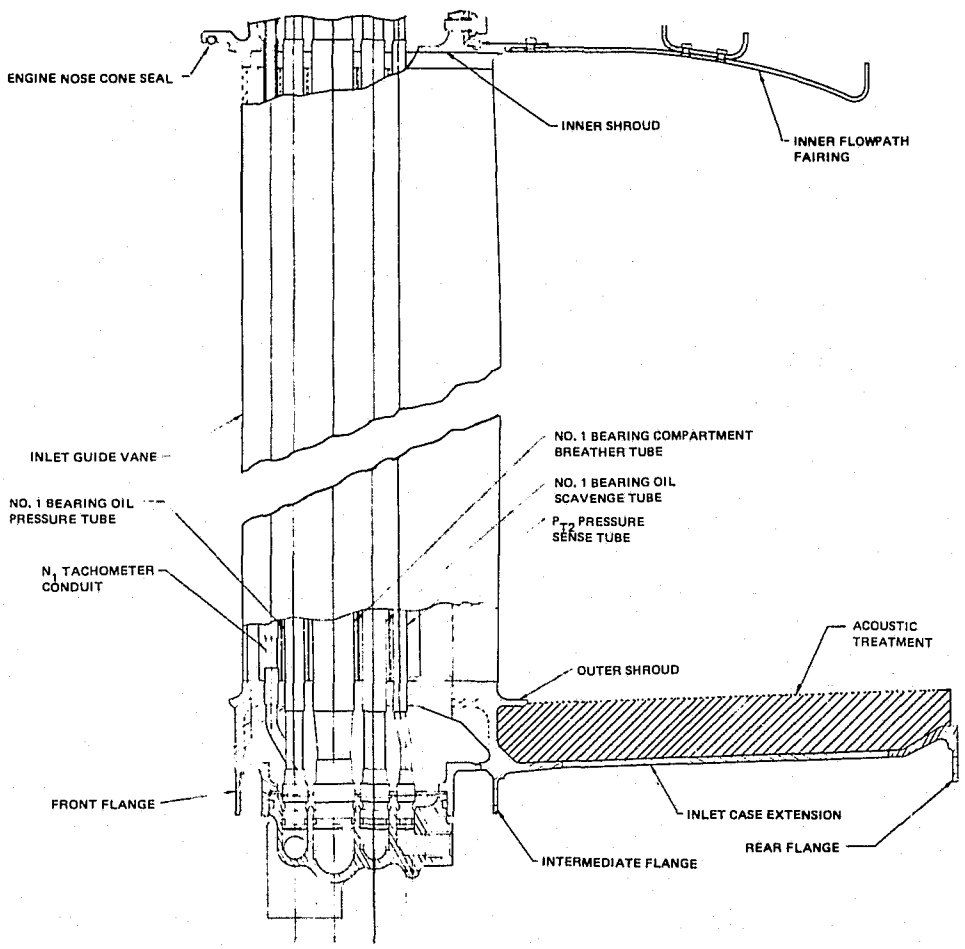

Figure A-6 JT8D-100 Inlet Cross Section View

a) Inlet Guide Vanes

The addition of an IGV aided in achieving fan stress and surge margin goals by permitting a lower fan rotor tip speed for a given root loading and pressure ratio. The IGV turns the air opposite to the direction of rotor rotation at the root and in the direction of rotation at the tip, thereby raising the root Mach number and lowering the tip Mach number, relative to designs without the IGV, as indicated in Figure A-7. In addition, the IGV allows an increase in fan root work without raising the root loading and acts as a case stiffener to help reduce tip clearance.

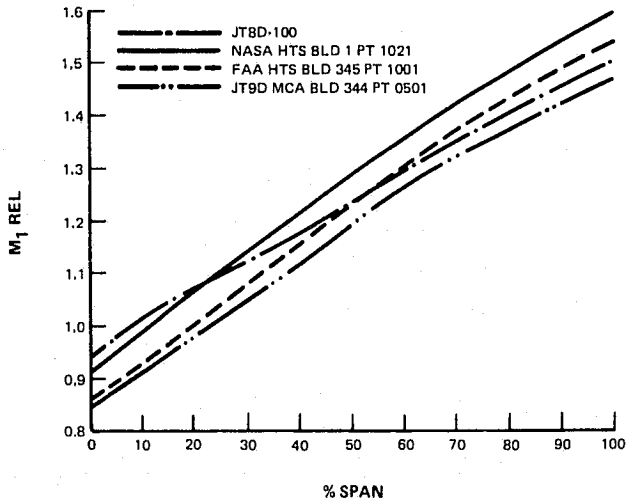

Figure A-7 JT8D-100 Fan Inlet Relative Mach Number Comparison

The inlet guide vanes are NACA 63 ($C_{10}A_4K_6$) series airfoils made of welded titanium sheet metal construction, similar to current JT8D vanes. An aerodynamic and geometric summary of the inlet guide vane is provided in Table A-II. The vane located on the bottom vertical centerline is thicker than the others to accommodate the N_1 tachometer wire conduit, No. 1 bearing compartment service tubes, and the compressor inlet total pressure (P_{t2}) sense tube. The number of vanes (23) and the axial spacing between the vanes and fan blades were selected to provide a low noise level configuration.

b) Outer Case Structure and Flowpath Extension

The outer case structure incorporates an outer vane structural shroud, external flanges and the inlet case flowpath extension. Gussets are machined integral with the outside of the outer shroud to provide a distributed load transition from the vanes to the O.D. of the outer ring and ultimately into the inlet case extension. The external front flange was designed to support the airframe-supplied inlet duct. The other flanges support airframe and engine accessories.

The inlet case outer flowpath extension is fabricated from titanium (AMS 4910 for the case and AMS 4920 for the flange) to be compatible with the inlet case outer shroud. This area is heated by 260°C (500°F) anti-icing air and thermal expansion considerations restricted material selections such as lightweight aluminum. The extension, which provides axial spacing between the vane and the fan blade to reduce noise generation, also incorporates perforated aluminum acoustic treatment to further suppress fan noise. Four 90° segmented panels are mechanically retained by extensions of the inlet case shroud and fan case assembly for ease of replacement. The panel structure consists of a perforated aluminum sheet inner wall, an aluminum honeycomb core and a solid sheet aluminum outer wall bonded together as a unit.

ORIGINAL PAGE IS
OF POOR QUALITY

TABLE A-II(a)
JT8D-100 INLET GUIDE VANE
AERODYNAMIC AND GEOMETRIC SUMMARY
23 NACA 63 ($C_{l_0}A_4K_6$) AIRFOILS

Percent Total Flow	Hub 0.0	3.0	9.0	15.0	21.0	27.0	Splitting Streamline 33.0	43.3	53.6	63.9	74.2	84.6	94.9	Tip 100.0
						Inlet								
Diameter – m	0.4064	0.4572	0.5450	0.6203	0.6872	0.7479	0.8039	0.8920	0.9720	1.046	1.115	1.1805	1.2425	1.2725
V – m/s	171.79	171.03	171.37	172.36	173.35	174.20	174.89	175.41	175.52	175.29	174.73	173.91	173.05	172.78
V_m – m/s	171.79	171.03	171.37	172.36	173.35	174.20	174.89	175.41	175.52	175.29	174.73	173.91	173.05	172.78
V_θ – m/s	0.0	0.0	0.0	0.0	0.0	0.0	0.0	0.0	0.0	0.0	0.0	0.0	0.0	0.0
β – deg	0.0	0.0	0.0	0.0	0.0	0.0	0.0	0.0	0.0	0.0	0.0	0.0	0.0	0.0
M	0.518	0.516	0.517	0.520	0.523	0.526	0.528	0.530	0.530	0.529	0.527	0.525	0.522	0.521
						Exit								
Diameter – m	0.4064	0.4616	0.5525	0.6278	0.6939	0.7537	0.8089	0.8956	0.9744	1.0471	1.1154	1.1802	1.2422	1.2725
V – m/s	165.53	168.50	172.99	175.85	177.75	178.91	179.64	181.09	181.93	182.22	182.03	81.20	179.53	178.46
V_m – m/s	155.55	161.46	169.81	174.77	177.47	178.81	179.63	181.05	181.66	181.58	180.90	179.49	177.17	175.75
V_θ – m/s	–56.61	–48.19	–32.98	–19.45	–10.42	–6.18	–2.21	4.10	9.88	15.23	20.19	24.79	29.01	30.99
β – deg	–20.00	–16.62	–10.99	–6.35	–3.36	–1.98	0.71	1.3	3.11	4.79	6.37	7.86	9.3	10.0
M	0.498	0.508	0.522	0.531	0.537	0.541	0.543	0.548	0.550	0.549	0.551	0.548	0.543	0.539
P_{03}/P_{02}	0.98403	0.98791	0.99258	0.99439	0.99500	0.99519	0.99526	0.99540	0.99545	0.99494	0.99333	0.98991	0.98464	0.98167
$\overline{\omega}$	0.09543	0.07286	0.04452	0.03330	0.02937	0.02800	0.02739	0.02645	0.02612	0.02909	0.03862	0.05890	0.09054	0.10657
D	1.7639	1.7589	1.6404	1.4412	1.0254	1.0271	1.0882	1.1572	1.3640	1.5826	1.8122	2.0471	2.2810	2.3957
						Geometry								
22 Thin Vanes	c = 0.1143m			t/c = 0.070			LER = 0.0013m							
Diameter – m	0.4064	0.4595	0.5486	0.6241	0.6904	0.7508	0.8065	0.8938	0.9733	1.046	1.115	1.180	1.242	1.273
RTE – m	0.0020	0.0013	0.0013	0.0013	0.0013	0.0013	0.0013	0.0013	0.0013	0.0013	0.0013	0.0013	0.0013	0.0020
β_2^* – deg	7.8	7.0	5.0	3.0	1.5	1.1	0.3	–1.0	–2.7	–4.5	–6.2	–8.2	–11.2	–12.1
ϕ – deg	27.7	23.5	19.2	9.5	5.5	3.4	1.3	–2.2	–6.3	–10.0	–13.4	–18.0	–23.5	–25.1
1 Thick Vane	c = 0.1143m			t/c = 0.15			RLE = 0.0018m		RTE = 0.0017m					
Diameter – m	0.4064	0.4595	0.5486	0.6241	0.6904	0.7508	0.8065	0.8938	0.9733	1.046	1.115	1.180	1.242	1.273
β_2^* – deg	8.5	7.5	5.5	3.2	2.0	1.0	0.3	–1.0	–2.7	–4.9	–6.2	–8.3	–11.2	–12.1
ϕ – deg	29.7	26.3	18.0	10.7	6.0	3.7	1.4	–2.2	–6.3	–10.0	–13.4	–18.0	–23.5	–25.1
σ	0.2059	0.1821	0.1525	0.1341	0.1212	0.1114	0.1038	0.0936	0.0860	0.0800	0.0750	0.0709	0.0674	0.0658

TABLE A-II(b)

JT8D-100 INLET GUIDE VANE
AERODYNAMIC AND GEOMETRIC SUMMARY
23 NACA 63 ($C_{l_0}A_4K_6$) AIRFOILS

Percent Total Flow	Hub 0.0	3.0	9.0	15.0	21.0	27.0	Splitting Streamline 33.0	43.3	53.6	63.9	74.2	84.6	94.9	Tip 100.00
						Inlet								
Diameter – in	16.000	18.001	21.456	24.421	27.054	29.445	31.649	35.117	38.269	41.182	43.906	46.477	48.920	50.100
V – ft/sec	563.61	561.11	562.24	565.47	568.74	571.51	573.77	575.50	575.84	575.11	573.27	570.58	567.76	566.87
V_m – ft/sec	563.61	561.11	562.24	565.47	568.74	571.51	573.77	575.50	575.84	575.11	573.27	570.58	567.76	566.87
V_θ – ft/sec	0.0	0.0	0.0	0.0	0.0	0.0	0.0	0.0	0.0	0.0	0.0	0.0	0.0	0.0
β – deg	0.0	0.0	0.0	0.0	0.0	0.0	0.0	0.0	0.0	0.0	0.0	0.0	0.0	0.0
M	0.518	0.516	0.517	0.520	0.523	0.526	0.528	0.530	0.530	0.529	0.527	0.525	0.522	0.521
						Exit								
Diameter – in	16.000	18.175	21.750	24.717	27.319	29.675	31.846	35.261	38.361	41.226	43.913	46.463	48.908	50.100
V – ft/sec	543.08	552.82	567.54	576.94	583.16	586.99	589.38	594.14	596.88	597.84	597.20	594.48	589.00	585.50
V_m – ft/sec	510.33	529.73	557.13	573.40	582.16	586.64	589.33	593.98	595.99	595.75	593.52	588.89	581.26	576.60
V_θ – ft/sec	–185.74	–158.10	–108.21	–63.81	–34.19	–20.27	–7.26	13.45	32.43	49.97	66.25	81.34	95.18	101.67
β – deg	–20.00	–16.62	–10.99	–6.35	–3.36	–1.98	.71	1.3	3.11	4.79	6.37	7.86	9.3	10.0
M	0.498	0.508	0.522	0.531	0.537	0.541	0.543	0.548	0.550	0.549	0.551	0.548	0.543	0.539
P_{03}/P_{02}	0.98403	0.98791	0.99258	0.99439	0.99500	0.99519	0.99526	0.99540	0.99545	0.99494	0.99333	0.98991	0.98464	0.98167
$\overline{\omega}$	0.09543	0.07286	0.04452	0.03330	0.02937	0.02800	0.02739	0.02645	0.02612	0.02909	0.03862	0.05890	0.09054	0.10657
D	1.7639	1.7589	1.6404	1.4412	1.0254	1.0271	1.0882	1.1572	1.3640	1.5826	1.8122	2.0471	2.2810	2.3957
						Geometry								
22 Thin Vanes	c = 4.5 in.			t/c = 0.07			LER = 0.05 in.							
Diameter – in	16.000	18.09	21.60	24.57	27.18	29.56	31.75	35.19	38.32	41.20	43.91	46.46	48.91	50.10
RTE – in.	0.080	0.050	0.050	0.050	0.050	0.050	0.050	0.050	0.050	0.050	0.050	0.050	0.050	0.080
β_2^* – deg	7.8	7.0	5.0	3.0	1.5	1.1	0.3	–1.0	–2.7	–4.5	–6.2	–8.3	–11.2	–12.1
ϕ – deg	27.7	23.5	19.2	9.5	5.5	3.4	1.3	–2.2	–6.3	–10.0	–13.4	–18.0	–23.5	–25.1
1 Thick Vane	c = 4.5 in.			t/c = 0.15			LER = 0.0717 in		TER = 0.0675 in.					
Diameter – in	16.000	18.09	21.60	24.57	27.18	29.56	31.75	35.19	38.32	41.20	43.91	46.46	48.91	50.10
β_2^* – deg	8.5	7.5	5.5	3.2	2.0	1.0	0.3	–1.0	–2.7	–4.5	–6.2	–8.3	–11.2	–12.1
ϕ – deg	29.7	26.3	18.0	10.7	6.0	3.7	1.4	–2.2	–6.3	–10.0	–13.4	–18.0	–23.5	–25.1
σ	0.2059	0.1821	0.1525	0.1341	0.1212	0.1114	0.1038	0.0936	0.0860	0.0800	0.0750	0.0709	0.0674	0.0658

c) Inner Structural Shroud Ring and Flowpath Fairing

The titanium inner structural shroud ring has a scalloped front flange which permits passage of the service tubes from the inner ring to the No. 1 bearing compartment cover and allows anti-icing air to flow from the inner ring to the engine nose cone. The N_1 tachometer conduit and the P_{t2} pressure sense tube are supported on the front flange and the oil pressure, oil scavenge, and breather tubes are supported on the rear flange.

The inner flowpath fairing is a riveted aluminum assembly attached to and extending rearward from the aft flange of the inner ring. It was designed to withstand aerodynamically and mechanically induced vibratory stresses. A small cut-out is provided at the aft end of the fairing near the bottom centerline to permit inserting a rivet tool to install trim balance weights on the No. 1.0 stage blade lock flange. The predicted flowpath fairing resonance diagram is shown in Figure A-8.

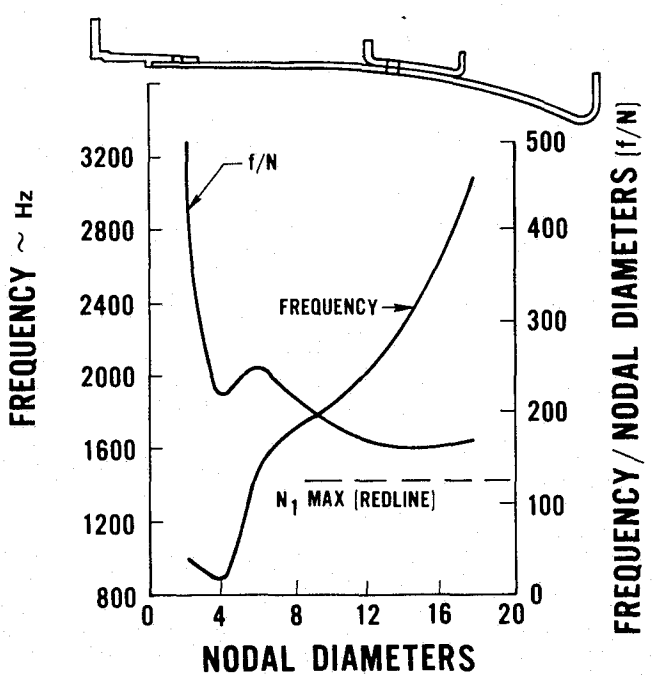

Figure A-8 Predicted JT8D-100 Inlet Case Inner Fairing Resonance Diagram

d) Inlet Case Design Features

Air from the compressor eighth stage is piped to the outer ring manifold to prevent vane icing. This hot air is distributed to the vanes where it flows radially inward through the forward section of the 22 thin vanes and through the forward and aft sections of the thick vane to the inner ring. It then exits through the scallops of the inner ring front flange where it is used to anti-ice the engine nose cone. Two bosses for connection of

anti-icing air tubing are welded into the outer wall of the outer ring. The locations have been changed from the current JT8D for better flow distribution in the manifold. The cross-sectional area of the opening in each boss has been increased 50% to permit use of larger diameter external piping to increase the flow and reduce the pressure drop.

A boss was provided at the bottom of the outer ring to support a five-passage service tube connector and a water drain.

A small drilled hole is provided in the outer shroud near the bottom to prevent an oil-leak from filling the anti-icing manifold with oil. The pumping action of high velocity inlet air will remove oil from the manifold when the engine is operating.

A tight-fitting dowel pin assembled into the rear face of the outer ring serves as an anti-rotation lug for the acoustic panels.

A 45° beveled surface is provided on the front face of the outer ring to align the airframe supplied inlet duct.

The N_1 tachometer conduit has a formed elbow at the inner end to facilitate wire insertion.

The O-ring seal on the front cover was relocated from outboard of the jumper tubes on current JT8D engines to inboard on this design. This eliminated the need for jumper tubes from the connectors on the inner ring to the front cover for the N_1 tachometer conduit and the P_{t2} pressure sense tube, and eliminated twelve O-rings. The number of O-rings on each of the other three tubes was reduced from six to four. Eliminating the two jumper tubes and improving the visibility of the remaining jumper tubes eases assembly of the front cover to the inlet case.

Self-locking helical inserts requiring tapped holes are used to eliminate lockwiring for all bolt connections. Both self-locking inserts and lockwire are used at the attachment of the fairing to the inner ring to prevent loss of bolt heads and/or shanks into the engine flowpath.

Component evaluations conducted during Phase II of this program have shown that the basic design of the inlet case structure is acceptable. However one design modification is recommended to eliminate a potential assembly problem which could be caused by the present method of retaining the acoustic panels. During assembly, it was found that several inlet case acoustic panels had an interference fit with the front retaining lip on the outer shroud. The interference was caused by misalignment of the inlet case extension with the outer vane shroud during the weld operation. This operation consisted of machining the outer vane shroud extension round, mating it to the thin inlet case, and welding them together. The weld fixturing caused the inlet case extension to locally vary from a true cylinder along the weld joint. This variation along with the variable height of the weld bead, caused the interference fit. To alleviate this problem, the following solutions are considered acceptable:

- The acoustic panel can be redesigned to provide an undercut at the weld joint location.

- The acoustic panel design can be modified to permit direct bonding of the acoustic honeycomb structure to the case. This would simplify the design and reduce weight and cost. An "on-the-wing" repair appears feasible for foreign object damage (FOD), thus the maintainability impact would be minimal.

2) Fan Containment Case, Fan Blade Tip Treatment, and Forward Fan Case

Figure A-9 shows the final configuration and relative locations of the fan containment case, the fan blade tip treatment (tip seals), and the forward fan case. The design of both the fan containment case and the blade tip treatment were modified during this component development phase of the Program. These modifications are discussed later in this section. The design of the forward fan case as presented in Reference 3 was considered acceptable and has been retained.

The fan containment case is an AMS 4928 titanium forging, machined all over, with conventional flanges at both ends. The containment case is made of titanium to take advantage of its relatively light weight, while retaining containment capability similar to steel. The design incorporates a removable, steel, tip treatment retention ring, which for purposes of this report is considered a part of the containment case. It provides the capability for removing both the blade tip treatment and the acoustic panels.

The fan blade tip treatment consists of removable cartridges of solid abradeable material held in place by radial screws and the steel retention ring. The solid material replaced the expandable honeycomb structure specified in the preliminary design.

The forward fan case is an AMS 4153 aluminum extrusion. This case forms the outer fan flowpath between the fan exit guide vanes and the intermediate case (front mount structure) with a flange at each end to attach to the containment case and the intermediate case. An intermediate dummy flange is provided to mount accessories and support the forward end of the accessory gearbox. The rear portion of the case has integral aluminum acoustical treatment.

The duct area was sized downstream of the FEGV so that the local corrected specific flow would be the same as that in the JT8D-9 to keep the duct losses at least as low as in the current engine. The flow path was contoured at the intermediate case to minimize the blockage effects caused by the fairings and struts.

Development testing conducted during Phase II of this Program resulted in modifications to both the fan containment case and the fan blade tip treatment.

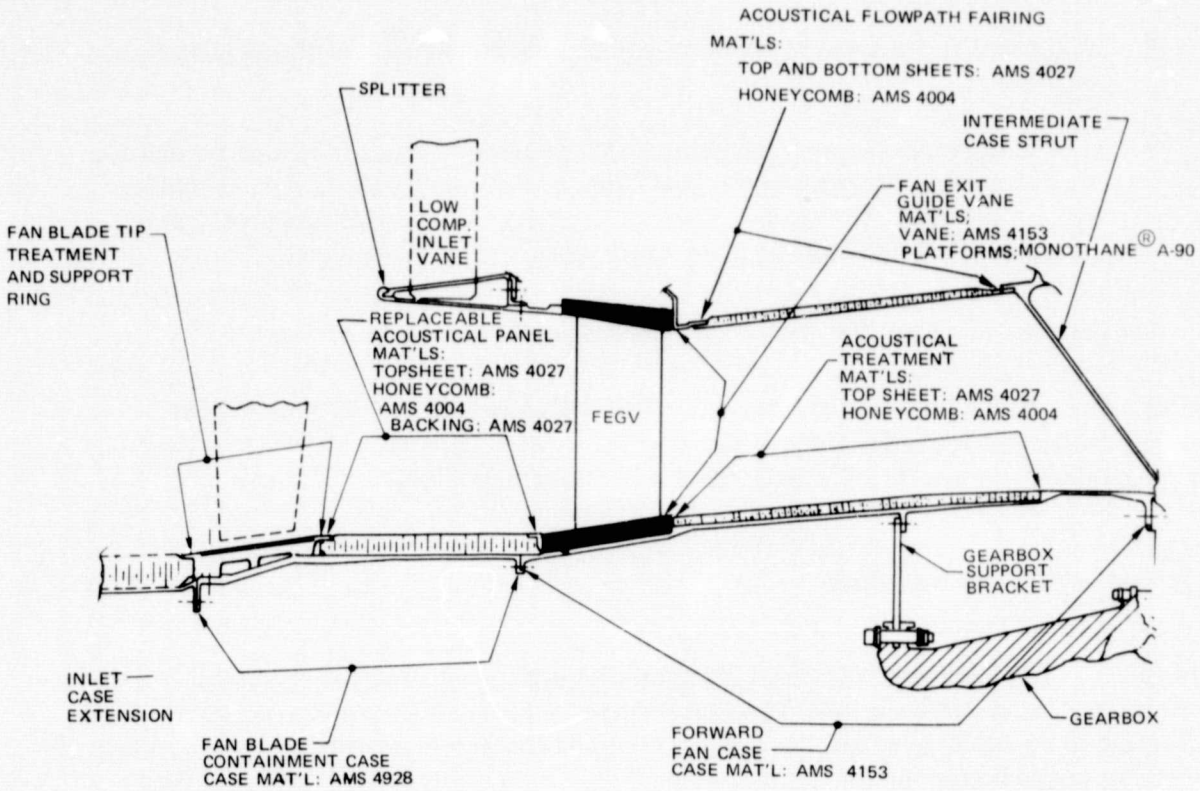

Figure A-9 JT8D-100 Forward Fan Case Area

The initial fan blade containment test was unsuccessful. The primary cause of the unsucessful test was the rig design which made the results of the test inconclusive. It is believed that when the airfoil of the failed blade contacted the aluminum ring, placed inside the containment case to support the fan blade tip seal, the velocity of the blade tip was severely retarded. The following blade impacted this slower moving blade and fractured. The second fan blade behind the initial failure blade also failed at high speed. The resultant unbalance load from these high speed failures caused the rig shaft to shear. Excessive radial clearances between the rig shaft and the upper and lower shaft guides and between the rig shaft and the fan disk allowed the rig shaft and fan disk assembly to accelerate prior to contacting the rig support structure producing an extremely high impact load. The sheared rig shaft and fan rotor assembly subsequently separated the containment case from the spin pit cover. Prior to conducting a repeat containment test, the rig hardware and fan blade tip seal support ring were redesigned. The rig hardware redesign included changes to the support structure and a reduction in clearances. The fan blade tip seal support ring was fabricated from steel rather than aluminum and was designed to have sufficient thickness to contain a fan blade fractured at 8000 rpm. This steel ring was placed inside the titanium containment case. The function of the titanium containment case was thus changed to an outer fan case to hold the steel containment ring. This case would be redesigned to a reduced thickness, reduced weight configuration prior to production release. The repeat containment test was successful.

The original fan blade tip treatment design was modified as a result of engine testing during this phase of the program. Originally the tip treatment was fabricated from angled or skewed honeycomb to improve fan blade tip surge margin. The honeycomb was formed into curved panels, bonded to aluminum backing sheets, and the forward and aft edges of the skewed cells were filled with epoxy foam. Ten such panels, or cartridges, were secured by radial screws to an aluminum retention ring tightly fitted into the containment case. Engine testing revealed persistent delamination of the honeycomb from the backing sheet. It was determined that the delamination resulted from either a poor honeycomb/sheet bond or blade passing frequencies, or a combination of these two conditions. To eliminate the problem a solid abradeable material was substituted for the honeycomb. Subsequent engine testing showed that satisfactory blade tip surge margin was maintained when the solid blade tip treatment material was installed.

At the request of the NASA, an alternate fan blade tip seal scheme was provided utilizing axial skewed grooves (ASG) of cast glass-reinforced epoxy, similar to that presently used in the JT9D engine. However, surge margin with the solid tip treatment proved to be adequate and this alternate design was not used.

3) Fan Exit Guide Vanes (FEGV)

The fan exit guide vanes (FEGV) are eighty-four solid aluminum vanes positioned in the fan case aft of the fan blades and the engine flow splitter. The number of vanes (84) was selected to be acoustically compatible with 34 fan blades (2N + 16 vanes required where N is the number of fan blades). The vanes are contoured to aerodynamically straighten the flow from the fan blades and improve overall fan performance. The type of airfoil series is 65/ circular arc. Pertinent information on the FEGV airfoil is summarized in Table A-III. Engine testing conducted during this Phase of the Program showed that the overall performance of the FEGVs was acceptable even though loss levels were 0.5% higher than predicted on the nominal operating line at 7450 $N_1/\sqrt{\theta}_{T2}$. These test results and possible remedial action to improve the FEGV performance are discussed later in this section.

The fan exit guide vane design was a compromise among the large incidence swing implied by the surge margin requirement, choking at the minimum cruise condition, and structural requirements of the aluminum strip stock vane. The vane was designed as thin as could be justified structurally and with incidence as large as could be justified at the surge condition. Surge incidence and loading are shown in Figure A-10 compared to the NASA low tip speed, redesigned stator. Figure A-11 is a predicted fan map and shows the points used in the choke analysis. It was anticipated that the resulting choke margin would not impose a significant penalty in the cruise range. Figure A-12 shows FEGV minimum A/A spanwise distribution at the aerodynamic design point and Figure A-13 is an estimate of the FEGV performance in the cruise operating range compared to the NASA low tip speed, redesigned stator performance.

TABLE A-III(a)

JT9D-100 FAN DUCT EXIT GUIDE VANE
AERODYNAMIC AND GEOMETRIC SUMMARY
84 STRIP STOCK AIRFOILS WITH NASA 65 SERIES THICKNESS DISTRIBUTION ON A CIRCULAR ARC MEAN LINE

Percent Duct Flow	Hub 0.0	15.38	30.77	46.15	61.54	76.92	92.31	Tip 100.0
				Inlet				
Diameter-m	0.8573	0.9169	0.9726	1.0254	1.077	1.1279	1.1822	1.2129
V-m/s	253.25	253.83	254.16	253.10	248.58	240.12	226.91	213.94
V_m-m/s	202.89	203.44	202.23	198.79	191.12	176.13	150.78	126.90
V_θ-m/s	151.56	151.79	153.96	156.66	158.94	163.21	169.57	172.24
β-deg	36.76	36.13	37.28	38.24	39.75	42.82	48.49	53.88
M	0.721	0.721	0.720	0.714	0.699	0.670	0.627	0.587
				Exit				
Diameter-m	0.8788	0.9310	0.9797	1.0263	1.0713	1.1158	1.1617	1.1862
V-m/s	221.09	218.58	215.35	211.70	206.79	198.58	181.31	169.08
V_m-m/s	219.79	218.55	215.31	211.65	206.72	198.47	181.31	166.43
V_θ-m/s	12.981	−3.191	−4.331	−4.523	−5.236	−6.721	.0640	29.852
β-deg	3.37	−0.84	−1.15	−1.23	−1.45	−1.94	0.02	10.17
M	0.622	0.613	0.601	0.589	0.573	0.547	0.494	0.458
P_{03}/P_{02}	0.9570	0.9820	0.9907	0.9907	0.9891	0.9840	0.9657	0.9619
$\overline{\omega}$	0.14716	0.06169	0.03184	0.03227	0.03908	0.06148	0.14739	0.18360
D	0.24538	0.28017	0.30567	0.32884	0.34881	0.37747	0.43151	0.42382
				Geometry				
		LER = 0.00036m			TER = 0.00036m			
Diameter-m	0.8680	0.9176	0.9671	1.0166	1.0662	1.1157	1.1652	1.1982
c-m	0.07416	0.07417	0.07409	0.07392	0.07363	0.07301	0.07155	0.06965
t/c	0.0477	0.0477	0.0477	0.0478	0.0480	0.0484	0.0494	0.0508
β_2^*-deg	35.84	35.61	36.30	37.51	39.58	43.75	51.71	62.37
ϕ-deg	44.49	44.27	45.19	47.12	50.29	56.49	68.92	82.48
σ	2.284	2.161	2.048	1.944	1.846	1.750	1.642	1.554

ORIGINAL PAGE IS
OF POOR QUALITY

TABLE A-III(b)

JT9D-100 FAN DUCT EXIT GUIDE VANE
AERODYNAMIC AND GEOMETRIC SUMMARY
84 STRIP STOCK AIRFOILS WITH NASA 65 SERIES THICKNESS DISTRIBUTION ON A CIRCULAR ARC MEAN LINE

	Hub							Tip
Percent Duct Flow	0.000	15.38	30.77	46.15	61.54	76.92	92.31	100.
				Inlet				
Diameter-in	33.750	36.099	38.291	40.372	42.387	44.404	46.542	47.750
V-ft/sec	880.87	832.77	833.87	830.38	815.54	787.80	744.46	701.91
V_m-ft/sec	665.66	667.46	663.47	652.19	627.05	577.85	494.70	416.35
$V\theta$-ft/sec	497.24	498.00	505.12	513.97	521.46	535.46	556.32	565.10
β-deg	36.76	36.13	37.28	38.24	39.75	42.82	48.49	53.88
M	0.721	0.721	0.720	0.714	0.699	0.670	0.627	0.587
				Exit				
Diameter-in	34.6	36.652	38.571	40.405	42.179	43.931	45.737	46.7
V-ft/sec	725.36	717.12	706.53	694.54	678.44	651.52	594.86	554.74
V_m-ft/sec	721.11	717.04	706.39	694.38	678.22	541.15	594.86	546.03
$V\theta$-ft/sec	42.59	−10.47	−14.21	−14.84	−17.18	−22.05	.21	97.94
β-deg	3.37	−.84	−1.15	−1.23	−1.45	−1.94	.02	10.17
M	0.622	0.613	0.601	0.589	0.573	0.547	0.494	0.458
P_{03}/P_{02}	0.9570	0.9820	0.9907	0.9907	0.9891	0.9840	0.9657	0.9619
ω	0.14716	0.06169	0.03184	0.03227	0.03908	0.06148	0.14739	0.18360
D	0.24538	0.28017	0.30567	0.32884	0.34881	0.37747	0.43151	0.42382
				Geometry				
		LER = 0.014 in.			TER = 0.014 in.			
Diameter-in	34.175	36.125	38.075	40.025	41.975	43.925	45.875	47.75
c-in	2.9195	2.9202	2.9171	2.9104	2.8989	2.8743	2.8168	2.7422
t/c	0.0477	0.0477	0.0477	0.0478	0.0480	0.0484	0.0494	0.0508
β^*_2-deg	35.84	35.61	36.30	37.51	39.58	43.75	51.71	62.37
ϕ - deg	44.49	44.27	45.19	47.12	50.29	56.4902	68.92	82.48
σ	2.284	2.161	2.048	1.944	1.846	1.750	1.642	1.554

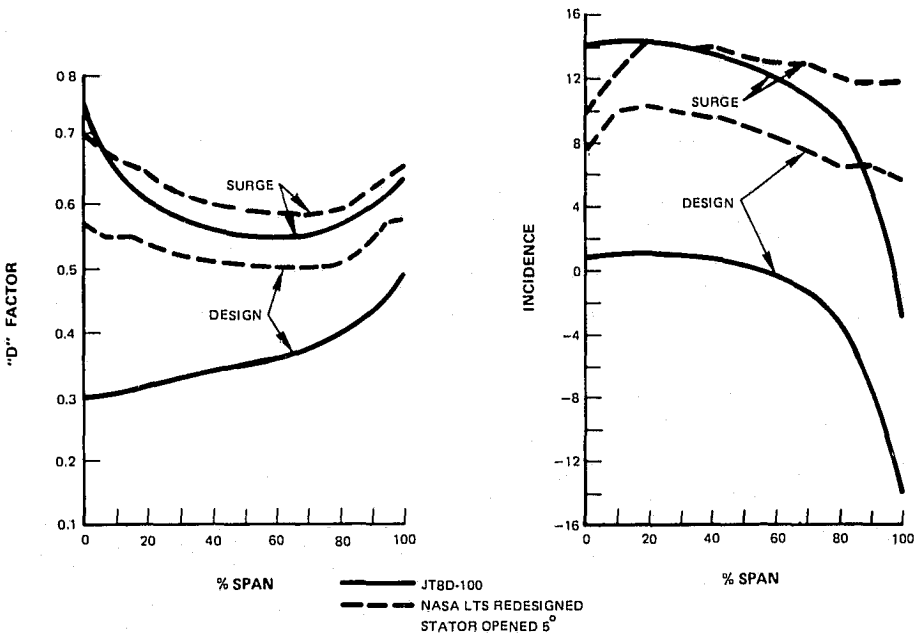

Figure A-10 JT8D-100 Fan Exit Guide Vane - Estimated Surge Incidence and Loading Compared to the NASA Low Tip Speed Redesigned Stator

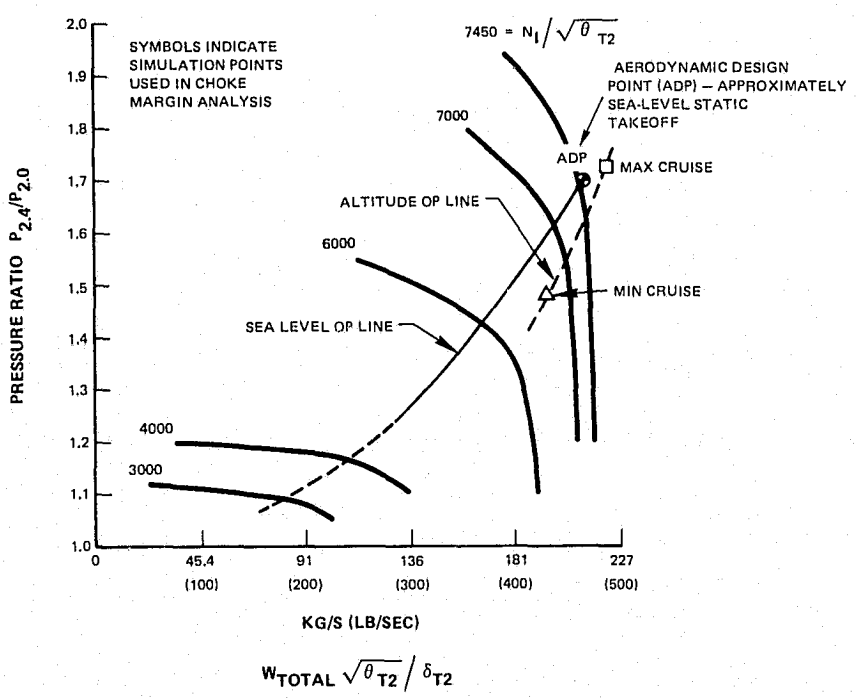

Figure A-11 JT8D-100 Fan Exit Guide Vane - Predicted Fan Map

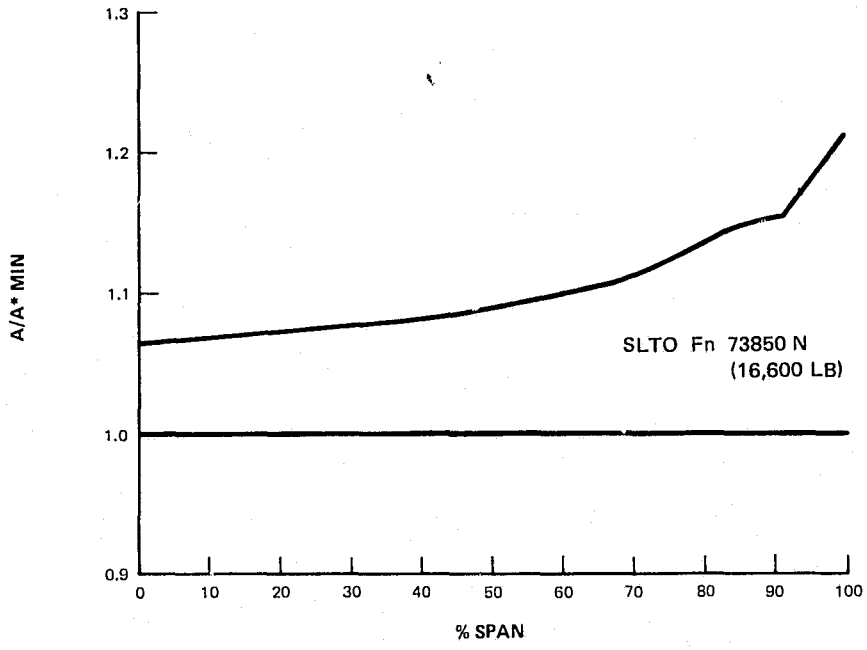

Figure A-12 JT8D-100 Fan Exit Guide Vane - Spanwise Distribution of Choke Margin at the Aerodynamic Design Point (ADP in Figure A-11)

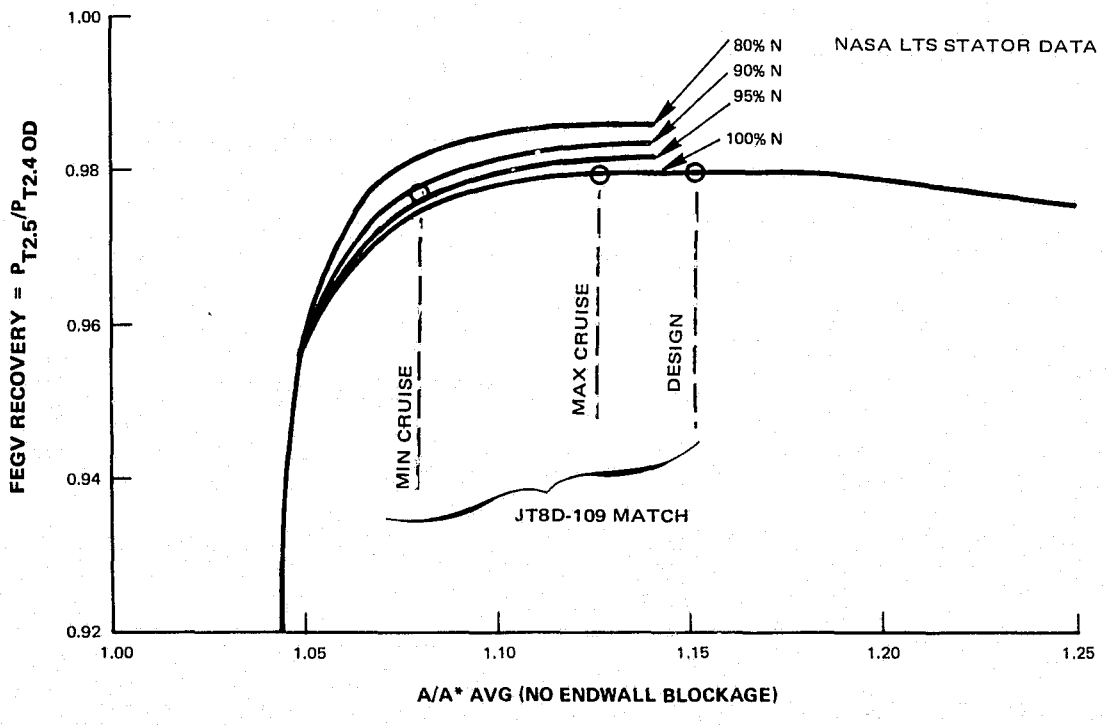

Figure A-13 JT8D-100 Fan Exit Guide Vane - Estimated Total Pressure Recovery vs. Choke Margin at Cruise Compared to NASA Low Tip Speed Redesigned Stator Performance

The FEGV was configured in four clusters of twenty-one vanes. The vane detail is an aluminum (AMS 4153) extrusion, coined to final shape. The vanes are fixtured together with inner and outer thin aluminum shrouds and potted with Monothane® A-90 polyurethane elastomer. The elastomer acts as the structural member and the aluminum shrouds act primarily as forms for fabricating these shrouds. Each cluster of vanes is attached to the fan duct outer wall by six bolts. At the root, the platforms have slots between vanes that engage lugs on the aluminum splitter fairing to provide tangential restraint but still allow the vanes radial freedom for thermal expansion.

Engine testing showed that the FEGV loss exceeded predicted loss levels between 0% and 60% span as shown in Figure A-14. Incidence variation, in this critical high Mach number region, moved the vane from one side of its minimum loss point to the other, but there was no tendency to drop below the design point level. From 60% to 100% span the FEGV followed the predicted loss level although it was matched more toward choke than anticipated.

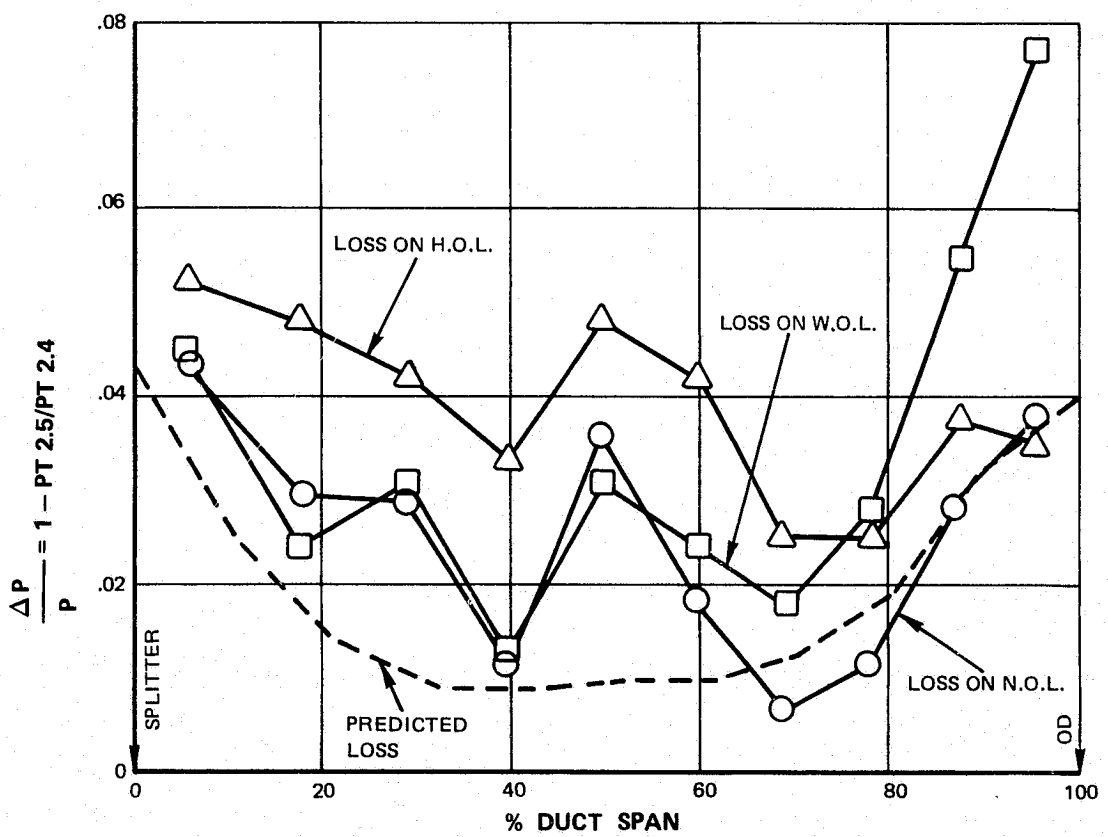

Figure A-14 JT8D-100 Fan Exit Guide Vane Losses With Fan on Nominal Operating Line, Wide Open Operating Line and High Operating Line at 7,450 $N_1\sqrt{\theta}_{T2}$

Loading levels of the FEGV are shown in Figure A-15 for three match points at design speed. These points show the change in loading as the fan is matched on a low operating line, a nominal operating line, and a point near surge. Design loading levels and those predicted at surge are presented for comparison. The overall performance on the nominal operating line most closely approximates the design point of the fan and therefore can be compared. This comparison shows good agreement from 0 to 50% span and that test loadings from 50% to 100% span are lower than predicted. This reduced loading is attributed to the higher than anticipated flow in the duct that manifests itself as higher local velocities in the more efficient outer percent spans. A comparison of loading of the near surge data point and that predicted at surge shows differences that reflect that (1) the near surge point is higher in flow than predicted and contributory to loading level differences, (2) the prediction did not account for the considerable increase in losses experienced in the shroud area of the fan blade near surge and (3) increased losses were incurred in the FEGV. These combine to redistribute the flow toward the walls thus maintaining lower than predicted loadings in those areas.

FEGV performance could best be improved with a redesign of the 0% to 60% span region where losses are high compared to other similar vanes. Additional performance gains could be realized through a simple leading edge angle change in the 60% to 100% span region.

4) Low-Pressure Compressor Splitter, Stators, and Fairing

Figure A-16 shows the final arrangement of the low pressure compressor splitter, the stage 1.0, 1.5, and 2.0 stators, and the fairing of the JT8D-100 engine. The remaining three stators of the low-pressure compressor were not redesigned and remain identical to those used in the basic JT8D turbofan engine.

The aluminum splitter divides the incoming air between the primary and fan streams and consists of an inner and outer section. The inner section supports the No. 1 stator while the outer section supports the fan exit guide vane. Figure A-17 presents the predicted resonance diagram for the splitter. The splitter configuration as presented in Reference 3 has proved acceptable and has not been modified during the development phase of the program.

The No. 1.0 stator vanes, described in Table A-IV, are fabricated of AMS 5613 steel and are damped by potting both the vane root and tip in silicone rubber. This damping scheme, as well as the vane support brackets and the vane stagger angle, are modifications to the original design and are discussed later in this section.

The Nos. 1.5 and 2.0 stators, also described in Table A-IV, are fabricated from AMS 4135 aluminum forgings and are of single-rail design at the tip and conventional JT8D double-rail construction at the root. The single-rail design provides lightweight and low cost.

The aerodynamic and geometric summaries for Stage 1.0, 1.5, and 2.0 stators are presented in Tables A-V, -VI, and -VII.

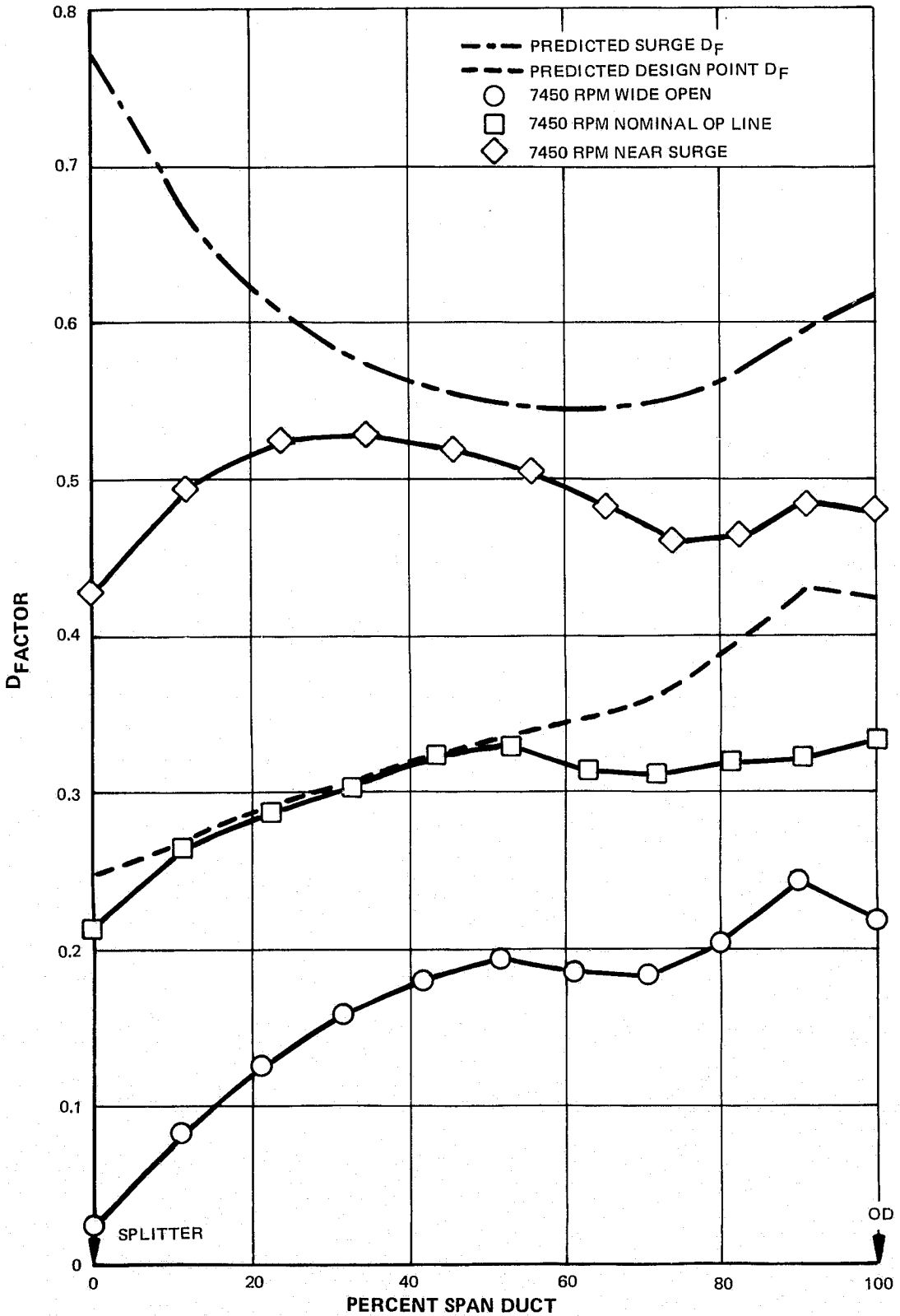

Figure A-15 JT8D-100 Fan Exit Guide Vane Loading

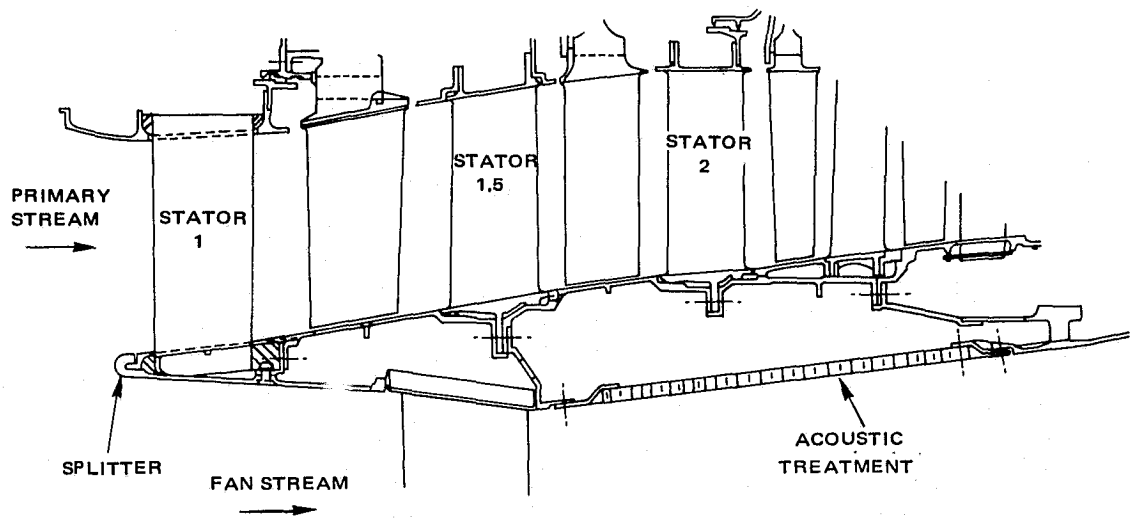

Figure A-16 JT8D-100 Low Pressure Compressor Fairing, Stators and Splitter

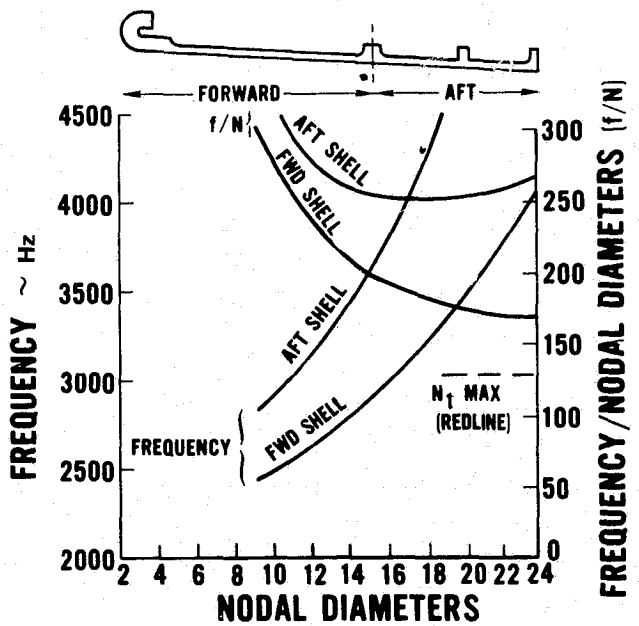

Figure A-17 JT8D-100 Predicted Resonance Diagram for Splitter

TABLE A-IV

SUMMARY OF NOS. 1, 1.5, AND 2.0 STAGE STATORS

	LPC Stator		
	No. 1	No. 1.5	No. 2
Material	AMS 5613	AMS 4135	AMS 4135
No. of Airfoils	56	53	59
Type of Airfoil	Circular Arc	65 series/ Circular Arc	65 series/ Circular Arc
Airfoil Chord, cm (inches)			
Root	6.02 (2.372)	5.25 (2.069)	4.69 (1.846)
Tip	6.04 (2.378)	5.79 (2.278)	5.17 (2.035)
Airfoil Thickness, cm (inches)			
Root	0.304 (0.120)	0.368 (0.145)	0.327 (0.129)
Tip	0.304 (0.120)	0.404 (0.159)	0.361 (0.142)
Airfoil Setting Angle, degrees			
Root	69.03, 72.03*	68.31	69.13
Tip	62.10, 62.10*	62.69	61.40

*After rotating 3° open.

TABLE A-V(a)

JT8D-100 STATOR 1
AERODYNAMIC AND GEOMETRIC SUMMARY
56 STRIP STOCK DOUBLE CIRCULAR ARC AIRFOILS

	Hub						Tip
Percent Engine Flow	0.0	9.09	27.3	45.5	63.6	81.8	100.0
				Inlet			
Diameter-m	0.5702	0.5951	0.6420	0.6867	0.7302	0.7723	0.8128
V-m/s	326.47	307.86	283.07	267.40	255.88	247.08	240.25
V_m-m/s	244.44	237.54	214.05	206.36	194.26	186.54	179.36
$V\theta$-m/s	216.40	195.84	176.08	170.06	166.56	162.02	159.85
β-deg	41.52	39.50	38.46	39.49	40.61	40.97	41.71
M	0.953	0.894	0.816	0.767	0.730	0.702	0.680
				Exit			
Diameter-m	0.5639	0.5882	0.6342	0.6775	0.7190	0.7595	0.8001
V-m/s	218.49	208.85	206.34	201.80	196.15	188.58	176.28
V_m-m/s	213.55	205.41	201.93	286.44	188.06	179.87	163.25
$V\theta$-m/s	42.217	37.655	42.449	51.956	55.781	56.641	66.495
β-deg	12.21	10.39	11.87	14.92	16.52	17.48	22.16
M	0.608	0.582	0.577	0.565	0.548	0.525	0.489
P_{03}/P_{02}	0.9516	0.9583	0.9843	0.9914	0.9898	0.9807	0.9616
$\bar{\omega}$	0.1094	0.1030	0.0443	0.0266	0.0342	0.0687	0.1444
D	0.4753	0.4679	0.4130	0.3851	0.3771	0.3846	0.4066
				Geometry			
		LER = 0.00020m		TER = 0.00020m			
Diameter-m	0.5696	0.5909	0.6406	0.6879	0.7234	0.7707	0.8062
c-m	0.06024	0.06065	0.06104	0.06109	0.06099	0.06076	0.06040
t/c	0.0506	0.0503	0.0500	0.0499	0.0500	0.0502	0.0505
β_2^*-deg	47.10	38.85	36.99	39.27	41.77	45.23	48.75
ϕ-deg	44.26	37.71	30.81	29.46	31.32	35.83	41.71
σ	1.885	1.829	1.698	1.583	1.503	1.405	1.336

TABLE A-V(b)

JT8D-100 STATOR 1
AERODYNAMIC AND GEOMETRIC SUMMARY
56 STRIP STOCK DOUBLE CIRCULAR ARC AIRFOILS

	Hub						Tip
Percent Engine Flow	0.0	9.09	27.3	45.5	63.6	81.8	100.0
				Inlet			
Diameter - in.	22.450	23.429	25.275	27.036	28.747	30.407	32.00
V - ft/sec	1071.09	1010.03	928.72	877.29	839.51	810.63	788.23
V_m - ft/sec	801.98	779.33	702.26	677.02	637.32	612.02	588.46
V_θ - ft/sec	709.96	642.51	577.68	557.93	546.45	531.55	524.43
β - deg	41.52	39.50	38.46	39.49	40.61	40.97	41.71
M	0.953	0.894	0.816	0.767	0.730	0.702	0.680
				Exit			
Diameter - in	22.200	23.156	24.969	26.672	28.309	29.902	31.500
V - ft/sec	716.83	685.19	676.98	662.07	643.55	618.71	578.34
V_m - ft/sec	700.62	673.93	662.50	639.75	616.98	590.14	535.61
V_θ - ft/sec	151.63	123.54	139.27	170.46	183.01	185.83	218.16
β - deg.	12.21	10.39	11.87	14.92	16.52	17.48	22.16
M	0.608	0.582	0.577	0.565	0.548	0.525	0.489
P_{03}/P_{02}	0.9516	0.9583	0.9843	0.9914	0.9898	0.9807	0.9616
$\bar{\omega}$	0.1094	0.1030	0.0443	0.0266	0.0342	0.0687	0.1444
D	0.4753	0.4679	0.4130	0.3851	0.3771	0.3846	0.4066
				Geometry			
		LER = 0.008 in.		TER = 0.008 in.			
Diameter - in.	22.425	23.263	25.220	27.082	28.480	30.343	31.74
c - in.	2.3715	2.3878	2.403	2.405	2.401	2.392	2.378
t/c	0.0506	0.0503	0.0500	0.0499	0.0500	0.0502	0.0505
β_2^* - deg.	47.10	38.85	36.99	39.27	41.77	45.23	48.75
ϕ - deg.	44.26	37.71	30.81	29.46	31.32	35.83	41.71
σ	1.885	1.829	1.698	1.583	1.503	1.405	1.336

TABLE A-VI(a)

JT8D-100 STATOR 1.5
AERODYNAMIC AND GEOMETRIC SUMMARY
53 AIRFOILS WITH NASA 65 SERIES THICKNESS DISTRIBUTION ON A CIRCULAR ARC MEAN LINE

	Hub						Tip
Percent Engine Flow	0.0	9.09	27.3	45.5	63.6	81.8	100.0
				Inlet			
Diameter-m	0.5248	0.5522	0.5989	0.6421	0.6830	0.7219	0.762
V-m/s	216.95	227.68	230.18	227.23	224.79	219.90	199.67
V_m-m/s	162.93	186.72	191.79	186.67	183.21	178.14	151.58
V_θ-m/s	143.25	130.22	127.27	129.57	130.24	128.93	129.96
β-deg	41.32	34.91	33.57	34.77	35.41	35.90	40.61
M	0.567	0.620	0.634	0.626	0.619	0.600	0.543
				Exit			
Diameter-m	0.5024	0.5319	0.5804	0.6238	0.6640	0.7026	0.7417
V-m/s	147.43	173.60	188.67	191.91	193.82	191.82	172.82
V_m-m/s	144.59	171.50	185.22	186.52	186.34	182.24	159.10
V_θ-m/s	28.80	26.93	35.87	45.20	53.328	59.85	67.47
β-deg	11.27	8.92	10.96	13.62	15.92	18.18	22.98
M	0.391	0.466	0.510	0.521	0.526	0.519	0.466
P_{03}/P_{02}	0.9879	0.9913	0.9952	0.9967	0.9962	0.9949	0.9946
$\overline{\omega}$	0.05831	0.03812	0.02059	0.01452	0.01671	0.02356	0.02965
D	0.4784	0.3762	0.3094	0.2830	0.2615	0.2468	0.2589
				Geometry			
		t/c - 0.070	LER = 0.00020m		TER = 0.00030m		
Diameter-m	0.5136	0.5375	0.5850	0.6327	0.6685	0.7160	0.7518
c-m	0.05255	0.05306	0.05413	0.05522	0.05601	0.05704	0.05786
β_2^*-deg	45.59	40.16	36.72	38.53	39.94	41.642	43.77
ϕ-deg	47.80	39.47	31.34	30.12	29.31	29.766	32.90
σ	1.726	1.666	1.561	1.472	1.413	1.344	1.298

TABLE A-VI(b)

JT8D-100 STATOR 1.5
AERODYNAMIC AND GEOMETRIC SUMMARY
53 AIRFOILS WITH NASA 65 SERIES THICKNESS DISTRIBUTION ON A CIRCULAR ARC MEAN LINE

	Hub						Tip
Percent Engine Flow	0.0	9.09	27.3	45.5	63.6	81.8	100.0
				Inlet			
Diameter-in	20.66	21.74	23.58	25.28	26.89	28.42	30.00
V-ft/sec	711.77	746.99	755.17	745.51	737.49	721.46	655.07
V_m-ft/sec	534.54	612.60	629.24	612.43	601.09	584.44	497.31
V_θ-ft/sec	469.98	427.24	417.54	425.11	427.30	423.00	426.37
β - deg.	41.32	34.91	33.57	34.77	35.41	35.90	40.61
M	0.567	0.620	0.634	0.626	0.619	0.600	0.543
				Exit			
Diameter-in	19.78	20.94	22.85	24.56	26.14	27.66	29.20
V - ft/sec	483.69	569.56	618.98	629.64	635.88	629.33	566.99
V_m - ft/sec	474.37	562.67	607.69	611.93	611.34	597.91	521.99
V_θ - ft/sec	94.49	88.34	117.68	148.31	174.96	196.37	221.35
β - deg.	11.27	8.92	10.96	13.62	15.92	18.18	22.98
M	0.391	0.466	0.510	0.521	0.526	0.519	0.466
P_{03}/P_{02}	0.9879	0.9913	0.9952	0.9967	0.9962	0.9949	0.9946
$\overline{\omega}$	0.05831	0.03812	0.02059	0.01452	0.01671	0.02356	0.02965
D	0.4784	0.3762	0.3094	0.2830	0.2615	0.2468	0.2589
				Geometry			
			t/c = 0.070	LER = 0.008 in.	TER = 0.012 in.		
Diameter-in	20.22	21.16	23.03	24.91	26.32	28.19	29.60
c - in	2.069	2.089	2.131	2.174	2.205	2.246	2.278
β_2^* - deg.	45.59	40.16	36.72	38.53	39.94	41.642	43.77
ϕ - deg	47.80	39.47	31.34	30.12	29.31	29.766	32.90
σ	1.726	1.666	1.561	1.472	1.413	1.344	1.298

TABLE A-VII(a)

JT8D-100 STATOR 2
AERODYNAMIC AND GEOMETRIC SUMMARY
59 AIRFOILS WITH NASA 65 SERIES THICKNESS DISTRIBUTION ON A CIRCULAR ARC MEAN LINE

	Hub						Tip
Percent Engine Flow	0.0	9.09	27.3	45.5	63.6	81.8	100.0
				Inlet			
Diameter-m	0.4928	0.5210	0.5669	0.6091	0.6490	0.6873	0.7264
V-m/s	196.11	215.10	218.69	216.92	216.63	215.98	203.41
V_m-m/s	144.17	174.90	183.94	181.44	178.45	173.03	149.27
V_θ-m/s	132.95	125.21	118.29	118.88	122.82	129.25	138.18
β-deg	42.69	35.62	32.75	33.23	34.54	36.76	42.79
M	0.513	0.567	0.582	0.578	0.577	0.574	0.538
				Exit			
Diameter-m	0.4928	0.5197	0.5644	0.6055	0.6441	0.6812	0.7188
V-m/s	153.95	181.81	189.50	188.02	186.63	184.31	169.26
V_m-m/s	150.55	179.79	187.03	184.40	181.79	177.73	157.05
V_θ-m/s	32.18	27.08	30.52	36.75	42.21	48.80	63.13
β-deg	12.07	8.57	9.27	11.27	13.09	15.35	21.9
M	0.398	0.475	0.500	0.497	0.493	0.485	0.444
P_{03}/P_{02}	0.9887	0.9911	0.9946	0.9957	0.9949	0.9935	0.9934
$\bar{\omega}$	0.06895	0.04529	0.02659	0.0218	0.02516	0.03240	0.03678
D	0.3563	0.2853	0.2557	0.2549	0.2640	0.2781	0.3043
				Geometry			
	t/c = 0.070	LER = 0.00020m			TER = 0.00030m		
Diameter-m	0.4928	0.5156	0.5618	0.6078	0.6421	0.6881	0.7226
c-m	0.04689	0.04739	0.04835	0.04932	0.05004	0.05098	0.05169
β_2^*-deg	43.65	40.179	39.155	40.391	42.764	45.413	48.42
ϕ-deg	45.57	40.143	36.632	35.737	36.347	37.889	39.64
σ	1.787	1.726	1.6166	1.524	1.463	1.391	1.343

TABLE A-VII(b)

JT8D-100 STATOR 2.0
AERODYNAMIC AND GEOMETRIC SUMMARY
59 AIRFOILS WITH NASA 65 SERIES THICKNESS DISTRIBUTION ON A CIRCULAR ARC MEAN LINE

	Hub						Tip
Percent Engine Flow	0.0	9.09	27.3	45.5	63.6	81.8	100.0
				Inlet			
Diameter-in	19.40	20.51	22.32	23.98	25.55	27.06	28.60
V-ft/sec	643.40	705.71	717.50	711.67	710.73	708.60	667.34
V_m-ft/sec	472.99	573.82	603.47	595.28	585.46	567.70	489.73
V_θ-ft/sec	436.18	410.80	388.10	390.03	402.96	424.06	453.34
β - deg.	42.69	35.62	32.75	33.23	34.54	36.76	42.79
M	0.513	0.567	0.582	0.578	0.577	0.574	0.538
				Exit			
Diameter-in	19.40	20.46	22.22	23.84	25.36	26.82	28.30
V - ft/sec	505.08	596.50	621.72	616.87	612.29	604.69	555.33
V_m-ft/sec	493.92	589.85	613.60	604.98	596.42	583.10	515.26
V_θ-ft/sec	105.59	88.85	100.14	120.58	138.49	160.12	207.12
β - deg.	12.07	8.57	9.27	11.27	13.09	15.35	21.9
M	0.398	0.475	0.500	0.497	0.493	0.485	0.444
P_{03}/P_{02}	0.9887	0.9911	0.9946	0.9957	0.9949	0.9935	0.9934
$\overline{\omega}$	0.06895	0.04529	0.02659	0.0218	0.02516	0.03240	0.03678
D	0.3563	0.2853	0.2557	0.2549	0.2640	0.2781	0.3043
				Geometry			
	t/c = 0.070	LER = 0.008 in.		TER = 0.012 in.			
Diameter-in	19.40	20.30	22.12	23.93	25.28	27.09	28.45
c - in	1.846	1.8658	1.9035	1.9419	1.9702	2.007	2.035
β_2^* - deg.	43.65	40.179	39.155	40.391	42.764	45.413	48.42
ϕ - deg.	45.57	40.143	36.632	35.737	36.347	37.889	39.64
σ	1.787	1.726	1.6166	1.524	1.463	1.391	1.343

The inner fan duct fairing provides acoustic treatment in the duct and establishes the inner passage of the diffuser section of the fan duct. Existing clearances provide for recirculation of air under the fairing to minimize the temperature gradient across it. Bonded construction is the same as the outer fan ducts aft of the intermediate case.

The air seals are similar to current JT8D design except for the first stator air seal. Abradable material was specified at that location to make the seal more tolerant of deflections under maneuver conditions. The calculated resonance diagrams for the 1.0, 1.5, and 2.0 stage labyrinth air seals are shown in Figures A-18, -19 and -20, respectively. The calculated resonance diagram for the 1.0 stator inner shroud is shown in Figure A-21.

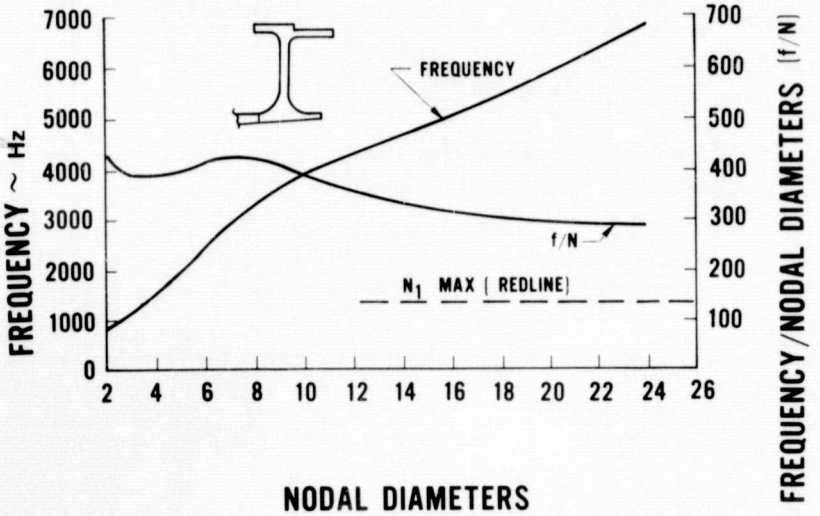

Figure A-18 Calculated JT8D-100 No. 1 Stator Labyrinth Seal Resonance Diagram

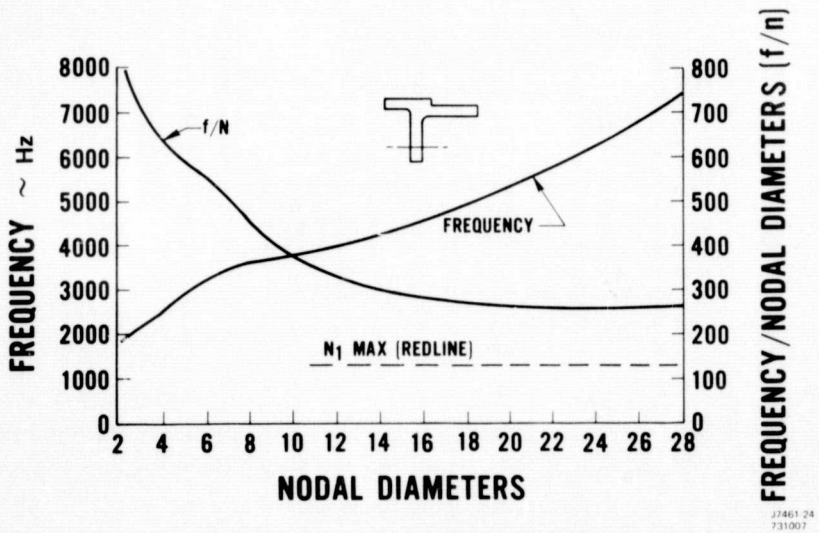

Figure A-19 Calculated JT8D-100 No. 1.5 Stator Labyrinth Seal Land Resonance Diagram

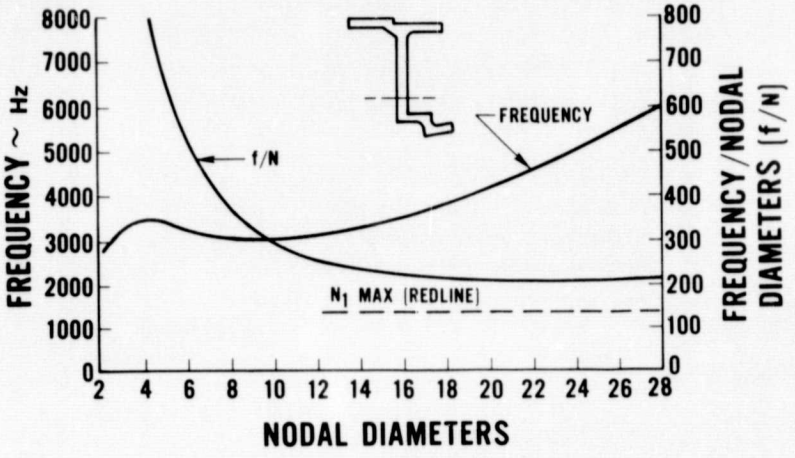

Figure A-20 Calculated JT8D-100 No. 2 Stator Labyrinth Seal Land Resonance Diagram

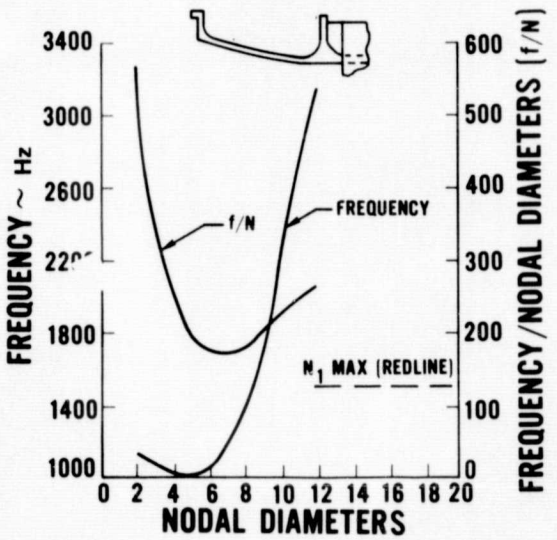

Figure A-21 JT8D-100 LPC No. 1 Stator Inner Shroud Resonance Diagram

The LPC cases and stators are free of engine ordered resonances over the full range of nodal diameters. Figures A-22 through A-26 present the predicted resonance characteristics of these shells. The f/N vs. nodal diameter curves represent the locus of resonance conditions existing on a Campbell diagram. Values of f/N above redline speed (133 hz) indicate that resonance occurs above the engine operating range.

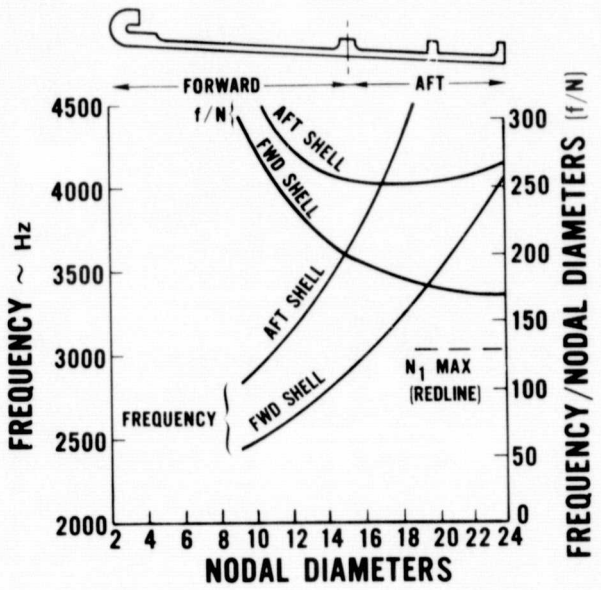

Figure A-22 Calculated JT8D-100 Outer Splitter Resonance Diagram

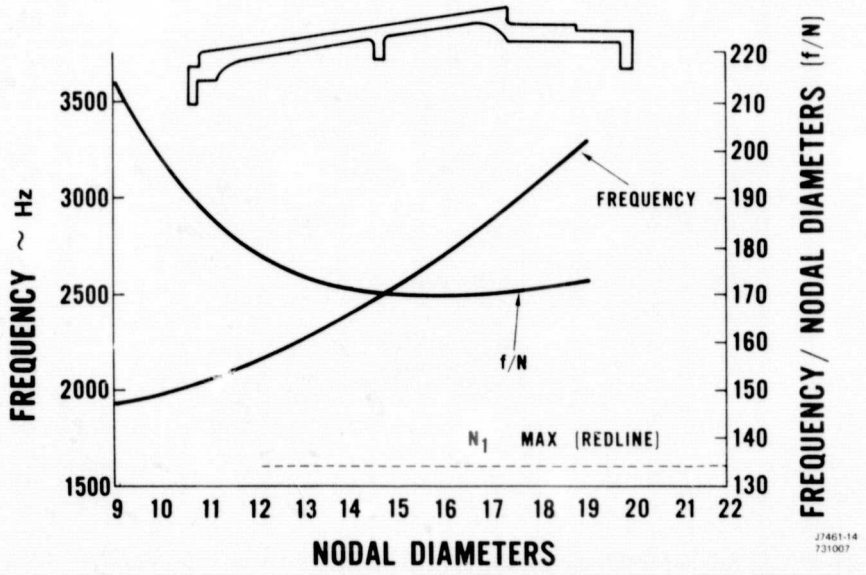

Figure A-23 Calculated JT8D-100 No. 1 Rotor Case Resonance Diagram

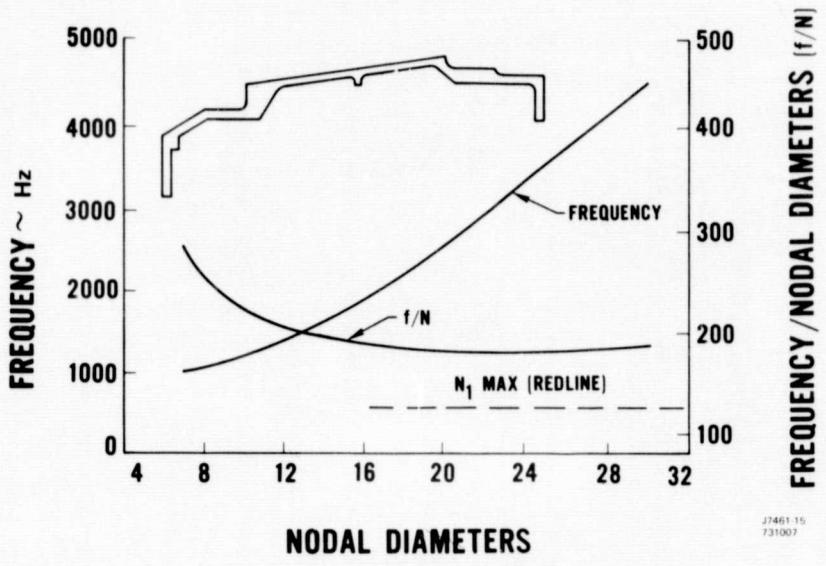

Figure A-24 Calculated JT8D-100 No. 2 Rotor Case Resonance Diagram

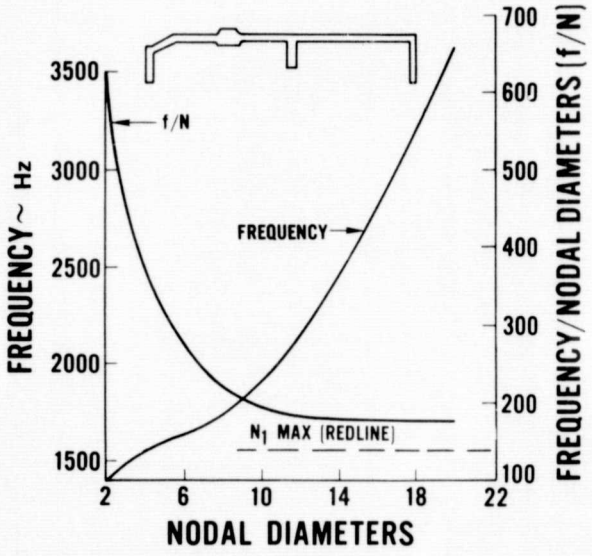

Figure A-25 Calculated JT8D-100 No. 3 Rotor Outer Case – Resonance Diagram

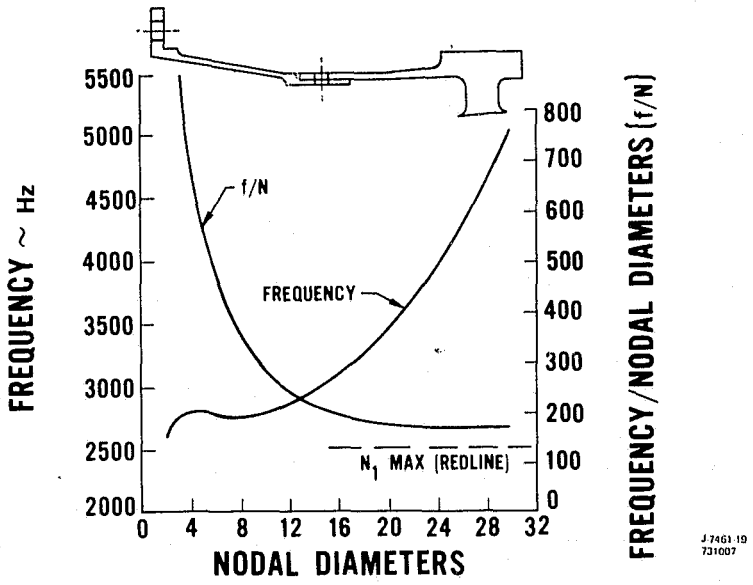

Figure A-26 Calculated JT8D-100 LPC Positioning Ring Resonance Diagram

The No. 1 stator vanes were initially damped by potting the vane root in silicone rubber and riveting the vanes to the stator outer shroud at the tip. However, to alleviate a first stator shroud cracking problem revealed during testing, a more flexible damping system was incorporated. The brackets retaining the vane tips were reduced in thickness from 0.127 cm (0.050 in.) to 0.102 cm (0.040 in.) and the vane tips were completely potted in silicone rubber in order to improve damping at the O.D.

Analysis of the aerodynamic data showed that stator 1 and, to a lesser extent, rotor 1.5 and stator 1.5 were operating closer to a choke condition than anticipated. To help alleviate this condition, the 1st stator was restaggered open three degrees relative to Phase I design goals.

The No. 2.0 stage stator case thickness was increased from 0.190 cm (0.075 inch) minimum to 0.310 cm (0.122 inch) minimum to improve No. 2 stage blade containment capability.

During the development program cracking of the Nos. 1.5 and 2.0 stage stator outer shrouds was encountered. The cause for the cracking was a combination of blade tip rub (as discussed in paragraph (c) page 69) and material residual stresses. A review of the aluminum material fabrication experience indicated the stator material could have considerable residual stresses introduced during cold water quench. These stresses are increased if the forged ring is relatively thick or massive since the center section of the ring cross section cools at a slower rate than the outer periphery. These residual stresses cause the distortion during subsequent machining operations seen on this part. Thus the final machined part will contain residual stresses which can be significant depending on the cross section of the part compared to the cross section of the heat treated forging. To reduce this residual stress problem, the forging can be quenched in hot water. This change reduces the material ultimate strength by approximately 10%, and has been incorporated for some commercial engine parts which exhibited a distortion problem after manufacture.

5) Fan Rotor

Figure A-27 shows the final design of the JT8D-100 titanium fan rotor assembly. This configuration, an extensive modification of the basic JT8D turbofan engine fan rotor assembly, provides approximately twice the fan duct airflow relative to the current JT8D fan and produces additional fan duct thrust at moderately lower pressure. This increase in fan duct thrust permits core engine thrust to be reduced which is required in order to reduce core engine jet velocity and thus jet noise. The fan size was limited by the low turbine shaft torque-carrying capability and work extraction capability of the current three stage low pressure turbine. Current fan tip speed technology is the basis for the upper limit of 8,000 rpm redline for the low rotor speed.

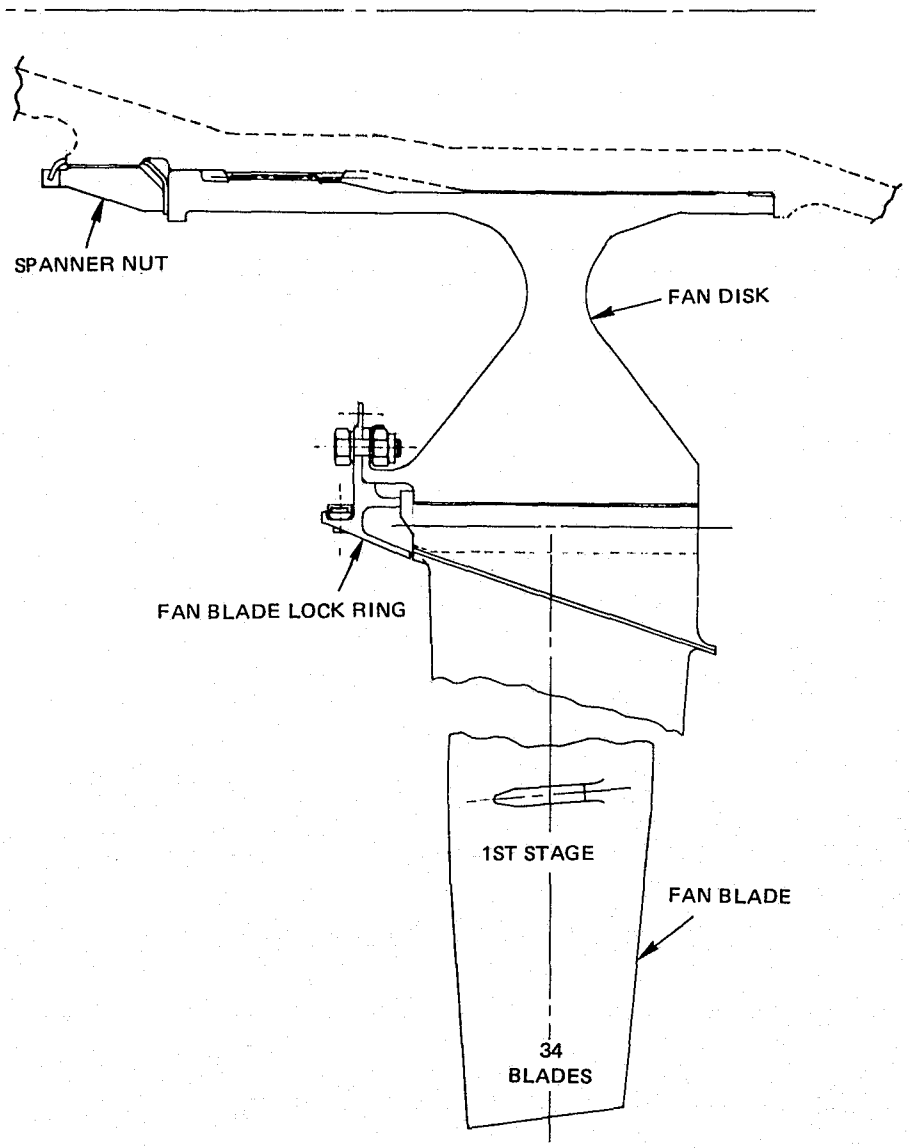

Figure A-27 Final Design of JT8D-100 Fan Rotor Assembly

The major modifications to the current JT8D fan rotor incorporated into the JT8D-100 fan rotor assembly design include:

- A single stage fan [1.25 m (49.2 inch) diameter] replaces the two stage smaller diameter fan rotor [1.03 m (40.5 inch) diameter] to significantly increase fan duct airflow at moderately reduced fan duct pressure.

- The number of fan blades (34) and the axial spacing relative to the inlet guide vanes and the first stator vanes were selected to reduce noise.

- The fan disk is double piloted and splined to the front hub. The disk is readily removable by disengaging the spanner nut.

- A blade lockplate attached to a wing on the fan disk incorporates fan rotor balance and trim balance provisions.

The blade material is AMS 4928, the same material as is used in current JT8D engines.

The final design of the JT8D-100 fan rotor assembly is essentially identical to that presented in Reference 3. The only modification incorporated during the development phase was an increase in the number of retaining bolts securing the blade lock ring. This modification is discussed in Paragraph (c), page 61.

a) Fan Blade

The final design of the fan blade is identical to that presented in Reference 3. Possible modifications to improve the performance characteristics of the blade are discussed later in this section.

The fan blade airfoil is multiple circular arc (MCA) and has a single part-span shroud to damp vibrations. This airfoil design was selected for the fan rotor because it has demonstrated better performance than the double circular arc airfoils used in the present JT8D fan at the higher Mach numbers required for this design. The principle design considerations were to keep the design loading sufficiently low to obtain 25% surge margin and to efficiently pass the flow required at the maximum cruise condition. Overall fan design parameters are compared to previous designs in Table A-VIII. Spanwise distribution of loss is shown in Figure A-28 and is within the design experience of previous successful MCA fans. Surge limits for the fan rotor were based on D factor. The JT8D-100 fan is tip limited, and the tip D factor/aspect ratio correlation was used to set the surge point. Figure A-29 compares D factor vs. % span for the JT8D-100 rotor and the FAA high tip speed design at the design point. An aerodynamic and geometric summary of the fan blade is provided in Table A-IX.

TABLE A-VIII

FAN DESIGN PARAMETERS

	JT8D-100	NASA HIGH TIP SPEED	FAA HIGH TIP SPEED	JT9D MULTIPLE CIRCULAR ARC 105% N_1
Corrected Flow/ Area, Rotor Inlet	205.06 kg/s/m^2 (42.0 lb/sec/ft^2)	202.6 kg/s/m^2 (41.5 lb/sec/ft^2)	204.6 kg/sec/m^2 (41.9 lb/sec/ft^2)	209.5 kg/s/m^2 (42.9 lb/sec/ft^2)
$P_{T2.4}/P_{T2}$ Full Span	1.693	1.762	1.623	1.620
$\eta_{2.4}/2$ Full Span	0.843	0.840	0.848	0.843
$U_{TIP}/\sqrt{\theta_{T2}}$	488 m/s (1600 ft/sec)	488 m/s (1600 ft/sec)	483 m/s (1586 ft/sec)	455 m/s (1492 ft/sec)
Fan Tip Relative Mach No.	1.50	1.59	1.54	1.46
No. Part Span Shrouds	1	0	2	2
Hub/Tip Ratio	0.389	0.5	0.384	0.384
Span/Root Chord	3.57	1.66	4.75	4.59
Span/Tip Chord	2.50	1.66	3.29	3.55
Surge Margin	25%	23%	25%	22%

The shroud is located at 65.7% span and is 0.635 cm (0.250 inch) thick. A shroud interference fit of 0.010 cm (0.004 inch), which creates a 0.2 degree assembly pretwist of the airfoil, was designed into the blade to assure shroud contact at idle speed under adverse tolerance conditions. Flame deposited tungsten carbide (hardcoat) is provided on the contacting surfaces to minimize wear and an anti-galling compound consisting of molybdenum disulfide, antimony trioxide and lead phosphate in a thermo setting resin carrier is applied over the hardcoat to facilitate assembly. An angle of 60° between the contacting surfaces and a tangential line was chosen to provide damping while still avoiding lock-up of the shrouds. When blades are assembled, the shrouds, which are formed by flat planes, will approximate a cone parallel to the air streamliners.

The airfoil is mounted on a platform that forms the entire root flowpath at the fan disk location. The platform is made up of flat planes that intersect at a ridge line, forming an approximation of the desired conical shape. A minimum thickness of 0.127 cm (0.050 inch) is maintained at the platform edges.

The blade and platform are attached to the disk by means of a conventional dovetail, broached 16° off the axial plane to lie as nearly as possible beneath the airfoil root. Fillet radii of 0.368 cm (0.145 inches) have been used to reduce stress concentrations. The front of the attachment has a protruding tang that acts as a stop to prevent blade rearward movement. The axial positions of the airfoil, root attachment and disk web were chosen to provide optimum balance and avoid bending stress. Table A-X presents fan blade properties.

TABLE A-IX(a)

JT8D-100 ROTOR 1 (FAN)
AERODYNAMIC AND GEOMETRIC SUMMARY ON CONICAL SURFACES
34 MULTIPLE-CIRCULAR-ARC AIRFOILS

Percent Total Flow	Hub 0.0	3.0	9.0	15.0	21.0	27.0	Splitting Streamline 33.0	43.3	53.6	63.9	74.2	84.6	94.9	Tip 100.0
Fan Rotor Inlet														
Diameter-m	0.4856	0.5290	0.6023	0.6648	0.7209	0.7726	0.8209	0.8980	0.9691	1.0357	1.0991	1.1604	1.2202	1.2497
V-m/s	200.77	207.62	216.25	219.73	220.36	219.59	218.50	218.27	216.83	213.70	208.79	202.26	195.56	193.31
V_m-m/s	195.10	203.32	214.13	218.96	220.13	219.51	218.49	218.23	216.60	213.14	207.78	200.68	193.32	190.71
V_θ-m/s	−54.90	−46.86	−32.330	−19.20	−10.34	−6.16	−2.22	4.12	9.96	15.37	20.39	25.02	29.22	31.17
β-deg	−13.65	−11.69	−8.04	−4.84	−2.62	−1.58	−0.57	1.07	2.63	4.13	5.63	7.16	8.69	9.39
β'-deg	50.52	50.7	51.62	51.75	52.92	54.47	55.88	57.78	59.52	61.26	63.03	64.85	66.59	67.3
V'-m/s	306.83	321.01	340.85	353.64	365.07	377.73	389.46	409.25	427.07	443.21	458.07	472.38	486.51	494.20
V'_θ-m/s	−236.82	−248.41	−265.19	−277.70	−291.24	−307.40	−322.41	−346.22	−368.07	−368.07	−408.24	−427.42	−446.46	−455.92
U-m/s	189.44	206.36	234.94	259.26	281.21	301.37	320.22	350.30	378.01	403.99	428.73	452.64	475.99	487.48
M	0.611	0.634	0.663	0.674	0.676	0.674	0.670	0.669	0.665	0.654	0.638	0.616	0.594	0.587
M'	0.934	0.980	1.044	1.085	1.121	1.159	1.194	1.255	1.309	1.357	1.399	1.439	1.479	1.501
Fan Rotor Exit														
Diameter-m	0.5512	0.5798	0.6325	0.6820	0.7299	0.7761	0.8205	0.8919	0.9576	1.0190	1.0776	1.1355	1.1958	1.2294
V-m/s	308.94	290.93	267.92	253.47	242.55	233.63	228.17	227.48	227.99	228.72	227.29	223.22	215.93	206.07
V_m-m/s	212.95	210.19	199.30	186.62	176.19	169.24	164.57	165.82	166.22	165.93	162.96	153.87	136.63	117.21
V'_θ-m/s	223.81	201.15	179.06	171.53	166.70	161.06	158.04	155.73	156.05	157.32	158.44	161.71	167.21	169.48
β-deg	46.42	43.74	41.94	42.59	43.41	43.58	43.84	43.2	43.19	43.46	44.19	46.42	50.75	55.33
β'-deg	−2.37	6.79	18.75	26.86	34.83	40.93	45.56	50.21	52.61	55.34	58.11	61.31	66.46	70.29
V'-m/s	213.13	211.68	210.47	209.19	212.08	220.71	230.96	253.83	273.72	291.96	308.46	320.56	328.98	331.54
V'_θ-m/s	8.809	−25.03	−67.67	−94.52	−118.04	−141.67	−162.04	−192.18	−217.47	−240.17	−261.91	−281.21	−299.27	−310.06
U-m/s	215.01	226.18	246.73	266.04	284.74	302.73	320.08	347.91	373.52	397.49	420.34	442.92	466.48	479.55
M	0.894	0.838	0.767	0.722	0.688	0.661	0.643	0.640	0.639	0.640	0.634	0.619	0.594	0.564
M'	0.616	0.610	0.603	0.596	0.602	0.624	0.651	0.714	0.767	0.817	0.860	0.889	0.905	0.907
P_{02}/P_{01}	1.74911	1.71432	1.68333	1.67634	1.67727	1.68120	1.68747	1.69781	1.71138	1.72498	1.72879	1.72128	1.70350	1.67441
$\bar{\omega}$	0.16902	0.13641	0.10156	0.09234	0.07947	0.07705	0.07998	0.08883	0.09912	0.10885	0.12169	0.15303	0.20458	0.24373
D	0.51425	0.52908	0.53810	0.55871	0.56932	0.55971	0.54677	0.51237	0.48529	0.46122	0.44106	0.43228	0.43412	0.43886
EFF-AD	0.85062	0.86781	0.89135	0.90269	0.90689	0.91282	0.90101	0.88738	0.87253	0.85756	0.83628	0.79052	0.72077	0.67053
Fan Geometry														
c-m	0.1059	0.1059	0.1063	0.1072	0.1084	0.1099	0.1115	0.1152	0.1201	0.1255	0.1309	0.1362	0.1412	0.1441
c_f-m	0.0302	0.0317	0.0360	0.0403	0.0446	0.0493	0.0536	0.0607	0.0675	0.0734	0.0794	0.0853	0.0655	0.0937
t/c	0.08700	0.08498	0.07897	0.07278	0.06668	0.06032	0.05150	0.04925	0.04617	0.04076	0.03390	0.02858	0.02345	0.02020
%c at Max. t	50.01096	50.28827	50.75844	51.16664	51.53568	51.87581	52.19383	52.69847	53.16339	53.59895	54.01305	54.41302	54.80473	54.99797
a/c	0.51112	0.50685	0.50331	0.51570	0.53378	0.56034	0.58715	0.57416	0.45510	0.46905	0.68506	0.73318	0.76017	0.76001
RLE-m	0.0006	0.00057	0.00048	0.00041	0.00038	0.00038	0.00038	0.00038	0.00038	0.00038	0.00038	0.00038	0.00038	0.00038
RTE-m	0.00055	0.00050	0.00044	0.00039	0.00036	0.00024	0.00032	0.00029	0.00028	0.00027	0.00027	0.00027	0.00027	0.00027
$\beta'_{1_{SS}}$-deg	52.51071	52.65497	53.1972	53.7534	54.2302	54.89381	55.5600	56.8517	58.0935	59.3683	60.6166	62.0151	63.5939	66.2214
β'^*_1-deg	44.82831	45.11729	45.98997	46.9468	47.9394	49.2013	50.380	52.21875	53.81355	55.66385	56.9807	58.5686	61.67044	64.6330
ϕ-deg	59.2059	51.9108	38.4790	30.2723	23.0441	17.4477	13.1527	8.8723	6.2939	4.8513	3.1961	2.9898	2.7416	4.7110
ϕ_e-deg	57.15515	50.09895	37.11734	29.38626	22.53027	17.23366	13.15274	9.28687	7.10419	6.10397	4.94468	5.17477	5.03368	6.72578
ϕ_f-deg	13.5796	13.9032	12.4790	9.6913	6.8530	4.3062	2.4316	2.9470	4.5581	3.4584	−1.10864	−3.7696	−5.8036	−6.3143
ϕ_{ef}-deg	12.28294	12.8903	11.89912	9.27393	6.60997	4.20156	2.43164	3.17212	5.02148	4.19873	−0.0443	−2.3997	−4.32788	−5.000
ϵ	17.46538	13.97819	8.73466	5.16499	2.81042	1.12215	0.0	−2.14693	−4.23977	−6.4494	−8.71519	−10.60235	−10.97494	−9.46254
σ	2.2160	2.0713	1.8657	1.7233	1.6177	1.5361	1.4703	1.3924	1.3482	1.3209	1.3009	1.2839	1.2641	1.2576

ORIGINAL PAGE IS
OF POOR QUALITY

TABLE A-IX(b)

JT8D-100 ROTOR 1 (FAN)
AERODYNAMIC AND GEOMETRIC SUMMARY ON CONICAL SURFACES
34 MULTIPLE-CIRCULAR-ARC AIRFOILS

Percent Total Flow	Hub 0.0	3.00	9.00	15.00	21.0	27.0	Splitting Streamline 33.0	43.3	53.6	63.9	74.2	84.6	94.9	Tip 100.00
							Fan Rotor Inlet							
Diameter – in	19.120	20.827	23.712	26.174	28.382	30.417	32.319	35.355	38.152	40.774	43.271	45.684	48.041	49.200
V – ft/sec	658.68	681.17	709.49	720.89	722.96	720.45	716.87	716.10	711.37	701.11	685.00	663.58	641.60	634.21
V_m – ft/sec	640.08	667.05	702.51	718.36	722.21	720.18	716.83	715.97	710.63	699.29	681.70	658.41	634.24	625.70
V_θ – ft/sec	–180.11	–153.73	–106.07	–62.98	–33.93	–20.21	–7.27	13.52	32.69	50.44	66.90	82.08	95.88	102.28
β – deg	–13.65	–11.69	–8.04	–4.84	–2.62	–1.58	–0.57	1.07	2.63	4.13	5.63	7.16	8.69	9.39
β' – deg	50.52	50.7	51.62	51.75	52.92	54.47	55.88	57.78	59.52	61.26	63.03	64.85	66.59	67.3
V' - ft/sec	1006.66	1053.17	1118.26	1160.24	1197.75	1239.27	1277.77	1342.70	1401.16	1454.10	1502.87	1549.18	1596.17	1621.40
V'_θ - ft/sec	–776.96	–814.99	–870.04	–911.10	–955.52	–1008.53	–1057.76	–1135.88	–1207.59	–1274.91	–1339.36	–1402.30	–1464.75	–1495.81
U – ft/sec	621.53	677.03	770.79	850.58	922.61	988.75	1050.60	1149.29	1240.20	1325.43	1406.60	1485.03	1561.65	1599.33
M	0.611	0.634	0.663	0.674	0.676	0.674	0.670	0.669	0.665	0.654	0.638	0.616	0.594	0.587
M'	0.934	0.980	1.044	1.085	1.121	1.159	1.194	1.255	1.309	1.357	1.399	1.439	1.479	1.501
							Fan Rotor Exit							
Diameter – in	21.700	22.828	24.902	26.851	28.738	30.554	32.305	35.114	37.699	40.117	42.424	44.703	47.080	48.400
V – ft/sec	1013.57	954.50	879.01	831.61	795.77	766.49	748.59	746.33	748.00	750.39	745.69	732.34	708.43	676.07
V_m – ft/sec	698.66	689.61	653.87	612.28	578.06	555.24	539.94	544.03	545.35	544.39	534.65	504.83	448.25	384.56
V_θ – ft/sec	734.29	659.93	587.47	562.75	546.90	528.41	518.50	510.92	511.96	516.14	519.80	530.53	548.58	556.05
β – deg	46.42	43.74	41.94	42.59	43.41	43.58	43.84	43.2	43.19	43.46	44.19	46.42	50.75	55.33
β' – deg	–2.37	6.79	18.75	26.86	34.83	40.93	45.56	50.21	52.61	55.34	58.11	61.31	66.46	70.29
V' – ft/sec	699.26	694.48	690.53	686.33	695.79	724.11	757.73	832.78	898.04	957.89	1012.02	1051.70	1079.33	1087.73
V'_θ – ft/sec	28.90	–82.12	–222.00	–310.09	–387.27	–464.80	–531.62	–630.52	–713.50	–787.95	–859.27	–922.61	–981.85	–1017.27
U – ft/sec	705.40	742.05	809.48	872.84	934.17	993.22	1050.13	1141.44	1225.46	1304.09	1379.07	1453.14	1530.43	1573.32
M	0.894	0.838	0.767	0.722	0.688	0.661	0.643	0.640	0.639	0.640	0.634	0.619	0.594	0.564
M'	0.616	0.610	0.603	0.596	0.602	0.624	0.651	0.714	0.767	0.817	0.860	0.889	0.905	0.907
P_{02}/P_{01}	1.74911	1.71432	1.68333	1.67634	1.67727	1.68120	1.68747	1.69781	1.71138	1.72498	1.72879	1.72128	1.70350	1.67441
$\overline{\omega}$	0.16902	0.13641	0.10156	0.09234	0.07947	0.07705	0.07998	0.08883	0.09912	0.10885	0.12169	0.15303	0.20458	0.24373
D	0.51425	0.52908	0.53810	0.55871	0.56932	0.55971	0.54677	0.51237	0.48529	0.46122	0.44106	0.43228	0.43412	0.43886
EFF-AD	0.85062	0.86781	0.89135	0.90269	0.90689	0.91282	0.90101	0.88738	0.87253	0.85756	0.83628	0.79052	0.72077	0.67053
							Fan Geometry							
c – in	4.17	4.17094	4.18706	4.21968	4.26799	4.32653	4.39080	4.53428	4.72643	4.93905	5.15312	5.36387	5.55835	5.67500
c_f – in	1.19	1.24861	1.41928	1.58654	1.75539	1.93956	2.11112	2.39026	2.65737	2.89160	3.12601	3.35877	3.57698	3.69000
t/c	0.08700	0.08498	0.07897	0.07278	0.06668	0.06032	0.05150	0.04925	0.04617	0.04076	0.03390	0.02858	0.02345	0.02020
% c at Max. t	50.01096	50.28827	50.75844	51.16664	51.53568	51.87581	52.19383	52.69847	53.16339	53.59895	54.01305	54.41302	54.80473	54.99797
a/c	0.51112	0.50685	0.50331	0.51570	0.53378	0.56034	0.58715	0.57416	0.45510	0.46905	0.68506	0.73318	0.76017	0.76001
RLE – in	0.02450	0.02235	0.01872	0.01600	0.01507	0.01500	0.01500	0.01500	0.01500	0.01500	0.01500	0.01500	0.01500	0.01500
RTE – in	0.02150	0.01953	0.01723	0.01524	0.01412	0.01326	0.01250	0.01158	0.01106	0.01058	0.01050	0.01050	0.01050	0.01050
$\beta'_{1\ ss}$ –deg	52.51071	52.65497	53.1972	53.7534	54.2302	54.8938	55.5600	56.8517	58.0935	59.3683	60.6166	62.0151	63.5939	66.2214
$\beta'_1{}^*$ – deg	44.82831	45.11729	45.98997	46.9468	47.9394	49.2013	50.380	52.21875	53.81355	55.66385	56.9807	58.5686	61.67044	64.6330
ϕ – deg	59.2059	51.9108	38.4790	30.2723	23.0441	17.4977	13.1527	8.8723	6.2939	4.8513	3.1961	2.9898	2.7416	4.7110
ϕ_e – deg	57.15515	50.09895	37.11734	29.38626	22.53027	17.23366	13.15274	9.28687	7.10419	6.10397	4.94468	5.17477	5.03368	6.72578
ϕ_f – deg	13.5796	13.9032	12.4790	9.6913	6.8530	4.3062	2.4316	2.9470	4.5581	3.4584	–1.10864	–3.7696	–5.8036	–6.3143
ϕ_{ef} – deg	12.28294	12.8903	11.89912	9.27393	6.60997	4.20156	2.43164	3.17212	5.02148	4.19873	–0.0443	–2.3997	–4.32788	–5.000
ϵ	17.46538	13.97819	8.73466	5.16499	2.81042	1.12215	0.0	–2.14693	–4.23977	–6.4494	–8.71519	–10.60235	–10.97494	–9.46254
σ	2.2160	2.0713	1.8657	1.7233	1.6177	1.5361	1.4703	1.3924	1.3482	1.3209	1.3009	1.2837	1.2641	1.2576

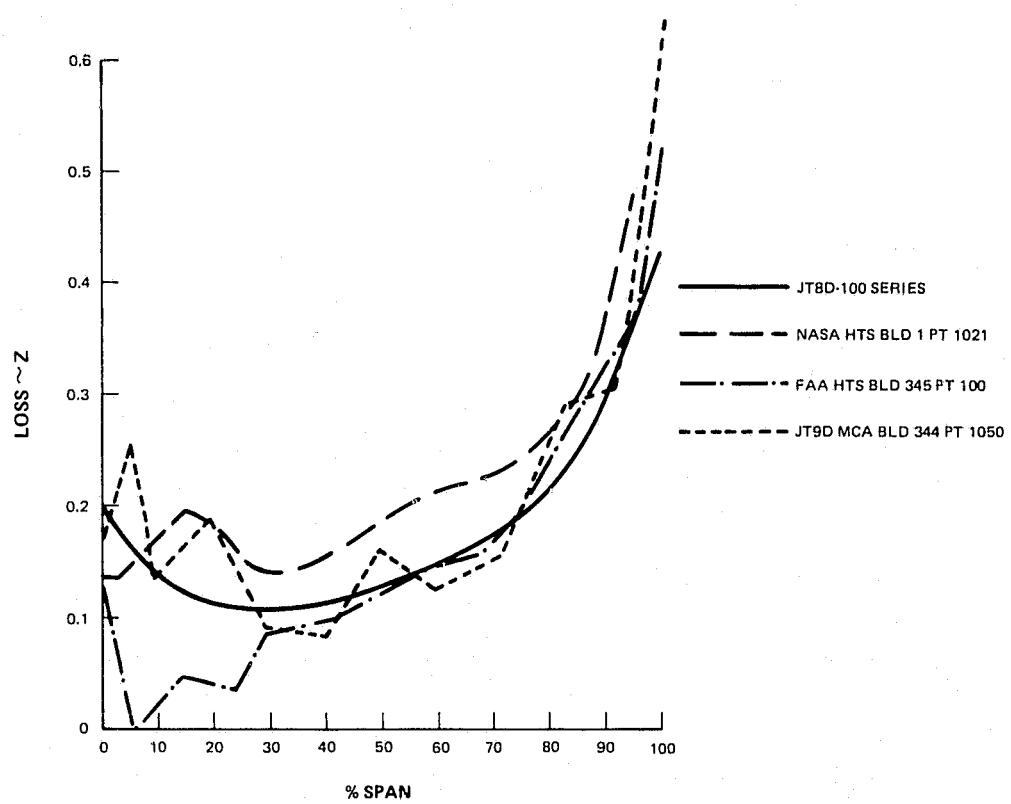

Figure A-28 Predicted JT8D-100 Fan Rotor Loss

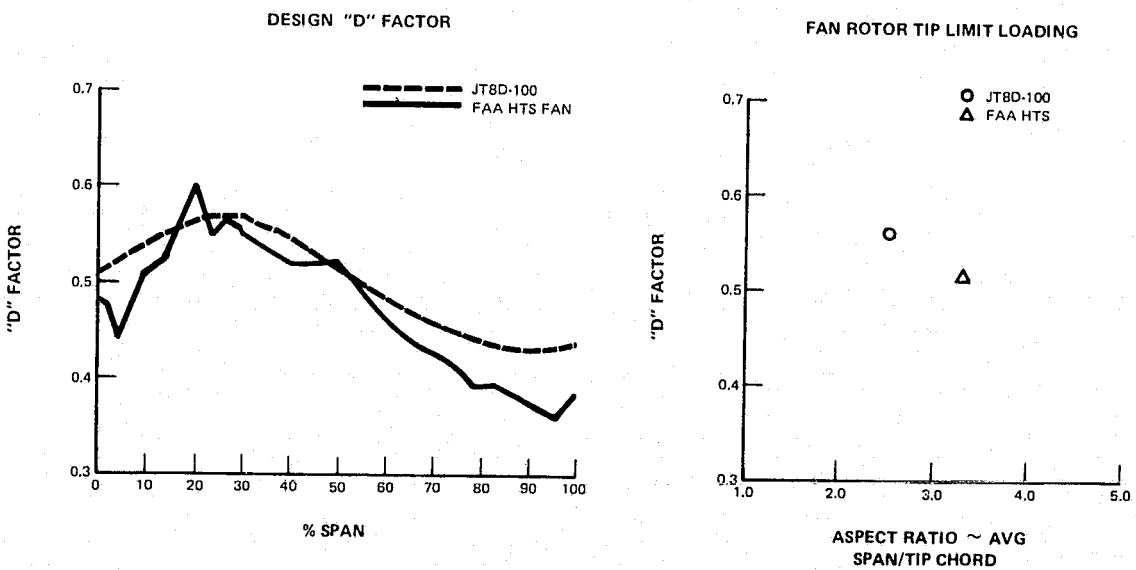

Figure A-29 Predicted JT8D-100 Fan Rotor "D" Factor and Tip Loading

TABLE A-X

FAN BLADE PROPERTIES

Material	AMS 4928
Modulus of Elasticity	10.8×10^{10} N/m^2 (15.7×10^6 psi)
Density	4.43×10^3 kg/m^2 (0.160 lb per in^3)
Poissons Ratio	0.35
No. of Blades	34
Airfoil Series	Multiple Circular Arc
Root Chord – C_r	0.101 m (3.974 inch)
Tip Chord – C_t	0.144 m (5.679 inch)
Airfoil Length	0.361 m (14.2 inch)
Aspect Ratio	3.57
Root Thickness Ratio – t/Cr	0.09
Tip Thickness Ratio – t/Ct	0.02
Chord Angle – Root	73.7605°
Chord Angle – Tip	22.7131°
Shroud Location	65.7% 0.497 m (19.58 inch)
Shroud Angle From Tangential	60°
Shroud Fit – Nom.	0.010 cm (0.004 inches) Tight
Shroud Thickness	0.635 cm (0.250 inch)
Rad_{root}/Rad_{tip}	0.418

Results of the development testing conducted during this phase of the program verified that maximum vibratory stress levels were relatively low, as anticipated. A summary of fan vibratory stresses versus various inlet and exhaust configurations is shown in Table A-XI.

Maximum fan blade static stresses agreed well with predicted levels except as follows: The airfoil root leading edge stress was considerably lower than predicted and probably caused by the airfoil root leading edge overhanging the attachment. This effect was not considered in the original analysis. The below-shroud airfoil stress was considerably higher than predicted by the original analysis. A subsequent revised analysis, which properly accounts for shroud boundary conditions, adequately calculates this stress. The magnitude of the below shroud stress does not create a life limiting situation at this location. A summary of measured fan static stresses is shown in Table A-XI.

TABLE A-XI

JT8D-100 MEASURED FAN BLADE STRESSES

STATIC STRESSES

Location Number (See Illustrations Below)	Gage Location	Maximum Measured Stress @ 7566 RPM N_1 $N/m^2 \times 10^{-7}$	(KSI)
1	Root Maximum Thickness, Convex	34.47	(50.0)
2	Root, ¾ Chord, Convex	68.60	(99.5)
3	Root Trailing Edge, Concave	-17.85	(-25.9)
4	Root Leading Edge, Concave	11.72	(17.0)
5	Below Shroud, 1.2" From Trailing Edge, Concave	70.33	(102.0)
6	Shroud Surface	39.09	(56.7)

VIBRATORY STRESSES			STRESS ~ $N/m^2 \times 10^{-6}$ (KSI)						
Tailpipe Area – m^2 (ft^2)			0.77 (8.3)	1.00 (10.8)	0.71 (7.6)	0.77 (8.3)	0.77 (8.3)	0.77 (8.3)	0.77 (8.3)
Inlet Configuration			Clean	Clean	Clean	18.0 m/sec (35 kt) X-wind Center Engine	15.4 m/sec (30 kt) X-wind Pod Engine	S. L. S. Center Engine	midspan Radial
Loc No. (See Illus. Below)	Gage Location	Excitation Order							
1	Root Max. Thickness Convex	3E	15.2 (2.2)	14.5 (2.1)	15.9 (2.3)	20.7 (3.0)	24.8 (3.6)	17.6 (2.55)	14.5 (2.1)
7	Above Shroud Trailing Edge, Co. vex	3E	13.1 (1.9)	16.5 (2.4)	13.1 (1.9)	19.3 (2.8)	21.4 (3.1)	16.5 (2.4)	17.2 (2.5)
4	Root Leading Edge, Concave	3E	13.8 (2.0)	13.8 (2.0)	16.5 (2.4)	23.4 (3.4)	20.0 (2.9)	26.2 (3.8)	17.2 (2.5)

ILLUSTRATIONS SHOWING GAGE LOCATIONS

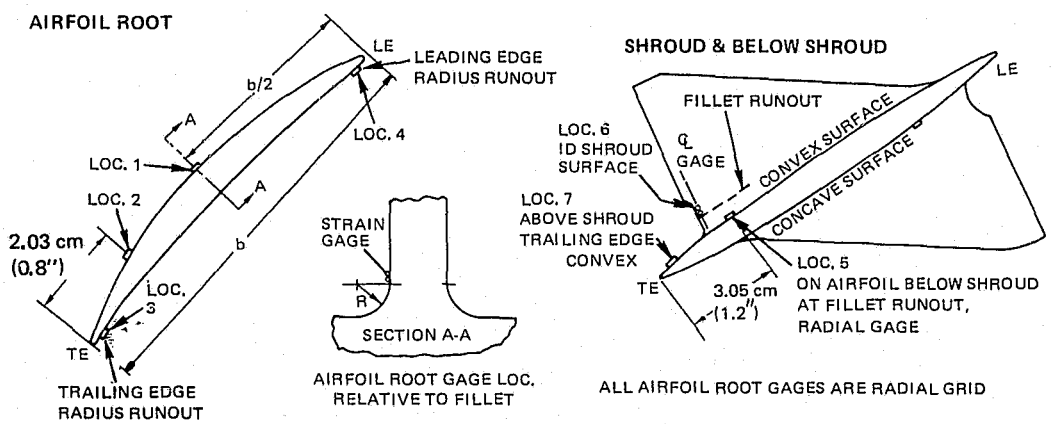

ORIGINAL PAGE IS
OF POOR QUALITY

Testing during this phase of the program verified that overall fan O.D. performance with the LPC on its nominal operating line (NOL) met design goals with the exception of producing 17% rather than 25% surge margin at the design point. Variations in LPC operating line (bypass ratio effects) caused little change in fan O.D. performance. Fan I.D. performance with the LPC on its NOL was low in pressure ratio and efficiency.

Fan losses from the root to the part span shroud were substantially higher than the predicted values but were lower than predicted from shroud to tip (Figure A-30). This result is consistent with the overall performance data. The high losses in the I.D. section produced the decreased efficiency and pressure ratio while the high and low losses bracketing the shroud cancelled each other to produce the predicted fan O.D. efficiency.

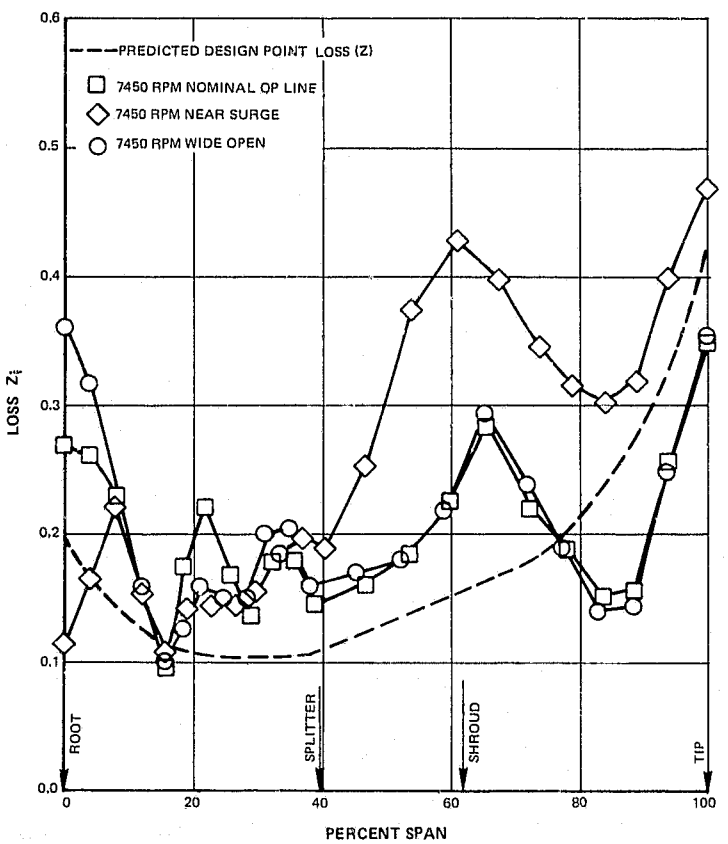

Figure A-30 JT8D-100 Full Span Fan Rotor Loss

Fan tip loading was substantially below its predicted limit and at near surge a loading peak appeared near the part span shroud (Figure A-31). It had been assumed that the loading in the tip region would set surge, but the peak level near the shroud is close to the maximum values seen on other single stage fans implying that the shroud region is setting surge.

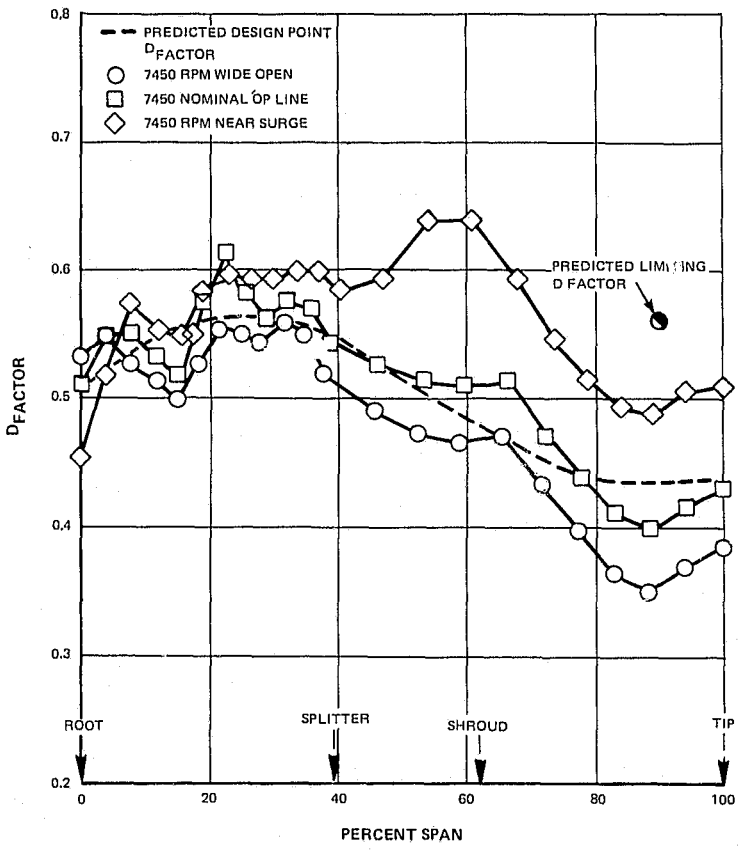

Figure A-31 JT8D-100 Full Span Fan Rotor Loading

Improvements to fan performance could be achieved by restaggering the fan blade root-to-shroud section and redesigning the fan shroud section (conical shroud) to reduce part span shroud losses.

During the engine development program abnormal fan performance modes characterized by a loss in flow capacity up to 5% and a loss in fan O.D. efficiency of up to 8% were observed. These modes occurred only at low rotor speeds above 7000 rpm. There was no measureable loss in stability. The abnormal performance was not observed during the fan/LPC rig program. Spanwise performance data taken during abnormal performance conditions indicated that, while the entire fan duct portion of the fan blade was affected, the greatest loss in efficiency occurred just under the part-span shroud. While no conclusive evidence exists, it appears that some complex mechanism produces shock wave spillage or partial span rotating stall when the fan operates in this mode. Possible causes for the spillage are condensation shocks in the presence of humidity, inlet vortices, and/or complex system unsteadiness. Rotating stall could be caused by FEGV and duct system instabilities, air leakage around the FEGV root, discontinuities in the duct I.D. wall aggravated by thermals or ovalization of cases. These hypotheses have not been investigated under controlled conditions with adequate instrumentation; consequently, configuration changes have not been established.

b) Fan Disk

The fan disk is made from PWA 1215 titanium alloy. The diameter of the cylindrical bore portion of the disk was determined by rotor critical speed requirements. The length of the cylinder provides isolation of the snaps and spline from the radial growth of the disk. The main concern in the spline area was wear resulting from uneven load distribution. To minimize this, (1) the length of the spline was chosen to give an average bearing pressure of 34.47 x 10^6 N/m^2 (5000 psi), and (2) the thickness of the cylinder in this spline area was chosen to closely match the flexibility of the shaft. An anti-galling compound is used on the spline. Refer to Figure A-32. The rim has elliptical dovetail slots. These blade slots are shot peened.

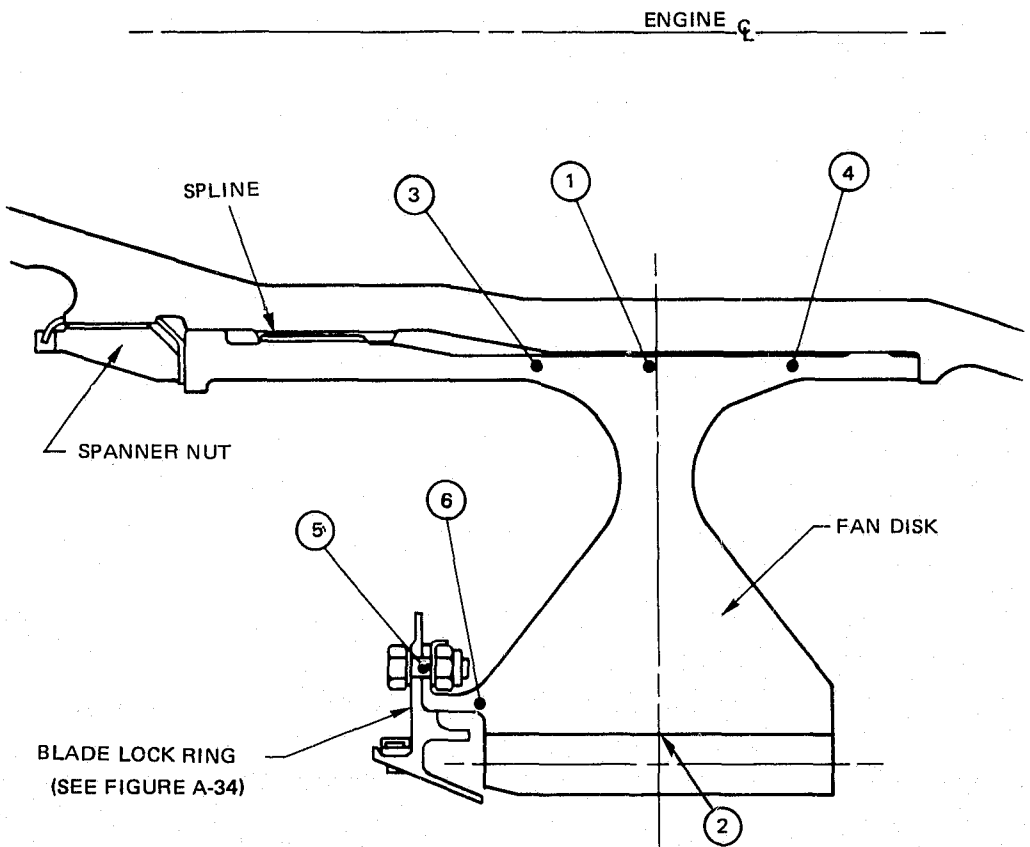

Figure A-32 JT8D-100 Fan Disk and Attachments

The final rim and web configuration gives a 6.5% 2E 1st mode margin and a 1 nodal diameter 2E 1st mode resonance at 5670 rpm, well below normal engine operating range. (See Figure A-33.) Detail balance is obtained by removing metal at the O.D. of the disk rim.

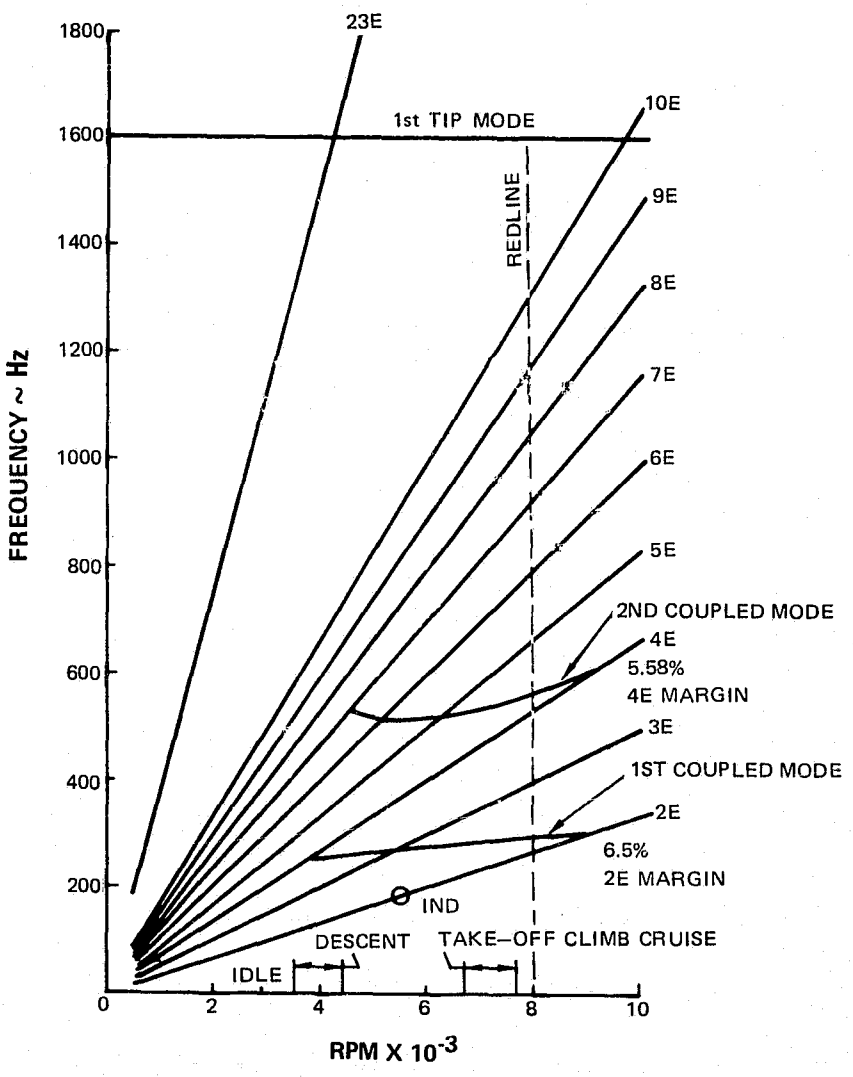

Figure A-33 Calculated JT8D-100 Fan Resonance Diagram

c) Blade Lock Ring

The blade lock ring shown in Figure A-34 holds the fan blades in position against the forward lands during engine operation and provides flanges for attaching trim balance and stage

balance weights. The trim balance weights can be attached to the outer set of balance holes with existing tools through a cutout at the bottom of the inlet case fairing. Stage balance can be accomplished through the same set of holes.

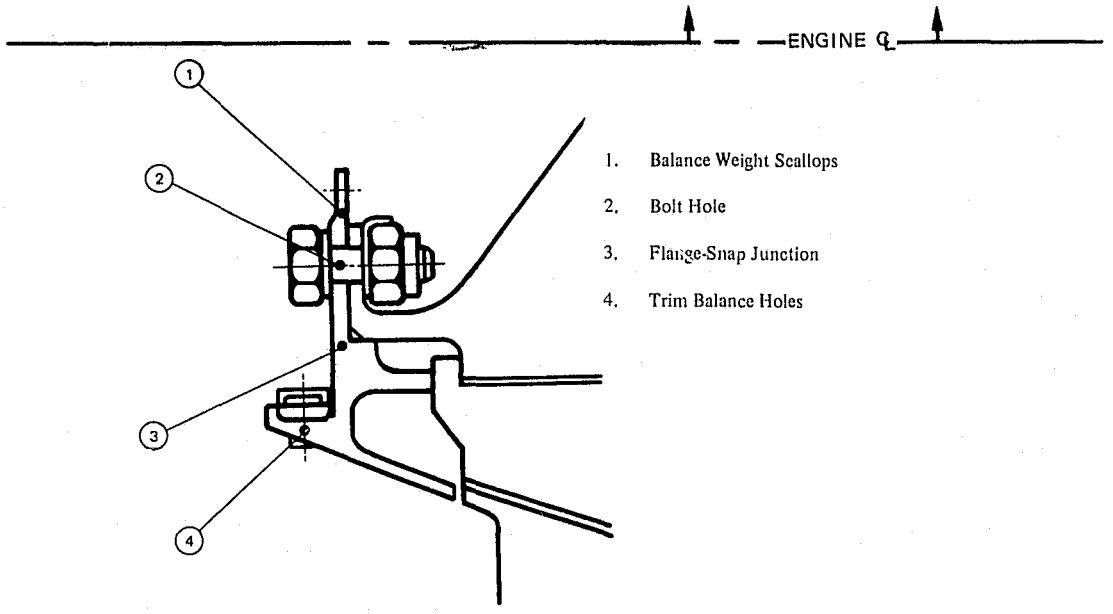

Figure A-34 JT8D-100 Fan Blade Lock Ring

Balancing of the lock ring is achieved by removing material at the rear of the conical surface. Provision for removing the lock ring is provided by a puller rail located at the front of the conical surface. The ring is fabricated from AMS4928 material and is secured to the fan disk by 60 bolts. This attachment scheme is a modification of the scheme presented in Reference 3.

Due to secondary damage resulting from a rig shaft failure which occurred during the blade containment test described in Paragraph (2), page 27, the fan blade lock ring was fractured. The blade lock ring retention scheme was reviewed and found to be marginal. Consequently, the design was modified to incorporate 60 retaining bolts rather than 20 as specified in the preliminary design.

d) Spanner Nut

The spanner nut, shown in Figure A-32, holds the fan rotor in position during engine operation. It is fabricated from AMS 5616 stainless steel. It incorporates Acme threads (16 per inch) rather than buttress threads to reduce cost and improve dimensional control.

The threads and thrust face of the nut are treated with an anti-galling compound to lower friction during torquing and prevent galling during operation. The nut is locked in place by bending two AMS 5510 tabs into the torque slots on the forward portion of the nut. These tabs will be bent in the same direction by centrifugal pull.

6) Low-Pressure Compressor (LPC) Rotor

Figure A-35 shows the final configuration of the JT8D-100 LPC rotor. It consists of a single fan stage and six core stages simply supported between the No. 1 (inlet case) roller bearing and the No. 2 (intermediate case) dual-ball thrust bearing. The LPC rotor incorporates substantial design changes from the basic JT8D turbofan engine design in order to best achieve the overall noise reduction, retrofit, reliability, maintainability, and performance goals of the quiet engine program. The more significant changes are:

- Replacement of the present two stage fan with a larger diameter single stage fan plus two new LPC compressor stages.
- The fan and the 1.5 stage rotor are not sandwiched in as an integral part of the structural rotor backbone. They have been configured for ease of removal in the event of ingestion damage.
- The distance between the supporting bearings has been increased 45% from 0.67 m (26.4 inches) to 0.97 m (38.1 inches). This is partly due to the additional rotor stage, but noise reduction was also a factor in setting this distance.

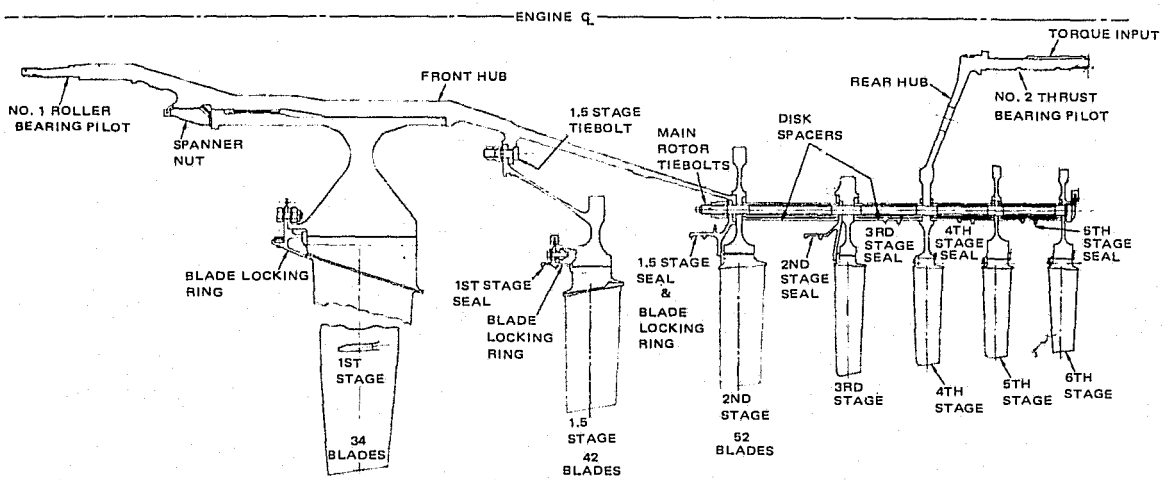

Figure A-35 JT8D-100 Fan, Low Pressure Compressor Rotor Cross Section

Reduced jet noise was the prime design objective. The larger fan is the mechanism through which turbine work is increased and jet velocity reduced, without loss in performance. The larger fan itself is a potential source of increased noise. To minimize this possibility, generous axial spacing has been used in the fan area. Also, the number of airfoils per stage has been carefully selected in order to achieve a minimum noise level.

The blade and disk assemblies of the last four stages, except where noted below, are common with corresponding parts in the current JT8D front compressor.

The final design of the LPC rotor is identical to the preliminary configuration presented in Reference 3 except for increased 1.5 and 2.0 stage tip clearances and modifications to these blade tips to reduce the impact of increased clearances on engine performance. These modifications as well as further analyses conducted during this phase of the program are discussed in Paragraph (c) page 69.

The basic rotor structure between the No. 1 and No. 2 bearings consists of:

- A long front hub-shaft extending from the No. 1 bearing pilot to the 2.0 stage disk,
- Cylindrical spacers from the 2.0 to the 3.0 and 3.0 to the 4.0 stage disks,
- The 2.0 and 3.0 stage disks.
- A conical rear hub which is integral with the 4.0 stage compressor disk. The rear of the cone extends aft to form the No. 2 bearing journal. At this location the low turbine shaft is splined to the LPC rotor. Driving torque from the turbine is applied here, and low rotor thrust is transmitted to the static structure via the thrust bearing.

The No. 1.0 stage (fan) rotor is double-piloted and splined to the front hub, and is retained by a spanner nut. The 1.5 stage rotor is fastened to a flange on the front hub located just aft of the No. 1.0 disk rear pilot. An integral cone, extending forward from the bore of the No. 1.5 disk, is attached to the hub flange with short tiebolts.

The Nos. 2.0 and 3.0 stage rotors are conventional pancake-type disks sandwiched directly into the basic rotor structure. The 5.0 and 6.0 rotors are overhung aft of the 4.0 stage hub. They are supported by cylindrical spacers. Twelve long tiebolts hold together the parts forming the basic rotor structure and the rear overhung stages.

In all new stages, the blades are secured to the disks by bolted-on annular plates or rings, similar to that found in the 3rd stage of current D-9, D-11 and D-15 JT8D models. Individually bent sheet metal tablocks serve this function in the final three (existing) stages.

The 1.0 interstage rotating knife-edge seal is an integral extension of the 1.5 stage blade locking ring. The 1.5 stage seal is integral with the 2.0 stage blade lock, as is the 2.0 stage seal with the 3.0 stage blade lock. The 3.0 through 5.0 stage seal knife-edges are part of the disk spacers.

The 3.0 to 4.0 stage disk spacer is common with current engines as is the 5.0 to 6.0 spacer. The 3.0 stage disk may be made by reoperating either the present steel or titanium parts, but only the current steel 4.0 stage hub-disk can be used as discussed in Paragraph i), page xx.

When a steel 3.0 stage disk is used, a thicker flange version of the blade lock-seal ring must be mated with it. The 4.0 to 5.0 disk spacer, the tiebolts, and all parts forward of the 3.0 stage blade locking ring are peculiar to the JT8D-100 engine.

Low compressor discharge pressurized air is bled into the center of the rotor drum through holes in the rear hub and then through holes at the forward end of the front hub to pressurize the No. 1 bearing compartment labyrinth seals.

The front hub is dynamically balanced in detail by removing material at two locations near the ends. The 1.5 stage disk and blade assembly is statically balanced by selective blade positioning. Subsequent correction for unbalance due to the addition of blade lock-seal attaching hardware may be made by attaching classified counterweights to the lock ring. The 4.0 stage blade-hub sub-assembly is balanced by the addition of trapped plugs and/or by blade position selection. The remaining four core blade-disk sub-assemblies are statically balanced by blade position selection alone. The entire primary compressor assembly (fan rotor omitted) is dynamically balanced by adding classified weights at the 1.5 and 6.0 stages. The independently balanced fan rotor assembly is then added without additional correction. A final trim correction may be made, if needed, in a plane at the fan stage after the entire rotor system is checked for vibration at operating speeds.

a) LPC Rotor Vibration Characteristics

The calculated stiff bearing critical speed (Figure A-36) of the fan-LPC rotor is greater than 20% above maximum operating speed. The two rotor hubs are stiffness-limited members. It was determined that the titanium rear hubs (4.0 stage hub-disk) in the field are not practical for use in the JT8D-100, due to their low modulus of elasticity.

The LPC rotor excited critical speed modes, Figures A-37, -38, and -39), as determined by a rotor-frame analysis (Figure A-40 and Table A-XII), indicate the presence of a new mode in the engine running range. The percentage of strain energy in this mode, however, is acceptable. In this respect, the rotor has a low sensitivity to unbalance, and will not constitute a vibration problem. Other modes in the operating range parallel those in existing JT8D models and will be similarly controlled through damping and trim balancing.

The short tiebolts for the 1.5 stage rotor assembly have adequate blade loss capability and are preloaded to avoid separation of rotor components during operation. Close fits are provided to minimize any possibility of rotor shift and resulting unbalance.

The JT8D-100 LPC rotor operates at lower RPM and similar temperature relative to the current models. All common disks, blades, spacers, hubs, etc. have equal or greater durability than in current applications.

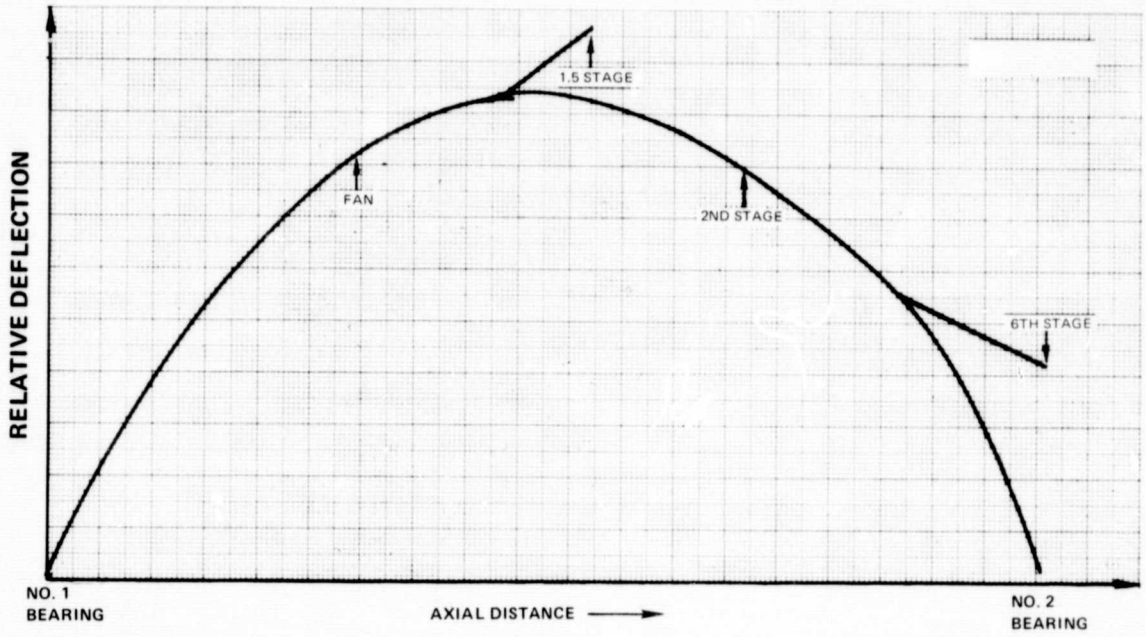

Figure A-36 Predicted JT8D-100 Low Rotor Excited Critical Speed, 9698 N_1

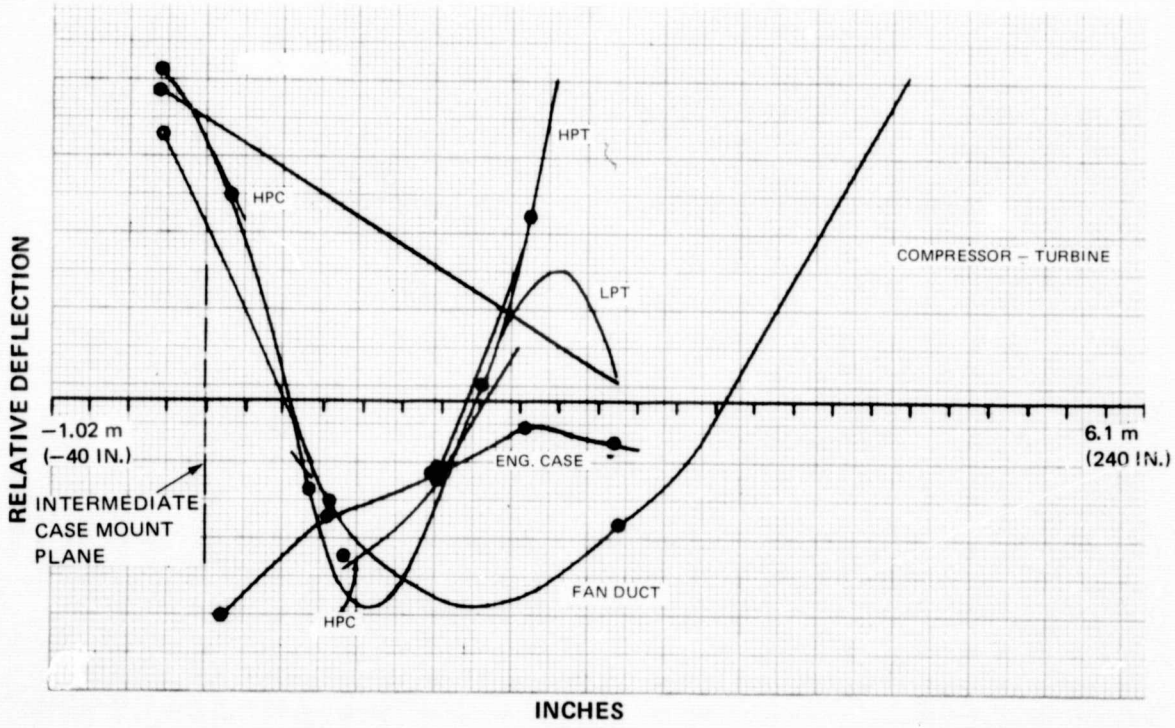

Figure A-37 Predicted JT8D-100 Low Rotor Excited Critical Engine Speed, 5771 N_1

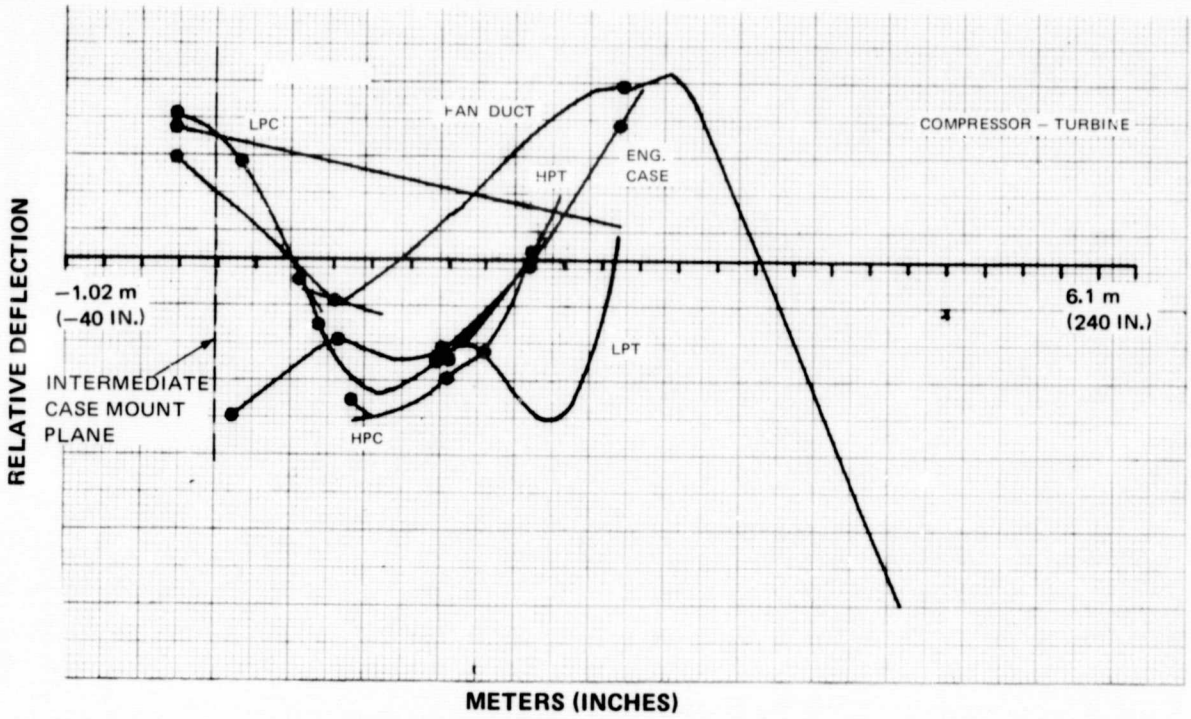

Figure A-38 Predicted JT8D-100 Low Rotor Excited Critical Engine Speed, 7208 N_1

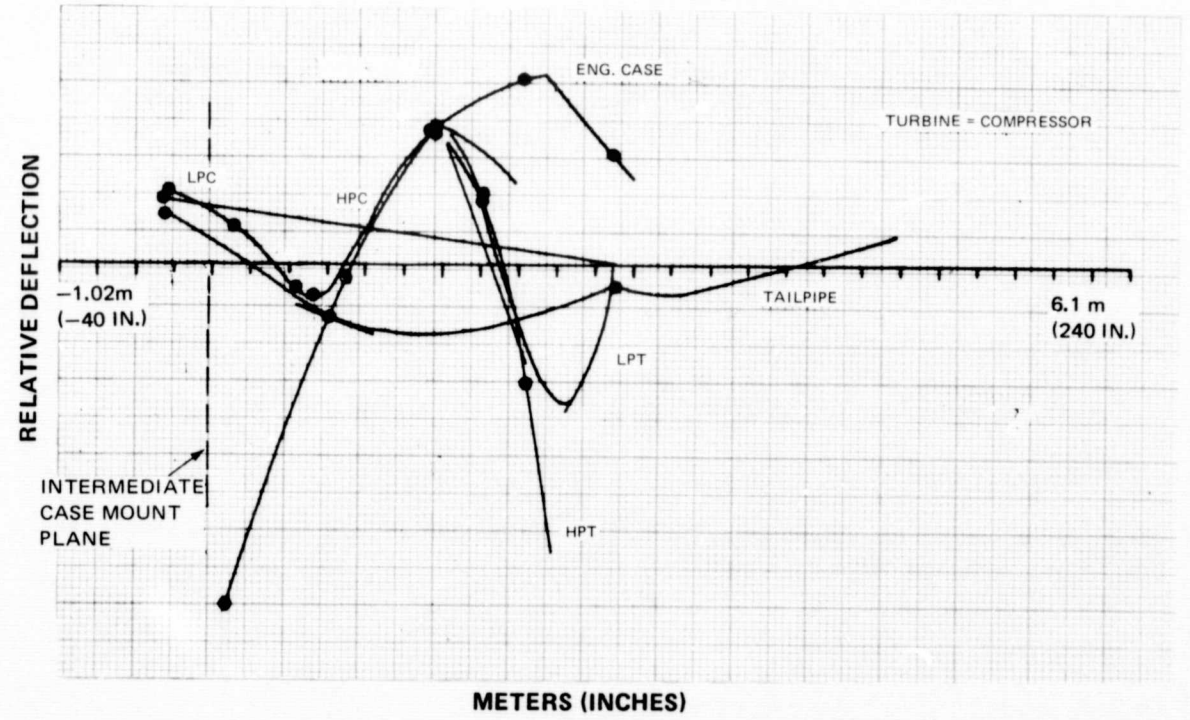

Figure A-39 Predicted JT8D-100 Low Rotor Excited Critical Engine Speed, 7659 N_1

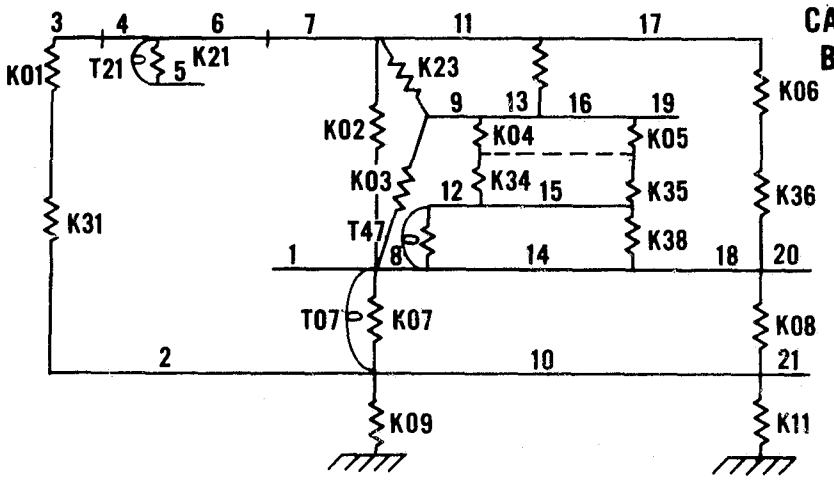

CALCULATED OR TESTED BEARING SPRINGRATES

K01 =	52.5×10^7	(3.0×10^6)
K02 =	13.8×10^7	(7.89×10^5)
K03 =	10.9×10^7	(6.21×10^5)
K04 =	35.0×10^7	(2.0×10^5)
K05 =	7.7×10^7	(4.4×10^6)
K06 =	7.7×10^7	(4.4×10^5)
K07 =	61.2×10^7	(3.5×10^6)
K08 =	7.0×10^7	(4.0×10^5)
K09 =	1.7×10^7	(1.0×10^5)
K11 =	1.7×10^7	(1.0×10^5)
K21 =	17.50×10^9	(1.0×10^8)
K23 =	1.5×10^7	(8.76×10^4)
K31 =	17.5×10^7	(1.0×10^6)
K34 =	39.75×10^8	(2.27×10^7)
K35 =	7.7×10^7	(4.4×10^5)
K36 =	5.6×10^7	(3.22×10^5)
K38 =	8.8×10^7	(5.0×10^5)
K45 =	55.8×10^7	(3.3×10^6)
K47 =	70.0×10^7	(4.0×10^6)
T07 =	2.5×10^6	(2.18×10^7)
T21 =	1.1×10^9	(1.0×10^{10})
T47 =	3.4×10^7	(3.0×10^8)

K = N/m (LB/IN)
T = M - N/RAD (IN LB/RAD)

SCHEMATIC NUMERAL REPRESENTATION FOR SPANS

3, 4, 5, 6, 7	– LPC	16	– HOT HIGH SHAFT	14	– OUTER COMBUSTION CASE
11	– LOW SHAFT	19	– HPT	18	– TURBINE CASE
17	– LPT	12	– DIFFUSER CASE	2	– FAN CASE
9	– HPC	15	– INNER COMBUSTION CASE	10	– FAN DUCTS
13	– COLD HIGH SHAFT	1	– LOW COMPRESSOR CASE	21	– TAIL PIPE
		8	– ENGINE CASE (INTERMEDIATE TO DIFFUSER)		

Figure A-40 JT8D-100 Rotor Frame Model

TABLE A-XII

STRAIN ENERGY COMPARISON OF JT8D-100 AND CURRENT JT8D
Maximum Redline Speeds – JT8D-100 – 8000 RPM
Current JT8D – 8600 RPM

	JT8D-100		CURRENT JT8D	
	RPM	% Strain Energy	RPM	% Strain Energy
Fan Case Mode	5707	6.1%	6692	10.6%
Fan Rotor Mode	7175	6.16%	8600	6.54%
Engine Case Mode	7649	7.52%	9200	4.83%

Percent Strain Energy is on a Basis of 100% for the Entire Engine System. Strain Energy Distribution above is Well within Successful P&WA Experience.

b) Front Hub

The front hub supports the Nos. 1.0 and 1.5-stage disks and blades and is connected to the main rotor by tiebolts. It is made of AMS 4928 titanium to assure compatibility with mating titanium disks.

c) Stage 1.5 and Stage 2.0 LPC Blades

Stages 1.5 and 2.0 are the JT8D-100 low-pressure compressor stages designed to replace the second fan stage in the current JT8D turbofan engines.

Stage 1.5 employs a circular arc airfoil whereas the stage 2.0 airfoil is a modified series 65 airfoil. The series 65 thickness distribution has been modified by incorporating a large leading edge and trailing edge radius on a circular arc mean line. The two supercharging stages are used with the existing four-stage LPC to achieve the required performance. Pertinent data on the stage 1.5 and stage 2.0 airfoils are summarized in Tables A-XIII and XIV. The primary aerodynamic considerations were to ensure sufficient choke margin to efficiently pass the required flow at the maximum cruise condition and to keep loading and incidence sufficiently low so that the supercharging stages would not initiate surge before the existing four-stage LPC, thereby maintaining current LPC surge margin. Table A-XV is a summary of critical supercharging-stage geometry and aerodynamics. Figure A-41 shows minimum A/A* vs. % span at design and maximum cruise (the critical LPC choke point). Figure A-42 shows D factor vs. incidence and % span at low speed surge (the most critical incidence and loading point) and includes a comparison with an advanced four-stage compressor.

Both blades are made of AMS 4928 titanium alloy because of its low density and high strength properties at low pressure compressor temperatures. The blades have dovetail roots which fit into mating disk slots. Rearward blade movement is prevented by a tang on the front of the blade root. Forward blade movement from gas loading is restricted by a ring which (for stage 2.0) is held in place by the rotor tiebolts or (for stage 1.5) by a separate bolt-circle.

The 1.5 stage blade platform configuration is similar to the fan blade in that adjacent platform edges form the complete inner flowpath, whereas the stage 2.0 blade platform is sunk into the disk rim, similar to current JT8D low pressure compressor stages 3.0 through 6.0.

Secondary gas leakage (recirculation) is restricted for stage 2.0 by the close fit between the blade root and disk slot. This type of leakage is minimized for stage 1.5 by providing a local close fit at the aft disk face between a disk "dam" and the blade platform under-surface.

TABLE A-XIII(a)

JT8D-100 ROTOR 1.5
AERODYNAMIC AND GEOMETRIC SUMMARY
42 DOUBLE CIRCULAR ARC AIRFOILS

	Hub						Tip
Percent Engine Flow	0.0	9.09	27.3	45.5	63.6	81.8	100.0
				Inlet			
Diameter-m	0.5578	0.5819	0.6276	0.6703	0.7109	0.7503	0.7899
V-m/s	220.19	212.03	211.33	207.97	203.23	196.32	185.11
V_m-m/s	215.18	208.58	206.93	201.23	195.24	187.77	172.43
V_θ-m/s	46.72	38.057	42.898	52.517	56.409	57.318	67.352
β-deg	12.25	10.34	11.71	14.63	16.12	16.98	21.34
β'-deg	38.45	42.17	44.30	46.07	48.53	51.43	54.39
V'-m/s	274.76	281.45	289.112	290.078	294.85	301.15	296.16
V'_θ-m/s	−170.86	−188.96	−201.91	−208.93	−220.95	−235.45	−240.79
U-m/s	217.58	227.02	244.81	261.45	277.36	292.77	308.14
M	0.613	0.592	0.592	0.583	0.569	0.548	0.514
M'	0.765	0.805	0.810	0.813	0.825	0.841	0.823
				Exit			
Diameter-m	0.5344	0.5616	0.5855	0.6513	0.6924	0.7318	0.7722
V-m/s	216.58	226.80	227.94	224.21	221.40	216.32	196.20
V_m-m/s	140.66	128.13	125.36	127.74	128.46	127.21	128.25
V_θ-m/s	164.68	187.14	190.37	184.26	180.43	174.96	148.49
β-deg	40.50	34.40	33.37	34.73	35.47	36.02	40.84
β'-deg	22.92	25.92	30.43	34.42	38.57	39.96	49.35
V'-m/s	178.09	208.06	220.78	223.38	229.27	235.90	227.95
V'_θ-m/s	−67.803	−90.937	−111.82	−126.28	−141.61	−158.22	−172.96
U-m/s	208.46	219.07	237.19	254.02	270.17	285.44	301.21
M	0.586	0.618	0.624	0.614	0.606	0.590	0.533
M'	0.481	0.597	0.604	0.612	0.493	0.643	0.619
P_{02}/P_{01}	1.1409	1.1929	1.200	1.1967	1.1997	1.2016	1.1778
$\bar{\omega}$	0.1686	0.0479	0.0281	0.0226	0.0247	0.0316	0.0419
D	0.4500	0.3555	0.3264	0.3164	0.3081	0.3021	0.3092
EFF-AD	0.7423	0.8166	0.8795	0.9008	0.9006	0.8836	0.8439
				Geometry			
Diameter-m	0.5461	0.5697	0.6048	0.6637	0.6988	0.7457	0.7811
c-m	0.06477	0.06561	0.06682	0.06894	0.07018	0.07186	0.07310
t/c	0.070	0.0680	0.0650	0.0601	0.0581	0.0531	0.050
RLE-m	0.00023	0.00023	0.00023	0.00023	0.00023	0.00023	0.00023
RTE-m	0.00023	0.00023	0.00023	0.00023	0.00023	0.00023	0.00023
β_1^*-deg	49.02	42.99	40.68	42.737	44.38	49.14	53.70
ϕ-deg	33.23	20.82	13.12	8.91	7.76	7.88	11.54
σ	1.586	1.540	1.477	1.389	1.342	1.288	1.251

ORIGINAL PAGE IS
OF POOR QUALITY

TABLE A-XIII(b)

JT8D-100 ROTOR 1.5
AERODYNAMIC AND GEOMETRIC SUMMARY
42 DOUBLE CIRCULAR ARC AIRFOILS

	Hub						Tip
Percent Engine Flow	0.0	9.09	27.3	45.5	63.6	81.8	100.0
				Inlet			
Diameter - in	21.96	22.91	24.71	26.39	27.99	29.54	31.10
V - ft/sec	722.41	695.63	693.33	682.32	666.75	644.10	607.33
V_m - ft/sec	705.96	684.33	678.89	660.21	640.55	616.04	565.71
V_θ - ft/sec	153.28	124.86	140.74	172.30	185.07	188.05	220.97
β - deg.	12.25	10.34	11.71	14.63	16.12	16.98	21.34
β' - deg.	38.45	42.17	44.30	46.07	48.53	51.43	54.39
V' - ft/sec	901.45	923.38	948.53	951.70	967.35	988.04	971.66
V'_θ - ft/sec	−560.57	−619.94	−662.43	−685.45	−724.89	−772.48	−790.00
U - ft/sec	713.85	744.80	803.18	857.76	909.96	960.53	1010.96
M	0.613	0.592	0.592	0.583	0.569	0.548	0.514
M'	0.765	0.805	0.810	0.813	0.825	0.841	0.823
				Exit			
Diameter - in	21.04	22.11	23.05	25.64	27.26	28.81	30.40
V - ft/sec	710.55	744.09	747.83	735.59	726.37	709.72	643.71
V_m - ft/sec	461.49	420.38	411.29	419.10	421.47	417.36	420.76
V_θ - ft/sec	540.28	613.97	624.58	604.52	591.59	574.03	487.16
β - deg	40.50	34.40	33.37	34.73	35.47	36.02	40.84
β' - deg	22.92	25.92	30.43	34.42	38.57	39.96	49.35
V' - ft/sec	584.28	682.62	724.36	732.86	752.21	773.94	747.88
V'_θ - ft/sec	-222.45	-298.35	-366.87	-414.30	-464.59	-519.11	-567.45
U - ft/sec	683.94	718.72	778.17	833.40	886.40	936.47	988.21
M	0.586	0.618	0.624	0.614	0.606	0.590	0.533
M'	0.481	0.597	0.604	0.612	0.493	0.643	0.619
P_{02}/P_{01}	1.1409	1.1929	1.200	1.1969	1.1997	1.2016	1.1778
$\overline{\omega}$	0.1686	0.0479	0.0281	0.0226	0.0247	0.0316	0.0419
D	0.4500	0.3555	0.3264	0.3164	0.3081	0.3021	0.3092
EFF-AD	0.7423	0.8166	0.8795	0.9008	0.9006	0.8836	0.8439
				Geometry			
Diameter - in	21.500	22.43	23.81	26.13	27.51	29.36	30.750
c - in	2.550	2.583	2.631	2.714	2.763	2.829	2.878
t/c	0.070	0.0680	0.0650	0.0601	0.0581	0.0531	0.050
RLE - in	0.009	0.009	0.009	0.009	0.009	0.009	0.009
RTE - in	0.009	0.009	0.009	0.009	0.009	0.009	0.009
β'_1 - deg.	49.02	42.99	40.68	42.737	44.38	49.14	53.70
ϕ - deg.	33.23	20.82	13.12	8.91	7.76	7.88	11.54
σ	1.586	1.540	1.477	1.389	1.342	1.288	1.251

TABLE A-XIV(a)

JT8D-100 ROTOR 2
AERODYNAMIC AND GEOMETRIC SUMMARY
52 AIRFOILS WITH NASA 65 SERIES THICKNESS DISTRIBUTION ON A CIRCULAR ARC MEAN LINE

	Hub						Tip
Percent Engine Flow	0.0	9.09	27.3	45.5	63.6	81.8	100.0
				Inlet			
Diameter-m	0.5024	0.5319	0.5804	0.6238	0.6640	0.7026	0.7417
V-m/s	147.43	173.60	188.67	171.91	193.82	191.82	172.82
V_m-m/s	144.59	171.47	185.22	186.52	186.34	182.24	159.10
V_θ-m/s	28.801	26.926	35.869	45.205	53.325	59.854	67.467
β-deg	11.27	8.92	10.96	13.62	15.92	18.18	22.98
β'-deg	49.14	46.48	45.80	46.72	47.83	49.61	54.35
V'-m/s	221.03	249.03	265.70	272.08	277.56	281.23	273.00
V'_θ-m/s	−167.18	−180.57	−190.50	−198.08	−205.72	−214.19	−221.85
U-m/s	195.98	207.50	226.37	243.29	259.04	274.04	289.32
M	0.391	0.466	0.510	0.521	0.526	0.519	0.466
M'	0.587	0.668	0.719	0.738	0.753	0.762	0.736
				Exit			
Diameter-m	0.4928	0.5210	0.5669	0.6091	0.6490	0.6873	0.7264
V-m/s	196.11	215.10	218.69	216.92	216.63	215.98	203.41
V_m-m/s	132.95	125.21	118.29	118.88	122.82	129.25	138.178
V_θ-m/s	144.17	174.90	183.94	181.44	178.45	173.03	149.27
β-deg	42.69	35.62	32.75	33.23	34.54	36.76	72.79
β'-deg	22.35	24.03	29.21	33.20	36.14	38.75	44.21
V'-m/s	155.87	191.50	210.74	216.83	220.96	221.86	208.24
V'_θ-m/s	−59.27	−77.99	−102.85	−118.72	−130.31	−138.85	−145.19
U-m/s	192.22	203.20	221.14	237.60	253.14	268.11	283.37
M	0.513	0.567	0.582	0.578	0.577	0.574	0.538
M'	0.407	0.505	0.560	0.578	0.589	0.590	0.551
P_{02}/P_{01}	1.186	1.192	1.180	1.174	1.172	1.178	1.194
$\bar{\omega}$	0.0710	0.042	0.0194	0.0148	0.0200	0.0303	0.0302
D	0.4340	0.3515	0.3071	0.2950	0.2928	0.3026	0.3374
EFF-AD	0.7553	0.8255	0.8868	0.9071	0.9043	0.8851	0.8545
				Geometry			
Diameter-m	0.4976	0.5212	0.5682	0.6160	0.6513	0.6985	0.7341
c-m	0.05006	0.05060	0.05116	0.05237	0.05339	0.05443	0.05519
t/c	0.080	0.0760	0.0680	0.0620	0.0540	0.0441	0.040
RLE-m	0.00022	0.00022	0.00022	0.00022	0.00022	0.00022	0.00022
RTE-m	0.00025	0.00025	0.00025	0.00025	0.00025	0.00025	0.00025
β_1^*-deg	47.91	45.07	44.27	44.66	46.24	51.34	54.02
ϕ-deg	37.51	27.29	17.91	14.50	12.31	14.20	18.98
σ	1.666	1.606	1.502	1.435	1.357	1.289	1.244

TABLE A-XIV(b)

JT8D-100 ROTOR 2.0 AERODYNAMIC AND GEOMETRIC SUMMARY 52 AIRFOILS WITH NASA 65 SERIES THICKNESS DISTRIBUTION ON CIRCULAR ARC MEAN LINE

	Hub						Tip
Percent Engine Flow	0.0	9.09	27.3	45.5	63.6	81.8	100.0
				Inlet			
Diameter-in	19.78	20.94	22.85	24.56	26.14	27.66	29.20
V - ft/sec	483.69	569.56	618.98	629.64	635.88	629.33	566.99
V_m - ft/sec	474.37	562.56	607.69	611.93	611.34	597.91	521.99
V_θ-ft/sec	94.49	88.34	117.68	148.31	174.95	196.37	221.35
β - deg.	11.27	8.92	10.96	13.62	15.92	18.18	22.98
β'-deg.	49.14	46.48	45.80	46.72	47.83	49.61	59.35
V' -ft/sec	725.17	817.04	871.73	892.64	910.64	922.66	895.68
V'_θ -ft/sec	-548.49	-592.42	-625.00	-649.88	-674.92	-702.71	-727.84
U -ft/sec	642.98	680.76	742.68	798.19	849.87	899.08	949.20
M	0.391	0.466	0.510	0.521	0.526	0.519	0.466
M'	0.587	0.668	0.719	0.738	0.753	0.762	0.736
				Exit			
Diameter-in	19.40	20.51	22.32	23.98	25.55	27.06	28.60
V -ft/sec	643.40	705.71	717.50	711.67	710.73	708.60	667.34
V_m -ft/sec	436.18	410.80	388.10	390.03	402.96	424.06	453.34
V_θ - ft/sec	472.99	573.82	603.47	595.28	585.46	567.70	489.73
β - deg.	42.69	35.62	32.75	33.23	34.54	36.76	72.79
β' - deg.	22.35	24.03	29.21	33.20	36.14	38.75	44.21
V' -ft/sec	511.40	628.28	691.41	711.38	724.95	727.88	683.19
V'_θ -ft/sec	-194.45	-255.87	-337.44	-389.49	-427.54	-455.55	-476.36
U	630.63	666.67	725.54	779.52	830.50	879.61	929.69
M	0.513	0.567	0.582	0.578	0.577	0.574	0.538
M'	0.407	0.505	0.560	0.578	0.589	0.590	0.551
P_{02}/P_{01}	1.186	1.192	1.180	1.174	1.172	1.178	1.194
$\overline{\omega}$	0.0710	0.0420	0.0194	0.0148	0.0200	0.0303	0.0302
D	0.4340	0.3515	0.3071	0.2950	0.2928	0.3026	0.3374
EFF-AD	0.7553	0.8255	0.8868	0.9071	0.9043	0.8851	0.8545
				Geometry			
Diameter-in	19.590	20.52	22.38	24.25	25.64	27.50	28.900
c - in	1.971	1.992	2.014	2.062	2.102	2.143	2.173
t/c	0.080	0.0760	0.0680	0.0620	0.0540	0.0441	0.040
RLE - in	0.0086	0.0086	0.0086	0.0086	0.0086	0.0086	0.0086
RTE - in	0.0100	0.0100	0.0100	0.0100	0.0100	0.0100	0.0100
B'^*_1 - deg.	47.91	45.07	44.27	44.66	46.24	51.34	54.02
ϕ - deg.	37.51	27.29	17.91	14.50	12.31	14.20	18.98
σ	1.666	1.606	1.502	1.435	1.357	1.289	1.244

TABLE XV

JT8D-100 LOW PRESSURE COMPRESSOR SUPERCHARGING STAGES GEOMETRY AND AERODYNAMICS

Geometry at Midspan

Locations	S1	R 1.5	S 1.5	R 2	S 2
Series	CA	CA	65/CA	65/CA	65/CA
Gap/Chord	0.632	0.72	0.679	0.707	0.647
Span/Chord	1.94	1.71	2.16	2.25	2.33
Max T/Chord	0.05	0.06	0.07	0.06	0.07

Span-Average Aerodynamics at Design Point

Inlet Mach No.	0.778	0.814	0.607	0.721	0.567
"D" Factor	0.408	0.328	0.301	0.320	0.278
$\Delta P/q$	0.429	0.361	0.298	0.344	0.251

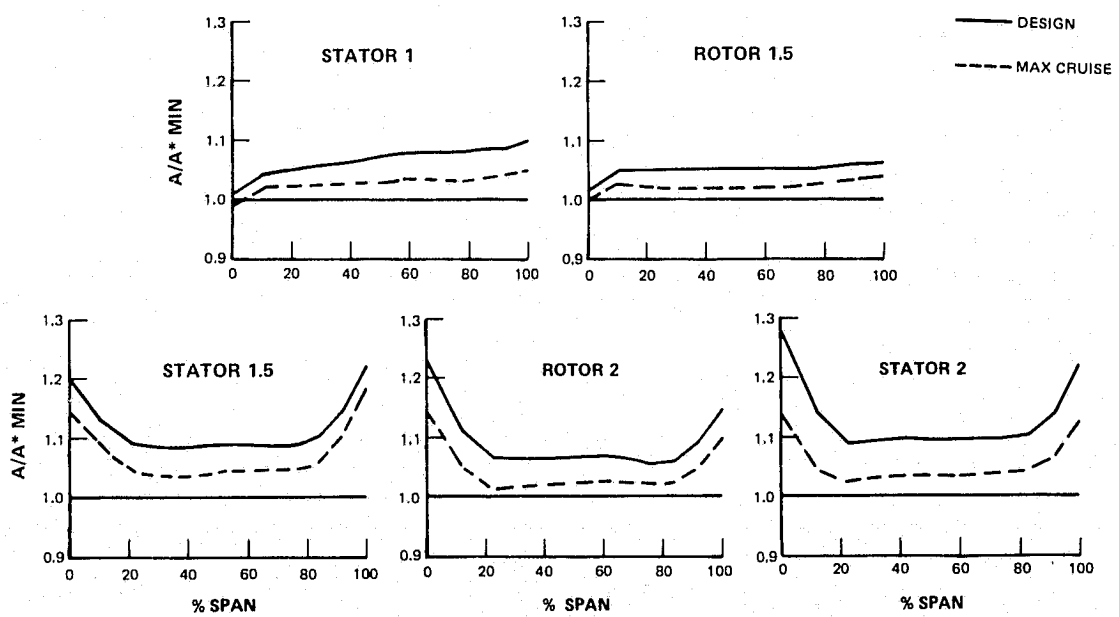

Figure A-41 JT8D-100 Low Pressure Compressor Supercharging Stages - Predicted Choke Margin at Design Point and Max. Cruise

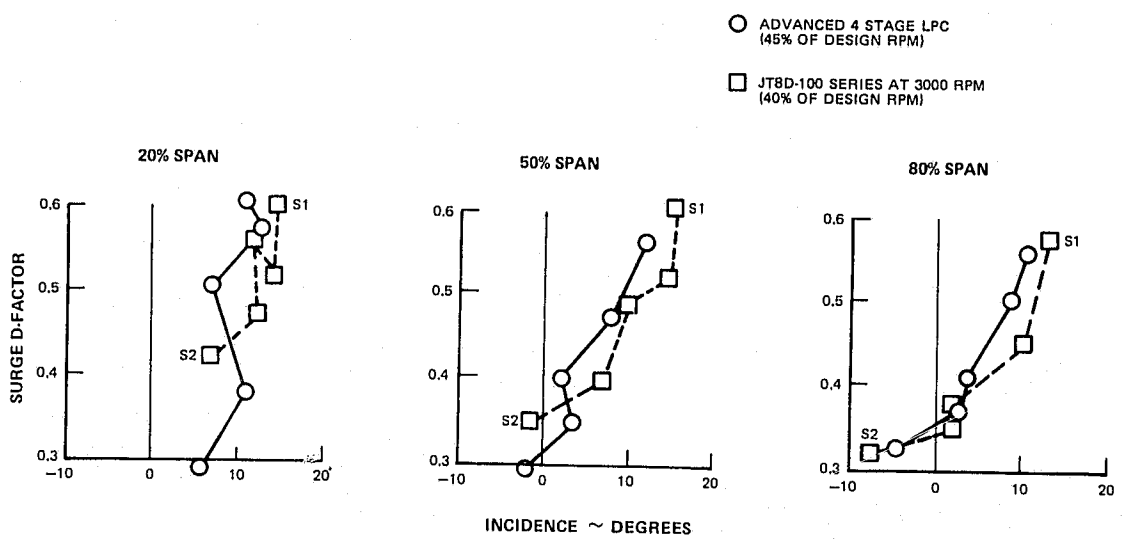

Figure A-42 Predicted JT8D-100 Low Pressure Compressor Supercharging Stages "D" Factor at Low Speed

These latter two figures demonstrate that the supercharging stages are designed up to both surge and choking limits. Figure A-43 is a predicted supercharging map and shows the points used in the surge-choke analysis.

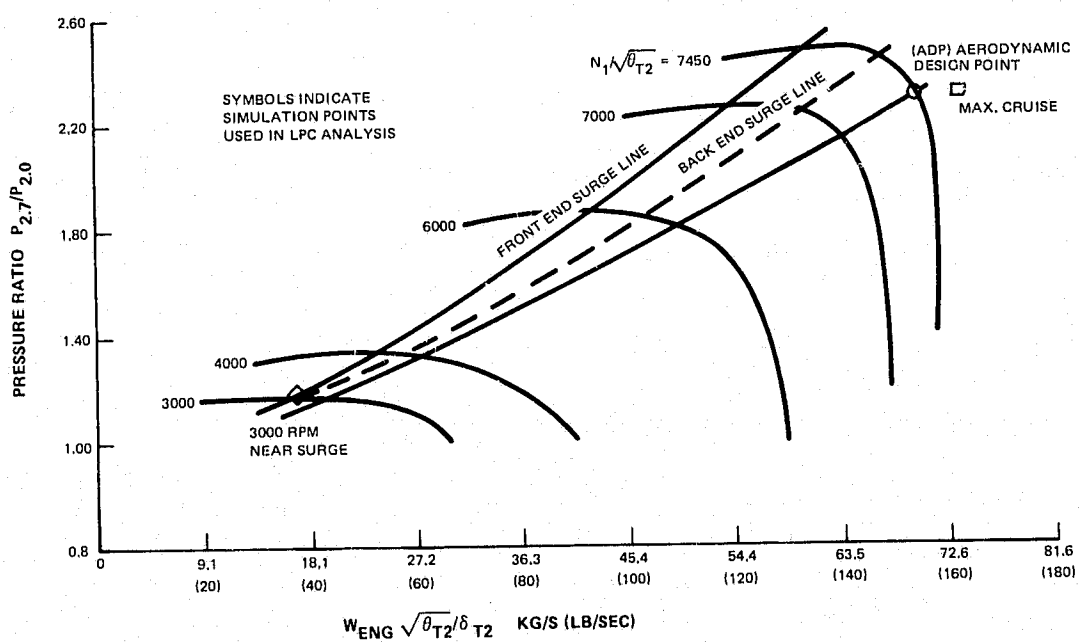

Figure A-43 Predicted Map for JT8D-100 Low Pressure Compressor Supercharging Stages

Stage 1.5 has been designed so the blades are accessible from the front of the engine. The bolted-on ring which retains the blades is independent of the disk mounting bolts, and the blades, which are moment-weight classified, can be replaced without subsequent rotor rebalancing.

An examination of blade tip chordwise bending modes reveals that first mode resonances at the passing orders of adjacent stators occur at engine speeds below the take-off, climb, and cruise speed range. See tip chordwise bending resonance diagrams, Figures A-44 and A-45.

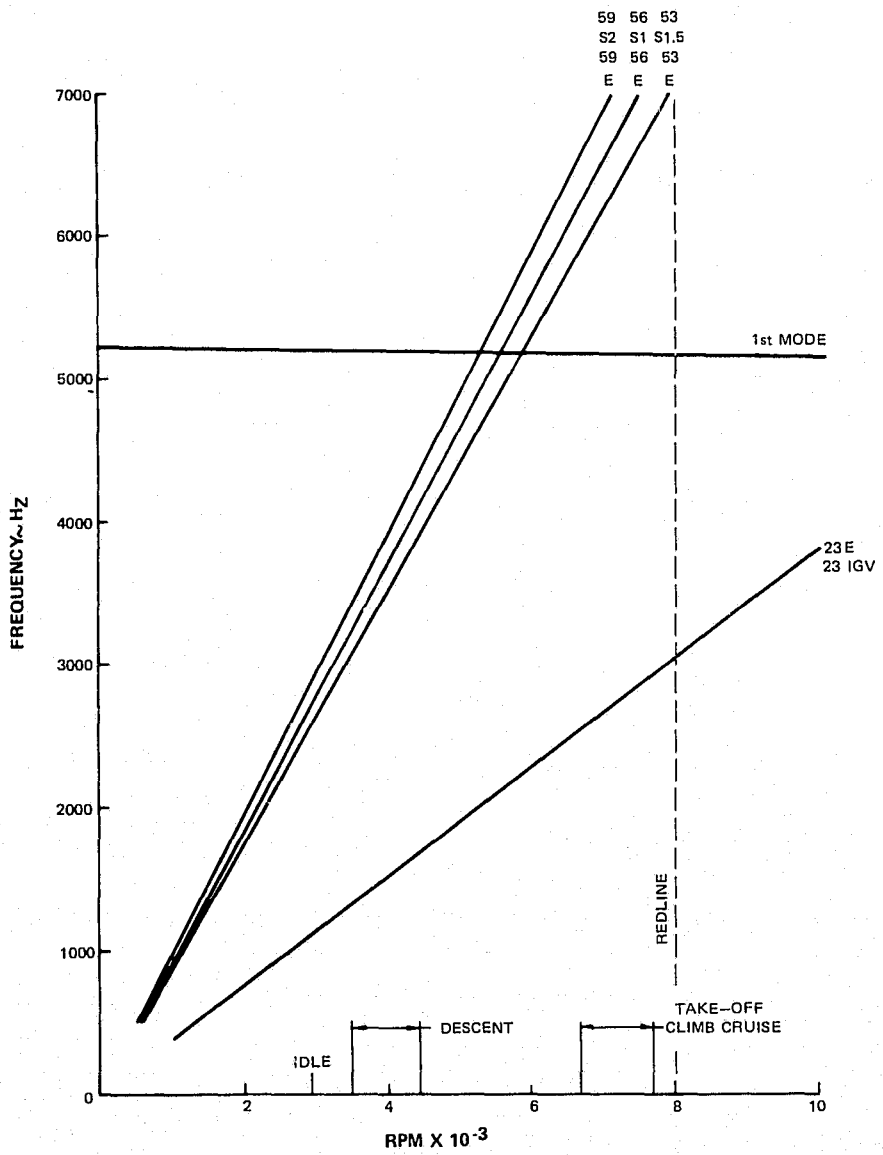

Figure A-44 Predicted JT8D-100 No. 1.5 Rotor Resonance Diagram – Tip Chordwise Bending Frequency

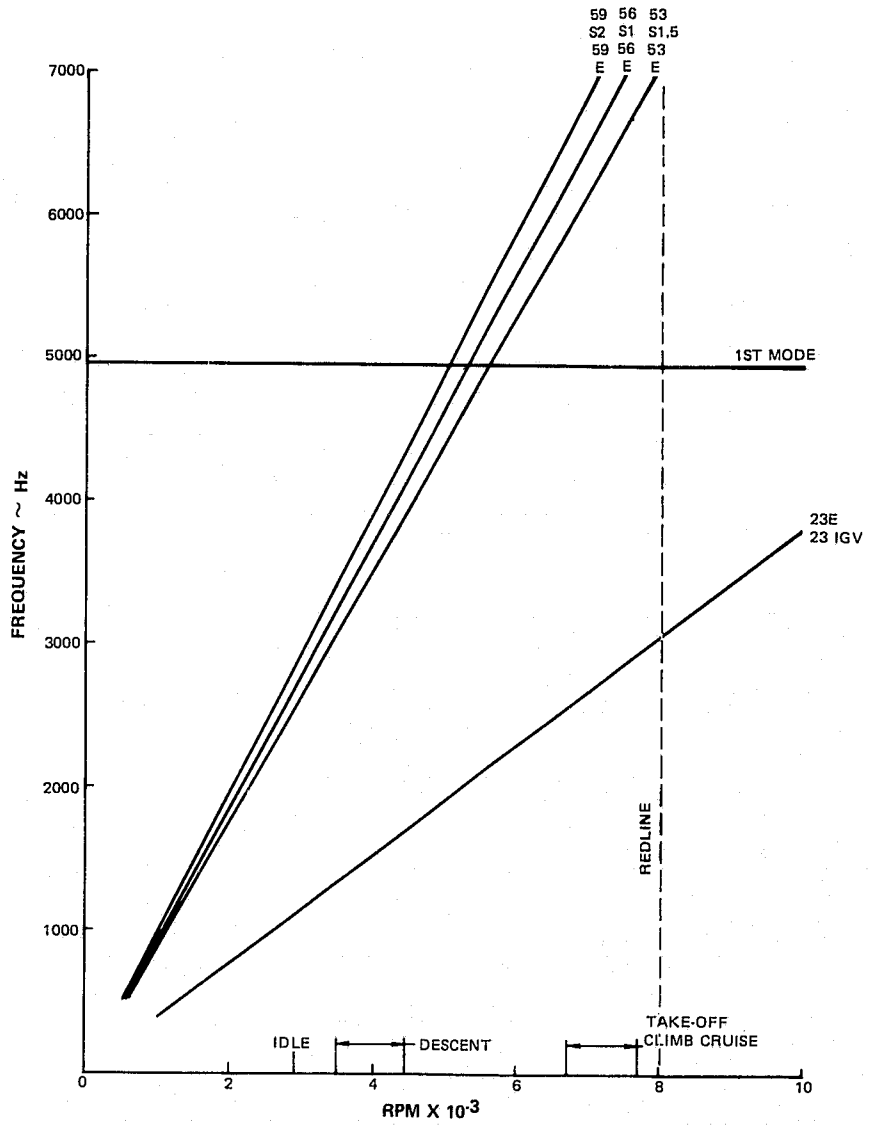

Figure A-45 Predicted JT8D-100 No. 2 Rotor Resonance Diagram – Tip Chordwise Bending Frequency

Except for slight modifications to the blade tips, the designs of the 1.5 stage and 2.0 stage low-pressure compressor blades are identical to the designs presented in Reference 3.

The stage 1.5 and 2.0 compressor blade tip clearances were increased from the preliminary design values of 0.053 cm (0.021 inch) and 0.055 cm (0.022 inch) respectively to 0.011 cm (0.045 inch). The increase was accomplished to alleviate a potential blade tip rub condition

revealed during testing. To reduce the impact of increased clearances on engine performance, squealer cuts were incorporated on the cut-back blade tips. The squealer cut was made by removing approximately .127 cm (.050 inch) of material on the blade tip concave surface. This cut reduced the blade-to-shroud annular ring effective area, thereby reducing tip leakage.

d) Stage 1.5 Compressor Disk and Stage 1.5 Blade Lock and Seal Ring

The 1.5 stage disk (Figure A-46) is made of AMS 4928 forged titanium. It has an integral cone projecting forward from the disk bore. This conical appendage extends inward to an attaching flange by which the stage is bolted to the center portion of the rotor front hub. The cone is long enough to isolate the disk growth from the flange to avoid snap separation, while at the same time providing the required stiffness for satisfactory disk-blade coupled vibration characteristics.

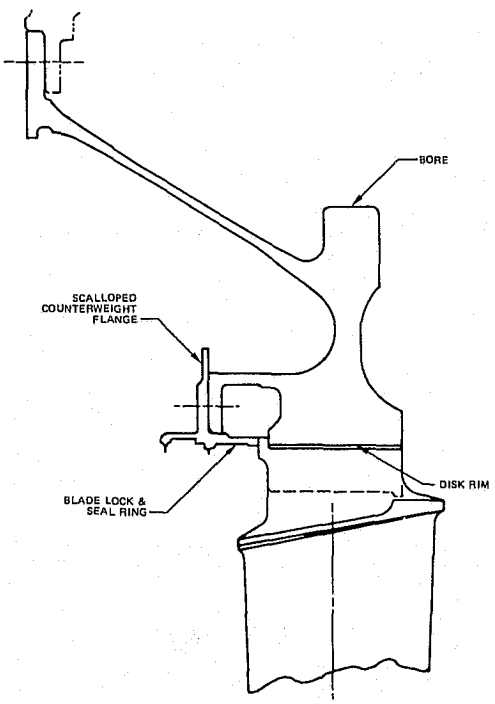

Figure A-46 JT8D-100 Stage 1.5 Disk

A bolted-on blade locking ring, also made of titanium, has been used in preference to a bent tab sheet metal lock. This improves reliability and facilitates blade replacement. The first interstage airseal knife-edges have been made an integral part of this ring. Positioning the seal at this location eliminates the need for a large area diaphragm on the stator and results in a smaller rotor root cavity, which helps to maintain compressor stability. The ring is held in place by bolts with adequate strength and sufficiently close spacing to withstand any blade root movement. Counterweight mounting provisions are also incorporated in the ring.

Disk and blade coupled vibratory modes were analyzed. The 1st mode 3E frequency was calculated to be less than 80% of red-line rotor speed. Experience with similar parts has shown this to be acceptable. Other significant modes are 1 nodal diameter, 2E with an 8% margin and 2 nodal diameter, 2E with a 24% margin (see Figure A-47). The blade lock-seal ring is completely free of engine ordered resonances over the entire running range (see Figure A-48). The f/N vs. nodal diameter curve represents the locus of resonance conditions on a Campbell diagram.

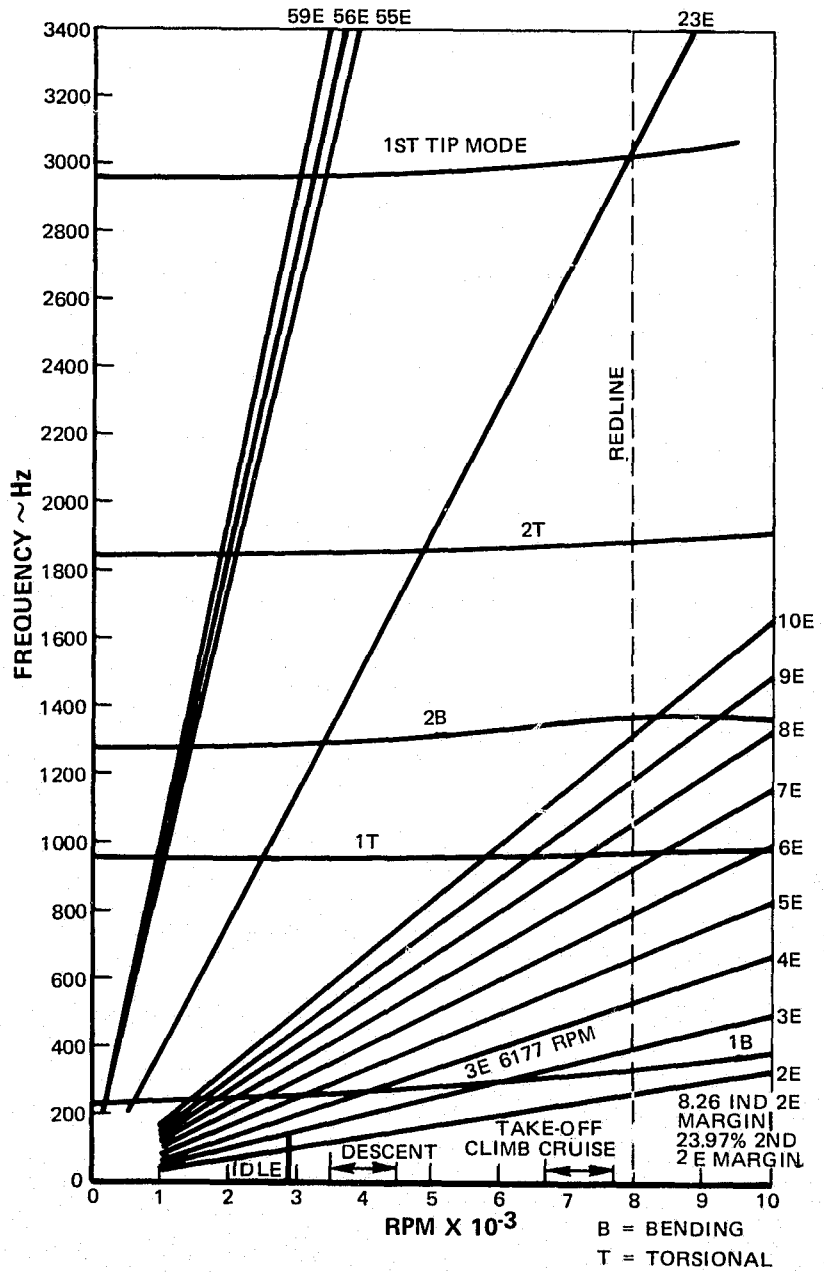

Figure A-47 Predicted JT8D-100 Stage 1.5 Rotor Resonance Diagram

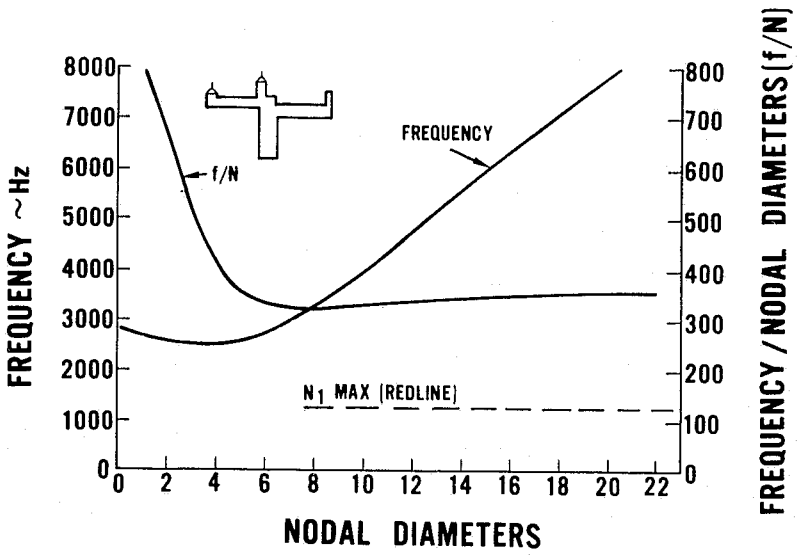

Figure A-48 Predicted JT8D-100 First Stage Labyrinth Seal – Stage 1.5 Blade Lock Resonance Diagram

e) Stage 2.0 Compressor Disk

A new 2.0 stage disk was designed to accommodate the new 2.0 stage blade. A snap diameter on the front face of the disk mates tightly with the hub flange to maintain concentricity. A similar snap is located on the rear face to maintain concentricity with the 2.0 to 3.0 stage rotor spacer. The front and rear snap diameters differ by 0.254 cm (0.100 inch) to ensure proper installation.

The coupled blade and disk resonances were calculated and there is a 21% 2E frequency margin in the first coupled mode. There is a 3E first coupled mode resonance at 5550 RPM which is well below the normal operating range. The web thickness and rim depth were established to ensure that a highly coupled second mode would not occur in the operating speed range. (see Figure A-49).

f) Stage 1.5/2.0 Airseal

The 1.5 to 2.0 stage air seal reduces the recirculation of air from the 1.5 stage stator exit. The seal consists of two knife-edges radially positioned very close to lands mounted on the I.D. of the 1.5 stage stator. In addition to sealing, this ring also prevents the second stage blades from moving forward out of their disk slots. It is held in position by the low pressure compressor tiebolts and a snap diameter on the No. 1 hub flange.

A small radial flange has been added to the cylindrical portion of the seal ring to support the weights used for rotor balancing. (See Figure A-46). Holes are provided to accommodate the rivets which retain the balance weights to the flange.

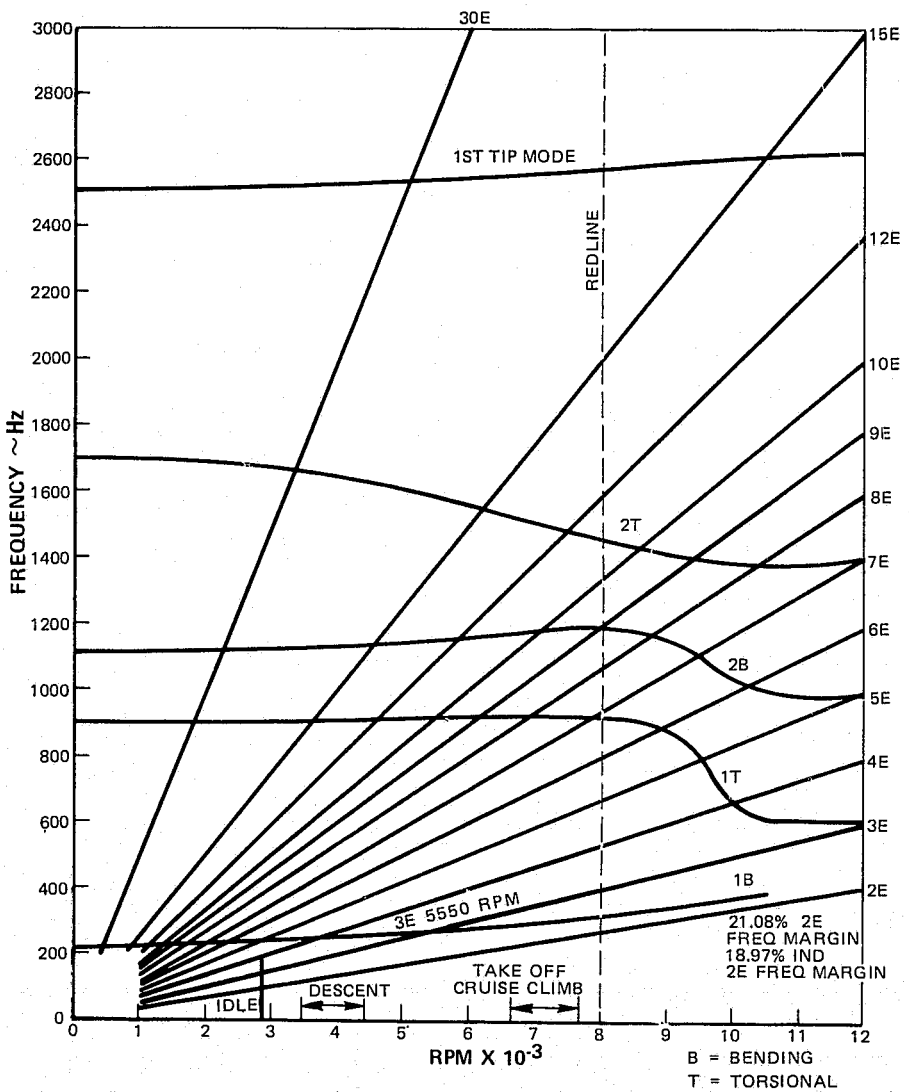

Figure A-49 Predicted JT8D-100 Stage 2 Rotor Resonance Diagram

The axial restraint afforded the blades by the seal is comparable to the restraint offered by the similar 2.0 to 3.0 stage air seal which has seen extended service on current JT8D engines. The airseal was analyzed and found to be free of engine ordered resonances over the engine operating range (see Figure A-50).

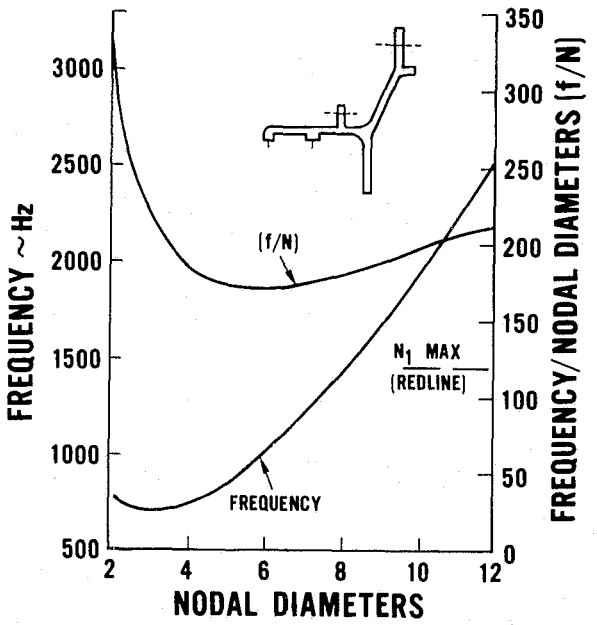

Figure A-50 JT8D-100 No. 1.5 Stage Labyrinth Seal Resonance Diagram

g) Stage 2.0/3.0 Spacer

Due to the wider stage spacing required for acoustic treatment and redesigning the front part of the low compressor, a longer 2.0 to 3.0 stage spacer was required. A conventional AMS 4928 titanium spacer with sleeves at each tierod location was designed. The spacer is positioned radially at each end by snap diameters on the adjacent disks. Because of the assembly of sleeves into the spacer, an unbalance of the assembly was corrected by adding clip weights to the sleeves of the spacer assembly.

h) Stage 2.0/3.0 Airseal

A new 2.0 to 3.0 stage airseal is required for use with the AMS 6415 steel 3.0 stage disk, because that disk is thinner than the titanium disk used in certain models. The new airseal has a thickened flange at the tiebolt hole locations to compensate for the thinner disk.

A snap diameter is provided on the front face of the new seal to accommodate the 2.0 to 3.0 stage rotor spacer. This spacer configuration is identical in all JT8D-100 engines (see Figure A-51).

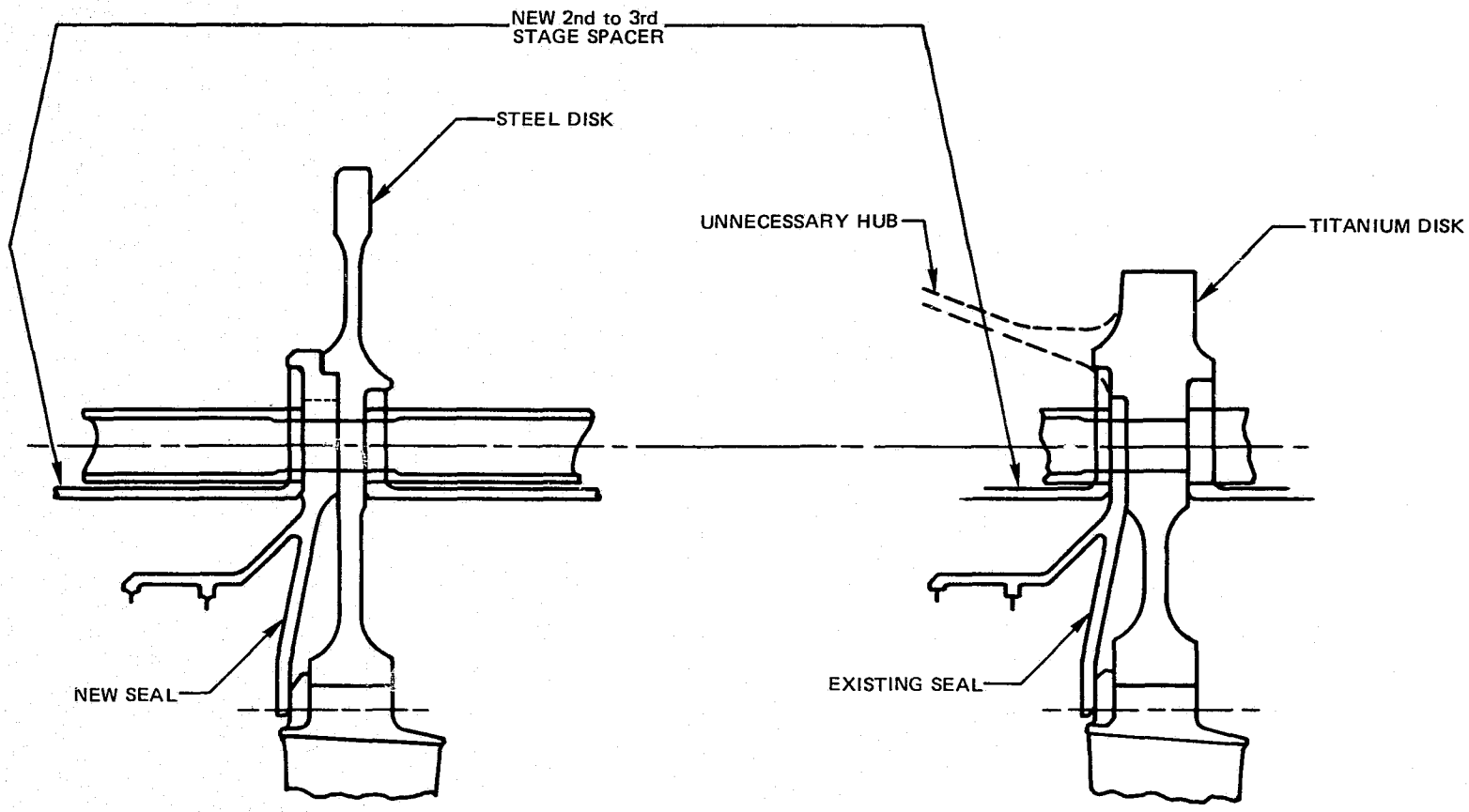

Figure A-51 JT8D-100 Third-Stage Disk

The seal flange has additional holes between the tiebolt holes to increase the LCF life of the flange. These added holes are on a different diameter circle than the tiebolt holes to avoid misassembly. Vibration analysis has shown this seal to be completely free of engine ordered resonances over the entire engine running range.

i) Stage 3.0 Disk

Two different third stage disks are used in JT8D engines currently in service. One is steel (AMS 6415), and the other is titanium (AMS 4928). Both disks may be reoperated to the new configurations used in the JT8D-100.

The steel disk is considerably thinner than the titanium disk. To avoid unequal stack lengths, a new airseal with a thicker flange is used with the steel disk. This allows using the same configuration 2.0 to 3.0 stage rotor spacer for all engines (see Figure A-51).

The steel disk requires a shorter length snap diameter to accommodate the new seal. The anti-galling compound currently used in the broached slot has been replaced with an improved compound, which has better lubricating characteristics.

In its present configuration the titanium disk has an integral hub which is not used in the JT8D-100 models. This hub was removed and an additional snap diameter was machined to receive the 2.0 to 3.0 stage rotor spacer and maintain concentricity with the adjacent forward stage. The improved anti-galling compound is also used on this disk.

Blade retention is accomplished by extending a radial flange outward from the seal ring, which limits the forward travel of the blade by contacting the blade tang.

Because existing blades are used in the 3.0 stage disk and the disk geometry is essentially the same, static stresses have not increased. The dynamic stresses are also essentially the same as in current engines.

j) Stage 4.0/5.0 Spacer

The original design objective was to retain the current JT8D 4-5 spacer, but the same rotor moments that required redesigning the tiebolt (see paragraph k) page 85) would have caused elastic buckling of the 0.011 cm (0.045 in) thick spacer. A new spacer with a 0.190 cm (0.075 in) thick wall is provided to avoid buckling.

The spacer resonance characteristics are presented in Figure A-52. The plot of f/N vs. nodal diameter represents the locus of resonance conditions existing on a Campbell diagram. Values of f/N above redline speed (133 Hz) show resonance occurring outside the engine running range and the spacer design is considered acceptable.

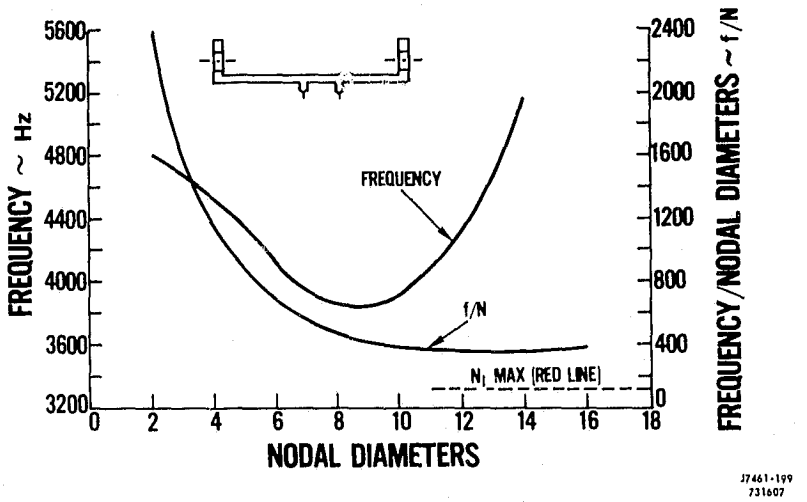

Figure A-52 Predicted JT8D-100 LPC No. 4-5 Spacer Resonance Diagram

k) Low-Pressure Compressor Tiebolt

The increased length of the fan portions of the LPC rotor required increasing the tensile capability of the tiebolt to prevent rotor bending in the event of blade loss. The increased strength was obtained by changing the bolt material to AMS 5617. The new bolt incorporates a larger cold-formed head which reduces stress concentrations in the fillet adjacent to the head. Land diameters are the same as in the current JT8D bolt, with three of the five lands being dimensionally identical to the old bolt. The use of a 65° asymmetric thread will increase fatigue life by a factor of approximately three over conventional 60° threads.

b. High Pressure Compressor, Burner and Turbine

The seven-stage high pressure compressor, the can-annular burner, and the air-cooled or uncooled single-stage high pressure (HPT) of the various current JT8D models were retained. The three-stage low pressure turbine (LPT) has also been retained except that the second stage vane flow area was reduced to achieve the desired engine match, the fourth-stage blade of the JT8D-9, -11, -15 models was replaced to reduce the turbine rotor exit Mach number, and the fourth-stage vane area was increased to reduce the fourth-rotor airflow incidence angle. The existing four exhaust case exit vanes were recambered and four additional exit vanes have been added to further reduce exit swirl to the level being experienced on the current JT8D engine models. An improved LPT shaft was required to maintain adequate strength at the increased torque. The maximum turbine temperature levels of the JT8D-100 derivative of a particular JT8D engine model are comparable to the levels for that particular current JT8D engine model being retrofitted.

Modification to the LPT and exhaust duct assembly were required to accommodate the re-fan engine cycle characteristics. The primary features that affect performance are: (1) the requirement to increase by-pass ratio without increasing the gas generator flow rate, turbine inlet temperature or pressure; and (2) the reduction in low-rotor speed imposed by noise and fan blade stress considerations. Table A-XVI shows a comparison of significant turbine cycle parameters for the JT8D-9 and JT8D-109 engines.

TABLE A-XVI

COMPARISON OF JT8D-9, JT8D-109 TURBINE CYCLE PARAMETERS AT DESIGN POINT

Parameter	JT8D-9	JT8D-109
By-Pass Ratio	1.04	2.00
Engine Airflow	70.7 kg/s (156 lb/sec)	69.8 kg/s (154 lb/sec)
Turbine Inlet Temp., T_{t5}	1236°K (1766°F)	1236°K (1766°F)
Burner Pressure P_{t5}	147.56 N/cm^2 (214 psia)	144.8 N/cm^2 (210 psia)
N_2 - RPM	11,365	11,380
ΔH_{HPT}	251204 J/kg (108 BTU/lb)	248878 J/kg (107 BTU/lb)
T_{T6}	1010.93°K (1360°F)	1010.93°K (1360°F)
P_{T6}	60.75 N/cm^2 (88.1 psia)	60.07 N/cm^2 (87.12 psia)
N_1 - RPM	8045	7450
ΔH_{LPT}	244226 J/kg (105 BTU/lb)	279116 J/kg (120 BTU/lb)

The turbine work requirement is increased by more than 14% and the rotor speed is reduced 7.4% in the D-109 relative to the D-9. The increased work requirement, at constant turbine inlet temperature, resulted in an increase in low pressure turbine expansion ratio of 22%. Table A-XVII shows a comparison of high- and low-pressure turbine design parameters for the D-9 and D-109 engines. The increase in turbine expansion ratio resulted in an increase in turbine exit flow parameter. The combined effects of increased exit flow parameter and reduced shaft speed resulted in increased Mach number and swirl levels entering the turbine exhaust case.

TABLE A-XVII

COMPARISON OF JT8D-9, JT8D-109 TURBINE DESIGN PARAMETERS

HIGH PRESSURE TURBINE

Parameter	JT8D-9	JT8D-109	% Change
Pressure Ratio	2.43	2.42	−0.4
Speed Parameter – $N/\sqrt{T_{t5}}$ $(rpm/\sqrt{°R})^*$	240	241	+0.04
Flow Parameter – $W\sqrt{T_{t5}}/P_{t5}$ $\left(\frac{lbm/sec\sqrt{°R}}{lb/in^2}\right)^*$	33.34	33.46	+0.36
Mean Velocity Ratio $\sqrt{\frac{\Sigma U^2_{mean}}{2gJ\Delta H}}$	0.480	0.485	+1.04
Rim Velocity Ratio $\sqrt{\frac{\Sigma U^2_{rim}}{2gJ\Delta H}}$	0.413	0.417	+0.97

LOW PRESSURE TURBINE

Pressure Ratio	2.96	3.62	+22
Speed Parameter – $N/\sqrt{T_{t6}}$ $(rpm/\sqrt{°R})^*$	189	175	−7.4
Flow Parameter – $W\sqrt{T_{t6}}/P_{t6}$ $\left(\frac{lbm/sec\sqrt{°R}}{lb/in^2}\right)^*$	75.82	75.69	−0.17
Mean Velocity Ratio $\sqrt{\frac{\Sigma U^2_{mean}}{2gJ\Delta H}}$	0.604	0.525	−13
Rim Velocity Ratio $\sqrt{\frac{\Sigma U^2_{rim}}{2gJ\Delta H}}$	0.456	0.380	−13
Exit Flow Parameter – $W\sqrt{T_{t7}}/P_{t7}$ $\left(\frac{lbm/sec\sqrt{°R}}{lb/in^2}\right)^*$	201.2	239.9	+19.3

*These parameters are used as non-dimensional factors and consequently equivalent S.I. units are not provided.

To minimize turbine and exhaust case performance penalties resulting from the increased loading and Mach number levels, several modifications relative to the basic JT8D turbofan engine were made to the LPT and exhaust case. These changes were determined to be the maximum possible within the constraints of minimizing hardware changes from the JT8D-9 engine while maintaining an acceptable level of performance.

1) LPT Blades and Vanes

The fourth-stage vane and blade flow areas were increased to achieve a more favorable work distribution by unloading the last stage of the turbine and shifting work forward to the front stages. The second-stage vane flow area was reduced by 3.7% to achieve the desired engine match with the new cycle. In addition, the turbine exhaust case was redesigned to remove the swirl at the increased LPT exit Mach number level of the D-109. Table A-XVIII summarizes the flow area changes made to the D-9 LPT and the resulting incidence, Mach number and swirl levels of the D-109 fourth stage and exit guide vane with the incorporated changes.

TABLE A-XVIII

COMPARISON OF JT8D-9, JT8D-109 PREDICTED LOW-PRESSURE TURBINE STAGE PARAMETERS*

Parameter	JT8D-9			JT8D-109**		
2nd Vane Flow Area	1106.45 cm^2 (171.5 in^2)			1048.38 cm^2 (162.5 in^2)		
4th Vane Flow Area	2187.09 cm^2 (339 in^2)			2277.42 cm^2 (353 in^2)		
4th Blade Flow Area	2154.83 cm^2 (334 in^2)			2406.45 cm^2 (373 in^2)		
2nd Stage Work	90712 J/Kg (39 BTU/lb)			102343 J/kg (44 BTU/lb)		
3rd Stage Work	74431 J/kg (32 BTU/lb)			88387 J/kg (38 BTU/lb)		
4th Stage Work	79283 J/kg (34 BTU/lb)			88387 J/Kg (38 BTU/lb)		
% Span	0	50	100	0	50	100
4th Blade Incidence	+5.4°	- 5.4°	+3.6°	+4.2°	- 4.1°	+8.9°
4th Blade Inlet Rel. Mach No.	0.47	0.374	0.438	0.618	0.459	0.456
4th Blade Exit Rel. Mach No.	0.717	0.759	0.801	0.907	0.889	0.852
Exhaust Guide Vane Inlet Mach No.	0.500	0.450	0.470	0.732	0.619	0.567
Exhaust Guide Vane Gas Swirl Angle	39.4°	21.8°	3.8°	37.9°	25°	6.9°

*Comparison based on controlled vortex turbine analysis
**Increased Flow Area 4th Vanes and Blades

The impact on LPT performance of the increased work and expansion ratio requirements of the D-100 cycle was minimized with the fourth-stage modifications. The fourth-stage blade flow area was increased 9.8% to re-distribute the work and reduce the rotor exit

absolute Mach number and swirl to a level that would provide for acceptable exhaust case performance. (The increase in area was accomplished by replacing the current D-9 blade with the D-1, D-7 blade which is of identical design restaggered 4° open). The flow area of the fourth-stage vane was increased 5% to improve the flow conditions, i.e, Mach number and incidence, entering the fourth-stage blade, particularly at the root section. The increase in vane area was accomplished by trimming back the trailing edges of the current D-9 vanes approximately 0.23 cm (0.09 in). Figure A-53 shows the JT8D-109 fourth-stage root pressure distribution compared to the basic JT8D-9 fourth blade root pressure distribution. While the root loading and Mach number levels have increased over those of the D-9, the pressure distribution is considered acceptable. An integral boundary layer calculation using this pressure distribution indicated that suction surface separation will not occur. Blade pressure distributions become more favorable at the outer spanwise locations. Figure A-54 presents the results of a pressure distribution calculation on the cut-back fourth-stage vane. These vane pressure distributions are also acceptable, and boundary layer analysis indicated no problem with separation.

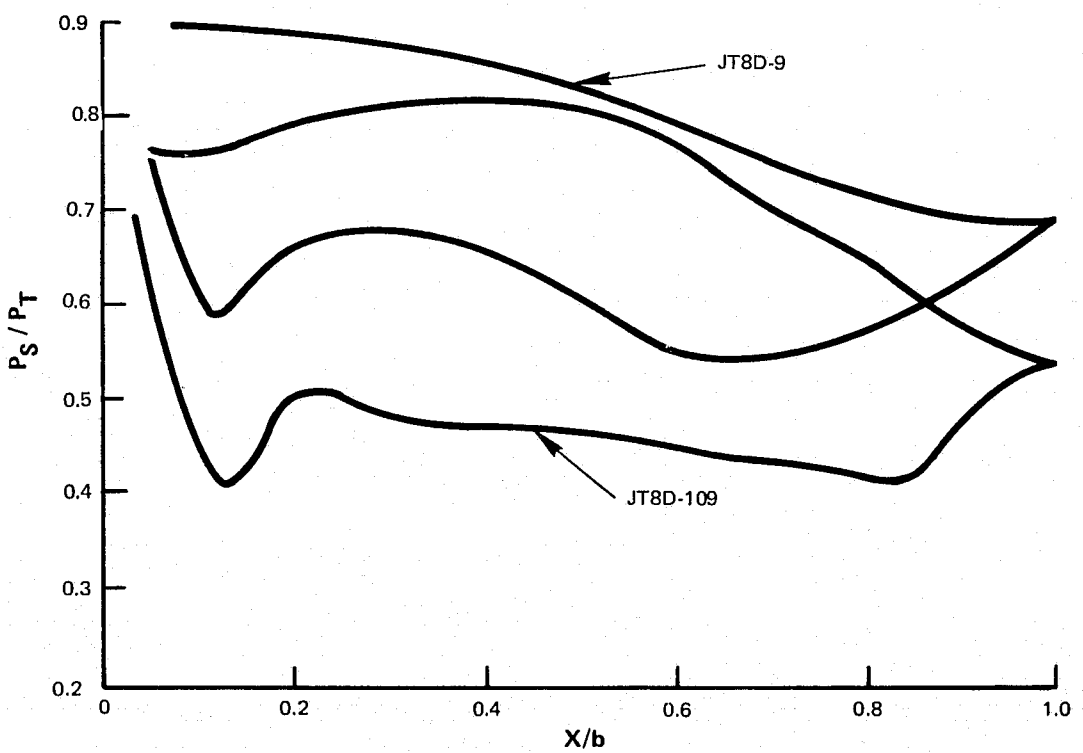

	JT8D-9	JT8D-109
INLET RELATIVE MACH NO.	0.48	0.618
EXIT RELATIVE MACH NO.	0.717	0.907
INCIDENCE	+5.4°	+4.2°

Figure A-53 JT8D-109 Low Pressure Turbine Fourth Blade Root Pressure Distribution Analysis

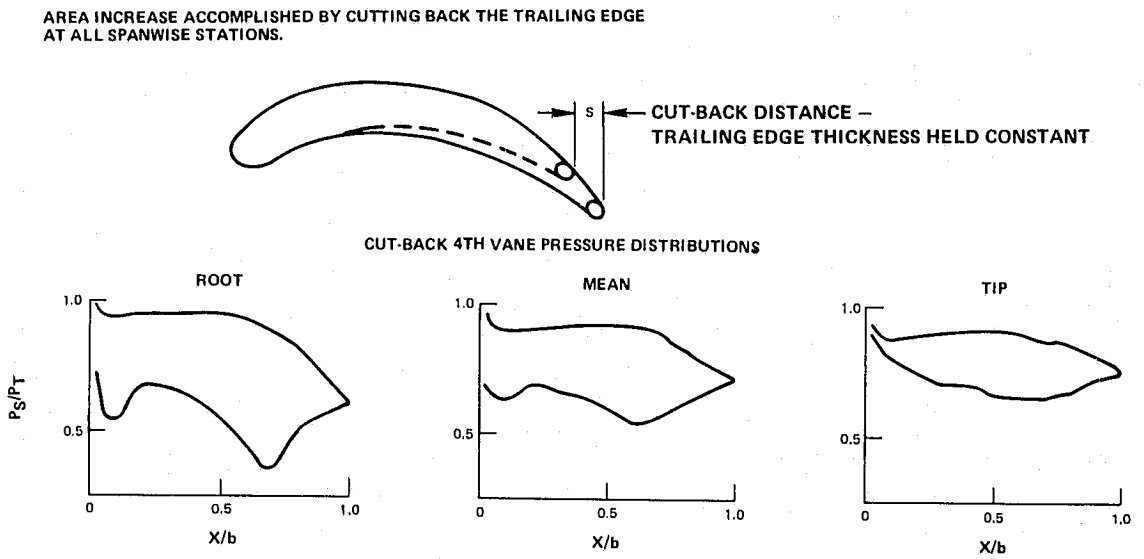

Figure A-54 JT8D-109 Low Pressure Turbine Fourth Vane Modification to Increase Flow Area

Table A-XIX summarizes the LPT cycle parameter changes from the JT8D-9 to the JT8D-109, along with the predicted performance of the D-109 cycle. The net LPT efficiency is the D-109 was predicted to be 1.4% lower than the D-9 LPT efficiency, resulting in a ΔTSFC penalty of 1.3%.

TABLE A-XIX

COMPARISON OF JT8D-9 AND JT8D-109 PREDICTED LOW PRESSURE TURBINE PERFORMANCE PARAMETERS

Parameter	JT8D-9	JT8D-109	% Change
T_{t6}	1010.93° K (1360°F)	1010.93° K (1360° F)	0
P_{t6}/P_{t7}	2.96	3.62	+22
Work	244226 J/kg (105 BTU/lb)	279116 J/kg (120 BTU/lb)	+13
N_1 – RPM	8045	7450	–7.4
Efficiency	89.3%	87.9%	–1.4
Δ TSFC	–	–	+1.3

a) Fourth-Stage Turbine Blade

To provide the power necessary to drive the new fan and low pressure compressor, it was necessary to extract more power from the turbine. This has been accomplished by modifying the fourth-stage turbine as follows:

- For the JT8D-1, -1A, -7, and -7A engines, the present blades were retained. These blades have the airfoil contours and stagger angles required to redistribute work to the forward LPT stages.

- For the JT8D-9 engine, the present blade will be replaced with a JT8D-7, -7A blade, which has 9.8% greater flow area (restaggered 4° open).

- For the JT8D-11, -15, and -17 engines, the present blades will be replaced with existing, previously unreleased, blades which are suitable for use with the elliptical broach slots in the fourth disk and have the 9.8% greater flow area of the JT8D-7, -7A blade.

None of the above changes caused any significant changes in blade or disk loading.

b) Fourth-Stage Turbine Vane

The fourth stage turbine vane trailing edge has been cut back approximately 0.229 cm (0.090 inch) to increase the total flow area through the fourth nozzle by 5.0%. This area increase was required to redistribute the stage work and minimize the effect of incidence angle and Mach number on fourth-stage blade performance. Stress levels in the nozzle were not significantly affected.

Radial transversing of the low-pressure turbine/exhaust case indicated that the modifications to the JT8D LPT fourth-stage, as incorporated into the JT8D-100, produced discharge spanwise Mach number and swirl characteristics that were acceptable in terms of impact on the redesigned exhaust vanes. The exit absolute Mach number was 5.7% less than estimated while the swirl was 8° greater than estimated. Presuming that the HPT performance remained at the level exhibited by the JT8D-9, the LPT efficiency ranged between 87.1% and 87.7%. This compares well with the estimated value of 87.9%.

2) LPT Shaft

The JT8D-100 LPT shaft is made of the same material (AMS 6304) and requires the same dual heat treatment as the present JT8D-15 shaft. Due to increased torque requirements for the JT8D-100, however, it is necessary to assure mechanical properties by specifying that an integral test specimen be taken from each shaft forging. Shaft geometry is identical with the JT8D-15 except for a radial thickness increase on the rear flange front snap diameter (i.e., second disk snap).

3) Turbine Exhaust Duct and Exit Guide Vanes (EGV)

Revisions within the JT8D-100 turbine necessary to meet the requirement for increased power extraction from the low-pressure turbine resulted in an increase in turbine exit swirl and Mach number. To minimize residual swirl, an eight-vane cascade of recambered airfoils has been included in the design to replace the JT8D four-vane design, which featured a low-camber airfoil contour. See Figure A-55.

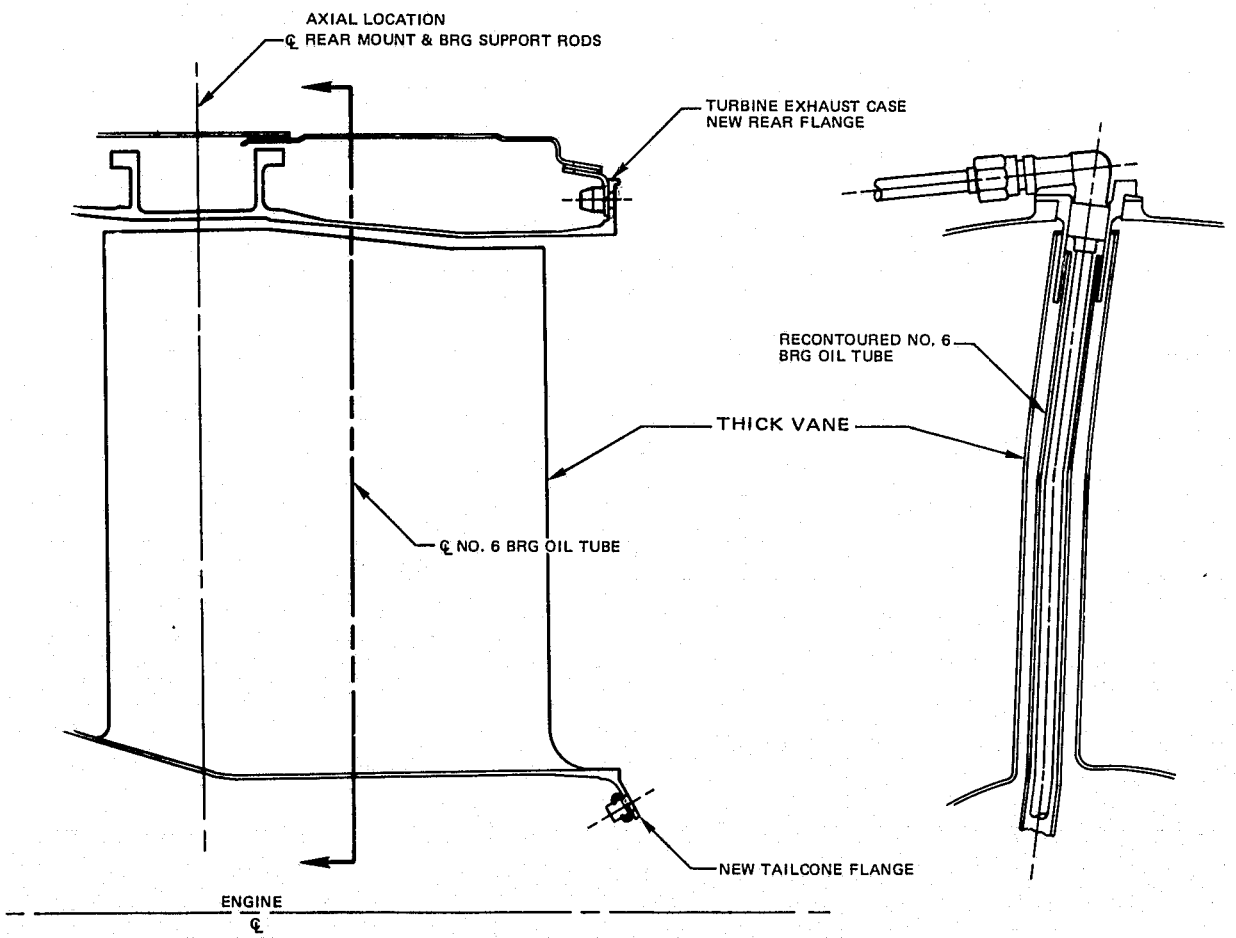

Figure A-55 JT8D-100 Turbine Exhaust Case & Exit Guide Vane Assembly

The turbine exit guide vane (EGV) assembly of the JT8D engine consists of four vanes which house the No. 6 bearing support rods. These vanes are also aerodynamic fairings which remove the swirl exiting from the low-pressure turbine. Table A-XX summarizes the EGV aerodynamic parameters for the JT8D-9 and JT8D-109. The D-109 inlet gas angles are of the same order of magnitude as the D-9 but the Mach number levels are considerably higher. Analysis has shown that the camber of the D-9 vanes is too low, the 400-series thickness shape has too low a critical speed, and the incidence angles would be too high for the D-9 vanes to give acceptable performance at the inlet swirl angles and the high inlet Mach numbers of the D-109 cycle conditions. The turbine exhaust case was redesigned, therefore, with higher-cambered 65-series airfoil vanes and vane twist was introduced to improve the incidence angle and increase the critical speed to retain essentially the same level of exit residual swirl without excessive losses.

Certain mechanical constraints, summarized in Figure A-56, had to be met in the design of the D-100 EGV's. The airfoil minimum thickness was established by the requirement to house the bearing support rods. The airfoil chord was established by turbine blade vibratory considerations and the location of the turbine case flange. The airfoil chord angle was restricted in range by the requirement for a strut to house both a bearing support rod and an oil line.

TABLE A-XX

COMPARISON OF JT8D-9, PREDICTED JT8D-109 TURBINE EXIT GUIDE VANE AERODYNAMIC PARAMETERS*

	JT8D-9			JT8D-109		
Parameters	**Root**	**Mean**	**Tip**	**Root**	**Mean**	**Tip**
Inlet Mach No.	0.500	0.450	0.470	0.732	0.619	0.567
Inlet Gas Angle	50.6°	68.2°	86.2°	52.1°	65°	83.1°
Incidence	+31.4°	+13.8°	-4.2°	+15.82°	-3.5°	-0.35°
Gas Turning Angle	27.5°	15.8°	3.8°	19.9°	16.0°	6.9°
Residual Swirl	13.7°	6°	0°	18.0°	9.0°	0.0°

***Comparison based on controlled vortex turbine analysis.**

Optimization studies were conducted to define the number of vanes required and the thickness distribution. Figure A-57 shows a comparison of various vane configurations and their effects on EGV choke margin. It was concluded that an eight-vane configuration with alternating thick and thin vanes was desirable. The configuration selected consists of eight series 65/circular arc vanes, four thick (0.18 thickness/chord) and four thin (0.07 thickness/chord). Tables A-XXI and A-XXII summarize the aerodynamic design conditions and geometry of the selected EGV designs.

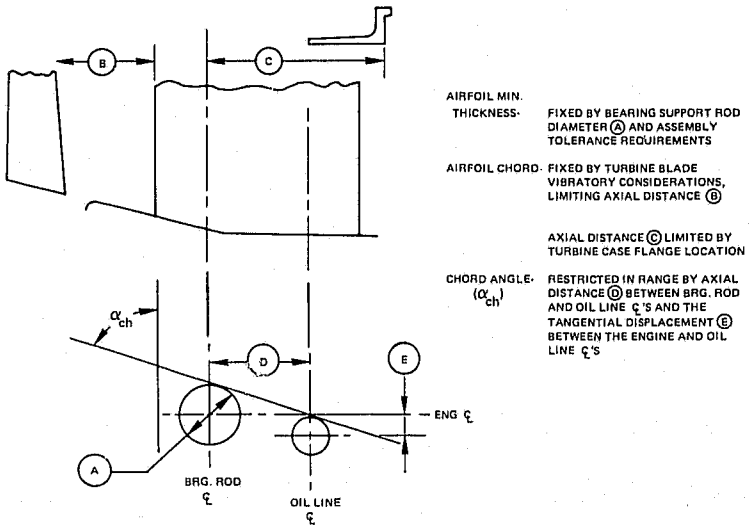

Figure A-56 JT8D-100 Turbine Exit Guide Vane Mechanical Constraints

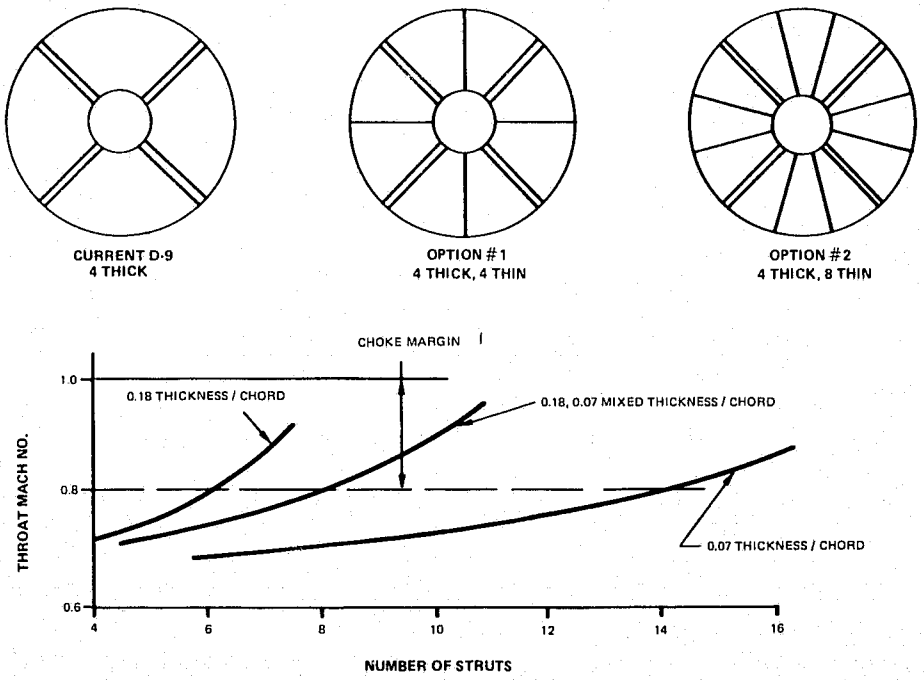

Figure A-57 JT8D-109 Turbine Exit Guide Vane Predicted Choke Margin

TABLE A-XXI

JT8D-109 TURBINE EXIT GUIDE VANE CASCADE SELECTION DESIGN POINT AERODYNAMIC INPUT

% Span	0	15	25	50	71.5	100
M_1	0.732	0.694	0.671	0.619	0.583	0.567
M_2	0.513	0.518	0.516	0.523	0.552	0.630
α_1	52.1°	55.8°	58.4°	65°	71.2°	83.1°
α_2	72°	74.7°	76.5°	81°	84.9°	90°
Gas Turning Angle	19.9°	18.9°	18.1°	16°	13.7°	6.9°
Residual Swirl	18°	15.3°	13.5°	9°	5.1°	0°

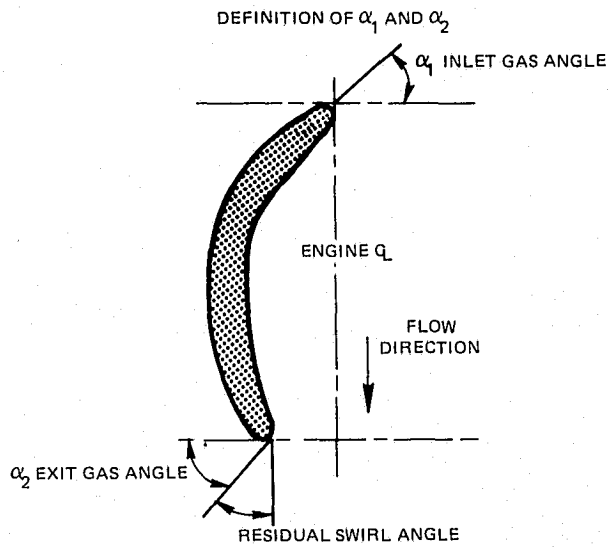

The selected vane configuration resulted in a predicted average residual primary stream swirl of 6° which approximates the D-9 residual value. Diffusion factors, defined and summarized in Table A-XXIII, are within P&WA experience. The selection of alternating thick/thin EGV's resulted in non-uniform flow channel geometry. The channel on either side of a strut is different, as shown in Figure A-58. Resultant mean section pressure distributions for each channel are also shown in Figure A-58. The channels are essentially similar in performance.

TABLE A-XXII

JT8D-109 TURBINE EXIT GUIDE VANE CASCADE GEOMETRY

Airfoil Type		Series 65 Circular Arc				
No. of Airfoils		8 Total (4 Thick and 4 Thin)				
Defining Radius-cm	16.12	19.43	21.77	27.47	32.32	38.81
(in)	(6.348)	(7.675)	(8.570)	(10.814)	(12.72)	(15.28)
% Span	0	15	25	50	71.5	100
θ^*	7.65°	9.91°	15.04°	30.6°	25.45°	11.4°
β_1^*	67.92°	67.84°	66.43°	61.5°	69.18°	82.75°
β_2^*	75.57°	77.75°	81.47°	92.09°	94.63°	94.15°
α_{ch}	71.75°	72.80°	73.95°	76.8°	81.9°	88.45°
Thickness/Chord-Thick	0.18	0.18	0.18	0.19	0.19	0.19
Thickness/Chord-Thin	0.07	0.07	0.07	0.07	0.07	0.07
Pitch/Chord	0.654	0.8	0.899	1.153	1.381	1.686
Chord-cm	19.35	19.16	19.03	18.69	18.39	17.98
(in)	(7.62)	(7.545)	(7.493)	(7.36)	(7.24)	(7.08)
Incidence Angle	+15.82°	+12.04°	+8.03°	-3.5°	-2.02°	-0.35°

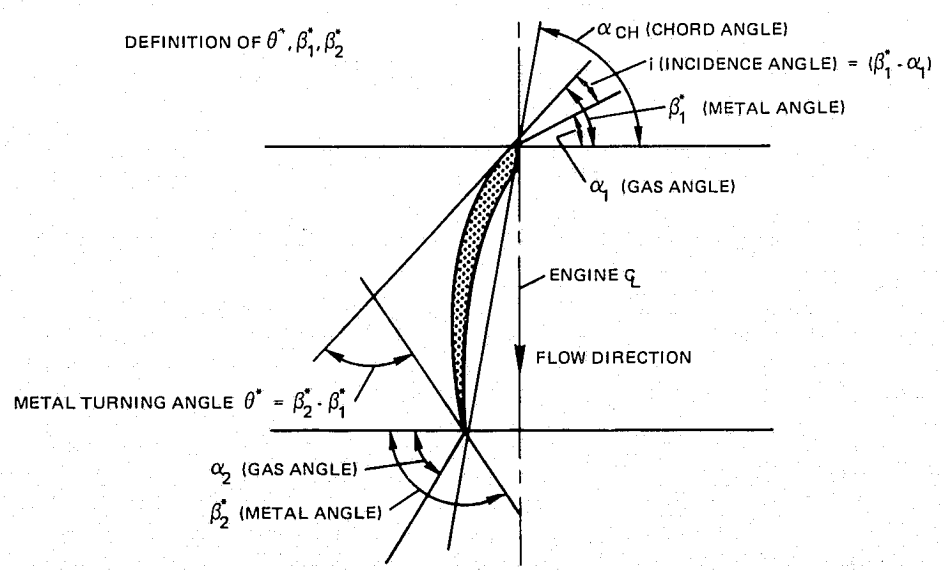

TABLE A-XXIII

JT8D-109 TURBINE EXIT GUIDE VANE DIFFUSION FACTORS

	Root	Mean	Tip
Diffusion Factor	0.413	0.312	0

$$\text{Diffusion Factor} = 1 - C_2/C_1 + \frac{\Delta C_u}{2C_1}\left(\tau/b\right)$$

C_1	Inlet Velocity Absolute
C_2	Exit Velocity Absolute
ΔC_u	Tangential Velocity change
τ/b	Gap/Chord

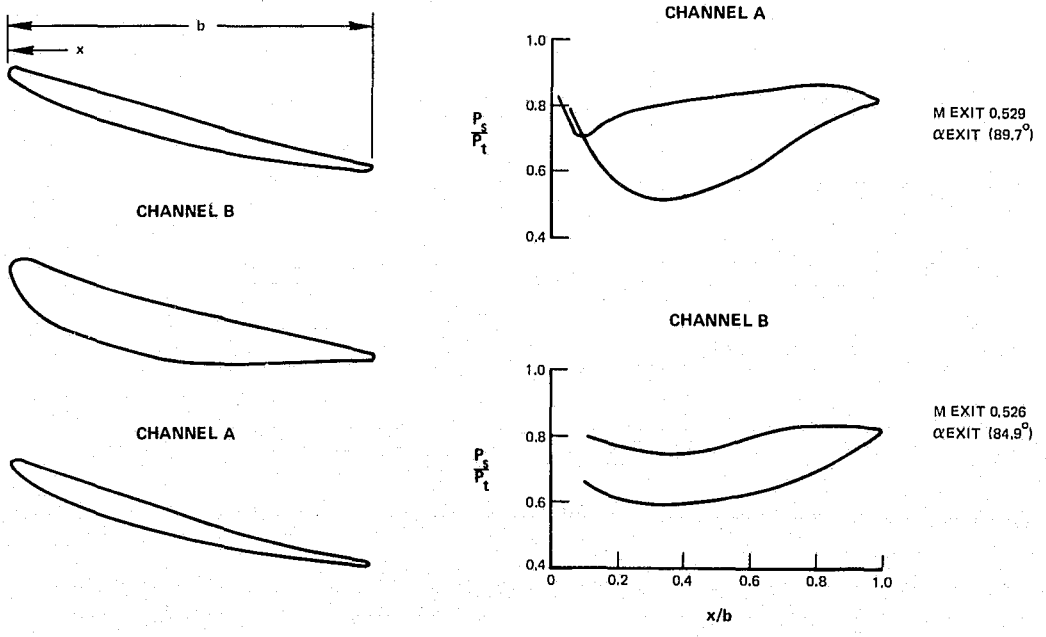

Figure A-58 Predicted JT8D-109 Turbine Exit Guide Vane Channel Performance and Pressure Distributions

Table A-XXIV shows a comparison of predicted exit Mach number and absolute gas angle at several spanwise locations for the two channels. Exit Mach numbers for the two channels show close agreement, while the computed exit angles vary by approximately 5° from channel A to channel B. This is considered to be satisfactory. An estimate of EGV total pressure loss was made, based on the P&WA cascade selection code and experience gained from other P&WA engines. The expected pressure loss ($\Delta P_o/P_o$) for the JT8D-109 EGV was 2.9% compared to 1.2% for the JT8D-9.

TABLE A-XXIV
JT8D-109 TURBINE EXIT GUIDE VANE
SUMMARY OF CASCADE PRESSURE DISTRIBUTION ANALYSIS

% Span	0	25	50	75	100
Channel			**M – Exit**		
A	0.489	0.505	0.529	0.599	0.669
B	0.496	0.561	0.526	0.593	0.661
			α – Exit		
A	85.6°	86.2°	89.7°	91.1°	93.1°
B	79.7°	88.9°	84.9°	86.7°	88.6°

A turbine exhaust case traverse program conducted during Phase II of the program indicated that the turbine exhaust case and instrumentation (6 P_T,and 8T_{T7} probes) pressure losses were 3.66% compared to an anticipated 2.9% for the design point; residual primary stream swirl was 8° more than the anticipated level. Measurement of strut fairing leading and trailing edge metal angles indicated significant deviation (3-5°) from design values which is believed to be the cause for the increase in residual swirl over design estimates. This increase in residual swirl together with possible losses due to unsealed radial gaps at thin vane tips would account for the extra 0.76% pressure loss. Instrumentation losses were as predicted. Table A-XXV presents a comparison of exhaust case design and measured data.

TABLE A-XXV
JT8D-109 TURBINE EXHAUST CASE PERFORMANCE

Configuration **TEGV** **Source**	**JT8D-109** **8 Vane** **Predicted**	**JT8D-109** **8 Vane** **Measured**
Mn Absolute - Mean	0.61	0.58
Swirl Before TEGV - Mean	24°CW	26°CW
Residual Swirl - Mean	6° CW	14° CW
LPT Efficiency – %	87.9	87.1 - 87.7
Total Primary $\Delta P/P$%	2.9	3.66
TEGV $\Delta P/P$ – %	0.6	1.52
P_t, T_t Instrumentation $\Delta P/P$ – %	2.3	2.14

Performance improvements can be made by maintaining required design strut fairing leading and trailing edge metal angles and combining the core engine P_{T7} and T_{T7} probes. There is also a possibility that removing the four thin vanes from the present case would improve the losses without increasing the exit swirl unacceptably. However, the effect of this change cannot be evaluated theoretically. Combined effects of reduced blockage and increased risk of flow separation can only be evaluated by test, which was not accomplished during the engine test program.

c. Fan and Primary Engine Cases

Increased diameter fan cases were incorporated into the JT8D-100 for compatibility with the increased diameter fan rotor. The current JT8D core engine cases were retained except in those instances where the core and fan cases are an integral assembly or where the fan flow path requirement necessitated the redesign of the core engine case. The tubing and manifold assemblies that cross the fan duct have been redesigned in conjunction with the increased diameter fan. The fairings used to aerodynamically enclose this plumbing have also been redesigned. Acoustic treatment has been provided on the inner walls of the fan cases and the outer walls of the engine core cases to reduce fan radiated noise.

Development testing conducted during this phase of the program verified the structural integrity of the case designs. However, on the basis of development test results, recommendations for design changes to improve performance of the fan ducts and fairings and the fan exhaust case components have been made. These recommendations are discussed subsequently in the appropriate sections.

1) Intermediate Case

The intermediate case assembly, shown in Figure A-59, includes the No. 2 and No. 3 bearing compartment, towershaft drive provisions, the sixth stage compressor vanes, high pressure compressor case, forward engine mounts, and support points for ground handling.

It was a requirement that the intermediate case for the JT8D-100 conversion kit be made by reoperating the inner portion of current JT8D engine intermediate case, retaining No. 2 and No. 3 bearing compartments, the sixth stage vanes, the integral portion of the No. 2 and No. 3 bearing oil pressure lines, and the upper towershaft drive system. The reoperated inner case incorporates welded-on radial flanges for bolting on a new outer case. The joints and bolts contain sealing provisions to ensure that the breather annulus is not subjected to either high or low pressure compressor air leaking in, or breather air leaking out into the rear compressor case and then into the cabin bleed system. The new intermediate cases uses "E" section seals between the mating bolted flanges, and capped anchor nuts which seal against the flange faces preventing air from leaking through the bolt holes.

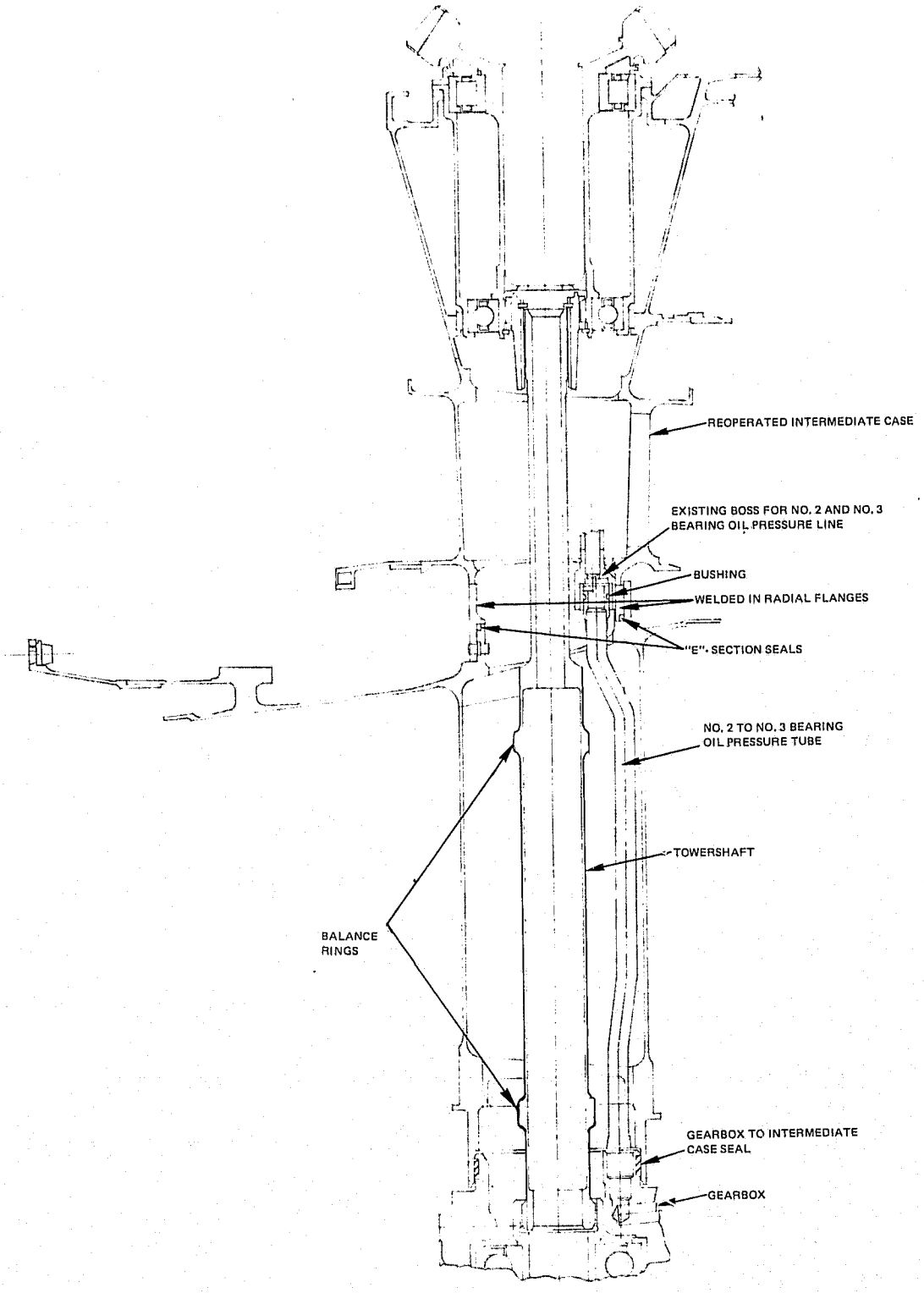

Figure A-59 JT8D-100 Intermediate Case – Towershaft Cross Section

ORIGINAL PAGE IS
OF POOR QUALITY

The new outer case features a large "T" section ring and twelve struts, six of which taper from 20.3 cm (8.0 inches) axial chord at the inner diameter to 10.7 cm (4.2 inches) at the outer diameter. Each of these tapered struts is radially aligned with a mount lug. This is a departure from the current engine design but is necessary because the increased radial depth of the fan annulus increased the couple due to thrust loads. The couple is almost double that of the existing engine. This dictates the use of struts utilizing a truss configuration rather than the conventional guided cantilever beam configuration. The large "T" section ring is necessary to react the forward-leaning strut punch loads. Loads acting radially through the engine mount points and struts dictate the inclusion of radial stiffening rigs in the thrust carrying struts. These struts are attached at the outside diameter such that punch loads cannot be carried through the strut leading edge. This is accomplished by overhanging the leading edge of the strut standup forward of the outer ring.

The remaining six struts have the same constant axial chord as the present engine. Five of these struts are the same width as the six thrust-carrying struts and are positioned radially at the three ground handling points and two gearbox mounting brackets. The sixth strut encloses the towershaft and No. 2 and No. 3 bearing oil pressure tube, and acts as a breather pipe between the inner engine and the gearbox. This strut has been resized to accommodate the larger diameter towershaft and maintain adequate breather area.

The integral boss which accepts the ferrule and O-ring for the No. 2 and No. 3 bearing oil pressure line has been retained as part of the reoperated inner case. The bore which accepts the aforementioned ferrule is enlarged, a bushing installed, and the bushing inner diameter is finished relative to features on the reoperated case to ensure alignment of the oil pressure tube. The fittings at the outer end of the oil pressure line are the same as used on the current engine. The housing forming the seal between the gearbox and intermediate case is the same configuration as is used on the current engine.

An axial flange is provided on the aft end of the outer case inner ring which will accept the existing high-pressure compressor case. This case is riveted on as in the current engine. A short case with a radial flange on the forward end and an axial flange on the aft end is riveted to the outer case assembly after the outer and inner assemblies have been bolted together. This short case provides attachment between the low-pressure compressor case stack-up and the intermediate case. When the aforementioned parts are riveted together a matched set is formed. The forward flange of the riveted-on case must be machined after assembly, relative to features on the inner intermediate case, in order to properly locate the front compressor. This is the only finishing required after assembly.

2) Compressor and Diffuser Fan Ducts

Figure A-60 shows the final configuration of the JT8D-100 compressor and diffuser fan ducts. These ducts were redesigned from the basic JT8D turbofan engine to accommodate the increased diameter fan section needed for the JT8D-100. In addition, aluminum acoustic treatment (honeycomb core and perforated face sheet) is bonded directly to the ducts.

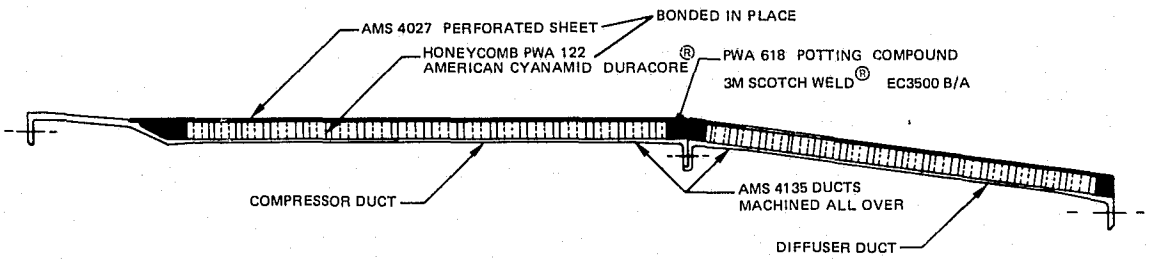

Figure A-60 JT8D-100 Compressor and Diffuser Fan Ducts

Both of the new ducts are AMS 4135 forgings whereas in the current engine the compressor duct is AMS 4135 and the diffuser duct is an AMS 4125 casting. The change to a forging reduces porosity which permits machining to a reduced wall thickness thereby reducing weight.

The compressor duct has also been changed by placing the major airbleed bosses on the skin outer surface only, rather than equally distributing the boss thickness between the inner and outer skin surfaces. This permits smooth turning of the I.D. and eliminates an expensive "Skip-turning" operation during manufacture. It also permits continuous I.D. tooling support for subsequent O.D. machining operations.

In the redesigned diffuser duct the flowpath is a cone rather than the "S" shape in current JT8D diffuser duct. This change allows more uniform tooling support for O.D. machining which permits machining to a reduced wall thickness.

As on the current parts the compressor duct O.D. is machined by skip turning and the diffuser duct O.D. by milling. Bosses on both parts are perimeter milled. Unlike the current parts, however, the new boss perimeters are designed to use end milling rather than arbor-type milling. The short, stiff end mill produces more accurate surfaces at lower cost than an arbor supported cutter.

Stresses adjacent to the compressor bleed bosses resulting from gas loads on the cantilevered fairings are 3.10×10^8 N/m^2 (45,000 psi).

Stress in the compressor duct wall transition between the tapered flowpath and honeycomb support is 3.37×10^8 N/m^2 (49,000 psi). A 2.5 G vertical, high angle of attack gust maneuver limits the duct at this location.

Evaluation testing conducted during the test phase of the program indicates that the fan duct pressure loss is approximately 1% greater than anticipated. One method recommended to reduce duct losses in this area is to provide a constant inner diameter flowpath from the intermediate case to the burner cover forward flange. This would entail modifying the compressor and diffuser fan ducts to maintain proper flow area which could affect airframe requirements.

3) Compressor and Fan Duct Fairings

Because of the increased diameter fan flowpath used in the JT8D-100 conversion kit, the aerodynamic fairings which enclose the plumbing that crosses the fan duct had to be redesigned.

In the new design the fairings do not use the intermediate case struts as leading edges as they do in the current JT8D, and the metal braces and trailing edges have been eliminated. The fairings are still made in three pieces and fitted together in the same fashion as in the current engine, but the segments, including the leading edge, are fabricated entirely from glass fabric, except for attachments and braces. This new construction method requires the fairings to be installed in the ducts before the plumbing is inserted across the fan flowpath.

The diffuser fan duct fairing nose section has been simplified to reduce molding and assembly costs. Glass fabric flanges have replaced the metal plate used to close off the tail section of the fairing on current JT8D engines.

Both fairings are cantilevered from the outer fan duct wall as in the current engine.

Due to the higher than anticipated fan duct losses encountered during engine and rig tests, the fan duct fairing design should be reviewed to determine if modifications which could reduce aerodynamic losses are possible.

4) Combustion Chamber and Turbine Fan Duct

Figure A-61 shows the final design of the combustion chamber and turbine fan duct. It is a two-piece cylindrical configuration, axially split along the horizontal centerline. Longitudinal flanges are provided and the two halves are joined with 66 bolts, 33 on each side. The split concept was retained from the current JT8D for ease of maintainability. A dummy flange is provided on the lower duct half, approximately four inches aft of the front flange, to accommodate mounting plumbing and accessories. Four pads are provided on the lower duct half for airframe bleed and/or the insertion of airframe accessories in the fan duct. The inside diameter of the duct is treated with integrally bonded acoustic treatment.

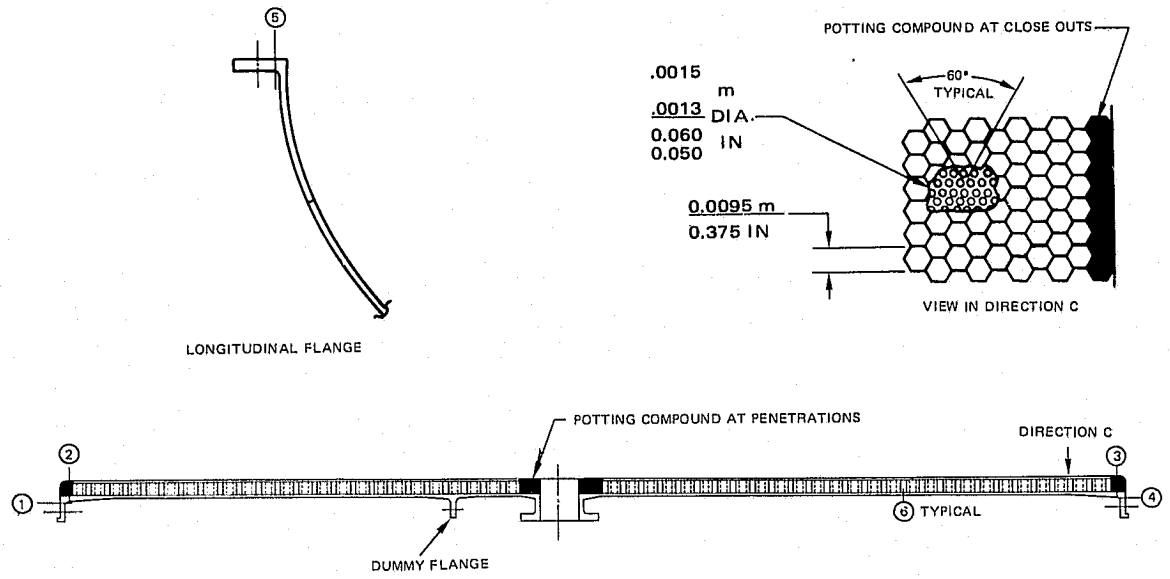

Figure A-61 JT8D-100 Combustion Chamber and Turbine Fan Duct

5) Turbine Case Acoustic Fairing

The turbine case acoustic fairing, shown in Figure A-62, forms a smooth flowpath around the turbine case. Due to its proximity to the turbine case, the resultant temperature level required welded stainless steel, AMS 5520, construction rather than the bonded aluminum constructuion used elsewhere in the JT8D-100. The 0.952 cm (0.375 inch) square honeycomb cell, which differs from the 0.952 cm (0.375 inch) hexagonal cell used elsewhere , was dictated by the structural requirements (size) and manufacturing process (shape). The different honeycomb cell shapes are acoustically equivalent. The fairing is made in two halves for assembly reasons, and is bolted to engine brackets at its front circumference. The longitudinal splits are bolted together. The aft cylindrical end of the fairing has a sliding fit on the engine brackets to allow for axial thermals. The aft end is hardfaced to prevent wear.

6) Turbine Exhaust Case

Revisions within the turbine necessary to meet the requirement for increased power extraction from the low-pressure turbine resulted in an increase in turbine exit swirl and Mach number. To minimize residual swirl, an eight vane cascade of recambered airfoils was incorporated into the conversion kit to replace the existing four strut design, which featured a low camber airfoil contour, as discussed in section (3) page 92 .

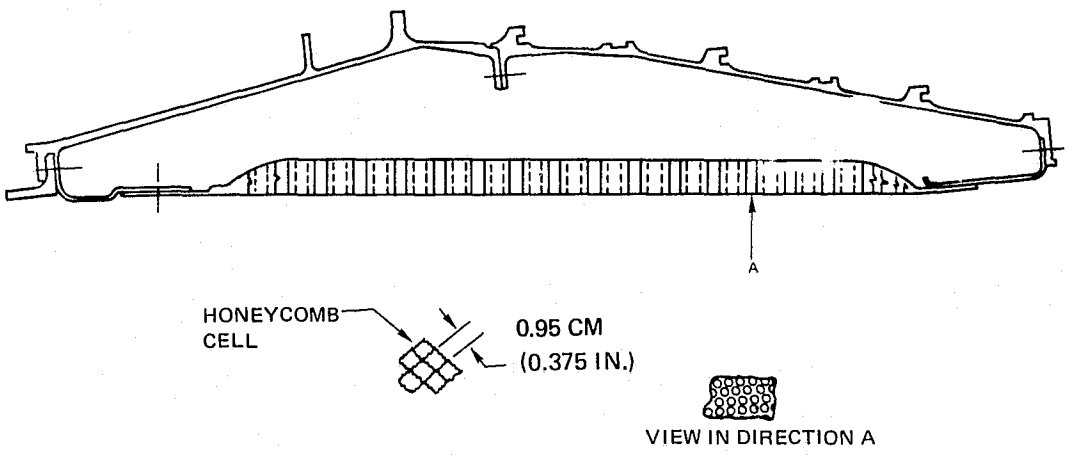

Figure A-62 JT8D-100 Turbine Case Acoustic Fairing

The eight vane design consists of four "thick" vanes, which provide enclosures for the No. 6 bearing support rods and No. 6 bearing oil supply line, and four "thin" vanes which were necessary to impose a cascade rather than an isolated airfoil flow field (reference Figure A-55).

Adding the thin vanes required developing a method of tip restraint. This restraint is provided by a pin and bushing configuration similar to existing thick vane hardware. An integral pin was added to the fan exhaust strut clevis to provide this support. Also, a pin clearance hole was necessary in the turbine exhaust case, which can be added by reoperation. The increased Mach number through the turbine exhaust case and increased turbulence due to flow restrictions prohibited the use of external axial stiffening ribs on the thin struts. Two additional internal radial stiffeners were used instead. This was not possible on the thick vanes due to the presence of the support rods and oil tube.

Due to a combination of vane aerodynamic requirements and the necessity of maintaining the present location of the No. 6 bearing support rods and oil tube boss in the turbine exhaust case, relocation and recontouring of the oil tube was required. Parts affected by the tube relocation included the No. 6 bearing scavenge pump housing, No. 6 bearing housing, No. 6 bearing heatshield, and the reoperation of the turbine exhaust case boss (i.e. resizing and reorientation of hole). In addition, a special adapter washer was required to mate the new oil tube assembly sleeve with the existing case boss.

In order to provide the customer with flexibility for designing his exhaust system, a reoperation of the turbine exhaust case was accomplished to provide a cylindrical exit contour and a redesigned rear flange. This flange is required for customer attachment of a splitter and/or mixer between core and fan exhaust. A new fan exhaust ID rear fairing design was also provided for an interface with the customer-supplied splitter fairing.

As a result of the turbine exhaust case flowpath revision, the ID flowpath diameter was increased to optimize exit Mach number. This inner flowpath revision, which is part of the turbine exhaust duct and fairing assembly, resulted in a new interface location for the customer-provided tailcone.

The design of the turbine exhaust case is considered acceptable from a structural standpoint based on development test experience. Revisions to the core engine temperature and pressure probes and struts for aerodynamic improvement are recommended as discussed in Paragraph (3), page 92.

7) Fan Exhaust Duct

It was necessary to reconfigure the current JT8D fan exhaust duct to accommodate the larger diameter fan flowpath needed for the JT8D-100 engine. Basically, all features were moved radially outward to provide this accommodation. The P_{t7} probe and oil line remain in the same respective axial and angular locations on the outside of the case. The rear mounts as well as those ground handling points required by the airframe manufacturers have also been retained in the same axial and angular positions as on the current engine.

Although the axial position of the principal features of the fan exhaust duct have been retained from the current JT8D turbofan engine, changes in the design of the engine tailpipe did result in shortening the overall exhaust duct relative to the current engine. The conical section of the duct on which the tailpipe flange was mounted was eliminated to provide greater flexibility in designing the exhaust system. Consequently, the flange is now positioned at the rear of the cylindrical duct.

The acoustic treatment is mounted on the inside of the case and forms the outer boundary of the flowpath. It is made in four 90° segments which are attached by radial bolts through the duct. Construction is similar to the other non-structural acoustic panels used on the JT8D-100 except for the outer (non-perforated) skin, which is made up of two layers of glass fabric rather than aluminum sheet.

Testing showed that the design of the fan exhaust duct is acceptable. However it is recommended that the design of fan duct flowpath components be reviewed for possible aerodynamic revisions which could reduce the fan duct pressure loss. This loss was found to exceed design predictions by approximately 1.0%.

d. Bearing and Support Structure

The No. 1 bearing compartment for the JT8D-100 series engine required redesign relative to the JT8D earlier engine models for two major reasons. First, the No. 1 bearing was relocated axially and radially. Second, the inlet case flowpath inner diameter was changed from 30.48 cm (12 in.) to 40.64 cm (16 in.) The final design is similar to the former JT8D bearing compartment except for size but includes the following improvements:

- Simplified plumbing to the front accessory cover
- More positive lubrication to No. 1 bearing
- Simplified aluminum bearing support casting.

All other bearings and their support structure remain unchanged. The redesigned bearing and support structure are considered acceptable. However, test results indicated areas of potential improvement which are discussed in paragraph (2) page 108.

Figure A-63 is a cross section view of the final No. 1 bearing compartment design.

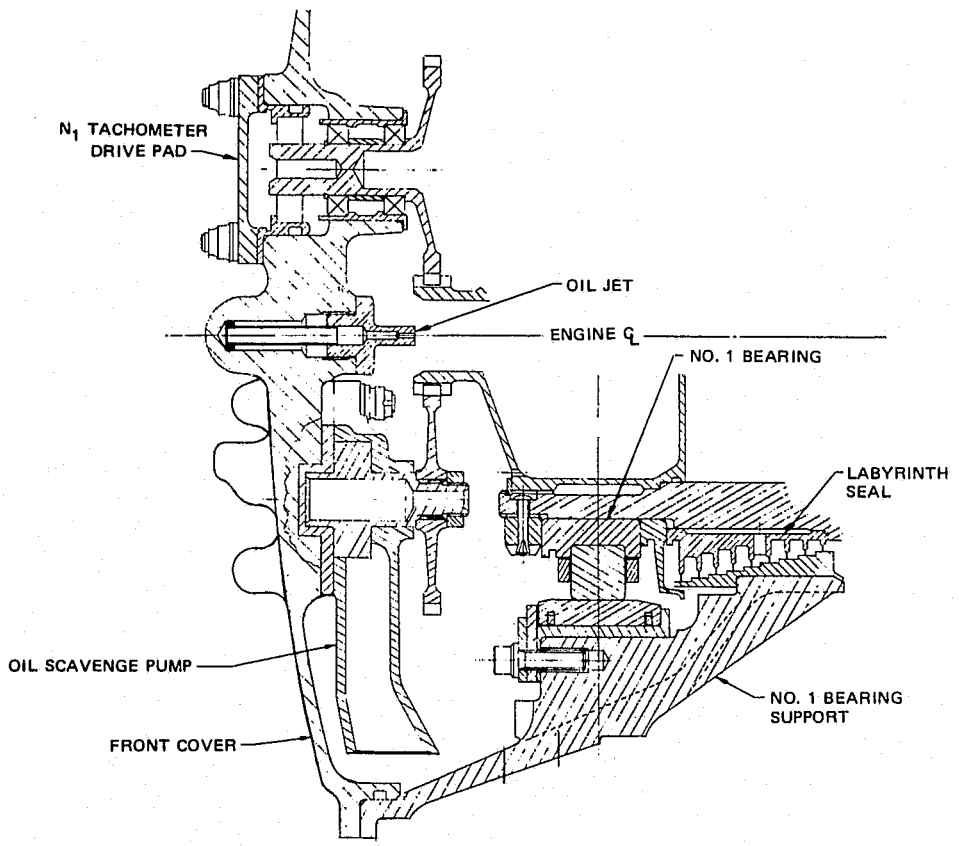

Figure A-63 JT8D-100 No. 1 Bearing Compartment – Cross Section

1) No. 1 Bearing

The JT8D-100 No. 1 bearing is a larger cross section bearing with an increased bore diameter compared to the current JT8D No. 1 bearing. The increased size was necessary to accommodate the large diameter hub which was required to maintain critical speed margin and by the requirement to have blade loss capability equal to the current JT8D No. 1 bearing. The increased bore diameter resulted in a bearing DN (Diameter Speed) level at which bearing preload is not required to preclude skid. The calculated skid potential of the JT8D-100 No. 1 bearing is less than the current JT8D bearing at equivalent "G" loads. The JT8D-100 No. 1 bearing fatigue life is comparable to the current JT8D No. 1 bearing (30,000 hours). A 0.014/0.016 cm (.0054/.0064 inch) tight fit between the JT8D-100 No. 1 bearing and hub has been selected to prevent race spinning.

The No. 1 bearing journal on the rotor front hub was increased in diameter from 9.50 cm (3.74 inches) to 11.99 cm (4.72 inches) to provide additional stiffness for critical speed margin. This required a new roller bearing of increased diameter. To obtain the required lubrication, a new oil jet was added, directed between the bearing cage O.D. and the outer race I.D.

2) Labyrinth Seal, Slinger, Scavenge Pump and Jets

The labyrinth seal axial position has been retained as on current JT8D engines, but has one extra knife-edge to compensate for the extra leakage expected from the larger diameter. The seal steps were increased in height from 0.025 to 0.127 cm (0.010 to 0.050 inches) to improve efficiency. The nose-up attitude angle possible before oil enters the labyrinth seal has been increased from 22° to 28°.

Scavenge pump capacity is adequate at the lower N_1 rotor speed. At 2930 rpm speed the calculated capacity is 0.166 Kg/sec (22 lbs/minute). Maximum lubrication flow into the compartment is 0.61 Kg/sec (8 lbs/minute).

A new oil jet was added to improve the lubrication of the No. 1 bearing. This jet was directed toward the space between the bearing cage O.D. and the outer race I.D. The former jet on the engine centerline was kept to lubricate splines, provide oil mist for gears, and to cool the shaft I.D. The size of passages through cast sections were made the same as the comparable tube I.D. passing through the inlet case large strut.

During engine testing oil leakage was noted from the No. 1 bearing compartment. The cause of this leakage was concluded to be the following. The breather line configuration to the No. 1 bearing compartment is such that flow through the line was subject to high losses. In addition, the inlet to the line faces into the spray from the scavenge pump gears. Finally, a low point in the line exists at the bottom of the inlet case, a possible oil collector site. During high-power operation, the compartment is pressurized by compressor bleed air which exits through the breather line along with some oil from the compartment due to its proximity to the scavenge pump gear. When the engine is decelerated to idle, compressor bleed air pressure to the compartment is reduced. However, due to oil collecting at the low point in the breather line and with its built-in pressure loss configuration, the high compartment pressure cannot exit through the breather line. This resulted in an air-oil mist backflow through the labyrinth seal causing external oil leakage.

Possible solutions to this problem are:

- Redesigning the breather tube configuration to eliminate low points and reduce the number of restrictions in the tube.
- Relocating the breather tube inlet toward a drier area of the compartment.
- Incorporating carbon type seals to provide positive oil retention capability.

3) Front Accessory Cover

The cover was positioned to maintain a reasonable clearance with the end of the low compressor rotor shaft. [0.322 cm (0.127-inch) minimum required] Identical gear mesh rates and internal parts were used from the current JT8D engine.

Because of the increased diameter bolt circle for joining the front accessory cover to the larger diameter inlet case, the number of bolts was increased from 12 to 15 at similar circumferential spacing. The studs for attaching the engine inlet center fairing were also increased from 4 to 5 and could be evenly spaced and symmetrical with the 15 flange bolts.

During engine testing cracks were discovered in the front accessory support structure around the N_1 tachometer pad and across the inlet nosecone mounting bosses. A combination of steady thermal stress and vibratory resonance was determined to have caused the crack. Revised covers were fabricated from both aluminum bar (AMS 4135) and steel (AMS 6415). These materials were chosen to facilitate material procurement and to maintain engine development and flight test schedules.

One solution to the cracking problem for production type engines would be to use high grade AMS 4418 cast magnesium with increased thickness in those areas where additional strength is required.

4) No. 1 Bearing Support Structure

The loads used for the No. 1 bearing support structural analysis were reaction loads due to fan blade loss, aircraft maneuvers, and rotor imbalance; and loads caused by thermal incompatibility and anti-icing air thermal gradients.

e. Towershaft

The towershaft of the JT8D-100 engine (shown in Figure A-59) is approximately 40% longer than the towershaft used on current JT8D engines. The added length was required due to the increased fan duct diameter of the JT8D-100. The towershaft transmits torque from the starter to the high-pressure compressor shaft while the engine is being started and extracts power during engine operation to drive fuel and oil system components as well as airframe electrical generation equipment through the externally mounted accessory gearbox.

The towershaft connects two regions capable of relative deflections, the high rotor shaft and the externally mounted accessory gearbox. Therefore, the configuration has loose splines at both ends to allow for misalignment without introducing high bending loads. The towershaft stiff bearing critical speed mode shape is illustrated in Figure A-64.

The material chosen for the towershaft was AMS 6487. It was selected because of its high yield strength and stiffness, good machinability and its suitability for adding spline treatment to impart acceptable wear characteristics.

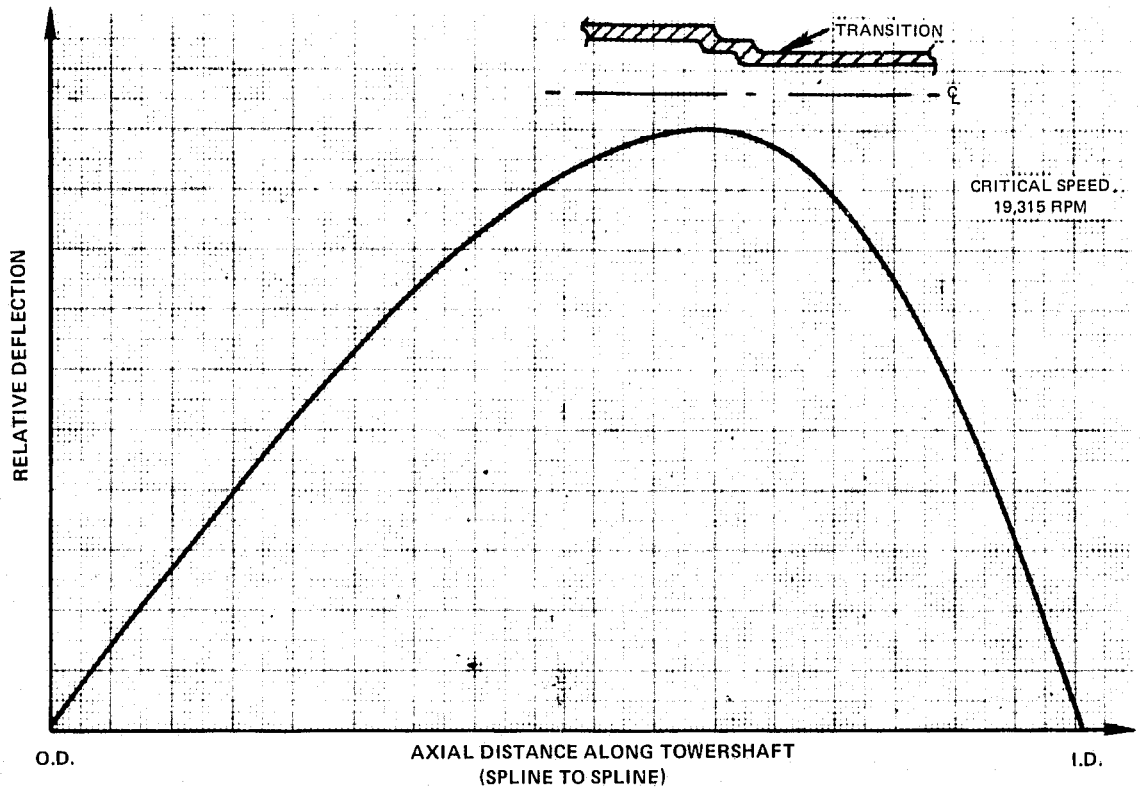

Figure A-64. Predicted JT8D-100 Towershaft Relative Deflection at Critical Speed

During the development phase of this program (prior to engine testing) it was found necessary to modify the towershaft design as presented in Reference 3. The shaft wall-thickness was increased to provide increased torque transmission capacity. This modification did not significantly affect the critical speed of the shaft.

f. External Tubing and Accessory and Control Location

The high rotor accessory gearbox, oil tank, oil pumps and oil system filters used on the current JT8D have been retained on the JT8D-100 design. The JT8D fuel control, fuel pump, fuel-oil cooler fuel filters, bleed control and pressurizing valve were also retained as well as the ignition system and the anti-icing and fuel de-icing valves. The fuel control would have to be revised to incorporate the capability of having a two-position idle setting (ground and approach) prior to certification of this engine model.

Due to the increased engine diameter and axial length and the change in relative locations of the engine flanges on the JT8D-100 as compared to current JT8D engines, it was necessary to relocate external controls and interconnecting plumbing. However, routing of the plumbing and placement of the controls and accessories was kept as close as possible to those of current engines. Controls and accessories were relocated only to accommodate the new flange locations or if required by airframe/engine mechanical interface limitations.

Locations of accessories and tubing was closely coordinated with the Boeing Company and McDonnell-Douglas to preclude interference between nacelle and engine components. This coordination indicated the need to relocate the fuel-oil cooler as well as to reroute several pipes. As a result of added flexibility caused by rerouting plumbing and relocating the fuel-oil cooler, the pipe connecting the pressuring valve to the fuel oil cooler required the addition of an anti-blow-off retaining fitting.

Tables A-XXVI, -XXVII, and -XXVIII and Figures A-65, -66, and -67 present the pertinent data about the external fuel, air, and oil plumbing systems, respectively.

TABLE A-XXVI

JT8D-100 FUEL SYSTEM PLUMBING

Tube No.	Description	Routing
F1	Main Fuel Supply	Fuel Control To Fuel Flowmeter
F2	Main Fuel Supply	Oil Cooler To Pressuring Valve
F3	Primary Fuel Manifold	Pressurizing Valve To Internal Pri. Manifold
F4	Secondary Fuel Manifold	Pressurizing Valve To Internal Sec. Manifold

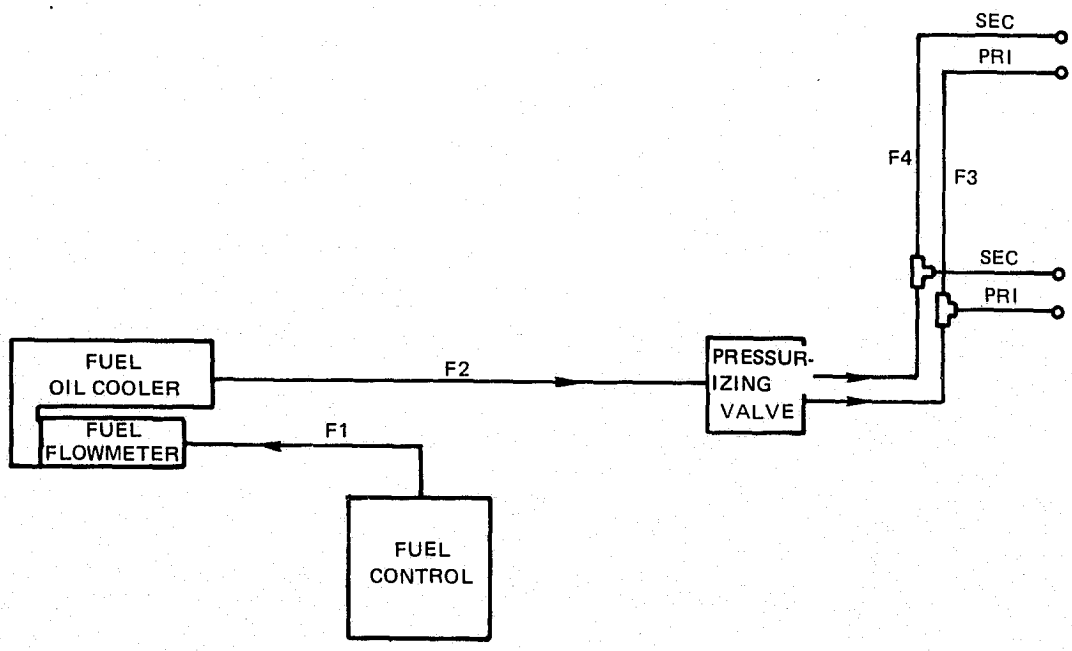

Figure A-65 JT8D-100 External Fuel Systems Plumbing Diagram

TABLE A-XXVII

JT8D-100 AIR SYSTEMS PLUMBING

Tube No.	Description	Routing
A1	IGV Anti-icing Left Side	Rear Compr. Fan Duct to Shut-off Valve
A2	IGV Anti-icing Left Side	Shut-off Valve to Inlet Case
A3	IGV Anti-icing Right Side	Rear Compr. Fan Duct to Shut-off Valve
A4	IGV Anti-icing Right Side	Shut-off Valve to Inlet Case
A5	Fuel De-icing Air Supply	Left & Right Fan Diffuser Duct Bleed Pads to Shut-off Valve
A6	Fuel De-icing Air Supply	Shut-off Valve to Fuel Heater
INSTRUMENTATION		
A7	Burner Pressure Sense (Pb)	Comb. Chamber & Turbine Fan Duct Boss to Water Trap
A9	Burner Pressure Sense (Pb)	Water Trap to Fuel Control
A10	Inlet Pressure Sense (P_{T2})	Inlet Case Boss to PRBC
A11	Lo Compr. Discharge Press. Sense (P_{S3})	Fan Diffuser Duct Boss to PRBC
A12	Bleed Valve Supply Pressure (P_{S4})	Tee on A5 to PRBC
A13	Bleed Valve Muscles Pressure	PRBC to Fan Diffuser Duct Boss
A14	Fan Duct Discharge Pressure (P_{tf7})	One O'Clock Probe to Two O'Clock Probe
A15	Fan Duct Discharge Pressure (P_{tf7})	Two O'Clock Probe to Four O'Clock Probe

*JT8D-117

TABLE A-XXVII (Continued)

Tube No.	Description	Routing
A16	Fan Duct Discharge Pressure ($P_{tf}7$)	Four O'Clock Probe to Seven O'Clock Probe
A17	Fan Duct Discharge Pressure ($P_{tf}7$)	Seven O'Clock Probe to Eight O'Clock Probe & Airframe Conn.
A18	Fan Duct Discharge Pressure ($P_{tf}7$)	Eight O'Clock Probe to Ten O'Clock Probe
A19	Fan Duct Discharge Pressure ($P_{tf}7$)	Ten O'Clock Probe to One O'Clock Probe

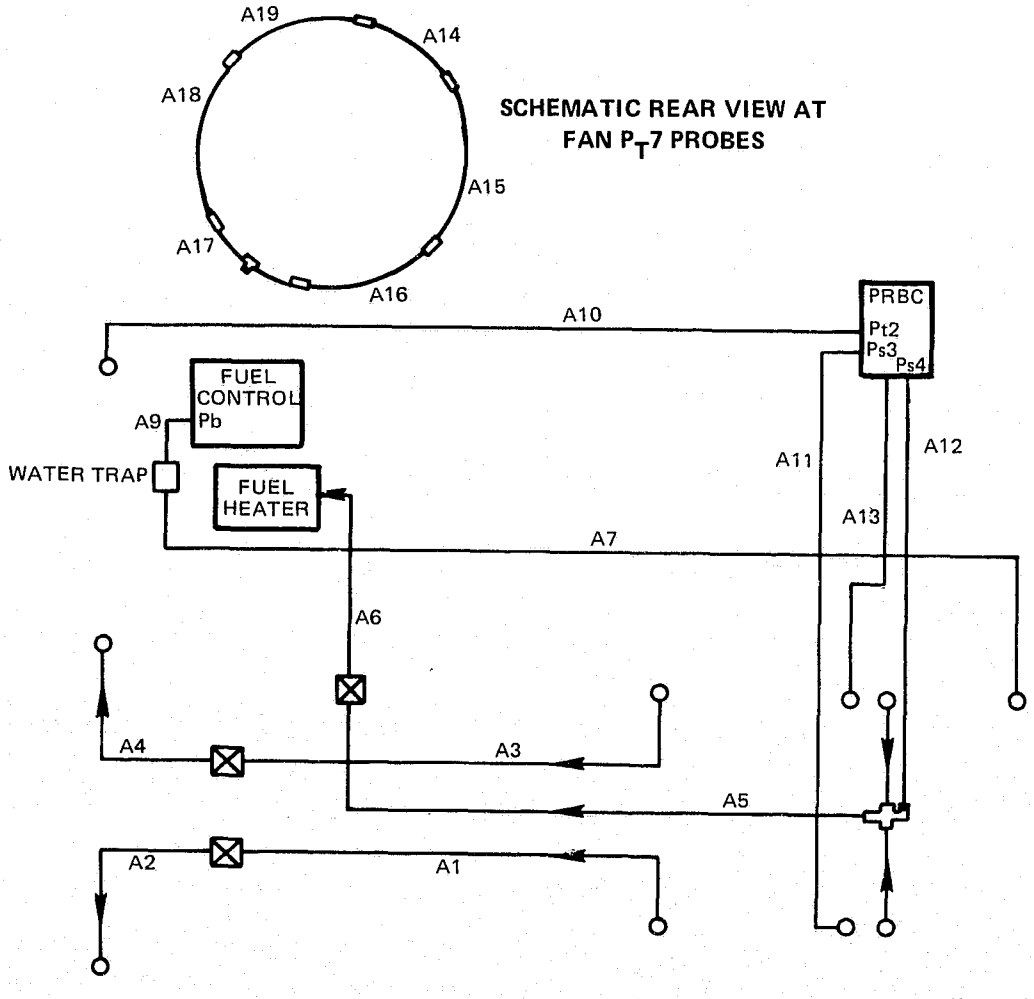

Figure A-66 JT8D-100 External Air Systems Plumbing and Instrumentation Diagram

TABLE A-XXVIII

JT8D-100 OIL SYSTEMS PLUMBING

Tube No.	Description	Routing
L1	Main Oil Supply	Gear Box Main Oil Filter to Fuel Oil Cooler
L2	Oil Pressure Supply #1 Bearing	Oil Cooler to Inlet Case Boss
L3	Oil Pressure Supply #4 & #5 Brg.	Oil Cooler to Fan Diffuser Duct Boss
L4	Oil Pressure Supply #2 & 3 Brg.	Tee on L3 to Gearbox Towershaft Housing
L5	Oil Pressure Supply #4½ & 6 Brg.	Diff. Fan Duct to Coupling on L6
L6	Oil Pressure Supply #4½ & 6 Brg.	Coupling on L5 to Internal #6 Oil Line in Fan Exh. Duct
L7	Oil Scavenge #1 Bearing	Inlet Case Boss to Gearbox
L8	Oil Scavenge #4, 4½, 5 & 6 Bearings	Fan Diffuser Duct Boss to Gearbox
L9	Oil Breather #1 Bearing	Inlet Case Boss to Gearbox
L10	Oil Breather #4 Bearing	Fan Diffuser Duct Boss to Gearbox
L11	Oil Pressure Sense	Oil Cooler to Gearbox Oil Press. Regulator

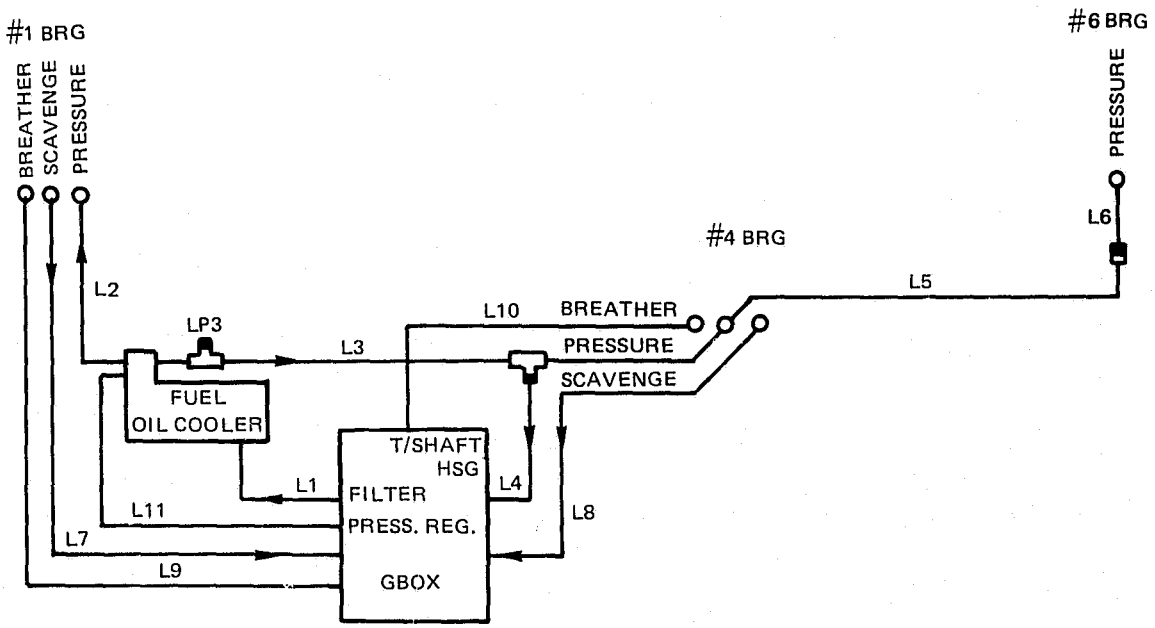

Figure A-67 JT8D-100 External Oil Systems Plumbing Diagram

No problems were encountered during the development testing except for the need to redesign the tube connecting the pressurizing valve to the fuel oil cooler. An anti blow off retention fitting was added to this tube in order to prevent tube disengagement under pressure.

3. Engine Installation and Weight

a. Installation Dimensions

Figure A-68 shows the pertinent installation differences between the JT8D and JT8D-100 engines.

All physical dimensions necessary for installation of the JT8D-100 engine are shown in Figures A-69A, B and C. The engine was designed to English units therefore S. I. units are not included on these drawings.

A reoperation scheme was devised to move the rear mount attachment points radially outward to accommodate Boeing mount links. It is noted that this resulted in non-interchangeability between McDonnell-Douglas and Boeing engines, a matter which will require resolution prior to attaining production status for the JT8D-100 engine. Figures A-69A, B, and C show the areas of non-interchangeability.

b. Mount and Maneuver Loads

Limit loads for engine mounts and customer attachment points are shown on Figures A-70 through A-78. Limit loads were established by analyzing engine stresses caused by application of the loads furnished by the customer. Customer loads were increased on the inlet cowl and tailpipe attachment flanges after the initial design was completed, requiring redesign to strengthen these attachment points.

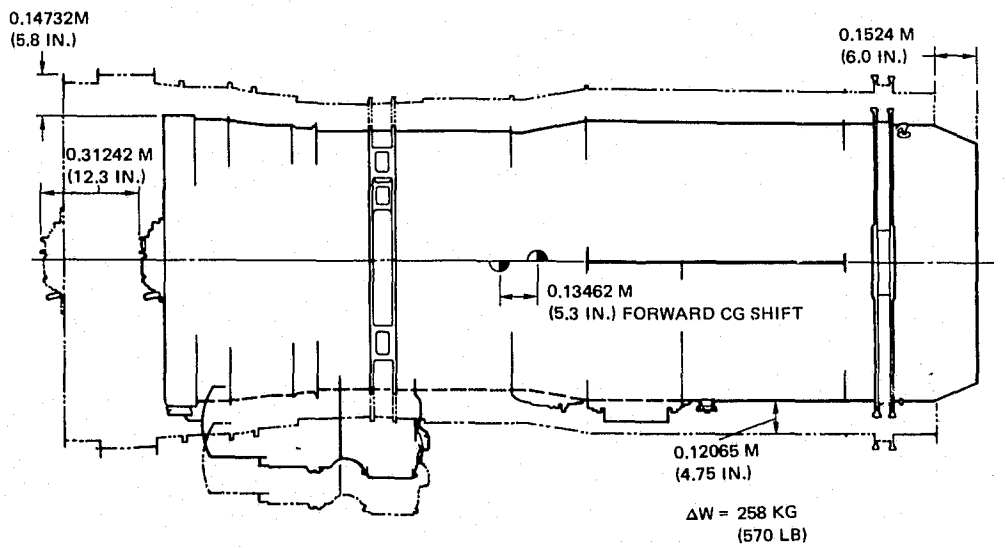

Figure A-68 Comparison of JT8D-JT8D-100 Installation Characteristics

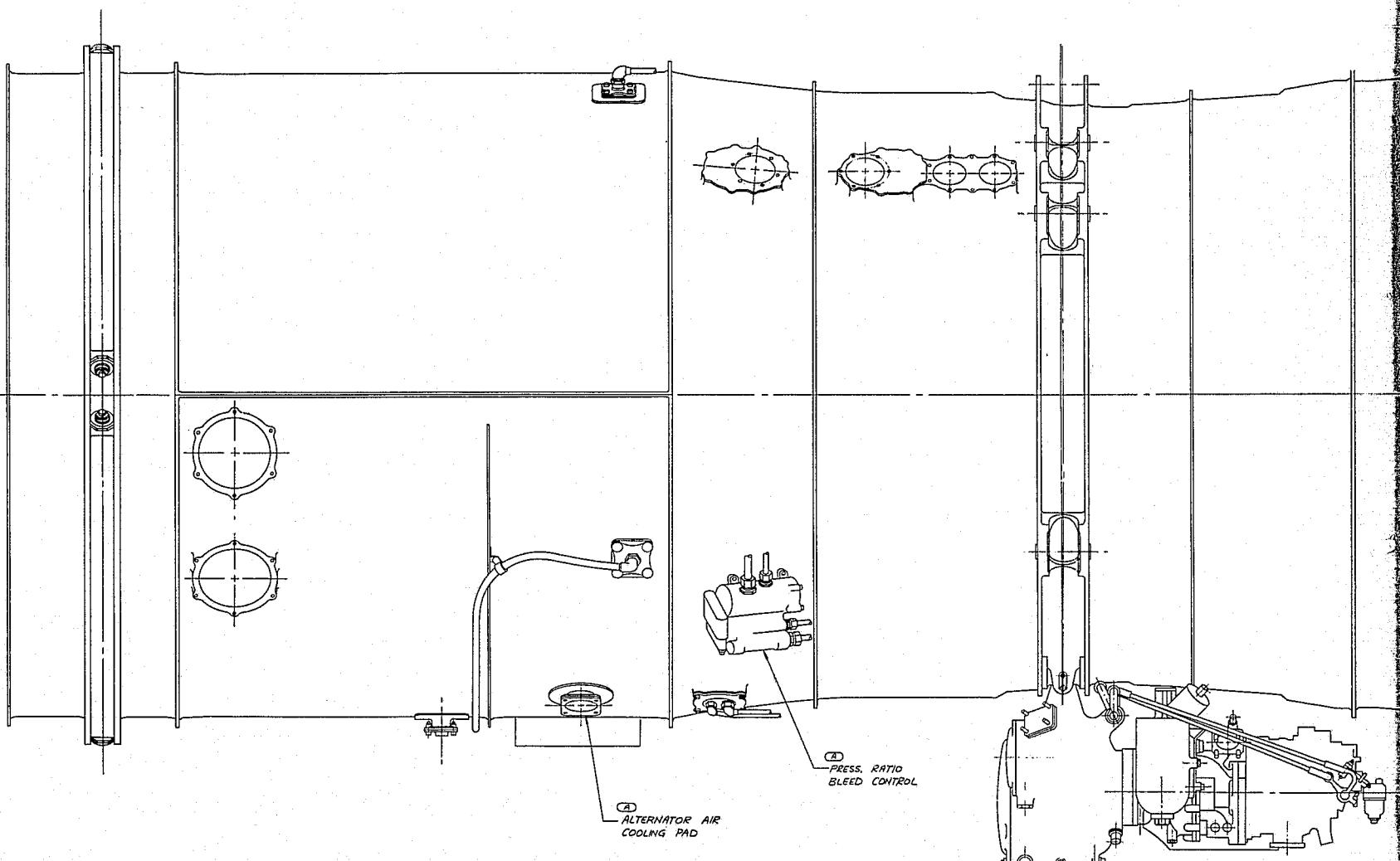

FOLDOUT FRAME 1

ORIGINAL PAGE IS
OF POOR QUALITY

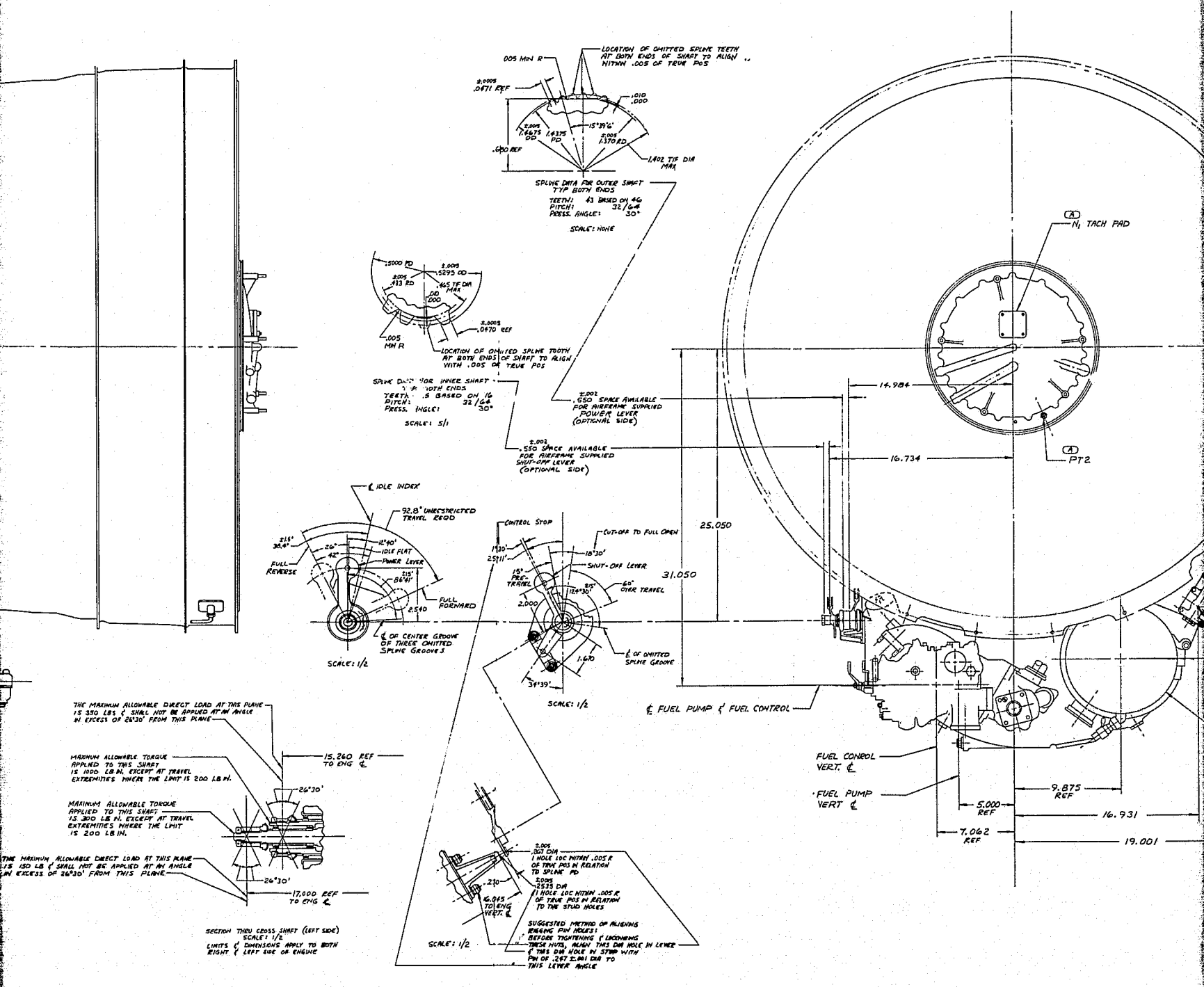

FOLDOUT FRAME 1

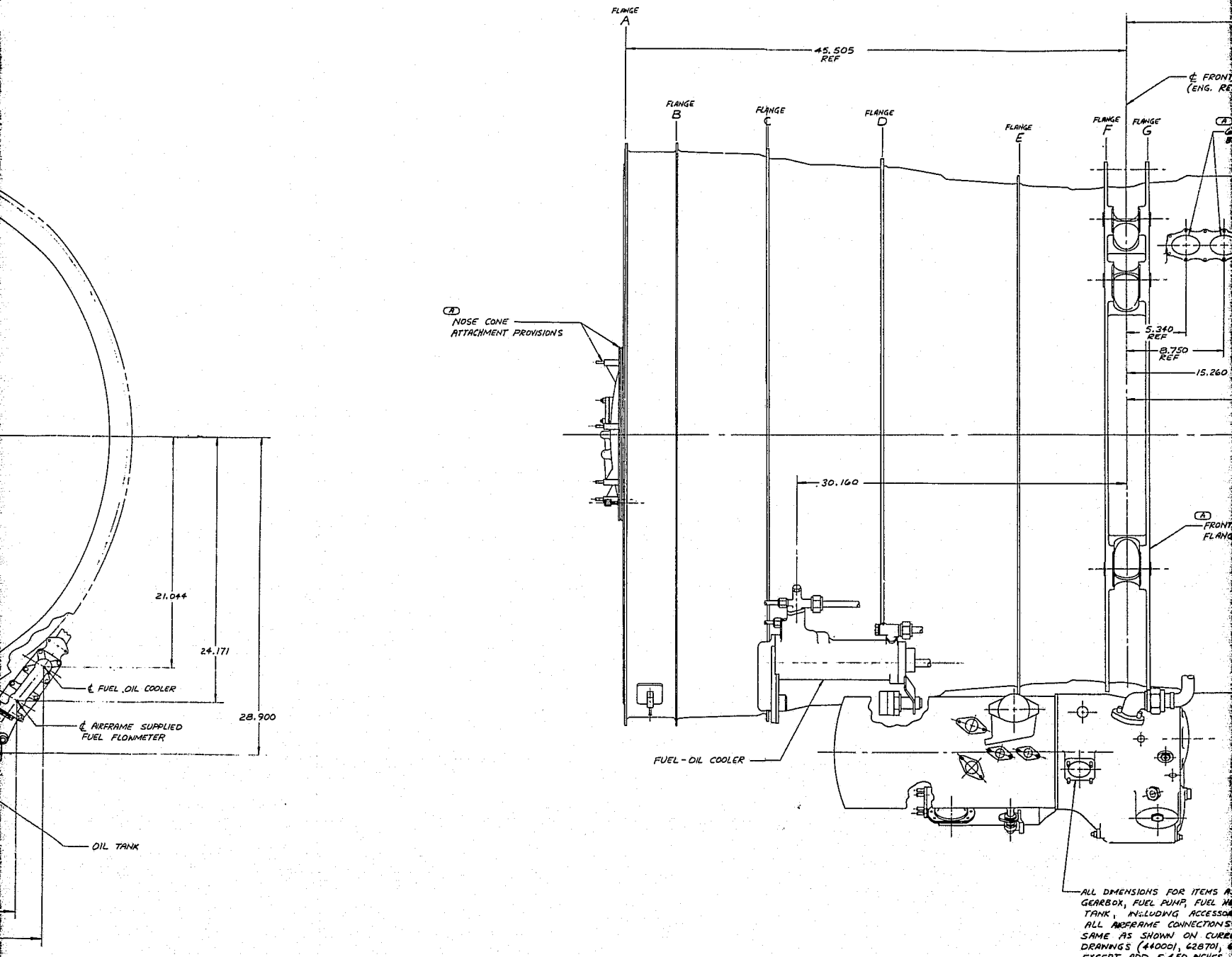

FOLDOUT FRAME 3

ORIGINAL PAGE IS
OF POOR QUALITY

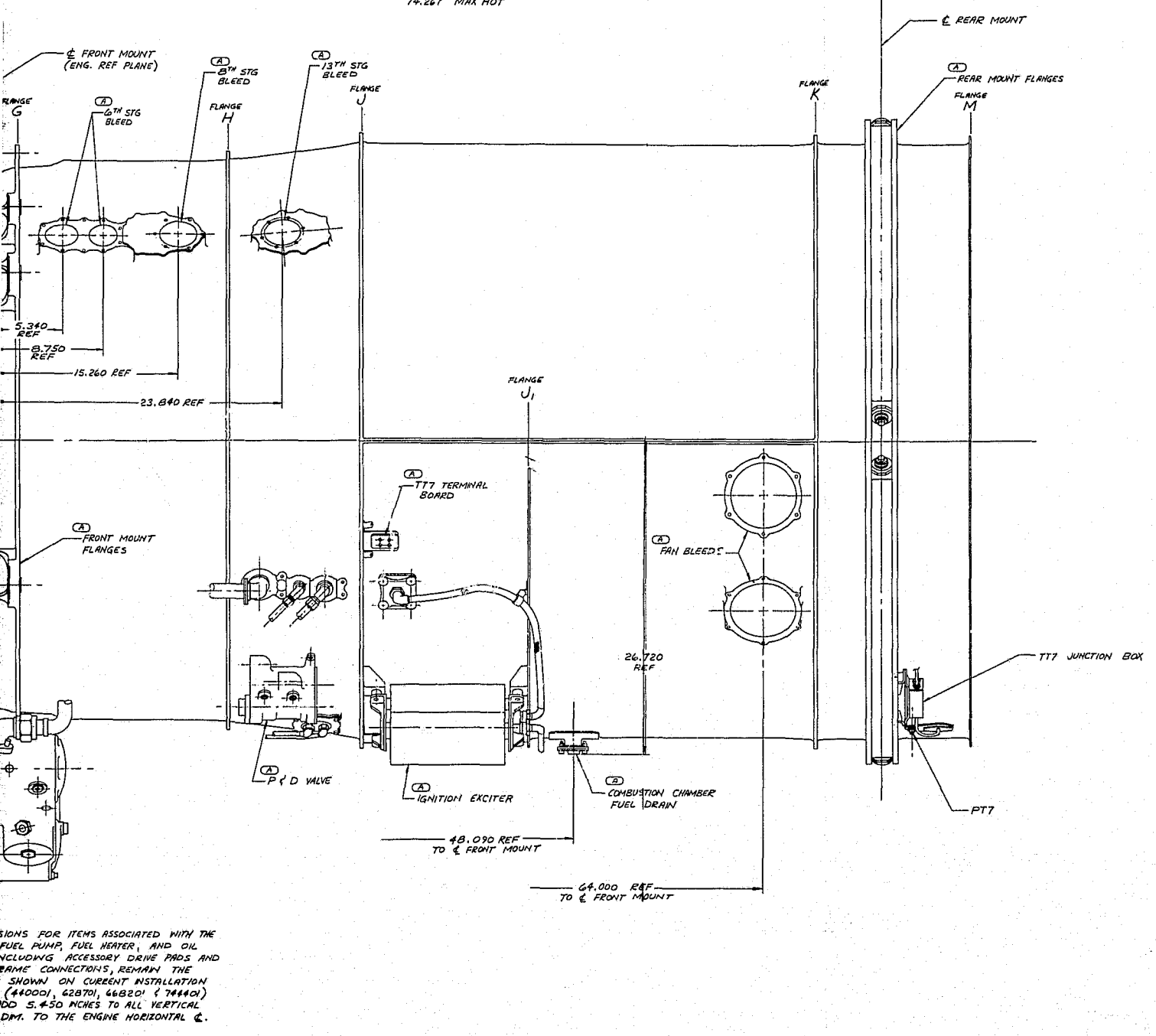

TORQUE & MOMENT		
DRIVE PAD	NOM. USE	T CONTINUO
A	STARTER	b
B	GENERATOR	1500
C	TACHOMETER	7
D	TACHOMETER	7
E	FUEL POWER PUMP	1000

1:1 RATIO REFERS TO LOW
1/2 RATIO REFERS TO HIGH
DIRECTION OF SHAFT ROTA
MAXIMUM ALLOWABLE CONTIN
OTHERWISE NOTED, PROVIDED
TORSIONAL VIBRATION ABS
a - MAXIMUM ALLOWABLE
AT FOUR HOUR R
b - STRENGTH OF THE
DELIVERING A MAX
SECTION IS DESIG
c - MAXIMUM TORQUE

NOTES —
1. (A) SEE SH
2. FOR SIZE
FOR AIRFR
APPLICABL
DRAWINGS
668201 (
3. [ ] INDIC
PRODUCTION

SIONS FOR ITEMS ASSOCIATED WITH THE FUEL PUMP, FUEL HEATER, AND OIL NCLUDING ACCESSORY DRIVE PADS AND RAME CONNECTIONS, REMAIN THE SHOWN ON CURRENT INSTALLATION (440001, 628701, 668201 & 744401) DD 5.450 INCHES TO ALL VERTICAL DIM. TO THE ENGINE HORIZONTAL ℄.

Figure A-69A JT

FOLDOUT FRAME

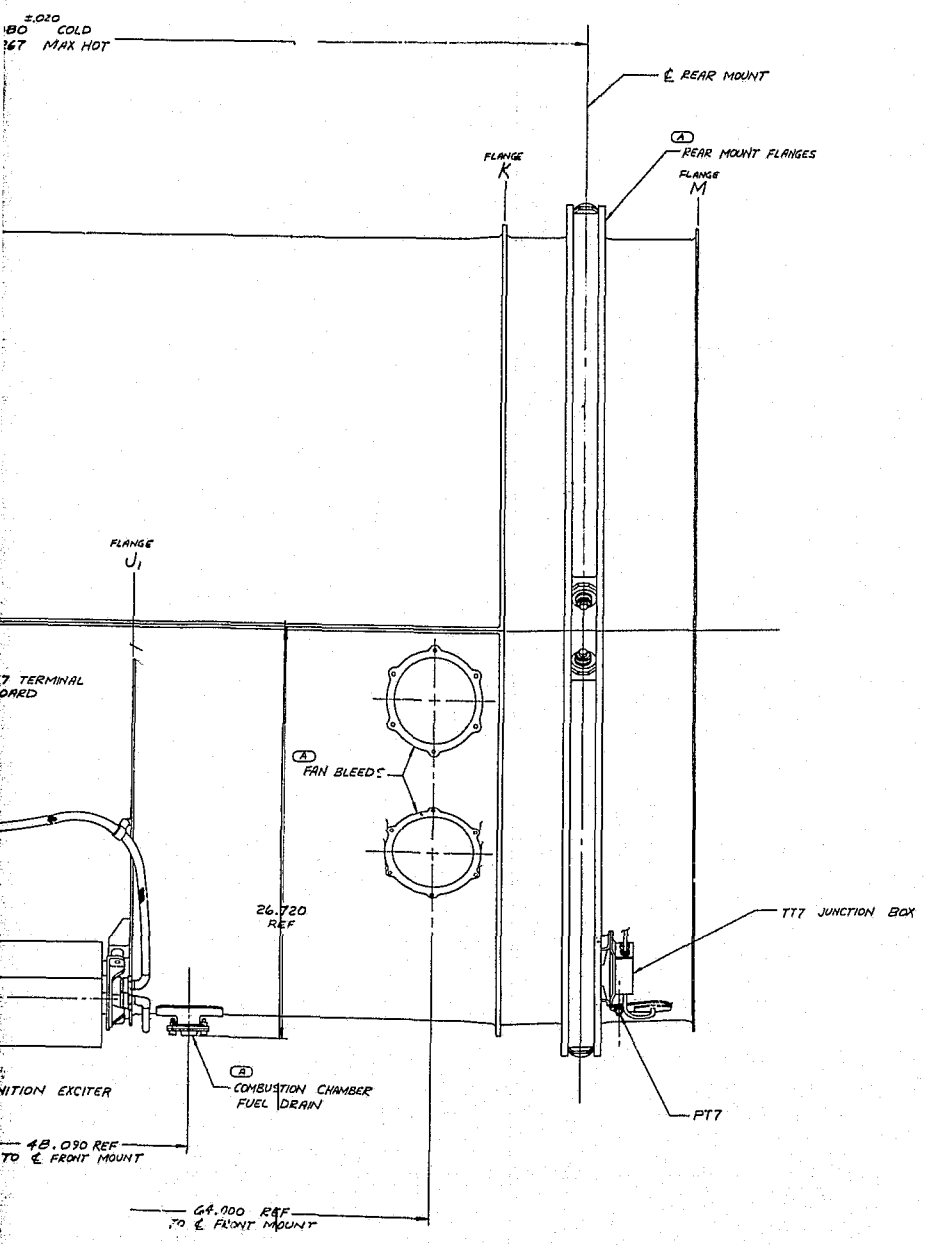

TORQUE & MOMENT LIMITATION TABLE - ACCESSORY DRIVES

DRIVE PAD	NOM. USE	TORQUE (LB IN.)			SPEED RATIO	N1 N2	ROTATION (FACING ENGINE PAD)	1G OVERHUNG MOMENT (LB IN.)
		CONTINUOUS	OVERLOAD	STATIC				
A	STARTER	b	b	b	.597:1	N_2	CW	625
B	GENERATOR	1500	2250a	6600c	.700:1	N_2	CW	2500
C	TACHOMETER	7	—	50	.699:1 (.532:1)	N_1	CW	—
D	TACHOMETER	7	—	50	.343:1	N_2	CCW	—
E	FUEL BOOST PUMP	1000	1500 a	4300	.292:1	N_2	CW	400

N1 RATIO REFERS TO LOW PRESSURE COMPRESSOR - TURBINE UNIT SPEED
N2 RATIO REFERS TO HIGH PRESSURE COMPRESSOR - TURBINE UNIT SPEED
DIRECTION OF SHAFT ROTATION FACING ENGINE PAD: CW- CLOCKWISE, CCW- COUNTERCLOCKWISE
MAXIMUM ALLOWABLE CONTINUOUS TORQUE VALUES ARE AT ANY ENGINE SPEED UNLESS OTHERWISE NOTED, PROVIDED NO DESTRUCTIVE FORCES RESULTING FROM ACCESSORY TORSIONAL VIBRATION ARE PRESENT.

a - MAXIMUM ALLOWABLE FOR FIVE MINUTE DURATION RECURRING NOT OFTENER THAN AT FOUR HOUR INTERVALS.

b - STRENGTH OF THE STARTER DRIVE SHALL BE ADEQUATE FOR A STARTER DELIVERING A MAX TORQUE OF 550 LB-FT ENGINE STARTER DRIVE SHEAR SECTION IS DESIGNED TO FAIL AT A STATIC TORQUE OF 850-950 LB-FT

c - MAXIMUM TORQUE WHEN USED AS A STARTER SHALL BE 410 LB-FT

NOTES —

1. (A) SEE SHEET 2 FOR DETAIL INFORMATION
2. FOR SIZE AND CONTOUR DIMENSIONS NOT SHOWN FOR AIRFRAME INTERFACE CONNECTIONS SEE APPLICABLE CURRENT ENGINE INSTALLATION DRAWINGS 440001 (JT8D-7A, 9A), 688701 (JT8D-[illegible]), 668201 (JT8D-15) & 744401 (JT8D-17).
3. [ ] INDICATES THIS DIMENSION APPLIES FOR PRODUCTION ENGINES ONLY.

FOLDOUT FRAME 5

Figure A-69A JT8D-100 Engine Installation

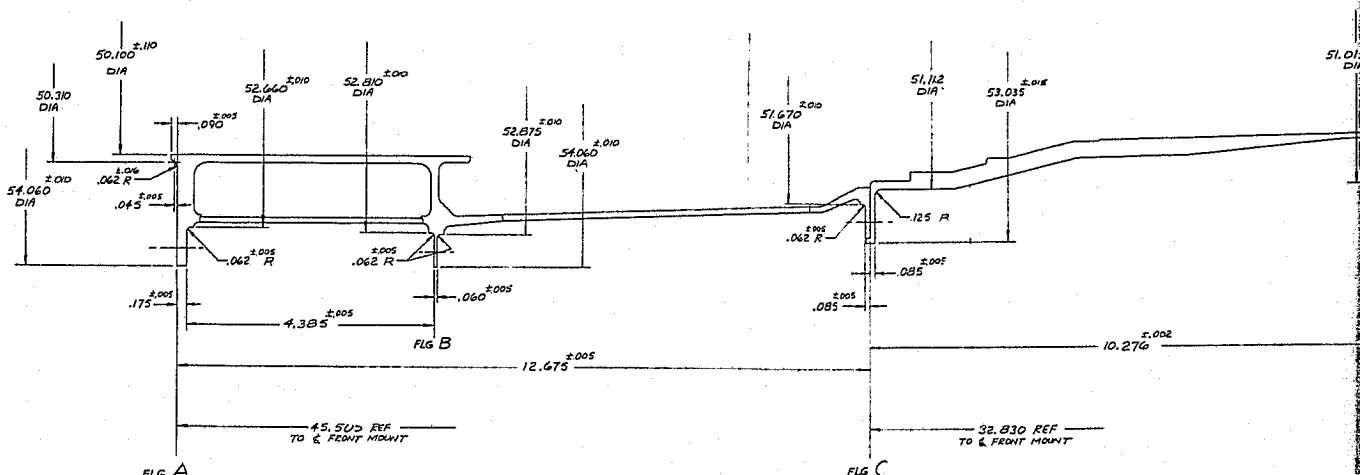

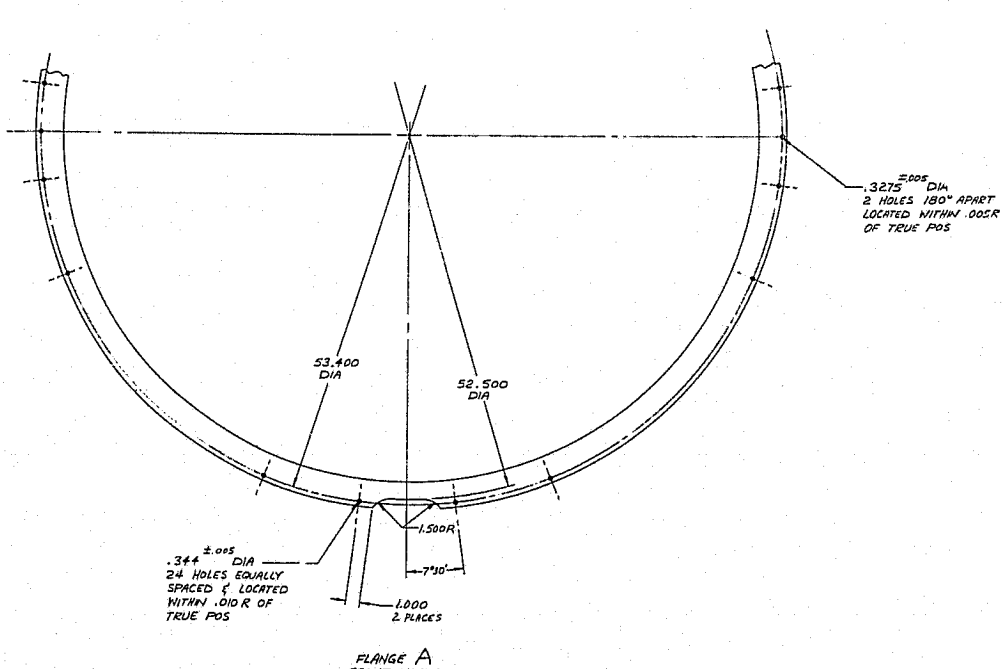

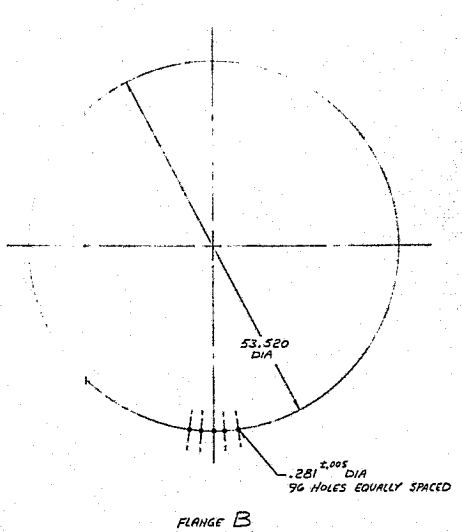

ORIGINAL PAGE IS
OF POOR QUALITY

Figure A-69B JT8D-100 Engine Installation

FOLDOUT FRAME

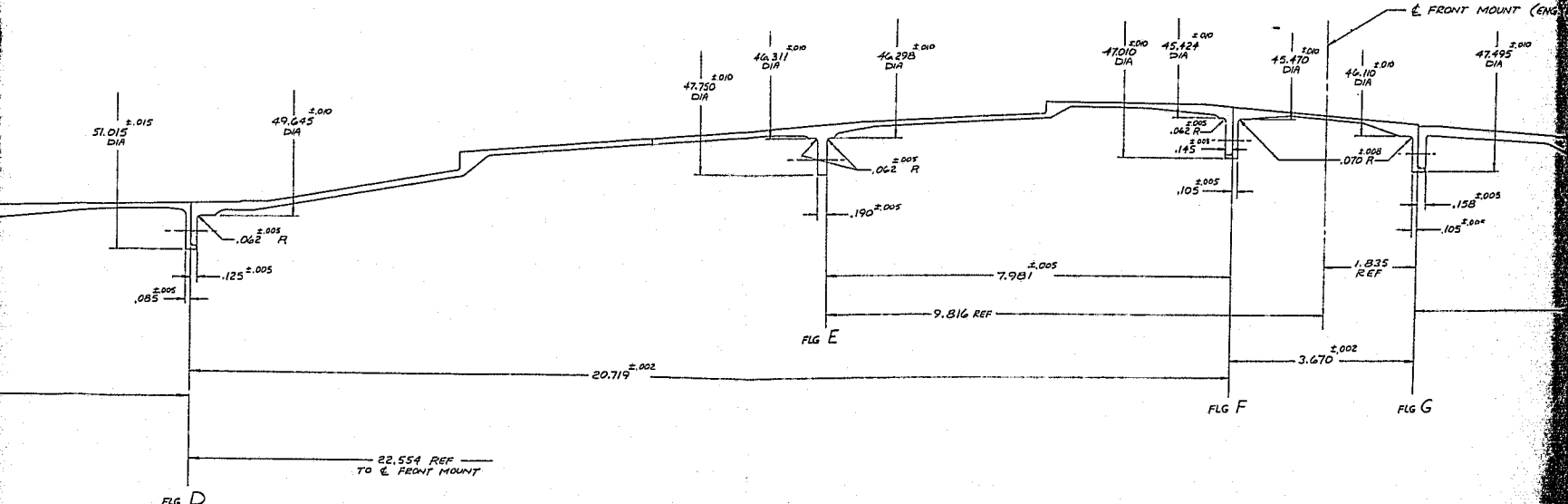

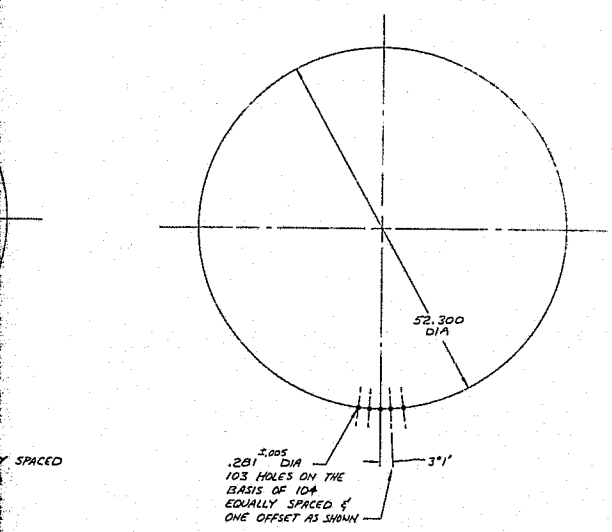

FLANGE C
FRONT VIEW

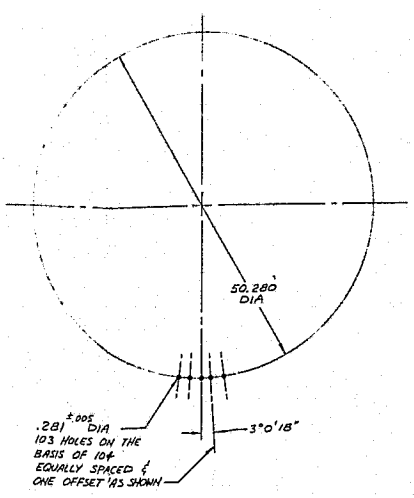

FLANGE D
FRONT VIEW

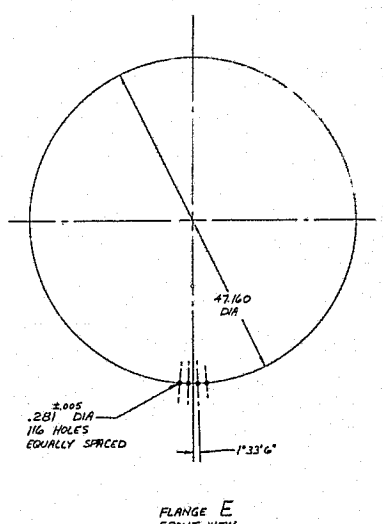

FLANGE E
FRONT VIEW

FOLDOUT FRAME 2

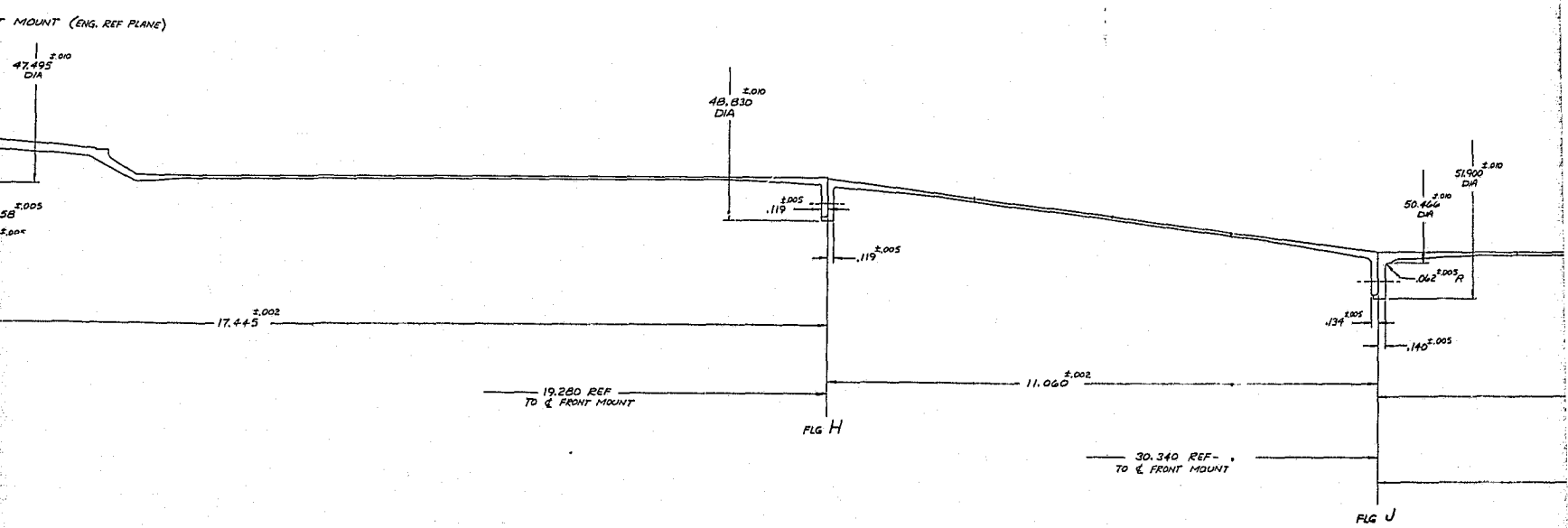

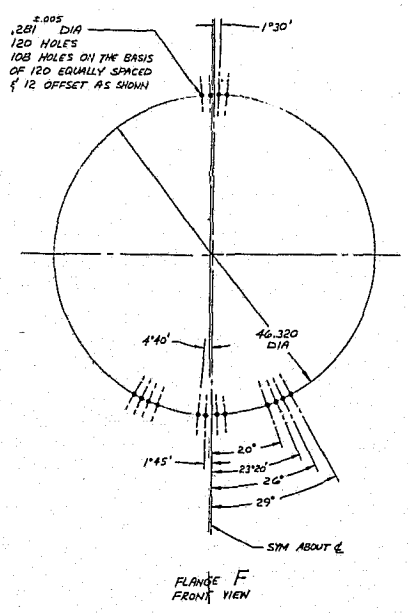

FLANGE F
FRONT VIEW

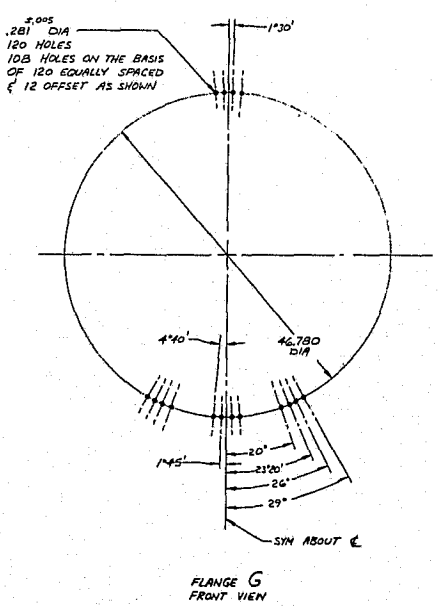

FLANGE G
FRONT VIEW

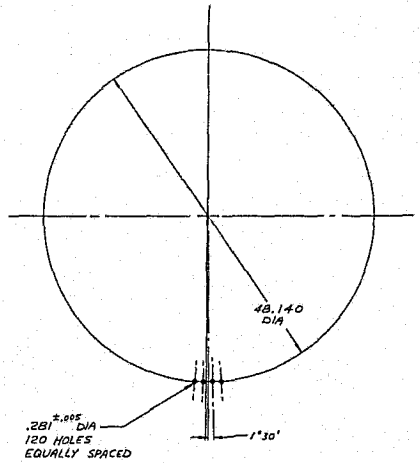

FLANGE H
FRONT VIEW

FOLDOUT FRAME 3

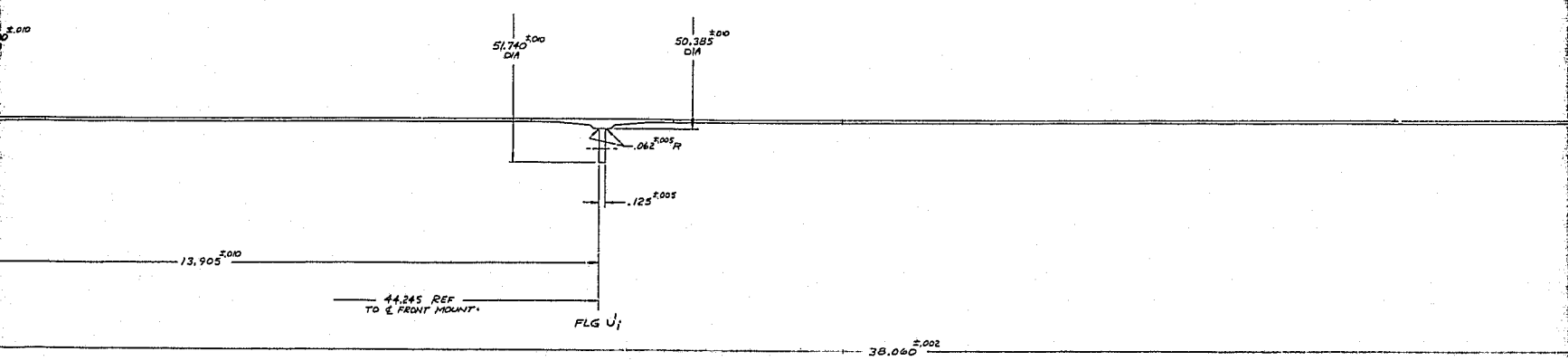

68.400 RE
TO ℄ FROM MO

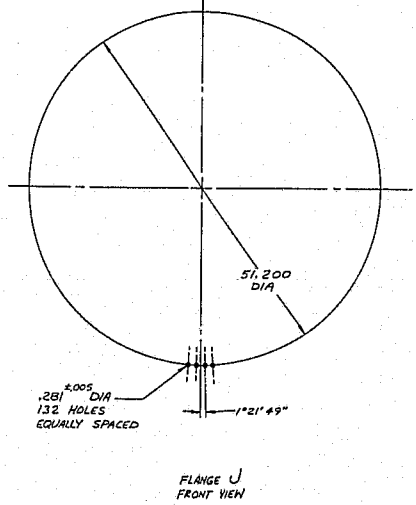

FLANGE J
FRONT VIEW

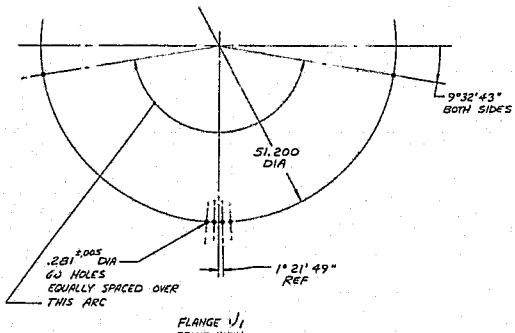

FLANGE J1
FRONT VIEW

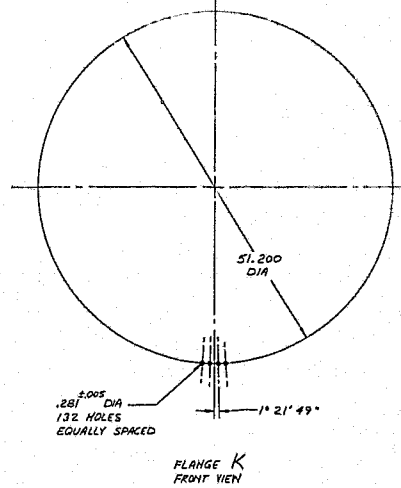

FLANGE K
FRONT VIEW

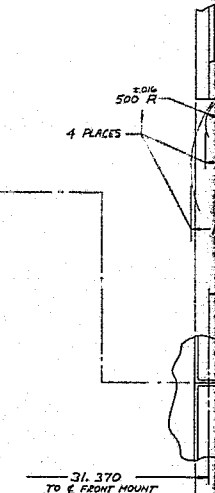

FOLDOUT FRAME 4

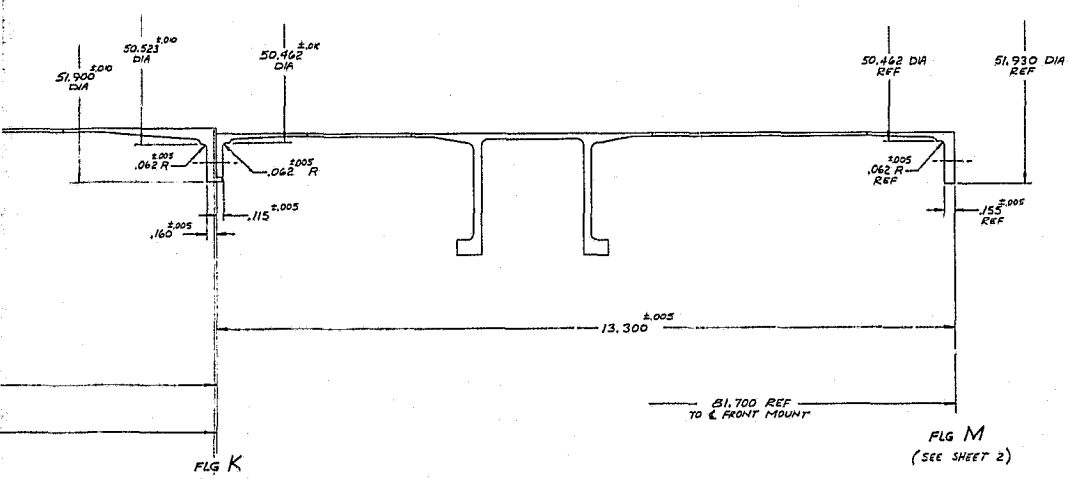

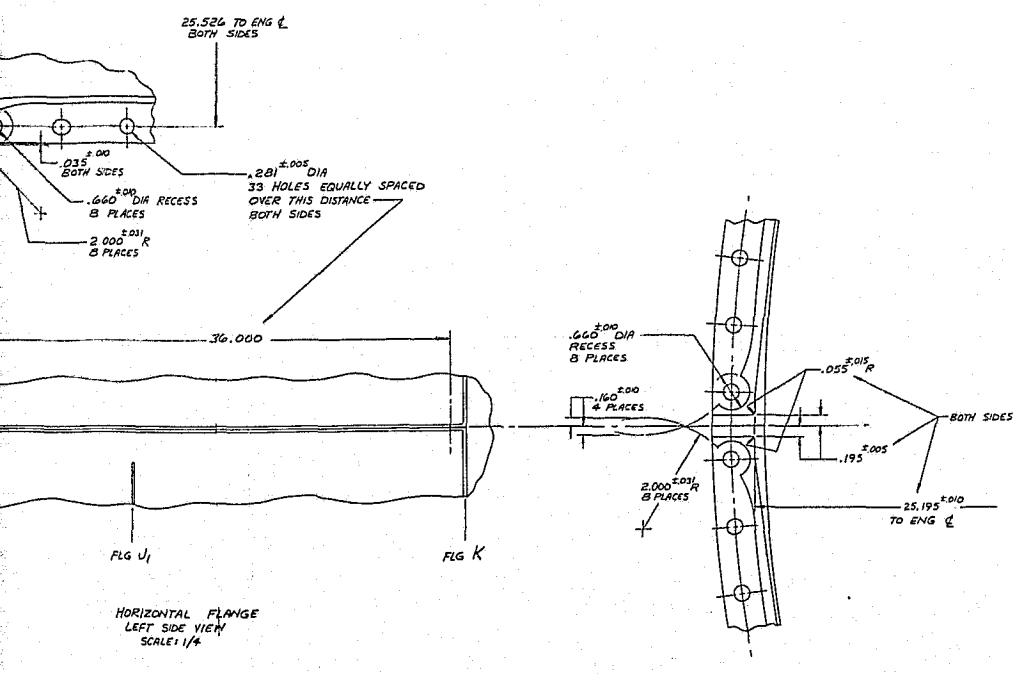

HORIZONTAL FLANGE
LEFT SIDE VIEW
SCALE: 1/4

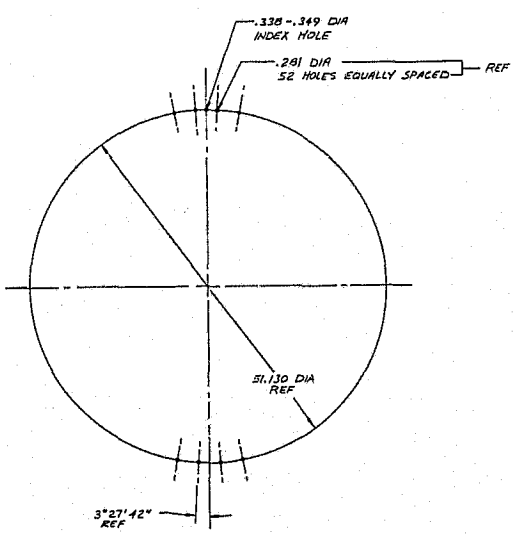

FLANGE M
FRONT VIEW
INFO FROM SHEET 2 REPEATED HERE FOR CONVENIENCE

ORIGINAL PAGE IS
OF POOR QUALITY

FOLDOUT FRAME 5

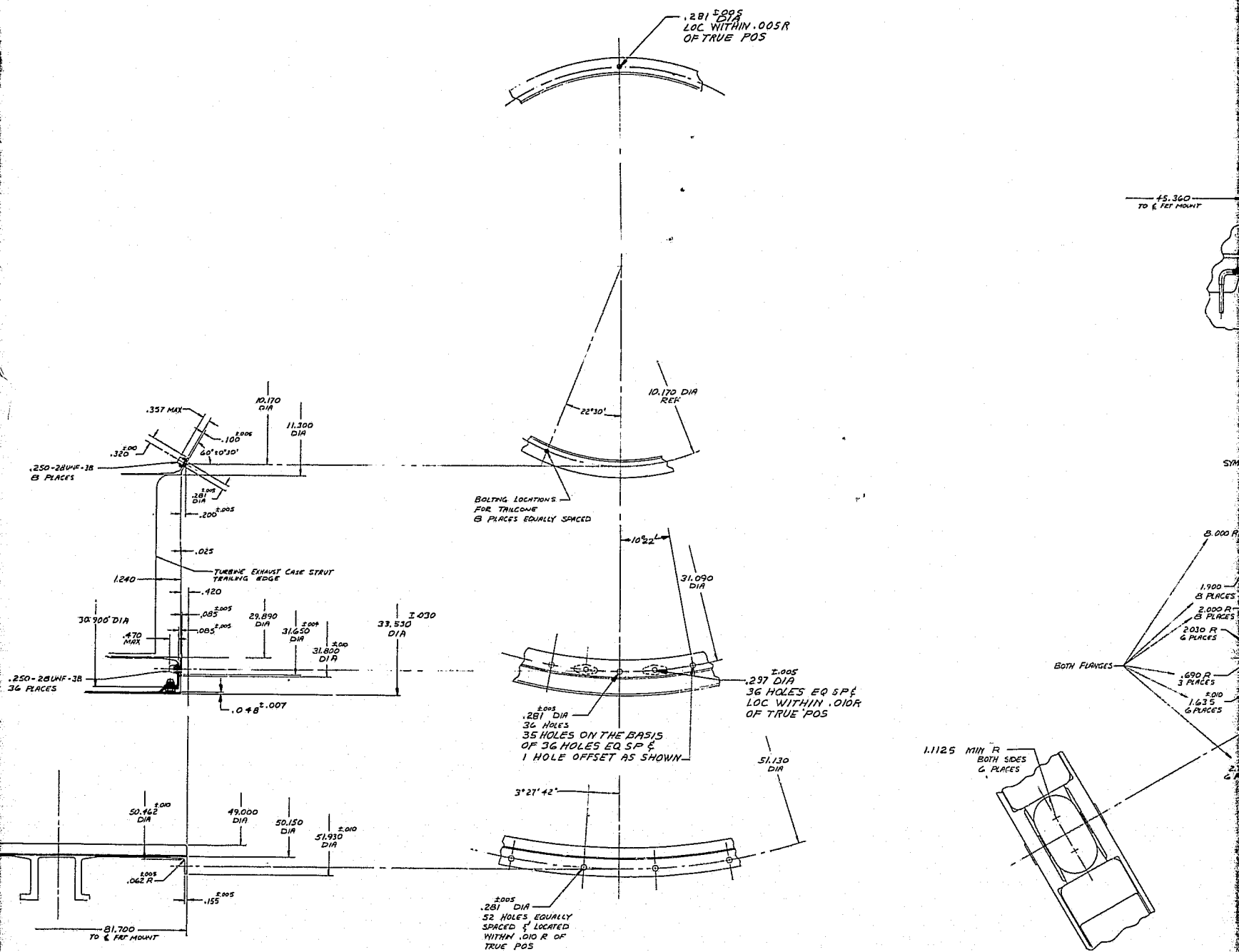

ENGINE REAR FLANGES
SCALE: 1/2

REAR VIEW

ORIGINAL PAGE IS
OF POOR QUALITY

FOLDOUT FRAME

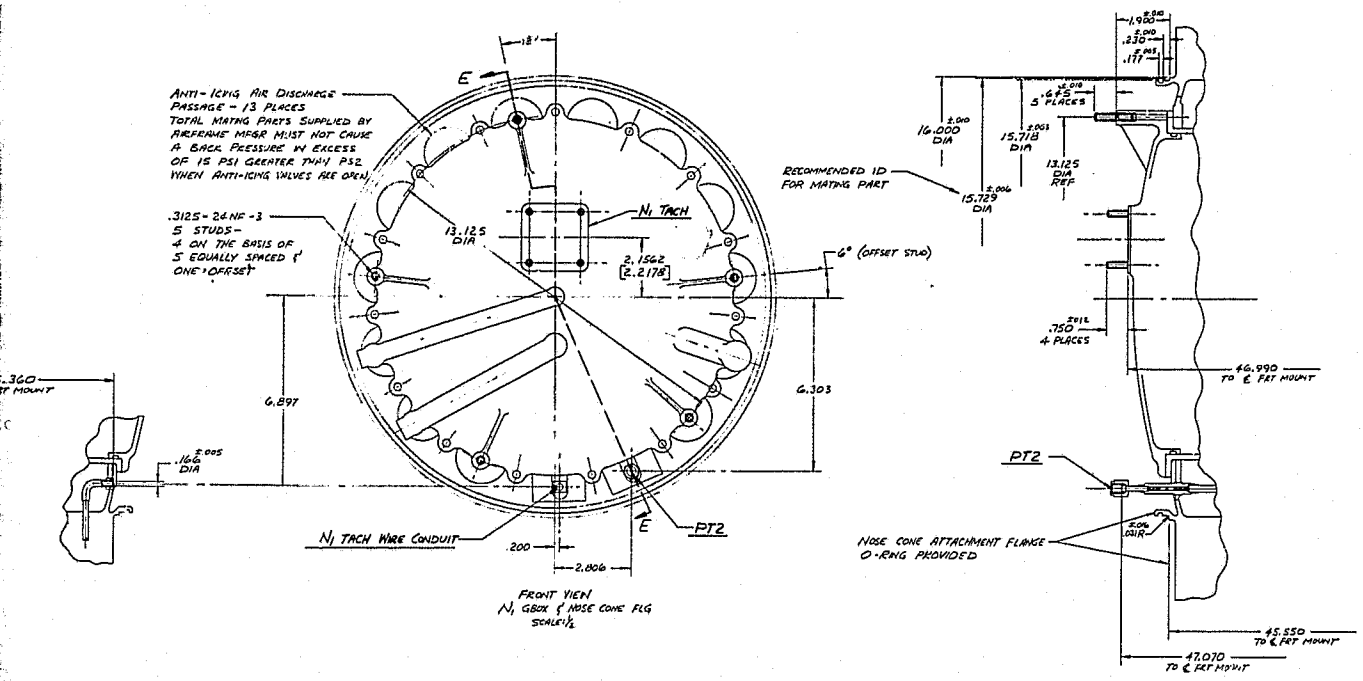

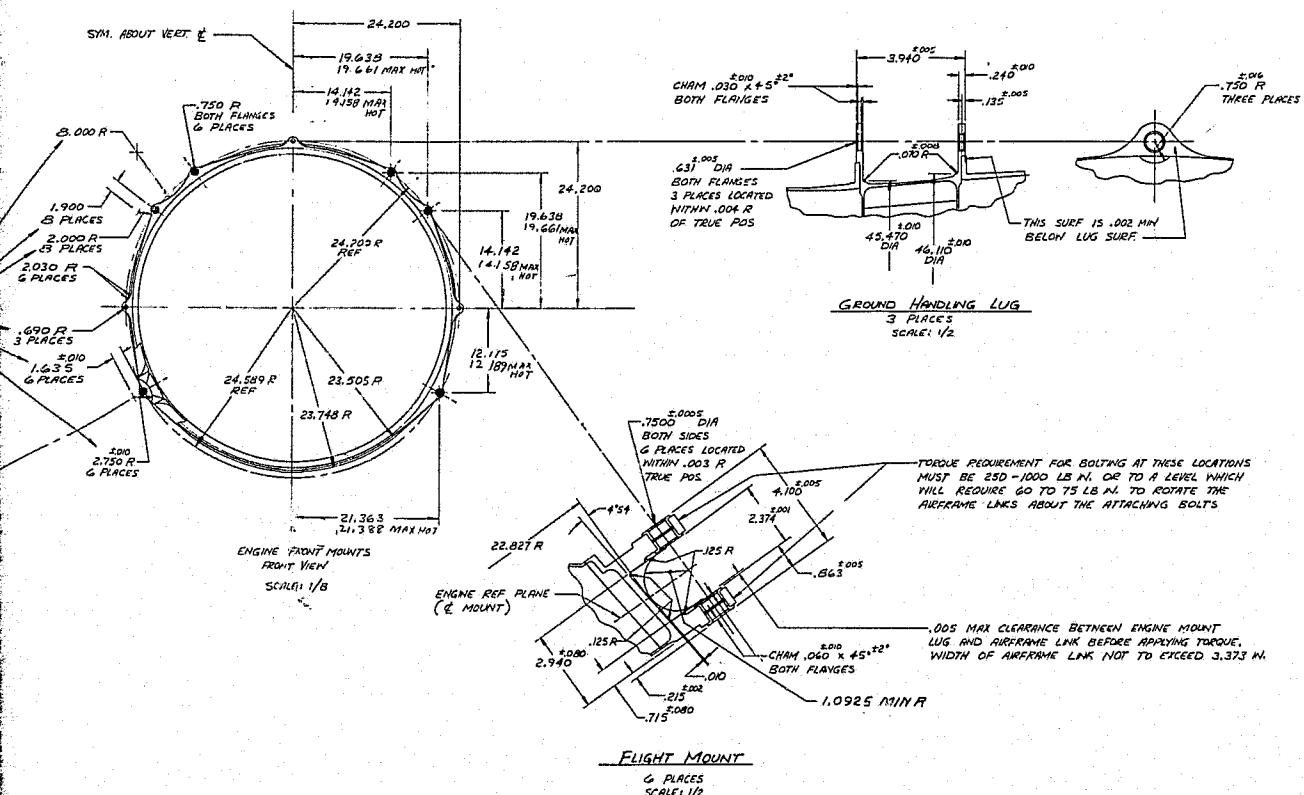

FOLDOUT FRAME 2

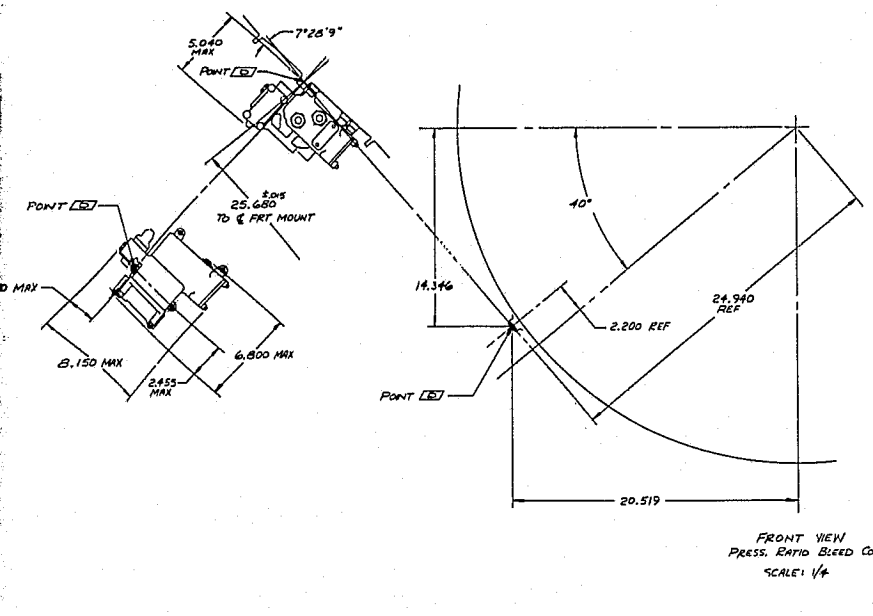

FRONT VIEW
PRESS. RATIO BLEED CONTROL
SCALE: 1/4

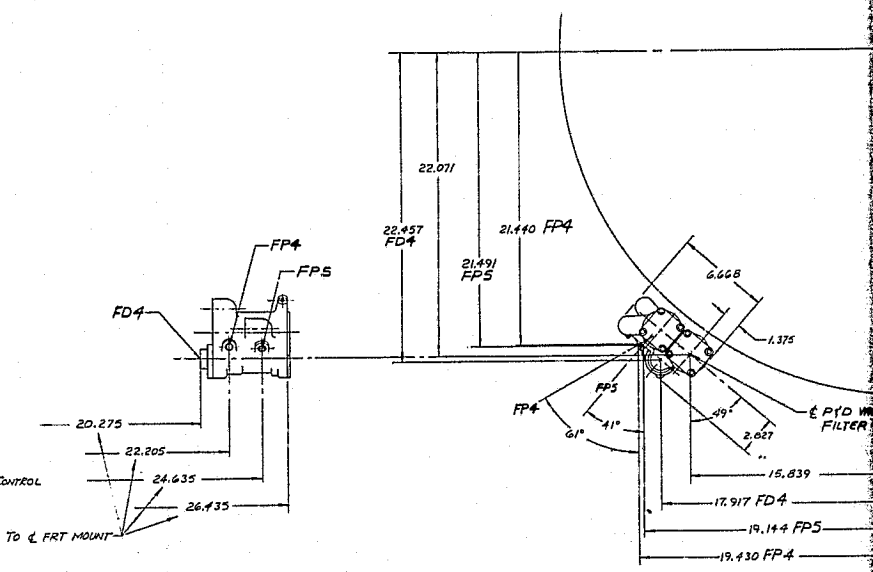

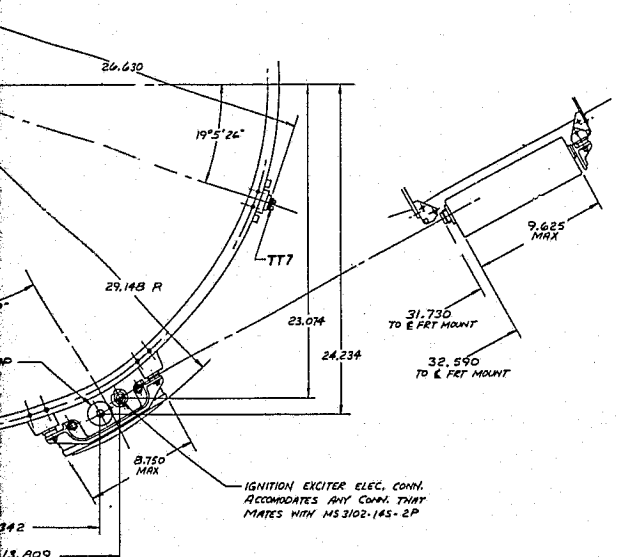

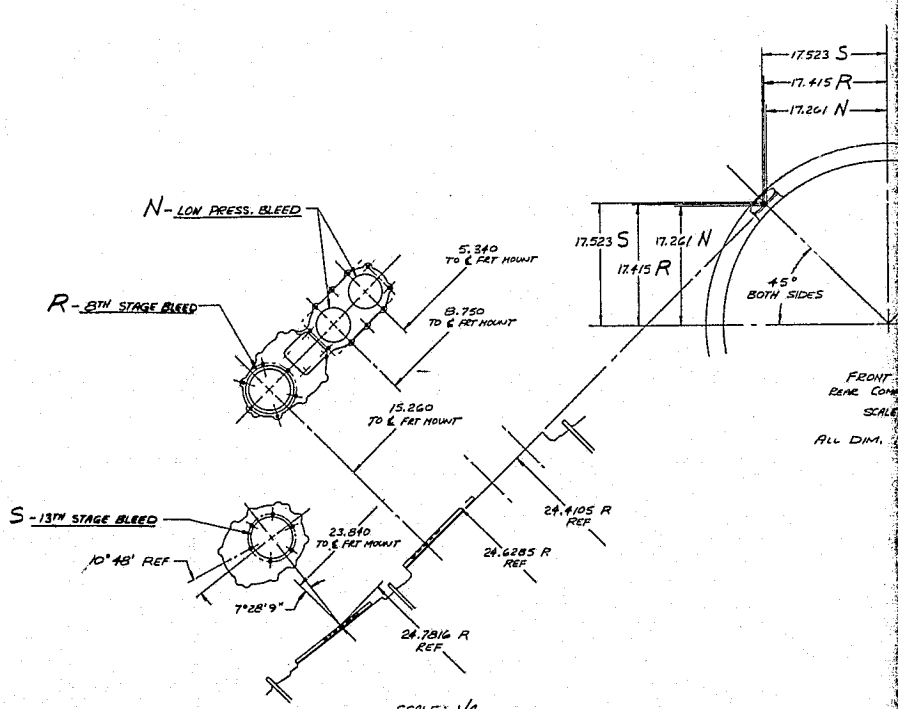

FRONT
REAR CONN
SCALE
ALL DIM.

SCALE: 1/4

FOLDOUT FRAME 3

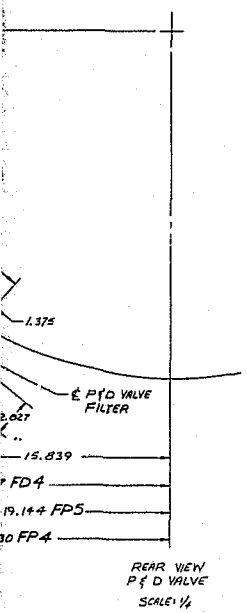

REAR VIEW
P℄D VALVE
SCALE: 1/4

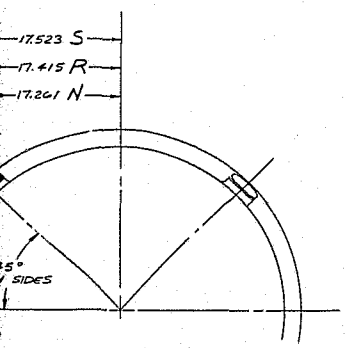

FRONT VIEW
REAR COMPR FAN CASE
SCALE: 1/8

ALL DIM. APPY 2 PLACES

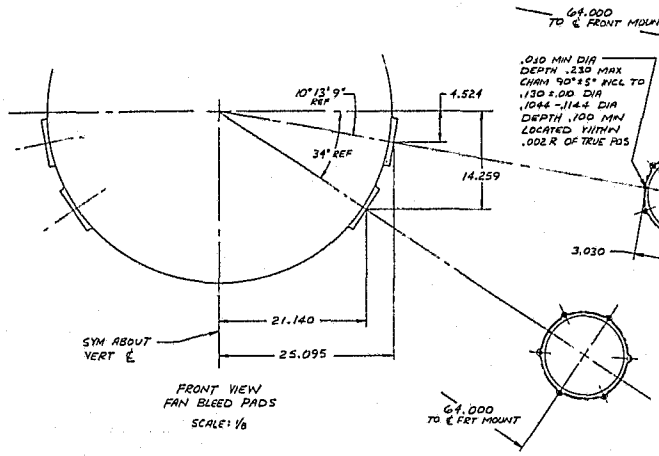

FRONT VIEW
FAN BLEED PADS
SCALE: 1/8

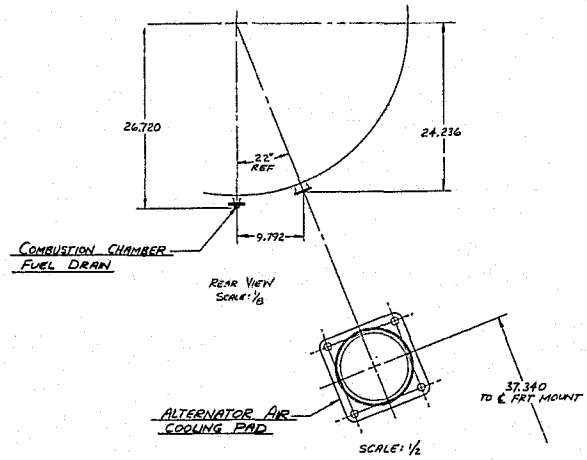

REAR VIEW
SCALE: 1/8

SCALE: 1/2

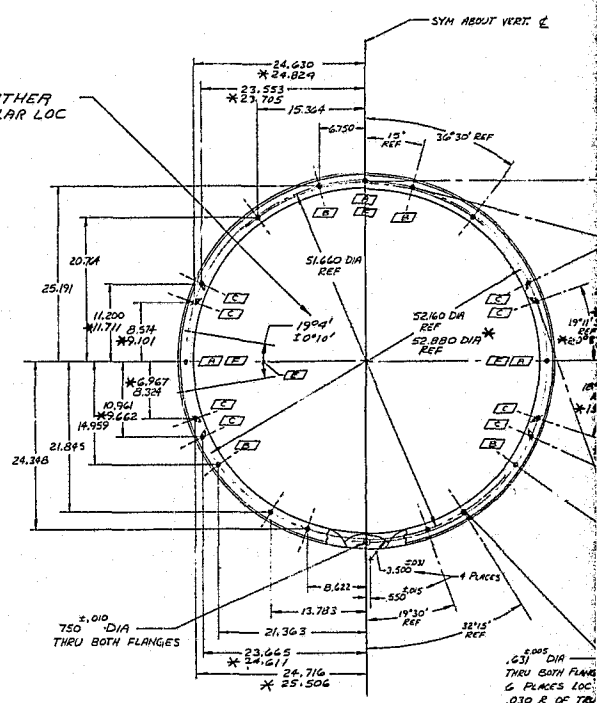

REAR VIEW
ENGINE REAR MOUNTS
SCALE: 1/8

FOLDOUT FRAME 4

ORIGINAL PAGE IS
OF POOR QUALITY

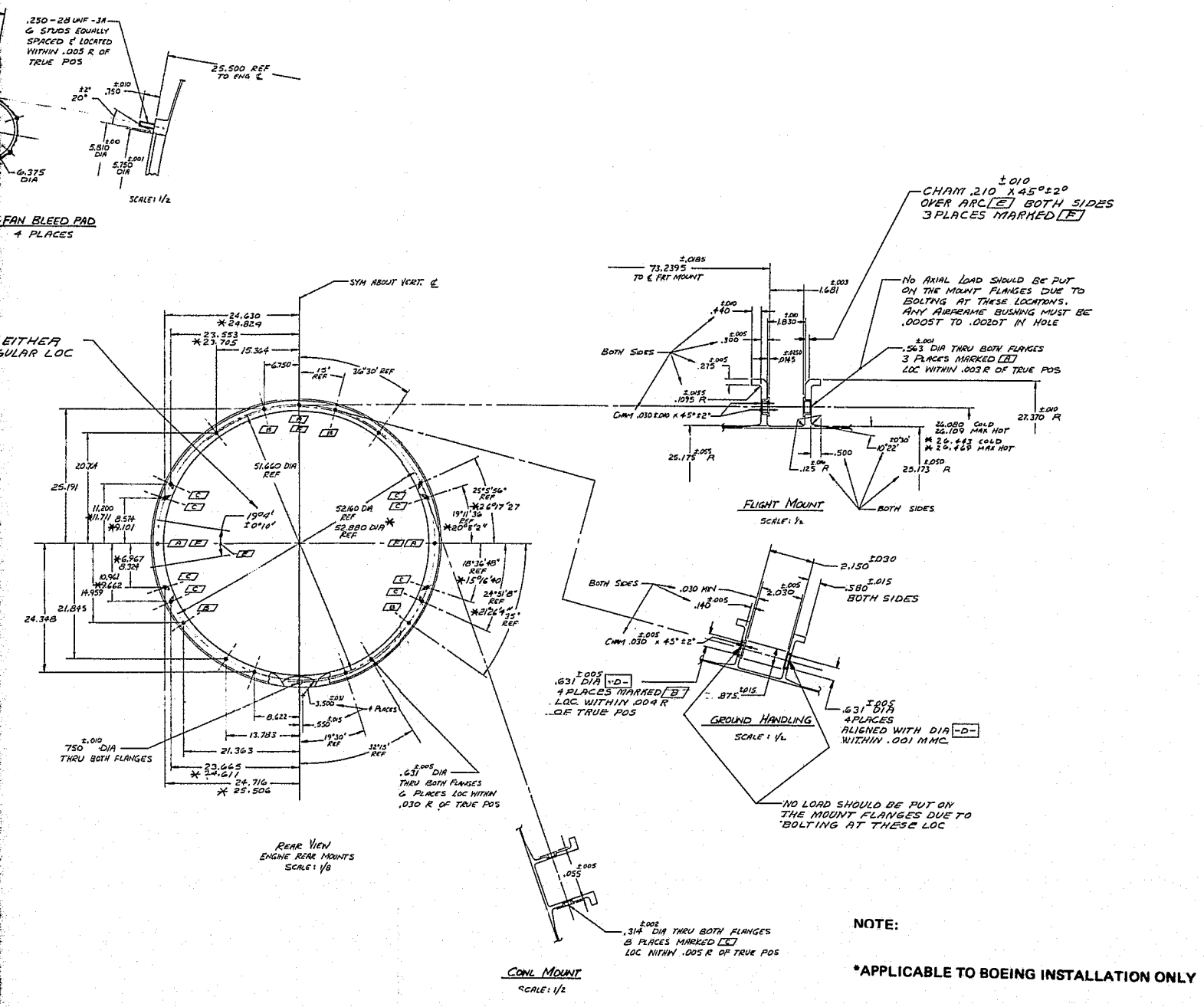

NOTE:

***APPLICABLE TO BOEING INSTALLATION ONLY**

Figure A-69C JT8D-100 Engine Installation

JT8D-100 TURBOFAN ENGINE
FLIGHT ALLOWABLE LIMIT LOADS

SCHEMATIC REAR VIEW OF FRONT MOUNT
DIRECTION OF LOADS POSITIVE AS SHOWN, NEGATIVE IN OPPOSITE DIRECTION.

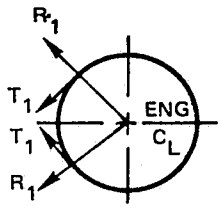

MOUNT TYPE "A" (SIDE)

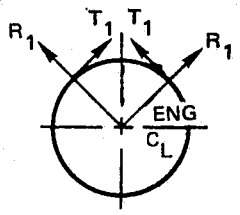

MOUNT TYPE "B" (TOP)

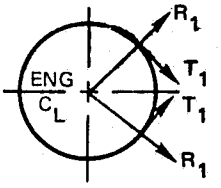

MOUNT TYPE "C" (SIDE)

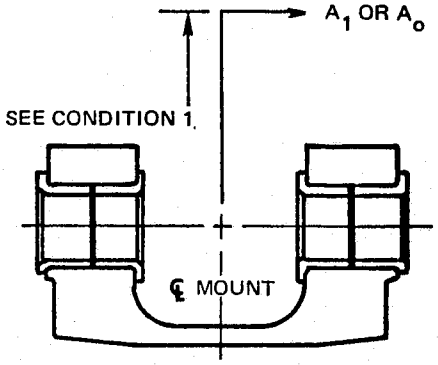

DEFINITIONS FOR EACH MOUNT TYPE:

A_1 = AXIAL LOAD ACTING ON FRONT MOUNT ATTACHMENT POINT (PAIR OF LUGS)
T_1 = TANGENTIAL LOAD ACTING ON FRONT MOUNT ATTACHMENT POINT (PAIR OF LUGS)
R_1 = RADIAL LOAD ACTING ON FRONT MOUNT ATTACHMENT POINT (PAIR OF LUGS)
A_o = MAX ALLOWABLE CRASH LOAD ACTING ON THE TWO FRONT MOUNT ATTACHMENT POINTS

LOADS BASED ON THE FOLLOWING CONDITIONS:

1. LOADS A_1 & A_0 ACTING ON FRONT MOUNT MUST BE APPLIED AT A RADIAL DISTANCE FROM ENGINE ℄ $\leqslant$ 0.71 M (27.9 INCHES)
2. LOADS A_1 & A_0 AND THEIR ACCOMPANYING AXIAL MOMENTS MUST BE EQUALLY DIVIDED BETWEEN BOTH LUGS OF EACH ATTACHMENT POINT.
3. THE THRUST OF A_1 OR A_o TO BE TAKEN BY PAIR OF LUGS AT EACH ATTACHMENT POINT AND THE OVER-TURNING MOMENT DUE TO A_1 OR A_o TO BE TAKEN BY PAIR OF LUGS AT EACH MOUNT ATTACHMENT POINT

THE ALLOWABLE LIMIT LOADS FOR EACH FRONT MOUNT ATTACHMENT POINT (PAIR OF LUGS) MUST SATISFY ALL THE EQUATIONS GIVEN BELOW.

1. $|A_0| \leq$ 346,944 N (78,000 LBS)
2. $|A_1| \leq$ 146,791 N (33,000 LBS)
3. $|T_1| \leq$ 57826 N (13,000 LBS)

| | = ABSOLUTE VALUES

4. $|R_1| \leq$ 164584 N (37,000 LBS)

Figure A-70

JT8D-100 TURBOFAN ENGINE
FLIGHT ALLOWABLE LIMIT LOADS

SCHEMATIC REAR VIEW OF REAR MOUNT
DIRECTION OF LOADS POSITIVE AS SHOWN, NEGATIVE IN OPPOSITE DIRECTION

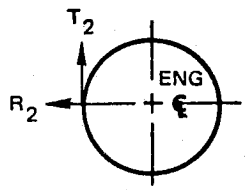

MOUNT TYPE "A" (SIDE)

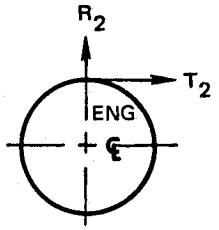

MOUNT TYPE "B" (TOP)

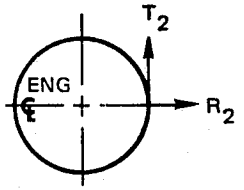

MOUNT TYPE "C" (SIDE)

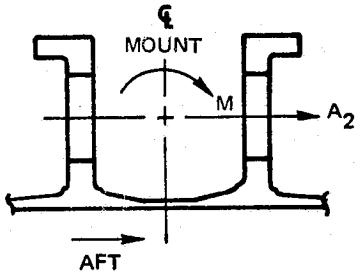

DEFINITIONS FOR EACH MOUNT TYPE:

- A_2 = AXIAL LOAD ACTING ON REAR MOUNT ATTACHMENT POINT APPLIED AT ℄ OF MOUNT HOLE
- M = OVERTURNING MOMENT ACTING ON REAR MOUNT ATTACHMENT POINT
- T_2 = TANGENTIAL LOAD ACTING ON REAR MOUNT ATTACHMENT POINT (BOTH FLANGES)
- R_2 = RADIAL LOAD ACTING ON REAR MOUNT ATTACHMENT POINT (BOTH FLANGES)

THE ALLOWABLE LIMIT LOADS FOR THE REAR MOUNT ATTACHMENT POINT MUST SATISFY ALL THE EQUATIONS GIVEN BELOW.

$|A_2| \leqslant 5337.86$ N (1200 LBS)

$|M| \leqslant 451.94$ M-N (4000 IN-LBS)

$|T_2| \leqslant 80067.96$ N (18,000 LBS)

-75,620N (-17,000 LB) $\leqslant R_2 \leqslant$ 97860.84 N (22,000 LB)

Figure A-71

[illegible]

JT8D-100 TURBOFAN ENGINE
SHIPPING AND GROUND HANDLING ALLOWABLE LIMIT LOADS
SCHEMATIC REAR VIEW OF FRONT MOUNT
DIRECTION OF LOADS POSITIVE AS SHOWN, NEGATIVE IN OPPOSITE DIRECTION
AXIAL LOADS ARE POSITIVE ACTING AFT

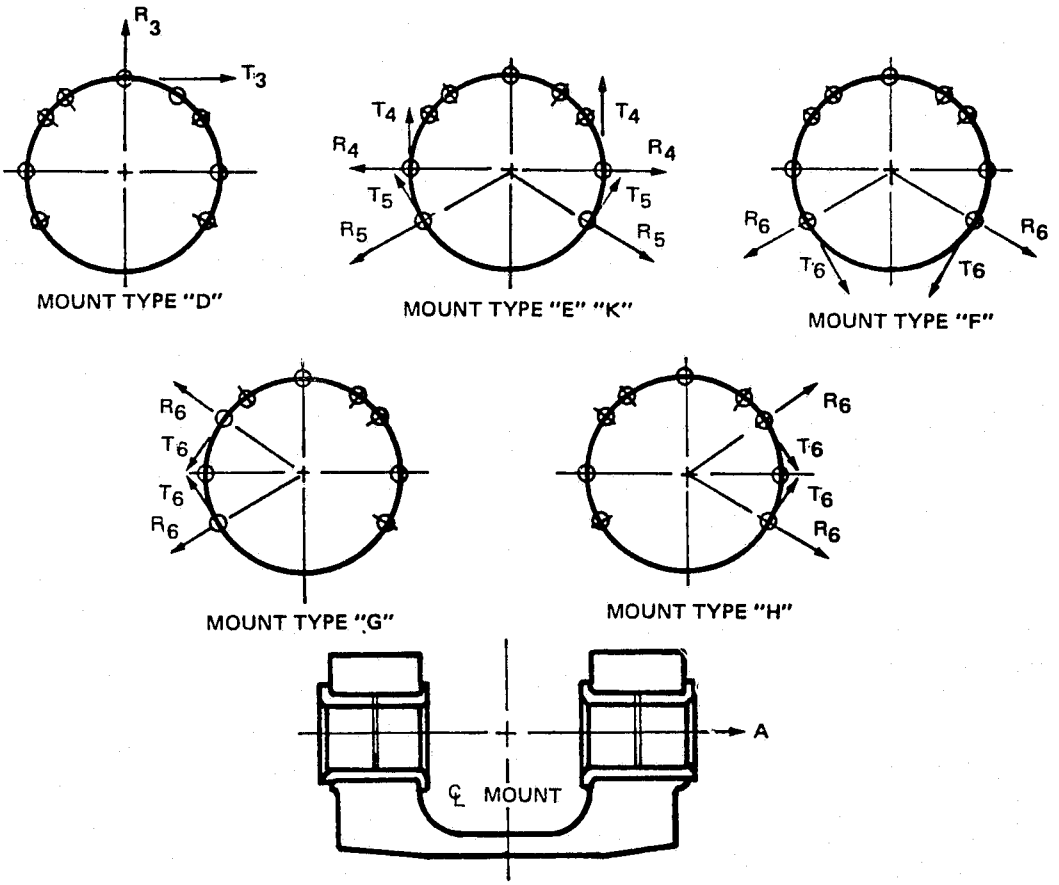

DEFINITIONS FOR EACH MOUNT TYPE:

A3-4 = AXIAL LOAD ON HANDLING ATTACHMENT POINT AT ℄ OF HOLE, WITH NO AXIAL MOMENT (SINGLE LUG).

A5-6 = AXIAL LOAD ON HANDLING ATTACHMENT POINT AT ℄ OF HOLE, WITH NO AXIAL MOMENT (BOTH LUGS).

R3-4-5-6 = RADIAL LOAD ON HANDLING ATTACHMENT POINT (BOTH LUGS).

T3-4-5-6 = TANGENTIAL LOAD ON HANDLING ATTACHMENT POINT (BOTH LUGS).

THE ALLOWABLE LIMIT LOADS FOR EACH FRONT MOUNT ATTACHMENT POINT (PAIR OF LUGS) MUST SATISFY ALL THE EQUATIONS GIVEN BELOW.

1. $|A_3| \leq$ 4626N (1040LBS)
2. $|R_3| \leq$ 80957N (18,200 LBS)
3. $|T_3| \leq$ 46261N (10,400 LBS)
4. $|A_4| \leq$ 4626N (1040 LBS)
5. $|R_4| \leq$ 1,165N (23,887N ULT) 2,510 LBS (5370 LBS ULT)
6. $|T_4| \leq$ 31,004N (74,730N ULT) 6970 LBS (16,800 LBS ULT)
7. $|A_5| \leq$ 146,790N (33,000 LBS)
8. $|R_5| \leq$ 164,583N (37,000 LBS)
9. $|T_5| \leq$ 57,827N (13,000 LBS)
10. $|A_6| \leq$ 146,790N (33,000 LBS)
11. $|R_6| \leq$ 164,583N (37,000 LBS)
12. $|T_6| \leq$ 57,827N (13,000 LBS)

$|\ |$ = ABSOLUTE VALUES

Figure A-72

JT8D-100 TURBOFAN ENGINE
SHIPPING AND GROUND HANDLING ALLOWABLE LIMIT LOADS

SCHEMATIC REAR VIEW OF REAR MOUNT
DIRECTION OF LOADS POSITIVE AS SHOWN, NEGATIVE IN OPPOSITE DIRECTION
AXIAL LOADS ARE POSITIVE ACTING AFT

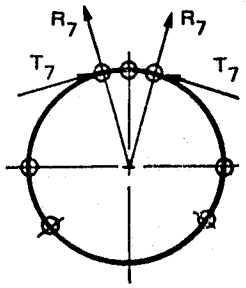

MOUNT TYPE "D"

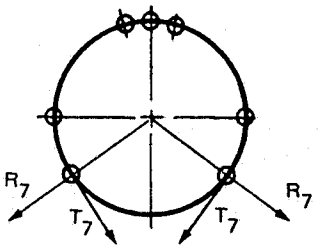

MOUNT TYPE "F" "G" "H"

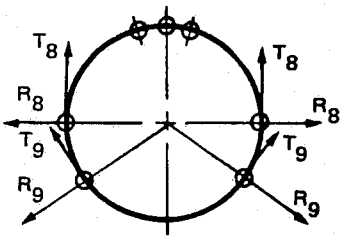

MOUNT TYPE "K"

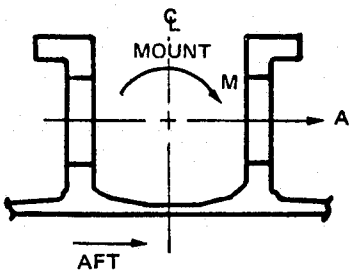

DEFINITIONS FOR EACH MOUNT TYPE:

$A_{7\text{-}8\text{-}9}$ = AXIAL LOAD ON HANDLING ATTACHMENT POINT AT ℄ OF HOLE, WITH NO AXIAL MOMENT (SINGLE FLANGE).

$R_{7\text{-}8\text{-}9}$ = RADIAL LOAD ON HANDLING ATTACHMENT POINT (BOTH FLANGES).

$T_{7\text{-}8\text{-}9}$ = TANGENTIAL LOAD ON HANDLING ATTACHMENT POINT (BOTH FLANGES).

THE ALLOWABLE LIMIT LOADS FOR THE REAR MOUNT ATTACHMENT POINT MUST SATISFY ALL THE EQUATIONS GIVEN BELOW:

1. $|A_7| \leqslant$ 5338N (1200 LBS)
2. $|R_7| \leqslant$ 21018N (65,611N ULT) / 4725 LBS (14,750 LBS ULT)
3. $|T_7| \leqslant$ 32,027N (7200 LBS)
4. $|A_8| \leqslant$ 5338N (1200 LBS)
5. $|R_8| \leqslant$ 37,899N (67,835N ULT) / 8520 LBS (15,250 LBS ULT)
6. $|T_8| \leqslant$ 16,903N (80,957N ULT) / 3800 LBS (18,200 LBS ULT)
7. $|A_9| \leqslant$ 5338N (1200 LBS)
8. $|R_9| \leqslant$ 10,676N (2400 LBS)
9. $|T_9| \leqslant$ 32,027N (7200 LBS)

$|\ |$ = ABSOLUTE VALUES

Figure A-73

JT8D-100 TURBOFAN ENGINE

ALLOWABLE LIMIT LOADS FOR INLET ATTACHMENT

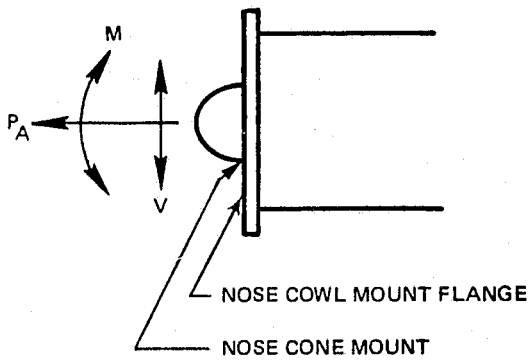

M_H = BENDING MOMENT IN HORIZONTAL PLANE
M_V = BENDING MOMENT IN VERTICAL PLANE
P_A = AXIAL LOAD
V_H = TRANSVERSE SHEAR IN HORIZONTAL PLANE
V_V = TRANSVERSE SHEAR IN VERTICAL PLANE
F_B = MAXIMUM BOLT TENSILE LOAD

NOSE CONE ATTACHMENT FLANGE	NOSE COWL MOUNT FLANGE
$(M_H^2 + M_V^2)^{0.5} \leqslant$ 1243M-N (11,000 IN-LBS)	$(M_H^2 + M_V^2)^{0.5} \leqslant$ 26,324M-N (233,000 IN-LBS)
$(V_H^2 + V_V^2)^{0.5} \leqslant$ 4448N (1000 LBS)	$(V_H^2 + V_V^2)^{0.5} \leqslant$ 43,592N (9800 LBS)
P_A = 13,789N (3100 LBS)	P_A = 30,693N (6900 LBS)
F_B = 5738N (1290 LBS)	F_B = 7740N (1740 LBS)

Figure A-74

JT8D-100 TURBOFAN ENGINE

ALLOWABLE LIMIT LOADS FOR FAN EXHAUST CASE ATTACHMENT

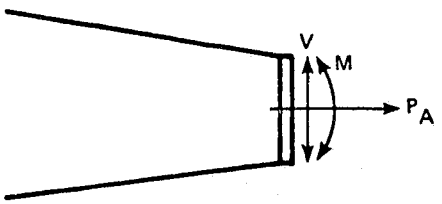

M_H = BENDING MOMENT IN HORIZONTAL PLANE

M_V = BENDING MOMENT IN VERTICAL PLANE

P_A = AXIAL LOAD

V_H = TRANSVERSE SHEAR IN HORIZONTAL PLANE

V_V = TRANSVERSE SHEAR IN VERTICAL PLANE

F_B = MAXIMUM BOLT TENSILE LOAD

$$(M_H^2 + M_V^2)^{0.5} \leqslant 34{,}007\text{M-N (301,000 IN-LBS)}$$

$$(V_H^2 + V_V^2)^{0.5} \leqslant 21{,}796\text{N (4900 LBS)}$$

$$P_A \leqslant 203{,}283\text{N (45,700 LBS)}$$

$$F_B \leqslant 6984\text{N (1570 LBS)}$$

Figure A-75

JT8D-100 TURBOFAN ENGINE

ALLOWABLE LIMIT LOADS FOR SPLITTER MOUNTING FLANGE (PRIMARY CASE OUTER ATTACHMENT)

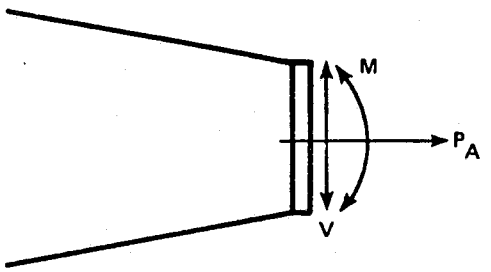

M_H = BENDING MOMENT IN HORIZONTAL PLANE

M_V = BENDING MOMENT IN VERTICAL PLANE

P_A = AXIAL LOAD

V_H = TRANSVERSE SHEAR IN HORIZONTAL PLANE

V_V = TRANSVERSE SHEAR IN VERTICAL PLANE

F_B = MAXIMUM BOLT TENSILE LOAD

$$(M_H^2 + M_V^2)^{0.5} \leqslant 1921\text{M-N (17,000 IN-LBS)}$$

$$(V_H^2 + V_V^2)^{0.5} \leqslant 8007\text{N (1800 LBS)}$$

$$P_A \leqslant 3336\text{N (750 LBS)}$$

$$F_B \leqslant 400\text{N (90 LBS)}$$

Figure A-76

JT8D-100 TURBOFAN ENGINE
ALLOWABLE LIMIT LOADS FOR TAILCONE MOUNTING FLANGE

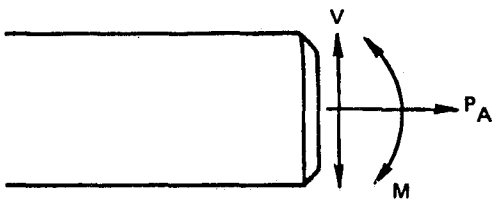

M_H = BENDING MOMENT IN HORIZONTAL PLANE

M_V = BENDING MOMENT IN VERTICAL PLANE

P_A = AXIAL LOAD

V_H = TRANSVERSE SHEAR IN HORIZONTAL PLANE

V_V = TRANSVERSE SHEAR IN VERTICAL PLANE

F_B = MAXIMUM BOLT TENSILE LOAD

$$(M_H^2 + M_V^2)^{0.5} \leqslant 452\text{M-N (4000 IN-LBS)}$$

$$(V_H^2 + V_V^2)^{0.5} \leqslant 1779\text{N (400 LBS)}$$

$$P_A \leqslant 2268\text{N (510 LBS)}$$

$$F_B \leqslant 1179\text{N (265 LBS)}$$

Figure A-77

T M–N (IN-LB) TORSION IN PLANE OF PAD M M–N (IN-LB) MOMENT ANY PLANE PERP TO PLANE OF PAD V N(LB) SHEAR ANY DIRECTION IN PLANE OF PAD P N(LB) RADIAL LOAD		
HIGH PRESS. PORT	0.94P + 6.2M + 0.16V $\leq$ 31,000 (4.2P + 0.7M + 0.7V $\leq$ 31,000)	T_{MAX} = 56 M-N (500 IN-LB)
8TH STAGE PORT	3.10P + 42.5M + 1.08V $\leq$ 31,000 (13.8P + 4.8M + 4.8V $\leq$ 31,000)	T_{MAX} = 34 M-N (300 IN-LB)
LOW PRESS. PORT	4.86P + 45.1M + 0.56V $\leq$ 31,000 (21.6P + 5.1M + 2.5V $\leq$ 31,000)	T_{MAX} = 34 M-N (300 IN-LB)
FAN PORT	1.17P + 28.6M + 0.4V $\leq 10^4$ (5.2P + 3.23M + 1.8V $\leq 10^4$)	T_{MAX} = 225M-N (2000 IN/LB)
ALTERNATOR	123.6P + 261.1M + 6.63V $\leq 10^4$ (550P + 29.5M + 29.5V $\leq 10^4$	T_{MAX} = 16.9 N-M (150 IN/LB)

SPRING RATES			
	CIRCUMFERENTIAL	RADIAL	LONGITUDINAL
BLEED	J	K	L
PORT	M – N (IN-LB/RAD)	N/M (LB/IN)	M – N (IN-LB/RAD)
HIGH	±46,550 ±(412,000)	±55,690,000 ±(318,000)	±64,970 ±(575,000)
8TH	±21,810 ±(193,000)	±48,160,000 ±(275,000)	±25,870 ±(229,000)
LOW	±29,040 ±(257,000)	±60,419,000 ±(345,000)	±69,490 ±(615,000)

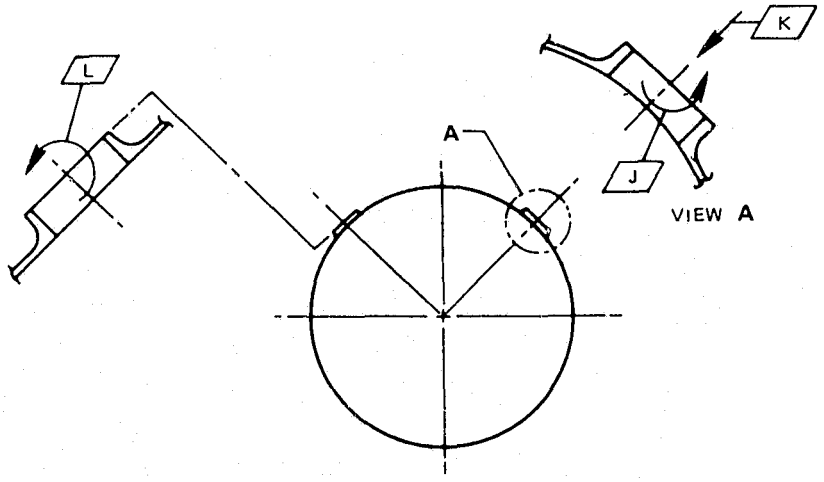

Figure A-78 JT8D-100 Allowable Loads for Airbleed Pads

ORIGINAL PAGE IS
OF POOR QUALITY

c. Engine Weight

1) Basic Engine Weight

It was estimated that the dry weight of the JT8D-109 engine, including the following items of standard and additional equipment would not exceed 1738 Kg (3832 lb). The estimated maximum differential weight was estimated at 258.8 Kg (570 lb). The average weight of the two McDonnell - Douglas JT8D-109 flight test engines was 1734 Kg (3822 pounds), including approximately 23Kg (50 lb) of additional blade containment not included in the estimate. This additional 23Kg (50 lb) would be essentially eliminated in a production version of the engine.

STANDARD EQUIPMENT

Fuel Control System Inlcuding Fuel Pump and Thrust and Speed Control Unit
Starting and Continuous Engine Ignition Systems Requiring External Power Source
Engine Anti-Icing System
Exhaust Thermocouple Probes and Exhaust Pressure Probes
AND Type Accessory Drives for Each of the Following:

Low Pressure Rotor – Tachometer
High Pressure Rotor – Tachometer, Starter, Generator, Fluid Power Pump

ADDITIONAL EQUIPMENT

Fuel Heater
Fuel-Oil Cooler
Oil Tank Assembly
Special Air Valves (Inlet Guide Vane Thermal Anti-Icing and Fuel Heater) in lieu of Standard Air Valves

The dry weight of the JT8D-109 engine does not include the following items of standard and additional equipment.

STANDARD EQUIPMENT

	Engine Dry Weight Change
Brackets for Attachment of Aircraft Equipment Wood Shipping Box	4.54 Kg (10 lb)

ADDITIONAL EQUIPMENT

	Engine Dry Weight Change
175 Micron Main Oil Filter (in lieu of Standard 40 Micron Main Oil Filter)	+ 0.45 Kg (1 lb)
15 Micron Main Oil Filter (in lieu of Standard 40 Micron Main Oil Filter)	– 0.45 Kg (1 lb)

Alternate A.C. Ignition System*	+	0.91 Kg (2 lb)
Provisions for the Incorporation of Chip Detectors in the Lubrication System	+	0.45 Kg (1 lb)

*Replaces ignition systems shown under standard equipment.

The weight of fluids remaining in the engine after operation and drainage, while the engine is in the normal attitude is estimated to be 4.5 Kg (10 lbs.).

2) Engine Center of Gravity

Horizontal – 45 cm (17.8 in.) aft of front mount (intermediate case) centerline

Vertical – 5.3 cm (2.1 in.) below engine centerline

3) Polar Moments

The estimated effective mass polar moments of inertia of the low and high pressure rotor assemblies about their axes are as follows:

Low rotor	17.08 Kg m^2 (12.6 slug ft^2)
High rotor	7.46 Kg m^2 (5.5 slug ft^2)

The estimated effective mass polar moment of inertia at the starter pad is 20.9 kg m^2 (15.45 slug ft^2)

4) Moments of Inertia

The following values represent the estimated moments of inertia of the engine in pitch, yaw and roll. These values are about axes through the engine center of gravity.

Pitch	1538.85 Kg m^2 (1135 slug ft^2)
Yaw	1593.09 Kg m^2 (1175 slug ft^2)
Roll	276.59 Kg m^2 (204 slug ft^2)

B. PERFORMANCE CHARACTERISTICS

Subsequent paragraphs in this section provide a detailed description of the performance characteristics of the JT8D-100 refan engine as determined from sea level and altitude development testing as conducted during Phase II of the refan program. Tables of estimated general performance parameters are presented in Ref. 4.

As part of the system development program, JT8D-100 engine testing was conducted to determine the performance characteristics of the refan engine. Testing was conducted at Pratt & Whitney Aircraft and Boeing Company sea level test facilities, at the NASA LeRC altitude test facility, and at McDonnell-Douglas in a DC-9 aircraft.

The performance criteria for the JT8D-100 refan program included goals of increasing sea level static standard day takeoff thrust from 64,499 N (14500-lbs) for a standard JT8D-9 engine to 73,840 N (16,600-lbs) for the refanned D-109 engine and from 68,947 N (15,500 lbs) for a standard JT8D-15 to 77,844 N (17,500-lbs) for the refanned D-115 engine. This increase in takeoff thrust was to be accompanied by a reduction in TSFC of 12.66% for the JT8D-109 and 13.8% for the JT8D-115. At altitude [9144 m (30,000 ft) 0.8 Mn] the JT8D-100 cycle was to increase cruise thrust by 5% and reduce TSFC by 1.25%. Similar thrust increases and TSFC reductions were to be obtainable by retrofitting any current JT8D engine model to a refan configuration. The JT8D-109/115 goals are stated here since these were the engines tested in the program.

Because the refan program was structured around a retrofit concept, the most meaningful evaluation of refan performance was on a percent improvement basis. The high compressor, high turbine, combustor, and parts of the low compressor and low turbine were essentially unchanged in the conversion from base engine to the refan configuration. Therefore, the performance of the refan engine was dependent to a large extent on the performance of the unchanged parts which could vary significantly according to their state of deterioration.

The JT8D-109 design goal performance predictions were based on JT8D-9 performance demonstrated by the average 1971 production engine. Based upon this criterion, takeoff TSFC would decrease from 0.05806 kg/hr/N (0.5694 lb/hr/lb) to 0.05071 kg/hr/N (0.4973 lb/hr/lb) (-12.66%) for a JT8D-109.

1. Sea Level Static Testing

Sea level static performance testing was conducted at P&WA on refan engines EE-1, EE-2 and EE-3 as both JT8D-9 and JT8D-109 models to establish the performance characteristics of the JT8D-109 engine in comparison to the JT8D-9 engine. After conversion, testing was also conducted on the two JT8D-109 engines used for DC-9 flight testing and the one JT8D-115 engine used for Boeing ground testing. These engines were not calibrated as base models immediately prior to conversion to the JT8D-100 configuration.

a. Test Procedure

Steady state performance data were recorded in 4,448 N (1000-lbs) thrust increments from 17,792 N (4000 lbs) of observed thrust to maximum power. A seven-minute stabilization time was observed at each power condition prior to data acquisition. Performance data were acquired through the use of the Steady State Data Acquisition System (SSDAS). Engine instrumentation was connected to a pressure measuring subsystem and an electrical subsystem. These systems were in turn connected to a central computer. Raw data plus selected computed results were sent back to the stand high speed printer for on-stand data validity checks and analysis during the test.

b. Test Results and Discussion of Results

Initial performance calibrations on engines EE-1 and EE-2 indicated that the fan operating line was approximately 3% higher than predicted. This resulted in loss of fan surge margin and lower than anticipated fan efficiency. To alleviate this condition, the engine area ratio was increased 26% and the jet nozzle area increased from 0.75 m^2 (8.08 ft^2) to 0.774 m^2 (8.33 ft^2). In addition to these modifications, the tip clearances on rotors 1.5 and 2.0 were increased due to blade tip rubs encountered in the initial testing. To reduce the impact of increased clearances on engine performance, "squealer cuts" were incorporated on the cut-back blade tips. The squealer cut was made by removing approximately 0.127 cm (0.050-in) of material on the blade tip concave surface. This cut reduced the blade-to-shroud annular ring effective area, thereby reducing tip leakage.

A final modification was made after analysis of fan/LPC rig data indicated the low compressor flow capacity to be approximately 3% below design goals. It was determined that stator 1 and, to a lesser extent, rotor 1.5 and stator 1.5 were operating closer to a choke condition than anticipated. To help alleviate this problem, the 1st stator vanes were restaggered open three degrees relative to initial design specifications.

Test results subsequent to these reoperations indicated that the low compressor flow capacity increased by 1.5 to 2.0%. Table B-I shows the percent TSFC improvement demonstrated by all refan engines with the modifications mentioned above, compared to the base engine model (JT8D-9 or JT8D-15). Figures B-1 through B-3 present the SLS TSFC curves for EE-1, EE-2 and EE-3 tested at P&WA in both the JT8D-9 and JT8D-109 configurations with the modifications mentioned above.

Engine EE-3 was the only engine tested at both sea level and simulated altitude conditions with sufficient experimental instrumentation to perform component performance analysis. Test results from this engine test program, therefore, permit the most comprehensive evaluation of refan engine performance and will represent the bulk of the discussion presented in this section. Additional sea level static test results from engines EE-1 and EE-2 and the flight test engines will be presented as required to complete the performance analysis of the JT8D-109 engine.

TABLE B-I

JT8D-109/D-9 THRUST SPECIFIC FUEL CONSUMPTION COMPARISON

Model	Engine	Base Model Configuration Takeoff TSFC kg/hr/N	(lb/hr/lb)	Refan Configuration Takeoff TSFC kg/hr/N	(lb/hr/lb)	Δ kg/hr/N	(Δ lb/hr/lb)	Δ%
JT8D-9/109	Design Goal	0.05806	(0.5694)	0.05071	(0.4973)	−0.00735	(−0.0721)	−12.66
JT8D-15/115	Design Goal	0.06128	(0.601)	0.05282	(0.518)	−0.00846	(−0.083)	−13.5
JT8D-9/109	EE-1	0.06078	(0.596)	0.05343	(0.524)	−0.00735	(−0.072)	−12.1
JT8D-9/109	EE-2	0.06047	(0.593)	0.05323	(0.522)	−0.00724	(−0.071)	−12.0
JT8D-9/109	EE-3*	0.05894	(0.578)	0.05190	(0.509)	−0.00707	(−0.069)	−12.0
JT8D-9/109	P-666995**	0.05833	(0.572)	0.05364	(0.526)	−0.00969	(−0.046)	− 8.1
JT8D-9/109	P-666996**	0.05772	(0.566)	0.05231	(0.513)	−0.00541	(−0.053)	− 9.4
JT8D-15/115	P-687547***	0.06139	(0.602)	0.05384	(0.528)	−0.00755	(−0.074)	−12.3

NOTES:

* The above data reflect EE-3 performance as a JT8D-9 with production instrumentation plus experimental instrumentation at stations 4 and 7F. As a JT8D-109 engine it was tested with full experimental instrumentation. The effects of this additional instrumentation will be addressed later in this section.

** These engines were tested in the JT8D-9 configuration in 1971. They were delivered to McDonnell-Douglas Corporation and accumulated approximately 115 hours of running time. The table shows Δ performance based on the 1971 engine calibration. The performance of these engines as JT8D-9 engines immediately prior to conversion is unknown.

*** This engine was tested in the JT8D-15 configuration in June 1974. It was delivered to The Boeing Company and accumulated approximately 30 hours of ground test running time. The table shows Δ performance based on the June 1974 engine calibration. The performance of this engine as a JT8D-15 engine immediately prior to conversion is unknown.

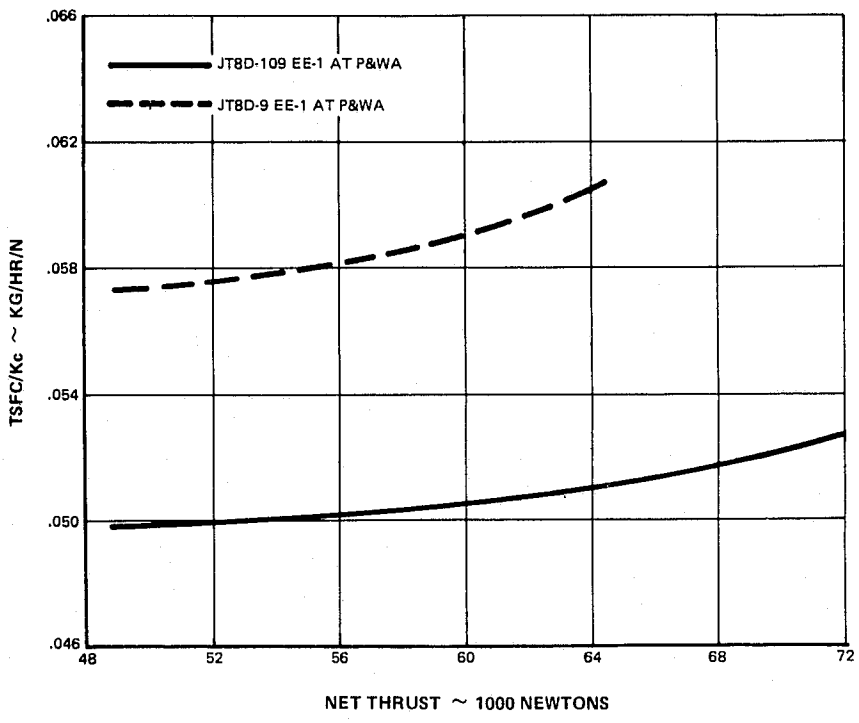

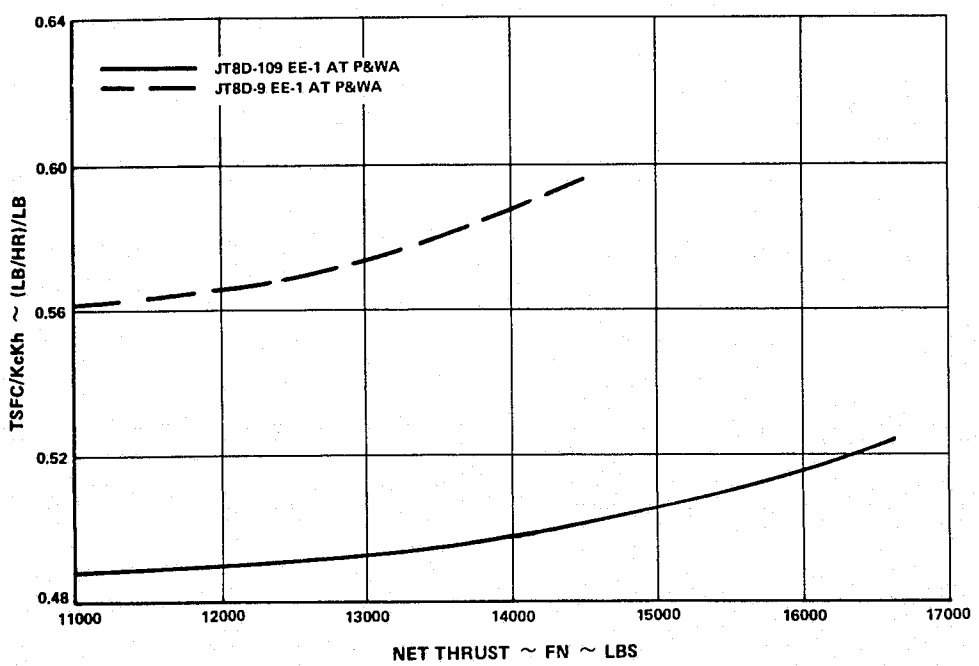

Figure B-1 JT8D-109/D-9 Engine EE-1 Steady State Static Sea Level Performance

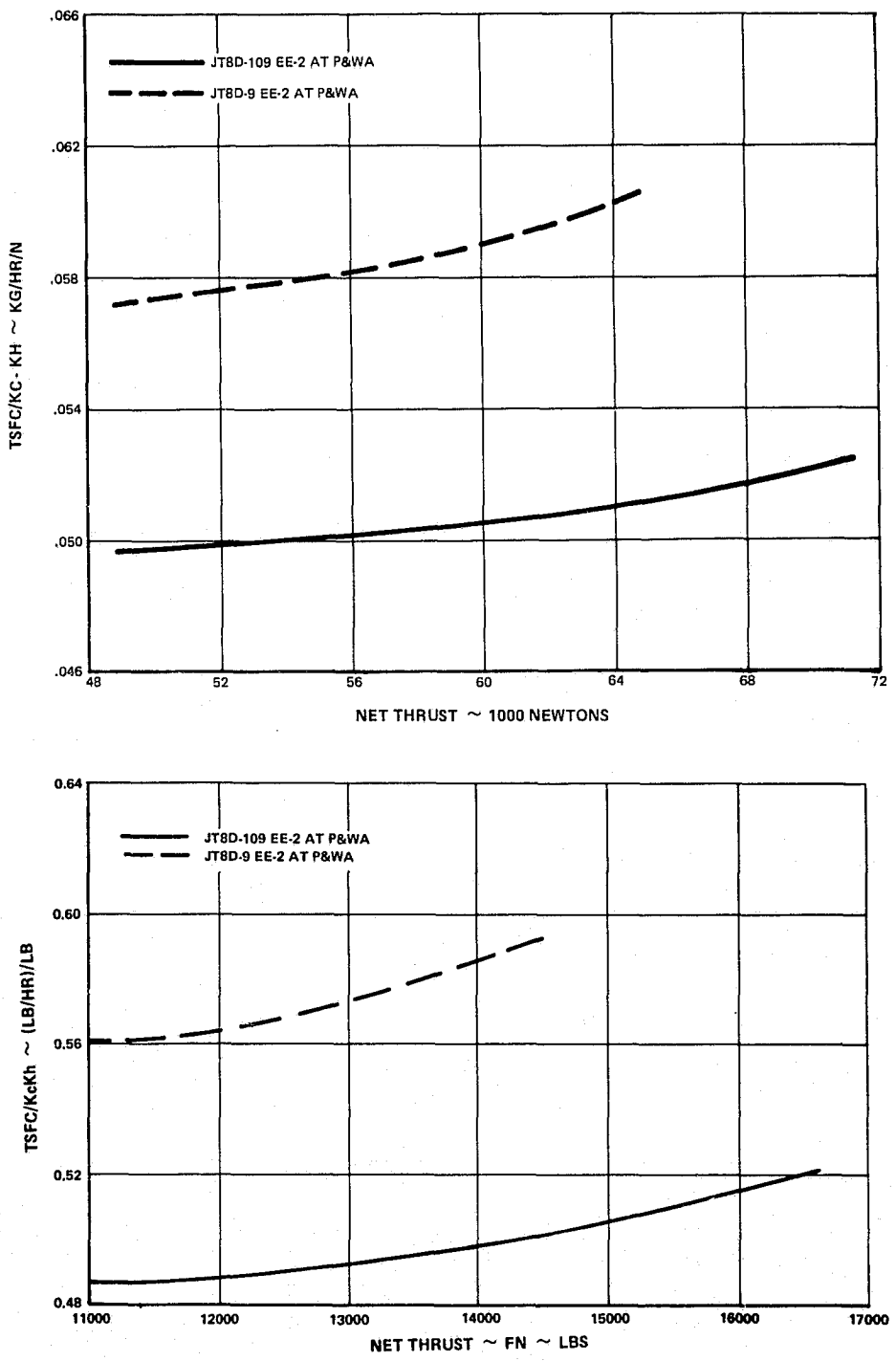

Figure B-2 JT8D-109/D-9 Engine EE-2 Steady State Static Sea Level Performance

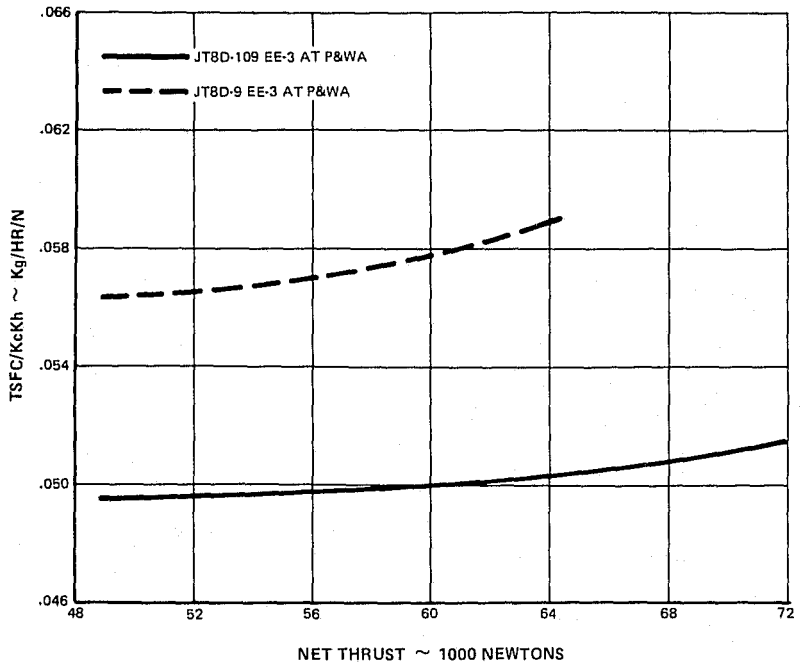

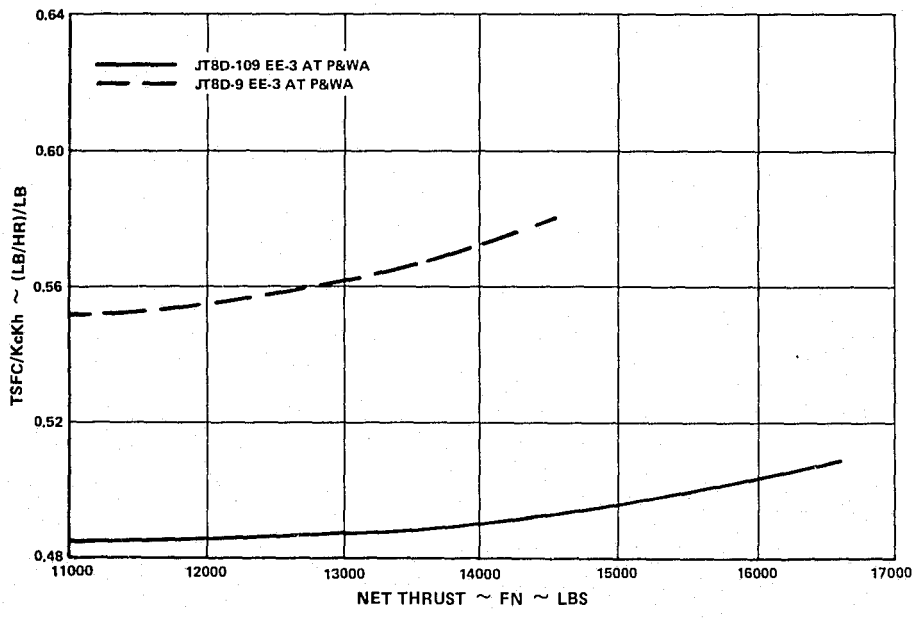

Figure B-3 JT8D-109/D-9 Engine EE-3 Steady State Static Sea Level Performance

Engine EE-3 was a new JT8D-9 engine, produced in 1974. When calibrated as a D-9 engine it demonstrated a TSFC at 64,499 N (14,500-lbs) [(D-9 takeoff rating)] of 0.05898 kg/hr/N (0.5784 lb/hr/lb.) This value was 1.6% higher than the 1971 JT8D-9 production average TSFC level of 0.05806 kg/hr/N (0.5694 lb/hr/lb) which was used in the refan design studies as typical, or baseline, JT8D-9 performance. There were two minor differences between engine EE-3 and the standard production engine configuration. Engine EE-3 had two experimental instrumentation probes inserted through the fan ducts and into the primary gas stream at station four to record total pressure and temperature at the exit of the high compressor. Engine EE-3 was also equipped with total pressure probes at station 7F to record fan duct exit total pressure. The performance penalty due to the pressure loss generated by this experimental instrumentation was not measured but is considered small. Table B-II summarizes engine EE-3 performance as a JT8D-9 relative to the average 1971 production engine.

TABLE B-II

JT8D-9 PERFORMANCE COMPARISON
ENGINE EE-3 VERSUS 1971 AVERAGE PRODUCTION ENGINE

Parameter	EE-3 as a D-9	1971 Prod. Avg.	% Diff.
FN/δT2 N (lbs)	64,499 (14,500)	64,499 (14,500)	0
TSFC/Kc Kh @ 18400 LHV kg/hr/N (lb/hr/lb)	0.05898 (0.5784)	0.05806 (0.5694)	+1.6
TT5 °K (°R)	1254 (2257)	1237 (2227)	+1.4
N1/$\sqrt{\theta}$T2, rpm	8010	8028	−0.2
N2/$\sqrt{\theta}$T2, rpm	11402	11400	0
PT7/PT2	2.015	2.025	−0.5
PS3/PT2	3.43	3.469	−1.1
PS4/PT2	15.2	15.28	−0.5
TT7/θT2 °K (°R)	785 (1413)	782 (1407)	+0.4

After conversion to a JT8D-109 configuration, EE-3 demonstrated the following at the JT8D-109 sea level static takeoff thrust rating of 73840 N (16,600 lbs)

- TSFC/KcKh, kg/hr/N (lb/hr/lb) = 0.05153 (0.5053)
- Corrected to 42,797,757 J/kg (18400 BTU/lb) LHV = 0.05189 (0.5089)
- Corrected for the presence of experimental instrumentation = 0.05145 (0.5046)

Therefore if the takeoff TSFC of EE-3 is adjusted for the pressure loss penalty induced by the presence of experimental instrumentation the TSFC improvement shown due to the refan conversion is:

$$\text{TSFC improvements} = [(0.05898 - 0.05145)/0.05898] \times 100 = 12.76\%$$

Comparing this with the previously stated design goal of 12.66% improvement indicates that EE-3 did achieve this design goal.

Table B-III presents the more significant performance parameters demonstrated on EE-3 compared to the original performance goals.

TABLE B-III

JT8D-109 ENGINE EE-3
MEASURED PERFORMANCE COMPARISON WITH DESIGN GOALS
(SLS TAKEOFF)

Parameter	JT8D-109 Design Goal		JT8D-109 EE-3 Measured		Δ Parameter		Δ TSFC Impact
TSFC/Kc Kh, kg/hr/N (lb/hr/lb)	0.05071	(0.4973)	0.05189	(0.5089)	+2.3%		
TT5/θT2, °K (°R)	1236.67	(2226)	1269.44	(2285)	32.8	(+59°)	
N1/√θ T2, rpm	7450		7340		−110		
N2/√θ T2, rpm	11240		11400		+160		
WAT√θ T2/δT2, kg/sec (lbs/sec)	211.83	(467)	212.28	(468)	+0.45	(+1)	
WAE√θ T2/δT2 kg/sec (lbs/sec)	70.76	(156)	68.04	(150)	−2.72	(−6)	
ηFan %	82.45		84.95		+2.5		−1.2%
ηLPC %	86.61		86.28		−0.33		+0.2%
ηSTO %	89.36		88.61		−0.75		+1.4%
ΔP/P(PT2.4 - PT7F)/PT2.4	0.042		0.064		+0.022		+2.2%
Gross Thrust Coefficient (CV)	0.980		0.984		+0.004		−0.4%

As can be seen from Table B-III, the TSFC differences from the design goals primarily resulted from turbine efficiency and fan duct (including fan exit guide vanes) pressure loss penalties. These losses were partially offset by an improved fan efficiency. When tested as a JT8D-9, engine EE-3 was not sufficiently instrumented to define the component performance in detail; however, computer simulations indicated JT8D-9 base line performance was deficient in terms of LPC and turbine efficiencies which would impact refan performance in a similar manner. In addition, the 2.2% duct loss increase can be reduced to 1.5% after an adjustment is made for instrumentation losses. Therefore, it is concluded from EE-3 testing that the fan efficiency improvement of 1.2% over design goals was offset by a fan stream pressure loss increase of 1.5%. Analysis of full-scale JT8D-100 fan/LPC rig wake rake survey data behind the fan exit guide vanes indicated that the exit guide vane loss was approximately 0.5% higher than predicted, leaving the fan duct loss about 1% higher than predicted.

Unlike TSFC, the turbine inlet temperature (TT5) difference noted in Table B-III would not be eliminated entirely by baseline performance differences and offsetting component performance shifts. The TT5 difference between EE-3 in the baseline and refan configurations at the takeoff rating was 16.6°F (30°F) after these adjustments. This remaining 16.6°K (30°F) can be attributed to fan root flow deficiencies noted during fan/LPC rig testing (only partially offset by the first stator vane restagger) and the reduction in takeoff rotor speed from 7450 rpm to 7340 rpm for the exhaust system match which together reduced primary flow 2.72 kg/sec (6 lb/sec).

Table B-IV presents the more significant component performance parameters demonstrated on JT8D-109 engines EE-1 and EE-2 compared to EE-3.

TABLE B-IV

JT8D-109 MEASURED PERFORMANCE COMPARISON
(SLS TAKEOFF)

Parameter	EE-1		EE-2		EE-3	
$N1/\sqrt{\theta}$ T2, rpm	7350		7400		7340	
$N2/\sqrt{\theta}$ T2, rpm	11430		11470		11400	
$WAT\sqrt{\theta}$ T2/δ T2 kg/sec (lbs/sec)	212.28	(468)	212.28	(468)	212.28	(468)
$WAE\sqrt{\theta}$ T2/δ T2 kg/sec (lbs/sec)	66.63	(147)	66.13	(147)	68.04	(150)
ηFan %	83.80		84.45		84.95	
ηLPC %	86.90		85.80		86.28	
ηSTO %	88.60		88.30		88.61	
ΔP/P(PT2.4 - PT7F)/PT2.4	0.057		0.058		0.064	

Engines EE-1 and EE-2 indicated similar component performance trends to EE-3 with somewhat less improvement in fan efficiency but improved fan stream pressure loss levels.

During SLS engine development testing abnormal fan performance modes characterized by a loss in flow capacity up to 5% and a loss in fan O.D. efficiency of up to 8% were observed on EE-1 and EE-2. These modes occurred only at low rotor speeds above 7000 rpm. There was no measurable loss in stability. The abnormal performance was not observed during the fan/LPC rig program, nor in the testing of the other four engines in the program.

The abnormal fan mode was observed to develop either gradually or as a discontinuous loss in fan performance. Accompanying changes in gas generator characteristics were evident and consistent with the loss in fan flow capacity and fan efficiency. The change back to normal performance was usually noted upon power reduction; however, a trend toward a gradual change back was observed on some occasions.

2. Altitude Testing

a. Test Procedure

Engine EE-3, after being baseline tested at the P&WA facility, was moved to the NASA LeRC for testing at altitude conditions. Steady state performance testing of EE-3 was conducted at the flight conditions shown in Table B-V. Steady state data were acquired at the specified altitude and Mach No. conditions over a range of approximately 8 throttle settings from idle to take-off power.

TABLE B-V

JT8D-109 ENGINE EE-3
TEST CONDITIONS

Altitude Meters	(Ft.)	Mach No.
3,048	(10,000)	0.1
3,048	(10,000)	0.4
4,572	(15,000)	0.5
5,791	(19,000)	0.2
7,620	(25,000)	0.6
7,620	(25,000)	0.8
9,144	(30,000)	0.4
9,144	(30,000)	0.7
9,144	(30,000)	0.8
9,144	(30,000)	0.85
10,668	(35,000)	0.7
10,668	(35,000)	0.85
10,668	(35,000)	1.05
12,192	(40,000)	0.85

b. Test Results and Discussion of Results

Analysis of results was complicated by two basic uncertainties in the data. First, there was a 3-3.5% variation (scatter) in TSFC values at constant thrust. "Average" lines were constructed through these data sets, but an undetermined level of uncertainty is contained in each "average" value. Secondly, the facility airflow measuring system required adjustments for the presence of static and total pressure gradients in the facility inlet duct to the engine. These gradients were not measured by the boundary layer instrumentation used in determination of airflow. The data presented have been adjusted by decreasing the measured total airflow by approximately 1.25%.

Figures B-4 through B-8 present thrust vs. fuel consumption test results at flight conditions in and around the airplane cruise environment. The results can be summarized by noting that the as-measured results show a deficiency of 2-3% in TSFC at the average cruise thrust setting of all the cruise conditions tested, except the 7620m (25,000 ft.) 0.8 Mn condition. A 4.7% deficiency at the 7620 m (25,000 ft) 0.8 Mn condition is not consistent with other average cruise conditions. Data analysis indicated this was due to a lower thrust indication at this condition. These data are considered questionable.

Engine EE-3 at sea level static showed an as-run deficiency of approximately 2.3% in TSFC relative to the design goal. Based on this, it can be concluded that EE-3 was approximately 0.5% higher than the design sea-level-to-altitude TSFC increment at average cruise power. A 4-6% deficiency exists at the maximum cruise thrust setting. Thus, at maximum cruise power the performance was 1.7% to 3.7% higher than the design sea level-to-altitude TSFC increment at maximum cruise power. Tables VI and VII show the measured vs. design goal values of important parameters for average cruise and maximum cruise power at 9144 m (30,000 ft)/0.8 Mn.

As previously noted at SLS, the combination of other refan component changes, instrumentation adjustment and base JT8D-9 performance differences offset a fan stream pressure loss increase above design goals of about 2%. However, at max cruise the additional 2% increase in fan stream pressure loss above the SLS and average cruise tested levels would account for an additional 1.3% TSFC discrepancy. As noted in Table B-VII, the gross thrust coefficient, which characterizes in an overall fashion the partially mixed flow exhaust system performance, contributed an additional 0.6% to the TSFC discrepancy.

When the altitude cruise data were originally taken in October of 1974, the cruise discrepancies were approximately 2% larger than indicated above. Since the JT8D had never been calibrated under simulated altitude conditions with direct force measurement to calculate thrust, and the contribution of fan stream discharge, turbine discharge, and exhaust stream discharge pressure losses, fan and turbine discharge stream mixing, and residual turbine swirl were not defined by the gas path instrumentation available, an exhaust system pressure and temperature traverse survey was conducted. Although subsequent correction of airflow and thrust for static and total pressure gradients in the NASA LeRC altitude facility inlet duct alleviated a major concern, traverse programs were conducted at NASA and P&WA in December 1974 and January 1975.

In December of 1974, a station seven pressure traverse was conducted on JT8D-109 EE-1 to determine fan and engine pressure levels at the turbine and fan discharge plane upstream of the nozzle exit. Traverses were conducted with a standard exhaust nozzle [0.774 m^2 (8.33 ft^2)] and with a 10% larger nozzle selected to provide corrected flow conditions at the traverse plane equivalent to those at cruise conditions.

Data were obtained at 15 radial locations for seven circumferential positions of the traversing probe. Total pressure was then averaged using a stream thrust integrated routine. The fan stream integration agreed quite well with the values used in the test data analyses, the traverse data giving slightly higher losses. The engine stream traverse, however, implied levels so low it would be impossible for the engine to achieve the measured levels of thrust.

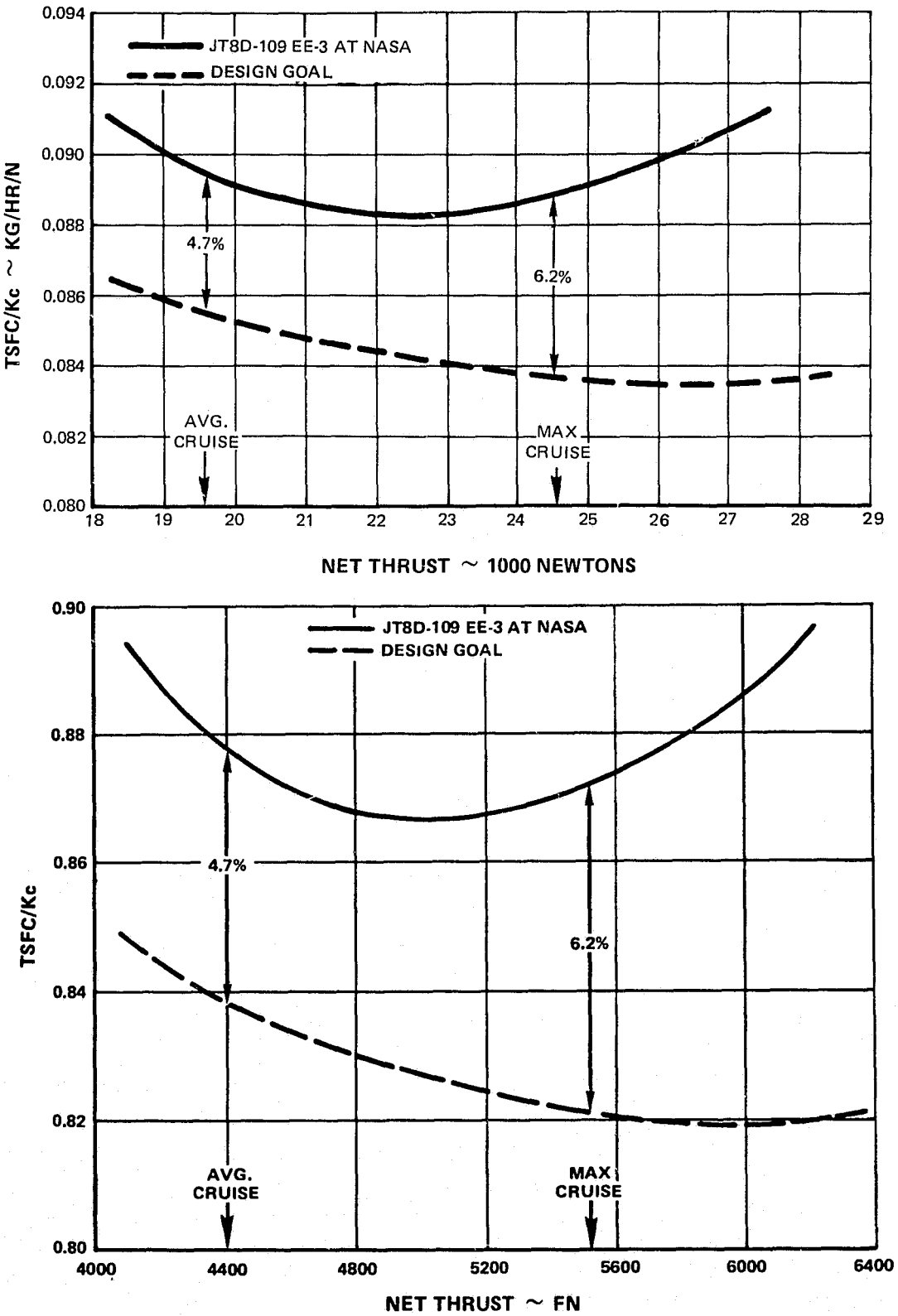

Figure B-4 JT8D-109 Engine EE-3 Steady State Performance Evaluation at 7,620 m (25000 Ft) Mn 0.80

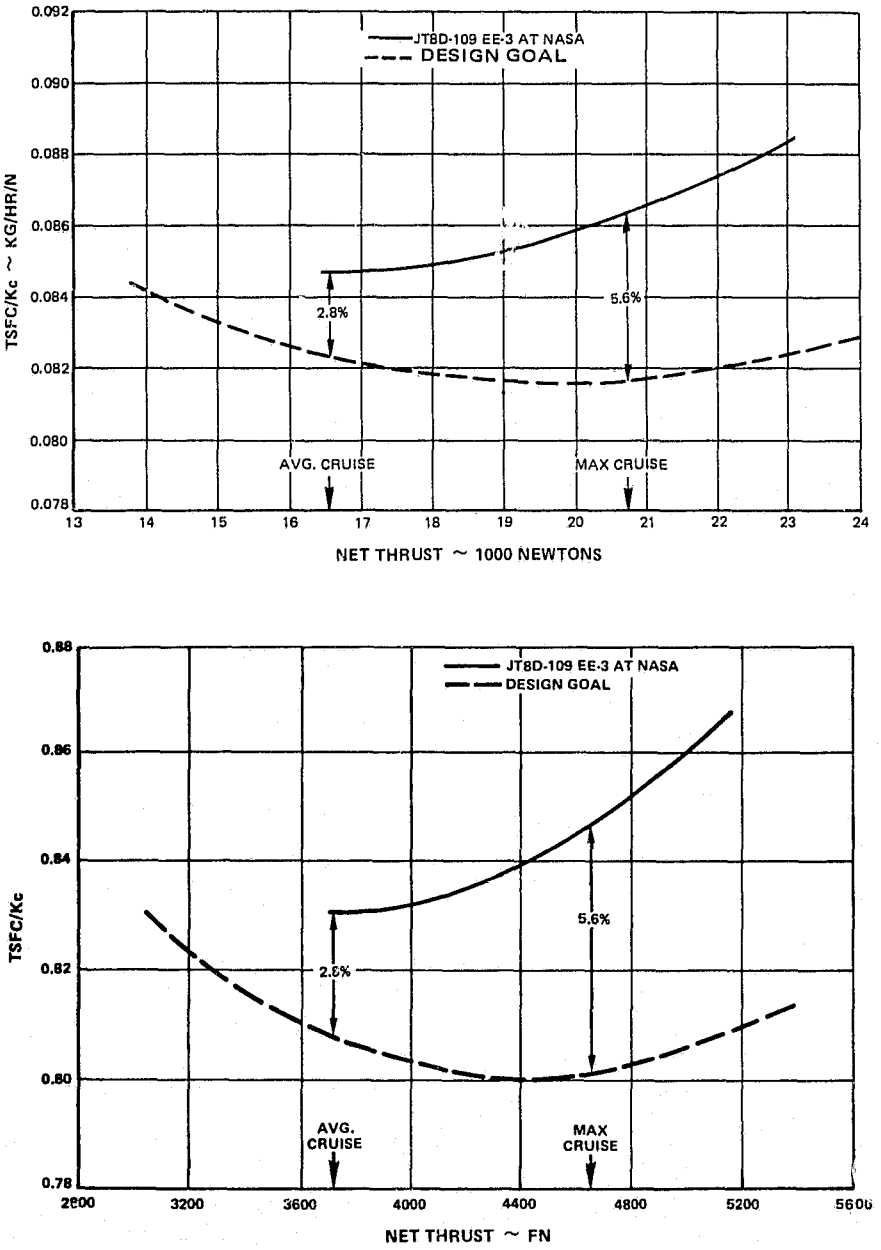

Figure B-5 JT8D-109 Engine EE-3 Steady State Performance Evaluation at 9144 m (30000 Ft) Mn 0.70

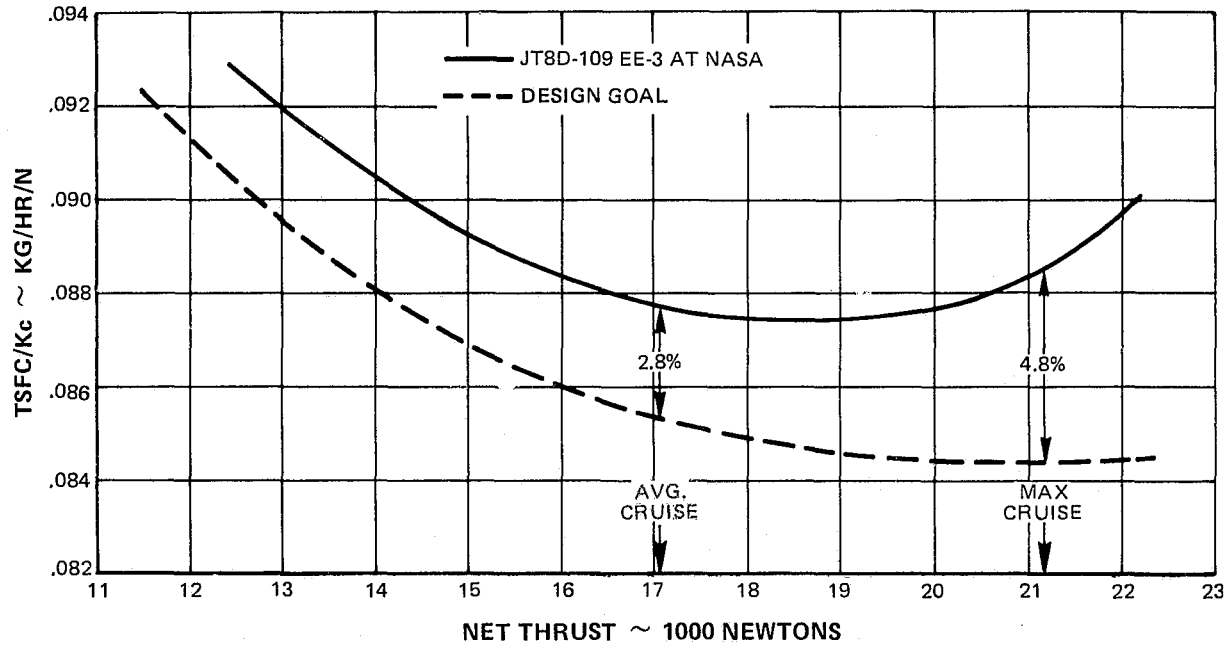

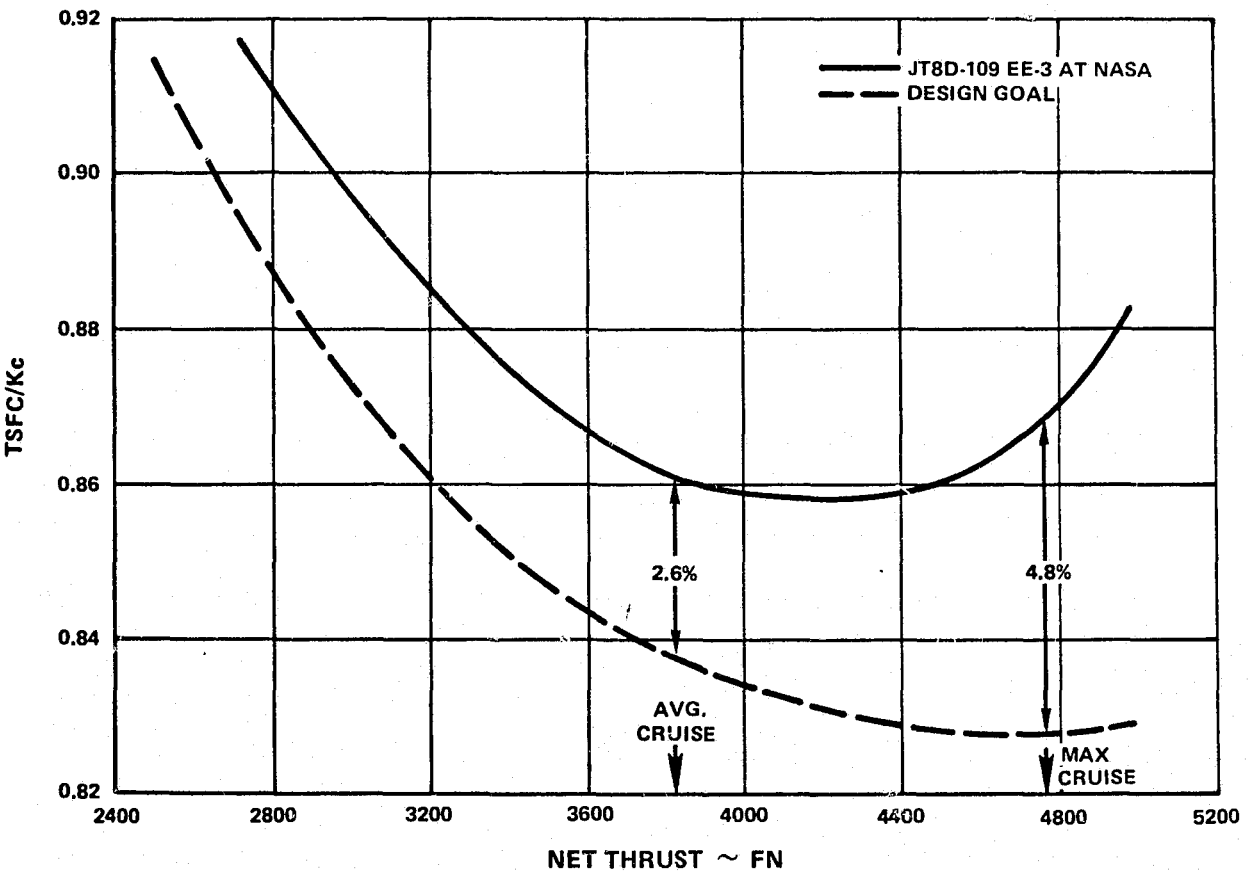

Figure B-6 JT8D-109 Engine EE-3 Steady State Performance Evaluation at 9144 m (30000 Ft) Mn 0.80

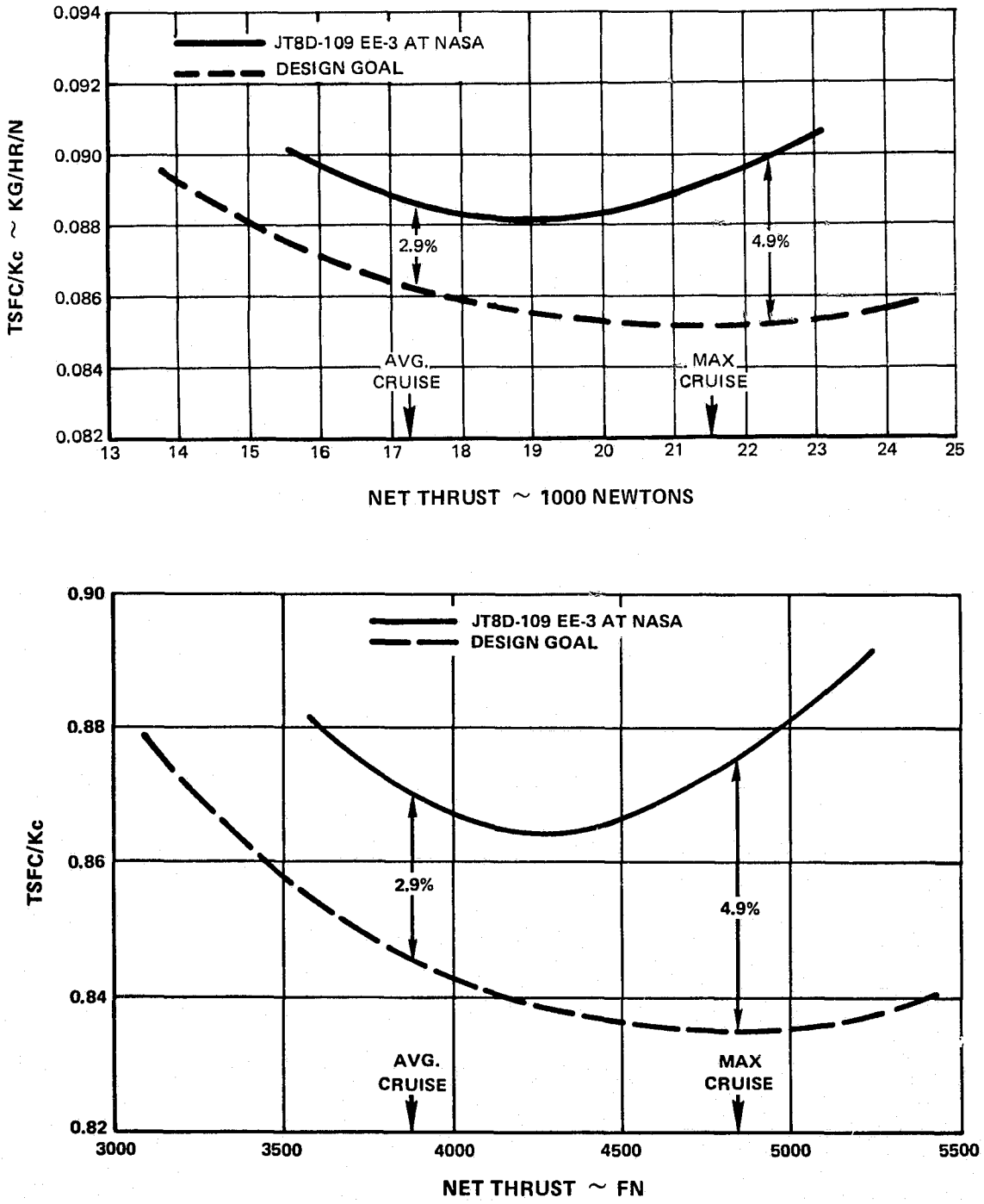

Figure B-7 JT8D-109 Engine EE-3 Steady State Performance Evaluation at 9144 m (30000 Ft) Mn 0.85

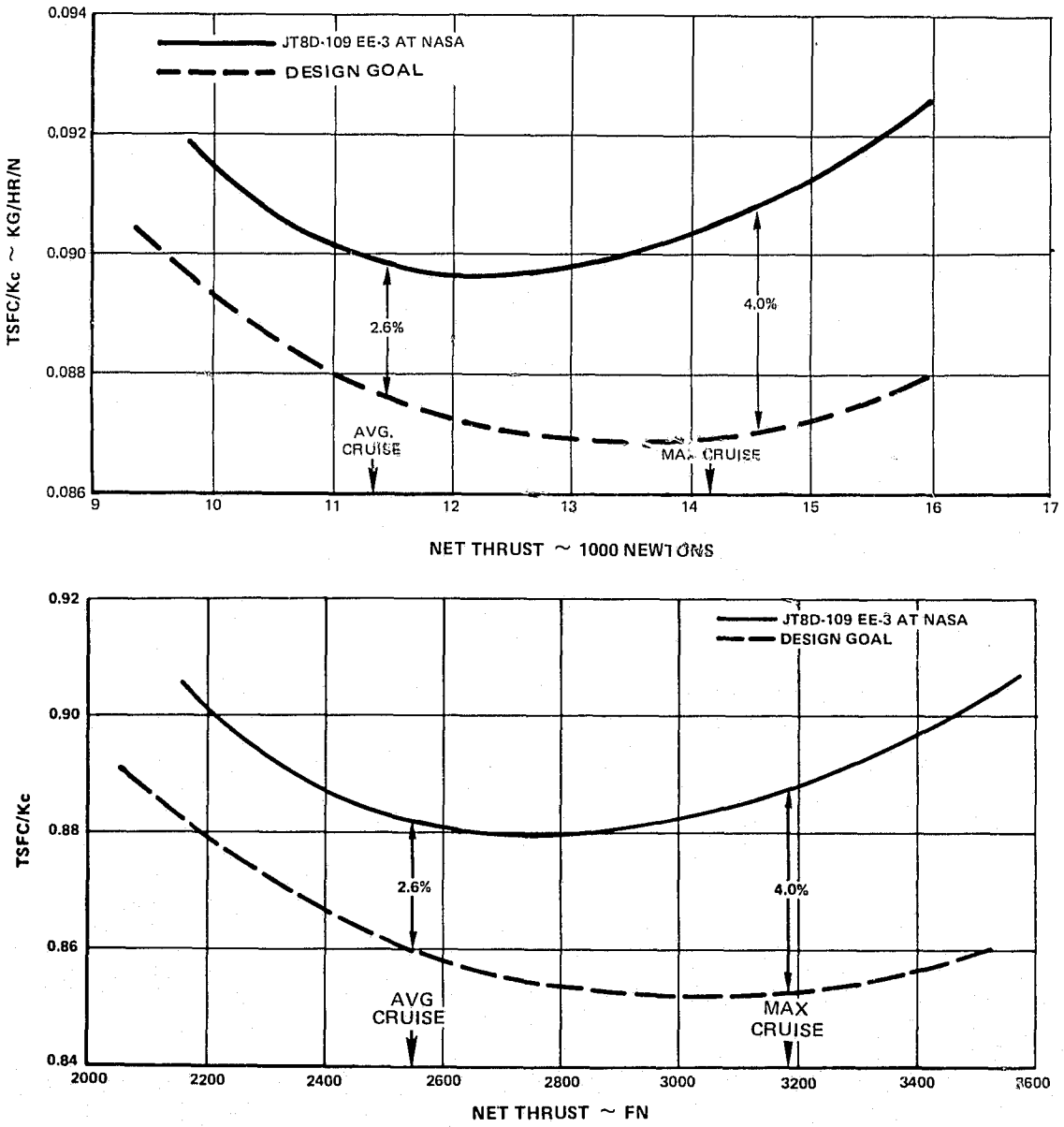

Figure B-8 JT8D-109 Engine EE-3 Steady State Performance Evaluation at 12,192 m (40000 Ft) Mn 0.85

TABLE B-VI

JT8D-109 ENGINE EE-3
MEASURED TEST RESULTS VERSUS DESIGN GOAL
COMPARISON AT AVERAGE CRUISE
9144 m (30,000 ft), 0.8 Mn

Parameter	Measured Data	Design Goal	Δ Parameter	Δ TSFC Impact
TSFC/KcKh Kg/hr/n (lb/hr/lb)	.08779 (0.861)	0.8545 (0.838)	+2.8%	
TT5/θT2 °K (°R)	1194 (2150)	1186 (2134)	+8.0 (+16)	
N1/$\sqrt{\theta T2}$, rpm	7140	7230	−90	
N2/$\sqrt{\theta T2}$, rpm	11030	11050	−20	
WAT$\sqrt{\theta T2}/\delta T2$ kg/sec (lbs/sec)	209.11 (461)	208.20 (459)	+0.91 (+2)	
WAE$\sqrt{\theta T2}/\delta T2$ kg/sec (lbs/sec)	64.41 (142)	66.68 (147)	−2.27 (−5)	
η Fan (%)	82.15	81.82	+0.33	−0.3
η LPC (%)	86.40	86.24	+0.16	−0.1
η STO (%)	88.88	89.34	−0.46	+0.8
ΔP/P(PT2.4−PT7F)/PT2.4	0.075	0.055	+0.02	+1.6
Gross Thrust Coefficient (CV)	0.988	0.988	0	0

TABLE B-VII

JT8D-109 ENGINE EE-3
MEASURED TEST RESULTS VERSUS DESIGN GOAL
COMPARISON AT MAXIMUM CRUISE
9144 m (30,000 ft), 0.8 Mn

Parameter	Measured Data	Design Goal	Δ Parameter	Δ TSFC Impact
TSFC/kcKh, kg/hr/N (lb/hr/lb)	0.08851 (0.868)	0.08443 (0.828)	+4.8%	
TT5/θT2, °K (°R)	1297 (2335)	1275 (2295)	22 (+40)	
N1/$\sqrt{\theta T2}$, rpm	7670	7735	−65	
N2/$\sqrt{\theta T2}$, rpm	11430	11400	+30	
WAT$\sqrt{\theta T2}/\delta T2$, kg/sec (lbs/sec)	220 (485)	217.3 (479)	2.7 (+6)	
WAE$\sqrt{\theta T2}/\delta T2$, kg/sec (lbs/sec)	69.9 (154)	71.7 (158)	1.8 (−4)	
η Fan (%)	81.04	80.72	+0.32	−0.1
η LPC (%)	83.00	82.82	+0.18	−0.1
η STO (%)	89.40	89.25	+0.15	−0.2
ΔP/P(PT2.4−PT7F)/PT2.4	0.0985	0.0574	+0.0411	+2.9
Gross Thrust Coefficient (CV)	0.9871	0.9903	−0.032	+0.6

The problem with the engine stream traverse appeared to be turbine exit guide vane (TEGV) tip vortices due to a gap between the vanes and the case. It is theorized that these holes in the total pressure map might be due to flow angularity relative to the pressure probe rather than a total pressure loss. Hence, including them into the integration produced an erroneous pressure level. Because of this, the decision was made to continue to use turbine discharge pressure levels taken earlier during a more detailed traverse on JT8D-109 EE-2. This turbine exit traverse indicated a 3.66% primary pressure loss. Measurements of strut fairing leading and trailing edge metal angles at this time indicated significant deviation from design values. This change in metal angle and the unsealed radial gaps at the thin vane tips account for the pressure loss level.

The 3.66% pressure loss was used on EE-3 when analyzing exhaust system performance. Because the fan duct did not have these complex flow patterns, fan duct discharge pressure loss levels from the traverse data from JT8D-109 EE-1 were used on EE-3 when analyzing exhaust system performance.

The fan stream traverse results confirmed the PT7F test data that fan duct pressure loss did not vary directly with the average duct $(Mn)^2$, as was assumed in making the original refan performance prediction. As noted above, the performance loss at altitude maximum cruise power relative to average cruise is primarily due to the increased duct pressure loss which was not anticipated based on the $(Mn)^2$ pressure loss relationship.

Exhaust nozzle discharge traverse results were obtained at simulated cruise conditions on EE-3 at NASA. Analysis of the data indicated that the measured facility thrust to airflow ratio was within 0.5% of the traverse calculated thrust to airflow ratio, thus matching the average exhaust velocity at the nozzle exit. The absolute integrated gross thrust and total airflow levels as obtained from the traverse data, however, were both 4% below measured facility values.

3. Flight Testing

Two JT8D-109 engines, P-666995 and P-666996, were delivered to McDonnell-Douglas for flight test in a modified DC-9 airplane. As can be seen from Table B-1, the TSFC at SLS takeoff power was considerably higher than the design goal, 5.8% for engine P-666995 and 3.2% for engine P-666996. This is an average value of 4.5% higher than the design goal for the airplane propulsion system. EE-3, which demonstrated a 2.3% TSFC deficiency (as-run) at SLS takeoff had a 2.8% (as-run) deficiency at 9144 m (30,000 ft) average cruise rating. Based on a straight ratio of these values, the airplane TSFC deficiency would be expected to be 5.4% at 9144 m (30,000 ft) average cruise power.

4. Potential JT8D-100 Performance Improvements

If a decision were made to proceed towards certification of the JT8D-100 engine series, extensive development testing would be conducted to evaluate performance improvement configurations. Potential performance improvement items that have been identified as a possible means to improve the deficiencies noted in the NASA refan programs are shown in Table B-VIII.

TABLE B-VIII

POTENTIAL JT8D-100 PERFORMANCE IMPROVEMENTS

Item	Pressure Loss Reduction (%)	Efficiency Improvement (%)	Δ Weight Increase kg (lbs)	Δ TSFC* Improvement (%)	Δ TT5** °K (°F)
Fan Rotor			0.9072 (2.0)	0.9	−8.9 (−16)
(a) Recontour airfoil root		3.0 primary			
(b) Conical shroud Streamline shroud Recontour airfoil below shroud		1.6 duct			
FEGV	0.6		0.4536 (1.0)	0.4	−2.2 (−4)
(a) Recontour spanwise					
(b) Root sealing					
Fan Duct Flowpath	1.1		6.3503 (14.0)	0.8	−4.4 (−8)
(a) Inner – Constant diameter from intermediate case to burner case					
(b) Outer – Increased inner diameter, intermediate to split fan burner case					
Combined PT7/TT7 Probes fore or aft of exhaust strut	1.0		0.7257 (1.6)	0.4	−2.2 (−4)
Summation			8.434 (18.6)	2.5	−17.9 (−32)

* 9144 m (30,000 ft) 0.8 Mn

** Sea Level Static, Takeoff

C. STARTING, TRANSIENT AND STABILITY CHARACTERISTICS

Subsequent paragraphs in this section provide a detailed description of the starting, transient and stability characteristics of the JT8D-100 refan engine as determined from sea level and altitude development testing as conducted during Phase II of the Refan program.

As part of the System Development Test Program, JT8D-109 engine starting, transient and stability testing was conducted by Pratt & Whitney Aircraft at sea-level static conditions, and by NASA LeRC at appropriate altitude test conditions. Selected data from the DC-9 flight testing are also included in this document.

1. Ground Starting Tests

Sea level static tests were conducted at P&WA on engines EE-1, EE-2 and EE-3 as both JT8D-9 and JT8D-109 models to establish the ground starting characteristics of the JT8D-109 engine in comparison to the baseline JT8D-9 engine.

a. Test Procedure

Normal engine starts were accomplished to document starting time-to-idle. The following were recorded:

- Starter drive pressure level
- Time to pressurization
- N1 speed at pressurization
- N2 speed at pressurization
- Time to engine light-off
- Maximum fuel flow
- Maximum exhaust gas temperature
- Time to idle – to within 100 rpm of the N2 defined by the idle trim curve

b. Test Results and Discussion of Results

The results of the JT8D-9 and JT8D-109 engine ground starting tests are shown in Table C-I. These results are consistent with typical JT8D-9 experience.

Table CII shows a comparison of the baseline JT8D-9 and refan JT8D-109 maximum exhaust gas temperature levels during ground start. These results are consistent with typical JT8D-9 experience.

TABLE C-I

JT8D-9/D-109 GROUND STARTING TIMES (SECONDS)*

	JT8D-9			JT8D-109		
Start No.	Typical D-9	EE-1	EE-2	EE-1	EE-2	EE-3
1	–	36	40.6	32.2	40.5	43.6
2	–	39.5	38.7	33.7	39.0	50.5
3	–	40.5	36.8	41.4	39.0	39.0
		38.7	38.7	35.8	39.5	44.3
Average	30-50	38.7			39.9	

*Timed from starter pressurization to idle N2-100 rpm

Table C-II shows a comparison of the baseline JT8D-9 and refan JT8D-109 maximum exhaust gas temperature levels during ground start. These results are consistent with typical JT8D-9 experience.

TABLE C-II

JT8D-9/D-109 MAXIMUM EXHAUST GAS TEMPERATURES °K (°F) DURING GROUND STARTING

JT8D-9		JT8D-109	
EE-1	EE-2	EE-1	EE-2
575	624	579	633
(575)	(663)	(582)	(680)

Additional representative JT8D-109 ground starting characteristics are compared to the JT8D-9 characteristics in Figures C-1 and C-2.

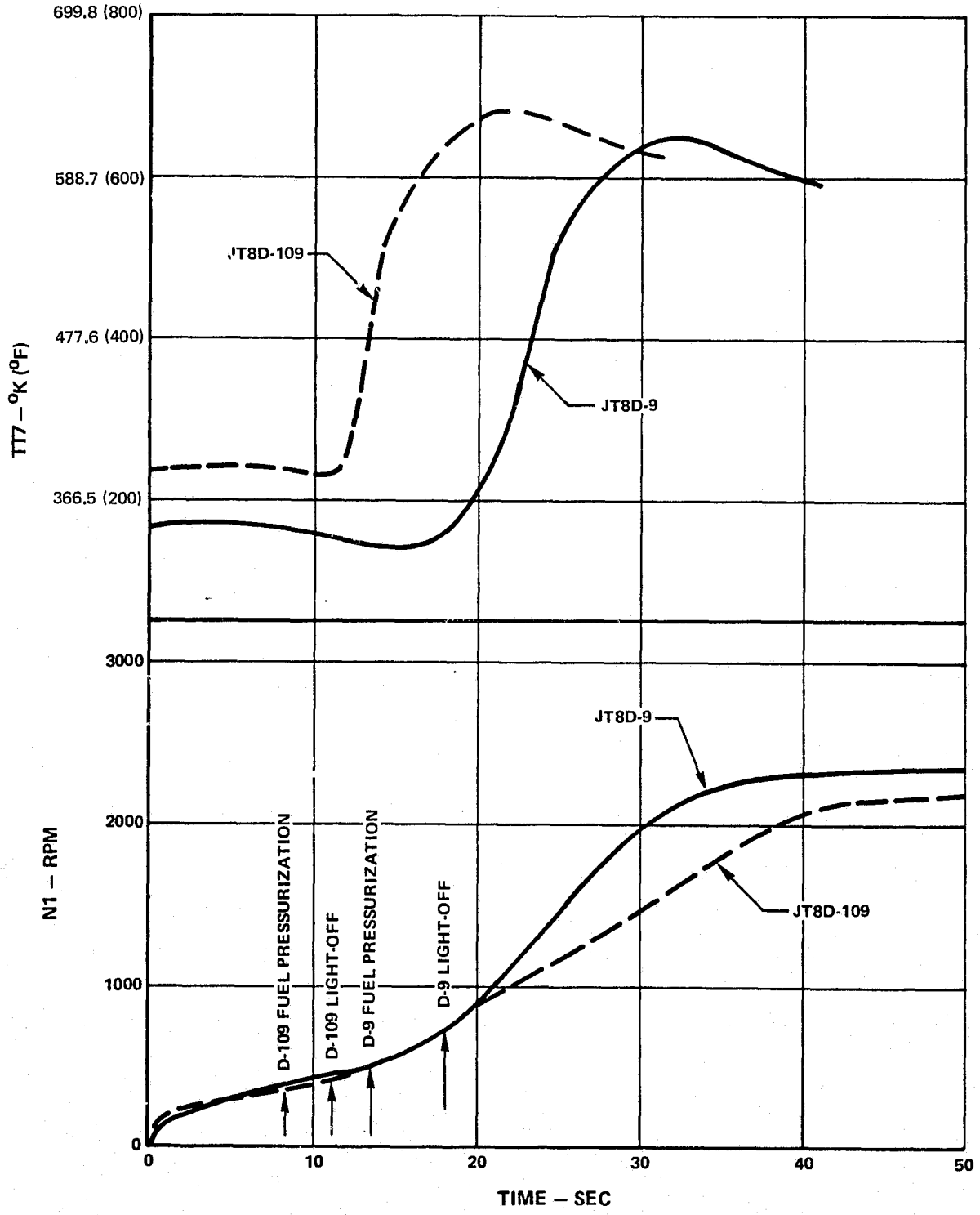

Figure C-1 JT8D-109/D-9 Typical Ground Starting Characteristics

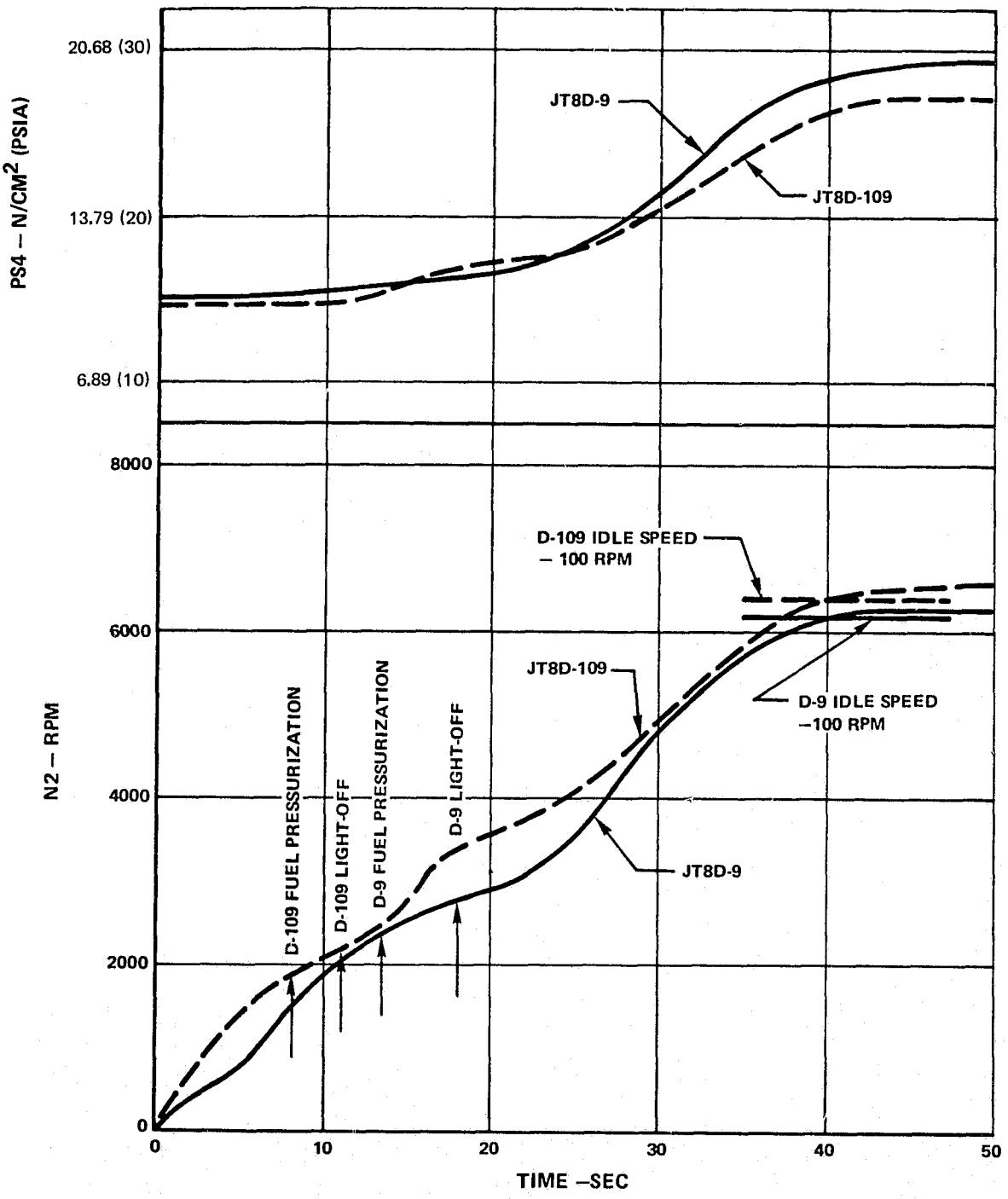

Figure C-2 JT8D-109/D-9 Typical Ground Starting Characteristics

2. Flight Starting Tests

Flight starting tests were conducted on JT8D-109 refanned engine EE-3 at the NASA Lewis Research Center (LeRC) altitude test facility. These tests were performed to demonstrate the capability of the JT8D-109 engine to start in flight without starter assist throughout the current JT8D-powered aircraft flight start envelope as shown in Figure C-3

Three categories of flight starting tests were conducted:

- Engine windmilling with TT7 - TT2 ≈ 255°K (0°F) (cold airstart)
- Engine windmilling with TT7 - TT2 ≈ 311°K (100°F) (airstart)
- Engine windmilling, restart after 45 sec shutdown from cruise power (relight)

a. Test Procedures

1) Cold Engine Airstart

Cold engine airstarts were accomplished from a free windmilling condition where TT7-TT2 across the engine was as close to zero as practical. An inlet distortion screen simulating the Boeing 727 center engine inlet distortion was utilized during the test. The test was conducted as follows:

- Test cell conditions (PT2, PO and TT2) were set with the bulkhead valve opened sufficiently so that total flow was 10 to 20 percent above idle value.
- Steady state data were recorded at the windmilling condition. While recording transient data, an engine start and acceleration to idle was accomplished.
- The engine was shut down upon reaching idle so as to obtain minimum Δ T (TT7-TT2) as quickly as possible for the next start.
- The above procedure was repeated with variations in Mn to establish the start-no start envelope, Ref. Table C-III.

TABLE C-III

JT8D-109 COLD AIRSTART TEST CONDITIONS

Altitude m	Altitude (ft)	Mn	TT2 °K	TT2 (°F)
3048	(10,000)	0.30	272	(30)
3048	(10,000)	0.75	285	(53)
3048	(10,000)	0.75	284	(51)
3048	(10,000	0.75	288	(58)
4572	(15,000)	0.30	260	(9)
4572	(15,000)	0.50	271	(28)
4572	(15,000)	0.80	285	(53)
4572	(15,000)	0.80	286	(55)
4572	(15,000)	0.80	289	(61)
6096	(20,000)	0.60	265	(18)
9144	(30,000)	0.90	265	(18)

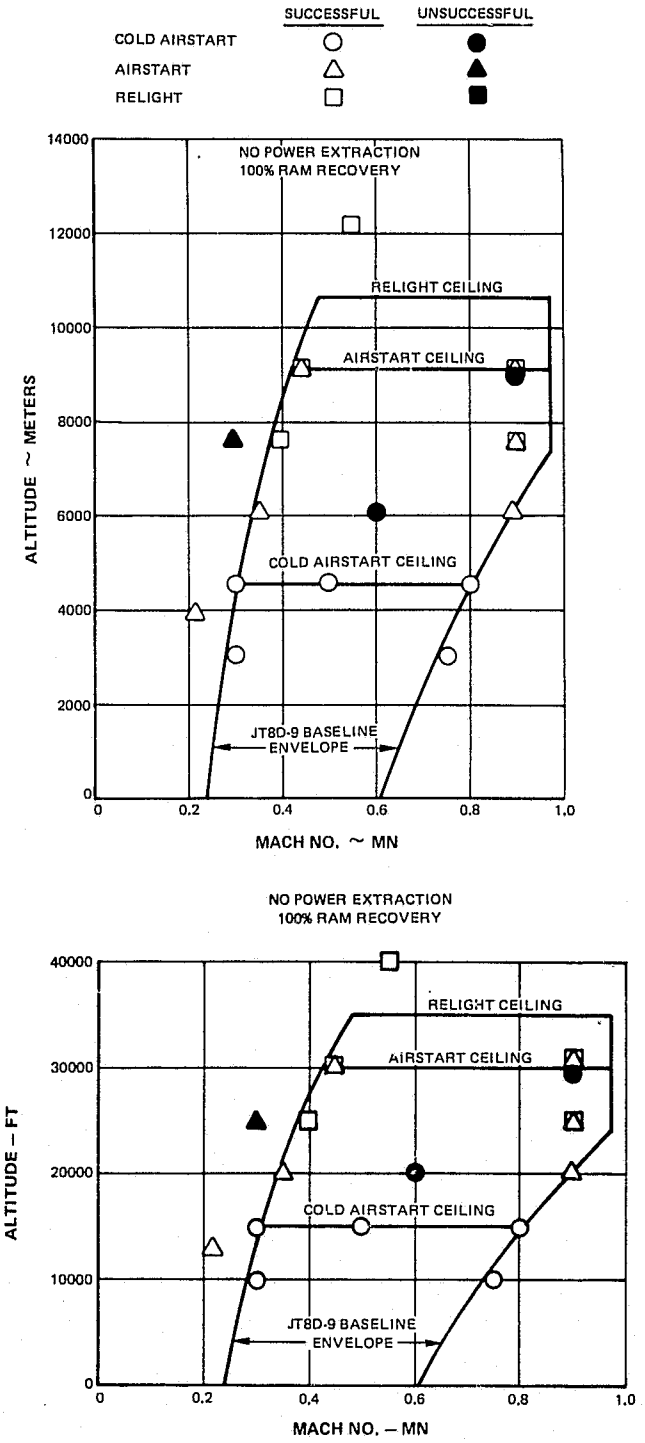

Figure C-3 JT8D-Powered Aircraft Flight Start Envelope

2) Engine Airstart

Engine airstart testing was conducted to simulate engine starts after engine shutdown from cruise power when the ΔT (TT7-TT2) across the engine was approximately 311°K (100°F). An inlet distortion screen simulating the Boeing 727 center engine inlet distortion was utilized during the test. The test was conducted as follows:

- Test conditions were set with the bulkhead valve slightly open.
- A steady state data point was recorded at cruise power.
- While recording transient data, the engine was shut down. A relight was attempted when the engine ΔT was approximately 311°K (100°F). The engine was then accelerated slowly to cruise power.
- The above procedure was repeated with variations in Mn to establish the airstart envelope. Ref. Table C-IV

TABLE C-IV

JT8D-109 AIRSTART TEST CONDITIONS

Altitude		Mn	TT2 °K (°F)	
m	(ft)			
4267.2	(14,000)	0.22	279	(42)
6096	(20,000)	0.35	280	(45)
6096	(20,000)	0.35	279	(42)
6096	(20,000)	0.90	284	(52)
7620	(25,000)	0.30	278	(41)
7620	(25,000)	0.90	280	(45)
7620	(25,000)	0.90	279	(43)
9144	(30,000)	0.45	276	(38)
9144	(30,000)	0.90	279	(43)

3) Engine Relight

Engine testing was conducted to simulate the engine starting capability 45 seconds after shutdown from cruise power. An inlet distortion screen simulating the Boeing 727 center engine inlet distortion was utilized during the test. The test was conducted as follows:

- The desired test conditions were set with the bulkhead valve slightly open.
- A steady state data point was recorded at cruise power.

- While recording transient data, the engine was shut down. An attempt was made to relight 45 seconds after engine shutdown. After relight, the engine was accelerated slowly to cruise power.

- The above procedure was repeated with variations in Mn to establish the relight envelope. Ref. Table C-V.

TABLE C-V

JT8D-109 RELIGHT CONDITIONS

Altitude m	(ft)	Mn	TT2 °K (°F)	
7620	(25,000)	0.40	278	(40)
7620	(25,000)	0.40	281	(46)
7620	(25,000)	0.90	280	(44)
7620	(25,000)	0.90	279	(43)
9144	(30,000)	0.45	276	(38)
9144	(30,000)	0.90	279	(43)
9144	(30,000)	0.90	279	(43)
9144	(30,000)	0.90	283	(50)
9144	(30,000)	0.90	280	(44)
12,192	(40,000)	0.55	275	(35)
12,192	(40,000)	0.55	279	(43)

b. Test Results and Discussion of Results

1) Cold Engine Airstart

Figure C-4 shows the JT8D-109 cold airstart envelope plotted against the JT8D-9 baseline envelope. As shown, the JT8D-109 engine is capable of cold airstarts within the JT8D-9 baseline envelope.

2) Engine Airstart

Figure C-5 shows the JT8D-109 airstart envelope plotted against the JT8D-9 baseline envelope. As shown, the JT8D-109 engine is capable of airstarts within the JT8D-9 baseline envelope.

3) Engine Relight

Figure C-6 shows the JT8D-109 relight envelope plotted against the JT8D-9 baseline envelope. As shown, the results of the engine relight tests are consistent with the JT8D-9 baseline envelope.

The results of the flight starting tests conducted on the JT8D-109 refan engine are consistent with typical JT8D-9 experience. The capability of the JT8D-109 engine to successfully perform flight starts within the current JT8D-9 flight start envelope was demonstrated by flight start testing. Further test data can be found in Reference 4.

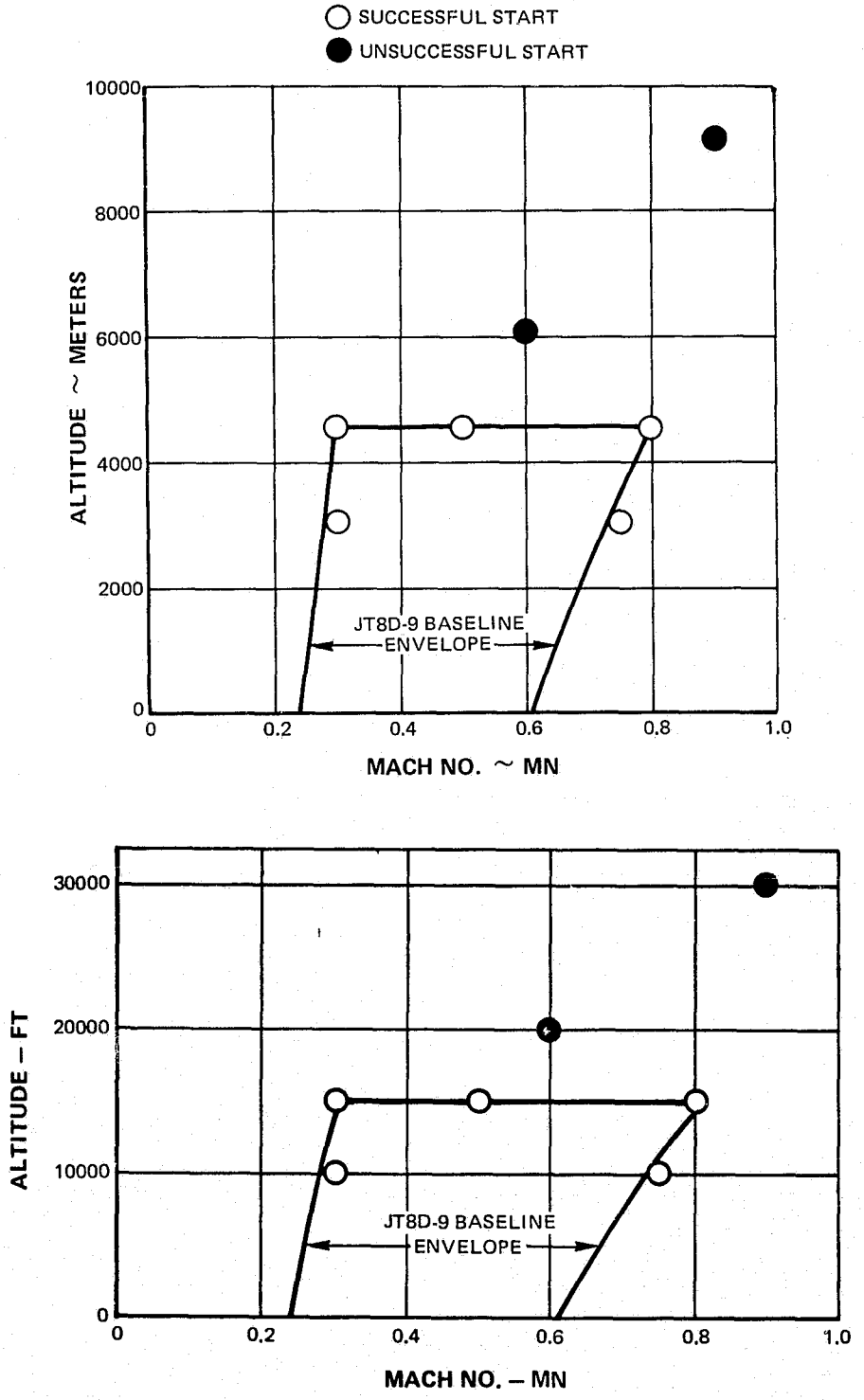

Figure C-4 JT8D-109 Cold Engine Airstarts [$\Delta T \approx 0°K$ (0°F)]

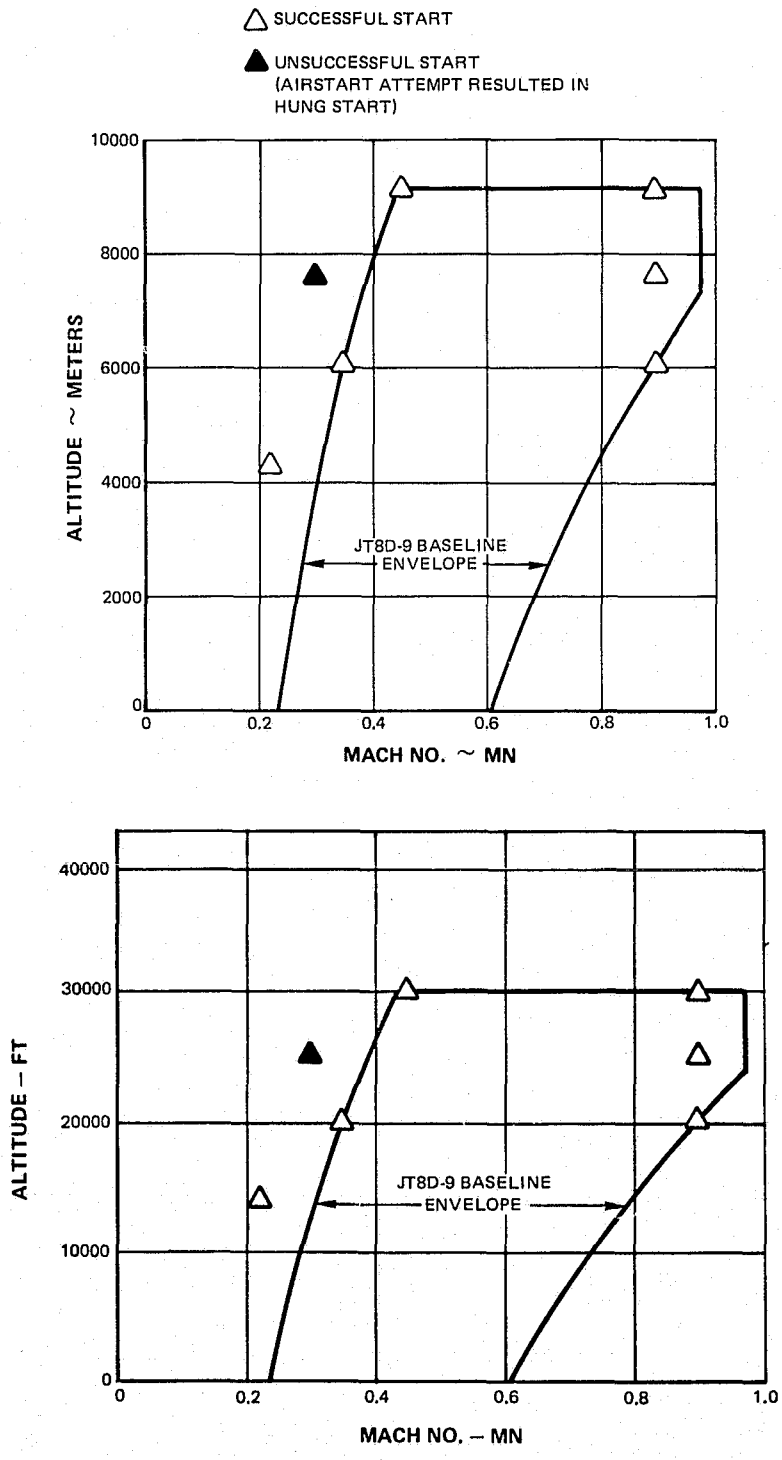

Figure C-5 JT8D-109 Engine Airstarts [$\Delta T \approx 55.6°K$ (100°F)]

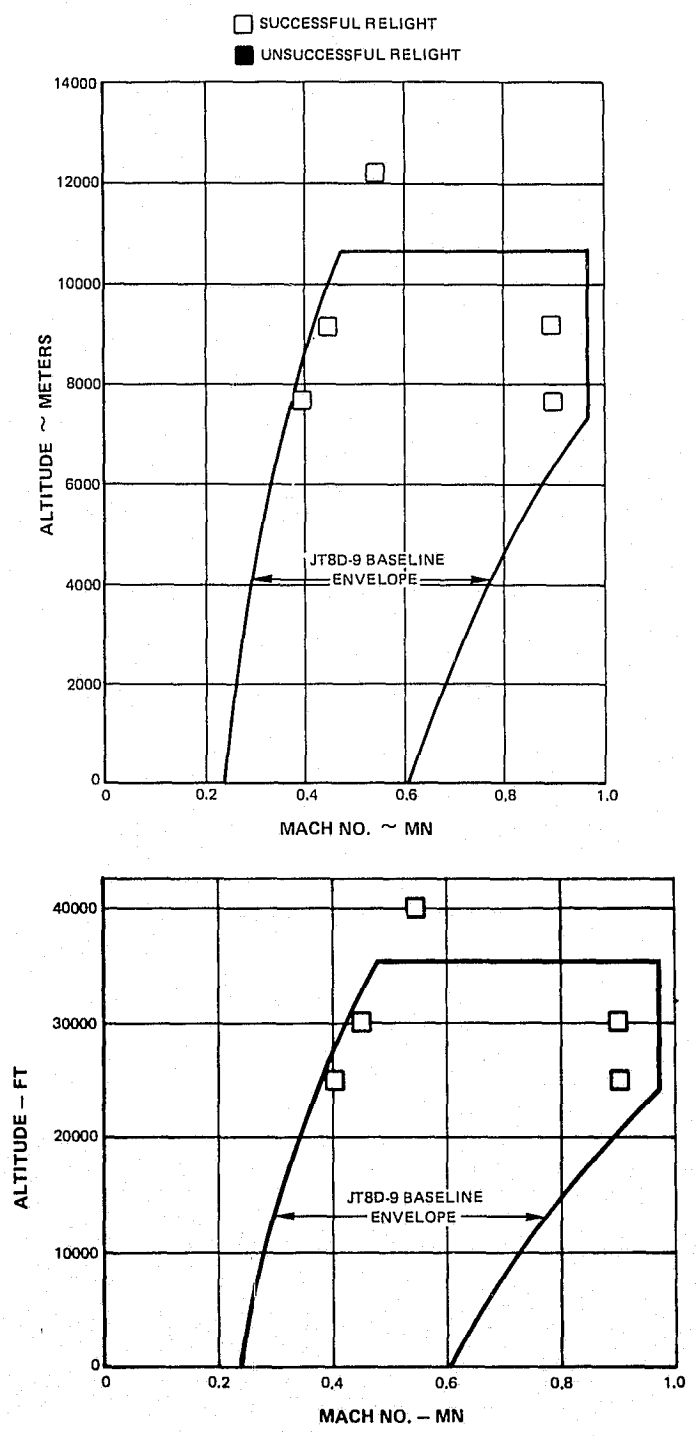

Figure C-6 JT8D-109 Engine Relights (45 sec shutdown)

3. Off-Idle Surge Tests

Engine surge margin tests were conducted to determine the JT8D-109 transient stability margin in the off-idle power region. A surge was identified by an audible thump, a jump in turbine cooling air pressure or burner pressure, hesitation in N2 speed, and/or torching in the engine tailpipe.

a. Test Procedures

For these tests, a special "flat ratio" fuel control was installed. This control was a standard fuel control modified to permit the engine to run on a constant ratio acceleration schedule as a tool to define HPC off-idle surge characteristics (surge bucket). The standard fuel control senses TT2 in the engine; the flat ratio control had a modified temperature sensing servo assembly that was actuated by externally supplied nitrogen pressure. By setting a specific nitrogen pressure, the control produced a constant acceleration schedule of fuel flow/burner pressure ratio (Wf/Pb). Changing the nitrogen pressure changed the schedule ratio.

A Hamilton Standard Model GS 7800 ratio plotter was utilized during the test. The ratio plotter is a self contained unit which is capable of plotting fuel flow/burner pressure (Wf/Pb) versus N2 speed (X-Y plot). A special fuel flow meter, N2 tachometer, and burner pressure transducer were installed on the engine to supply the necessary input signals to the ratio plotter.

The following procedure was used:

The engine was started and trimmed to 5000 rpm N2, and a steady state calibration performed at 5000, 6000, 7000, and 8000 rpm N2 to calibrate the ratio plotter. After this four-point calibration was completed, the X-Y plot of the fuel flow/burner pressure versus N2 speed was initiated.

For plotting the left side of the surge region, a reference stabilized starting speed of 5000 ± 100 rpm N2 was established, and nitrogen pressure set to provide an acceleration schedule equivalent to 32.89 to 39.46 kg/hr/N/cm^2 (55 to 60 lb/hr/psia) ratios fuel flow/burner pressure. A snap acceleration was made. The power was reduced when the first surge occurred, or at 8000 rpm N2 if no surge was encountered.

Nitrogen pressure was raised in 3.44 N/cm^2 (5 psig) steps, lowering the acceleration schedule until surge-free operation was achieved. Changes in nitrogen pressure were always made in an increasing direction. Reduction and reset of nitrogen pressure were made as required by test conditions.

When surge-free operation had been achieved under these conditions, the last surge point defined was repeated, and additional accelerations were made, raising the nitrogen pressure level in 0.688 N/cm^2 (one psig) increments until surge-free operation was again achieved for three consecutive accelerations.

This procedure defined the left side boundary of the surge bucket and partially defined the bottom.

In plotting the right side boundary of the surge bucket, the nitrogen level was initially set to obtain 30.26 kg/m/N/cm^2 (46 lb/hr/psia) ratios. Snap accelerations were made at several points (± 100 rpm, higher and lower than the apparent minimum bucket). The nitrogen pressure was then lowered 2.76 - 3.45 N/cm^2 (4-5 psig) and these speeds repeated.

This procedure was repeated until the right side of the curve bucket was defined. If surges were encountered further to the right, speeds were increased until maximum ratios were obtained with maximum speed, and surge-free operation was achieved.

Figure C-7 presents a typical JT8D-109 off-idle surge margin test sequence.

b. Results and Discussion of Results

A summary of results from the off-idle surge margin tests conducted on engines EE-1, EE-2 and EE-3 in the baseline JT8D-9 and refan JT8D-109 configurations is presented in Table C-VI.

TABLE C-VI

JT8D-9/D-109 MINIMUM OFF-IDLE SURGE LEVEL
WF/PB ~ KG/HR/N/CM^2 (LB/HR/PSIA)

Engine	JT8D-9	JT8D-109
EE-1	34.2 (52.0)	34.2 (52.0)
EE-2	32.9 (50.0)	32.8 (49.9)
EE-3	30.8 (46.8)	30.3 (46.1)

Figures C-8, -9, and -10 present comparisons of the baseline JT8D-9 and refan JT8D-109 engine off-idle surge minimum levels for engines EE-1, EE-2 and EE-3. The minimum surge bucket level for the JT8D-109 configuration is essentially the same as that of the JT8D-9 configuration. The right hand side of the surge bucket, which is the most significant side for tailoring an acceleration schedule, was also determined to be essentially the same as the JT8D-9 configuration.

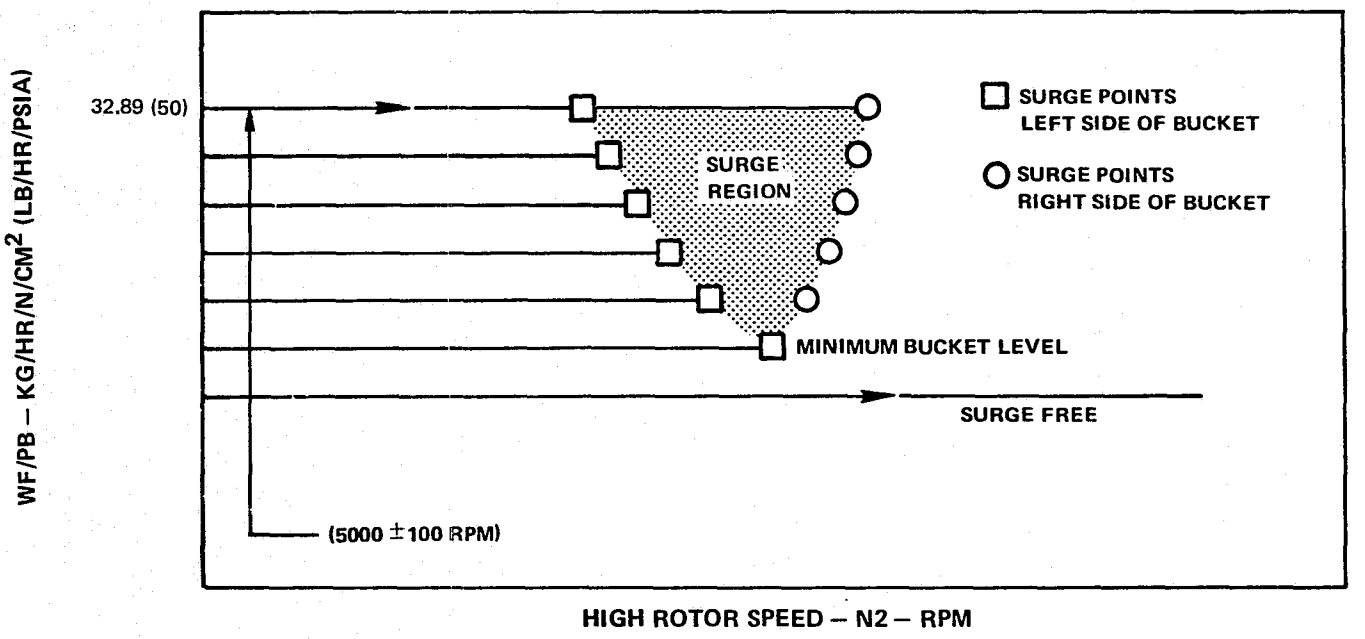

Figure C-7 Typical JT8D-109 Off-Idle Surge Margin Test Sequence

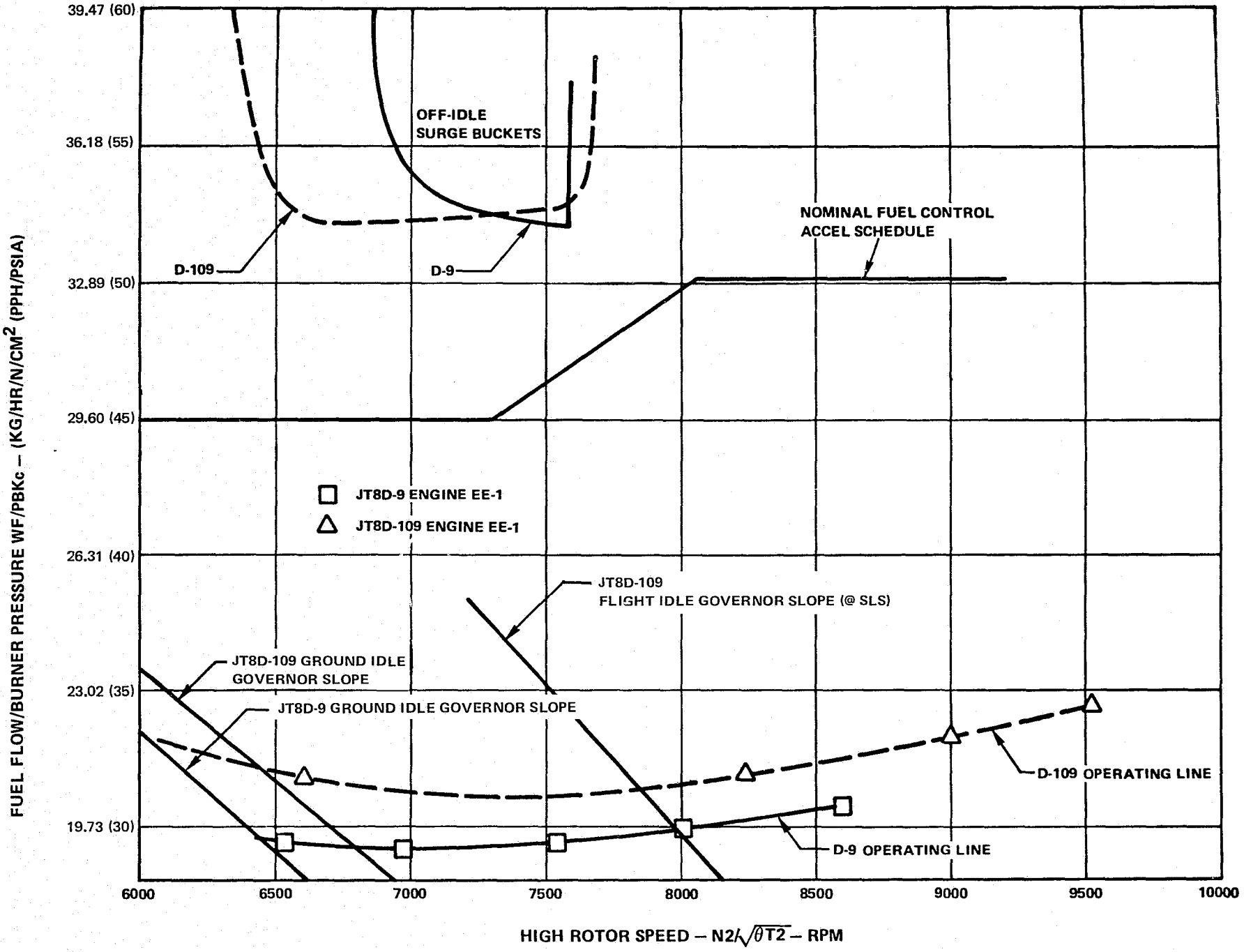

Figure C-8 JT8D-109/D-9 Engine EE-1 Off-Idle Surge Margin

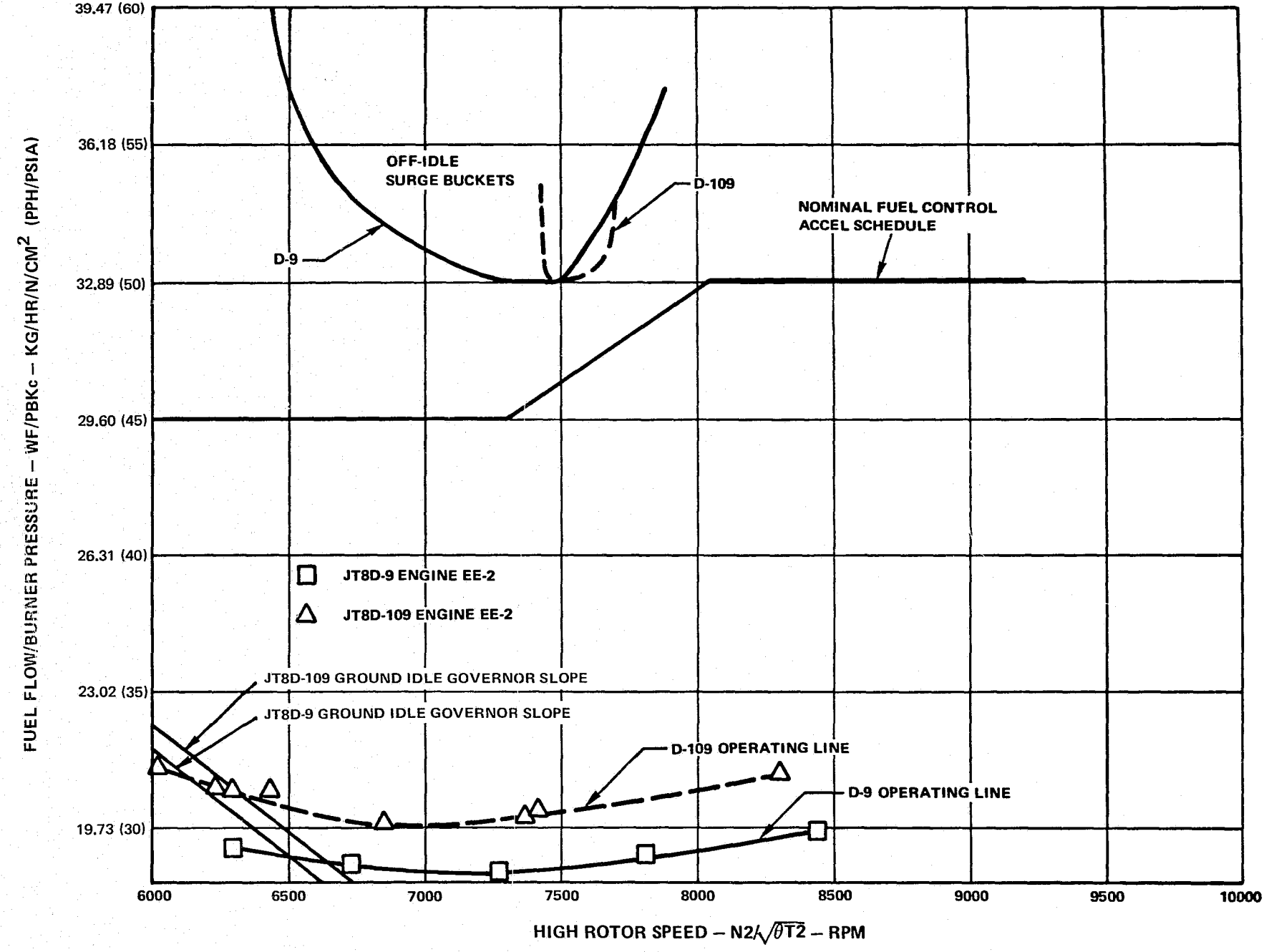

Figure C-9 JT8D-109/D-9 Engine EE-2 Off-Idle Surge Margin

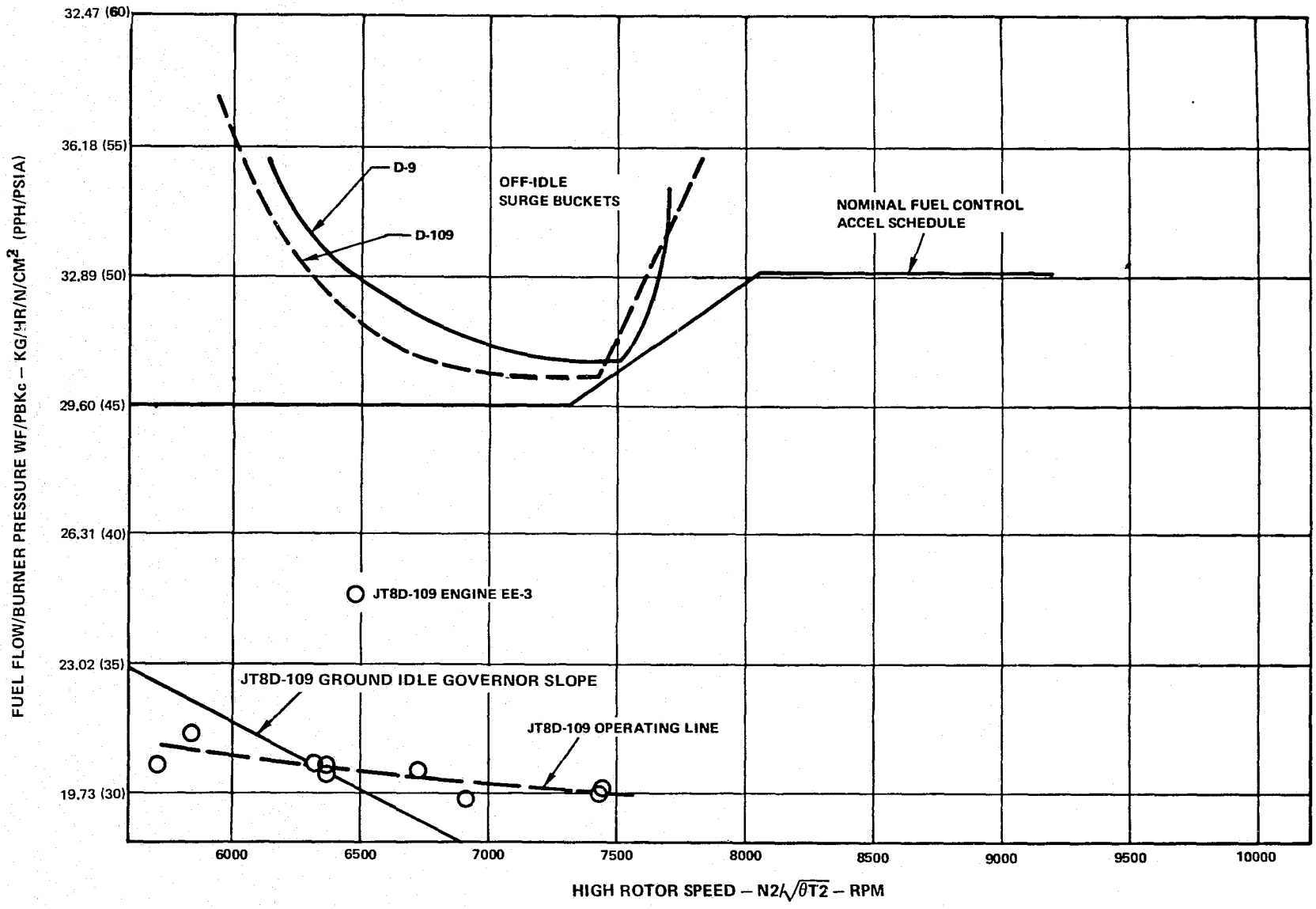

Figure C-10 JT8D-109/D-9 Engine EE-3 Off-Idle Surge Margin

4. Inlet Distortion Tests

The JT8D-109 engine and fan/LPC rig were run with inlet distortion screens simulating critical inlet patterns defined from inlet scale model tests to determine the tolerance of the JT8D-100 compressor system to inlet distortion. In addition, distortion effects of the Douglas DC-9 flight inlet on the JT8D-109 engine were determined during sea level static testing.

a. Fan/LPC Rig Inlet Distortion Test Procedures

Six inlet distortion patterns were tested. Three "classical" screens, I.D. radial, O.D. radial, and 180° full span circumferential, were selected to allow comparison of the distortion sensitivity of the compression system to previous experience. These screens are shown schematically in Figure C-11.

Three flight screen patterns were selected from Boeing inlet model test data to be representative of conditions expected to be encountered in actual service of the refanned 727 aircraft. The patterns represent the engine running at sea level static take-off power in the 1) center engine location with no crosswind, 2) center engine location with a 18 m/sec (35 knot) crosswind, and 3) pod engine location with a 15.4 m/sec (30 knot) crosswind. Further information about flight screen selection is presented in Reference 4.

To determine the inlet total pressure patterns, the inlet distortion screens were rotated with respect to the fixed pressure instrumentation. Data points were taken at eleven screen rotational positions, for each screen, at both nominal operating line and near surge, and the results were used to determine the true average conditions at major calculating stations.

Fan constant corrected speed lines were generated by setting the fan and low pressure compressor on their nominal operating line. The primary or engine discharge valve was kept at a position to maintain the nominal low pressure compressor operating line. The fan discharge valve was then opened to obtain data below the fan operating line and closed to obtain data above the fan operating line level. Data points were recorded at successively higher fan pressure ratios and/or lower total inlet flow until verge of surge was defined. When surge was encountered, the fan discharge valve was opened and speed reduced to idle, to restore stable operation.

LPC speed lines were run in the same manner except that the fan operating line was held constant, and the primary or engine discharge valve was used to vary LPC back pressure.

Occurrence of surge operation was determined from wall statics in the fan and LPC discharge ducts. Each static was fed to the two ports of a differential pressure transducer. One port had a snubber and the other was unrestricted. At steady state operating conditions both ports read the same, but at surge the snubber resulted in different levels in the two ports.

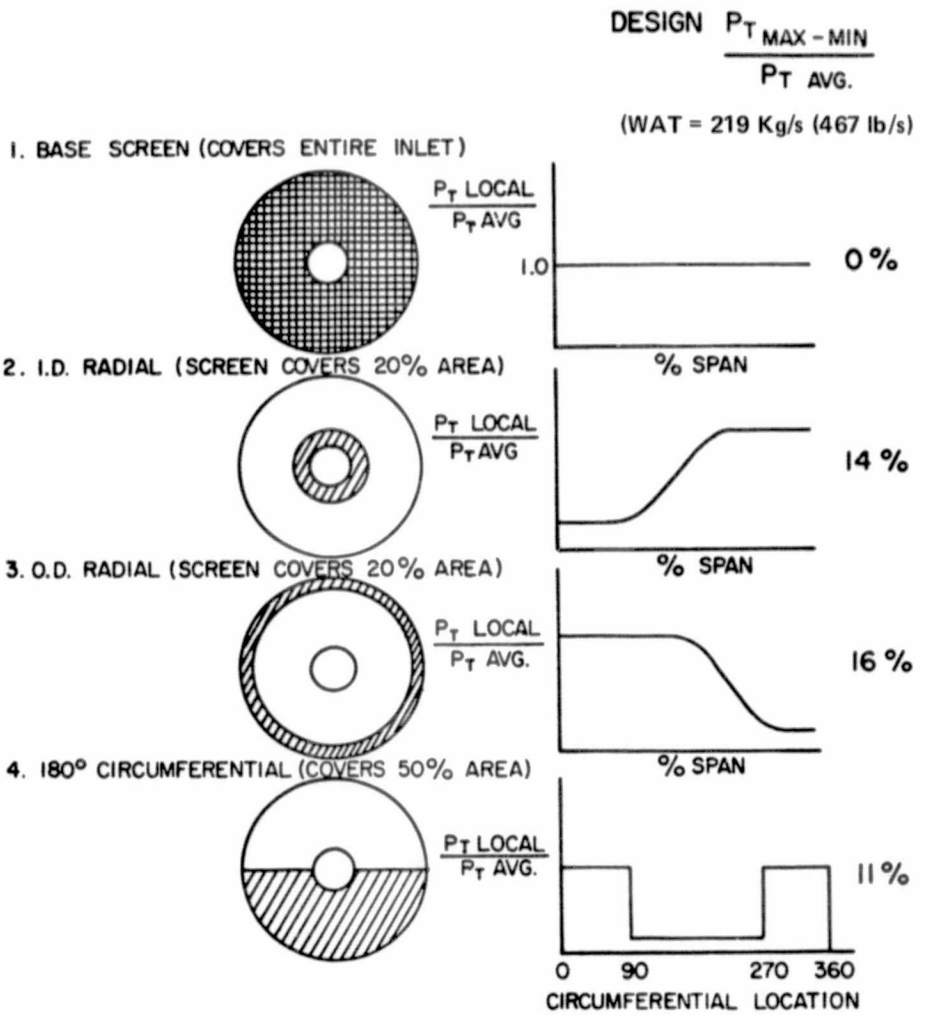

Figure C-11 JT8D-109 Classical Engine Inlet Screen Patterns and Predicted Distortion Levels

b. Fan/LPC Rig Test Results and Discussion of Results

1) Fan Surge Margin

Positive fan surge margin was attained with all inlet distortion patterns tested. The 15.4 m/sec (30 knot) crosswind pod engine distortion pattern yielded the largest surge margin loss. Surge margin increased with I.D. distortion and was slightly reduced by 180° circumferential distortion. These effects of distortion on surge margin were consistent with other single stage fan experience. Fan surge margins with distorted inlet flow are summarized in Figure C-12. Table C-VII, taken from Figure C-12, presents fan surge margins at two flows representing high and part speed operation, and presents the loss or gain in surge margin relative to the base grate surge margin at that flow. Fan sensitivity to distortion was similar to NASA single stage fan experience. Figure C-13 presents the JT8D-109 fan sensitivities to I.D. radial, O.D. radial, and 180° circumferential screens as compared to other single stage fans.

TABLE C-VII

JT8D-109 FAN SURGE MARGIN (2.4 O.D./2)

	Inlet Total Flow 145 kg/sec (320 lb/sec)		Inlet Total Flow 190.5 kg/sec (420 lb/sec)	
Inlet Screen	Surge Margin (%)	Δ Surge Margin (%)	Surge Margin (%)	Δ Surge Margin (%)
Clean Inlet	16.4	0	13.2	0
I.D. Radial	17.5	+1.1	15.0	+ 1.8
O.D. Radial	12.6	-3.8	4.0	- 9.2
180° Circum.	15.5	-0.9	12.6	-0.6
Sea Level Static Center	14.0	-2.4	10.6	- 2.6
18 m/sec (35 kt.) X-wind Center	15.0	-1.4	11.1	- 2.1
15.4 m/sec (30 kt.) X-wind Pod	7.7	-8.7	1.7	-11.5

2) LPC Surge Margin

Positive LPC surge margin was attained with all inlet distortion patterns tested. The LPC showed the largest surge margin loss with 180° circumferential distortion, which was consistent with previous experience. LPC surge margins, with distorted inlet, are summarized in Figure C-14. Table C-VIII, taken from Figure C-14, presents LPC surge margins at two flows representing high and part speed operation, and presents the loss or gain in surge margin relative to the base grate at that flow. LPC sensitivity agrees with previous P&WA experience. Figure C-15 presents the JT8D-109 LPC sensitivity to 180° circumferential as compared to other compressors.

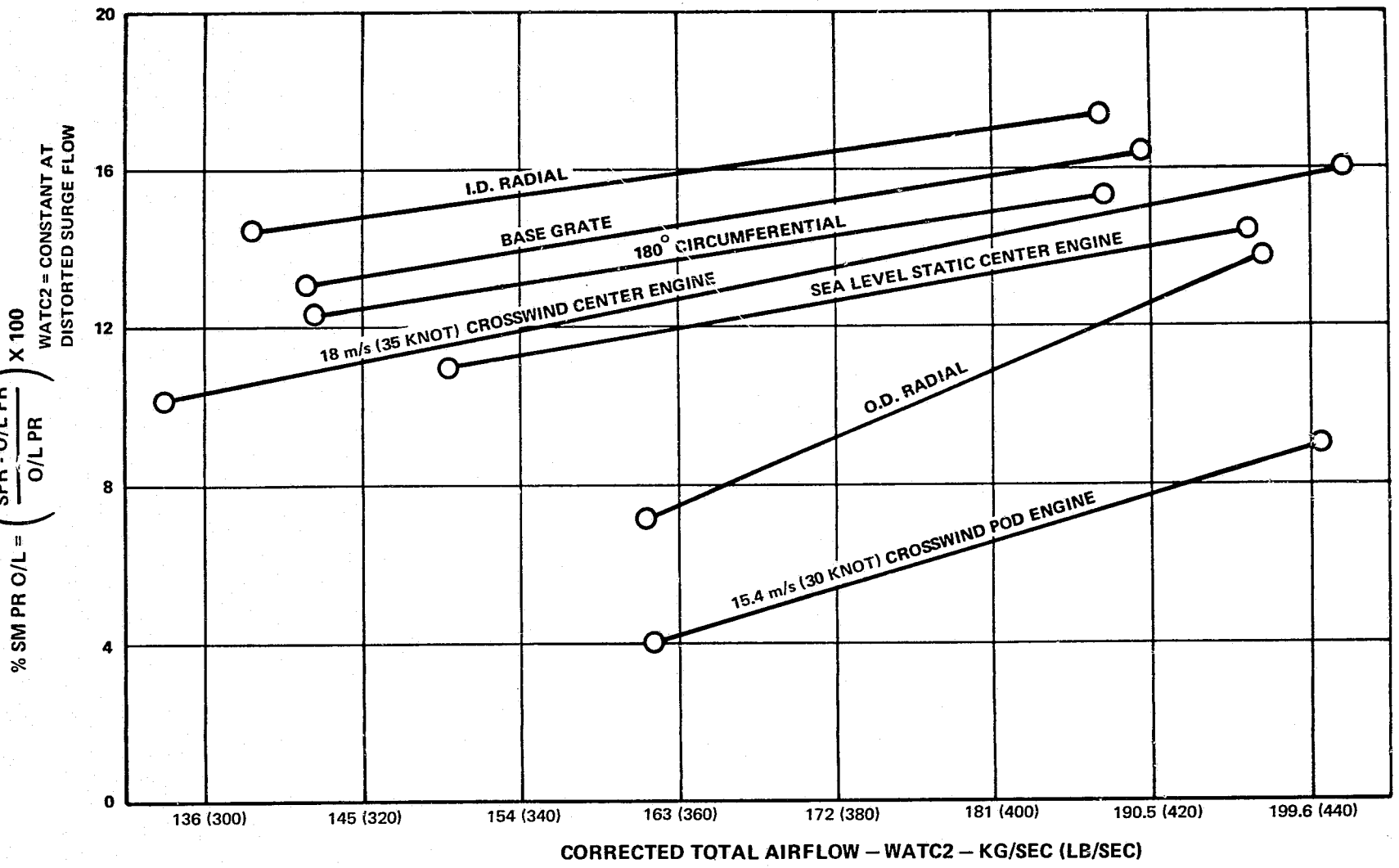

Figure C-12 JT8D-109 Fan Surge Margin (2.4 OD/2) with Distorted Inlet Flow

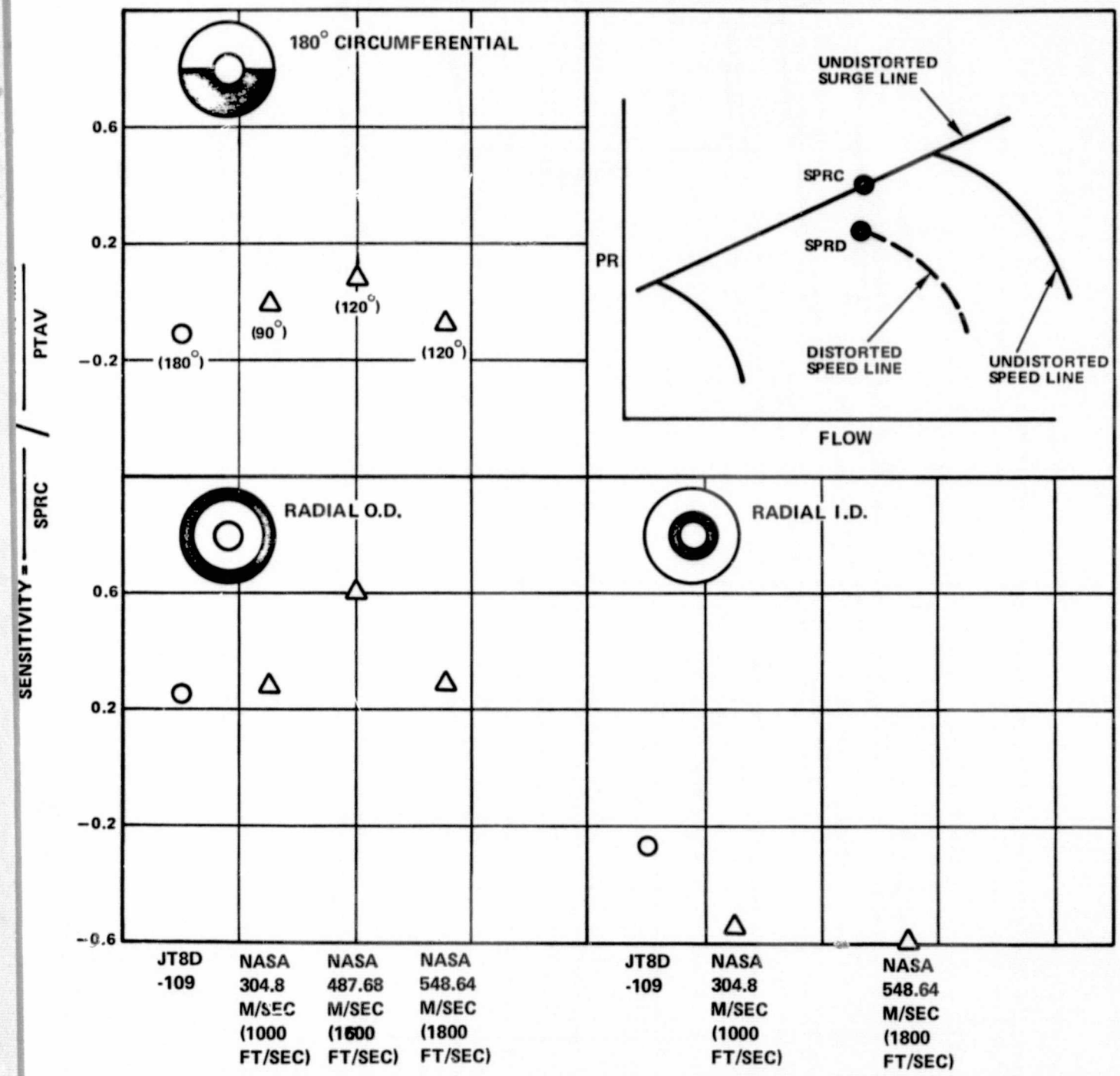

Figure C-13 JT8D-109 Fan High-Speed Sensitivity Compared to Other Single-Stage Fans

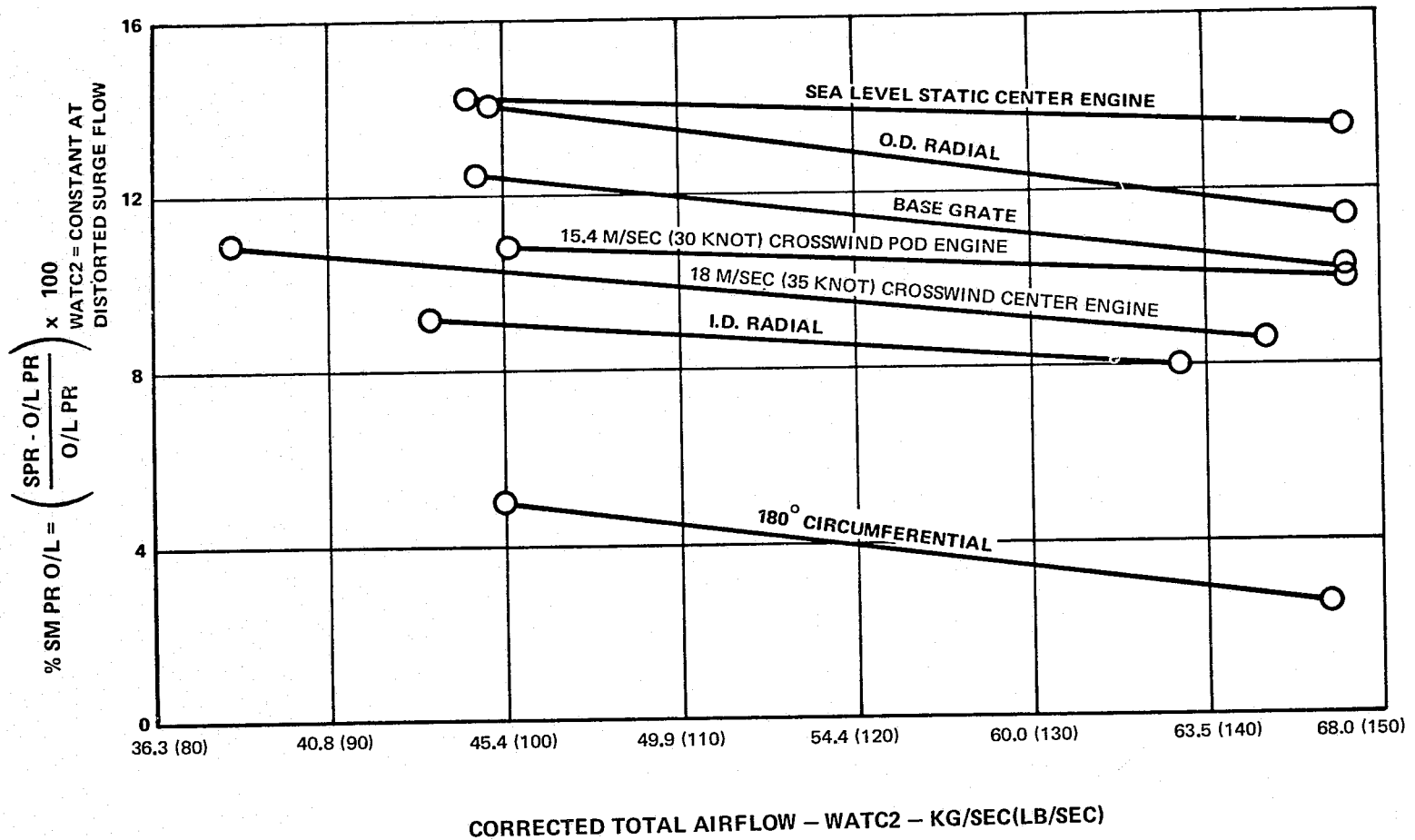

Figure C-14 JT8D-109 Low-Pressure Compressor Surge Margin (3/2) with Distorted Inlet Flow

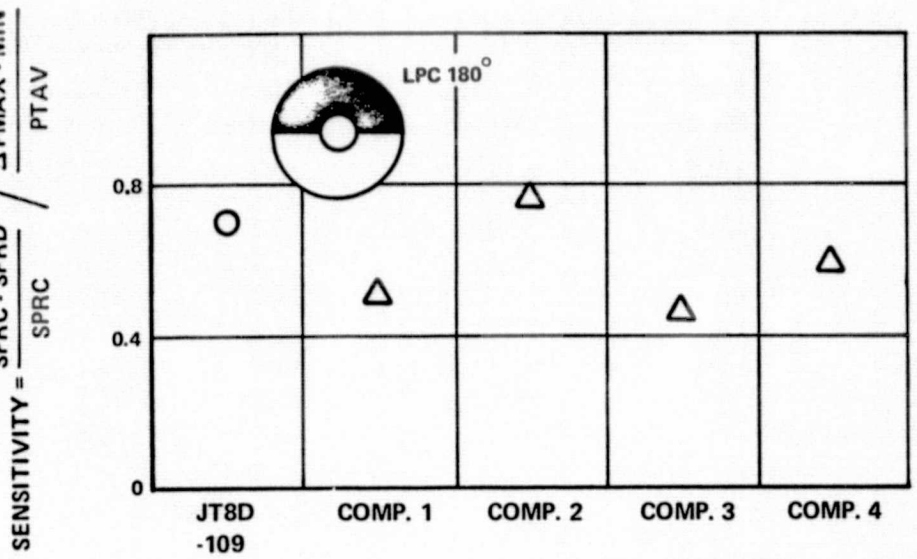

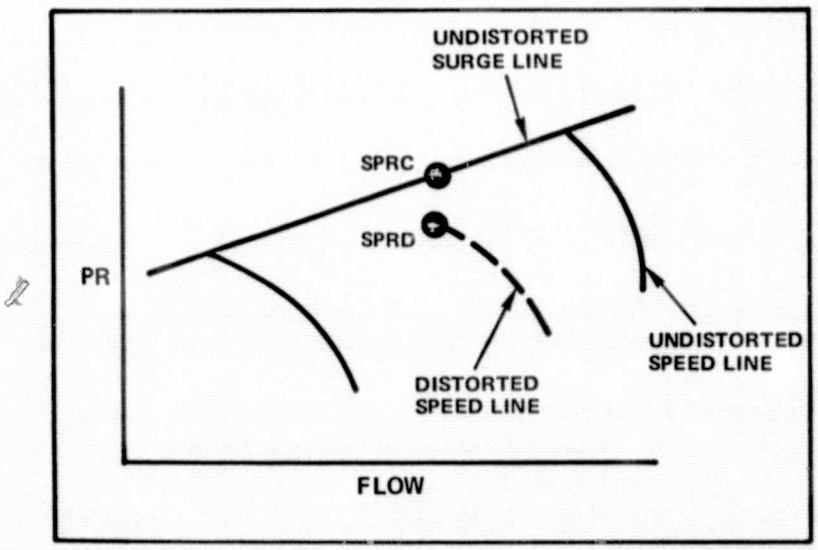

Figure C-15 JT8D-109 Low-Pressure Compressor High-Speed Sensitivity Compared to Other Compressors

TABLE C-VIII

JT8D-109 LPC SURGE MARGIN (3/2)

Inlet Screen	LPC Flow 67 kg/sec (148 lb/sec) Surge Margin (%)	LPC Flow 67 kg/sec (148 lb/sec) Δ Surge Margin (%)	LPC Flow 44.5 kg/sec (98 lb/sec) Surge Margin (%)	LPC Flow 44.5 kg/sec (98 lb/sec) ΔSurge Margin (%)
Clean Inlet	10.1	0	12.5	0
I.D. Radial	7.8	-2.3	9.1	-3.4
O.D. Radial	11.4	+1.3	14.2	+1.7
180° Circum.	2.4	-7.7	5.1	-7.4
Sea Level Static Center	13.4	+3.3	14.2	+1.7
18 m/sec (35 kt) X-wind Center	8.4	-1.7	10.4	-2.1
15.4 m/sec (30 kt) X-wind Pod	9.9	-0.2	10.9	-1.6

c. Engine Inlet Distortion Test Procedure

JT8D-109 engine inlet distortion testing was conducted with the same inlet distortion screens used during the fan/LPC rig test program to simulate the following conditions:

- Sea level static pattern – 727 center inlet duct at takeoff airflow.
- 18 m/sec (35-knot) crosswind pattern – 727 center inlet duct at takeoff airflow.
- 15.4 m/sec (30-knot) crosswind pattern – 727 pod inlet at takeoff airflow.

The following test procedure was followed for the engine testing with each distortion screen:

- A performance calibration was conducted at the following points: 22,241, 40,034, 57,827 and 73,840N (5000, 9000, 13000, and 16600 lbs) corrected thrust
- With the full span PT2 rakes removed, two slow accelerations and decelerations from idle to take-off and from take-off to idle were performed.
- Two snap accelerations and decelerations from idle to take-off and from take-off to idle were also performed.

d. Engine Inlet Distortion Test Results and Discussion of Results

JT8D-109 refan engine EE-1 was tested at sea level static conditions with and without the paragraph (c) inlet distortion screens installed to demonstrate D-109 engine stability with a clean inlet and with flight distortion patterns. With a clean inlet and with each distortion screen installed, a slow accelerarion and a slow deceleration were performed between idle and 8000 rpm N1 or maximum EGT (TT7 = 822°K (1020°F)). The test conditions are shown in Table C-IX. Stable engine operation existed at all test conditions.

TABLE C-IX

JT8D-109 ENGINE EE-1 INLET DISTORTION TEST
SLOW ACCELERATION TO MAXIMUM CONDITION
Aj = 0.774 m^2 (8.33 ft^2)

Inlet Screen	Max. EGT TT7 °K (°R)	Max. Corr. N1 $N1/\sqrt{\theta T2}$ (rpm)
Clean Inlet	822 (1020)	7676
Sea Level Static Center	822 (1020)	7453
18 m/sec (35 kt.) X-wind Center	822 (1020)	7274
15.4 m/sec (30 kt.) X-wind Pod	822 (1020)	7296

e. DC-9 Flight Inlet Distortion Test Procedure

A sea level static engine performance calibration was conducted on JT8D-109 engine EE-2 with the DC-9 flight inlet installed. Eight full span PT2 rakes, with 10 pressure sensory elements per rake, were installed aft of the flight inlet. In addition, four 10-element boundary rakes were installed equally spaced circumferentially and in the same axial plane as the PT2 rakes.

f. DC-9 Flight Inlet Test Results and Discussion of Results

Testing indicated that the lowest ring average pressure levels experienced in the inlet are: 3.5% below ambient for take-off flow, 2% for 75% flow and 1% at 50% flow (exclusive of the area within 1.27 cm (0.5 in) of the O.D. wall).

Figure C-16 shows the face average inlet recovery, PT2 avg/Pamb, over a wide range of power levels. Recovery was 99.5% at take-off flow and improved at lower flow. Further data can be found in Reference 4.

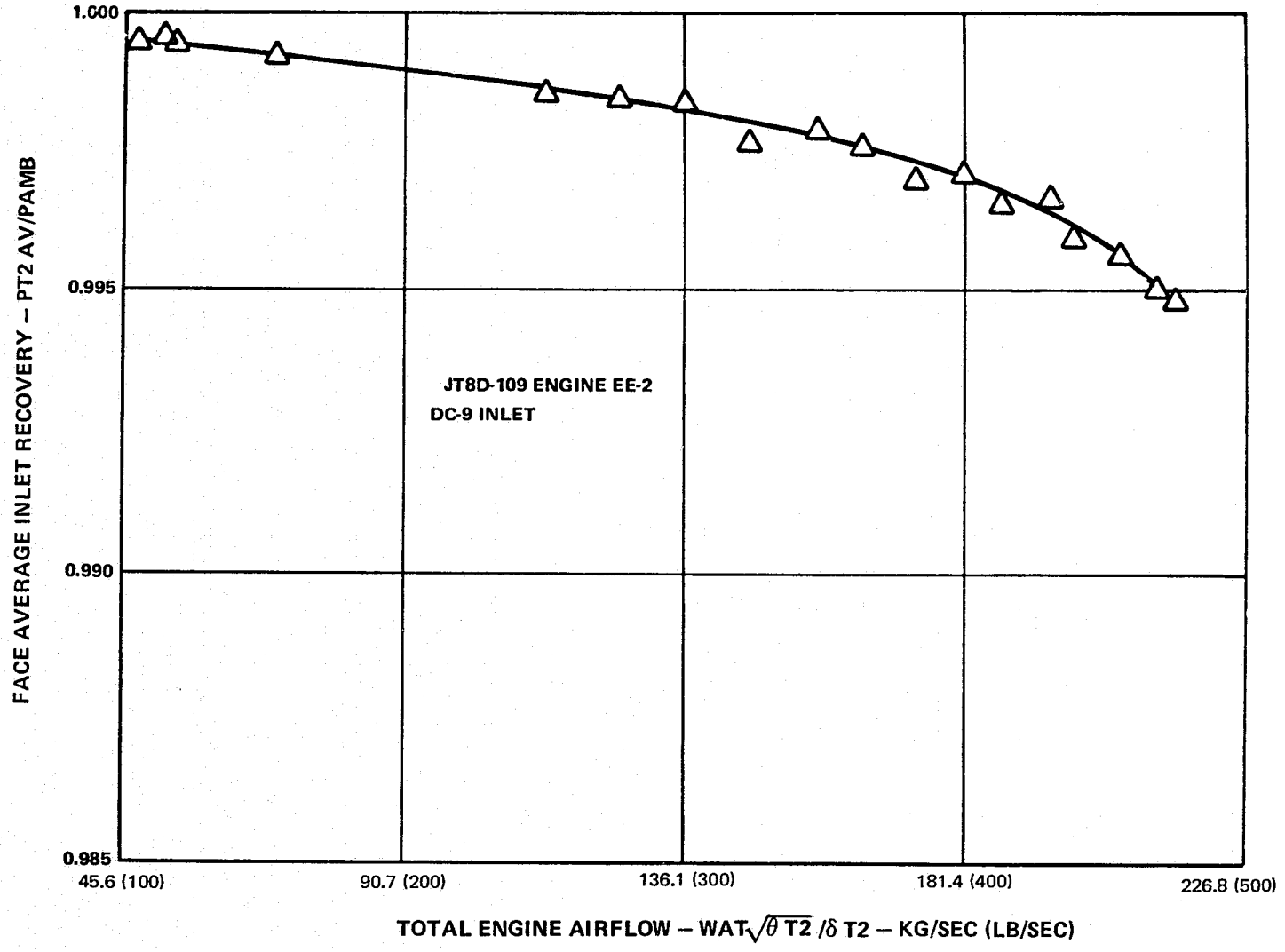

Figure C-16 JT8D-109 Face Average Inlet Recovery – DC-9 Inlet

5. Acceleration Response Test

JT8D-109 engine acceleration response characteristics were determined during sea level testing of engines EE-1, EE-2 and EE-3. Additional testing was conducted at the NASA LeRC altitude test facility on EE-3 and during the DC-9 flight test program.

a. Test Procedure

Acceleration response tests were conducted on EE-1, EE-2 and EE-3. The following procedure was used:

Timed accelerations from idle to takeoff corrected thrust were performed over the idle N2 speed range of 6000 to 9000 rpm.

The engines were set to takeoff corrected thrust and the N2 rpm recorded at this thrust. A response timer was set at 99% of this N2 rpm. The engines were reset to the desired idle N2 speed and stabilized for five minutes, after which the steady state operating point was recorded.

An oscillograph was then started, and a snap acceleration made from idle to maximum power lever angle. When the observed N2 rpm reached the preset response timer speed, the power lever was retarded to maintain this N2 rpm. The oscillograph was stopped and a full reading taken. The oscillograph recording included high rotor speed, low rotor speed, power lever angle, fuel flow, burner pressure, low pressure compressor static exit pressure, and high pressure compressor static exit pressure.

The engines were stabilized for five minutes, after which the steady state operating point was recorded.

In addition to the above tests, acceleration response characteristics with engine airbleed were determined on engines EE-2 and EE-3. Engine 13th stage airbleed amounts of up to 8% of primary airflow were tested.

b. Test Results and Discussion of Results

Table C-X compares the acceleration response characteristics of the JT8D-9 and JT8D-109 engines at sea level static conditions. As shown, the average D-109 engine accelerates from idle to takeoff about 2.9 seconds slower than the D-9 engine. The slower acceleration characteristics of the D-109 are attributable to a 40 percent increase in the low rotor polar moment of inertia relative to that of the baseline D-9 engine and an increase in the operating line relative to the D-9, as indicated in Figures C-8 and C-9. Figure C-17 shows the JT8D-9 and D-109 acceleration times vs. corrected high-rotor speed characteristics for no service bleed and for 4 percent and 8 percent 13th-stage service bleed at sea level static conditions.

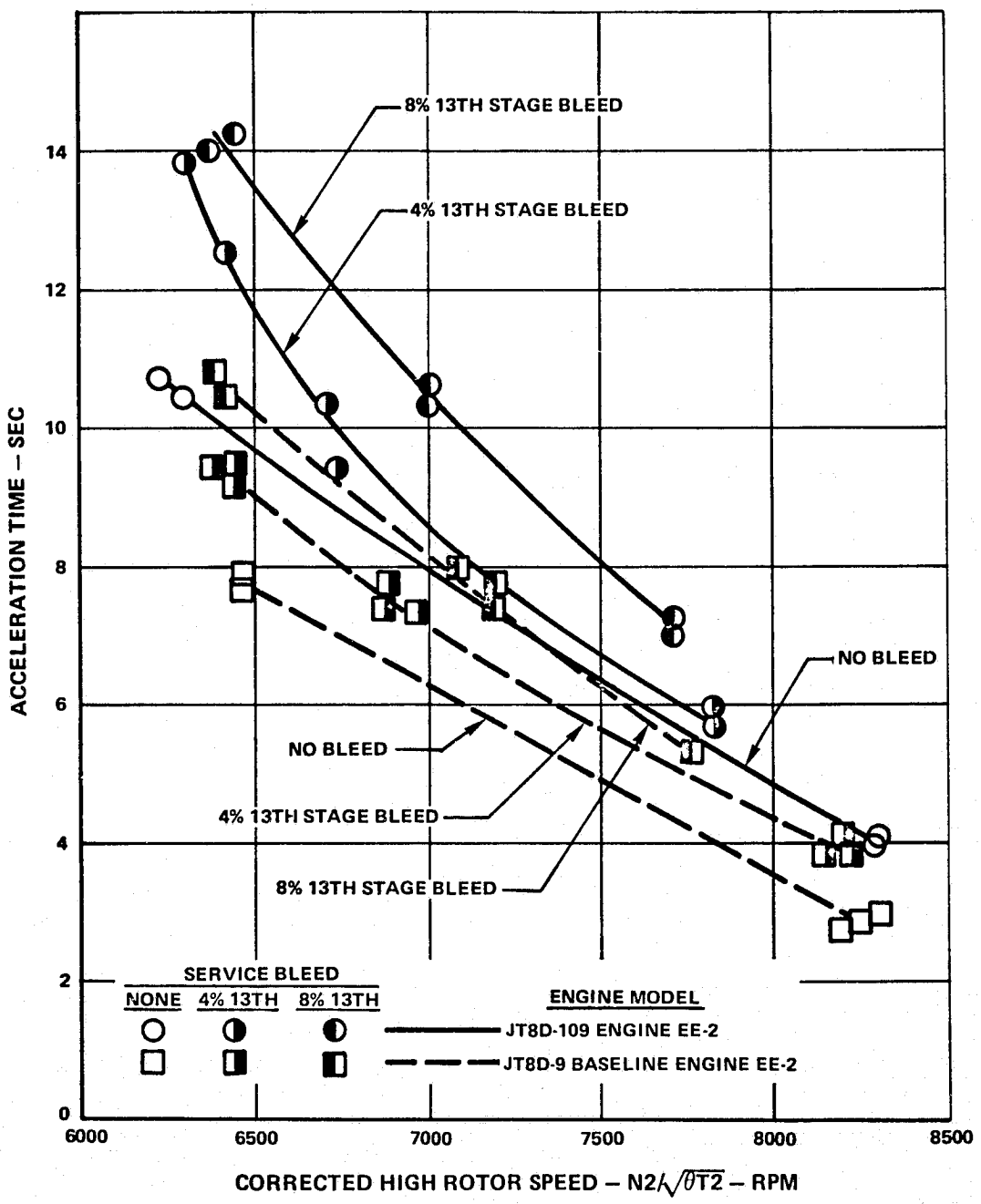

Figure C-17 JT8D-109/D-9 Sea Level Static Acceleration Comparison

TABLE C-X

JT8D-9/D-109 ACCELERATION TIMES (SECONDS)
(GROUND IDLE TO TAKEOFF – NO AIRBLEED)

Engine	JT8D-9	JT8D-109	Δ
EE-1	7.6	9.3	+1.7
EE-2	7.6	10.9	+3.3
EE-3	6.6	10.4	+3.8
Average	7.3	10.2	+2.9 sec

Dynamic simulation analytical studies predicted that the JT8D-109 engine would require the incorporation of a flight idle-minimum idle control system. The flight idle is required to provide acceptable aborted landing go-around acceleration capability. Analysis of DC-9 flight test results and EE-3 NASA test data indicated that a minimum JT8D-109 flight idle setting of 7.5 percent of takeoff thrust ($N2/\sqrt{\theta T2}$ = 7750 rpm) is required to achieve the acceleration requirement at an approach condition of 3048 m (10,000 ft), 0.2 Mn (see Figure C-18). Previous estimates based on dynamic simulation analysis predicted the flight idle setting to be at 6 percent of takeoff thrust ($N2/\sqrt{\theta T2}$ = 7600 rpm) at this approach condition. Minimum idle at this condition provides 3 percent of takeoff thrust. A comparison of dynamic simulator results, EE-3 NASA test data, and DC-9 refan flight test results is presented in Figure C-18. As shown, the DC-9 flight test results indicated a flight idle setting of $N2/\sqrt{\theta T2}$ = 7500 rpm at the 2652 m (8700 ft), 66 m/sec (140 knot) DC-9 approach condition. This flight idle setting was found acceptable during DC-9 flight testing.

6. Altitude Transient Tests

Engine tests were conducted at the NASA LeRC altitude facility to determine the JT8D-109 altitude transient characteristics. Testing was conducted with an inlet distortion screen simulating the 727 center engine distortion. Three test sequences were conducted as follows:

- Acceleration-deceleration
- Wave-off acceleration
- Decelerations

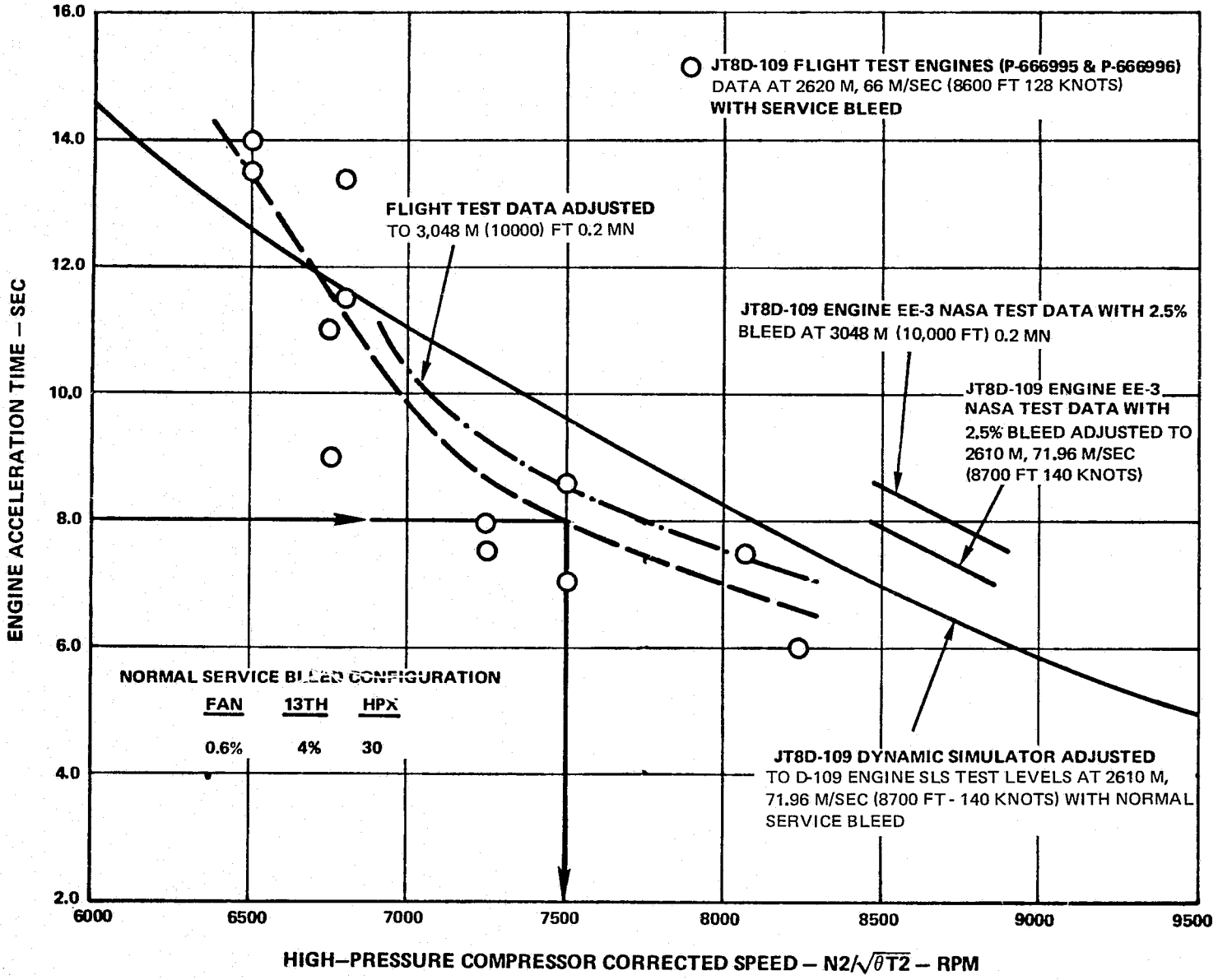

Figure C-18 JT8D-109/D-9 Acceleration Comparison – DC-9 Flight Test

a. Test Procedures

1) Acceleration-Deceleration Tests

Snap accelerations were made from a stabilized idle to maximum continuous power (cold acceleration). The engine was stabilized two minutes, and a snap deceleration to idle was performed; thirty seconds after snap deceleration initiation, a snap acceleration to maximum continuous power was made (hot acceleration). This procedure was repeated for two idle power settings, ground idle 3736 N (840 lb) Fn and flight idle as determined in Section 5 testing. Data were acquired at the conditions shown in Figure C-19.

2) Wave-off Accelerations

Snap accelerations from several part power throttle settings to maximum continuous power were performed at the following conditions:

Altitude	Mn	TT2
Meters (Ft)		°K (°F)
3048 (10,000)	0.2	270 (27)

3) Decelerations

Decelerations from maximum continuous power to idle were performed at the conditions shown in Figure C-19.

b. Test Results and Discussion of Results

The JT8D-109 engine demonstrated stable operation during both hot and cold snap accelerations from both ground and flight idle power settings around the DC-9/727 flight envelope as shown in Figure C-19.

Snap decelerations conducted during altitude tests at the NASA LeRC test facility indicated pressure fluctuations at altitudes above 4572 m (15,000 ft). It is suspected that these pressure fluctuations could have been caused by low-pressure compressor surge and surge bleed valve cycling, or induced by the test facility. Further testing at NASA indicated that the pressure disturbances could be eliminated by manually opening the 13th-stage surge bleeds. Snap engine accelerations were successfully performed from the apparent unstable condition.

Engine deceleration transients performed during the DC-9 refan flight test program demonstrated stable engine operation in the flight test envelope. Pressure fluctuations as experienced in the NASA LeRC testing were not evident. In addition, stable engine operation was also demonstrated during sea level testing conducted at P&WA test facilities.

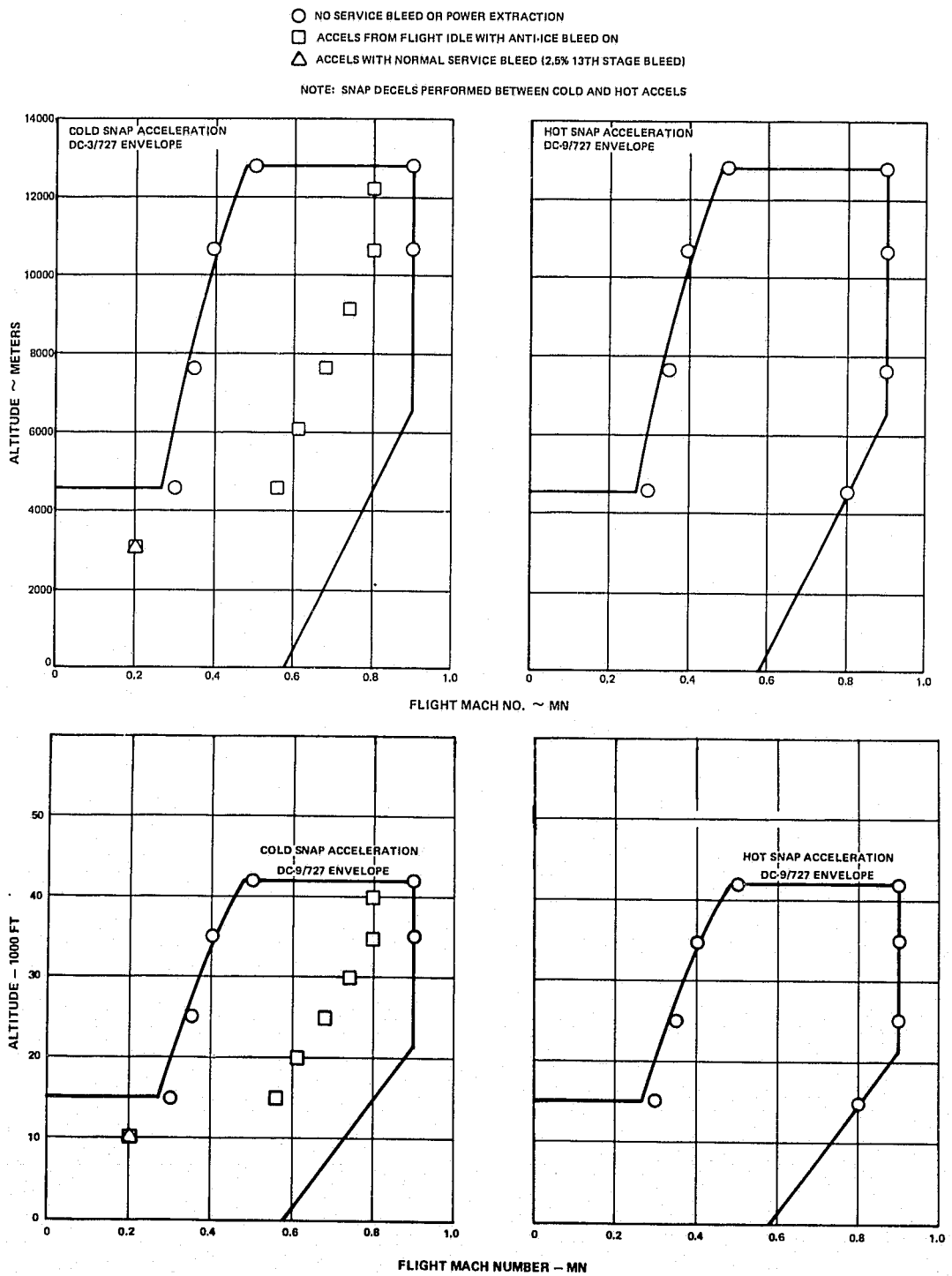

Figure C-19 **JT8D-109 Engine EE-3 Altitude Test Summary with 727 Center Inlet Distortion**

7. Low Pressure Compressor Surge Tests (Cross-Bleed Surge Check)

Tests were conducted to determine the low compressor surge margin characteristics of the JT8D-109 engine. The procedure used in this determination (known as cross-bleed surge check) involved the use of the high pressure bleed air available at the 13th-stage discharge to back pressure the low-pressure compressor, thus raising the low-pressure compressor operating line. The equipment used consisted of tubing to connect the 13th-stage bleed ports to the sixth-stage bleed ports on each side of the engine, an electrically operated shut-off valve in each tube, and provisions for installing various size orifices to control the flow recirculating from the 13th-stage discharge to the sixth-stage discharge, thus controlling the back pressure at the low-pressure compressor discharge.

a. Test Procedure

The following is a description of the test procedure normally utilized in conducting cross-bleed surge checks:

With the shutoff valves in the cross-bleed system closed, the engine is idled for five minutes and then slowly accelerated to the appropriate stabilizing speed for the orifice diameter being used. The engine is stabilized for one minute, and N1 rpm and engine inlet total temperature are recorded. Proper valve operation is checked by opening the cross-bleed system shutoff valves to confirm that the N1 speed reduction corresponds to that required for the orifice size being tested.

Following a ten minute stabilization period, the engine is accelerated slowly over a period of approximately two minutes or more until engine surge occurs, a corrected N1 speed of 7400 rpm is reached, or the engine exhaust gas temperature limit is reached. If no surge occurs, the engine is stabilized at a corrected N1 speed of 7400 rpm, or at the exhaust gas temperature limit, whichever occurs first. At this condition, a full instrumentation reading is taken.

b. Test Results and Discussion of Results

Operation was limited by exhaust gas temperatures or N1 speeds for all conditions tested. No surges were encountered. Table C-XI presents a summary of the cross-bleed results for testing conducted on refan engines EE-1 and EE-2 compared to the fan/LPC rig defined surge margin. As indicated, EE-1 and EE-2 exhibited LPC surge margin levels in excess of those previously attained by the rig with a clean inlet. The cross-bleed test data are presented in Figure C-20. These results indicate there is no detrimental effect on the JT8D-109 low compressor surge margin.

TABLE C-XI

JT8D-109 LOW PRESSURE COMPRESSOR SURGE TESTS
(Cross-Bleed Surge Check)

	% Surge Margin** at $N1/\sqrt{\theta T2} \approx 6500$ rpm			
Inlet Screen	Rig (D-109) Baseline LPC	EE-1 (D-9) Baseline LPC	EE-1 (D-109)	EE-2 (D-109)
Clean Inlet	10.4	>11.8*	>12.3*	>11.9*
Sea Level Static Center	12.2	–	> 9.9*	–
18 m/sec (35 kt.) X-wind Center	9.2	–	> 9.7*	–
15.4 m/sec (30 kt.) X-wind Pod	9.3	–	>10.9*	–

*Extrapolation based on passing the rig-defined surge line slope (for the appropriate inlet distortion) through the engine data.

**% Surge margin $= \frac{S/L - O/L}{S/L} \times 100$ at constant corrected airflow.

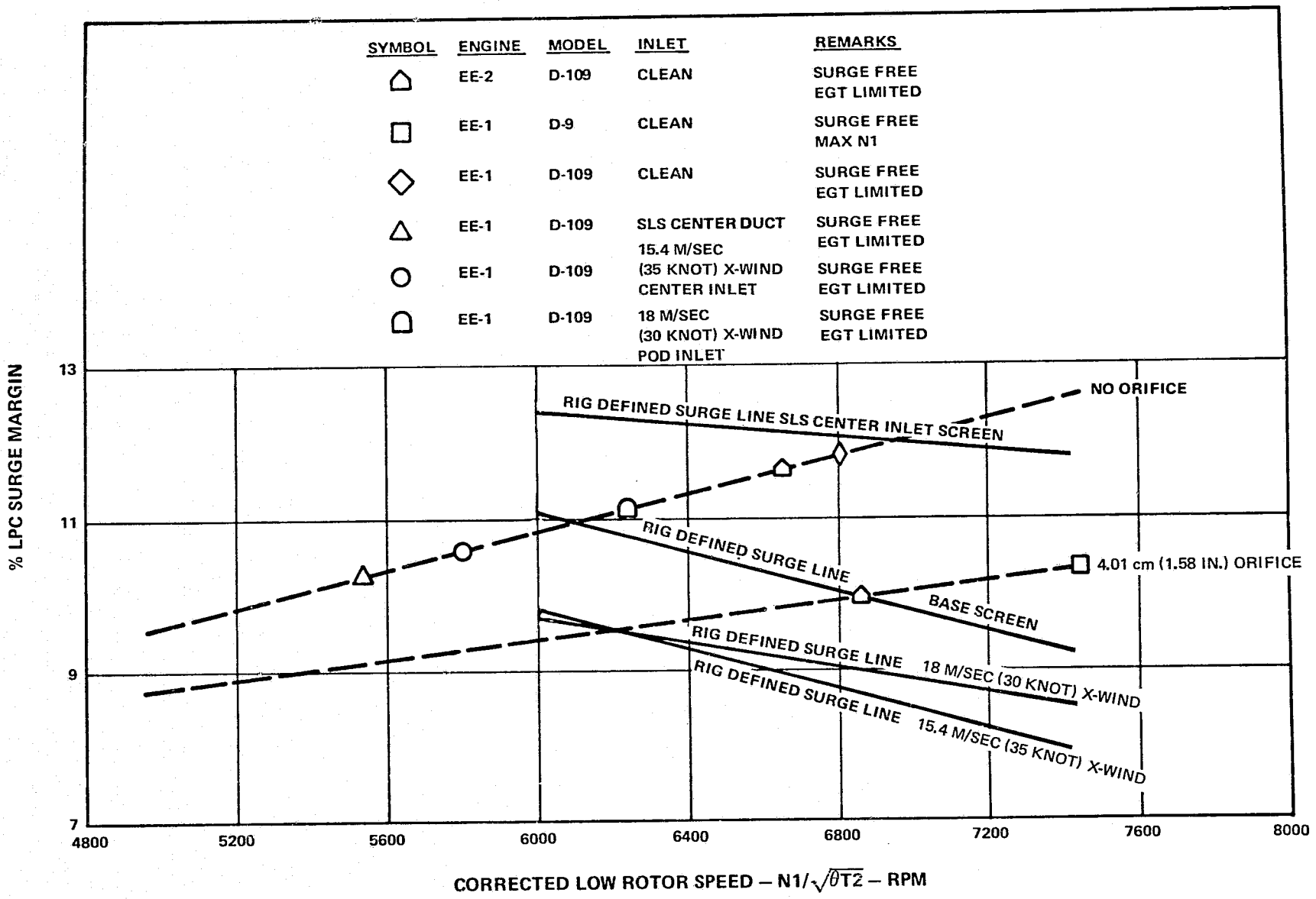

Figure C-20 JT8D-109 Cross-Bleed Low-Pressure Compressor Stall Check

D. ACOUSTIC CHARACTERISTICS

Subsequent paragraphs in this section of the report provide detailed acoustic characteristics of the JT8D-109 engine. In addition, a description of the procedure used to evaluate test data obtained during Phase II development testing as well as a description of the test facility and equpment used during this testing is also provided. Tables of measured and predicted acoustic data are presented in Reference 5.

1. Test Description

a. Test Configurations

Outdoor static noise tests were conducted on two JT8D-109 engines. Engine performance was also evaluated for both JT8D-109 engines to ensure that the engine was operating normally during the noise testing, and to provide the specific engine performance parameters upon which engine component noise levels are dependent. Since noise levels could be affected by the presence of probes in the engine gas path, complete standard performance instrumentation was not installed during the acoustic tests. Only those probes required to ensure proper engine performance, such as turbine exit pressure and temperature probes, were installed.

Table D-I presents comparisons of design point performance parameters affecting component noise levels for the JT8D-9, JT8D-109 design, and measured performance on the JT8D-109 engines tested for noise. Figures D-1 through D-5 show the variation in these parameters with engine thrust. (Detailed engine performance is provided in Ref. 4.)

TABLE D-I
PERFORMANCE COMPARISON

Parameter	JT8D-9 Design Point	JT8D-109 Design Point	JT8D-109 Engine 1	JT8D-109 Engine 2
Thrust, Fn/δ,N(lbs)	64,499 (14,500)	73,840 (16,600)	73,840 (16,600)	73,840 (16,600)
Low Rotor Speed, $N_1/\sqrt{\theta}$, rpm	8,040	7,450	7,226	7,440
Core Engine Jet Velocity, $V_{je}/\sqrt{\theta}$, m/s (ft/sec)	538 (1,766)	441 (1,446)	457 (1,500)	463 (1,520)
Fan Exhaust Jet Velocity, $V_{jd}/\sqrt{\theta}$, m/s (ft/sec)	350 (1,150)	300 (985)	305 (1,002)	292 (957)
Airflow, $Wa\sqrt{\theta}/\delta$, Kg/s (lbs/sec)	145 (319)	212 (467)	208 (458)	212 (468)
Fan Pressure Ratio	1.97	1.67	1.71	1.66
Tip Speed, U_{tip} m/s (ft/sec)	432 (1,416)	488 (1,600)	473 (1,551)	487 (1,597)

Different configurations were tested to evaluate the effectiveness of the engine inlet and tailpipe acoustic treatment, and to determine engine component noise characteristics. A summary of each configuration is presented in Table D-II.

The refan engine makes extensive use of sound absorbing liners in the fan duct. In order to evaluate the effectiveness of this treatment a baseline configuration with hardwall fan ducts was tested. These "hardwall" fan ducts were fabricated by applying a thin layer [0.051 cm (0.020 in.)] of fiberglass over the treatment panels.

As part of the overall NASA Refan Contract, the refan engine was demonstrated in flight using a DC-9-30 airplane. The flight hardware incorporated an acoustic nacelle with treatment in the tailpipe and a contoured inlet that was designed by McDonnell Douglas Corp. An identically treated nacelle was tested statically at P&WA to serve as a static baseline for the McDonnell Douglas flight test. To evaluate the effectiveness of the nacelle treatment statically, a hardwall nacelle configuration was also tested. The hardwall inlet was achieved by applying aluminum foil tape over the treated panels. A hardwall tailpipe was run in place of the treated tailpipe. The treated inlet and tailpipe are shown in Figures D-6 and D-7.

TABLE D-II

JT8D-109 CONFIGURATIONS TESTED

Test No.	Inlet Noise Suppression Tube	Inlet Treatment	Fan Duct Treatment	Tailpipe Treatment	Engine No.
1	No	Hard	Soft	Hard	1
2	No	Soft	Soft	Hard	1
3	Yes	Soft	Soft	Hard	1
4	No	Soft	Soft	Soft	2
5	Yes	Soft	Soft	Soft	2
6	Yes	Soft	Soft	Hard	2
7	No	Hard	Soft	Hard	2
8	No	Hard	Hard	Hard	2

Separation of fan noise into inlet and aft components required blocking the radiation of one of these components while measuring the other. This was accomplished by measuring aft noise levels with an inlet noise suppression tube installed. The tube, 4.88m (16 feet) in diameter and 6.10m (20 feet) in length, was successful in blocking inlet radiated fan noise from the far field at angles greater than 30° from the engine inlet centerline.

To assist in defining and locating the source of core engine and turbine noise, several flush mounted Kulite high response transducers were located internally to the engine. Two of these were located one inch upstream of the tailpipe exit plane. Another two probes were installed in the OD wall of the splitter (that separates the fan and primary air flow downstream of the turbine exit vanes) to measure the core engine noise exclusive of any low frequency fan noise contribution. In addition, two Kulites were located in the primary engine OD wall upstream of the turbine exit vanes.

A transducer was also installed in one of the combustors through an available ignitor port. The purpose of this installation was to obtain a true combustion noise spectrum free of any distortion due to transmission through the turbine.

Radial traverses were conducted to determine the fan blade passage tone sound pressure levels in the inlet and fan duct. The locations of these internal microphones are detailed in Figure D-8.

b. Outdoor Noise Test Facility

The P&WA X-314 test stand is a full-scale engine outdoor noise test facility located near the east boundary of Rentschler Field, East Hartford, Conn. The X-314 test stand has been designed to evaluate the noise and performance characteristics of turbofan and turbojet engines. The engine is supported by two large "I" beams cantilevered from a vertical open-truss structure in a manner to provide a noise radiation field free of acoustical shadow zones around the engine. Engines are installed with their centerline at a height of approximately 4.88m (16 feet) above the ground.

The test area provides a cleared and carefully graded controlled ground surface with uniform reflective characteristics. This surface extends from the test pad in a semicircle around the engine [arc of approximately 60.96m (200 foot) radius.] The controlled surface consists of a 0.3048m (12 inch) deep layer of 2.54 to 3.81 cm (1 to 1 1/2 inch) size trap rock provided with a drainage system of four-inch perforated pipe to maintain the water table at least 45.7 cm (18 inches) below the finished surface. A hard smooth asphalt surface exists on the opposite side of the engine covering an area from 90° through 160° within a 45.72m (150 foot) arc.

c. Test Sequence

For each of the hardware configurations tested, the engine was operated on a sea level static part power line. Noise data were taken at 13 or 14 different rotor speeds along this operating line. Data repeatability was established by running the majority of these points twice. Two repeat points were obtained at the relatively more important approach, cutback and take-off power settings. The lowest four rotor speed points, although well below approach power, were run to identify the internally generated low frequency core noise.

In order to prevent the necessity of applying extreme weather corrections to the acoustic data and to prevent large discrete frequency noise level fluctuations, the following limita tions were placed upon acoustic data acquisition:

- wind speed less than 4.11 m/s (8 miles per hour)
- relative humidity between 30% and 90%
- no precipitation
- engine speed variation ±25 RPM
- all engine bleeds closed

Table D-III shows the corrected low rotor speeds run and the type of noise data recorded for each configuration.

TABLE D-III

MICROPHONE LOCATIONS RECORDED

$N_1/\sqrt{\theta}$		3000	3700	4300	4800	5200	5350	5500	5650	5800	6100	6400	6800	7200	T/O	MAX POWER
DATA POINTS RECORDED		2	2	2	2	3	2	2	2	2	2	3	1	1	3	1
TEST NO.	1	●■▲	●■▲	●■▲	●■▲	●■▲		●■▲		●■▲	●■▲	●■▲	●■▲	●■▲	●■▲	●■▲
	2	●	●	●	●	●	●	●	●	●	●	●	●	●	●	●
	3			●■		●■◣				●■		●■◣			●■◣	
	4	●■▲	●■▲	●■▲	●■▲	●■▲	●■▲	●■▲	●■▲	●■▲	●■▲	●■▲	●■▲	●■▲	●■▲	
	5	●	●	●	●	●	●	●	●	●	●	●	●	●	●	
	6	●	●	●	●	●	●	●	●	●	●	●	●	●	●	
	7	●■▲	●■▲	●■▲	●■▲	●■▲	●■▲	●■▲	●■▲	●■▲	●■▲	●■▲	●■▲	●■▲	●■▲	
	8	●■▲	●■▲	●■▲	●■▲	●■▲	●■▲	●■▲	●■▲	●■▲	●■▲	●■▲	●■▲	●■▲	●■▲	

● FARFIELD POLE

■ FARFIELD GROUND

▲ TAILPIPE INTERNAL FLUSH MOUNTED

◣ INTERNAL RADIAL TRAVERSE

2. Results

a. Comparison with Baseline JT8D Engine

Results of static testing of the JT8D-109 engine with the treated nacelle are compared to data from similar tests on a JT8D-9 hardwall engine. The hardwall JT8D-9 configuration was chosen because it is representative of the majority of JT8D engine installations now in service. Acoustic test results obtained during outdoor testing on eight JT8D-109 engine configurations are presented in Appendix A of document Reference 5.

Figure D-10 shows the perceived noise level at the angle of aft peak noise at a 60.96m (200 ft.) sideline distance plotted as a function of engine thrust. At low thrust, typical of the approach condition, the aft fan noise has been reduced in the JT8D-109 engine by the acoustic treatment and is about 11 PNdB lower than the JT8D-9 engine at the same thrust. At the higher thrust levels, the significant reduction in jet noise results in the JT8D-109 engine being 8 PNdB quieter than the JT8D-9 engine at the same thrust. At their respective sea level static takeoff rated thrusts, 64,499 N (14,500 lbs) for the JT8D-9 and 73,840 N (16,600 lbs) for the JT8D-109, the PNdB difference is about 6, which meets the design goal of the refan engine.

Directivity curves are presented in Figures D-11, -12, and -13 at thrusts typical of approach, cutback and takeoff for each engine. It is seen that in the aft quadrant significant reductions in noise level exist at all angles and thrust settings.

A plot of overall sound pressure level (OASPL) vs. thrust is presented in Figure D-14 for the two engines. At thrusts above 44,480 N (10,000 lbs) the OASPL is controlled by the jet noise component. It is seen that at constant thrust the refan engine is between 6.5 and 8 dB lower than the JT8D-9 baseline engine. A directivity plot of OASPL vs. aft angles at a thrust typical of refan engine cutback power, Figure D-15, shows that the largest reduction in noise level (approximately 8 dB) occurs at 140°, the angle of peak jet noise. A one-third octave band spectral plot at the cutback condition at this peak aft angle, Figure D-16, shows that both engines exhibit spectral shapes characteristic of jet noise, with the refan being significantly lower in both peak frequency and level. A one-third octave band spectrum for each engine at takeoff thrust is shown in Figure D-17, at an angle representative of peak jet noise. It is seen that the refan engine with its lower primary jet velocity has significantly lower jet noise levels.

Noise levels in the inlet quadrant are compared in Figure D-18. PNdB at the angle of peak inlet noise is plotted against engine thrust. The lower noise levels of the refan engine at power settings typical of approach power are primarily due to the reductions in fan fundamental blade passage frequency noise achieved with the inlet treatment. A typical one-third octave band spectral comparison is shown in Figure D-19. At higher thrusts, the higher tip speed of the refan engine generates more combination tone noise. Although the inlet treatment remains effective, there is also an effect due to the inlet contour itself (Ref. 8). The main effect of the inlet contour is to reduce the levels of combination tone noise that are radiated from the inlet.

Figure D-20 is a comparison of the JT8D-9 engine and the JT8D-109 engine configured with a hardwall contoured inlet. Once again perceived noise level at the angle of peak inlet noise is plotted against engine thrust. It is seen that the refan engine is quieter than the JT8D-9 engine over the entire engine operating range.

Table D-IV summarizes the inlet and aft quadrant perceived noise levels of the JT8D-9 engine, and the three configurations of the JT8D-109, including the hardwall engine with hardwall nacelle, the treated engine with hardwall nacelle, and the treated engine with treated nacelle. The angles of peak levels are also shown.

Comparison of the baseline JT8D-9 and the treated nacelle JT8D-109 refan engine shows that the noise levels of the refan engine are 6 PNdB lower at takeoff thrust, 7 PNdB lower at cutback thrust and 11 PNdB lower at approach power. Table D-IV also indicates that at takeoff power, both engines are controlled by jet noise, as evidenced by the angle of peak noise being that of a typical jet. The refanned engine configurations with less acoustic treatment show that even at takeoff power, aft fan noise controls the engine noise levels, having angles of peak noise at 110 to 115 degrees.

At the approach power point, which was the design point for the majority of the fan duct acoustic treatment and the nacelle acoustic treatment, the perceived noise levels at both the inlet and aft angles of peak noise are the same, as seen in Table D-IV. Thus, a balanced engine acoustic design was achieved.

b. Effect of Fan Duct Treatment

The effects on fan noise of the acoustic treatment in the fan duct were determined by comparing noise data from a simulated hardwall configuration with that from a treated fan duct configuration. These tests were run with a hardwall tailpipe. The majority of the treatment was designed to attenuate fan blade passage frequency noise at an engine power setting typical of aircraft approach.

One-third octave band attenuation spectra for a series of aft quadrant angles that include the aft angle of peak fan noise are presented in Figures D-21, -22, and -23 for power settings typical of approach, cutback and takeoff, respectively. The one-third octave band that includes fan blade passage frequency is reduced by about 6-10 dB at the 120° angle with less attenuation in neighboring one-third octave bands and angles. Some attenuation is also observed at the second harmonic of the fan blade passage frequency. A plot of attenuation of the fundamental against angle at approach power (Figure D-24) shows that the peak attenuation occurs at 120°, with an abrupt drop in attenuation fore and aft of 120°.

PNdB reductions due to the fan duct treatment vary from 3.5 at approach to 1.5 at takeoff power (Figure D-25). Even though one-third octave band fundamental fan tone levels were reduced up to 10 dB, other noise sources such as the turbine at approach and jet at takeoff power limited the PNdB attenuation that could be achieved. However, Figure D-26, shows that the measured PNdB level was within 2 PNdB of the predicted level at approach thrust.

TABLE D-IV

SUMMARY OF 45.72 m (200 FT) SIDELINE MAXIMUM PERCEIVED NOISE LEVELS

Configuration	Approach					Cutback					Takeoff				
		Inlet		Aft			Inlet		Aft			Inlet		Aft	
	Fn/δ ,N (lbs)	∢	PNdB	∢	PNdB	Fn/δ,N (lbs)	∢	PNdB	∢	PNdB	Fn/δ,N (lbs)	∢	PNdB	∢	PNdB
JT8D-9 Hardwall Baseline	29,134 (6550)	60	115	110	118	52,709 (11850)	80	120	115	121	65,030 (14620)	80	119	140	126
JT8D-109 Treated Engine Treated Nacelle	28,912 (6500)	40	107	110	107	51,997 (11690)	50	112	115	114	73,837 (16600)	80	115	140	120
JT8D-109 Treated Engine Hardwall Nacelle	29,357 (6600)	60	110	115	111	51,597 (11600)	70	115	110	116	73,170 (16450)	80	117	110	121
JT8D-109 Hardwall Engine Hardwall Nacelle	29,134 (6550)	60	110	115	114	51,775 (11640)	60	116	115	118	73,392 (16500)	80	117	110	122

The problem of limited attenuation at aft arc angles other than 120° was studied, and, although not verified, is briefly discussed here. It is known that there are two distinct source mechanisms that generate tone noise at blade passage frequency during static engine testing. One of these is the classical interaction tone noise due to the chopping by the fan of the wakes from the inlet guide vanes. The other is generated by the fan interacting with long coherent eddies. These eddies are believed to originate from the large scale eddies present in the atmosphere close to the ground that become stretched and elongated as they enter the fan inlet. Since the blade passage frequency tone-noise due to inlet guide vane wake rotor interaction is propagated through the duct in both a 12 and an 11 circumferential lobe pattern, the far field directivity is more "peaked" than the directivity due to rotor/turbulence interaction which generates tone noise in all the circumferential modes that can exist in the duct (Ref. 9). It is believed that the largest attenuation occurring at 120° results from the treatment successfully suppressing tone noise due to inlet guide vane wake/rotor interaction which peaks at the 120° microphone location. Furthermore, this attenuation is believed to be limited by the relatively uniform tone directivity due to rotor/turbulence interaction, which does not seem to be significantly attenuated by the treatment. This apparent lack of attenuation at angles other than 120°, however, could be due to the possibility that the treatment is attenuating only those rotor/turbulence interaction modes that cannot propagate to the far field because they are reflected back by the common flow tailpipe that has a diameter 20% less than the fan. This reflection due to the geometry also occurs in the hardwall duct. Thus, the attenuation measured in the farfield is small. The idea is made more plausible by the fact that both the treatment and the tailpipe have the greatest effect on modes near cut-off.

If the theory presented here is correct, it means that the apparent limited attenuation at angles other than 120° is due to a contaminating noise source that is present only during static testing. It is believed that in a flight test, the full treatment effectiveness will be realized since the contaminating noise source will be reduced as the inflow to the fan is appreciably "cleaned up"

c. Effect of Treatment Between the Inlet Guide Vanes and the Fan Rotor

One type of fan noise, combination tone noise, or multiple pure tone noise, is generated from turbofan engines when the relative tip speed of the fan is supersonic. Because the refanned engine operated at higher tip speeds than the current JT8D engine, particular attention was paid to combination tone noise. Unlike the sound field produced by fans at subsonic speeds, where discrete tones are produced at harmonics of blade passage frequency, fans at supersonic speeds generate a multiplicity of tones at essentially all integral multiples of engine rotational frequency.

The essential features of combination tone noise are well established (Refs. 6, 10, and 11). Shock waves are produced at the leading edge of each blade and spiral forward of the fan conveying sound energy out of the inlet to the far field. As shown by the narrowband spectral plot in Figure D-27, a large number of tones are present in the far field. Work at Pratt & Whitney Aircraft (Ref. 10) has shown that the tones generated are due to the slight differences in amplitude of each shock causing different spacings to evolve between the

shock waves as they spiral forward in the inlet. This irregular pattern rotating with the fan results in the spectrum composed of a series of tones at harmonics of shaft rotation frequency.

Previous testing at Pratt & Whitney Aircraft (Ref. 6) has shown that combination tone noise levels were significantly reduced by a short length of acoustic treatment located upstream of the fan; therefore, a six inch long segment of treatment was placed in the outer duct wall between the inlet guide vanes and the fan of the JT8D-109 engine.

Narrowband spectra at the inlet angle of peak combination tone noise for the untreated engine are shown in Figures D-27 and D-29 at engine low rotor speeds typical of airplane cutback and takeoff conditions, respectively. Comparison of these Figures with Figures D-28 and D-30, for which combination tone treatment was installed, showed that, in general, combination tone levels are from 5 to 8 dB lower than the hardwall noise levels. Plots of one-third octave band attenuation at angles of 40°, 50°, 60°, and 70° from the inlet centerline are shown in Figures D-31 and D-32 for the same engine operating conditions as the previous figures. They show that the combination tone treatment is effective in the frequency range between 630 and 2500 Hz when tones are present in this range.

Predicted and measured attenuations are compared in Figures D-33 and D-34 at the angle of peak combination tone noise at rotor speeds of 6400 and 7200 RPM, respectively. They both show that the predicted attenuation was significantly less than the measured data indicated.

Figure D-35 shows a plot of the peak inlet perceived noise level (between 20° and 60°) on a 60.96m (200 ft) sideline vs. corrected low rotor speed. Despite the large reduction in combination tone noise, the reductions in perceived noise are modest. This effect is further illustrated in Figure D-36, which shows the PNdB directivity plot at 6400 RPM, the speed at which maximum combination tone noise reduction was obtained. Comparison of one-third octave band spectra at this speed, typified by the one comparison shown in Figure D-37, shows that at the frequencies controlling the perceived noise level(3150 and 4000 Hz), the levels of the hardwall and treated configurations are very close.

d. Effect of McDonnell Douglas Inlet Treatment

The effectiveness of the inlet treatment on fan noise is evaluated by comparison of the hardwall and treated inlet configurations. Because fan noise is the controlling noise component at rotor speeds simulating aircraft approach thrust, approximately 5500 RPM, the inlet treatment was patterned from the McDonnell Douglas treated inlet, which was designed to attenuate fan blade passing frequency noise at 5500 RPM.

Figure D-38 is a plot of the tone corrected perceived noise level (PNLT) at the angle of peak inlet noise along a 60.96m (200 ft) sideline distance from the engine centerline versus corrected low rotor speed. Significant reductions in PNLT are evident at all speeds except the takeoff condition, where the controlling influence is aft radiated low frequency jet noise. Largest reductions are noted at rotor speeds corresponding to approach power.

The third curve in Figure D-38 represents noise levels from a configuration in which a 4.88m (16 foot) diameter 6.1m (20 foot) long tube was placed over the inlet bellmouth. The curve is indicative of the noise levels in the inlet quadrant (aft of 20° -30°) that are radiated from the aft engine noise sources. This becomes more evident in some figures that follow.

Examination of approach power inlet spectra demonstrates that noise reductions due to inlet treatment are mostly attributable to attenuation of fan blade passage frequency noise (1F1H) and its harmonic (1F2H).

Results at typical inlet angles of 30° and 50° are shown in Figures D-39 and D-40. The blade passing frequency tones have been reduced by between 6 and 9 dB. It is also interesting to note that some noise reduction is seen over a larger frequency range (1-10 kHz).

By noting that the use of the inlet noise suppression tube further reduces the high frequency noise levels, it can be concluded that aft end noise sources are not limiting the noise reductions attributable to the inlet treatment at this rotor speed.

Figure D-41 shows reductions in perceived noise levels at approach power as a function of angle from the inlet centerline. Significant reductions are seen from 20° to 80° with the largest perceived noise level reduction occurring at the inlet angle of peak noise for the hardwall configuration.

At takeoff power corresponding to a corrected rotor speed of approximately 7200 RPM, jet noise controls the far field noise levels, so that effects of inlet treatment should have little effect on far field noise levels. Figure D-42 is a plot of PNL at 60.96m (200 ft) sideline versus angle. Inlet treatment is seen to have little effect on inlet perceived noise level, and then only between 20° and 80°. One-third octave band spectra, Figures D-43, -44, and -45, show that both blade passing frequency and combination tone noise (1250-2000 Hz range) are well attenuated by the inlet treatment. Below 1250 Hz, all three configurations tested exhibit the same spectral noise levels, confirming that aft end noise is controlling the low frequencies in the forward quadrant at takeoff power.

From the foregoing discussion it is apparent that the treated inlet effectively reduced fan generated inlet noise at all speeds. However, at speeds above 7000 RPM, inlet peak perceived noise levels and tone corrected perceived noise levels were not affected by the inlet treatment because the angles of peak noise in the inlet quadrant are controlled by jet noise.

e. Effect Of McDonnell Douglas Tailpipe Treatment

The turbine is a significant noise source in the JT8D-109 engine. This noise, produced in much the same manner as fan noise, is the result of turbine blade wakes chopping through downstream vane rows. Because of the high number of turbine blades, this noise is characterized by discrete tones at blade passage frequencies in 6300 Hz and 8000 Hz center frequency one-third octave bands when the engine is operating at approach power.

In order to attenuate the high frequency noise, use was made of acoustic treatment in the JT8D-109 tailpipe. The acoustic treatment was patterned after that designed by McDonnell-Douglas. In order to evaluate the reduction of the discrete tones themselves, data from the

hardwall and treated tailpipe configurations were examined. Figures D-46, -47, and -48 show these spectra at three angles while the engine was operating at approach power. Levels of both the fan rotor second harmonic and turbine fundamental discrete tones were substantially lowered.

One-third octave band attenuations for approach, cutback and takeoff thrust operation taken at a series of aft angles (100°, 110°, 120°, and 130°) are shown in Figures D-49, -50, and -51. At all conditions, the angles of peak attenuation are at 120° and 130°. It should be noted that due to the broadness in the treatment tuning, the fan rotor fundamental tone is also attenuated. The fact that this tone is lowered in addition to the turbine tones results in a 2 PNdB reduction over the entire operating range of the engine (Figure D-52).

In order to substantiate that the treated tailpipe noise levels are not being held up by inlet fan noise radiating rearward, treated tailpipe PNdB levels were compared with and without an inlet noise suppression tube. The results, shown in Figures D-53, -54, and -55, clearly indicate that blocking the inlet noise source does not lower aft measured PNdB levels.

f. Internal Traverses

Since knowledge of the radial distribution of fan noise is a benefit to the airframe manufacturer who designs the inlet and tailpipe acoustic treatment, radial traverse was conducted in an axial plane 6.86 cm (2.7 inches) upstream of the inlet guide vane assembly (Ref. Figure D-8) in order to document the inlet radial distribution of the fan rotor's discrete fundamental tone. With the engine in steady state operation, the probe was inserted to several depths. To separate the broadband and discrete portions of the noise signature, it was necessary to analyze these data on a narrow bandwidth filter (32 Hz). Radial variations in fan tone level such as seen in these results are typical of internal traverses conducted in fan rigs. Definition of circumferential and radial mode structure requires phase information and was not addressed in this program.

The variation of blade passage frequency tone level is shown in Figure D-56 for rotor speeds corresponding to typical aircraft approach and cutback conditions. At these low speeds, three peaks occur radially, corresponding roughly to the O.D., midspan and I.D. wall. The high fan tone levels predicted at the O.D. were not observed probably due to the 15.24 cm (six inches) of treatment between the fan and inlet guide vanes.

The radial traverse at the cutback speed, 6460 RPM, shows that the blade passage frequency levels are higher than those at approach power as a result of the increase in fan tip speed. At takeoff rotor speed, combination tone noise dominates the spectra. Blade passing frequency noise does not lie above the levels of the combination tones.

Narrowband spectra taken at ten radial positions for approach, cutback and takeoff rotor speeds are presented in Figure D-57 through D-78. At the low speed, discrete tones are found at the fan fundamental (1F1H), second and third harmonic frequencies (1F2H, 1F3H) over the entire annulus; and, although tones from the first and second low compressor

(1C1H, 2C1H) stages are present near the O.D., the second compressor tone predominates from approximately midspan to the I.D. The presence of these compressor tones, and even the summation of the fan and first compressor blade passage frequency tone, (1F1H + 1C1H), were expected in the near field spectra at low speeds. However, narrowband analysis of the far field data, a sample of which is shown in Figure D-79, shows that the predominating tone is that of the fan. At rotor speeds well below that typical of approach power, the other tones are present in the far field and at some angles, such as the 10° angle shown in Figure D-80, the compressor tones are seen to have the highest levels.

Returning to the internal narrowband spectra, the speed typical of cutback power (Figures D-67 through D-72), reveals the presence of combination tone noise from the O.D. to about nine inches inboard. At this speed, fan blade passage frequency still predominates at all radial locations. In the midspan area of the annulus a relatively broadband "haystack" (spectral peak) appears surrounding a frequency of 56E (i.e., 56 times the shaft rotation frequency). Although there are 56 low compressor inlet guide vanes, the noise generating mechanism is not understood. However, narrowband analysis of the far field data at this rotor speed, Figure D-81, does not show any indication of this haystack noise.

Internal narrowband spectra at takeoff power, 7285 RPM, show (Figures D-73 through D-78) that the combination tones predominate over most of the annulus, with broadband noise controlling near the I.D. Fan blade passage frequency noise is identifiable, but not significant.

Radial traverses similar to those made in the inlet were conducted in the treated fan discharge duct in an axial plane approximately two inches downstream of the aft engine flange (tailpipe attachment flange), as shown in Figure D-8. Narrowband analysis of these data, Figures D-82 through D-92, showed complete dominance by aerodynamic noise at all speeds and at all radial locations probed.

g. Internal Core Engine Measurements

The low levels of jet and fan noise components achieved in the JT8D-109 engine revealed a low frequency broadband noise centered at 400 Hz in the far field noise signature at low engine power settings. High response dynamic transducers were placed internal to the engine to determine the generation source. The locations of these high response Kulite transducers are shown in Figure D-8.

Spectra obtained from transducers internal to the engine are difficult to interpret because both aerodynamic noise due to the environment and acoustic signals are present simultaneously. Only the acoustic signals, whether discrete or broadband in nature, propagate to the far field and are of interest. Core engine noise, as defined from far field ground microphone data (see para b, page 204) is broadband in nature and has a peak frequency of about 400 Hz. Thus, the internal noise data of interest in this case are in the area of 400 Hz.

The noise levels within the tailpipe were measured at several engine speeds using a Kulite transducer located one-inch upstream of the nozzle exit plane. One-third octave band plots,

shown in Figures D-93 and D-94, did not reveal a 400 Hz broadband noise, as defined in the far field. The far field 400 Hz noise did not change with either speed or angle. However, it is to be noted that frequency of peak noise below 1600 Hz varies with engine rotor speed from 1000 Hz at the low speed to 500 Hz at takeoff speed. Thus, the 400 Hz signal of interest was being masked by other phenomena or was not present in the tailpipe.

Further upstream in the engine, noise levels were measured at the O.D. wall of the flow splitter near the mixing plane. One-third octave band analysis at several fan rotor speeds (Figure D-95) showed higher levels of noise being measured at this location than at the tailpipe. The one-third octave band levels were generally 10-15 dB higher than those in the tailpipe. Much of this increase in noise may be aerodynamic in nature due to higher flow velocities in this area of the engine. A predominant "haystack" of noise centered around 500 Hz was observed at the tailpipe when low rotor speeds exceeded 6000 RPM (Figures D-93 and D-94). No such "haystack" was seen at the splitter location (Figure D-95). Some indication of the presence of noise at 400 Hz is present, but once again, some masking has occurred.

In the combustor section of the engine noise levels were measured in a spare ignitor in one of the burner cans. One-third octave band levels for a series of engine rotor speeds are shown in Figure D-96. A low frequency peak appears in the spectra centered between 400 and 500 Hz.

Although the spectra measured internal to the engine did not show clearcut evidence of the core noise defined from far field data, correlation techniques were applied to the measured data in an attempt to separate the unwanted masking noises from the defined core engine noise. This is discussed in the following paragraphs.

1) Correlation of Measurements With Internal Kulites and Far Field Microphones

Cross-correlation of the internal Kulites with a far field microphone to determine the location(s) of the source(s) of core engine noise within the engine was accomplished. The cross-correlation results presented in this section were performed at two different engine speeds ($N_1/\sqrt{\theta}$ = 5195 and 7717 RPM). The 120° far field microphone was chosen because this is the angle at which core engine noise was found to peak.

The cross correlations were performed on a SAICOR Correlator Model 43A. In mathematical terms, the normalized cross correlation function is defined as

$$R_{xy}(\tau) = \frac{\lim_{T\to\infty} \frac{1}{T} \int_0^T f_x(t)\, f_y(t+\tau)\, dt}{\sqrt{f_x^2}\,\sqrt{f_y^2}}$$

where $f_x(t)$ is the magnitude of the signal observed at point x at an arbitrary instant of time t; and $f_y(t+\tau)$ is the magnitude of a signal observed at a point y at time τ later. The term $\sqrt{f_x^2}$ is the rms value of the signal at point x and $\sqrt{f_y^2}$ is the rms value of the signal

at point y. By varying τ, a complete function of the relationship between the signals at x and y as a function of the time delay, τ, is obtained (i.e., the cross-correlation function). The denominator in the above equation is the term which normalizes the cross correlation. Ideally, what this term does is to take into account the differences in the rms values of the two signals so that a meaningful cross correlation coefficient can be obtained. With regard to the instrumentation (SAICOR Correlator) used to perform these cross correlations, normalization is achieved by attenuating or amplifying the two input signals so that their auto-correlation amplitudes at $\tau = 0$ (i.e., their rms values) are equal. In this way, the mean square value of both signals are identical. As a result, the 0 to 1 correlation scale which is defined by the amplitude of the auto-correlation at $\tau = 0$ can be directly applied to the cross correlation results.

In addition, the input signals being cross-correlated were filtered through identical phase-matched filters. Since the frequency range of interest for core engine noise was around 400 Hz, a filter bandwidth of 300-500 Hz was used. Band pass filtering of the two signals generated secondary resonant peaks which were produced by the roll-off of the filters. This resonant frequency was found to be a function of the center frequency of the filter bandwidth. Increasing the filter bandwidth lowered the correlation levels, while narrowing the filter bandwidth tended to generate a discrete frequency sine wave.

Figure D-97 contains the cross-correlation of the tailpipe Kulite with the far field microphone at an engine speed of 5197 RPM. The full scale time delay range of 0 to 200 milliseconds contains a single distinct correlation peak at a time delay of 136 milliseconds. Multiplying this time delay by the acoustic speed of a sound [340.46 m/s (1117 ft/s)] yields a distance of 45.72m (150 feet) which is the distance from the tailpipe to the far field microphone. Therefore, the 136 milliseconds delay time corresponds to an acoustic wave propagating from the tailpipe to the far field. In addition, the correlation level of 32 percent is the equivalent of stating the following: "If the internal noise measured in the tailpipe is uncontaminated by sources other than core engine noise, then the correlated core noise in the far field spectrum is within 5 dB of the total measured noise in the frequency range between 300 and 500 Hz." These results confirm that significant levels of internally generated low frequency core noise do indeed radiate to the far field and contribute to the total far field noise levels.

At a higher engine speed ($N_1/\sqrt{\theta} = 7717$ RPM), the normalized cross-correlation coefficient has decreased to a level of 12 percent. This is due to the increase in jet noise signal, which at this high engine speed almost completely dominates the far field measured spectrum. The delay time obtained from this cross-correlation of the tailpipe Kulite with the far field microphone (Figure D-98) is exactly the same as that obtained at the lower engine speed, and this is as it should be, since the external speed of sound did not change.

Figure D-99 contains the cross-correlation (at 5195 RPM) of the splitter Kulite with the same 120° far field microphone. This time the correlation peak occurs at a delay time of 137.5 milliseconds. Using the result from Figure D-97 implies that the propagation time from the splitter to the tailpipe nozzle exit is 1.5 milliseconds. In addition, the peak correlation value of 16 percent in the 300-500 Hz frequency range again indicates that internally

generated core noise measured at the splitter can be detected in the far field. At the higher engine speed (Figure D-100), the cross-correlation coefficient decreases to four percent. This is probably due to internal flow noise contamination and to the increase in externally generated jet noise levels.

The differences in correlation level between Figures D-99 and D-100 are due to the high levels of low frequency aerodynamic noise generated by the swirling flows coming out of the last stage turbine blade row. Since this low frequency aerodynamic flow noise does not propagate to the far field, its overall effect is to lower the cross-correlation levels between the splitter Kulite and the far field microphone.

Figure D-101 contains the cross-correlation of the ignitor Kulite and the 120° far field microphone. The cross-correlation peak occurs at 139 milliseconds which implies that if the noise is generated near the burner ignitor it would take 1.5 milliseconds for the acoustic wave to travel from the ignitor to the splitter Kulite. However, in this region the acoustic speed of sound is difficult to calculate because the acoustic wave must travel through the turbine region, in which large temperature variations exists. These time delays do indicate, however, that the major source of correlated noise is in the burner region, and not in the tailpipe downstream.

At the higher engine speed (Figure D-102), the cross-correlation level is three percent, while the correlation delay time is approximately 138 milliseconds. This decrease is delay time is due to the increased internal temperatures, (T_{t4}, T_{t5}, T_{t6}, and T_{t7}), that control the acoustic speed of sound in each of their respective regions of the engine.

These cross-correlation results confirm that internally generated low frequency core noise does indeed radiate from the tailpipe and contributes to the total far field noise levels. In addition, these results indicate that the cross-correlation technique is a useful tool, which can lead to the location of internally generated core noise sources.

h. Component Noise

The far field noise signature of a gas turbine engine is primarily comprised of contributions from five noise generation sources: fan-generated noise radiated from the inlet, fan-generated noise radiated from the discharge, turbine, jet, and the core engine noise. Because installation and flight affect the radiated noise levels differently for each of these components, it is necessary to establish static component noise levels. After component noise levels have been determined, appropriate installation and flight effects can be applied to each component, then summed to yield more accurate aircraft noise predictions. Static noise data, obtained while running Test No. 1 (Ref. Table D-VI), was used to define the refan engine component noise levels. Predicted component levels, determined using the procedures described in this section, are presented in Appendix B Reference 5.

The following sections discuss the component noise definitions based on the first JT8D-109 engine acoustic tests.

1.) Inlet Fan Noise

The one-third octave band noise data were correlated with low rotor-speed on a one-third octave by one-third octave basis for each of the inlet angles. A least squares curve-fit was

made, by computer, for these data. Figure D-103 is a typical plot that shows the data points and the curve fit for one 1/3 octave band at one angle. This process smooths the data and allows fan and combination tone one-third octaves to be recalled with a second computer deck.

The second computer deck reads the least squares curves. This is done for the fan portion of the spectra, which extends from one 1/3 octave band below that containing the blade passage tone to the one-third octave band centered at 10 kHz, and for the combination tone portion of the spectra, which extends from two 1/3 octave bands below that containing the blade passage tone to between three and ten 1/3 octave bands below blade passage as a function of tip speed. Below the combination tone region, the fan noise is rolled off at 1 dB per one-third octave.

2. Aft Fan and Turbine Noise

The aft noise spectrum is a complex shape containing levels from the jet, core, turbine and aft fan sources. In order to separate this noise into its components, it is necessary to examine narrow band spectra. Figure D-104 is a typical approach power spectrum (110°). The fundamental of fan blade passage frequency (1F1H) is seen at 2.9 kHz.

Turbine tones (4T1H, 2T1H, 3T1H) at fundamental blade passing frequencies are found in the region between 6 and 8 kHz. A large "haystack" (peaked broadband spectrum) of broadband noise is visible in the region surrounding these tones. As the high temperature, high velocity primary jet stream interacts with the slower moving, cooler fan stream, as well as the ambient air, strong shearing effects take place. In order to reach the far field, the turbine tones must pass through this zone of high temperature gradients and pressure gradients. In doing so, the discrete turbine tones are scattered into many other frequency bands surrounding the fundamental. These "sidebands" are so close to each other that even when analyzed with a "narrow" 32 Hz bandwidth filter, they merge into a broadband type spectrum. The locus of these turbine tone sidebands forms a "haystack" shaped spectrum between 5 and 10 kHz, as shown in Figure D-104.

In a common flow engine such as the JT8D-109, the fan blade passage frequency must also pass through the external shear layer. Thus it is not unexpected that a "haystack" of broadband noise surrounding the fundamental of fan blade passage frequency is observed (Figure D-104).

a. Aft Fan Noise

From examination of the narrow band spectra, the aft fan noise spectrum was separated into broadband and discrete portions. The broadband portion was further divided into the "haystack" surrounding the fan blade passage fundamental and a high frequency segment. This high frequency section was determined by fitting a straight line through the lower bounds of the turbine "haystack".

This broadband portion was divided into one-third octave bands and an average level within each band was calculated. Because of the bandwidth differences between narrow and one-third octave bands, these broadband levels were corrected by 10 log of the bandwidth ratio (10 log BW/32).

Narrow band levels of the fan blade passage fundamental (1F1H) and its harmonic (1F2H) were then anti-logarithmically added to the broadband noise levels of the one-third octave bands that contained their respective frequencies. It is not necessary to correct these tone levels for bandwidth. Also, since the one-third octave band data has been corrected to an FAA day (77°F, 70% humidity) and corrected for microphone and cable response, the levels derived from the narrow band were similarly corrected in order to be consistent with the total "measured" data.

The low frequency portion of the spectrum (below about 2000 Hz) is controlled by jet and core noise. Spectra from numerous noise tests of fan rigs, which do not contain jet and core noise, indicate that low frequency fan broadband noise levels decrease by about 1 dB per one third octave band in the region below blade passage frequency. This slope was used for the refan engine noise data. The slope was applied to the noise level in the second one-third octave band below that containing the fundamental blade passage frequency, as this band is assumed to contain only fan broadband noise. Lower bands contain jet and core noise, while the next higher band noise level may be influenced by the blade passage frequency tone.

Thus, aft quadrant fan noise spectra were determined at several angles and rotor speeds. The data were plotted vs. rotor speed for each one third octave band and angle. Least square fits were generated, and generalized aft fan noise prediction curves were plotted (Figure D-105).

b) Turbine Noise

The procedure for defining the turbine noise is similar to that for the aft fan. The peak turbine level for a given speed and angle was determined by: 1) finding the one-third octave band into which the average turbine blade passage frequency fell, 2) determining an average sound pressure level for the turbine "haystack" and for the fan broadband in the average turbine blade passage frequency band, 3) subtracting on an anti-logarithmic basis the fan broadband level from the turbine "haystack" level to yield a turbine broadband level, 4) adding the bandwidth correction to the turbine broadband, and 5) adding, on an anti-logarithmic basis, the turbine blade passage tones contained in the band to the turbine broadband. As with the aft fan, these levels were weather, microphone, and cable corrected to be consistent with the total "measured" data.

The above method was used to define a peak turbine level for angles 90°, 100°, 110°, 120°, 130°, and 140° for all speeds where turbine noise could be discerned. Using these levels, an engine rotor speed dependence curve (Figure D-106) and a directivity curve (Figure D-107) were plotted.

Using these same techniques, the one-third octave bands adjacent to that containing the peak were analyzed to yield a spectrum at each angle and each speed. These spectra were found to be very similar so that one generalized spectrum for all angles was used. The spectrum is shown in Figure D-108.

3) Jet and Core Engine Noise

To define the jet and core noise components, detailed data analysis was conducted on the spectra measured with ground microphones at angles from 90° to 150°. The low frequency portion of these spectra have been separated successfully into core engine and jet noise components. All results are presented " as measured " by the ground microphones. A free field definition may be obtained by simply subtracting six dB.

a) JT8D-109 Jet Noise Definition

The SAE coaxial jet noise prediction procedure (October 1973) was first compared to measured spectra. Significant differences appeared in both spectra shape and levels, especially at the forward angles (90°-110°). Therefore, it was concluded that the SAE procedure was not applicable to, nor was it developed specifically for, the prediction of jet noise from common flow nozzles.

- Jet Noise Spectra – Ground microphone spectra for several high speed conditions were examined at 90°, 100°, 110°, 120°, 130°, 140°, and 150° independently. By positioning the measured spectra in both level and frequency, it was found that very similar shapes resulted at a given angle for all speeds examined. Therefore, a single spectrum shape was assumed to apply at each angle over the speed range. The resulting spectra are shown in Figure D-109.

To examine the validity of these spectra, comparisons were made with results from model jet noise tests on a scaled JT8D-109 configuration. A comparison at a simulated engine operating condition (near takeoff-thrust) is shown in Figure D-110 for seven angles. Fair agreement is seen at all angles, with the more significant deviations occurring at 90° and 110°.

A similar comparison was made with predictions from the SAE coaxial jet noise prediction procedure (October 1973) at the same power setting as shown in Figure D-111. Good agreement is apparent at the further aft angles, but at 90° and 110°, the SAE spectra appear too flat. In addition the peak frequency dependence and levels predicted by the SAE procedure were not in agreement with data and thus had to be redefined. This is discussed in the following paragraphs.

- Jet Noise Peak Frequency – The spectra of Figure D-109 were used, together with the data, to define the peak frequency dependence of jet noise for the JT8D-109. The results are shown in Figure D-112. Curves have been drawn through these data that always lie within one-half of a one-third octave band from the points shown for each angle. As expected the peak frequency increased with jet velocity and decreased toward the rearward angles.

- Jet Noise Levels – The next step in the analysis of the ground microphone spectra was to determine the noise level behavior with primary jet velocity. Figure D-113 shows the peak jet noise sound pressure level at each angle plotted versus jet velocity. A straight line was found to exist at all angles that fell within one dB of the points obtained from the spectra. The slopes and the levels increased with increasing angle.

- Jet Noise Directivity – The information contained in Figure D-113 was cross-plotted to obtain the directivity of peak jet spectral sound pressure level. Results are shown in Figure D-114 for primary jet velocities ranging from about 122 to 610 m/s (400 to 2000 ft/sec.) Also shown are the directivities obtained from JT8D-109 model jet tests at two conditions simulating the actual engine cycle. Very good agreement between the full scale definition and model jet directivities is apparent.

b) JT8D-109 Core Engine Noise Definition

Using the jet noise definition just described, it was possible to obtain a separation of jet and core engine noise from an examination of ground microphone spectra at low engine power settings.

- Core Engine Noise Spectrum – From an analysis of data at low speeds, the spectrum shown in Figure D 115 was found to apply at all angles.

- Core Engine Noise Levels – Using the spectrum shown in Figure D-115, together with the predicted jet and measured spectra, it was possible to determine core engine noise levels for at least three speeds at all angles, and as many as six speeds at an angle of 120° (near the core engine noise peak angle). Results of this analysis are shown in Figure D-116. At 120°, where the most data exist, a smooth curve fit was established through these points when plotted versus thrust. It was also possible to fit the data at the other angles with a curve parallel to that used for 120°. Thus, the core noise was defined for the other angles up to a thrust of 40,032N (9000 lbs) as shown in Figure D-116.

- Core Engine Noise Directivity – Since the core engine noise "slope" with thrust is the same for all angles, the directivity characteristics of JT8D-109 core engine noise are identical at all power settings. Figure D-117 shows the points obtained from cross-plotting the information shown in Figure D-116. The peak angle occurs at 125° from the inlet axis.

c) Results and Discussion

The curves shown in the previous jet and core noise figures were programmed so that overall and perceived noise levels could be obtained for each component. In addition, total low frequency (jet and core) spectra, and overall and perceived noise levels could be obtained on the computer and compared to the measured spectra. Figures D-118, -119, and -120 represent a comparison of the total low frequency spectra obtained from the current definition with the measured spectra at three engine operating conditions:

- $N1/\sqrt{\theta}$ = 3014 RPM where core engine noise is dominant (Figure D-118).
- $N1/\sqrt{\theta}$ = 5195 RPM where the jet and core engine levels are comparable (Figure D-119).
- $N1/\sqrt{\theta}$ = 7226 RPM where the jet noise is the dominant low frequency component (Figure D-120).

The comparisons are shown at an angle of 120°, very near where core engine noise peaks (Figure D-117). Good agreement is seen at all frequencies for the two speeds (always within 2 dB). Similar agreement was obtained at other angles and engine speeds. Also shown in Figures D-118 and D-119 are the individual jet and core engine noise spectra.

A comparison of overall sound pressure level (jet and core obtained from the current definition) with measured values is shown in Figure D-121 at an angle of 120°. Reasonable agreement is seen. Similar agreement was obtained at other angles and speeds.

4.) Comparison With Total Measured Data

Since the only noise component defined for the inlet was the inlet fan, the inlet comparison consists of comparing this definition with the measured inlet pole microphone data. However, in the aft direction, where all of the components were defined, the components were corrected to simulate pole microphones, where necessary (jet and core), and were anti-logarithmically summed to yield total noise. The total noise and its components are compared to the measured aft pole microphone data. Typical comparisons are presented in Figures D-122 through D-144. Six angles, 50°, 60°, 70°, 100°, 120°, and 140° at four engine speeds, 3698, 5208, 6397, and 7443 RPM were selected as approximations of idle, approach, cutback and takeoff power settings. (Note that since core noise is not defined above 40,032N (9000 lbs), there is no core component at the cutback and takeoff simulation.) All spectra are at 45.72m (150 foot) radius from the engine.

In general, the inlet fan agrees quite well with the fan and combination tone portion of the measured data. It is apparent that there is low frequency noise in the inlet region, especially at high power, which is unaccounted for by the fan. This is probably due to jet and core noise radiating from the back of the engine.

It is evident that at aft frequencies below about 1600 Hz, the total noise level is controlled by the jet and core engine noise components, while above this frequency the aft fan and turbine components determine the total spectral levels. Generally, the summation of component noise agrees quite well with the total aft quadrant measured data, being within about 2 dB. In the frequency region between 500 and 1250 Hz at the 100° and 120° angles, the combination of jet and core noise is consistently below the measured data, especially at the speeds where the jet and core components are close together in level. At the 140° angle, where the jet component is more dominant, the agreement is better.

The separation of the total noise signature into components required examination of the data at all speeds and all aft angles. Generalized curves were then drawn for each component, and of course, did not agree precisely with each point. Considering this procedure it is concluded that, with minor exceptions, the component agreement with the total noise measured is within 2 dB, representing an accurate assessment of component noise characteristics.

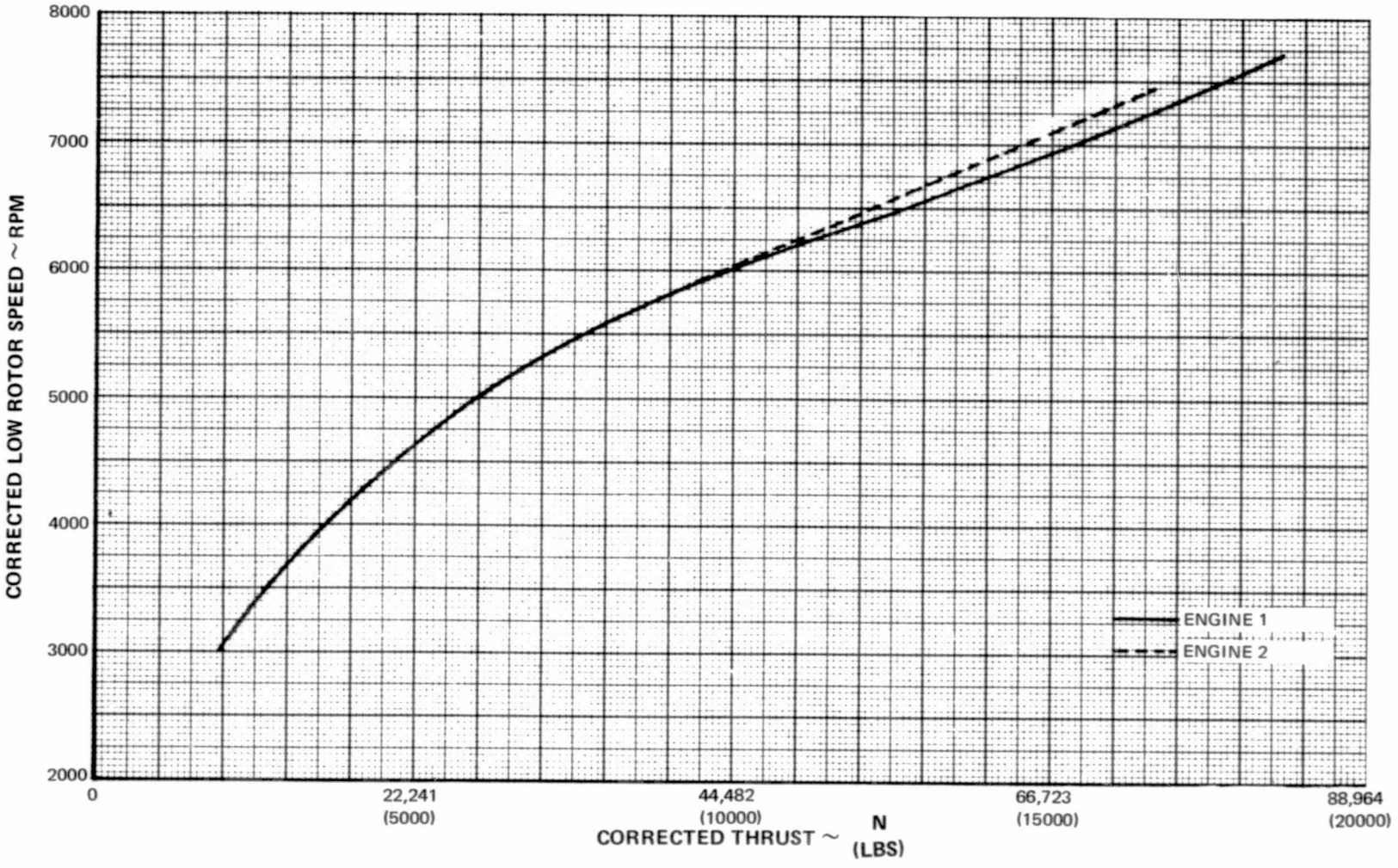

Figure D-1 JT8D-109 Engine Performance ~ Low Rotor Speed

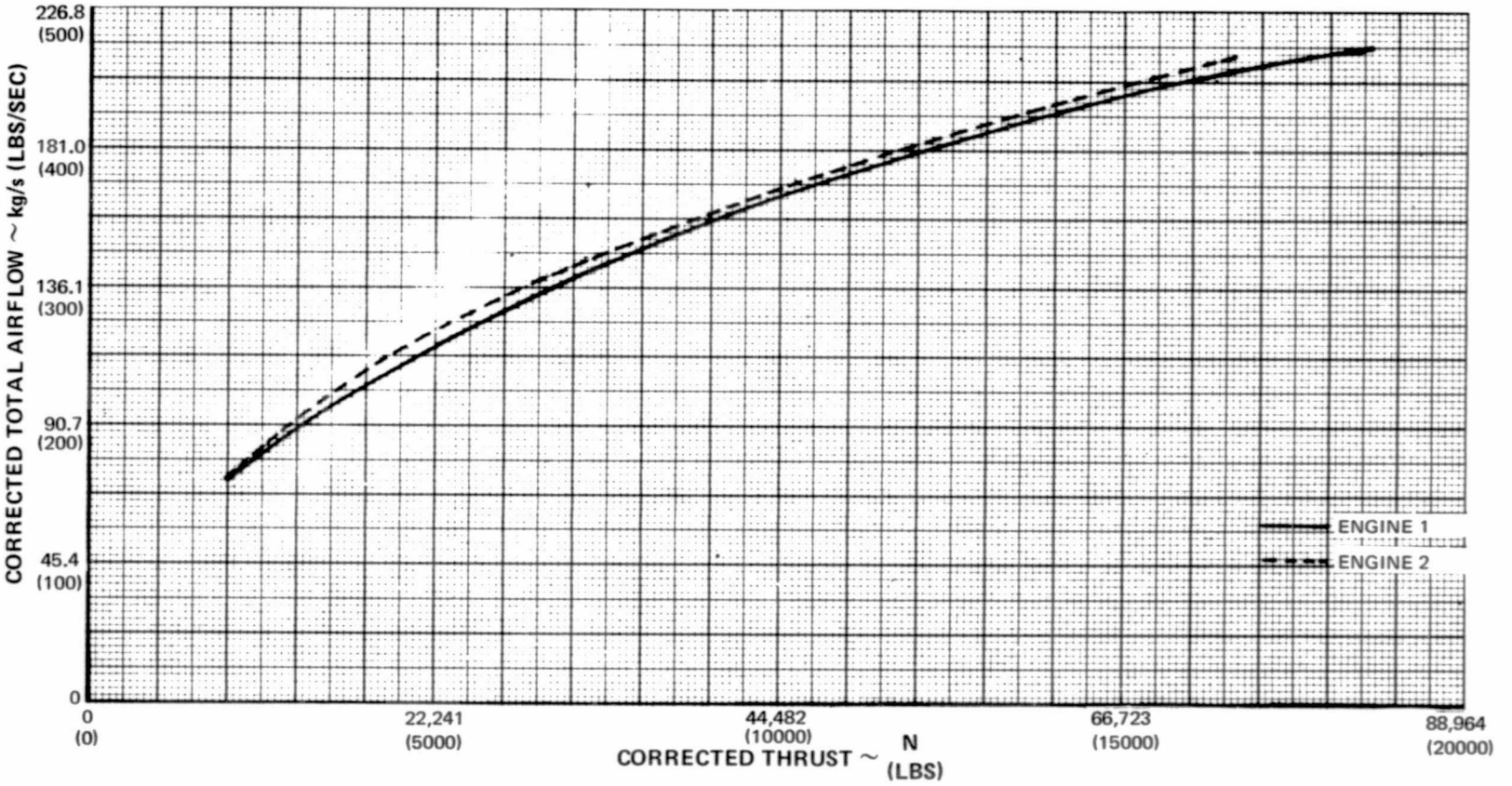

Figure D-2 JT8D-109 Engine Performance ~ Total Airflow

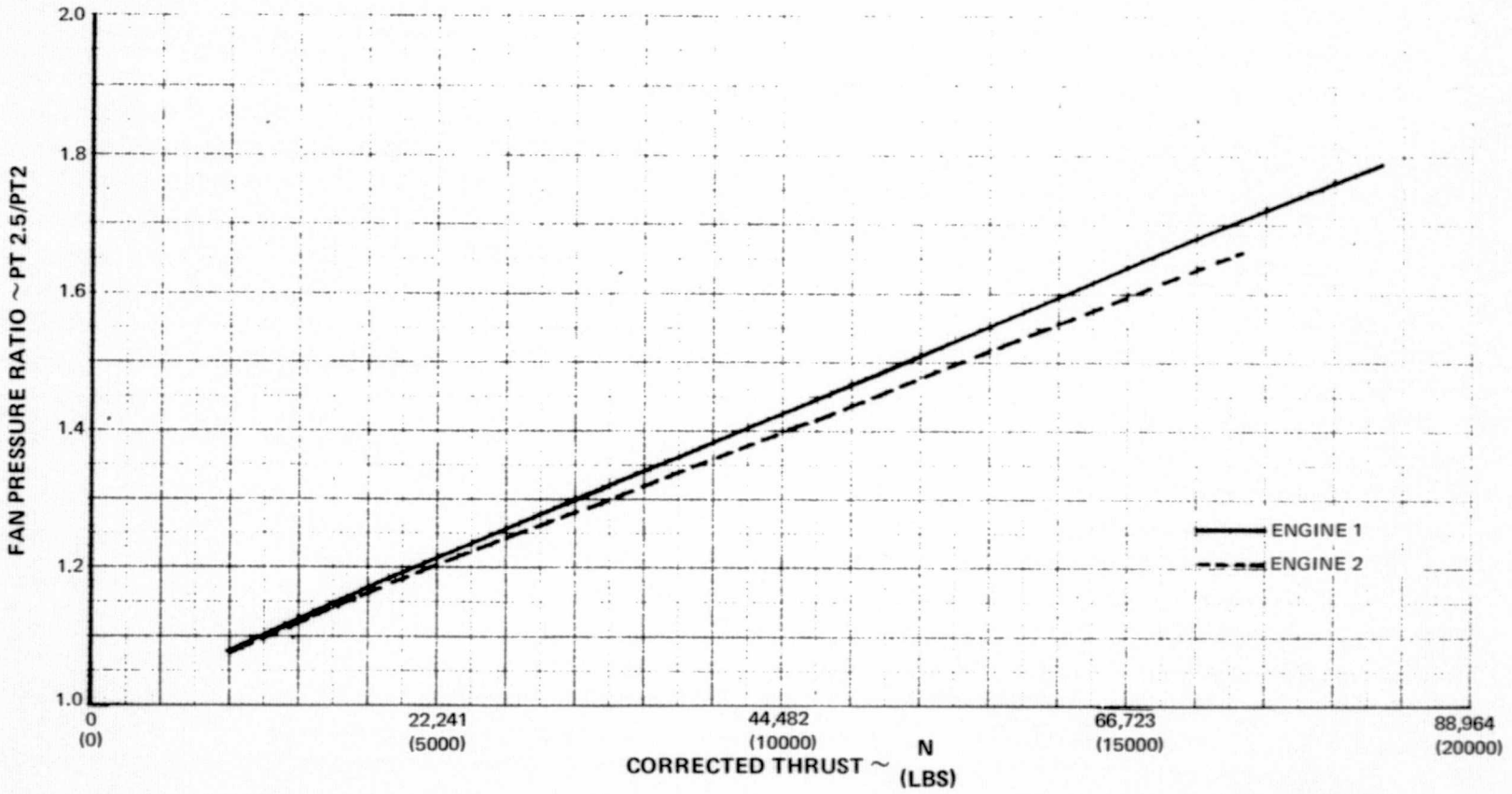

Figure D-3 JT8D-109 Engine Performance ~ Fan Pressure Ratio

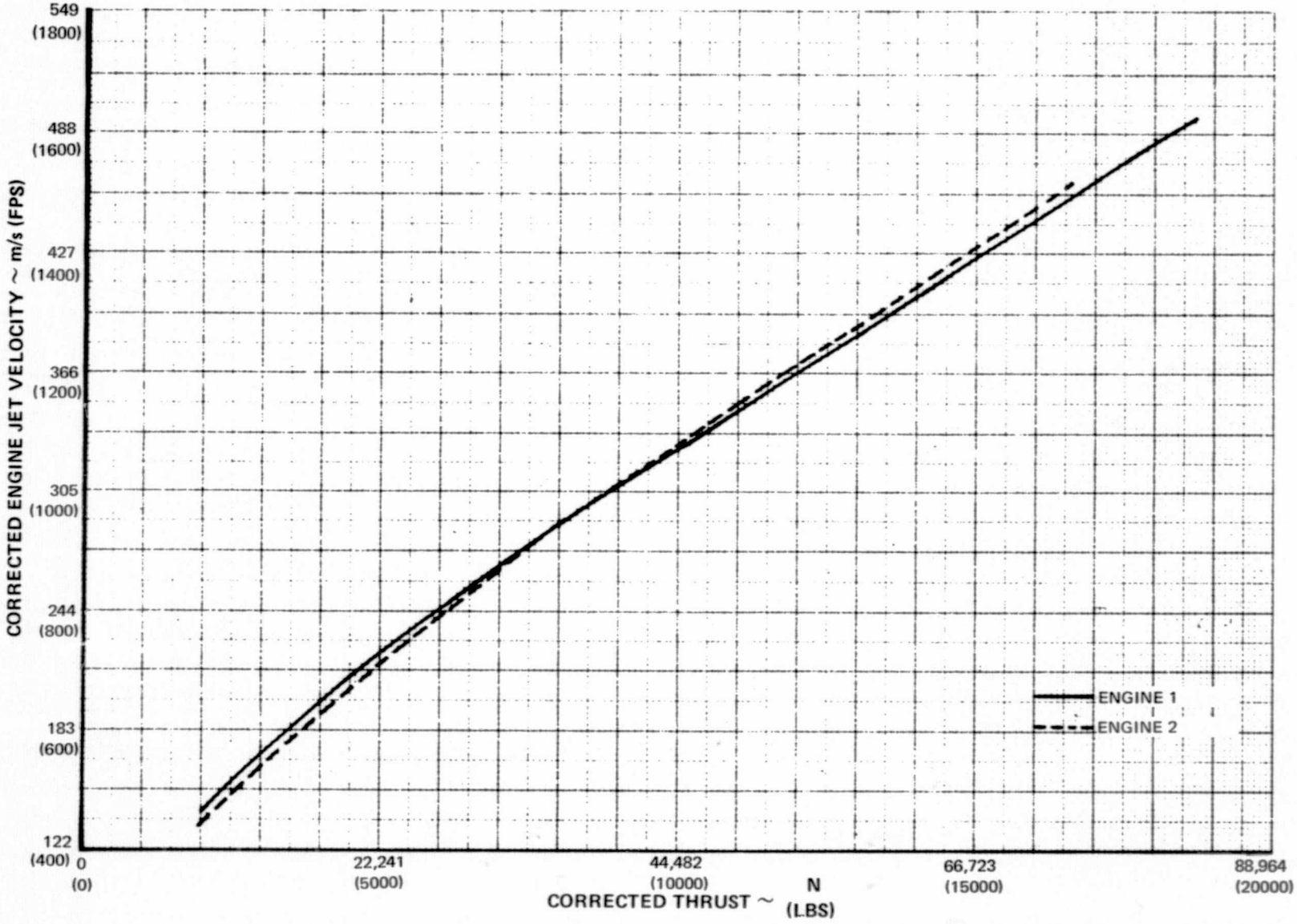

Figure D-4 JT8D-109 Engine Performance ~ Engine Jet Velocity

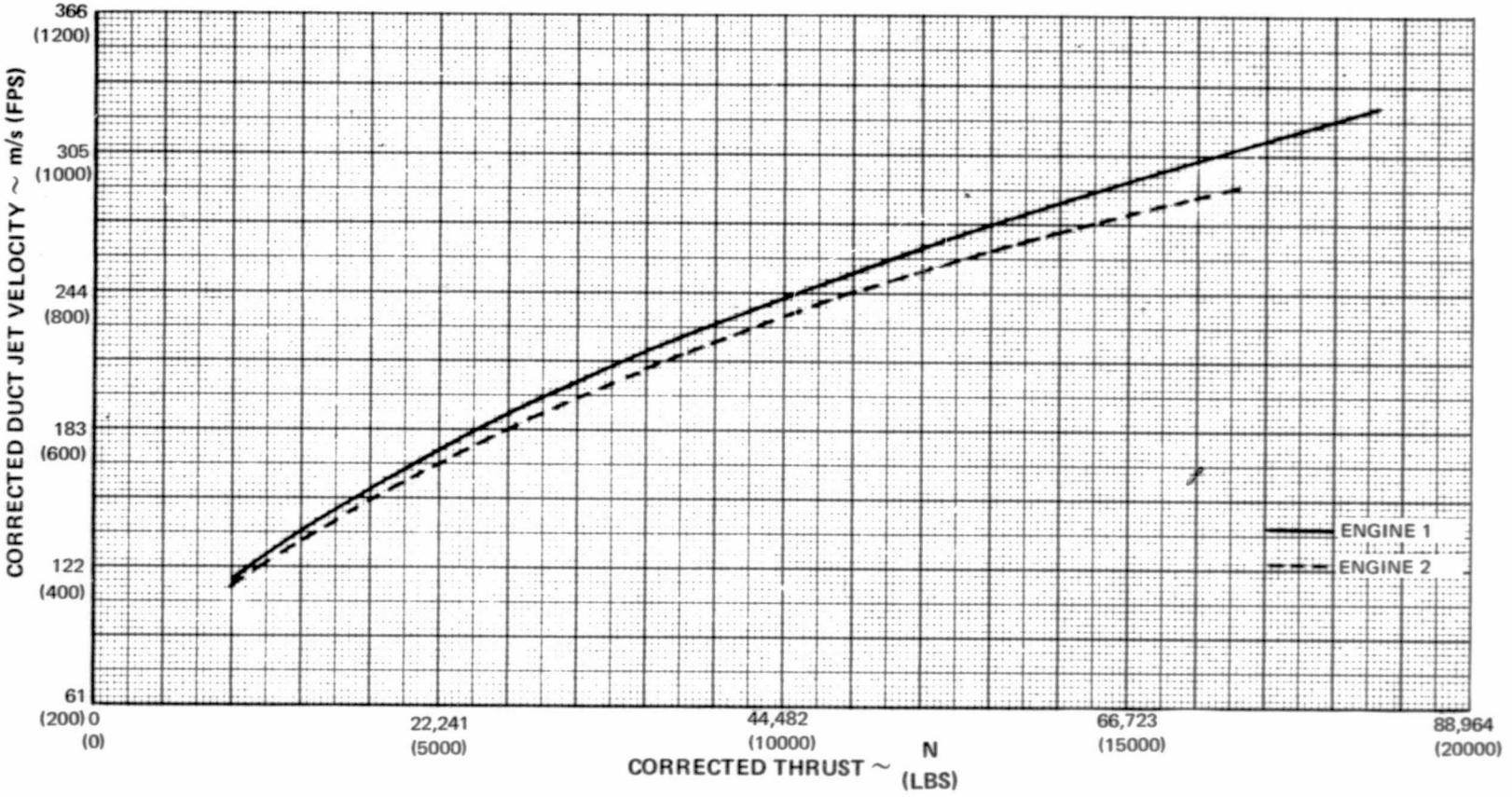

Figure D-5 JT8D-109 Engine Performance ~ Fan Duct Jet Velocity

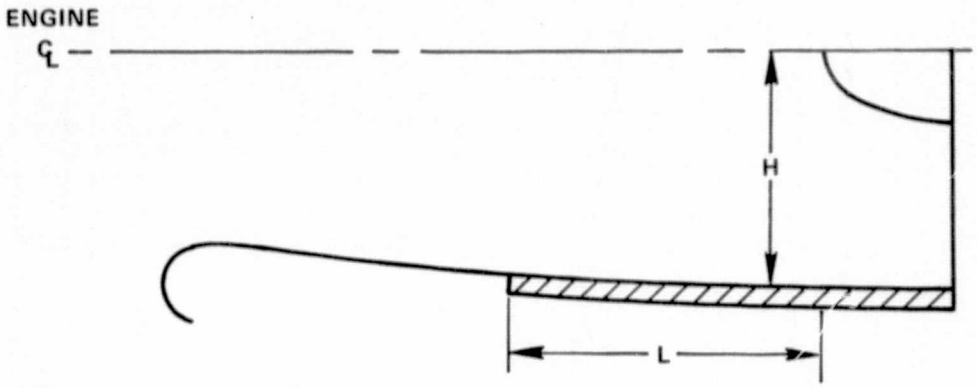

TREATMENT LENGTH ~ m (IN.)	% OPEN AREA	BACKING DEPTH ~ cm (IN.)	HOLE SIZE ~ cm (IN.)	L/H	TREATED AREA ~ SQ. m (SQ. FT.)
1.16 (45.6)	6	1.41 - 1.43 (0.555 - 0.565)	0.122 - 0.135 (0.048 - 0.053)	1.65	2.23 (24)

Figure D-6 JT8D-109 Inlet Acoustic Treatment

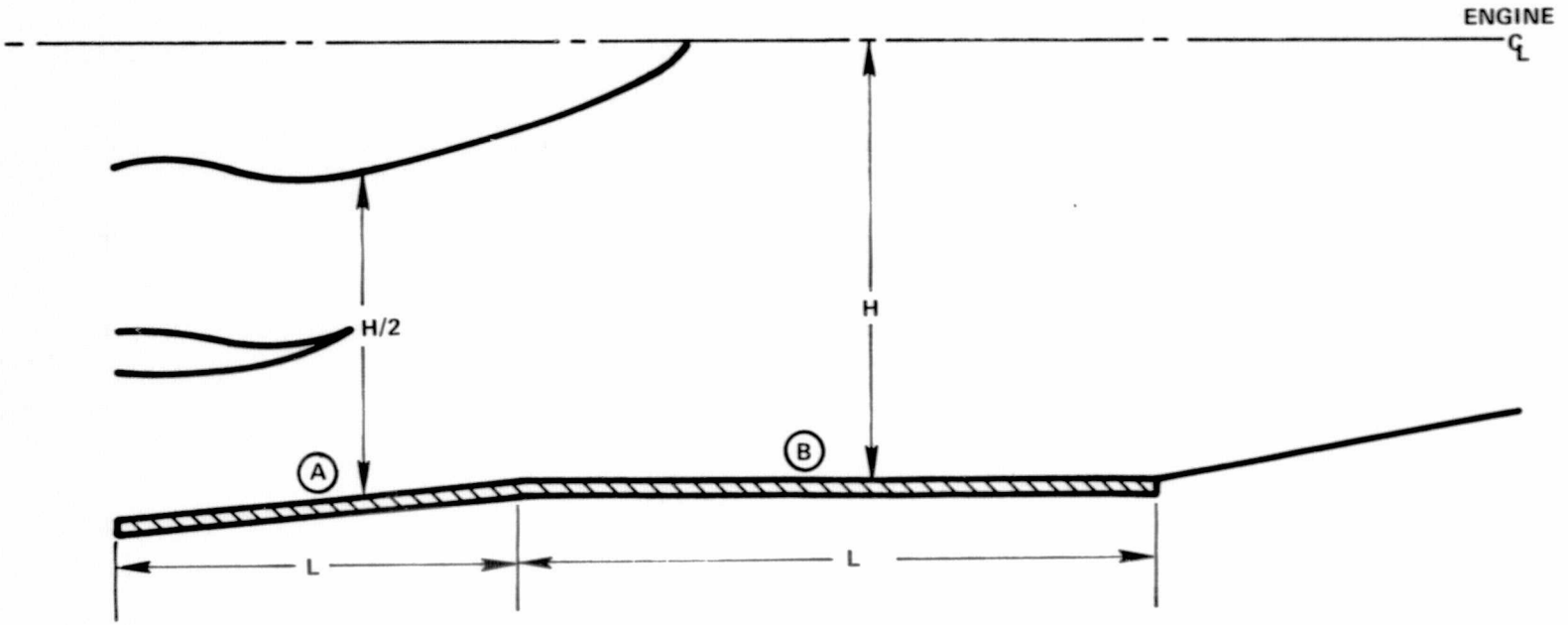

TAILPIPE	LENGTH m (IN.)	% OPEN AREA	BACKING DEPTH ~ cm (IN.)	HOLE SIZE ~ cm (IN.)	L/H	TREATED AREA ~ SQ. m (SQ. FT.)
(A)	0.53 (21)	12	0.876 - 0.902 (0.345 - 0.355)	0.119 - 0.145 (0.047 - 0.057)	1.0	2.02 (21.8)
(B)	0.85 (33.4)	12	0.876 - 0.902 (0.345 - 0.355)	0.119 - 0.145 (0.047 - 0.057)	1.48	3.02 (32.5)
TOTAL					2.48	5.04 (54.3)

Figure D-7 JT8D-109 Tailpipe Acoustic Treatment

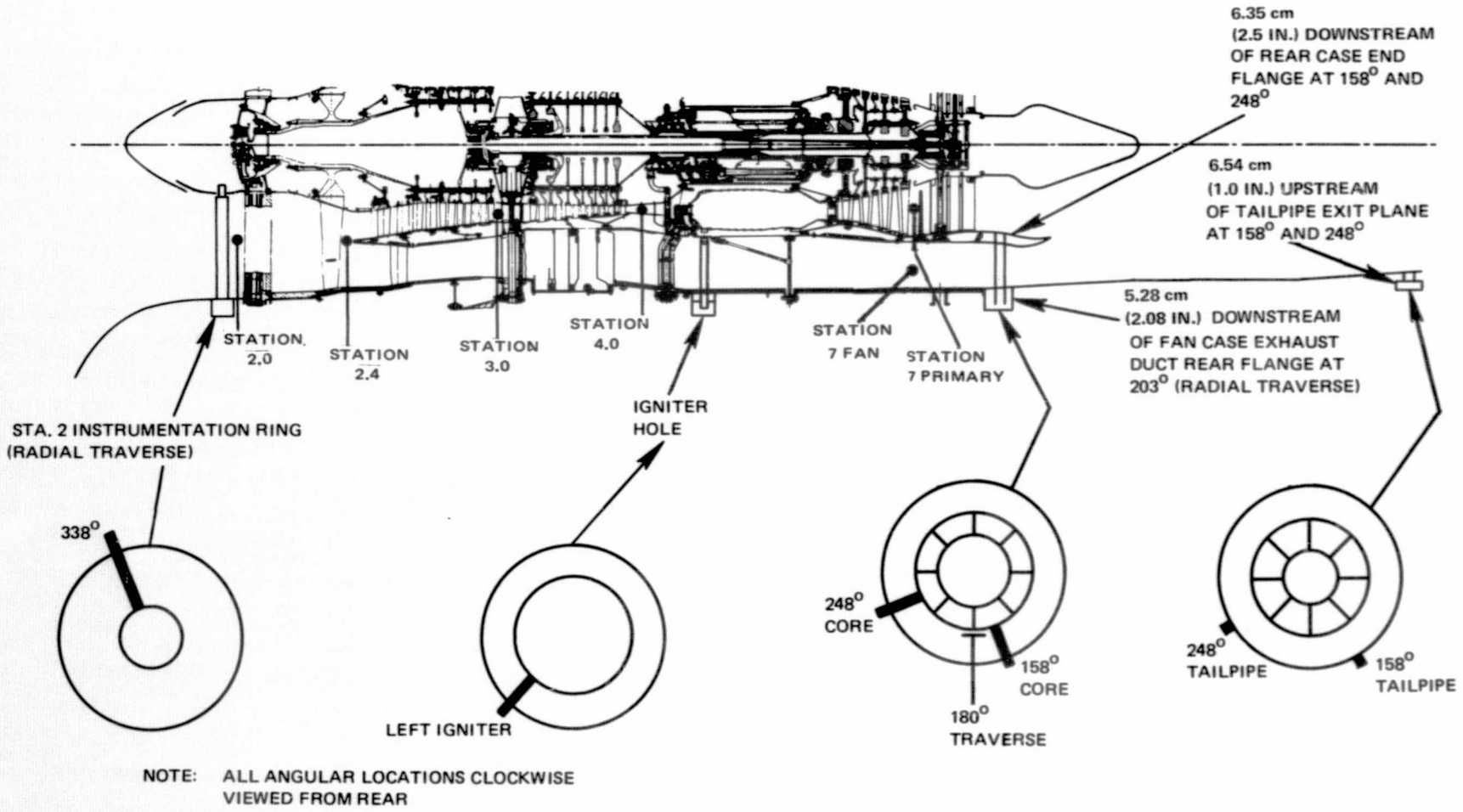

Figure D-8 JT8D-109 Internal Acoustic Instrumentation Locations

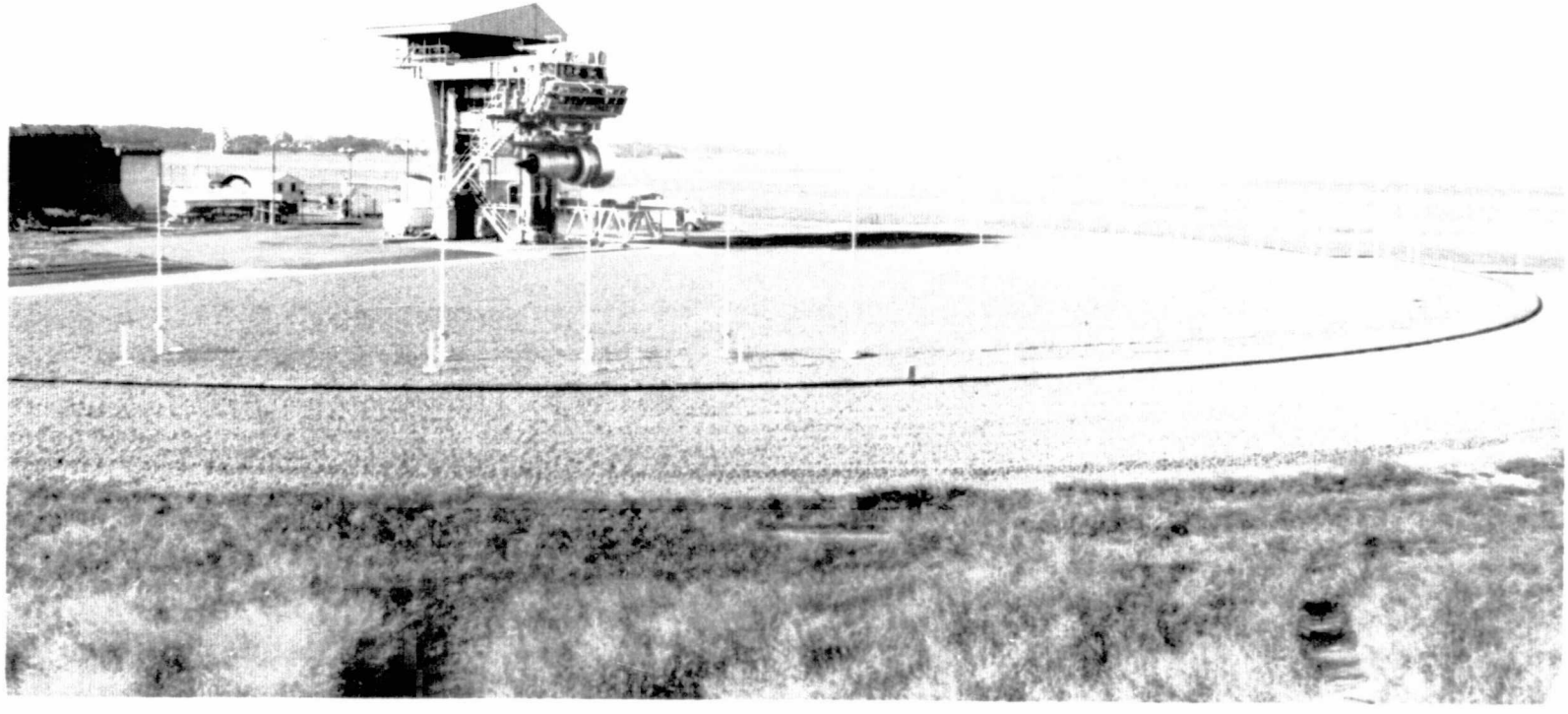

Figure D-9 Outdoor Noise Test Facility, X-314, Showing Location of Pole Microphones, CN-39419

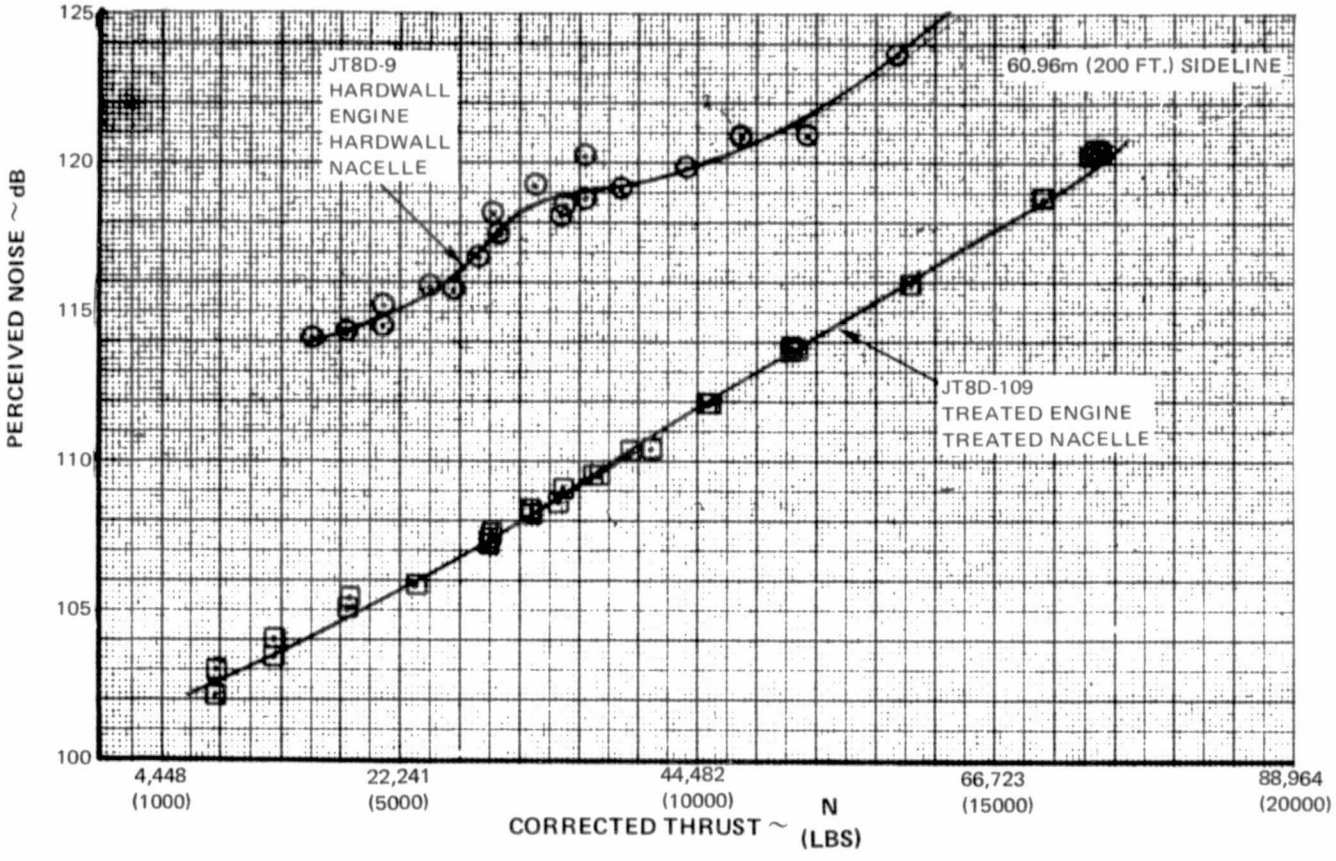

Figure D-10 Comparison of Peak Aft PNdB Levels of Current JT8D Engine and Refanned JT8D-109 Engine with Treated Nacelle

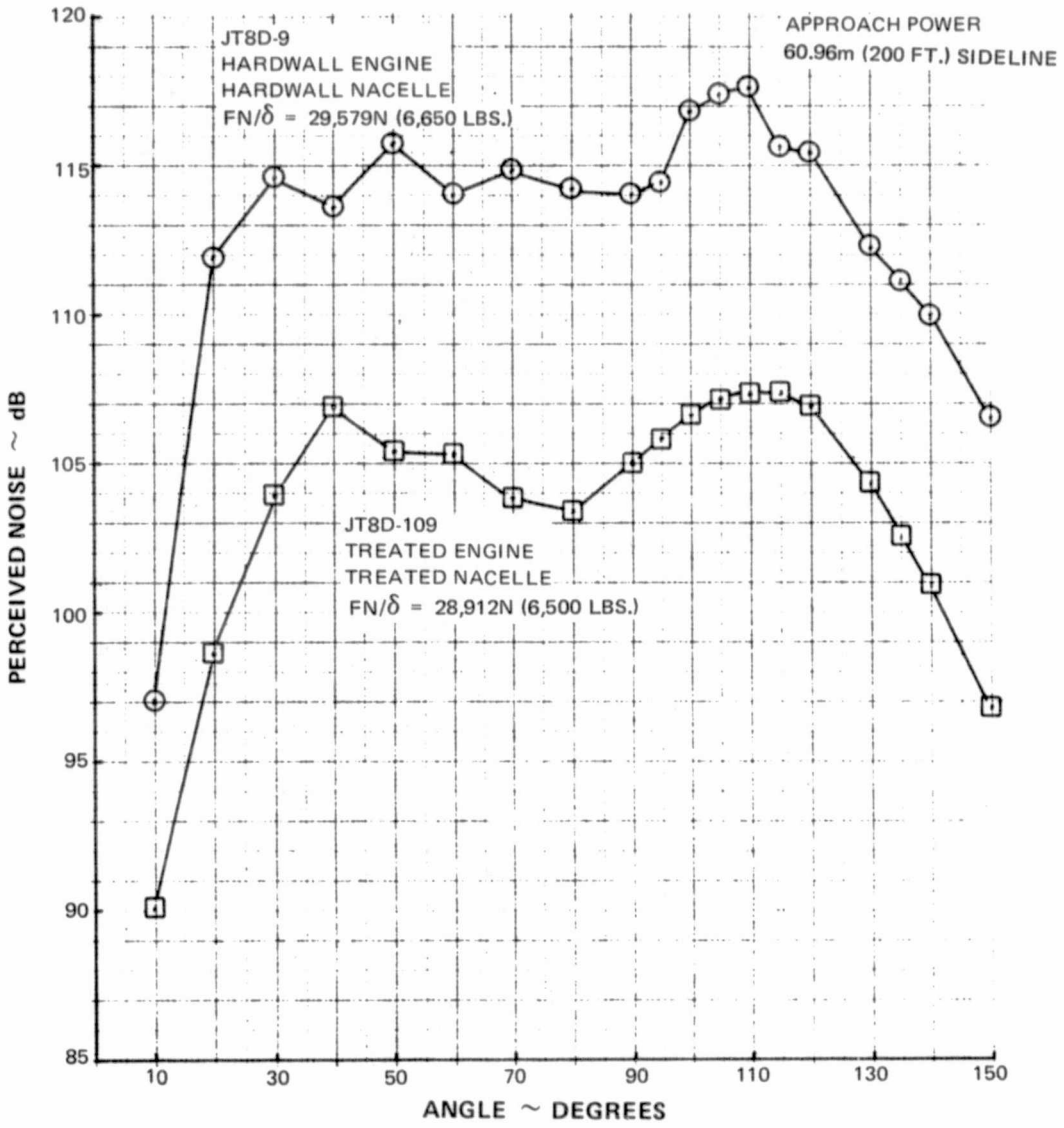

Figure D-11 Comparison of PNdB Directivity of Current JT8D Engine and Refanned JT8D-109 Engine with Treated Nacelle ~ Approach Power

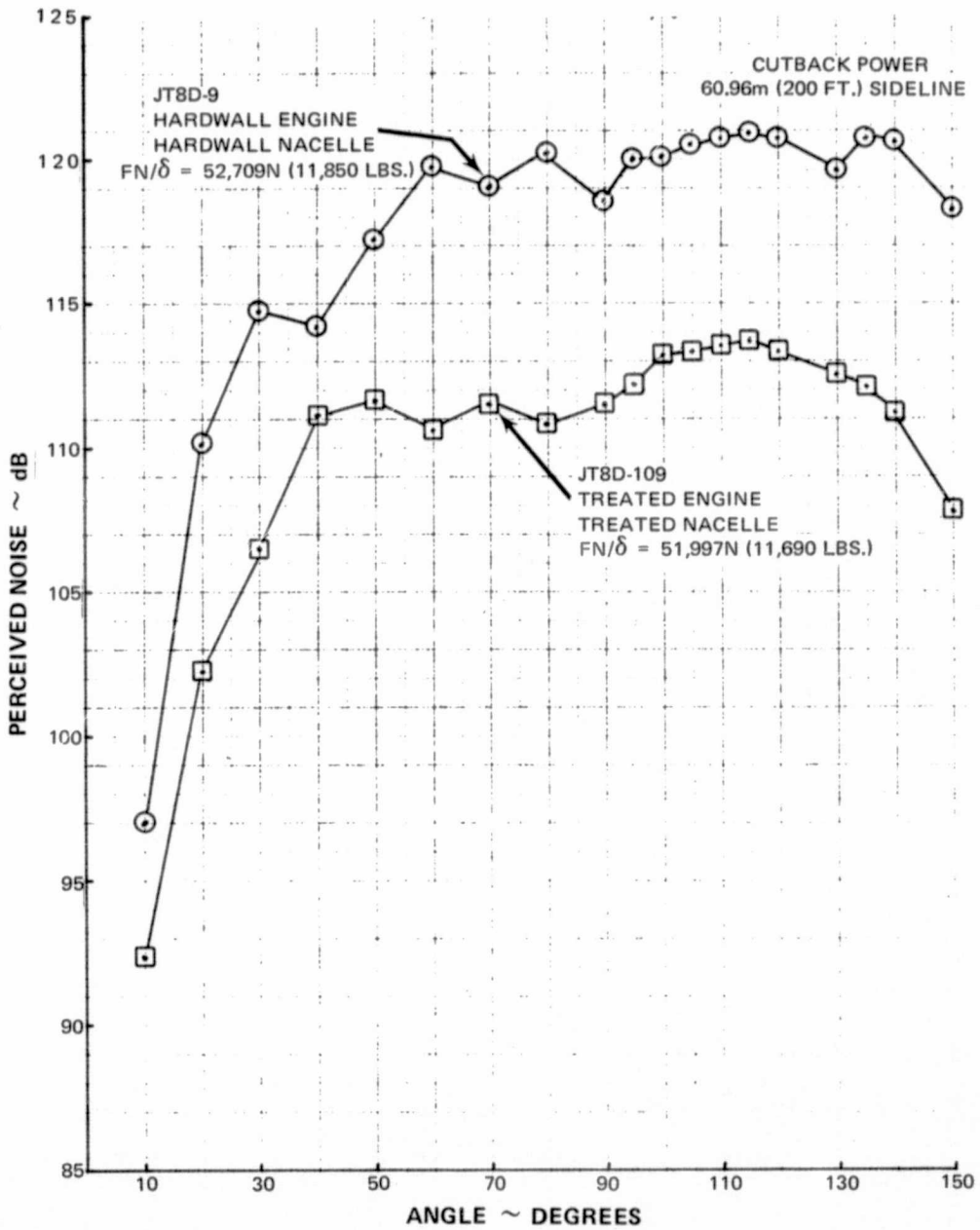

Figure D-12 Comparison of PNdB Directivity of Current JT8D Engine and Refanned JT8D-109 Engine with Treated Nacelle ~ Cutback Power

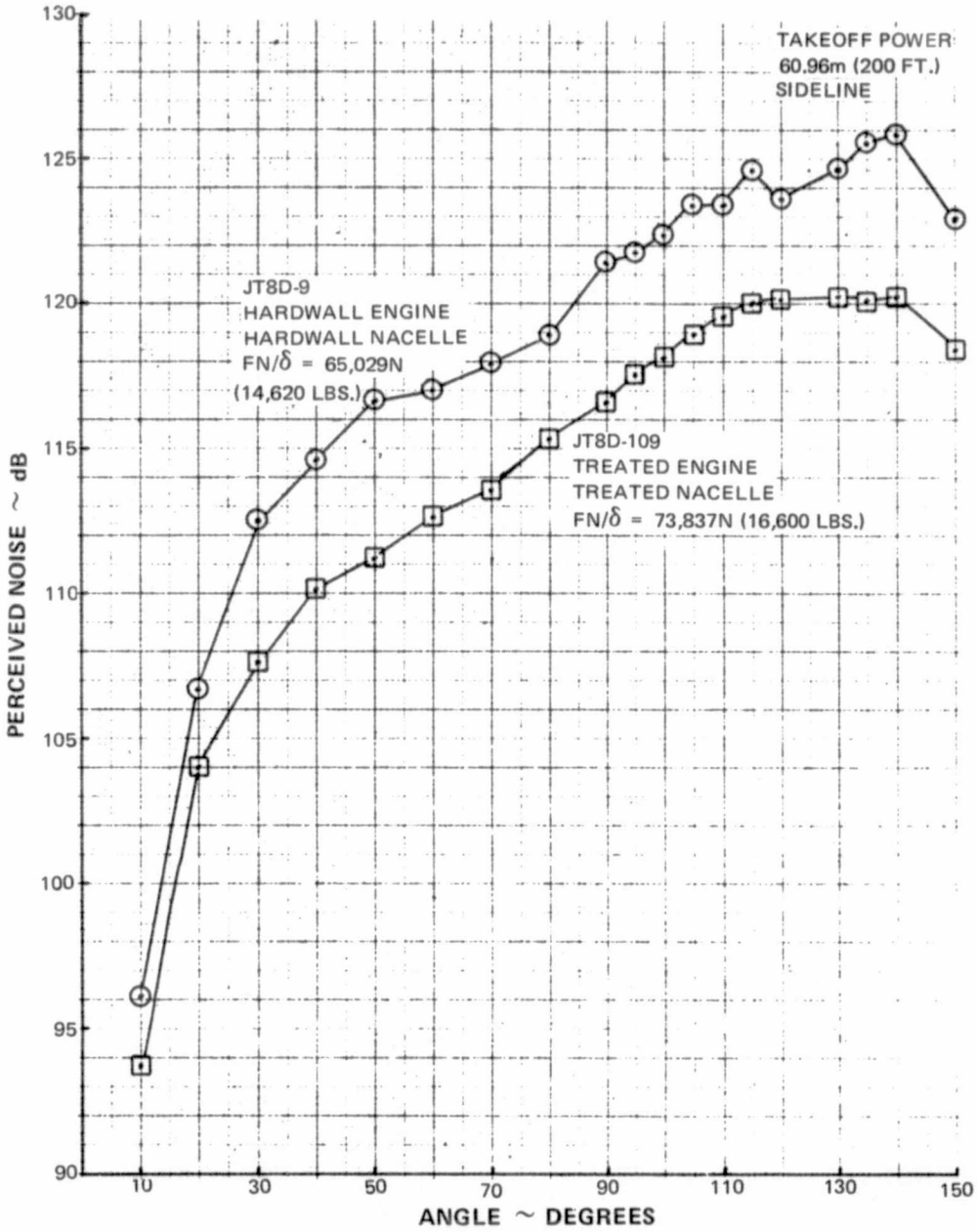

Figure D-13 Comparison of PNdB Directivity of Current JT8D Engine and Refanned JT8D-109 Engine with Treated Nacelle ~ Takeoff Power

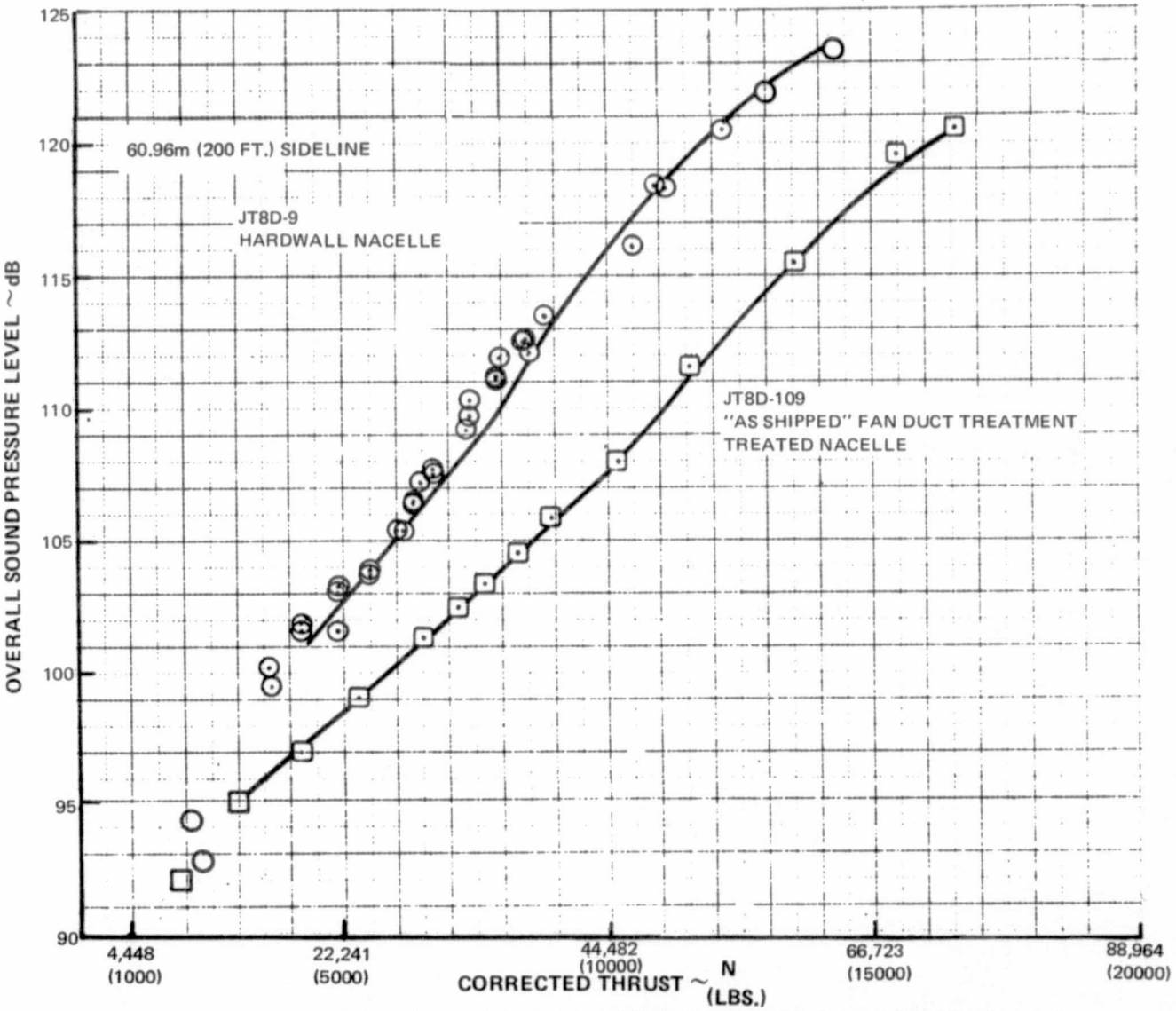

Figure D-14 Comparison of Peak Aft OASPL Levels of Current JT8D Engine and Refanned JT8D-109 Engine with Treated Nacelle

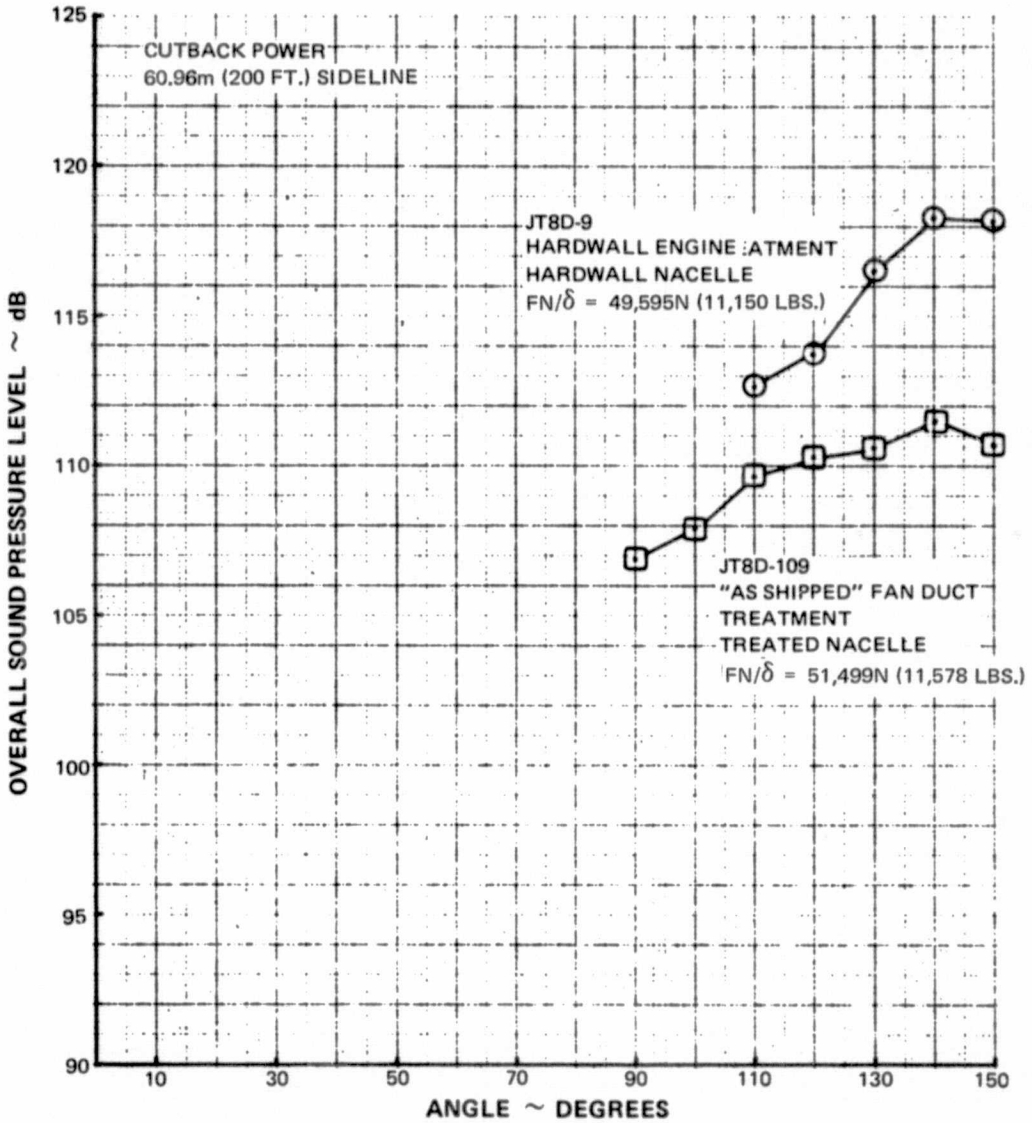

Figure D-15 Comparison of OASPL Directivity of Current JT8D Engine and Refanned JT8D-109 Engine with Treated Nacelle ~ Cutback Power

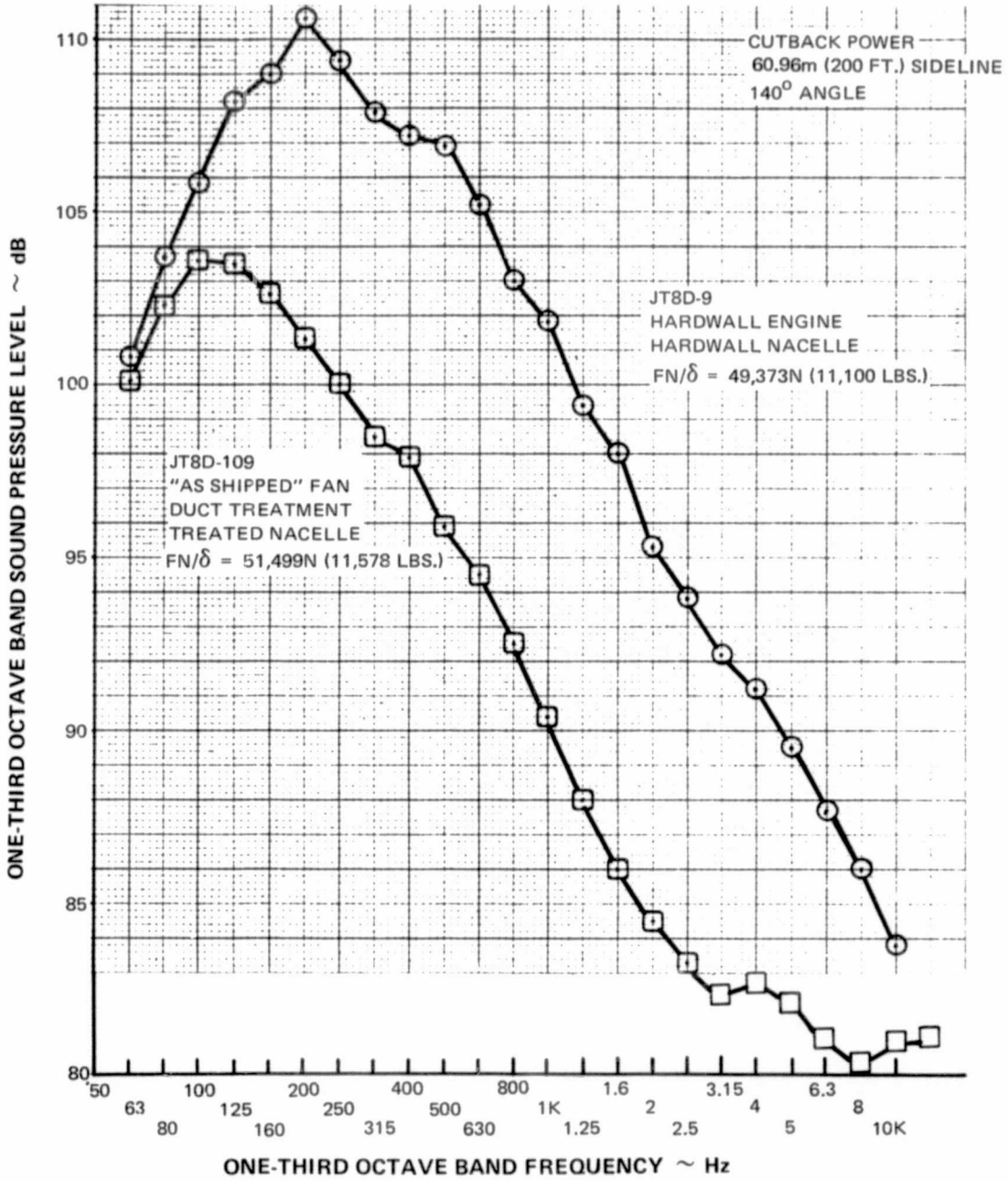

Figure D-16 Aft Quadrant Spectral Comparison of Current JT8D Engine and Refanned JT8D-109 Engine with Treated Nacelle ~ Cutback Power

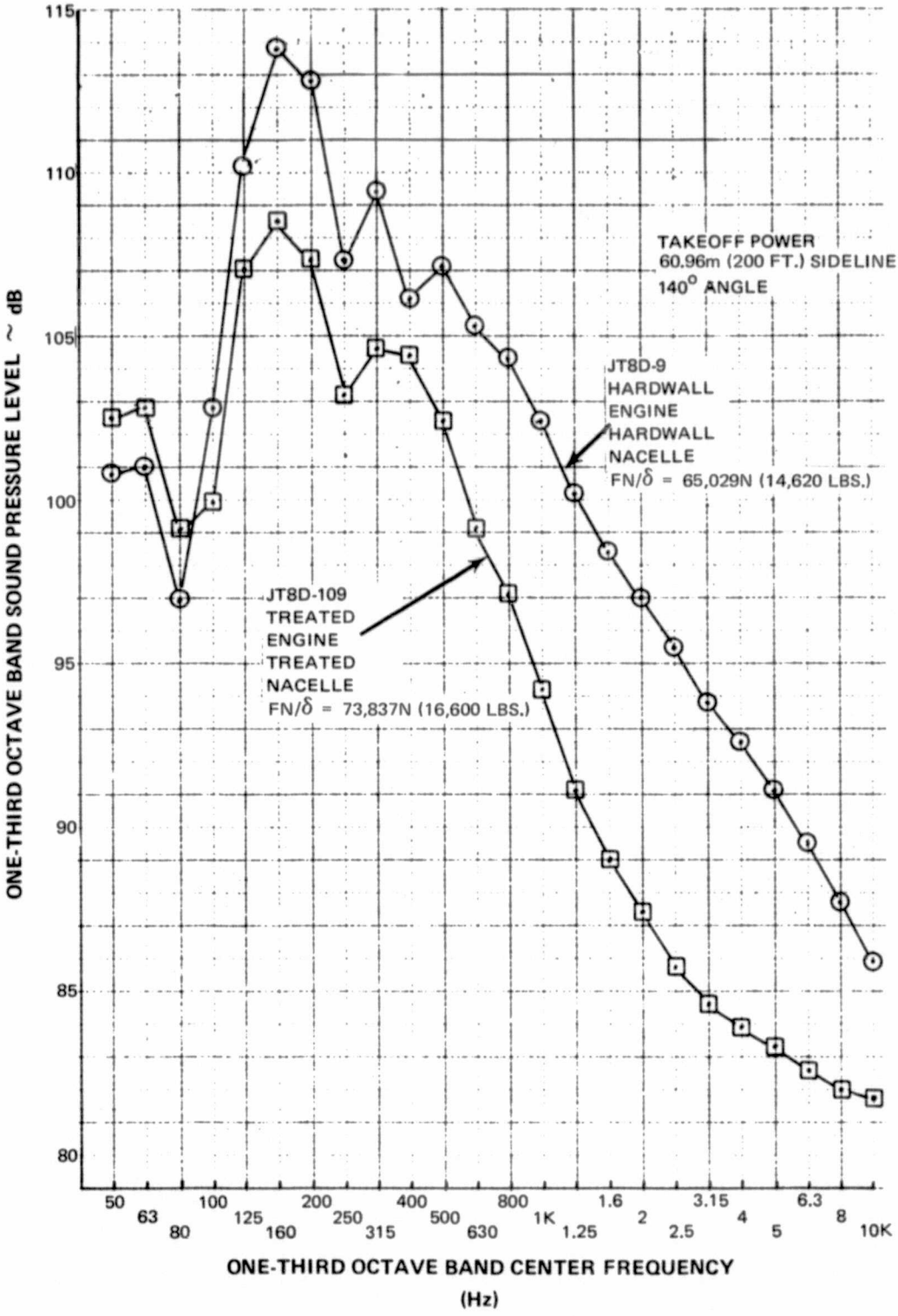

Figure D-17 Aft Quadrant Spectral Comparison of Current JT8D Engine and Refanned JT8D-109 Engine with Treated Nacelle ~ Takeoff Power

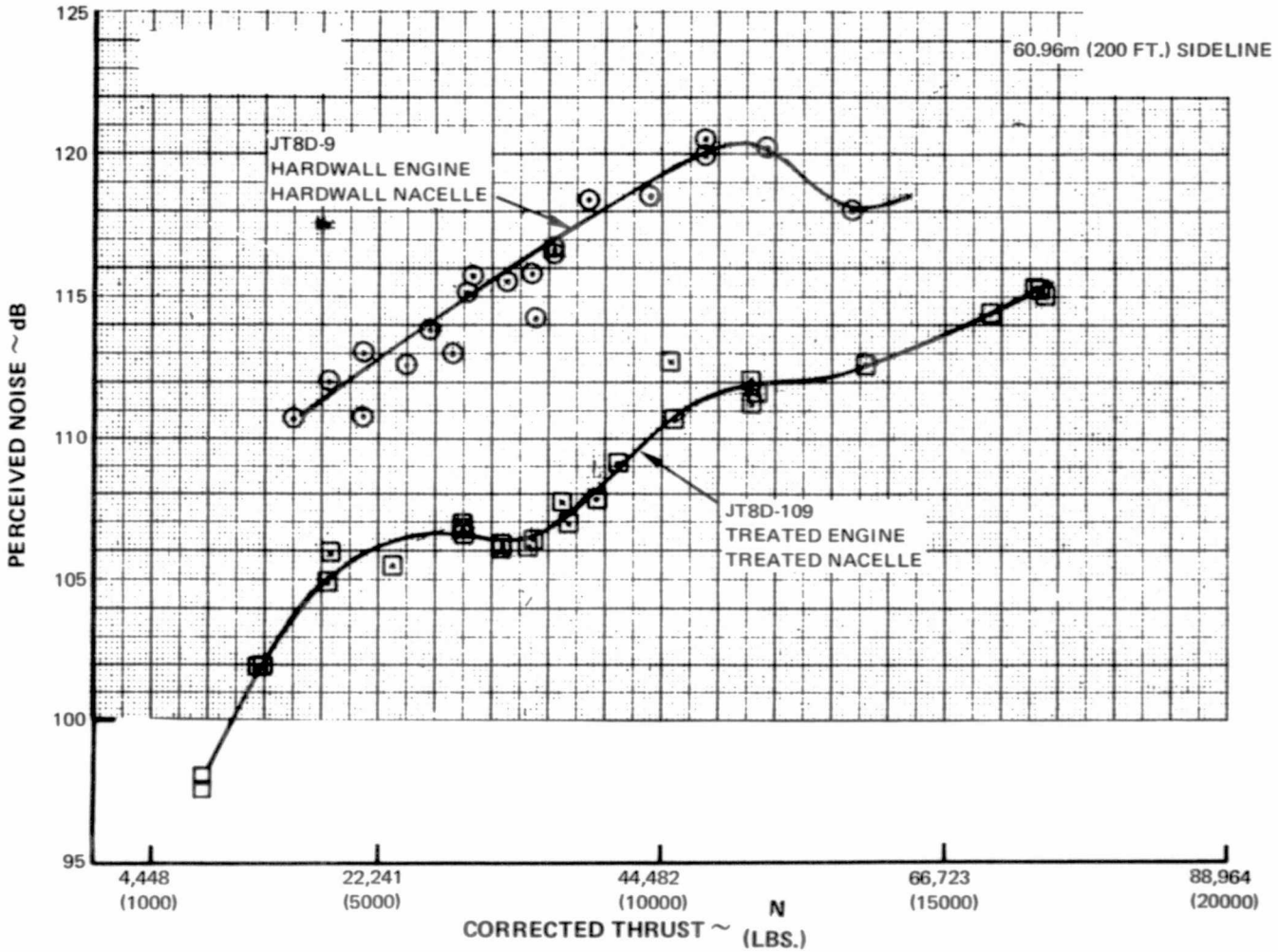

Figure D-18 Comparison of Peak Inlet PNdB Levels of Current JT8D Engine and Refanned JT8D-109 Engine with Treated Nacelle

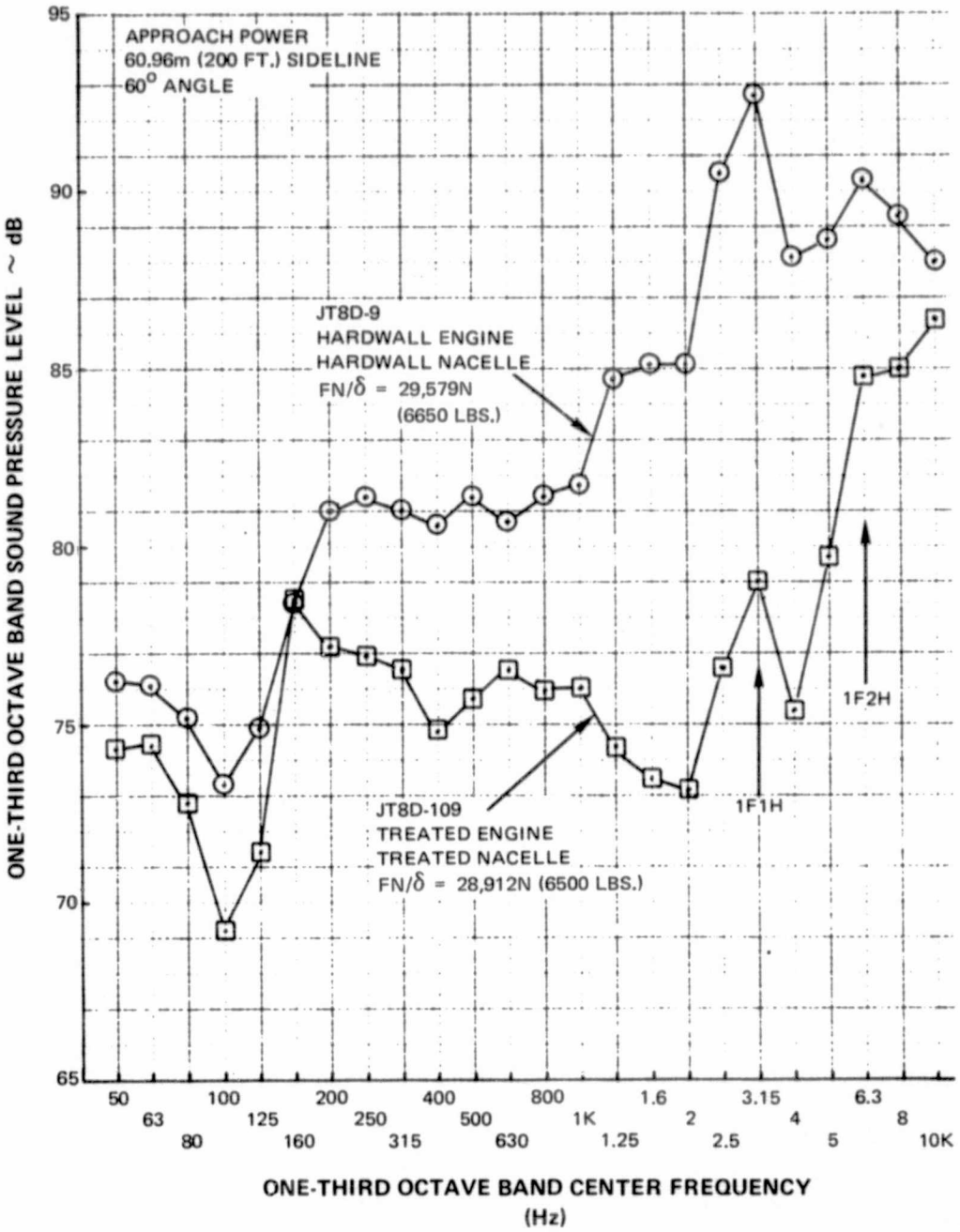

Figure D-19 Inlet Quadrant Spectral Comparison of Current JT8D Engine and Refanned JT8D-109 Engine with Treated Nacelle ~ Approach Power

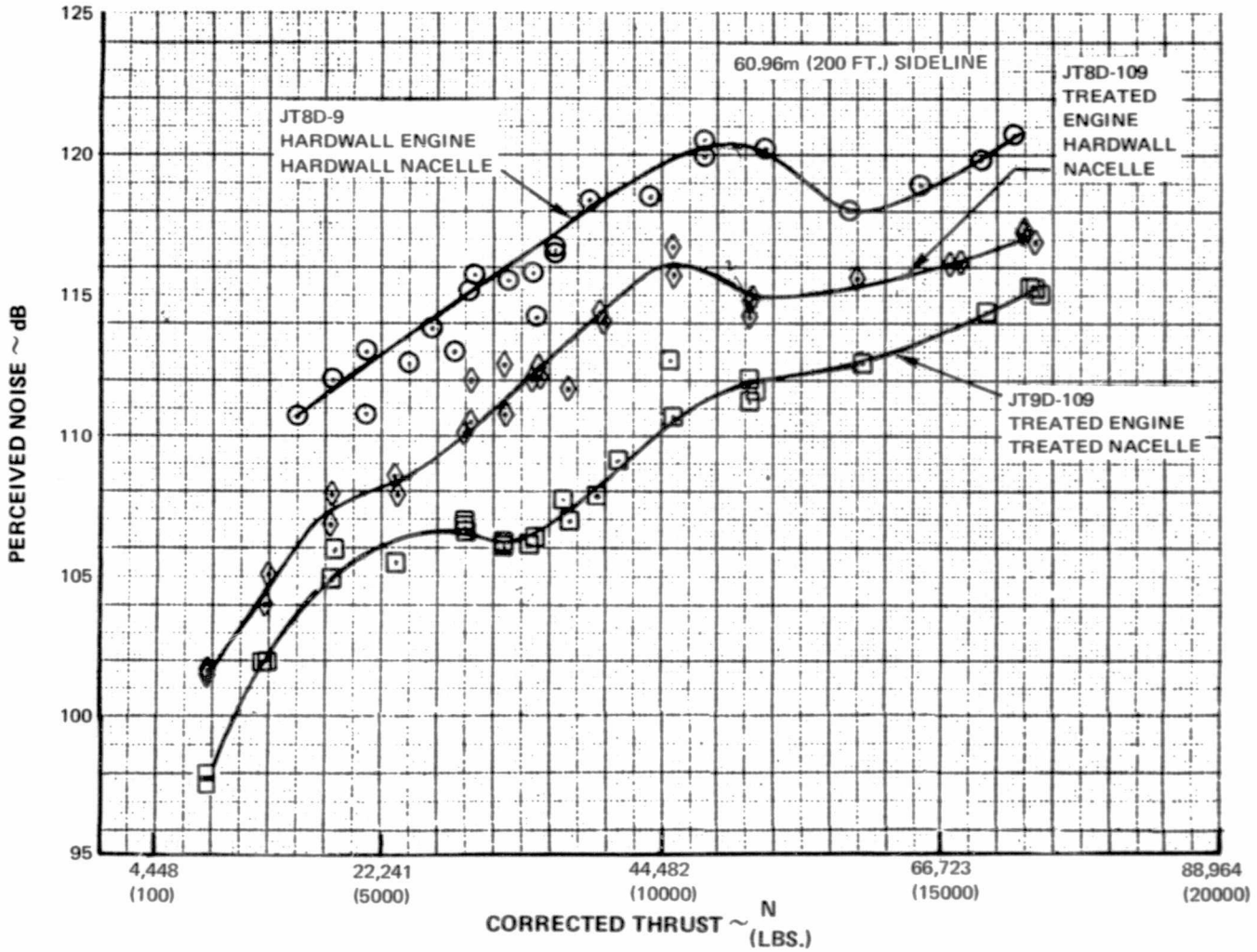

Figure D-20 Perceived Noise Comparison of Current JT8D Engine and Refanned JT8D-109 Engine

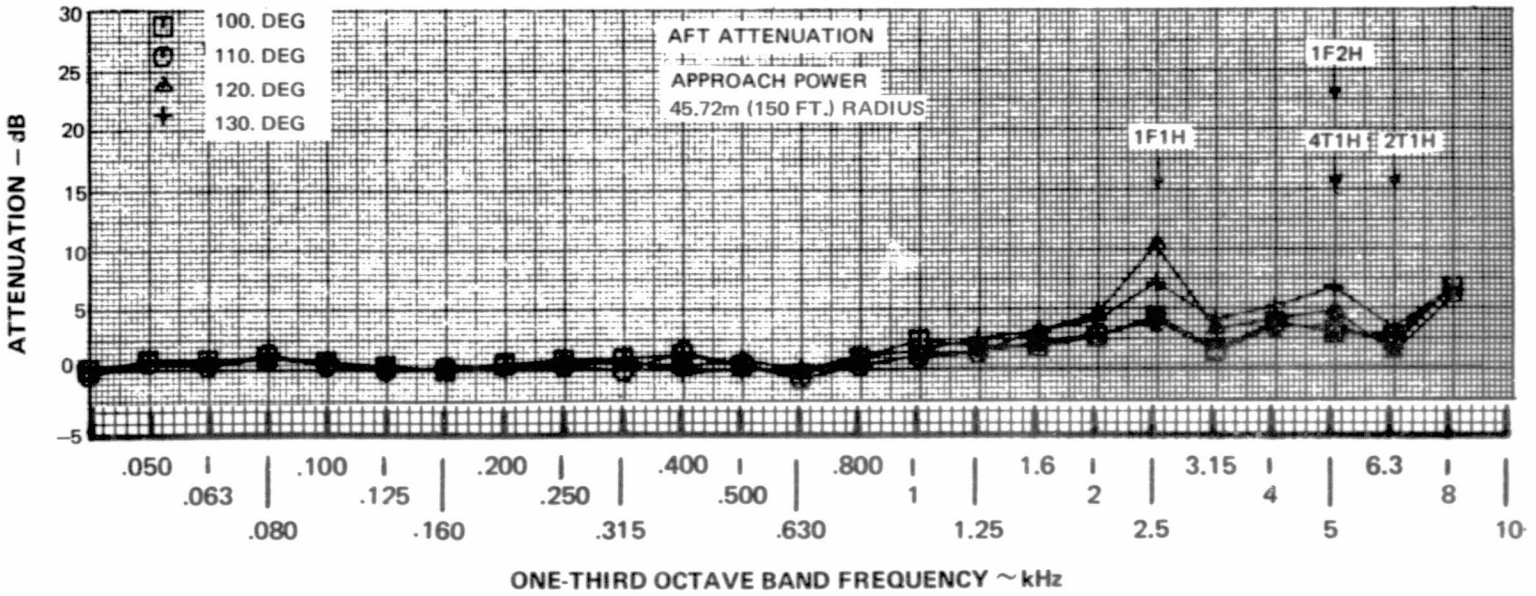

Figure D-21 One-Third Octave Band Aft Quadrant Attenuation Due to Fan Duct Treatment ~ Approach Power

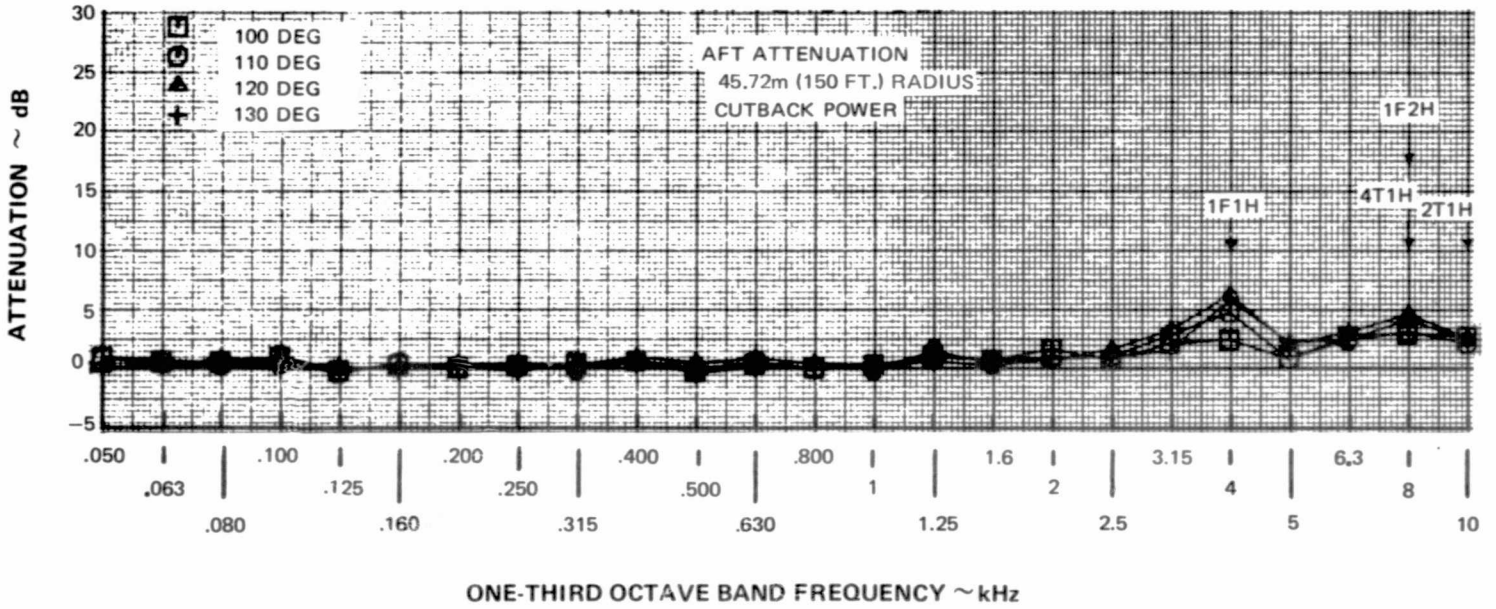

Figure D-22 One-Third Octave Band Aft Quadrant Attenuation Due to Fan Duct Treatment ~ Cutback Power

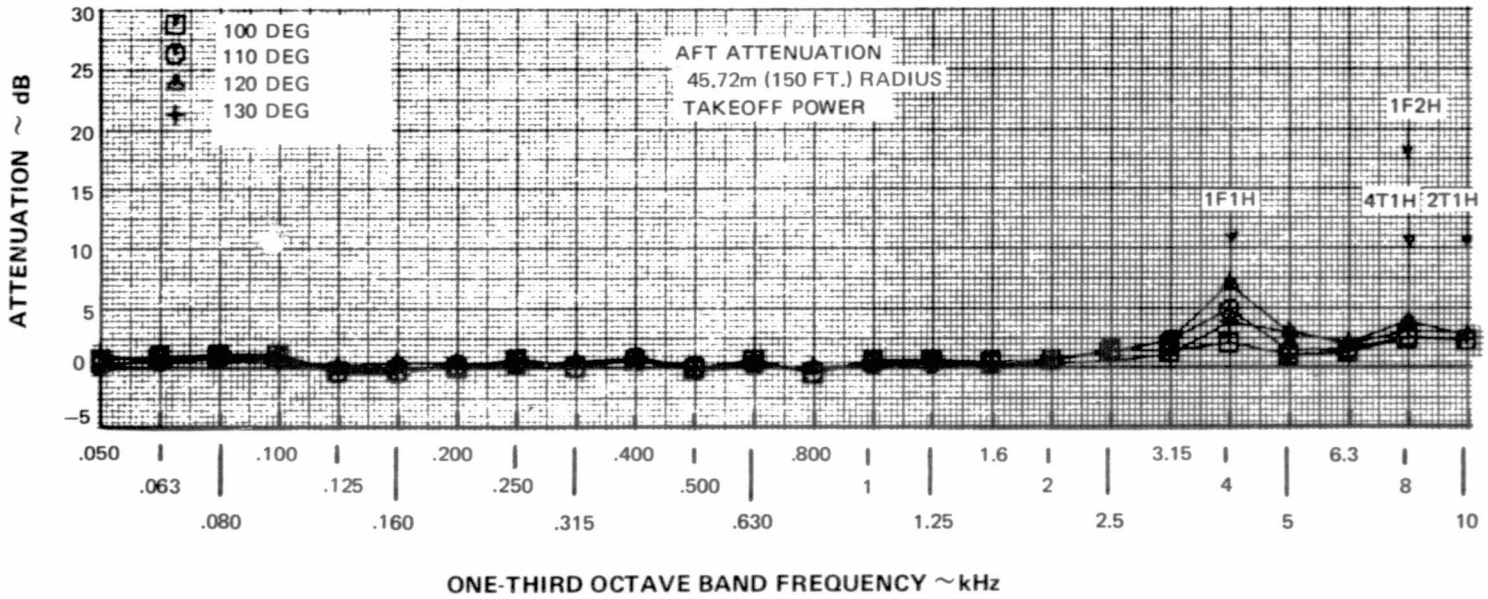

Figure D-23 One-Third Octave Band Aft Quadrant Attenuation Due to Fan Duct Treatment ~ Takeoff Power

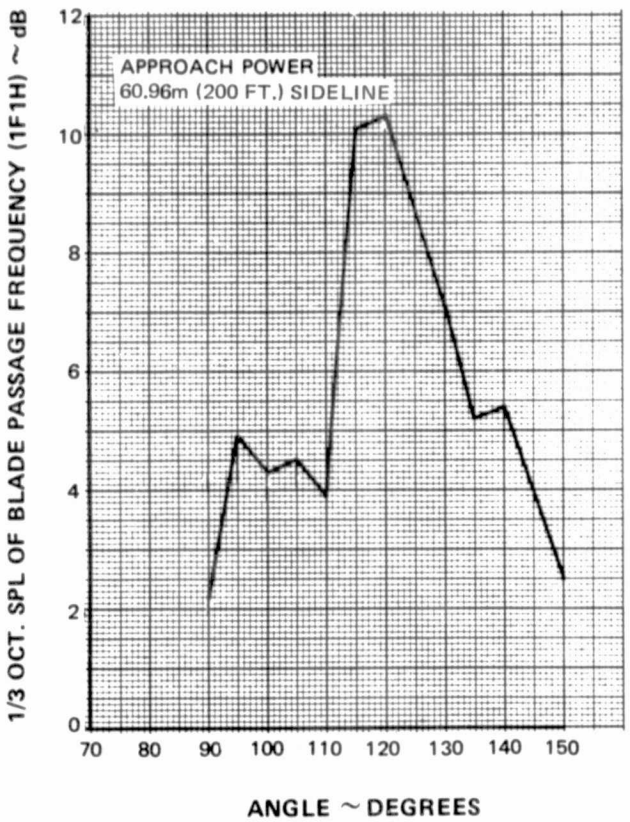

Figure D-24 One-Third Octave Band Attenuation of Blade Passage Frequency Tone (1F1H) Due to Fan Duct Treatment ~ Approach Power

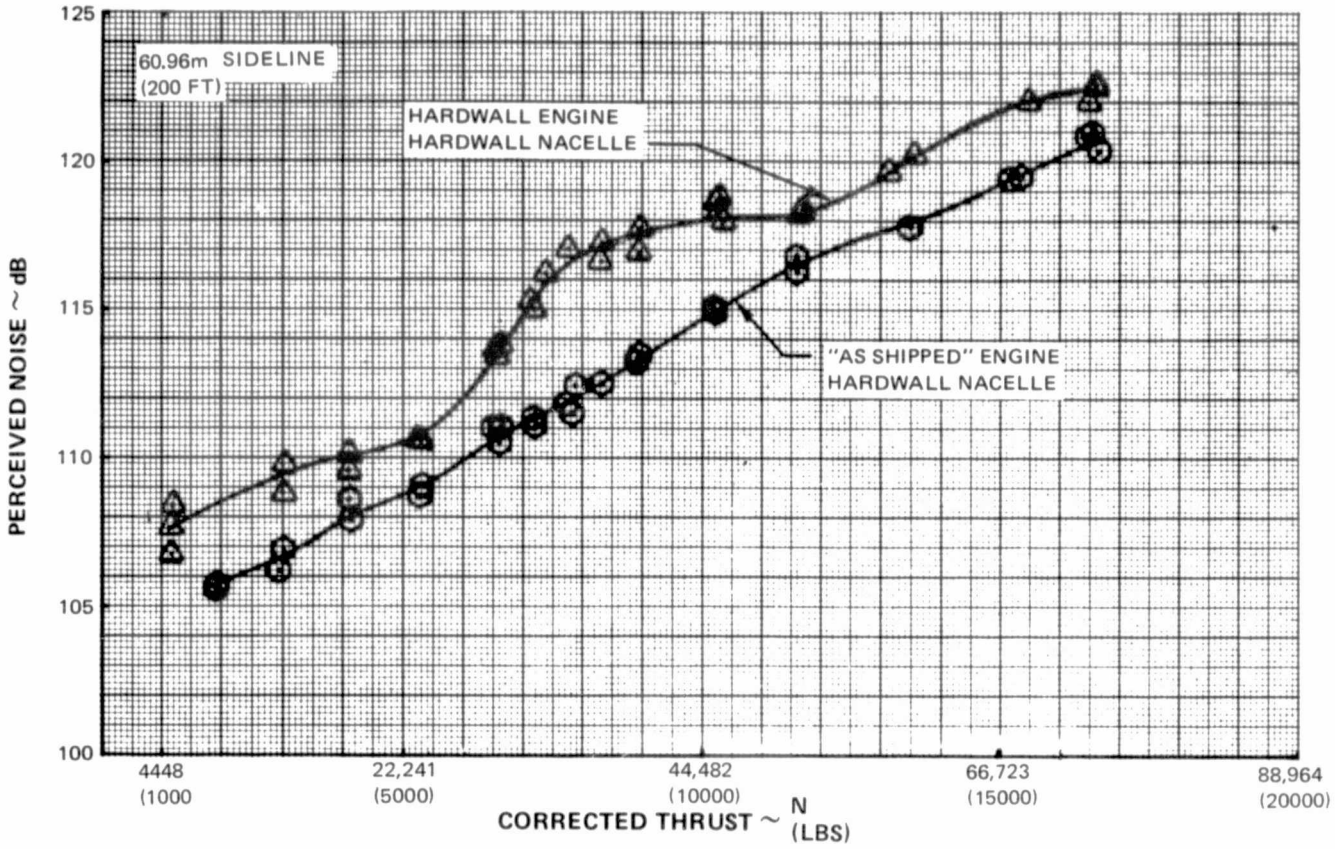

Figure D-25 Effect of Fan Duct Treatment on Measured Noise Levels at Angle of Peak Aft Noise

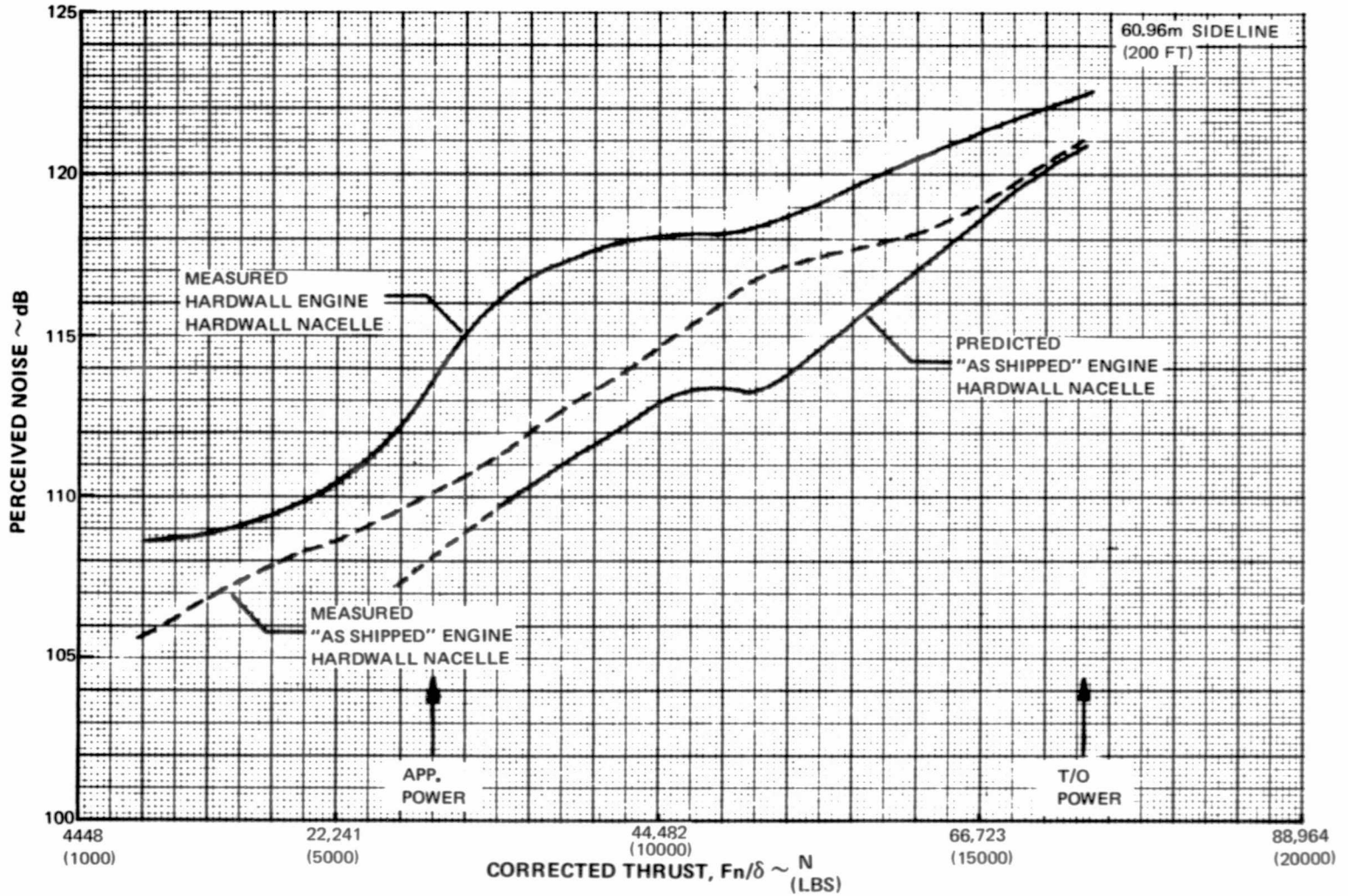

Figure D-26 Effect of Fan Duct Treatment on Measured Noise Levels at Angle of Peak Aft Noise Compared to Predicted Noise Levels

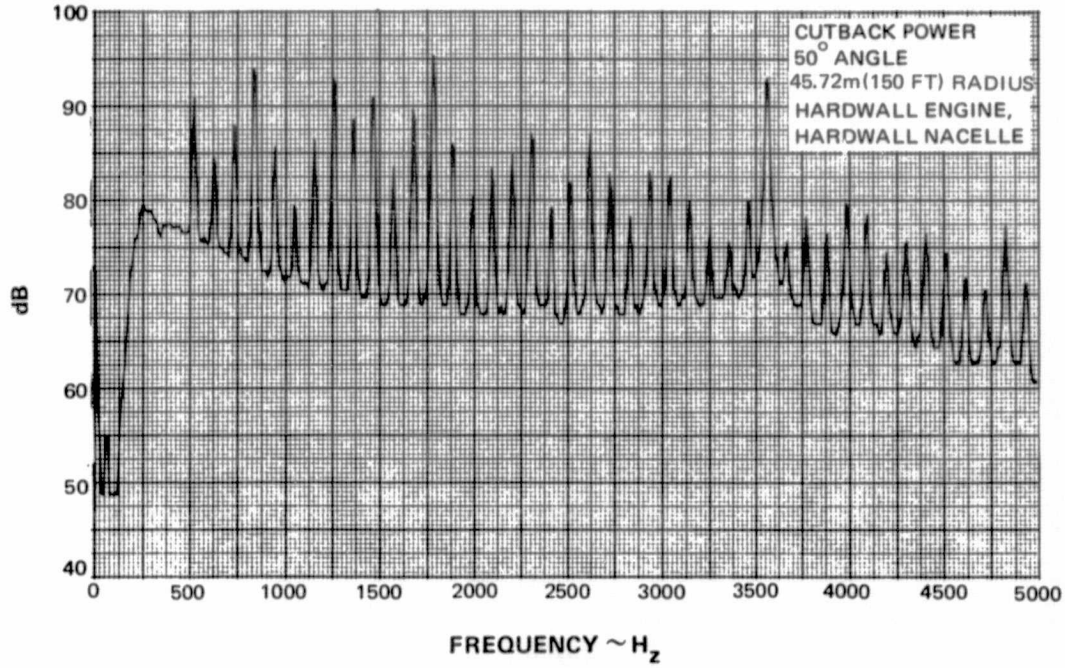

Figure D-27

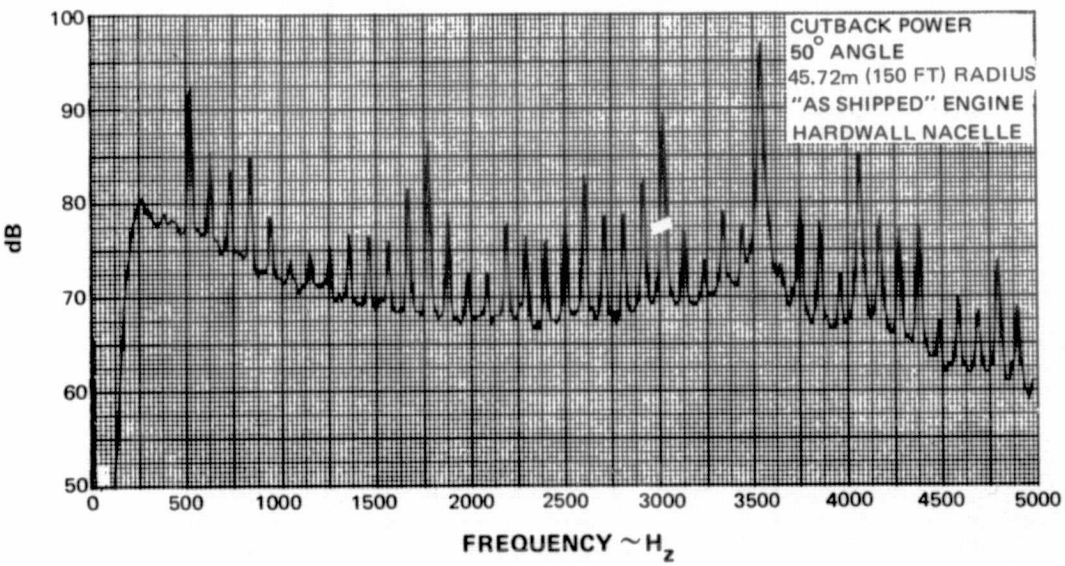

Figure D-28 JT8D-109 Inlet Narrowband Spectral Comparison Showing Effect of Acoustical Treatment ~ Cutback Power

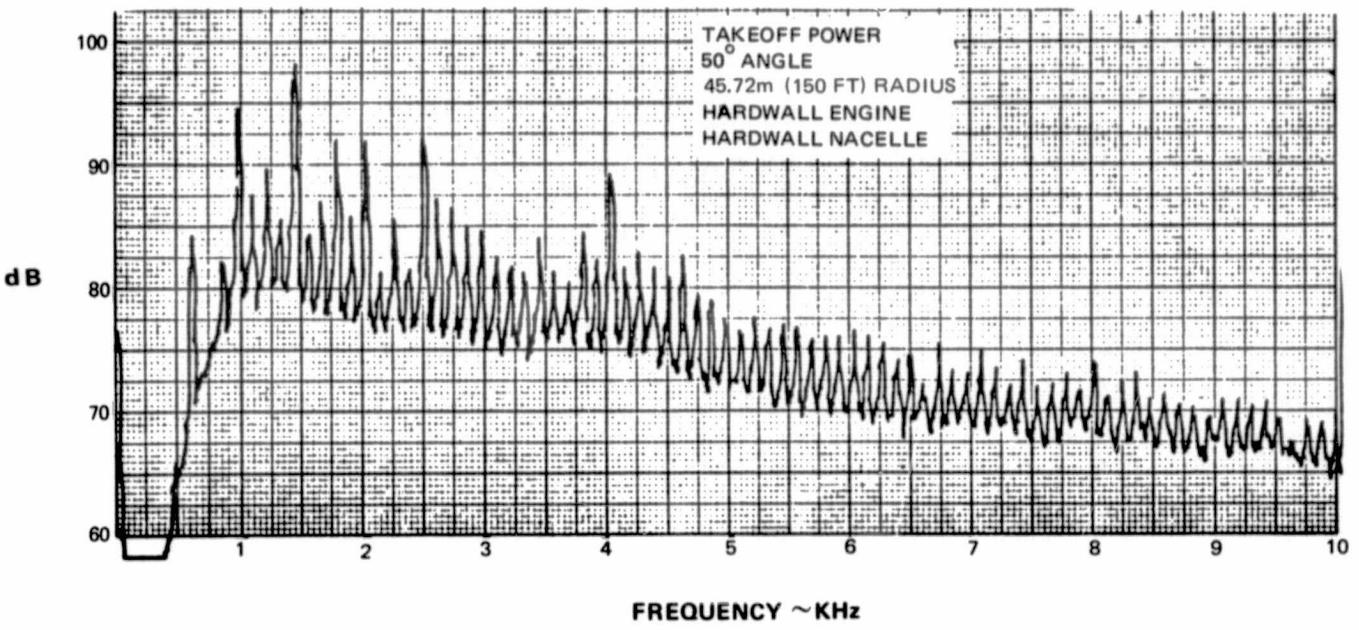

Figure D-29

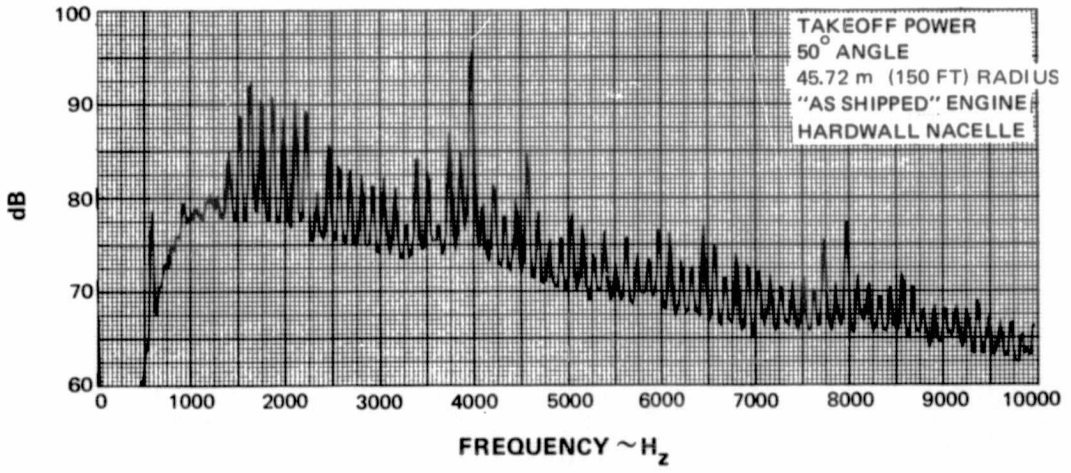

Figure D-30 JT8D-109 Inlet Narrowband Spectral Comparison Showing Effect of Acoustical Treatment ~ Takeoff Power

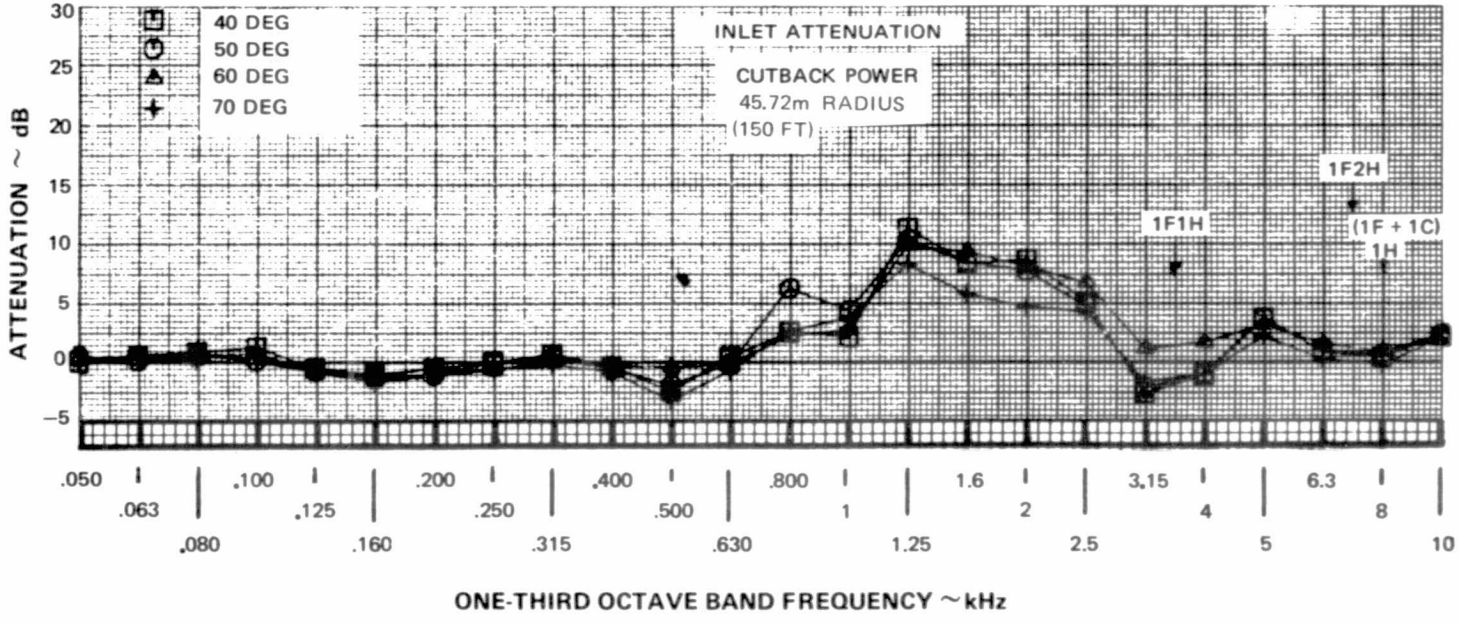

Figure D-31 Inlet Quadrant One-Third Octave Band Attenuation Due to Acoustical Treatment Between IGV and Fan ~ Cutback Power

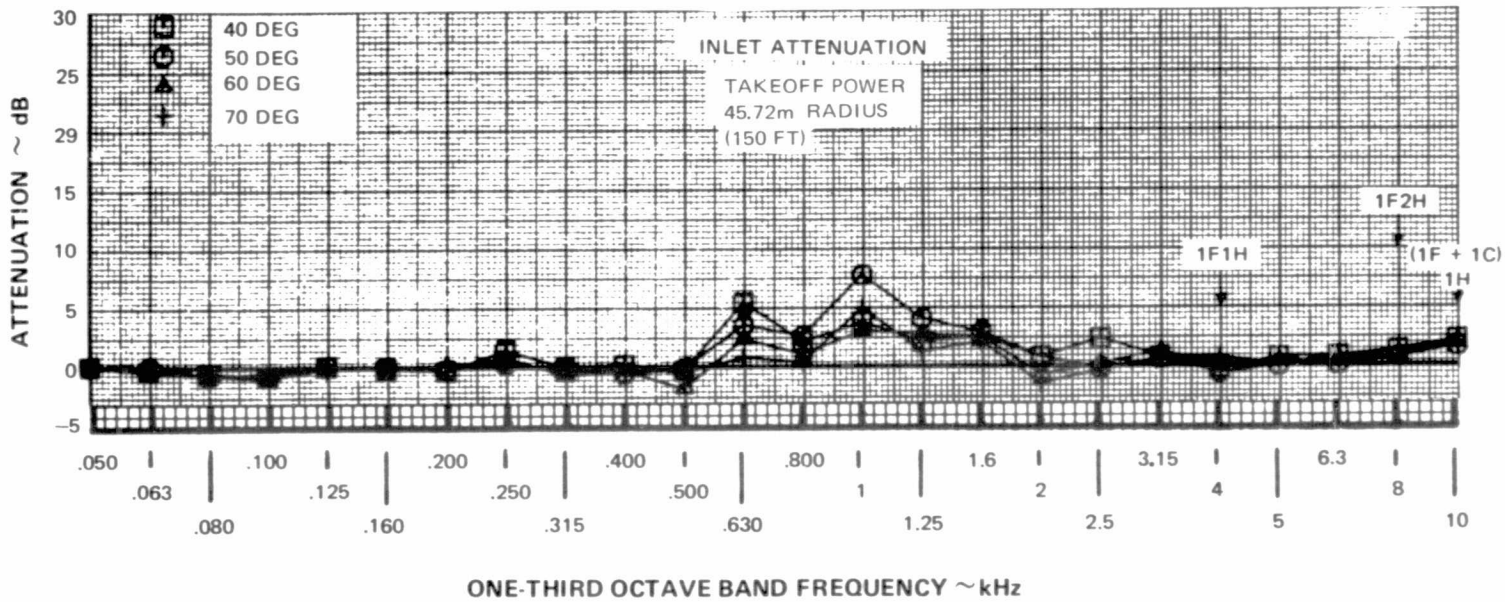

Figure D-32 Inlet Quadrant One-Third Octave Band Attenuation Due to Acoustical Treatment Between IGV and Fan ~ Takeoff Power

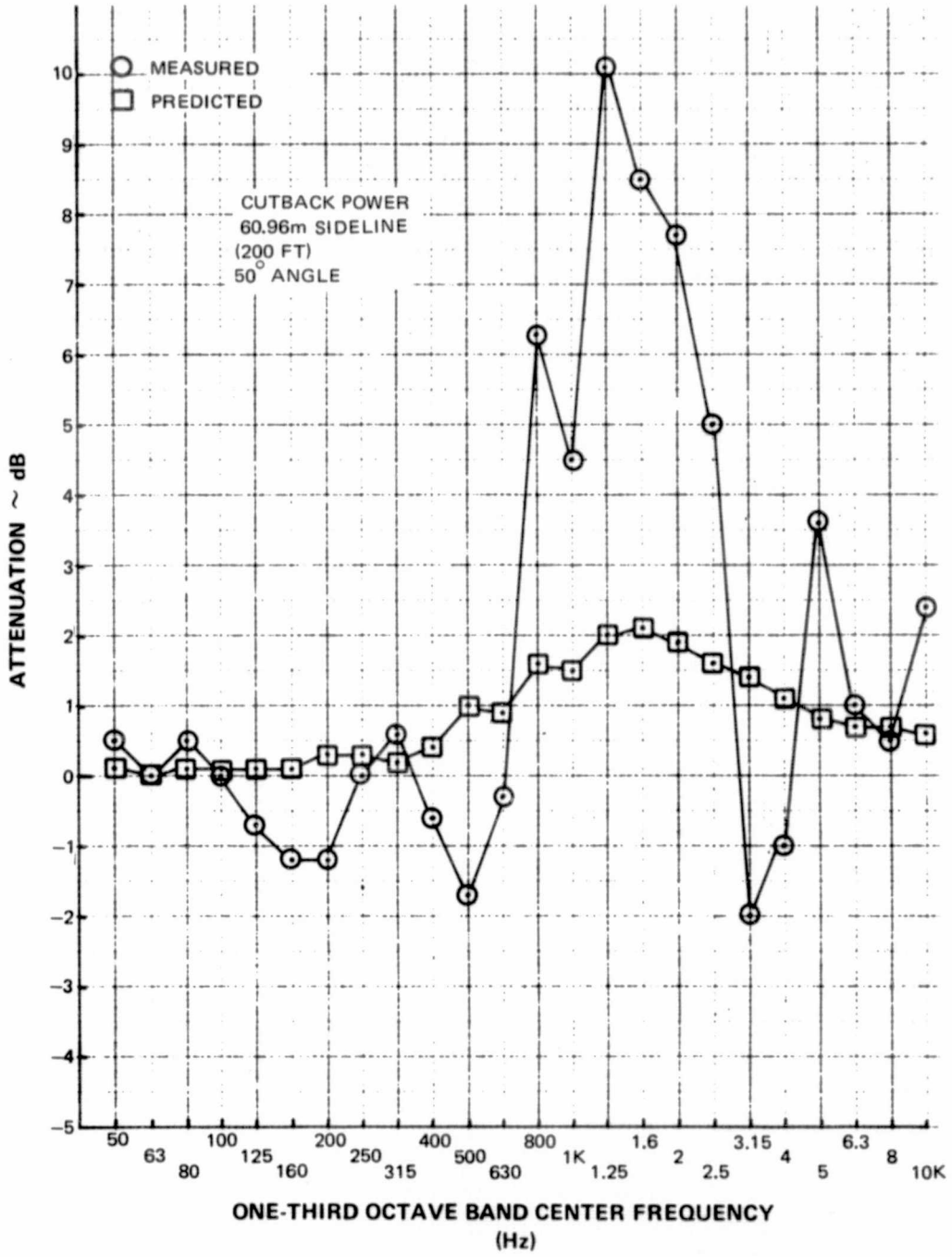

Figure D-33 Comparison of Predicted and Measured Attenuation Due to Acoustical Treatment Between IGV and Fan ~ Cutback Power

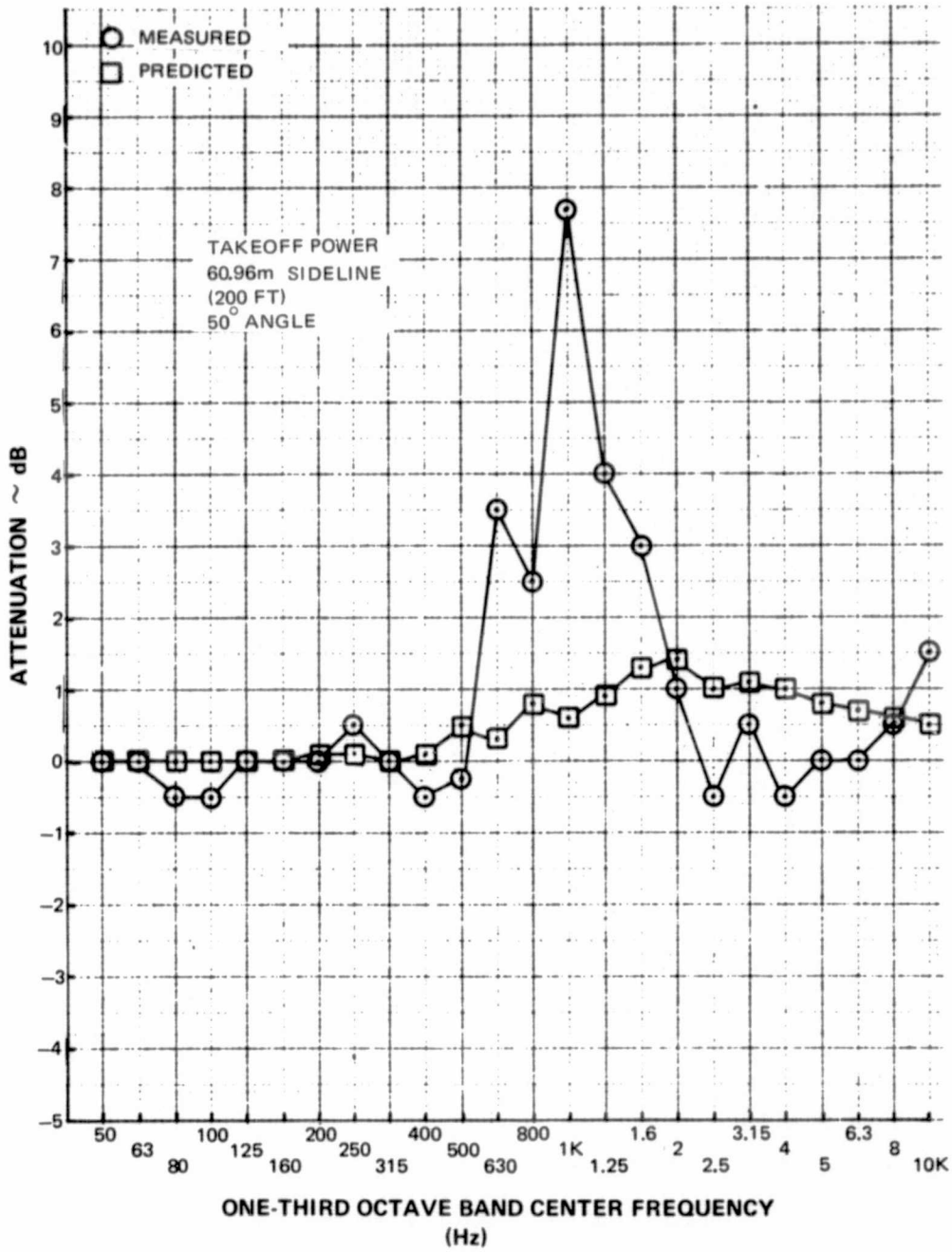

Figure D-34 Comparison of Predicted and Measured Attenuation Due to Acoustical Treatment Between IGV and Fan ~ Takeoff Power

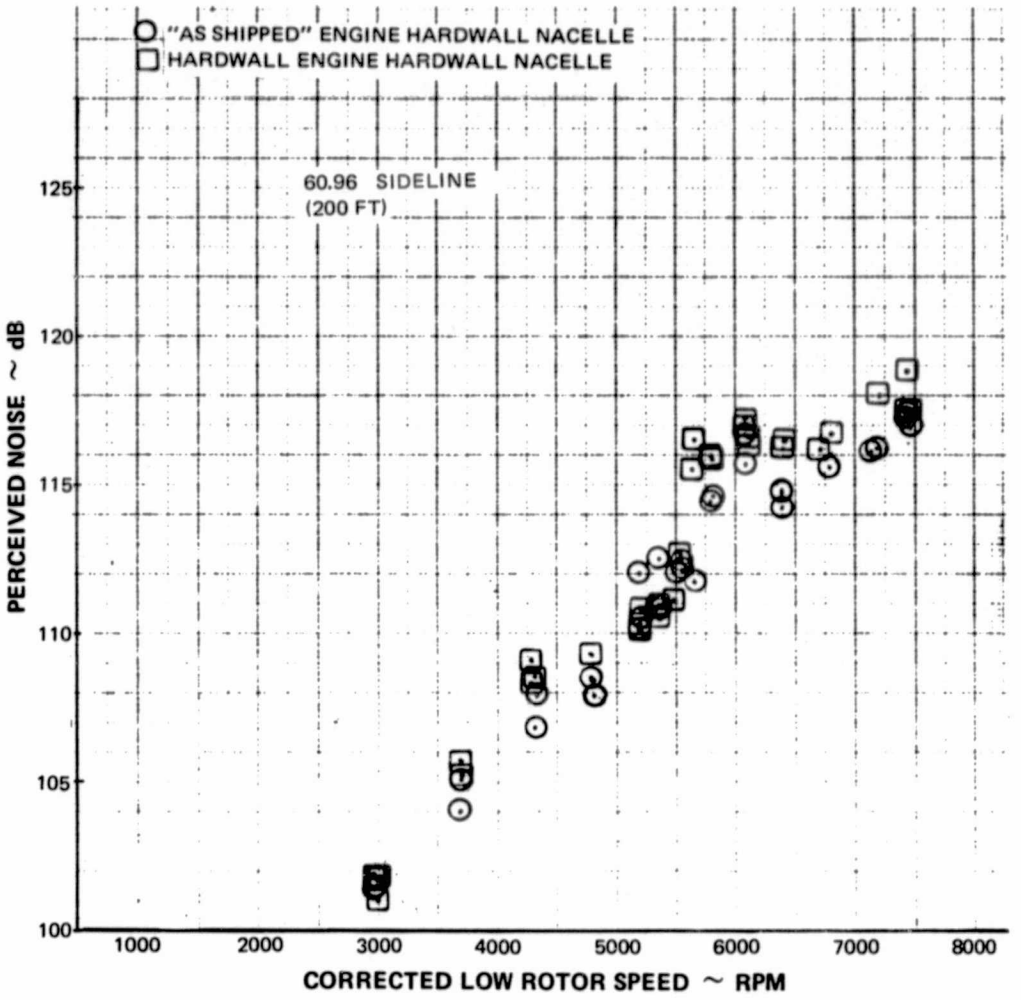

Figure D-35 Effect of Acoustical Treatment Between IGV and Fan on Peak Inlet PNdB

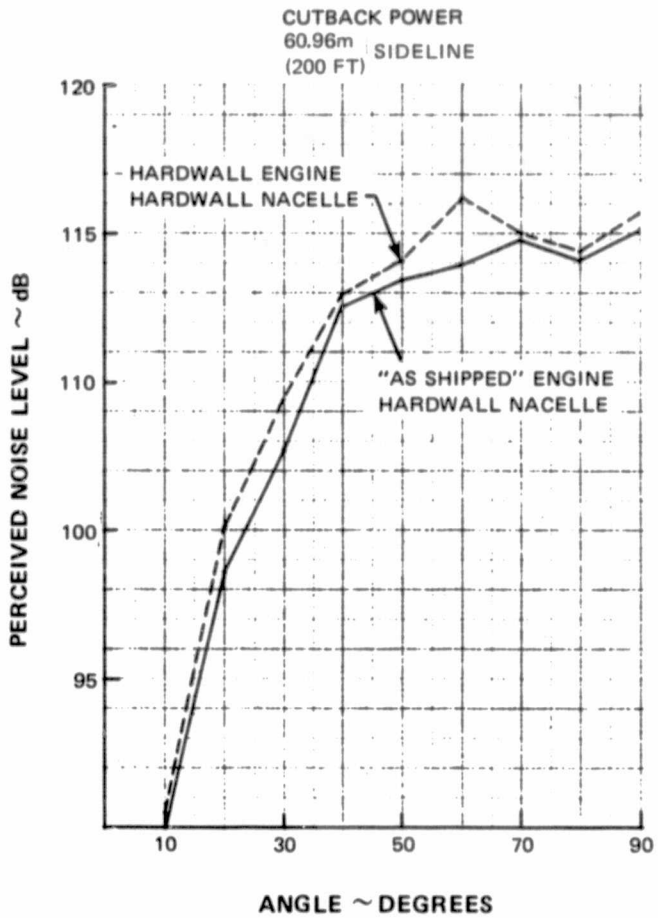

Figure D-36 Effect of Acoustical Treatment Between IGV and Fan on Peak Inlet PNdB Directivity - Cutback Power

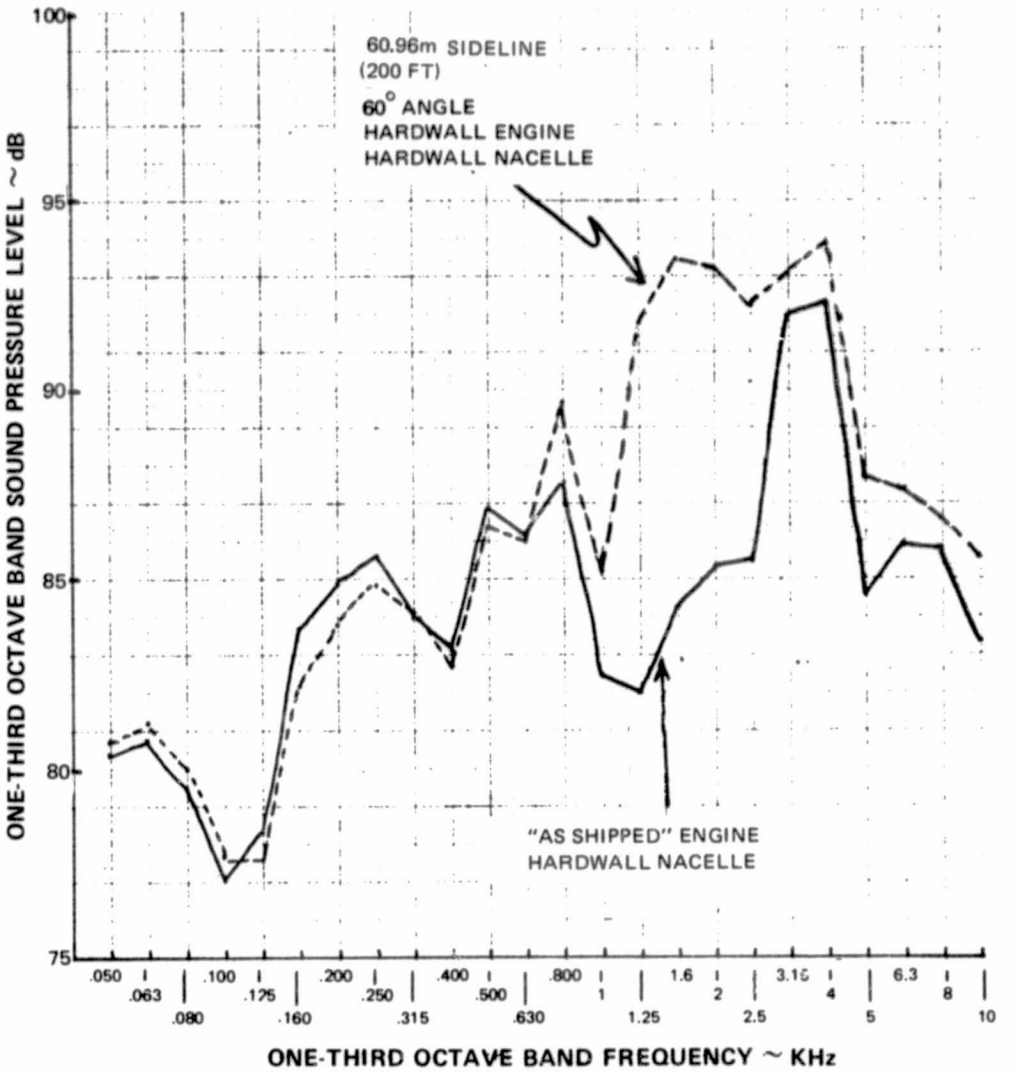

Figure D-37 Effect of Acoustical Treatment Between IGV and Fan on Inlet Spectra Cutback Power

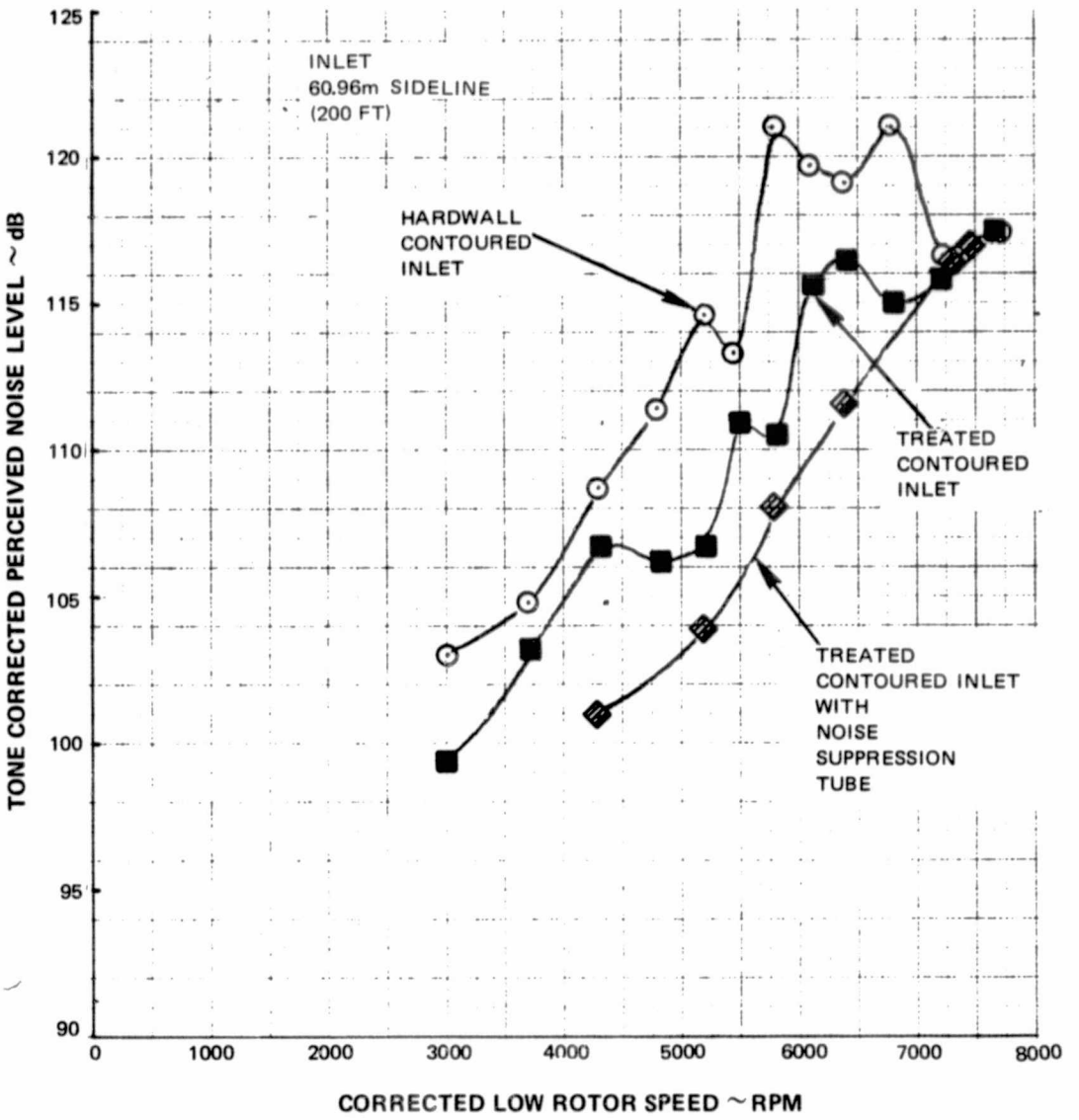

Figure D-38 Effect of Treated Inlet and Noise Suppression Tube on Peak Inlet Noise Level (Tone Corrected)

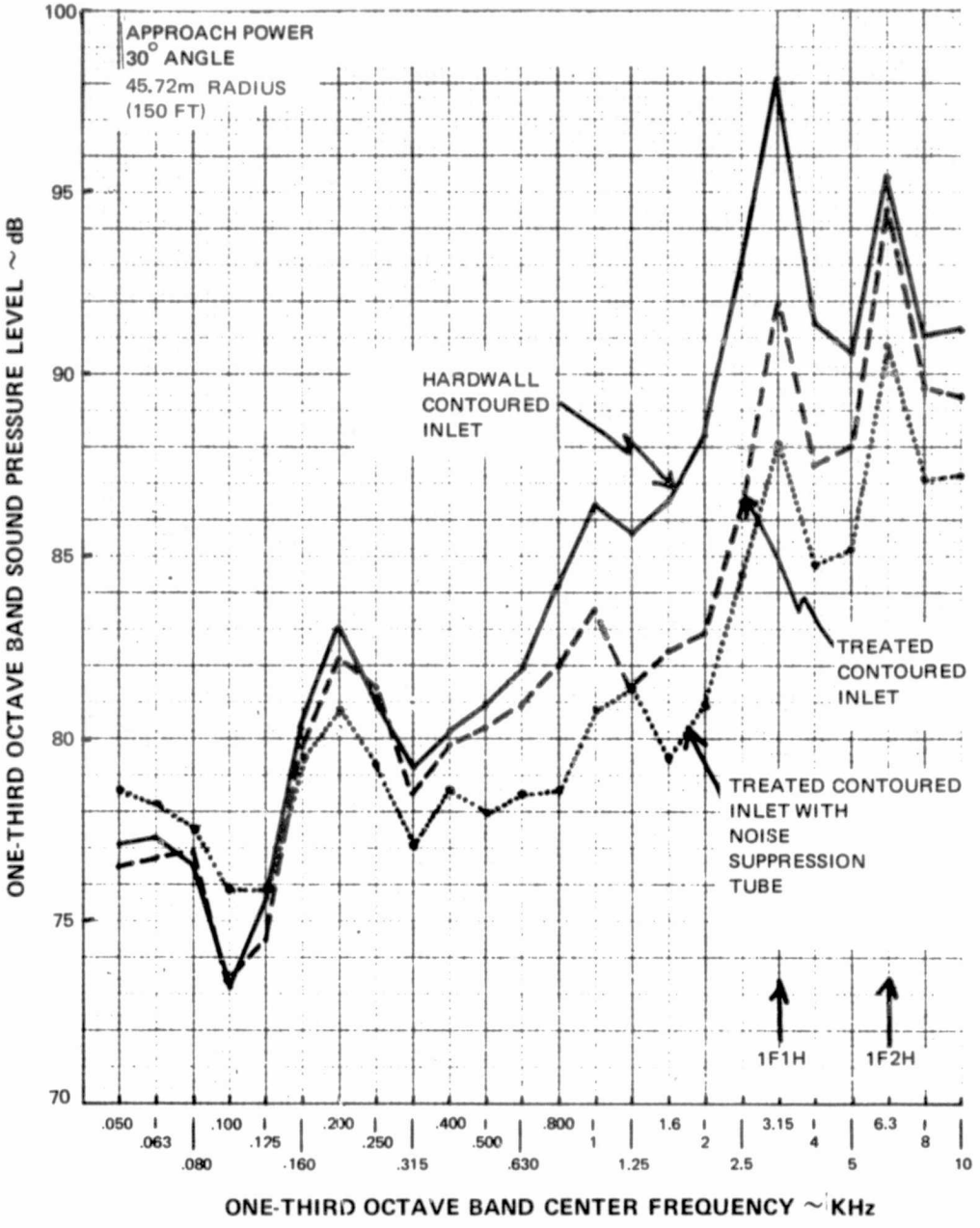

Figure D-39 Effect of Treated Inlet and Noise Suppression Tube on Inlet Noise Level ~ Approach Power, 30° Angle

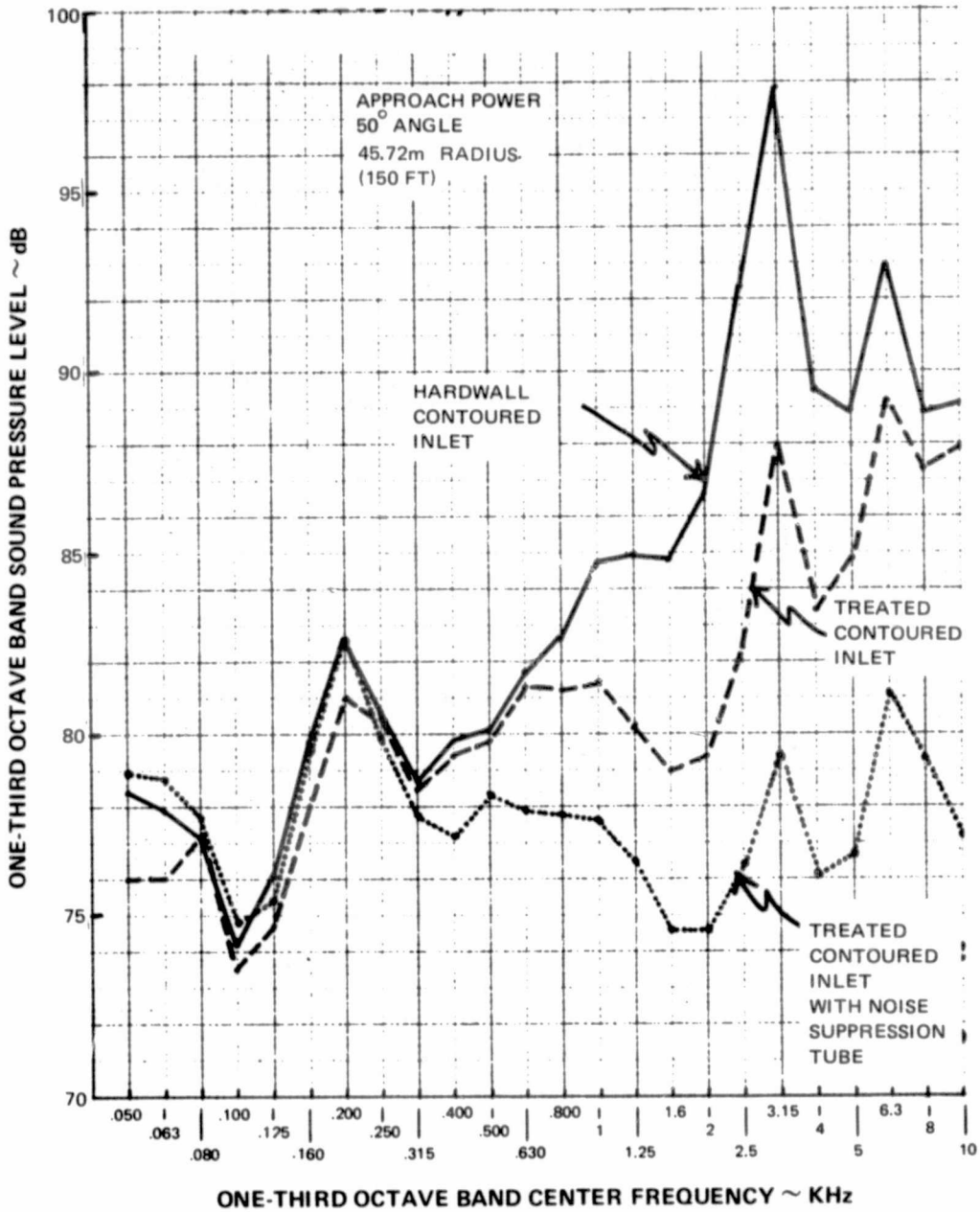

Figure D-40 Effect of Treated Inlet and Noise Suppression Tube on Inlet Noise Level ~ Approach Power, 50° Angle

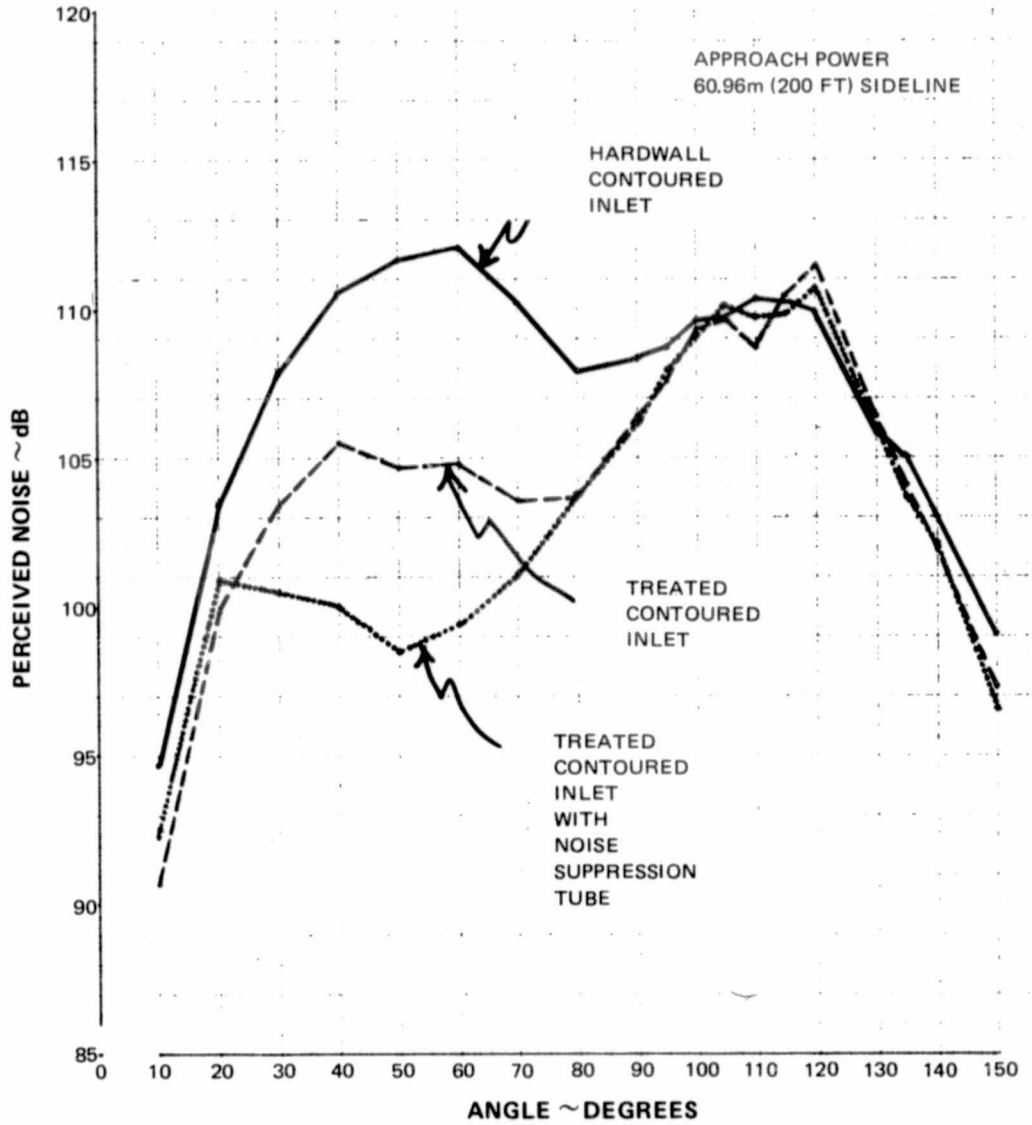

Figure D-41 Effect of Treated Inlet and Noise Suppression Tube on Perceived Noise Level Directivity ~ Approach Power

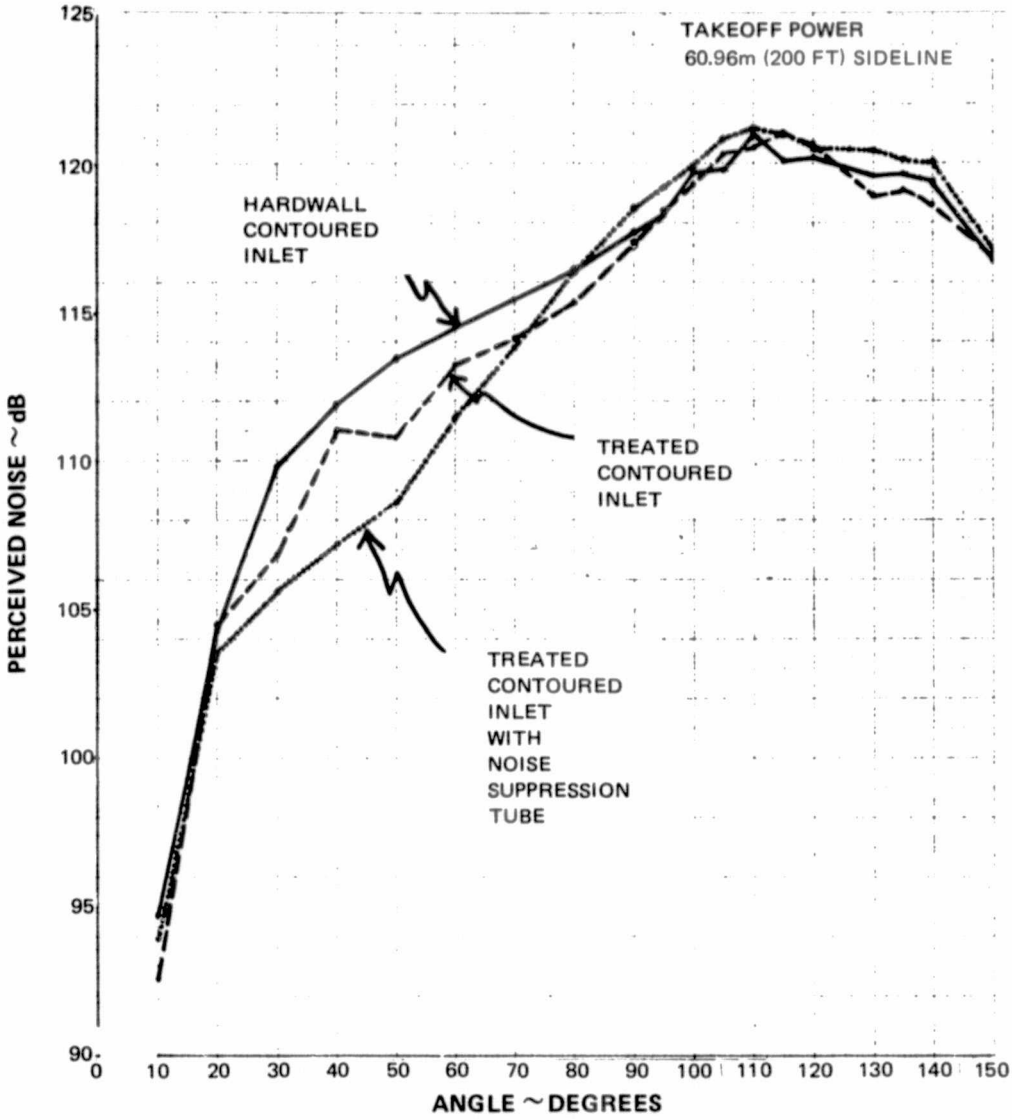

Figure D-42 Effect of Treated Inlet and Noise Suppression Tube on Perceived Noise Level Directivity ~ Takeoff Power

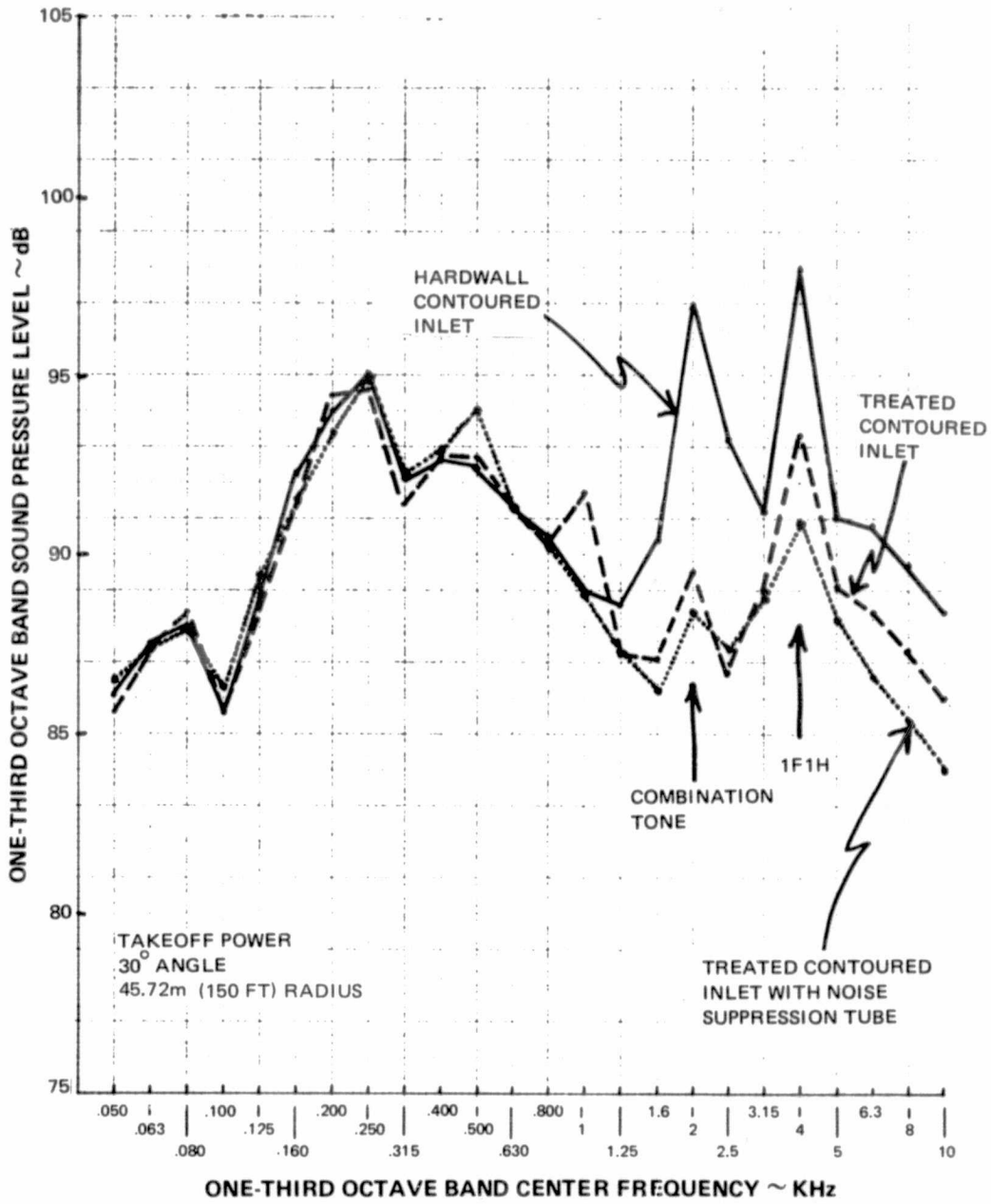

Figure D-43 Effect of Treated Inlet and Noise Suppression Tube on Inlet Noise Level ~ Takeoff Power, 30° Angle

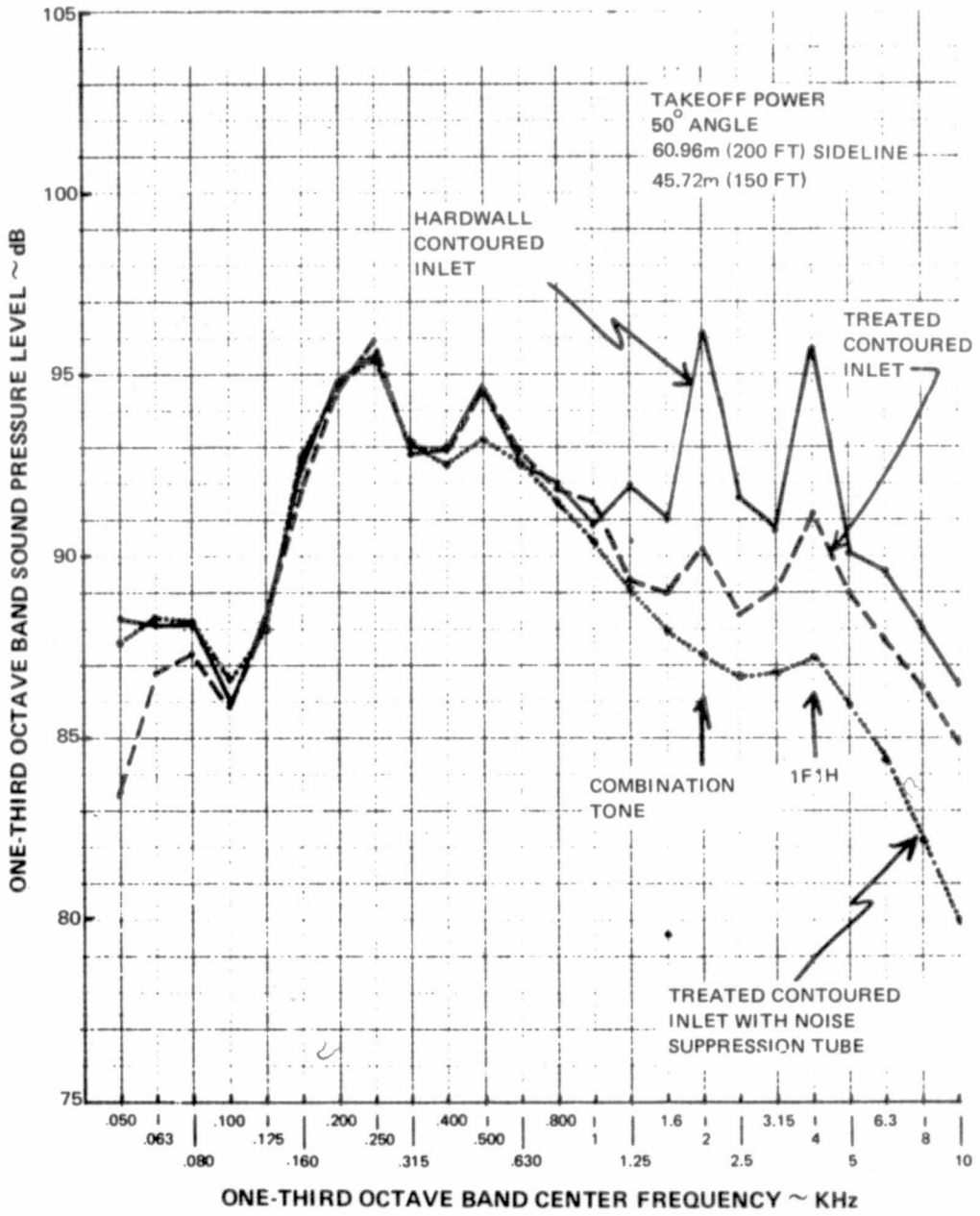

Figure D-44 Effect of Treated Inlet and Noise Suppression Tube on Inlet Noise Level ~ Takeoff Power, 50° Angle

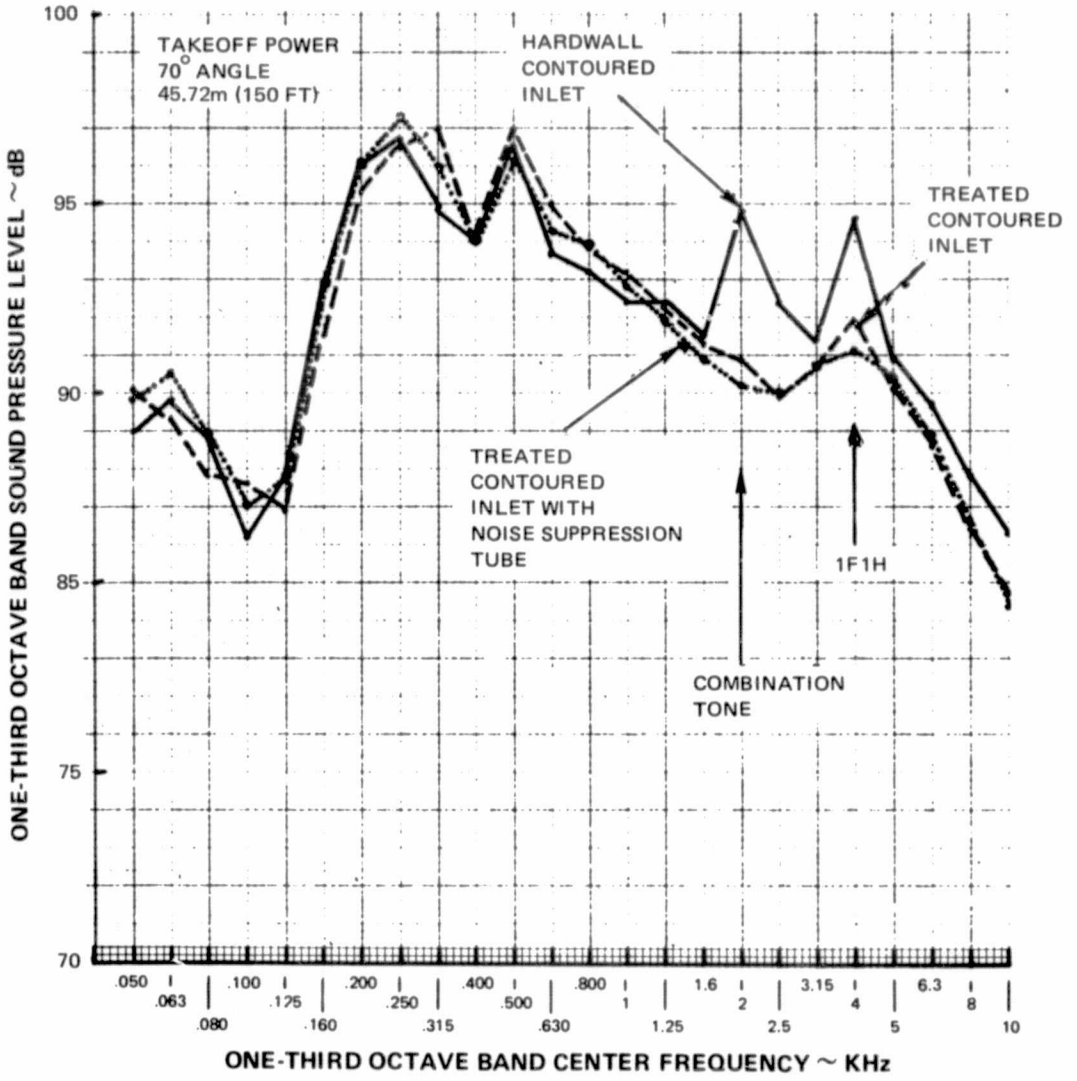

Figure D-45 Effect of Treated Inlet and Noise Suppression Tube on Inlet Noise Level ~ Takeoff Power, 70° Angle

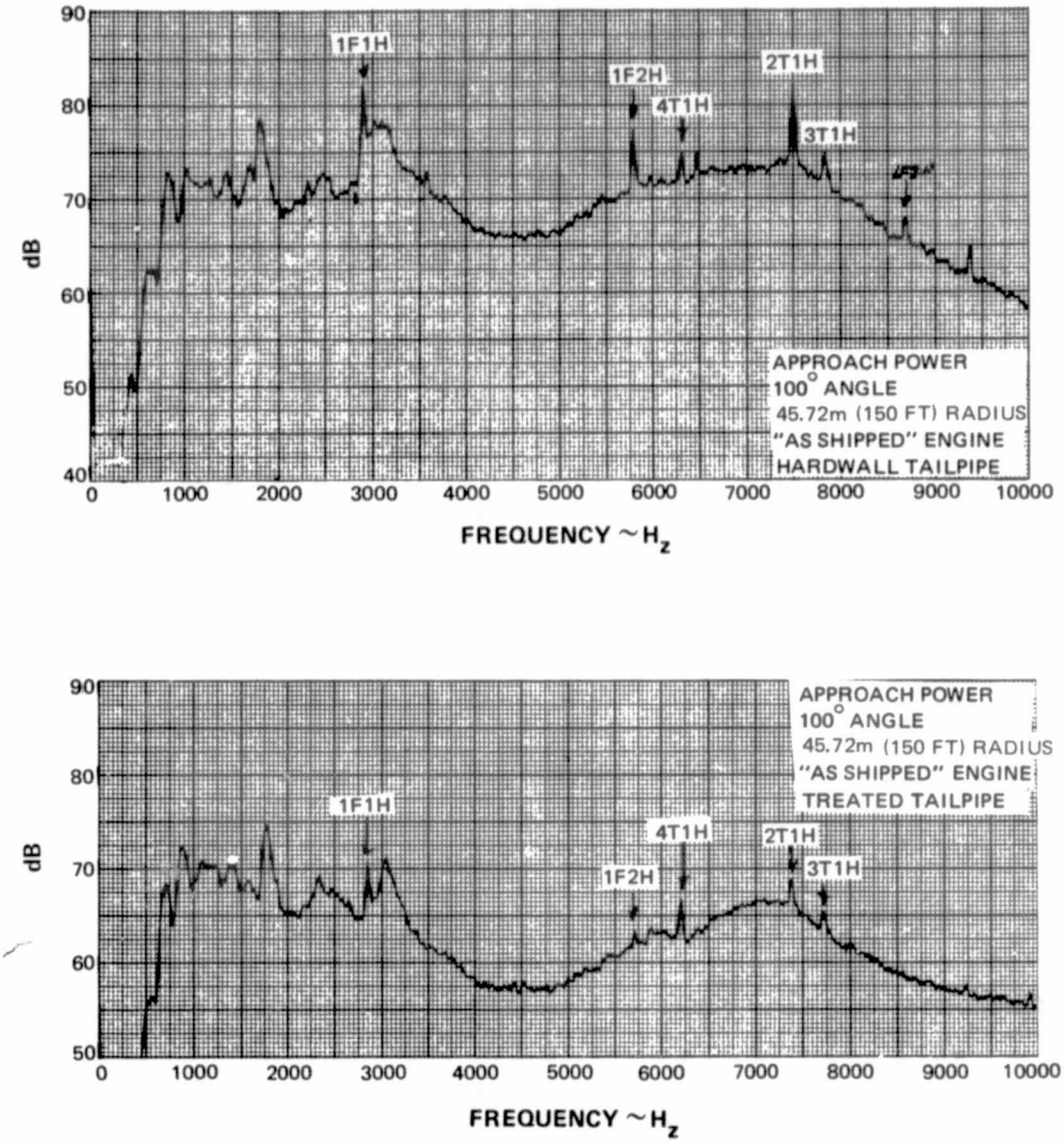

Figure D-46 Effect of Tailpipe Treatment on Narrowband Spectra ~ Approach Power, 100° Angle

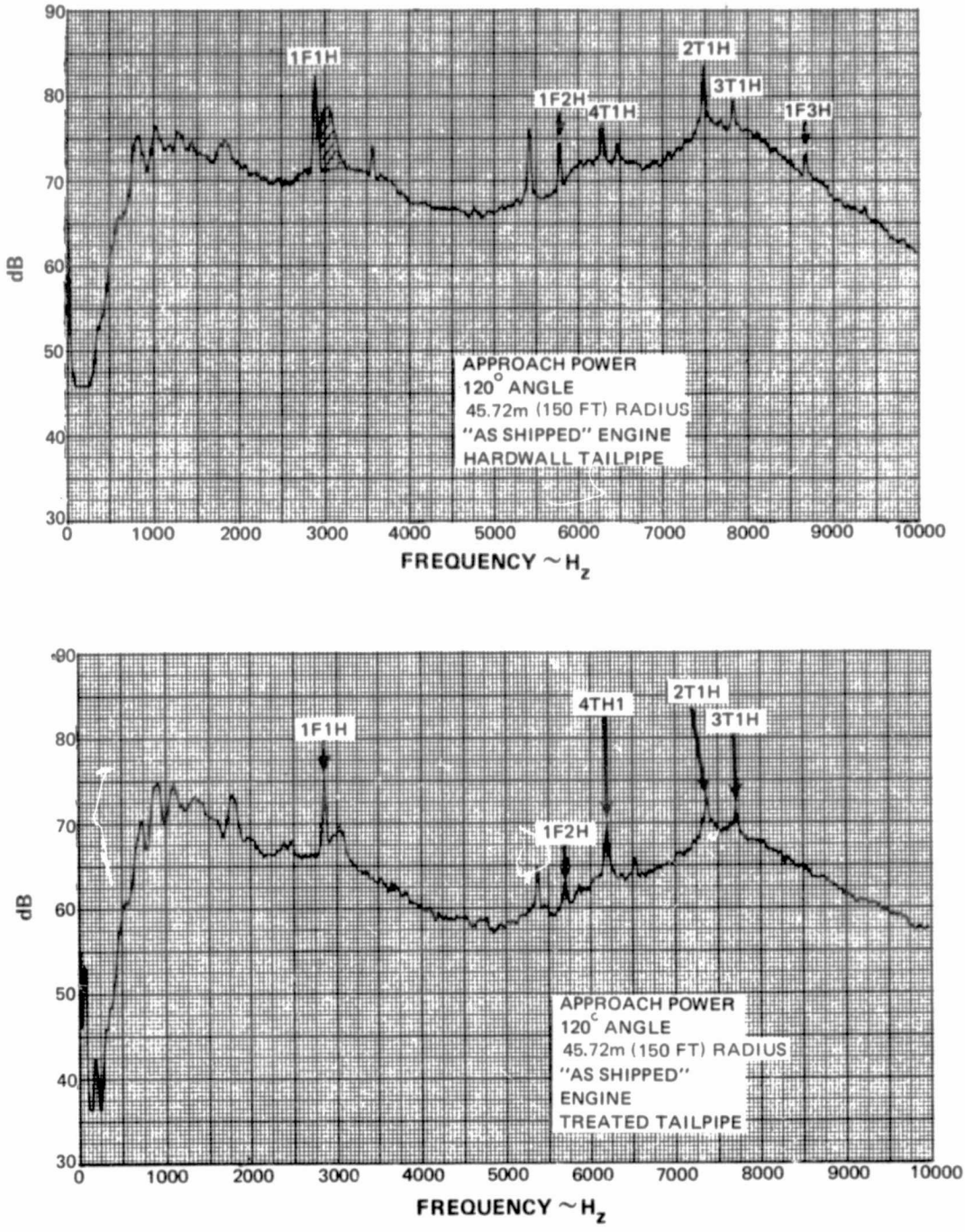

Figure D-47 Effect of Tailpipe Treatment on Narrowband Spectra ~ Approach Power, 120° Angle

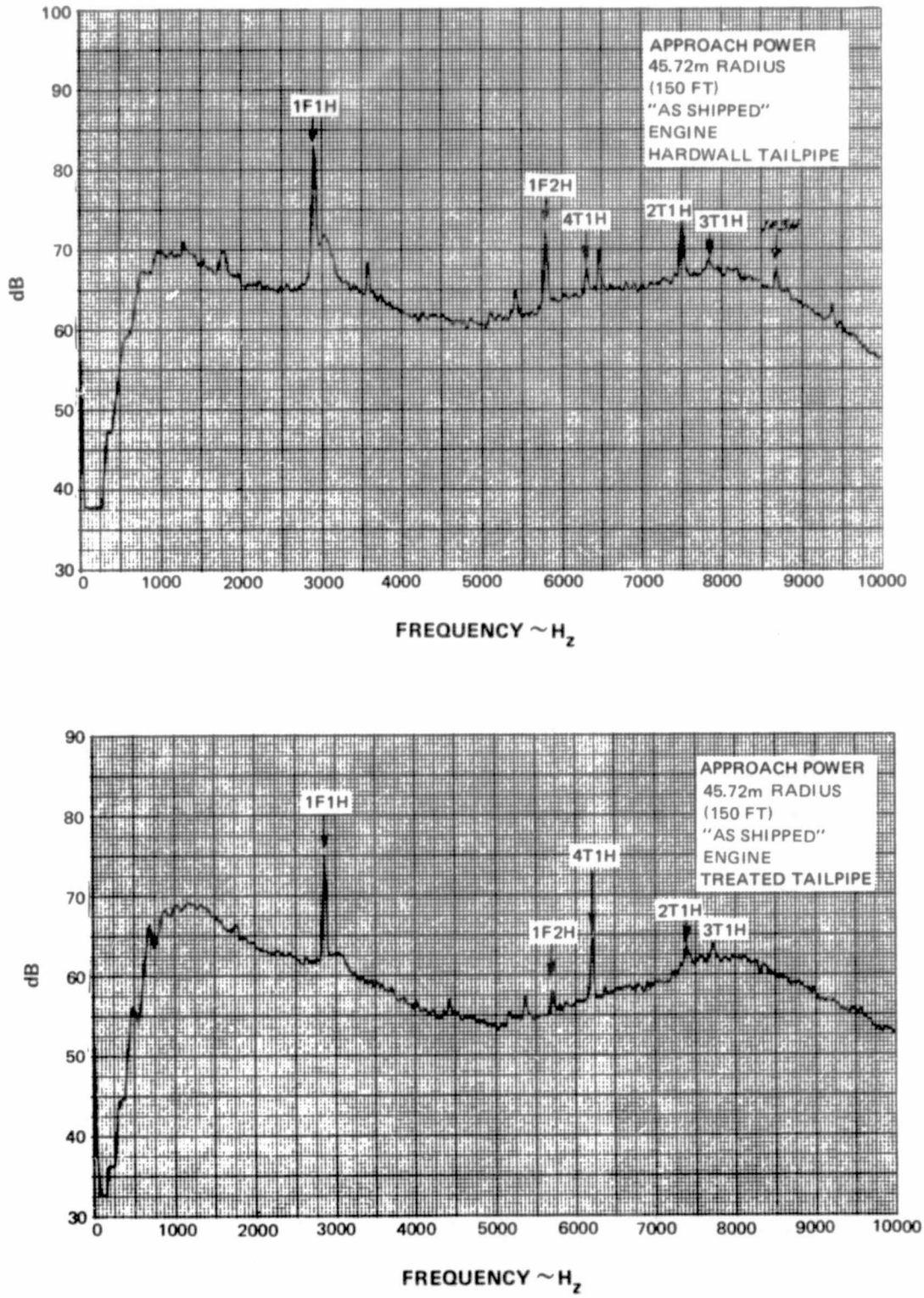

Figure D-48 Effect of Tailpipe Treatment on Narrowband Spectra ~ Approach Power, 140° Angle

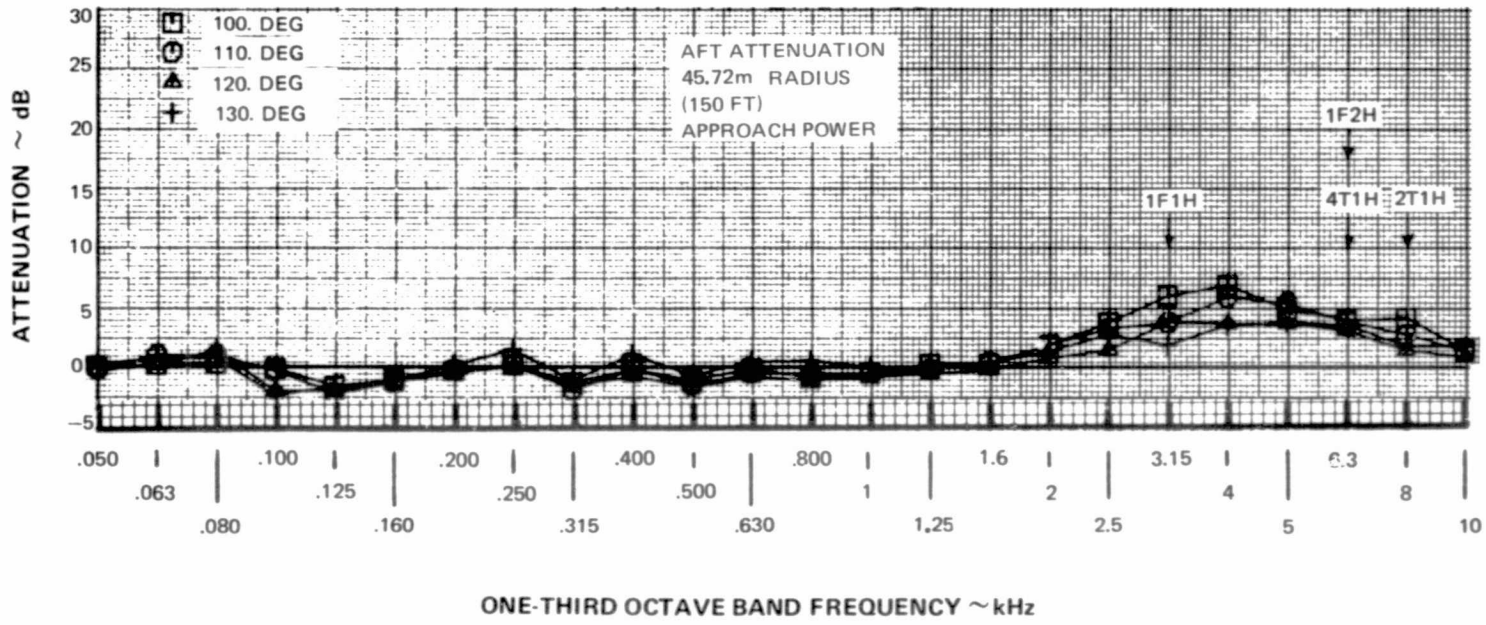

Figure D-49 Aft Quadrant ~ One-Third Octave Band Attenuation Due to Tailpipe Treatment ~ Approach Power

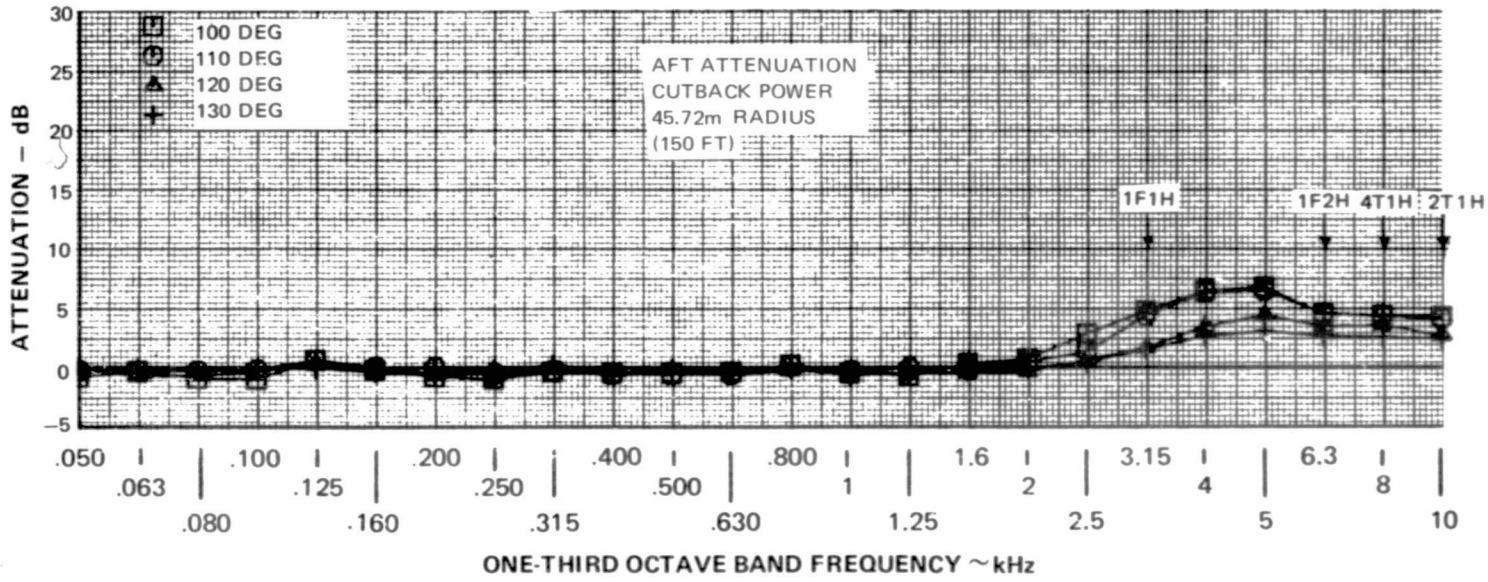

Figure D-50 Aft Quadrant ~ One-Third Octave Band Attenuation Due to Tailpipe Treatment ~ Cutback Power

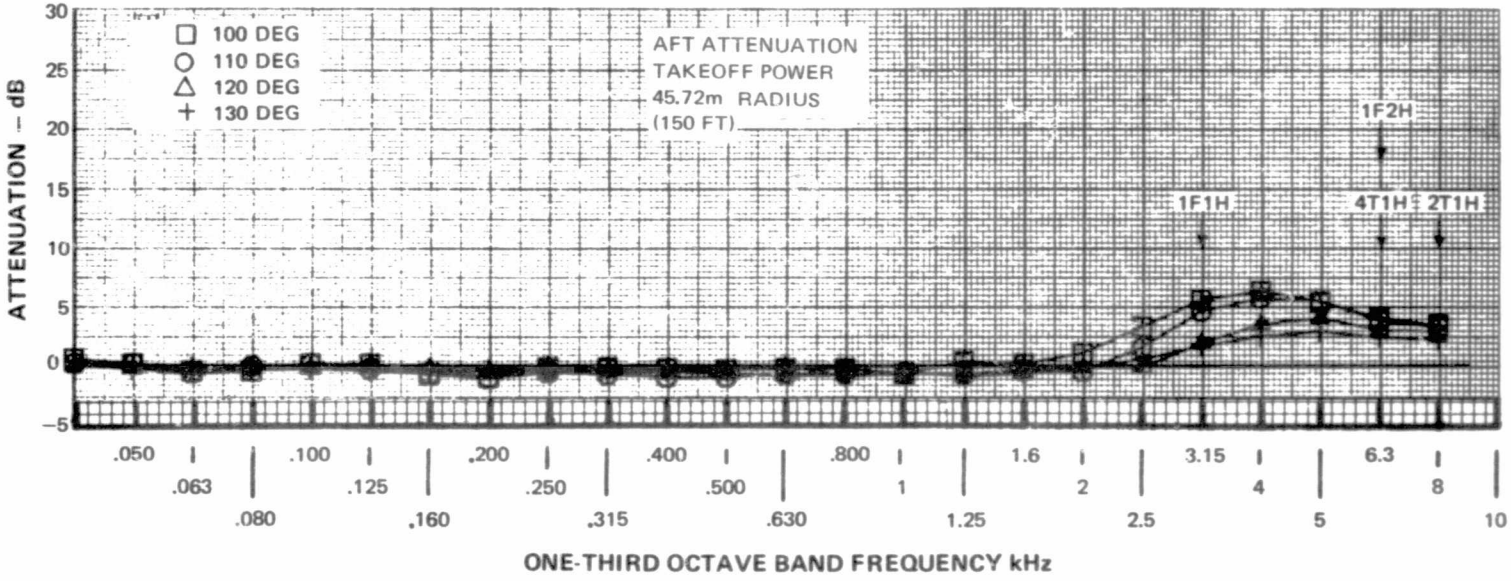

Figure D-51 Aft Quadrant ~ One-Third Octave Band Attenuation Due to Tailpipe Treatment ~ Takeoff Power

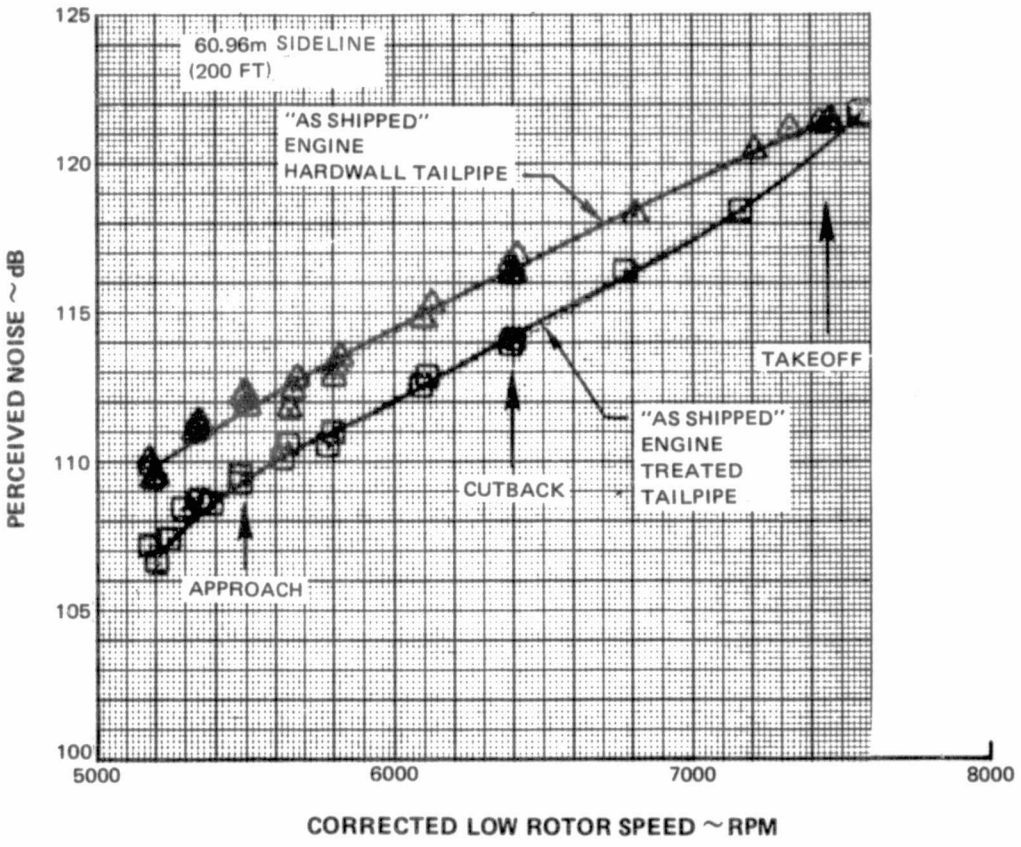

Figure D-52 Effect of Tailpipe Treatment on Peak Aft Quadrant PNdB

C, 4

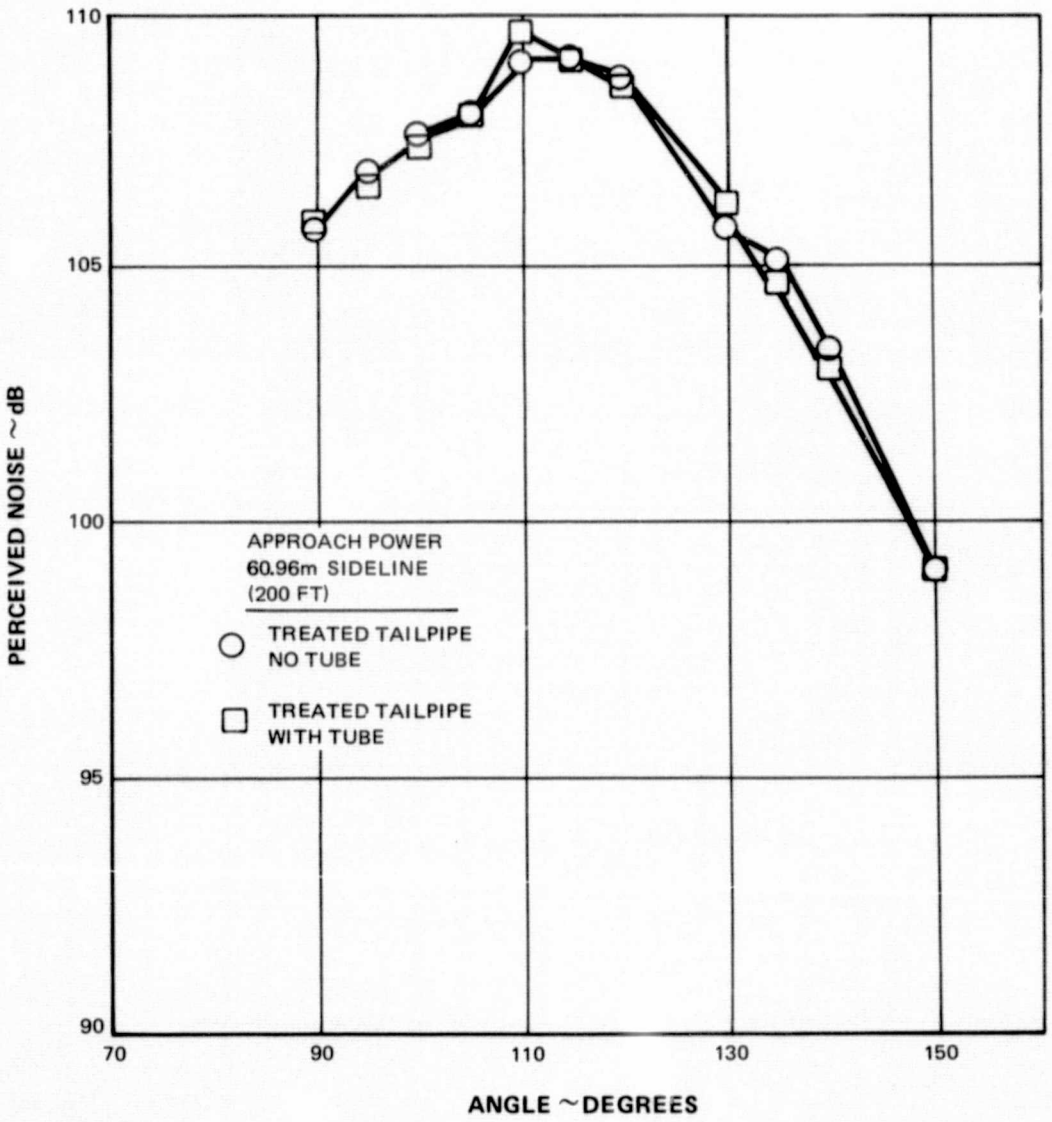

Figure D-53 Effect of Inlet Noise Suppression Tube on Treated Tailpipe Aft Quadrant PNdB ~ Approach Power

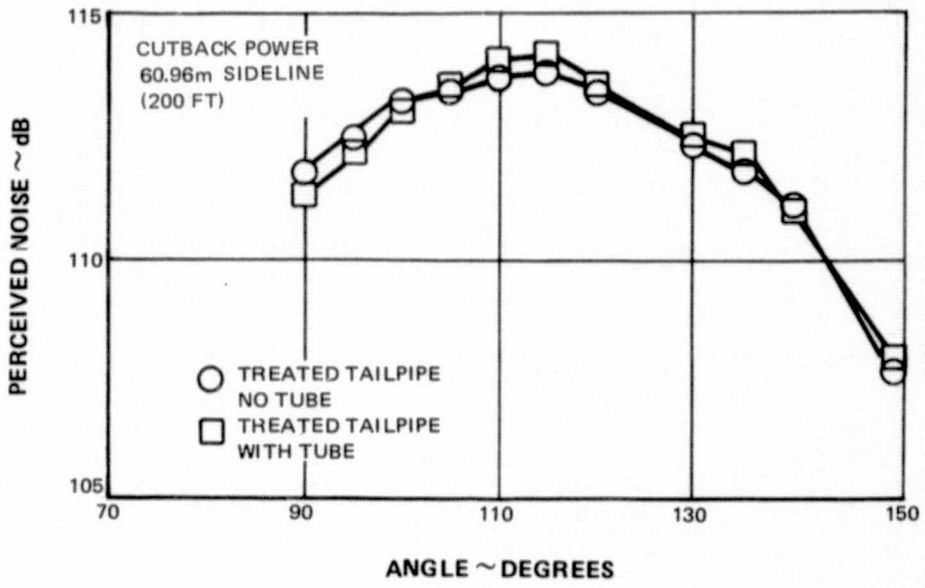

Figure D-54 Effect of Inlet Noise Suppression Tube on Treated Tailpipe Aft Quadrant PNdB ~ Cutback Power

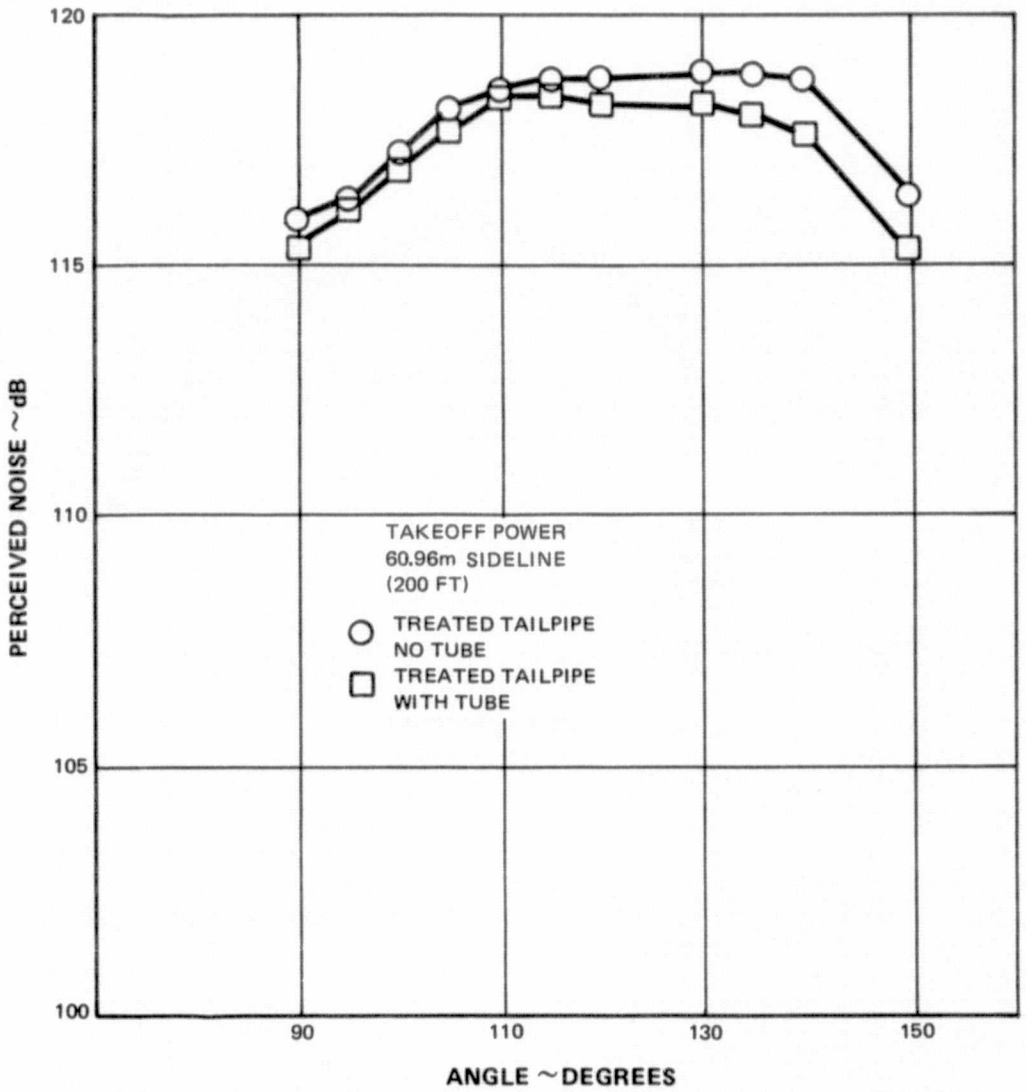

Figure D-55 Effect of Inlet Noise Suppression Tube on Treated Tailpipe Aft Quadrant PNdB ~ Takeoff Power

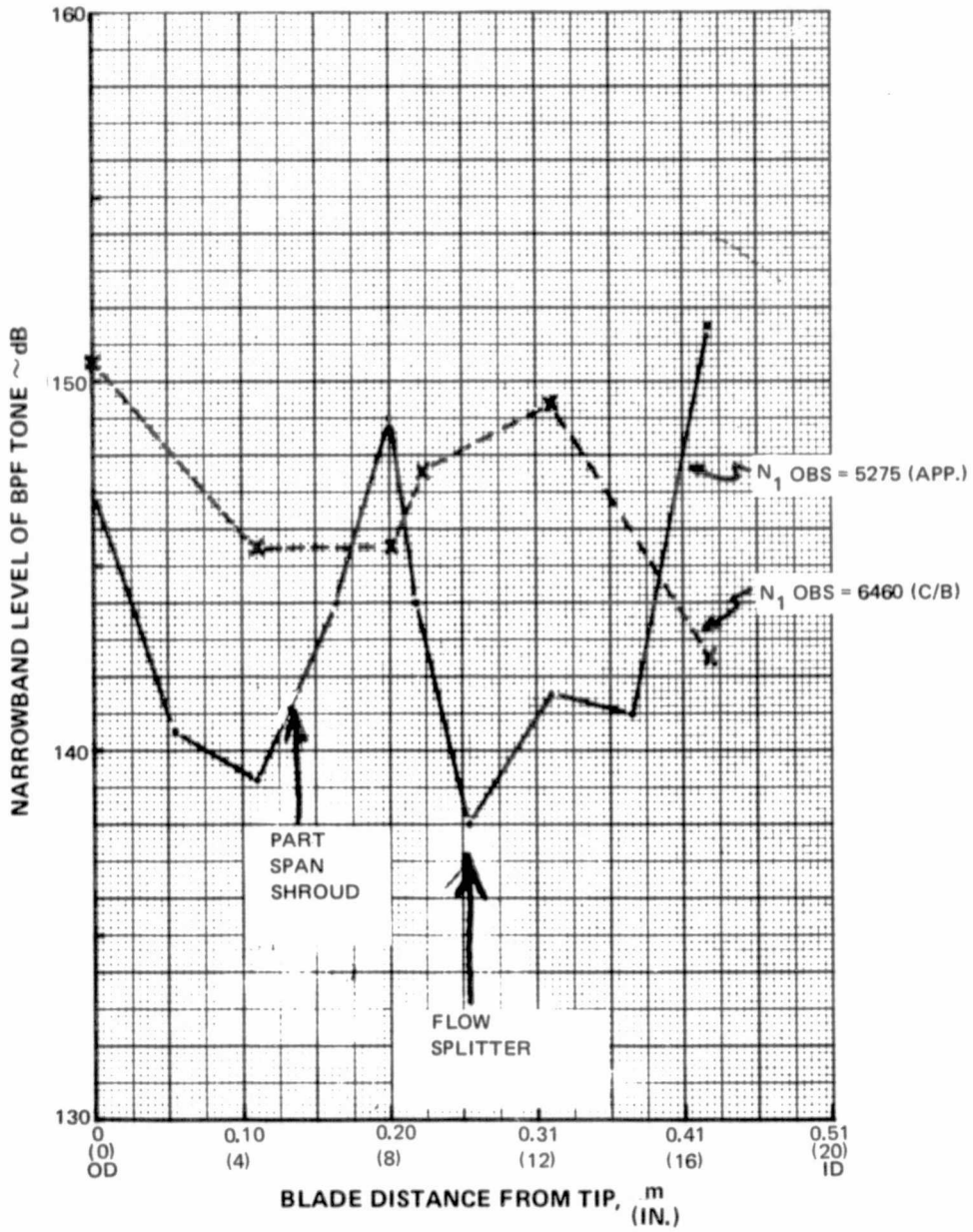

Figure D-56 Radial Distribution of Blade Passage Frequency Tone in Inlet

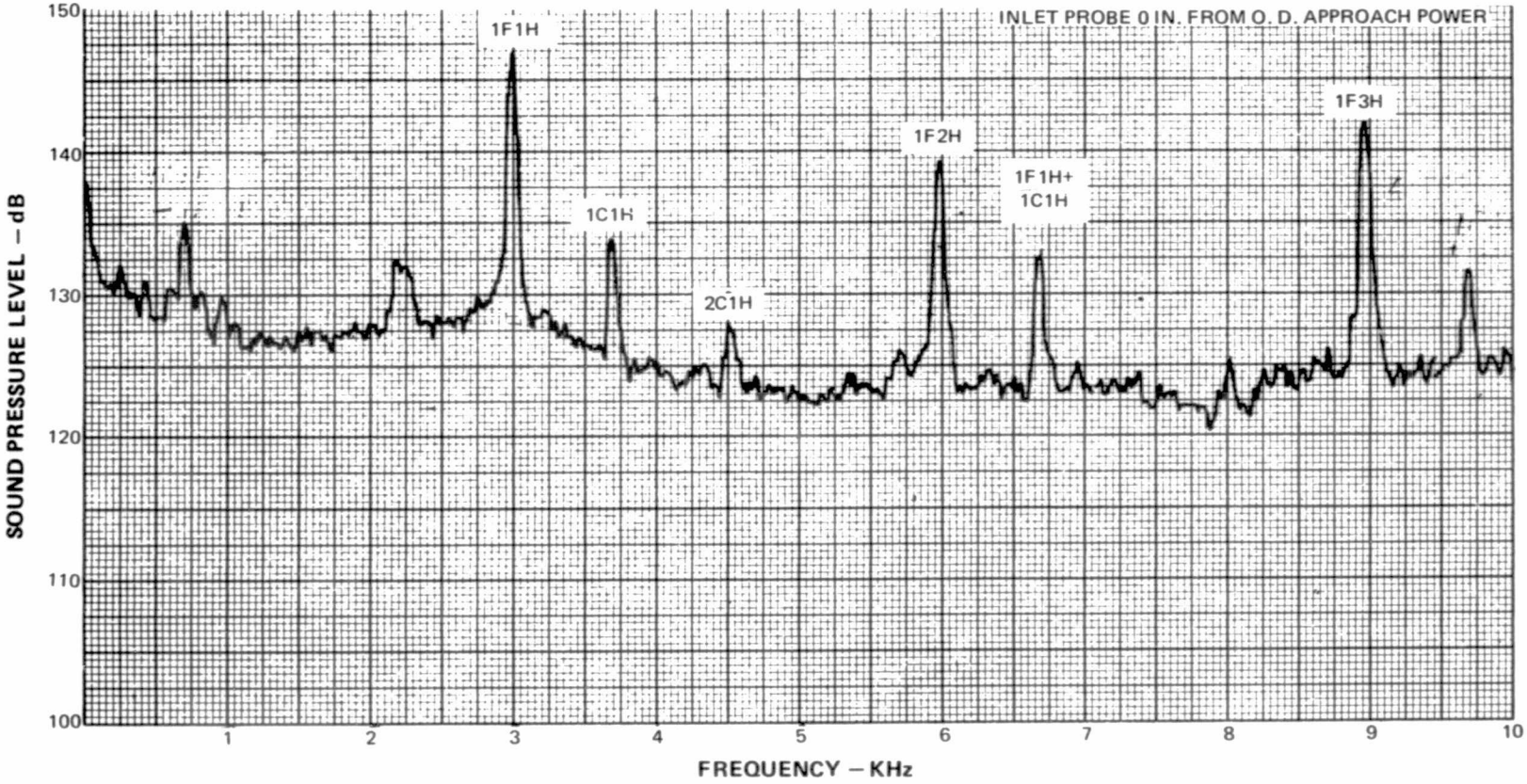

Figure D-57 Inlet Narrowband Spectra ~ Approach Power, Probe 0 in. from O. D.

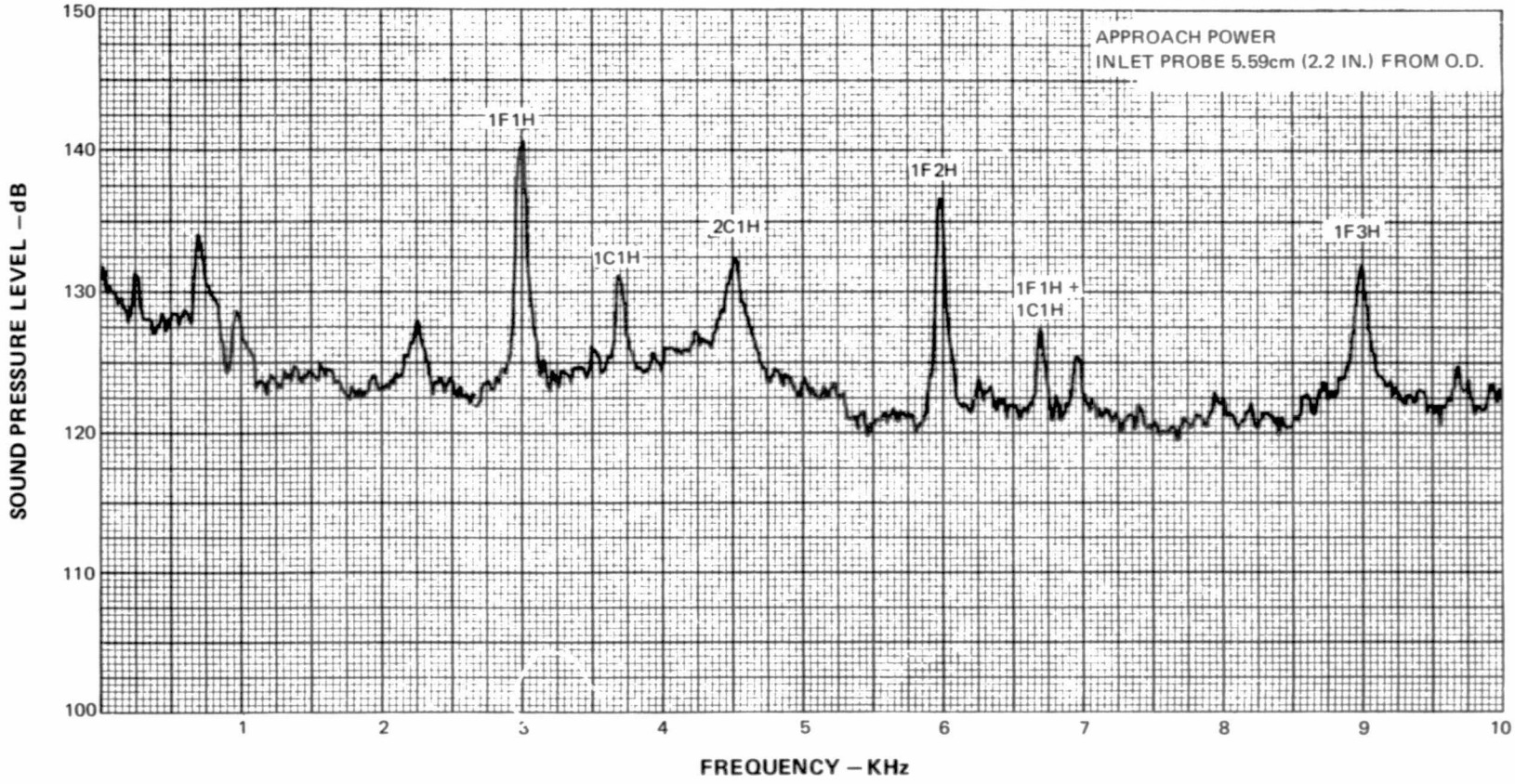

Figure D-58 Inlet Narrowband Spectra ~ Approach Power, Probe 5.59cm (2.2 In.) from O.D.

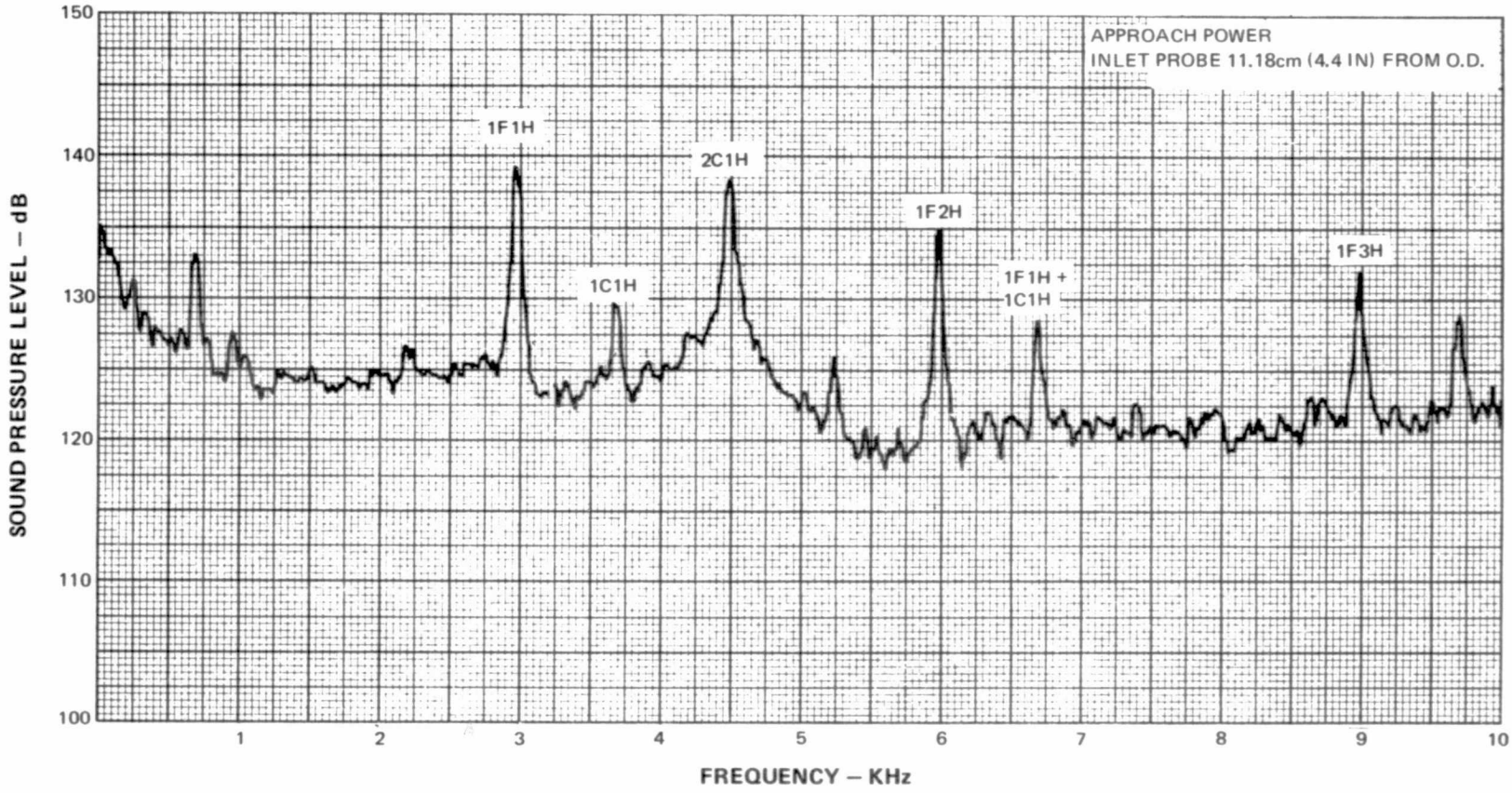

Figure D-59 Inlet Narrowband Spectra ~ Approach Power, Probe 11.18cm (4.4 In) from O.D.

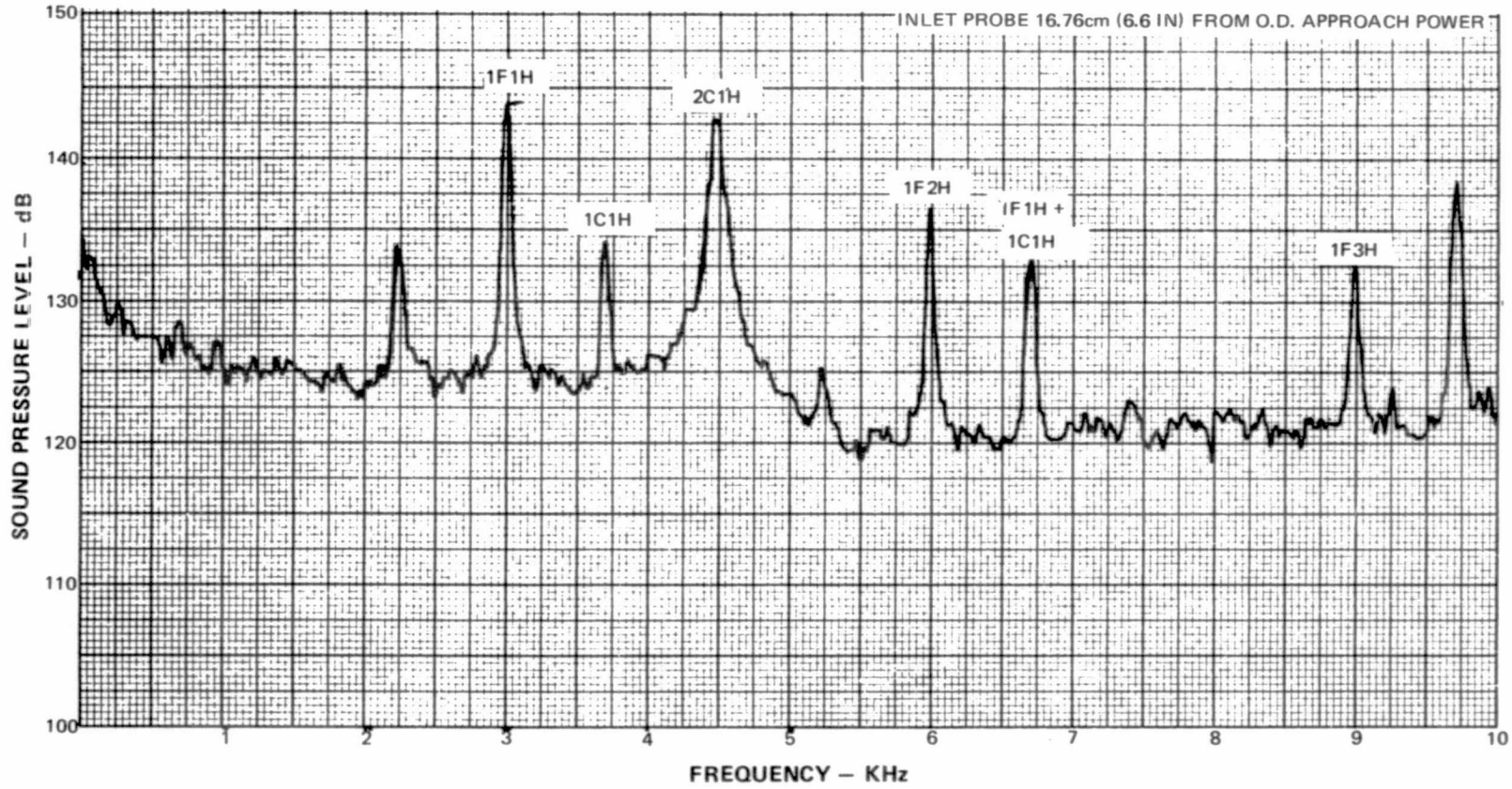

Figure D-60 Inlet Narrowband Spectra ~ Approach Power, Probe 16.76cm (6.6 In) from O.D.

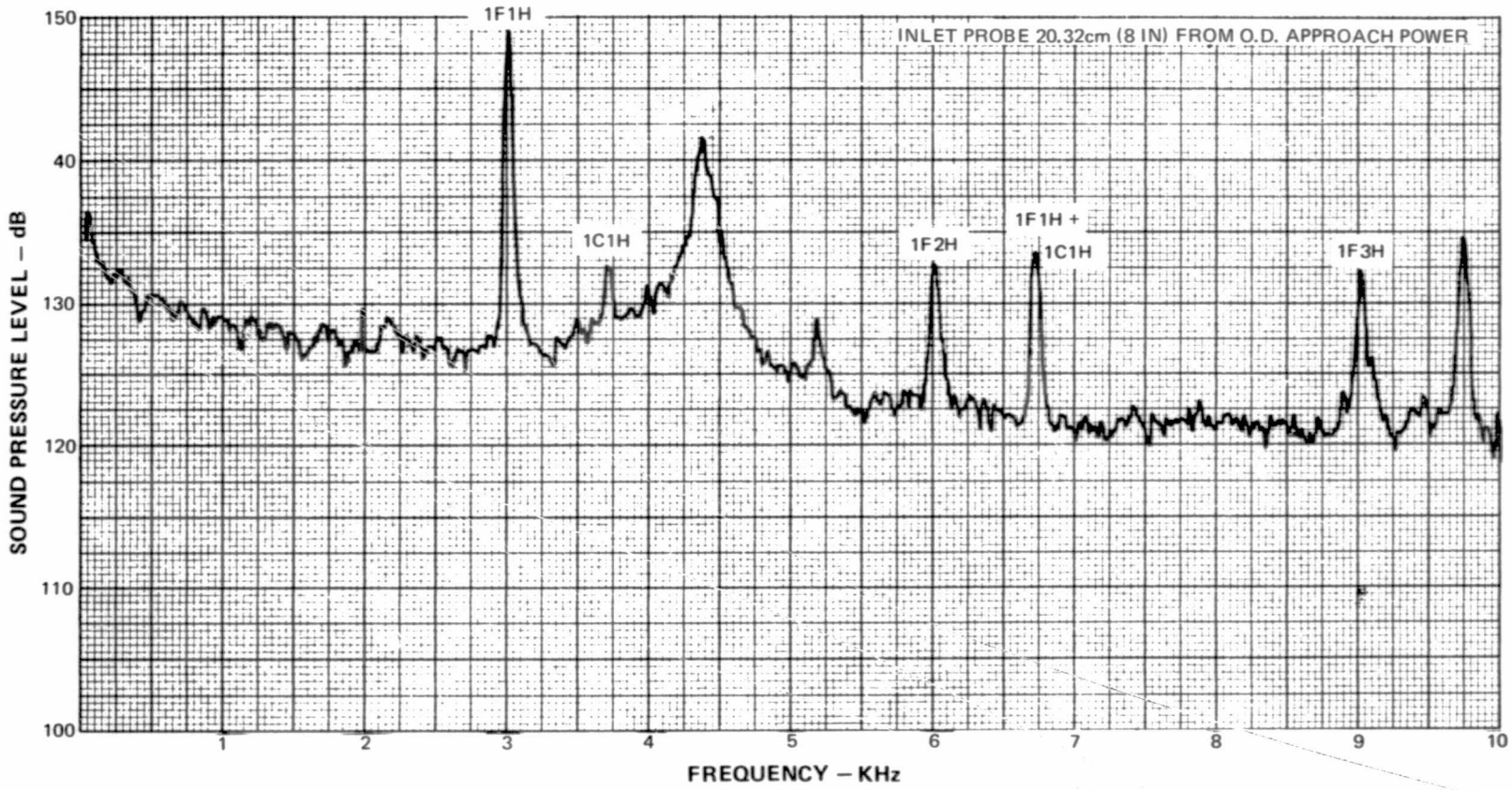

Figure D-61 Inlet Narrowband Spectra ~ Approach Power, Probe 20.32cm (8 In) from O.D.

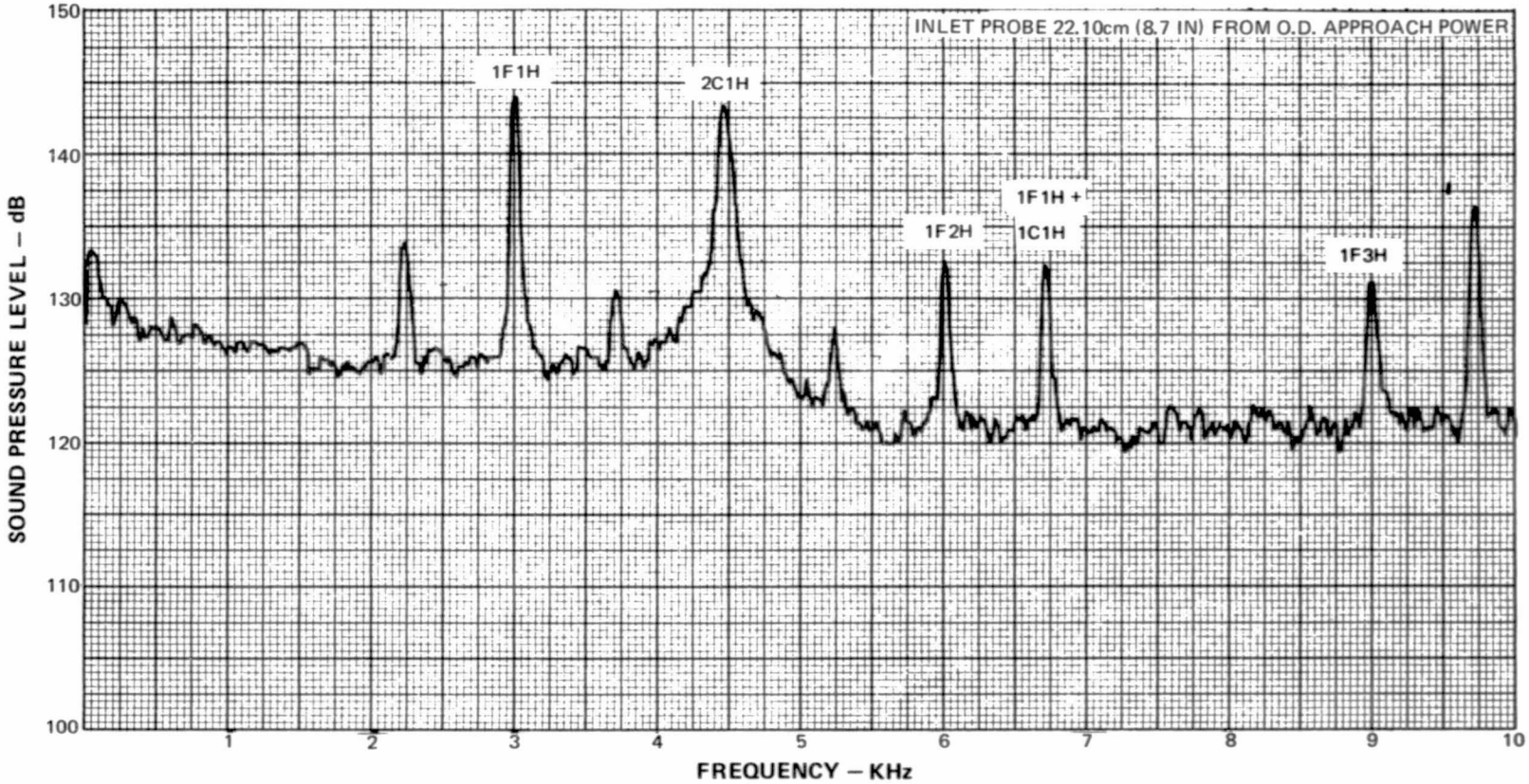

Figure D-62 Inlet Narrowband Spectra ~ Approach Power, Probe 22.10cm (8.7 In) from O.D.

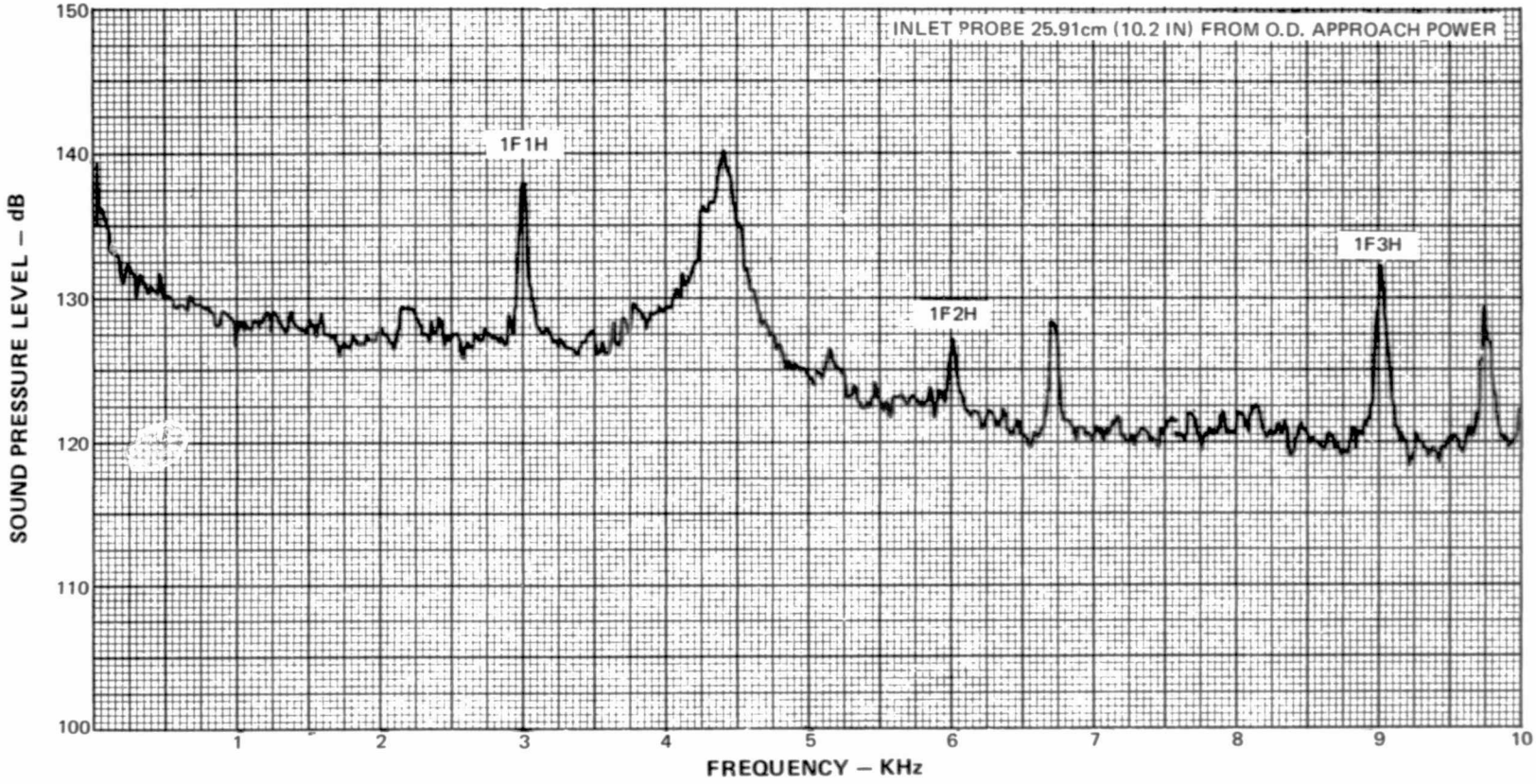

Figure D-63 Inlet Narrowband Spectra ~ Approach Power, Probe 25.91cm (10.2 In) from O.D.

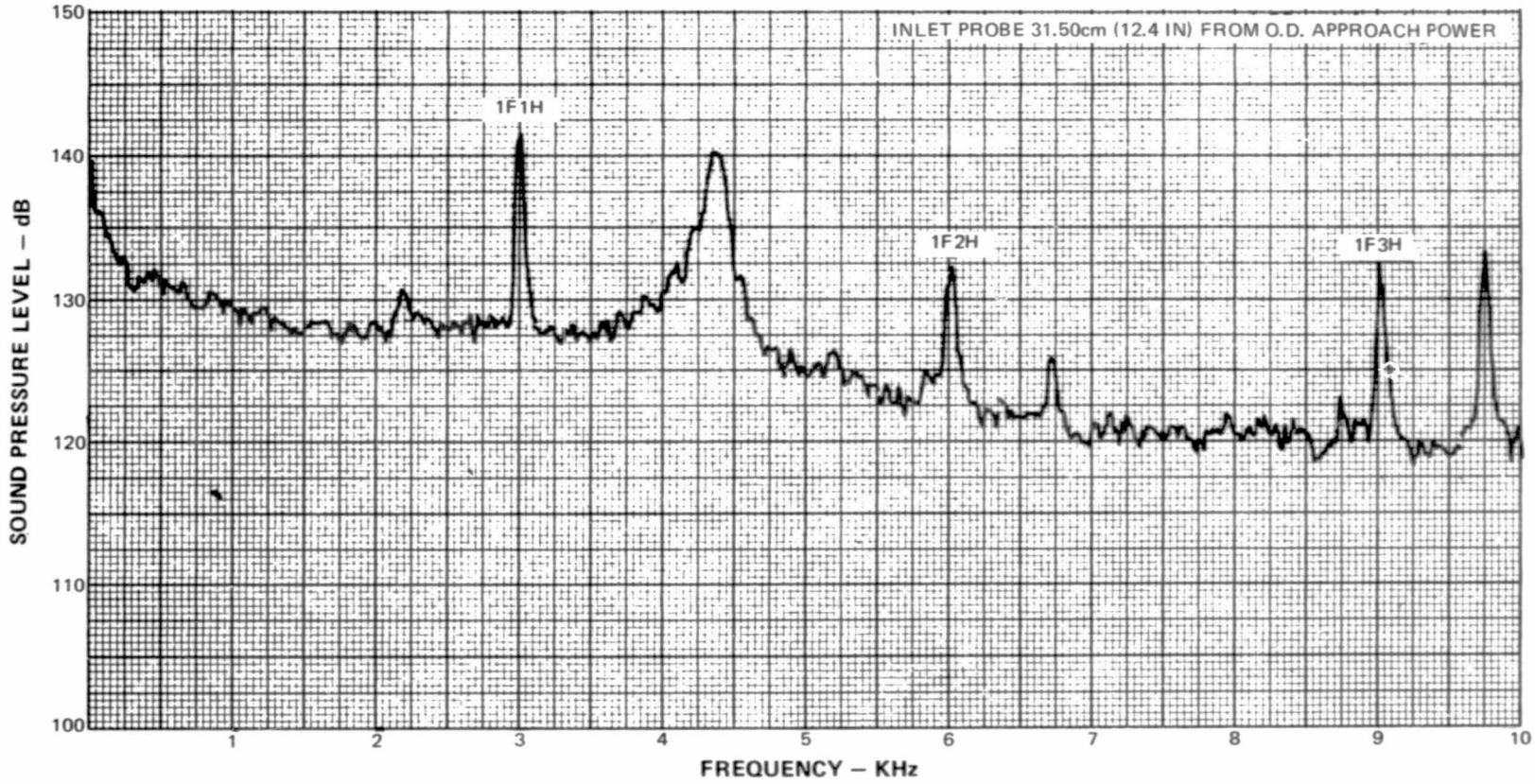

Figure D-64 Inlet Narrowband Spectra ~ Approach Power, Probe 31.50cm (12.4 In) from O.D.

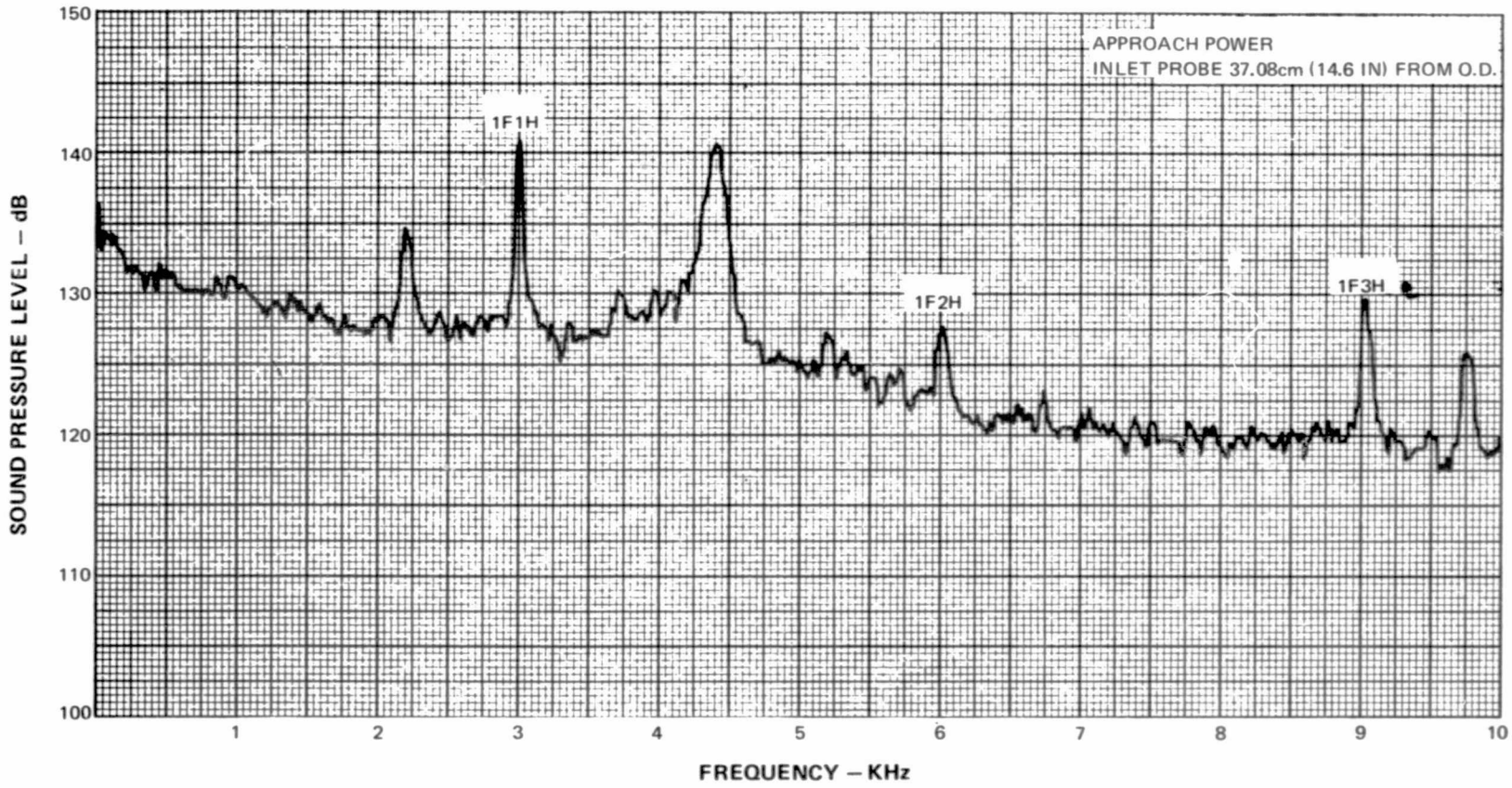

Figure D-65 Inlet Narrowband Spectra ~ Approach Power, Probe 37.08cm (14.6 In) from O.D.

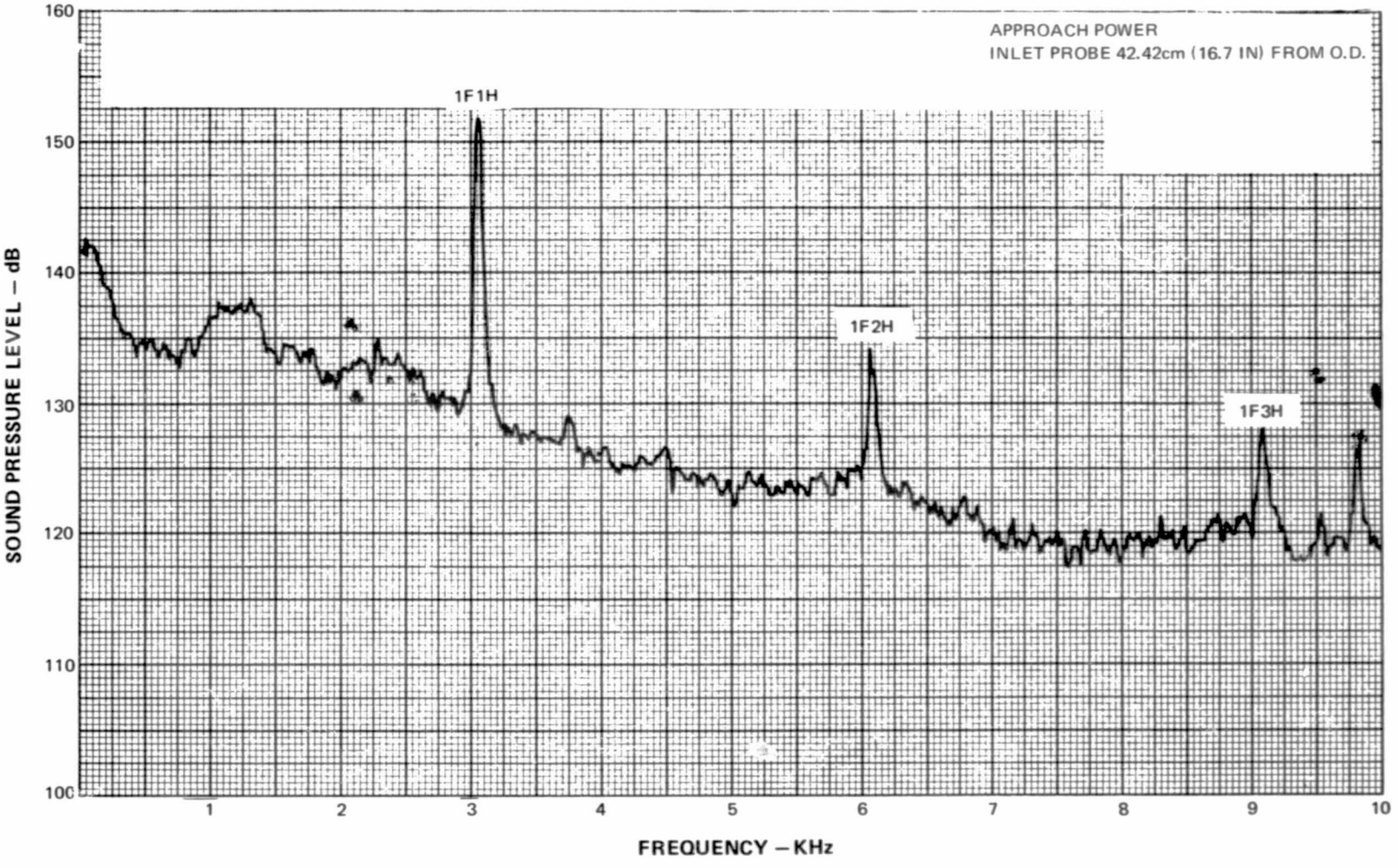

Figure D-66 Inlet Narrowband Spectra ~ Approach Power, Probe 42.42cm (16.7 In.) from O.D.

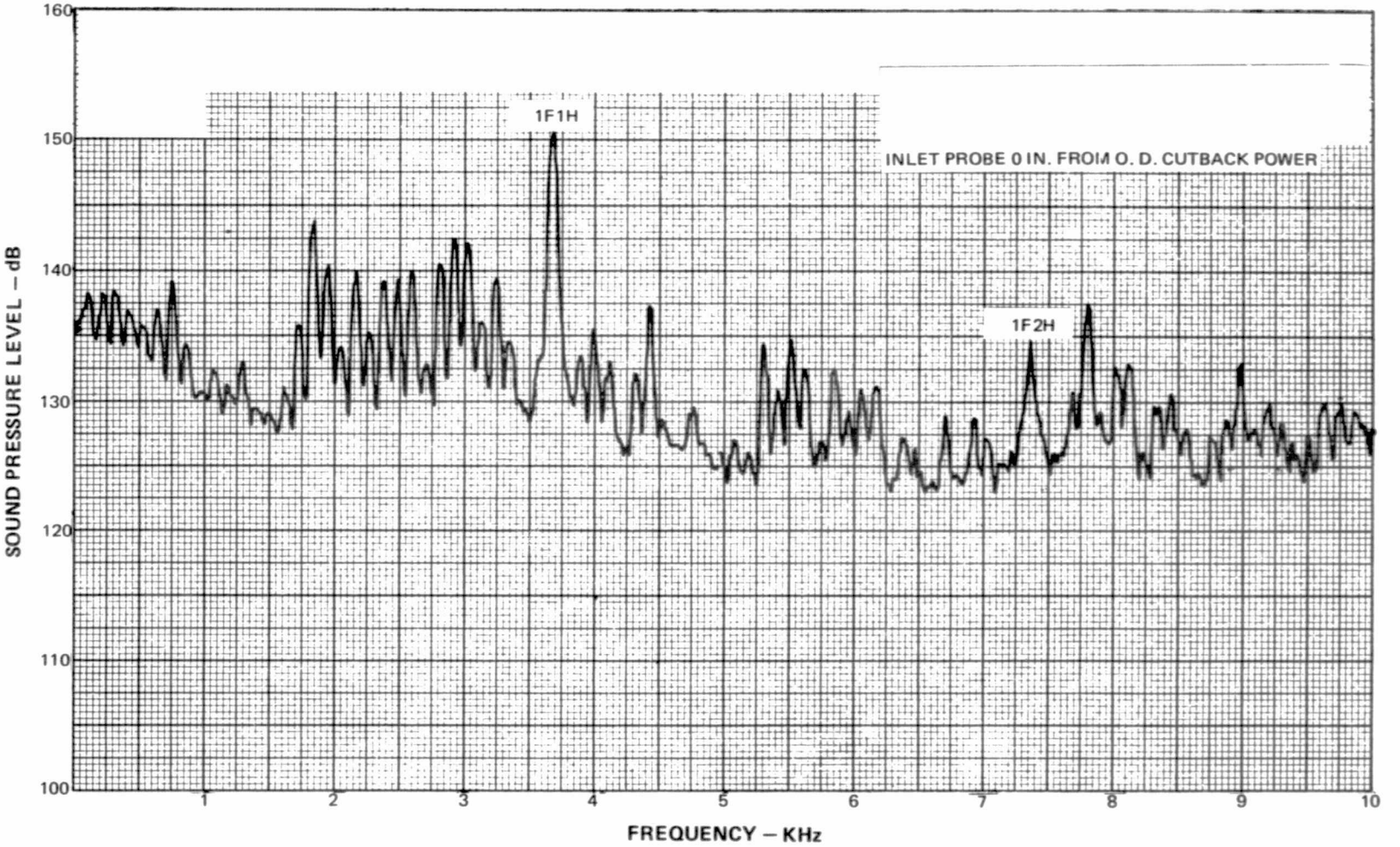

Figure D-67 Inlet Narrowband Spectra ~ Cutback Power, Probe 0 In. from O. D.

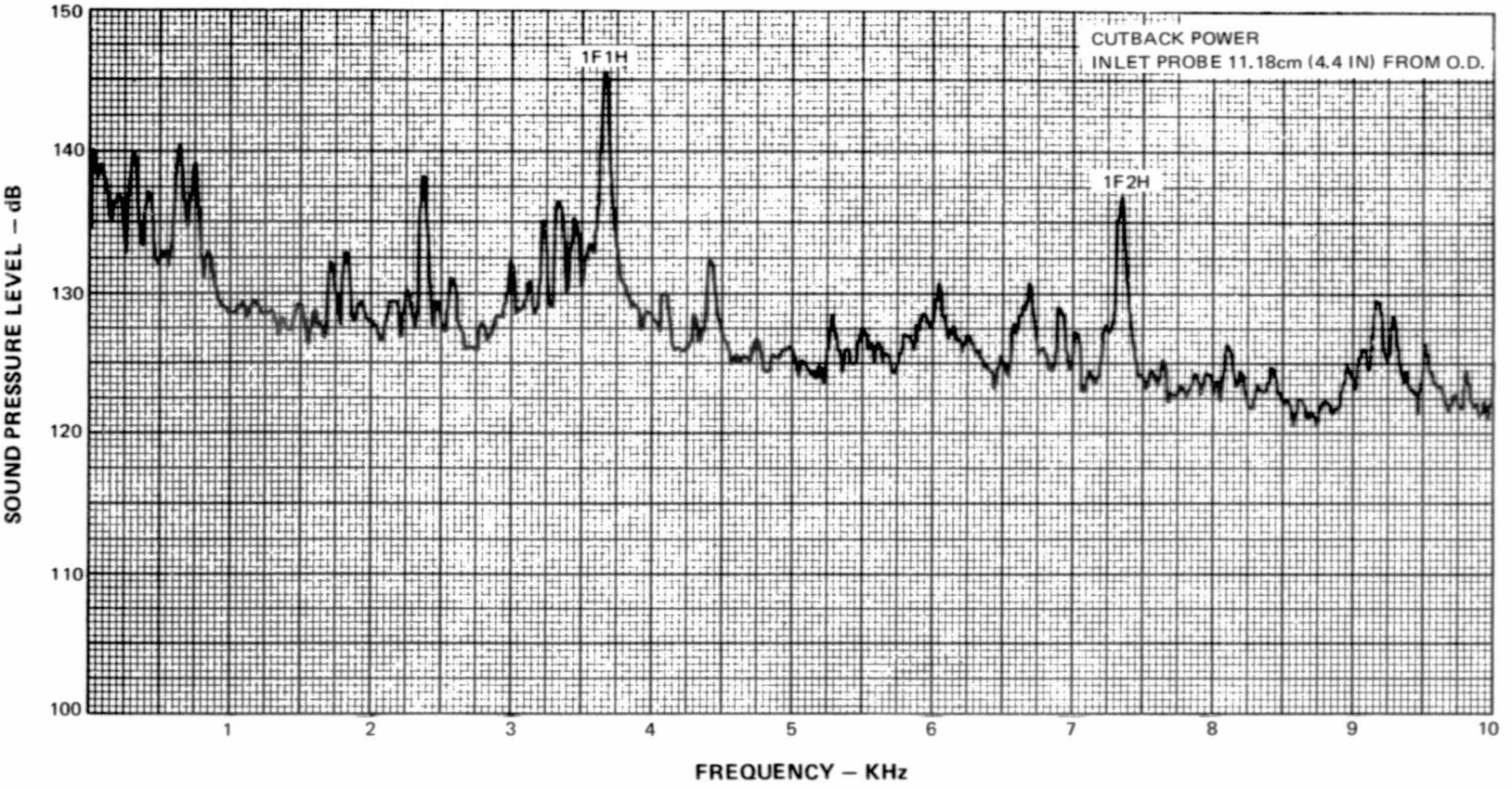

Figure D-68 Inlet Narrowband Spectra ~ Cutback Power, Probe 11.18cm (4.4 In.) from O.D.

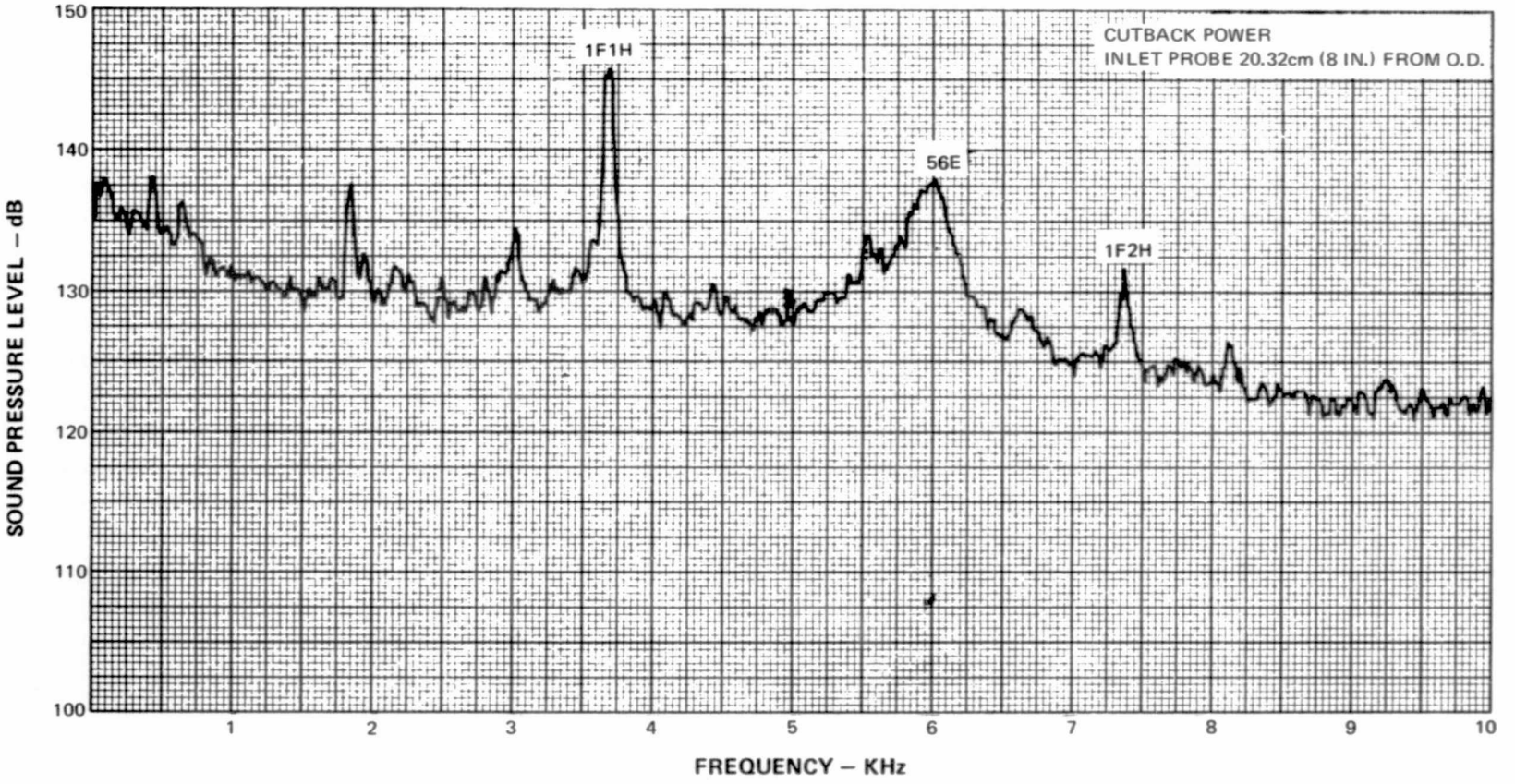

Figure D-69 Inlet Narrowband Spectra ~ Cutback Power, Probe 20.32cm (8 In.) from O.D.

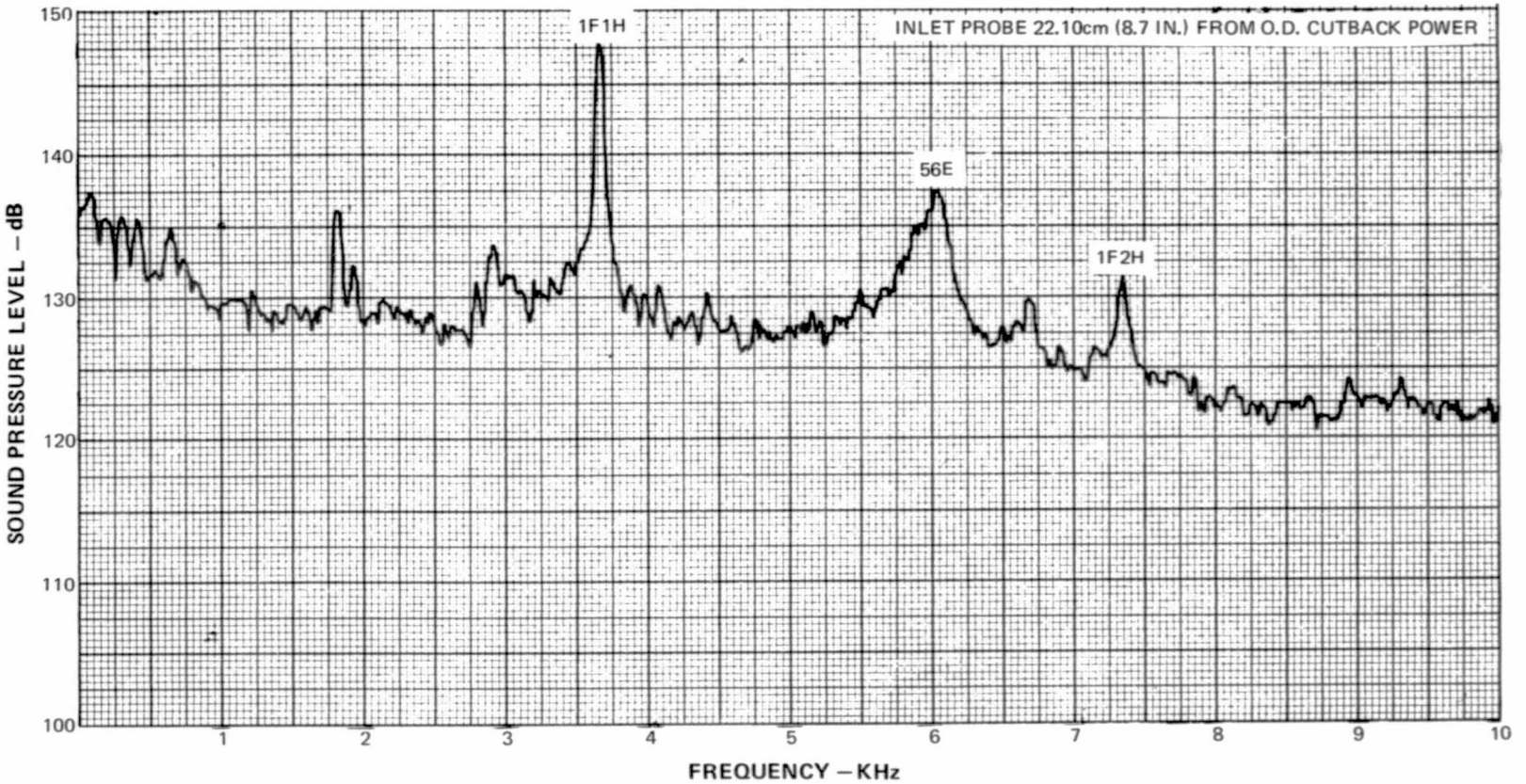

Figure D-70 Inlet Narrowband Spectra ~ Cutback Power, Probe 22.10cm (8.7 In.) from O.D.

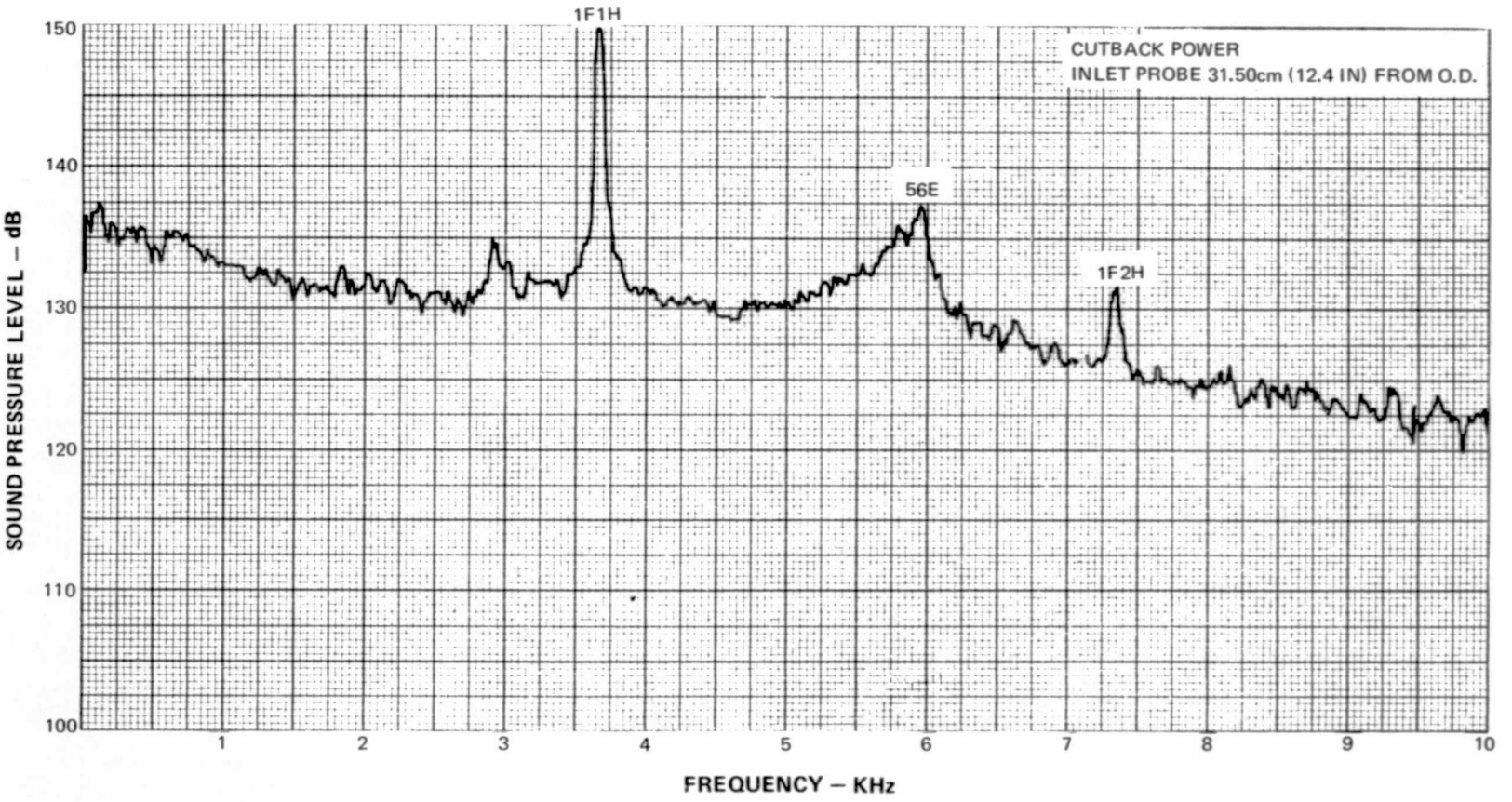

Figure D-71 Inlet Narrowband Spectra ~ Cutback Power, Probe 31.50cm (12.4 In.) from O.D.

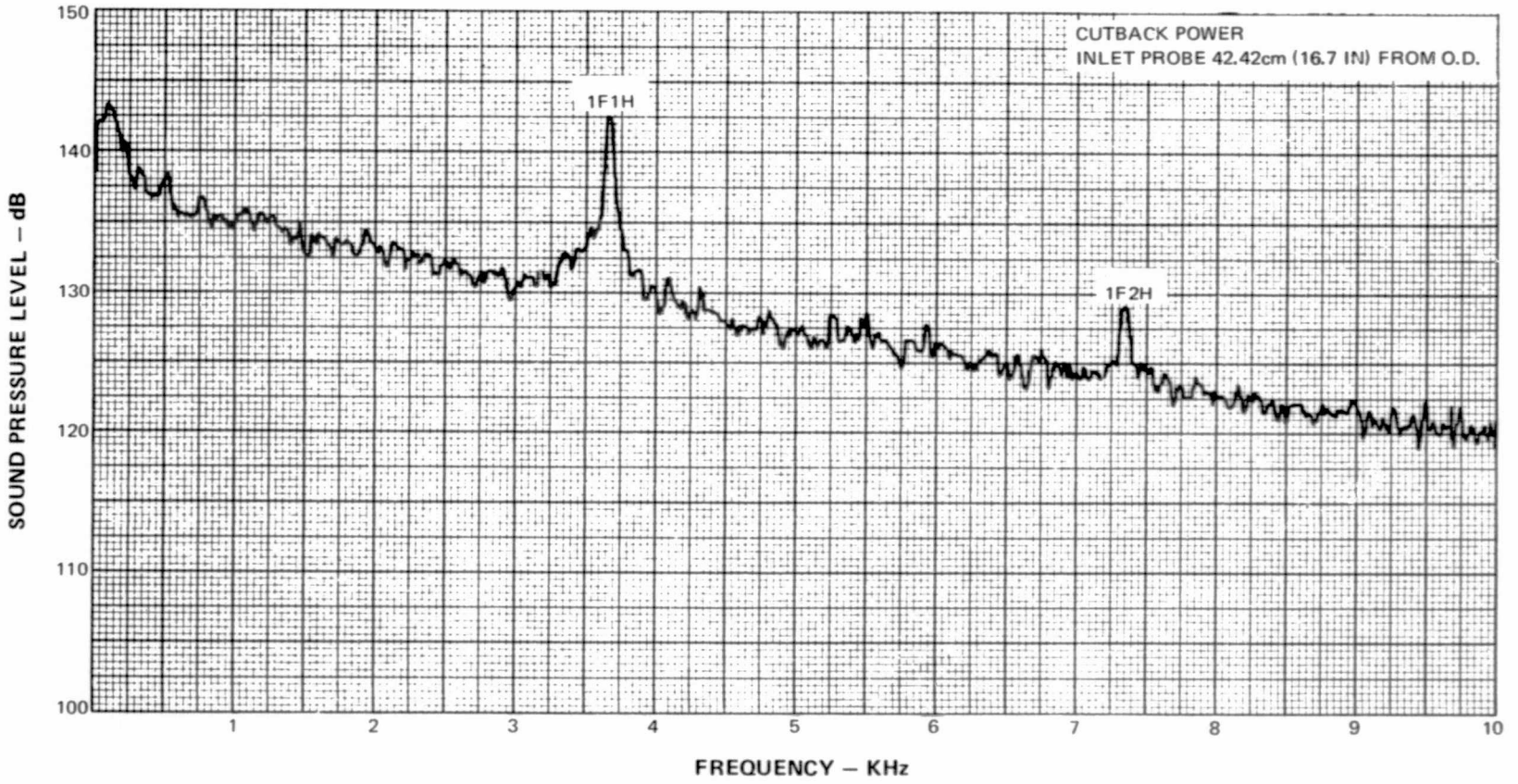

Figure D-72 Inlet Narrowband Spectra ~ Cutback Power, Probe 42.42cm (16.7 In.) from O.D.

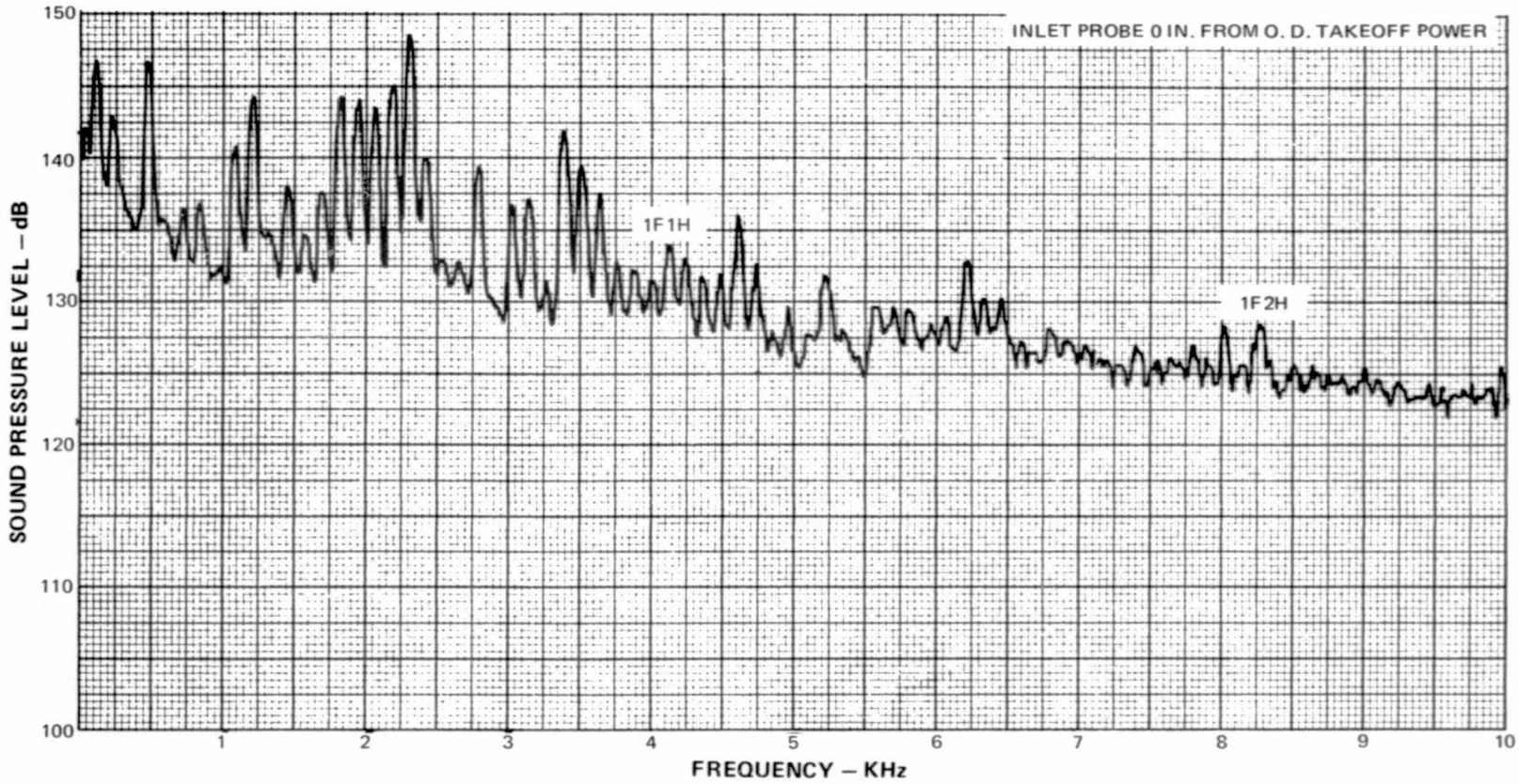

Figure D-73 Inlet Narrowband Spectra ~ Takeoff Power, Probe 0 In. from O. D.

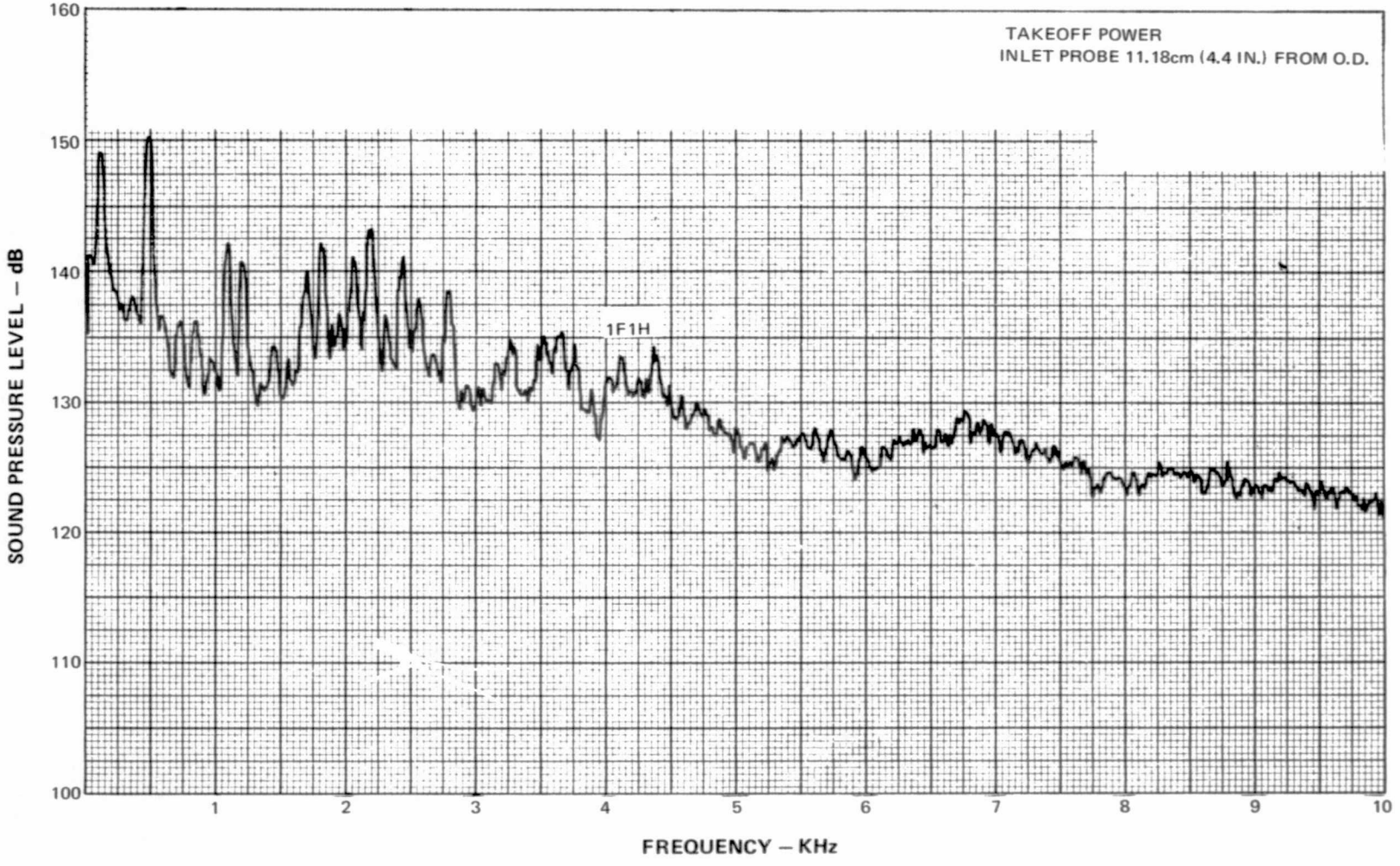

Figure D-74 Inlet Narrowband Spectra ~ Takeoff Power, Probe 11.18 cm (4.4 In.) from O.D.

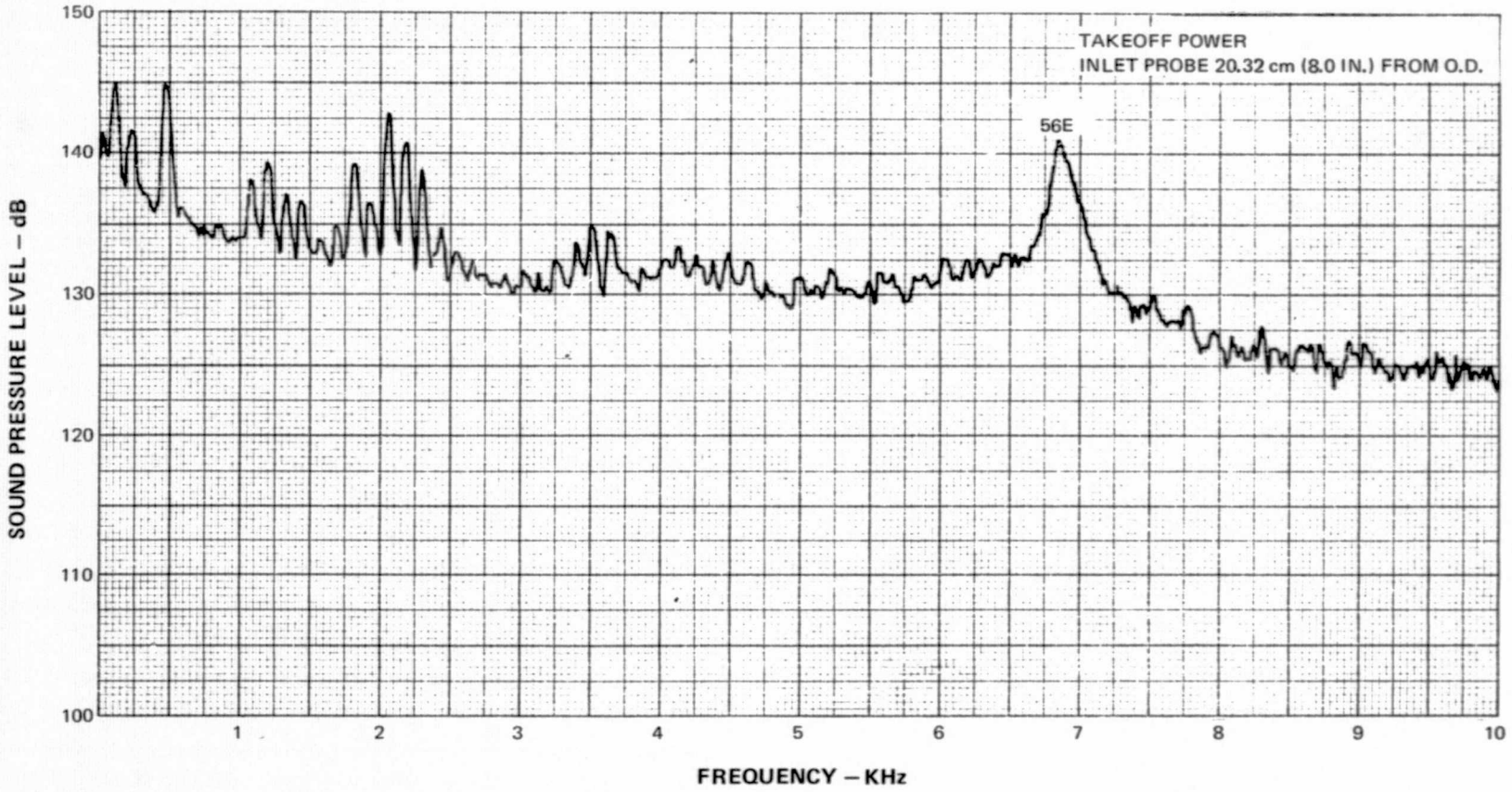

Figure D-75 Inlet Narrowband Spectra ~Takeoff Power, Probe 20.32 cm (8 In.) from O.D.

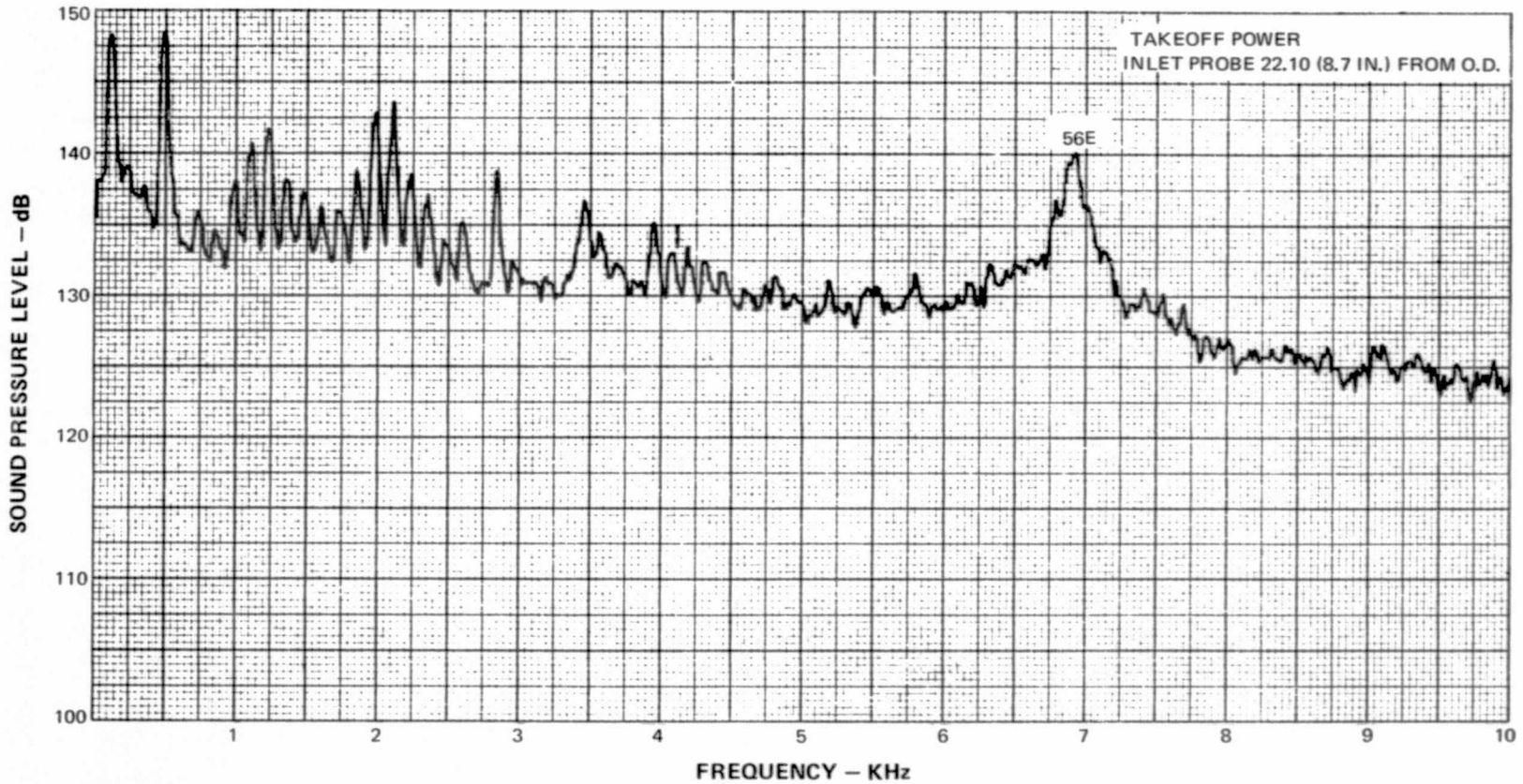

Figure D-76 Inlet Narrowband Spectra ~ Takeoff Power, Probe 22.10 cm (8.7 In.) from O.D.

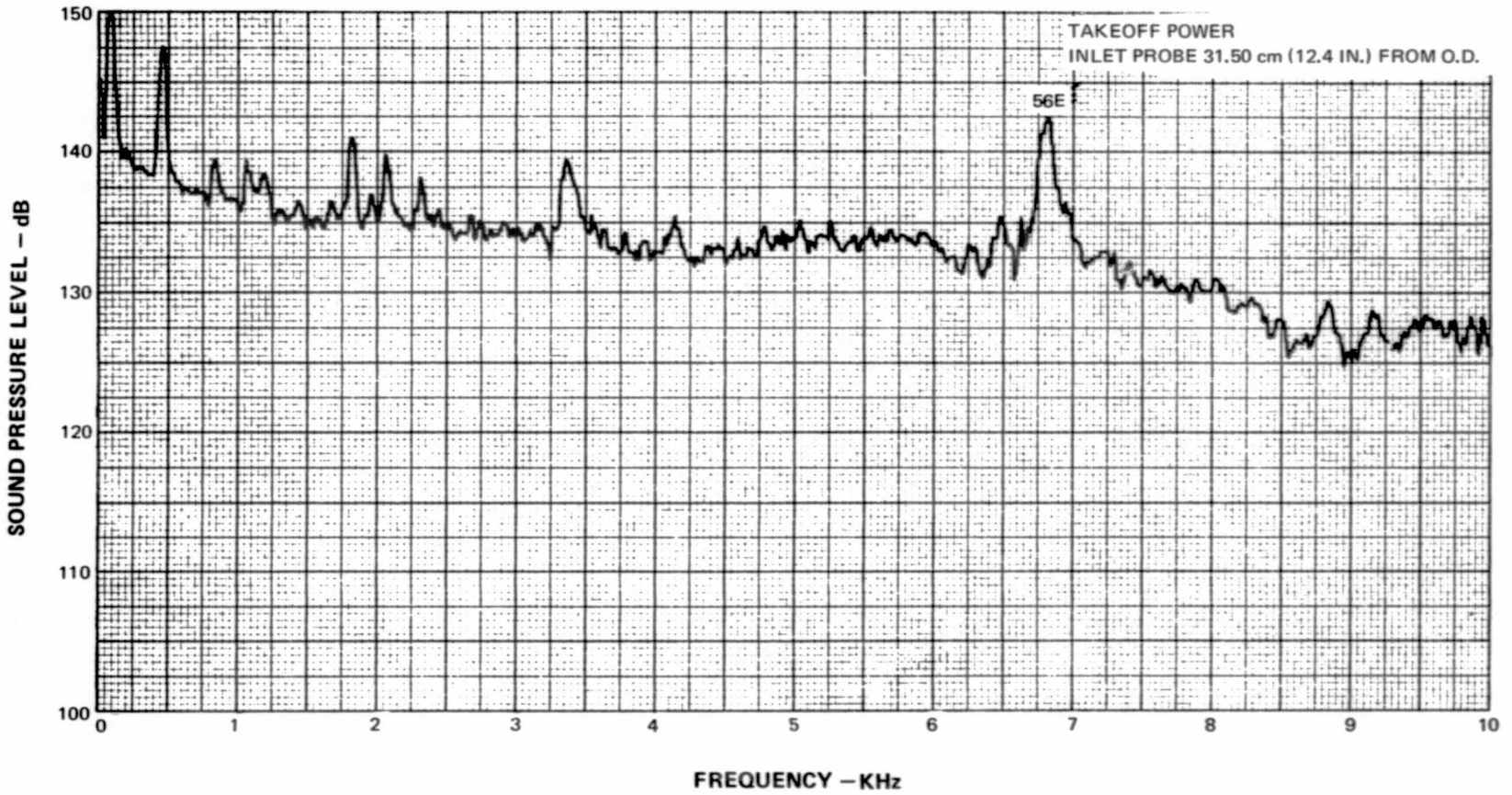

Figure D-77 Inlet Narrowband Spectra ~ Takeoff Power, Probe 31.50 cm (12.4 In.) from O.D.

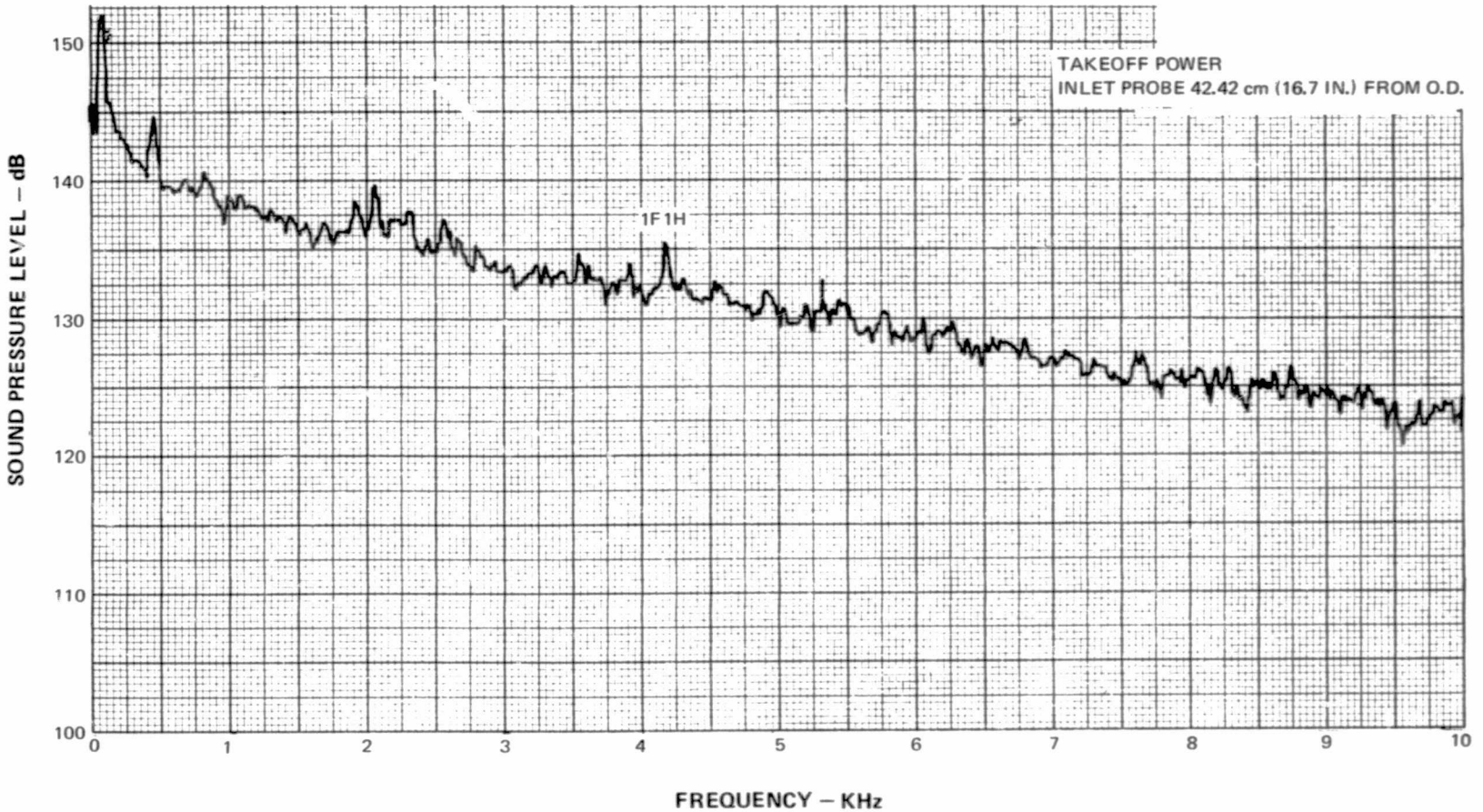

Figure D-78 Inlet Narrowband Spectra ~ Takeoff Power, Probe 42.42 cm (16.7 In.) from O.D.

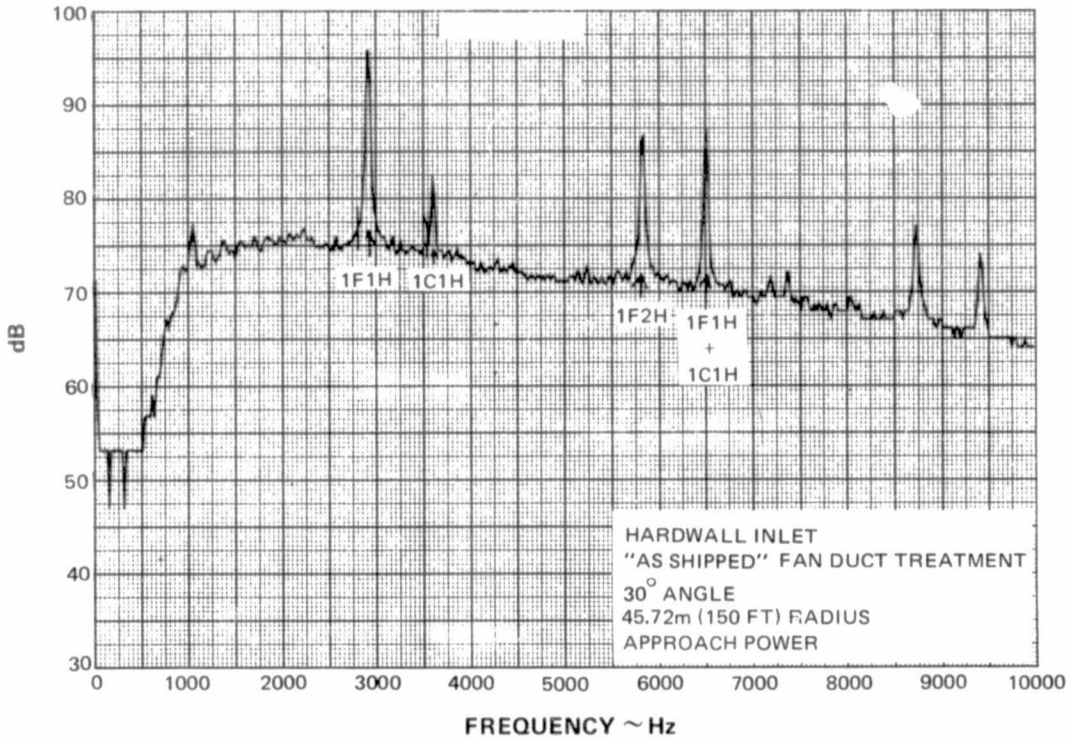

Figure D-79 Narrowband Analysis of Far Field Data ~ Approach Power, Treated Fan Duct

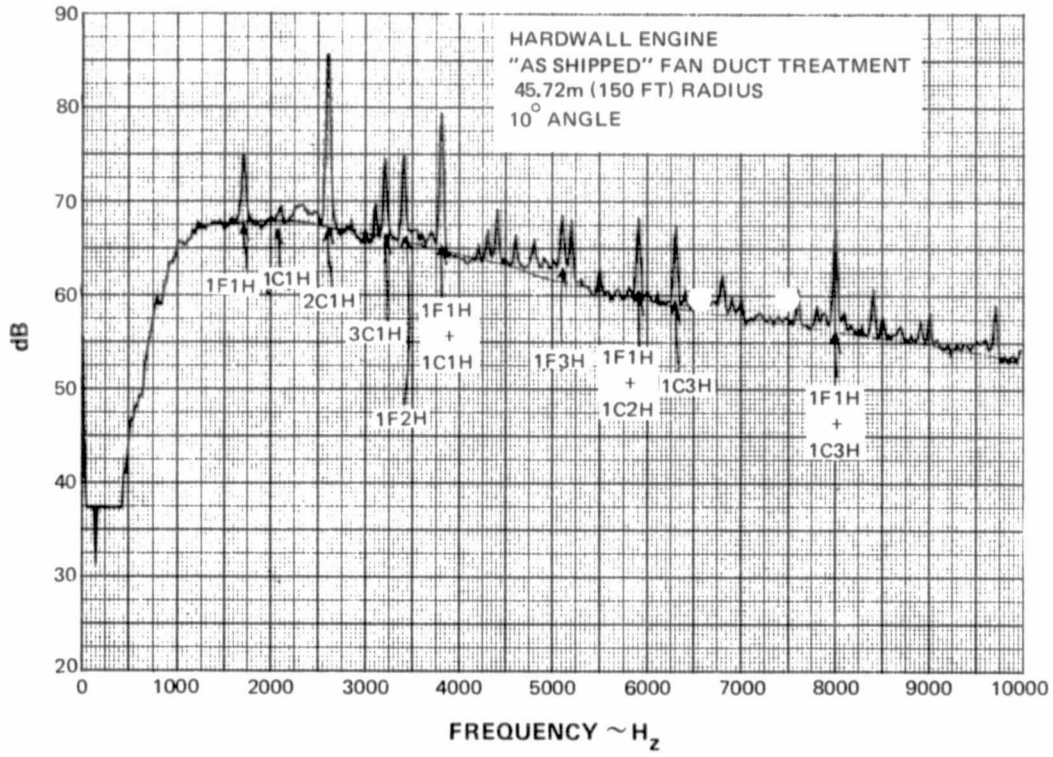

Figure D-80 Narrowband Analysis of Far Field Data ~ Below Approach Power, Treated Fan Duct

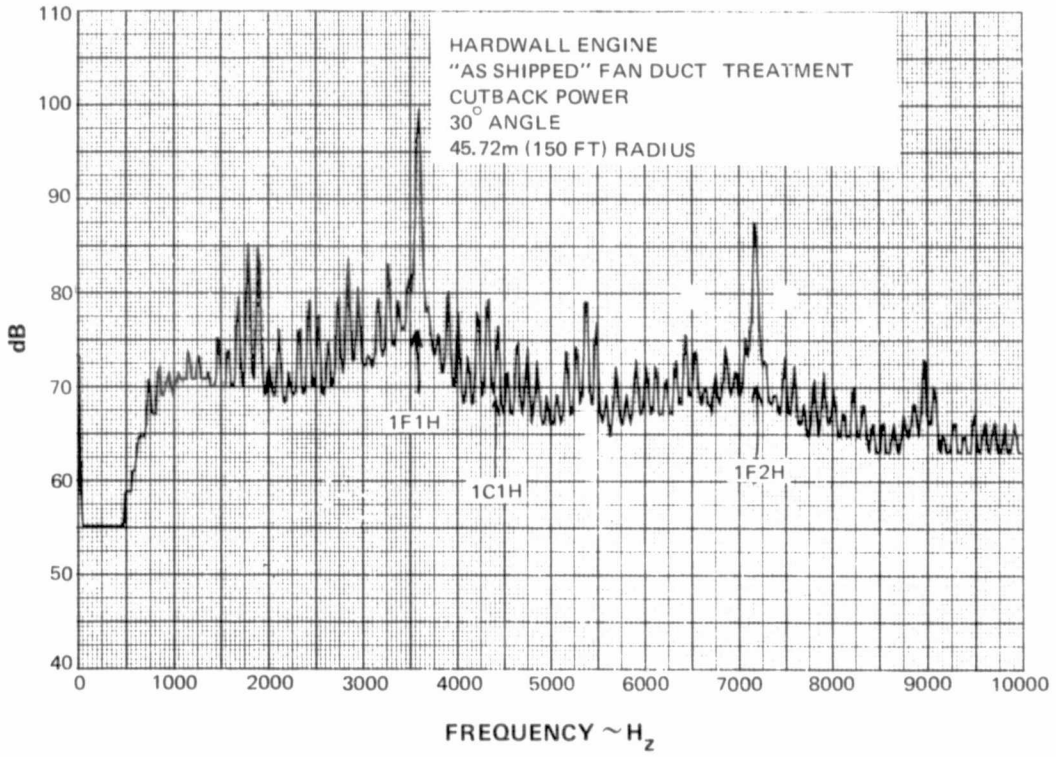

Figure D-81 Narrowband Analysis of Far Field Data ~ Cutback Power, Treated Fan Duct

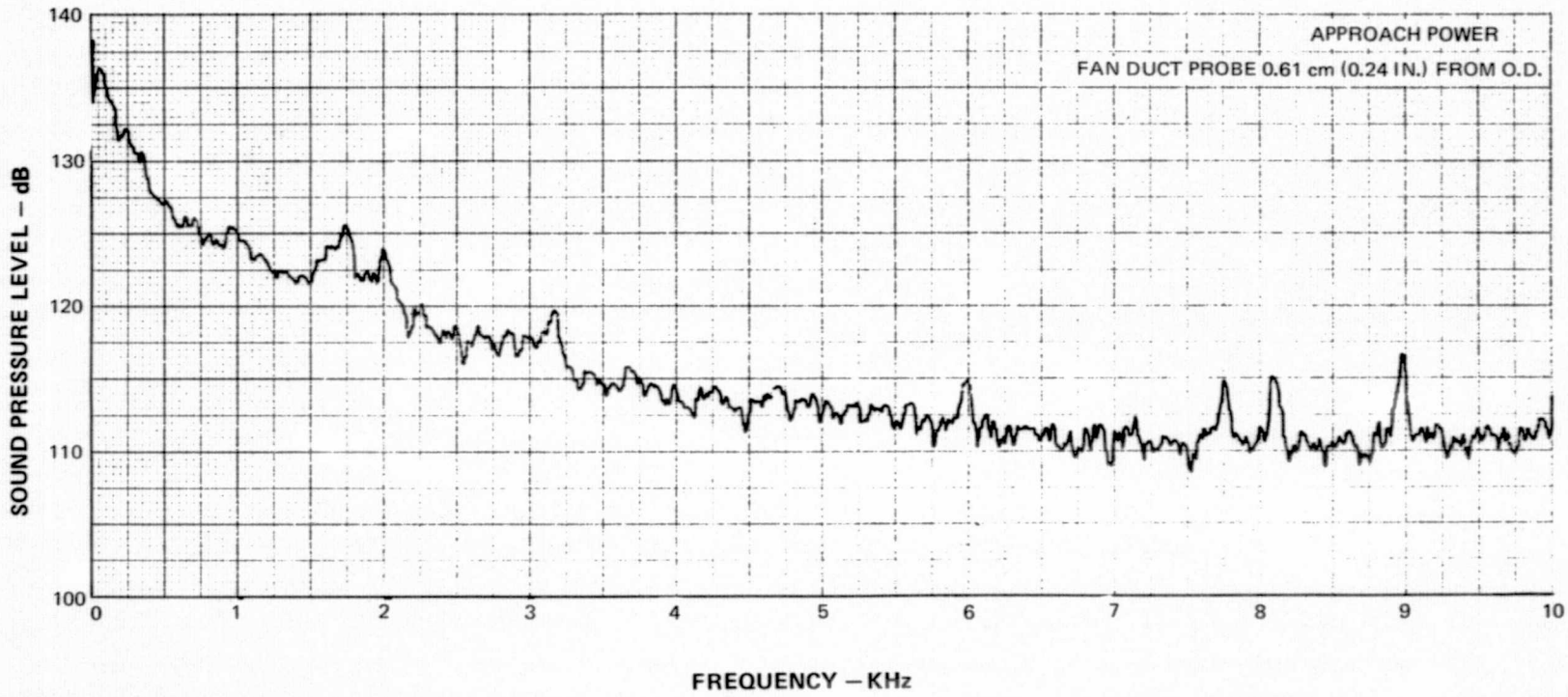

Figure D-82 Fan Duct Narrowband Spectra ~ Approach Power, Probe 0.61 cm (0.24 In.) from O.D.

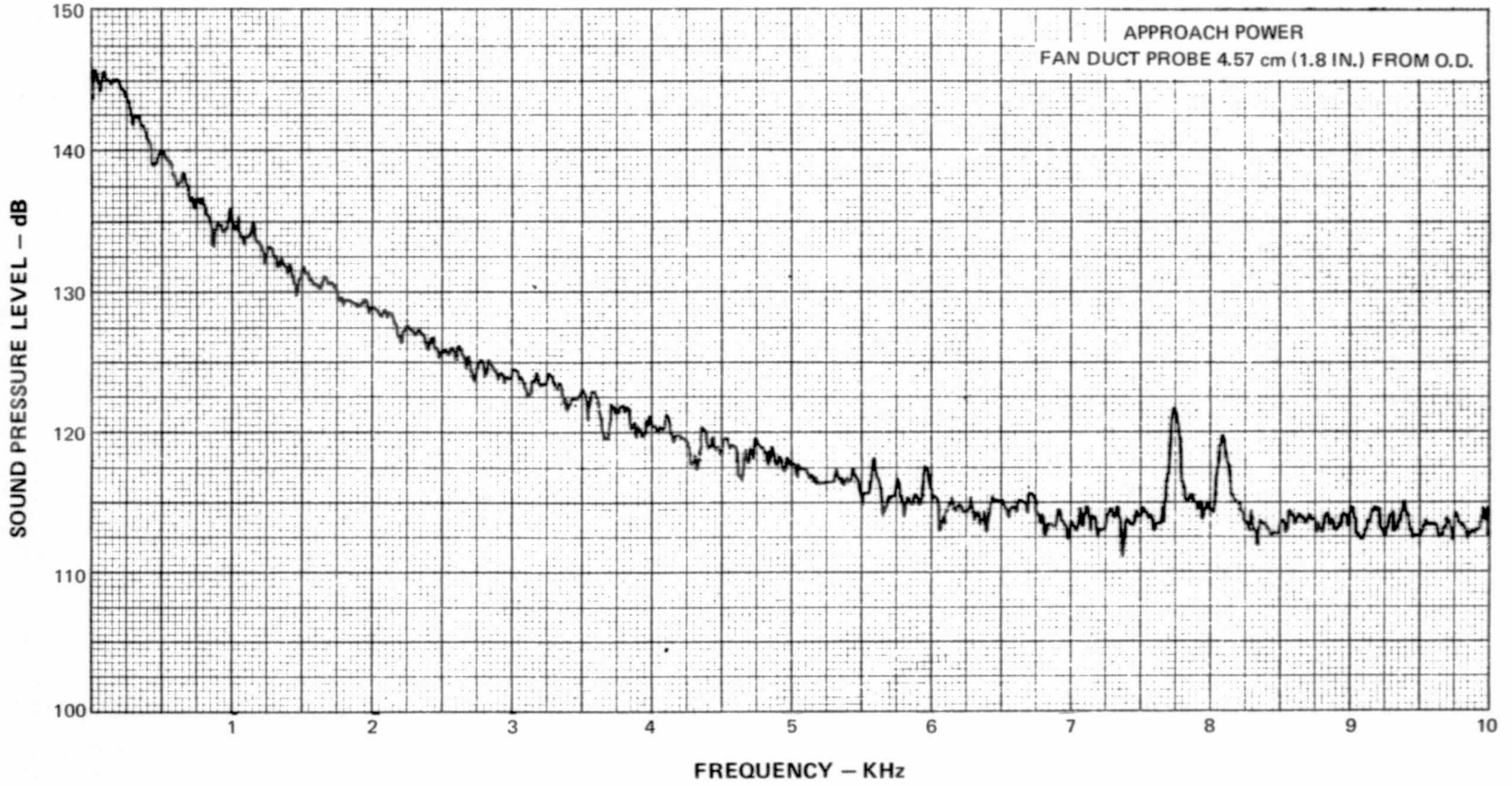

Figure D-83 Fan Duct Narrowband Spectra ~ Approach Power, Probe 4.57 cm (1.8 In.) from O.D.

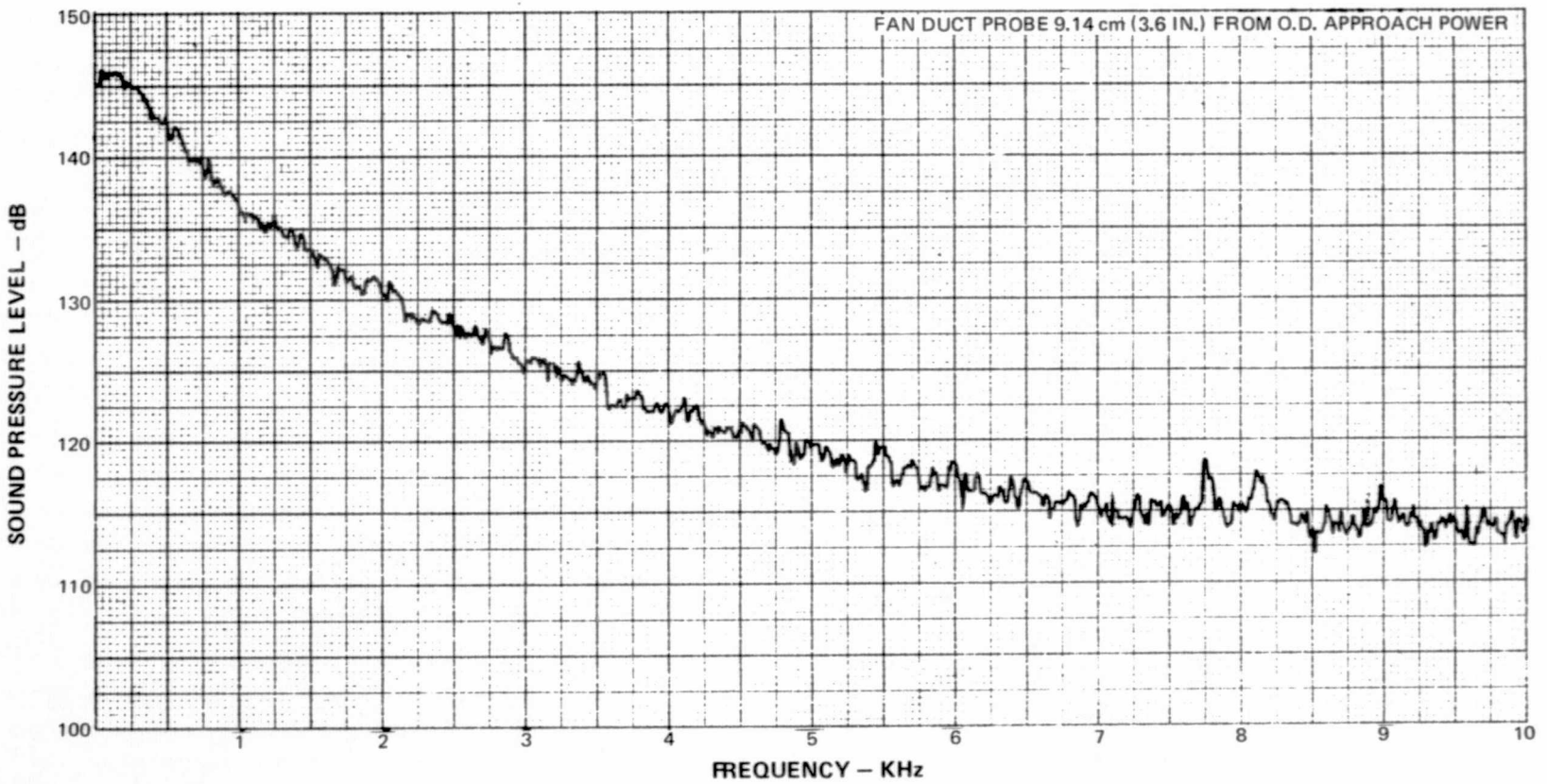

Figure D-84 Fan Duct Narrowband Spectra ~ Approach Power, Probe 9.14 cm (3.6 In.) from O.D.

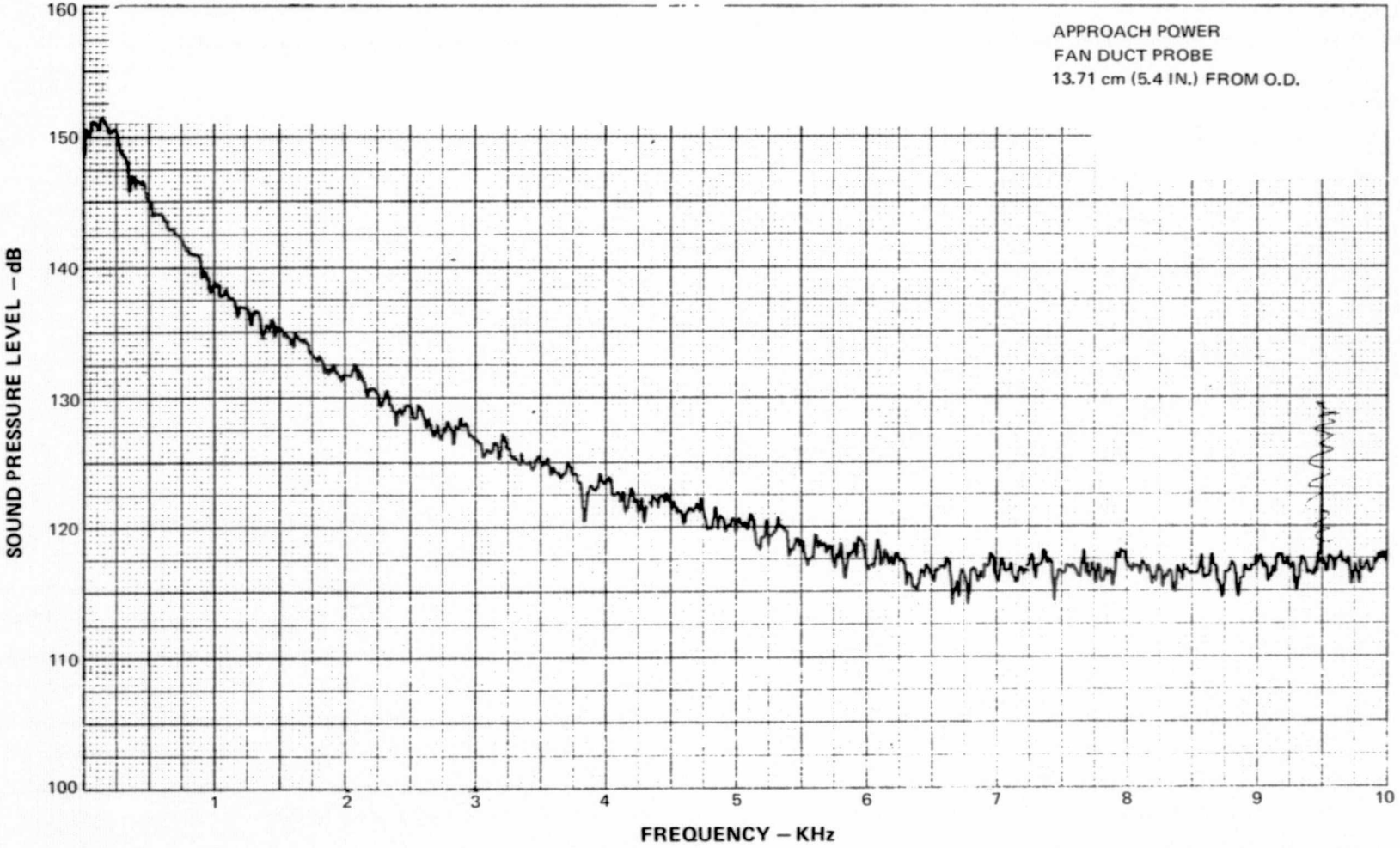

Figure D-85 Fan Duct Narrowband Spectra ~ Approach Power, Probe 13.71 cm (5.4 In.) from O.D.

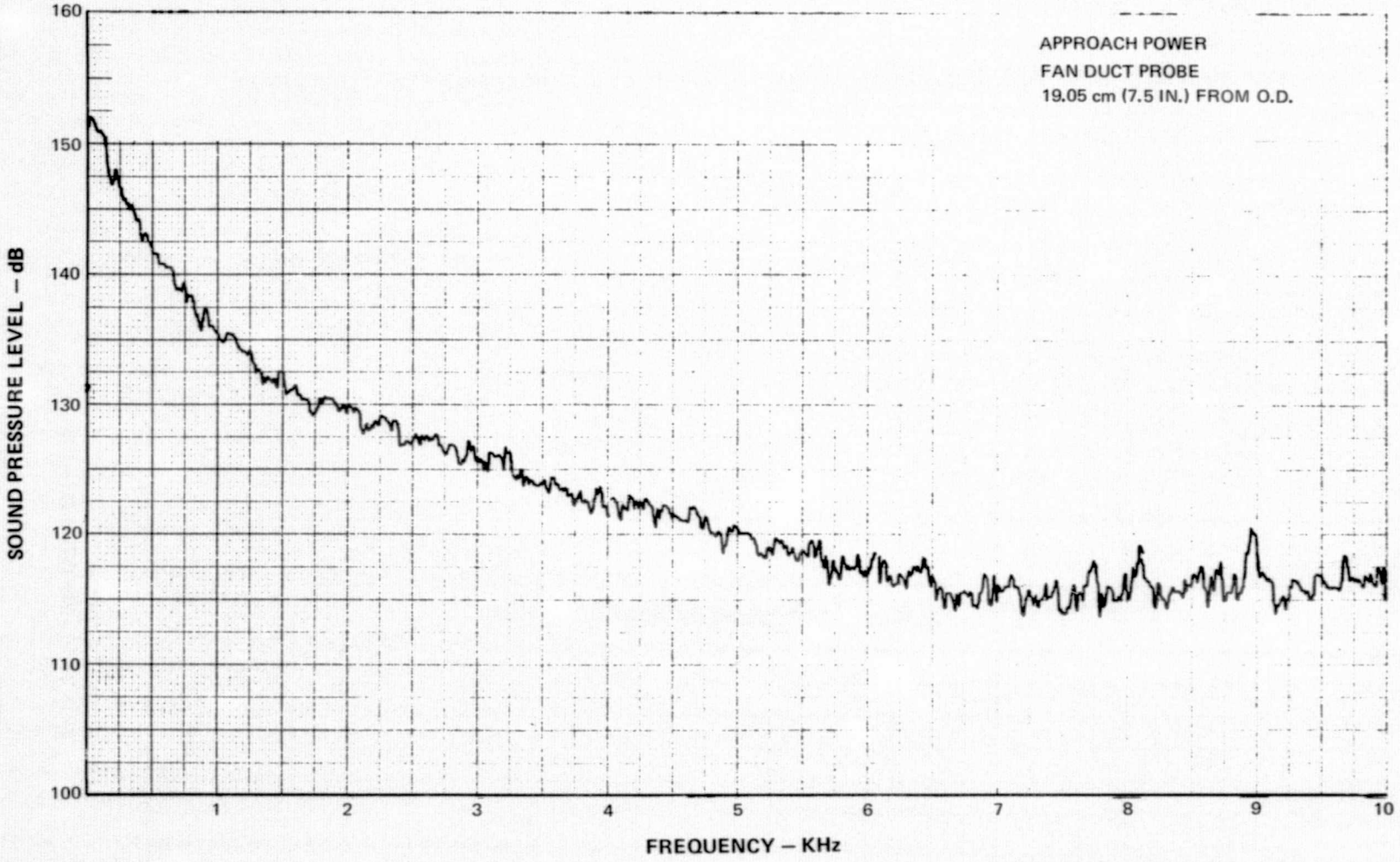

Figure D-86 Fan Duct Narrowband Spectra ~ Approach Power, Probe 19.05 cm (7.5 In.) from O.D.

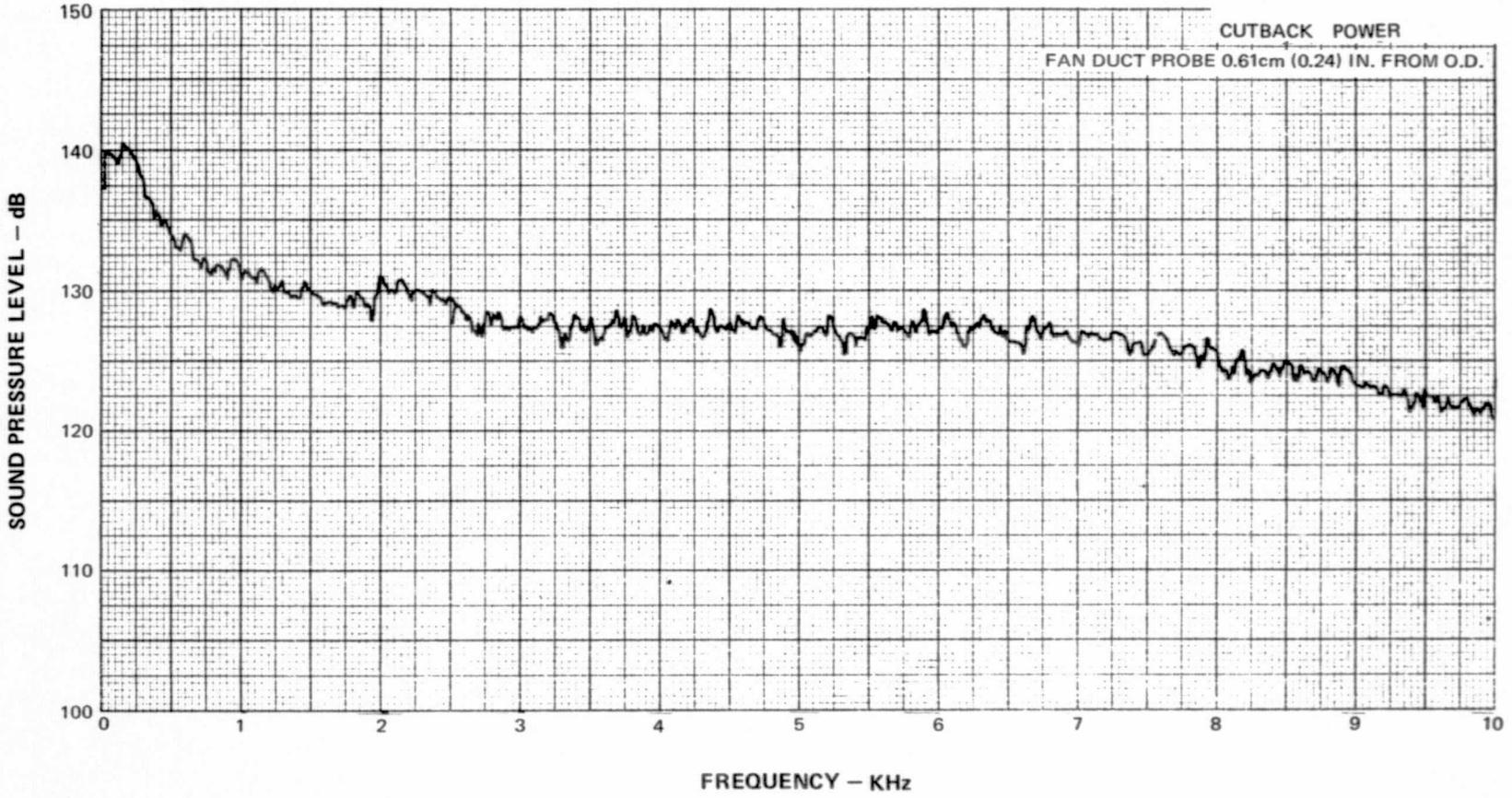

Figure D-87 Fan Duct Narrowband Spectra ~ Cutback Power, Probe 0.61cm (0.24 In.) from O.D.

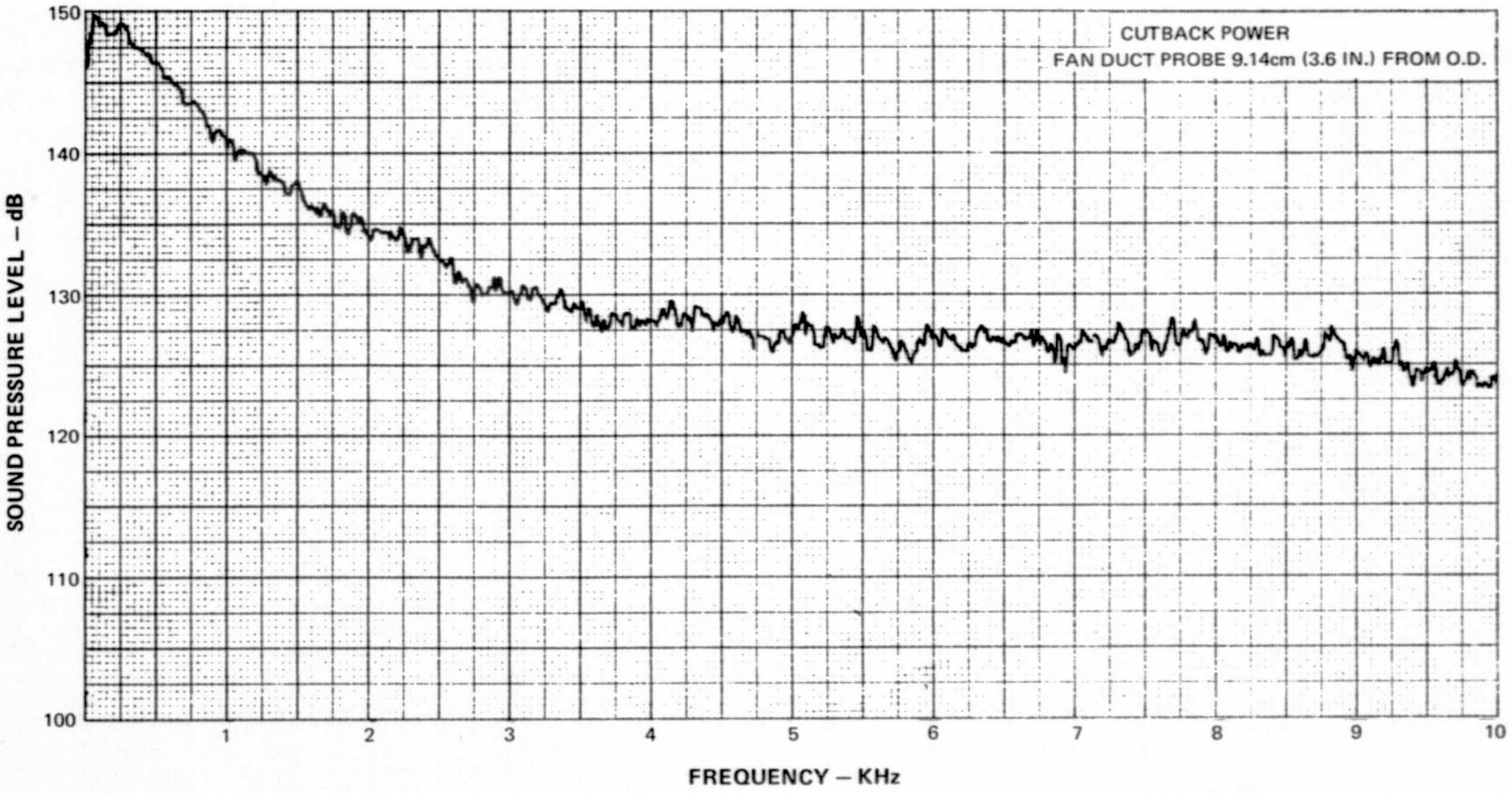

Figure D-88 Fan Duct Narrowband Spectra ~ Cutback Power, Probe 9.14cm (3.6 In.) from O.D.

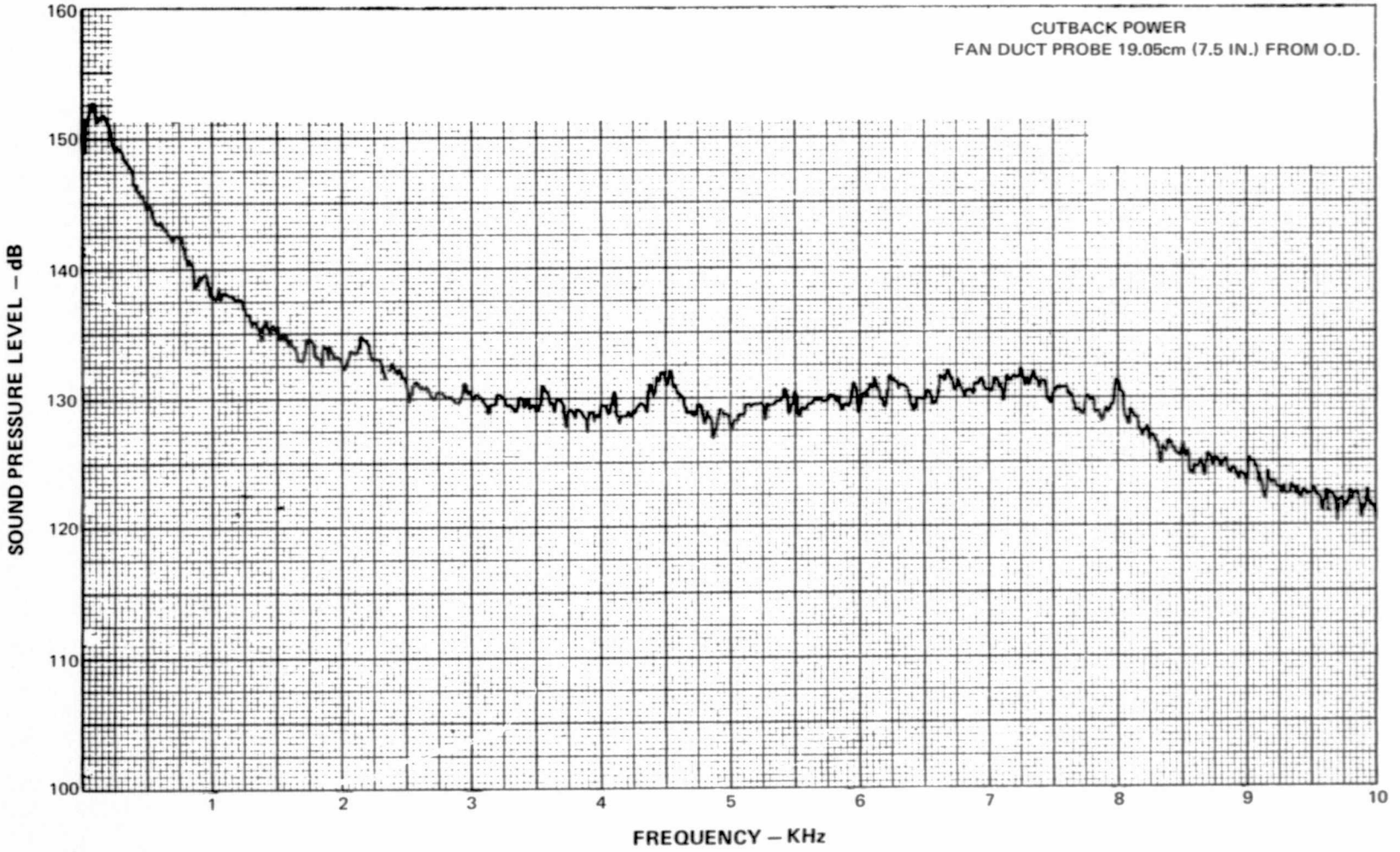

Figure D-89 Fan Duct Narrowband Spectra ~ Cutback Power, Probe 19.05cm (7.5 In.) from O.D.

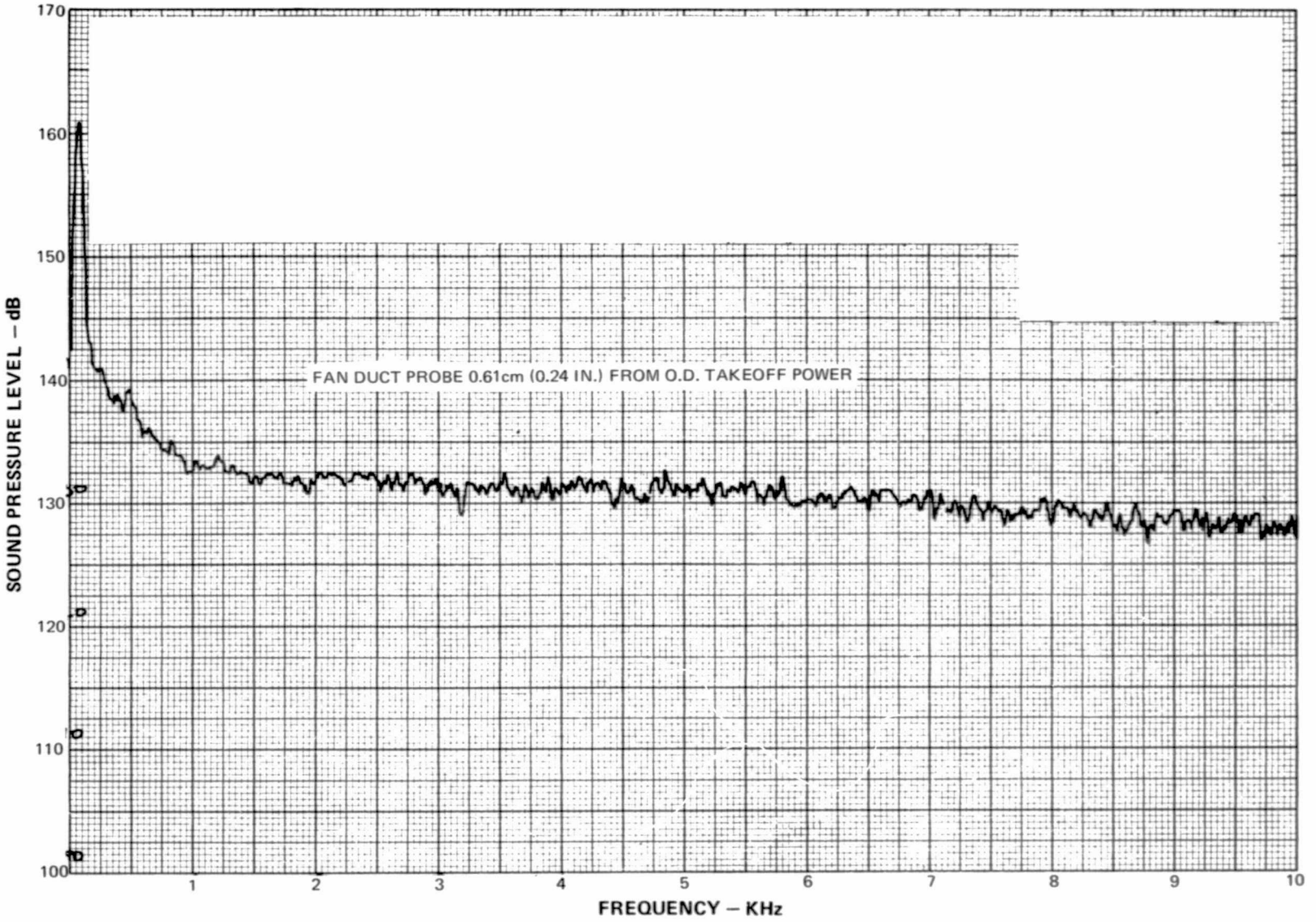

Figure D-90 Fan Duct Narrowband Spectra ~ Takeoff Power, Probe 0.61cm (0.24 In.) from O.D.

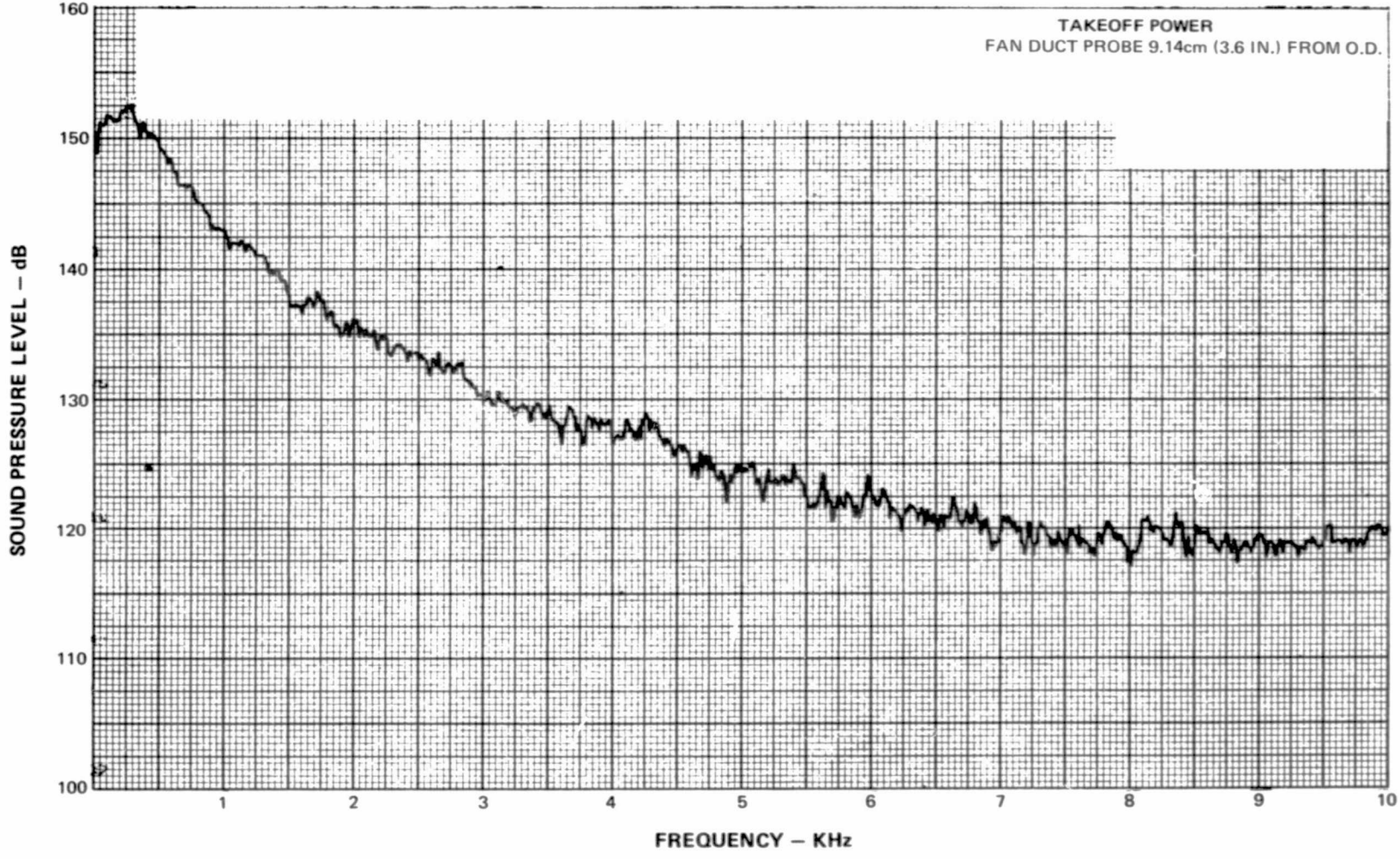

Figure D-91 Fan Duct Narrowband Spectra ~ Takeoff Power, Probe 9.14cm (3.6 In.) from O.D.

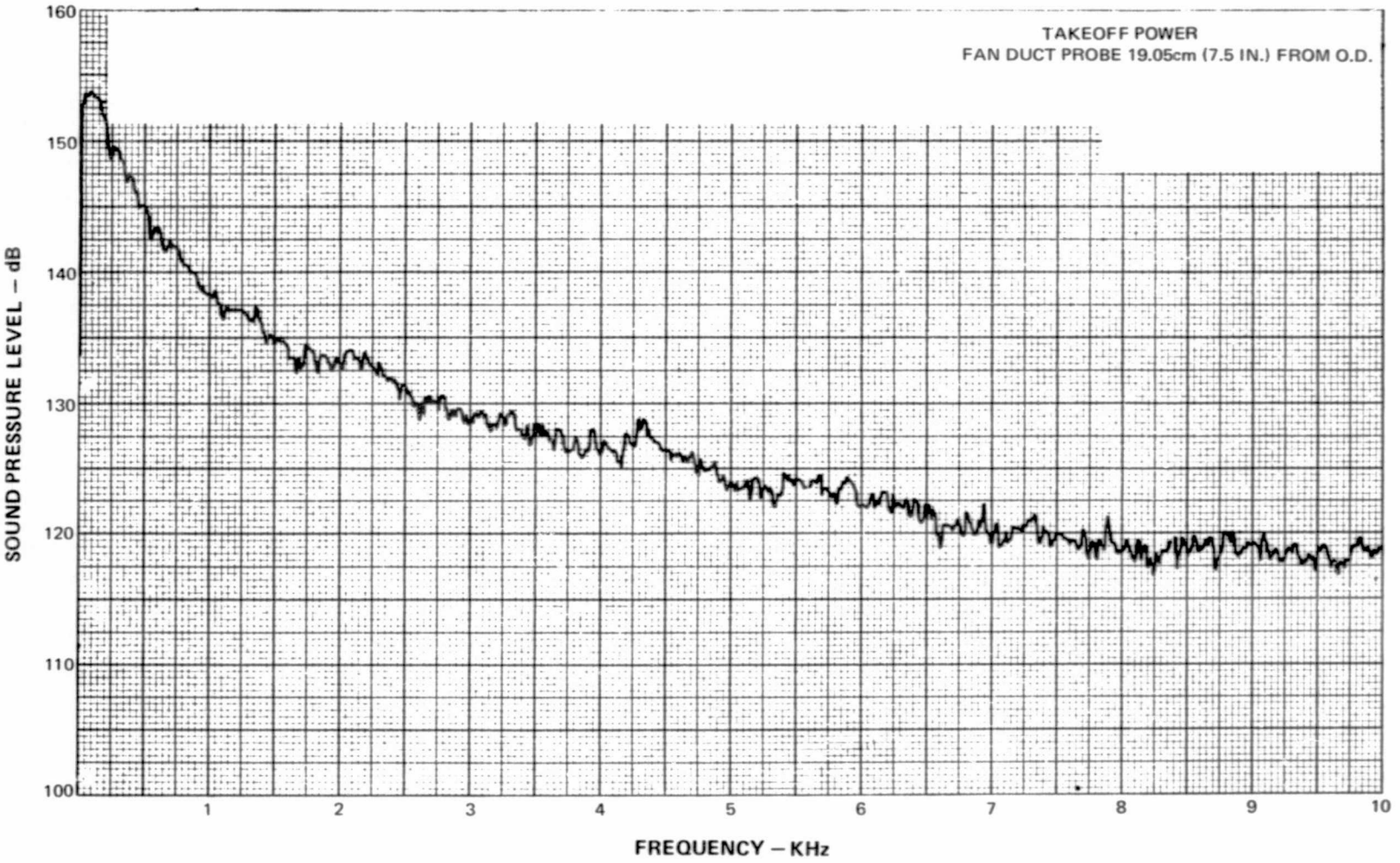

Figure D-92 Fan Duct Narrowband Spectra ~ Takeoff Power, Probe 19.05cm (7.5 In.) from O.D.

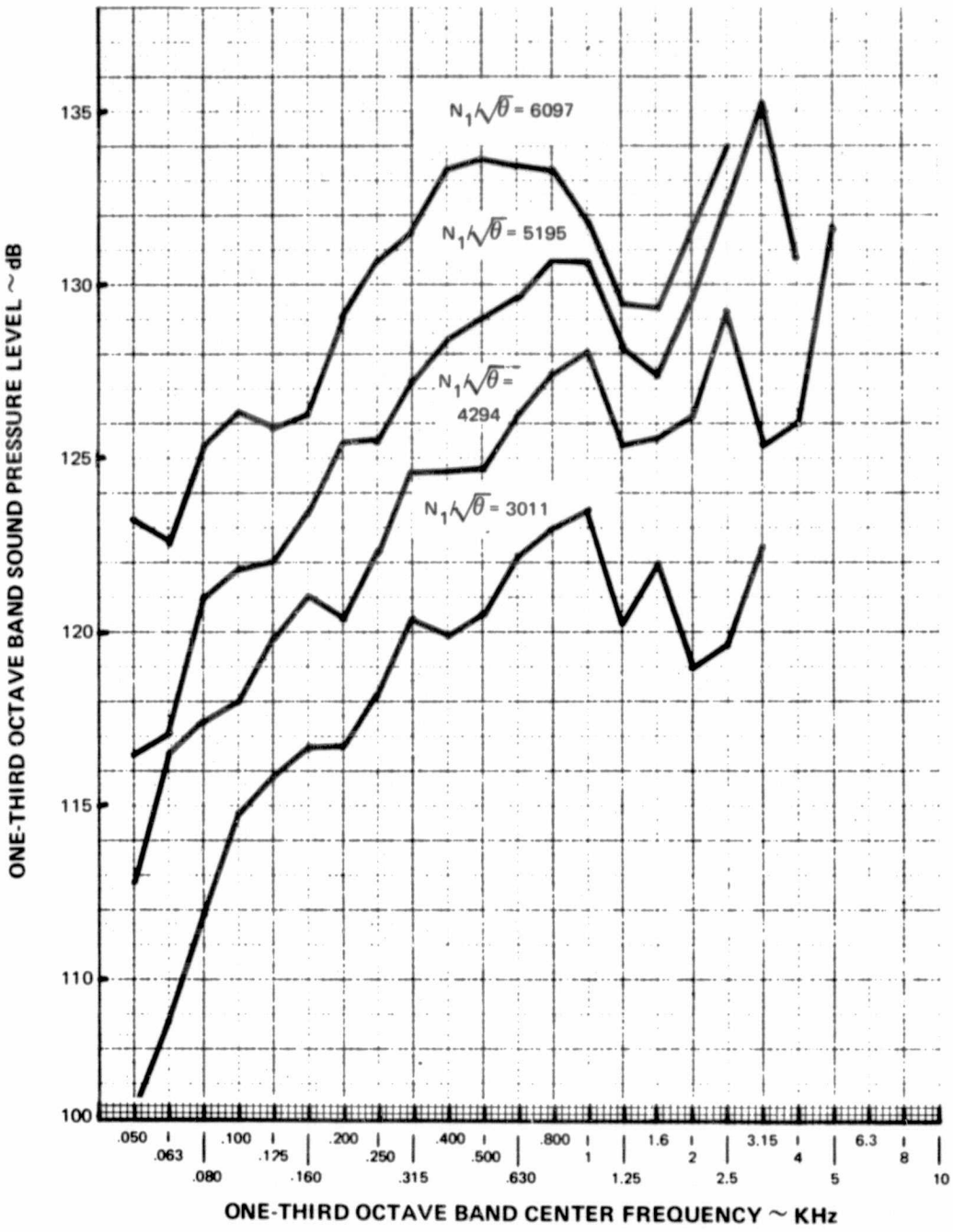

Figure D-93 Tailpipe Noise Spectra ~ Kulite Transducer

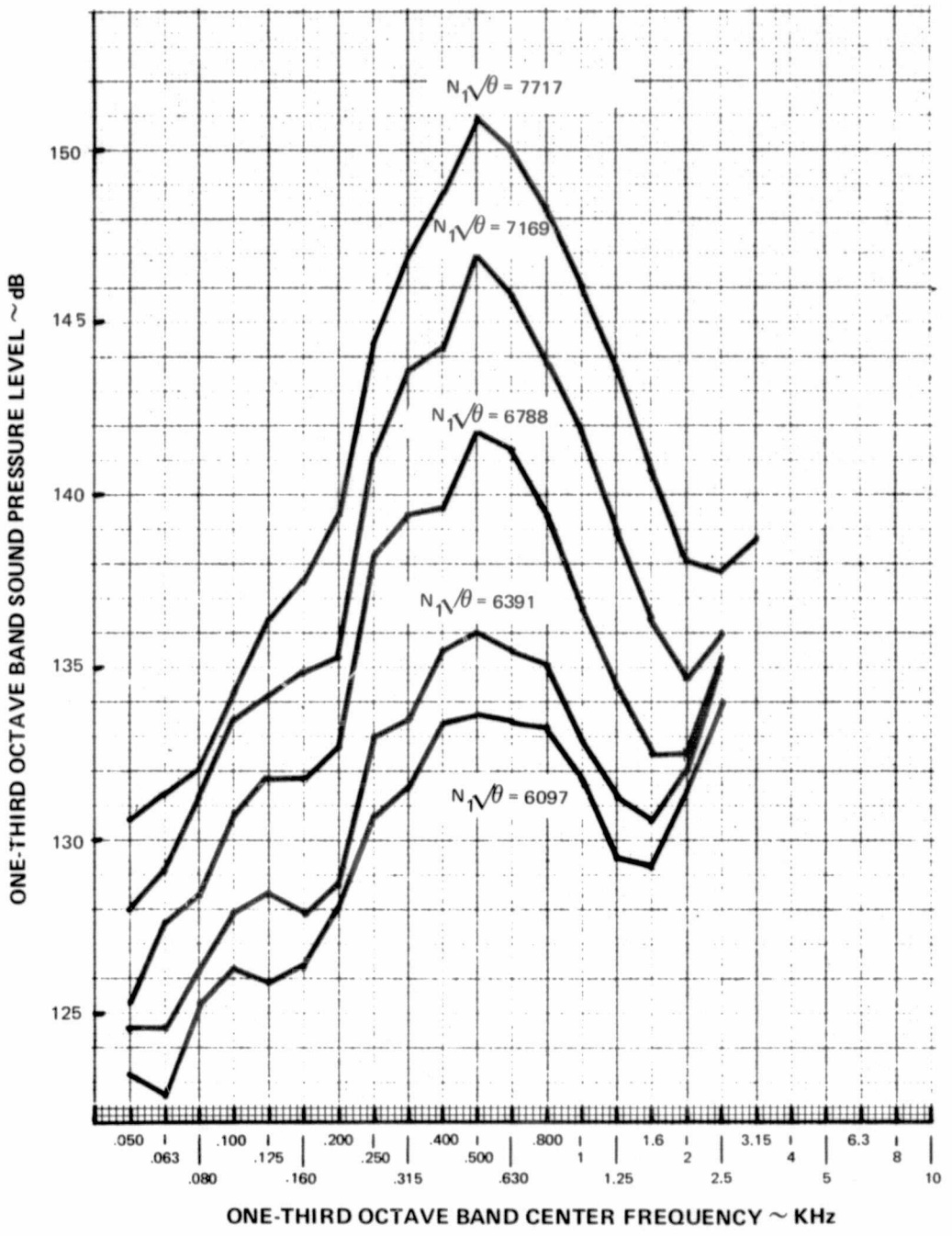

Figure D-94 Tailpipe Noise Spectra ~ Kulite Transducer

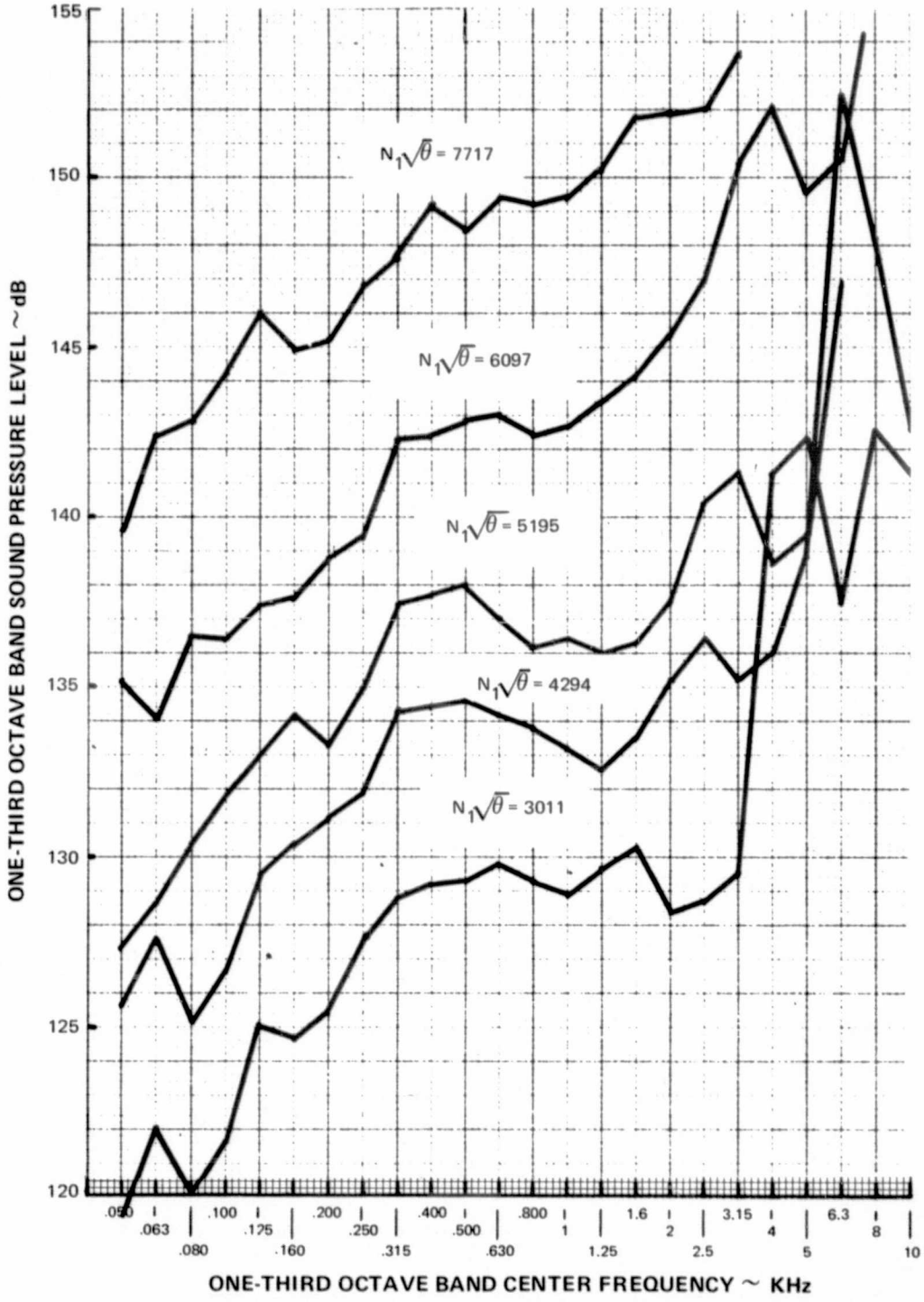

Figure D-95 Splitter Noise Spectra ~ Kulite Transducer

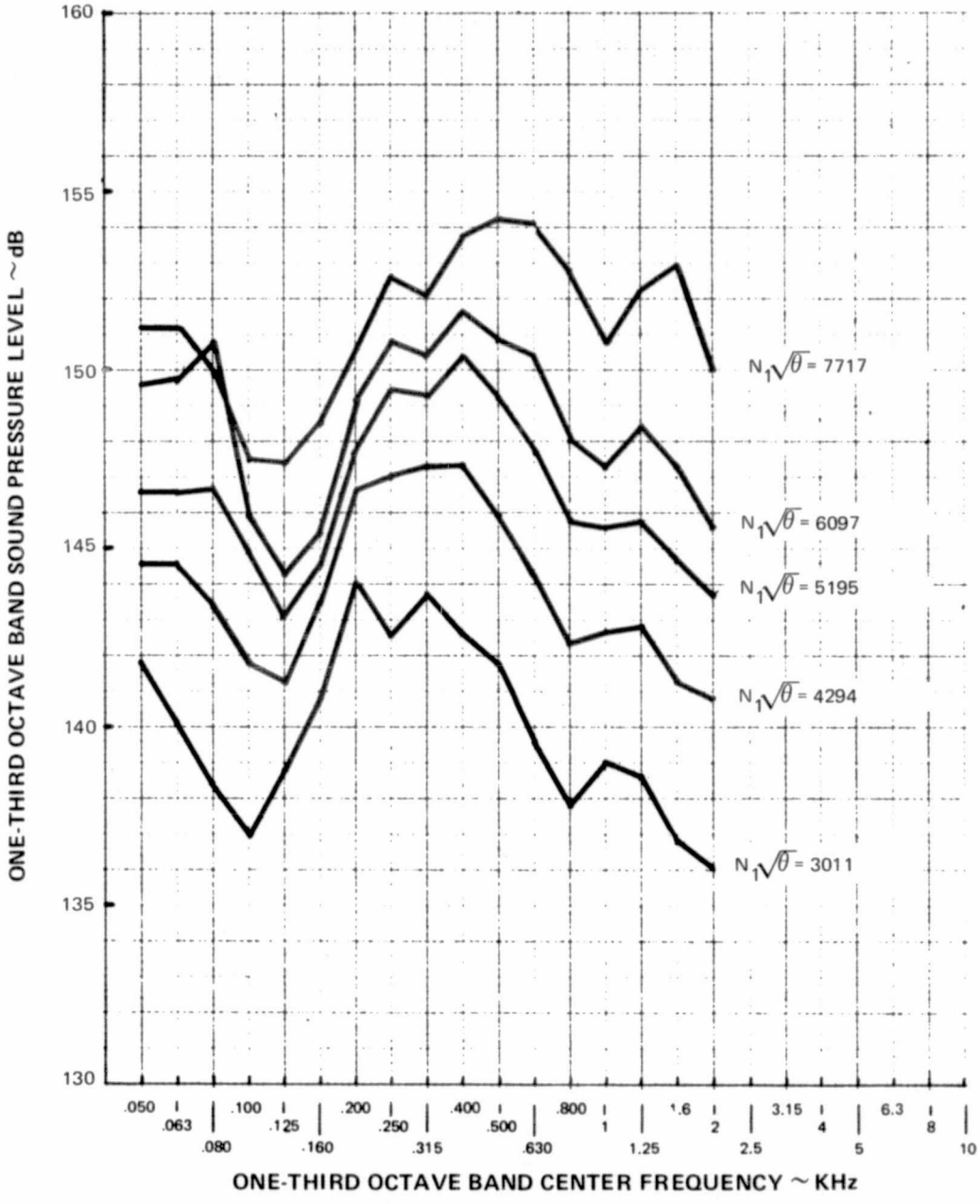

Figure D-96 Combustor Noise Spectra ~ Kulite Transducer

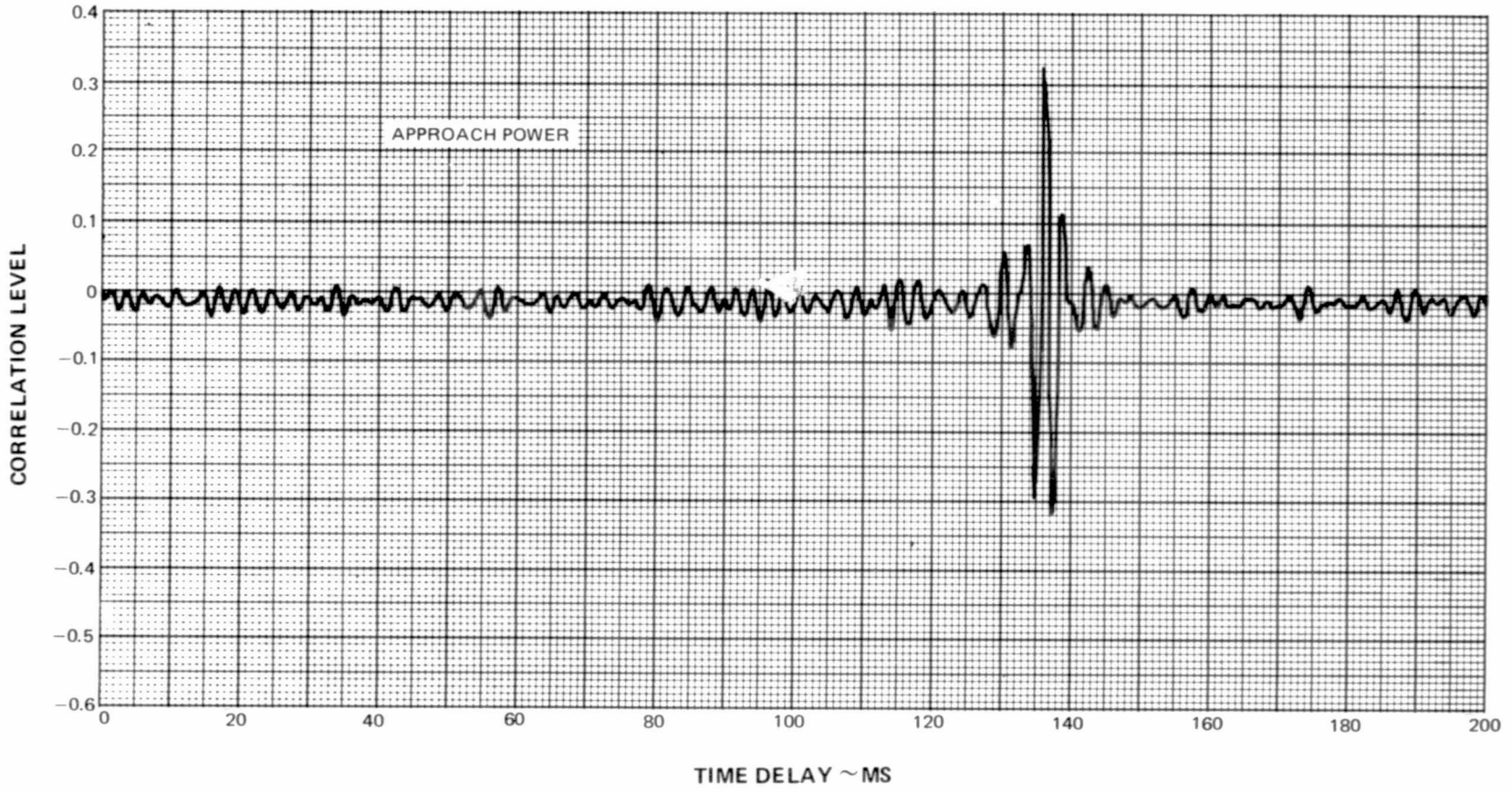

Figure D-97 Cross Correlation of Tailpipe Kulite with Far Field Microphone (120°) ~ Approach Power

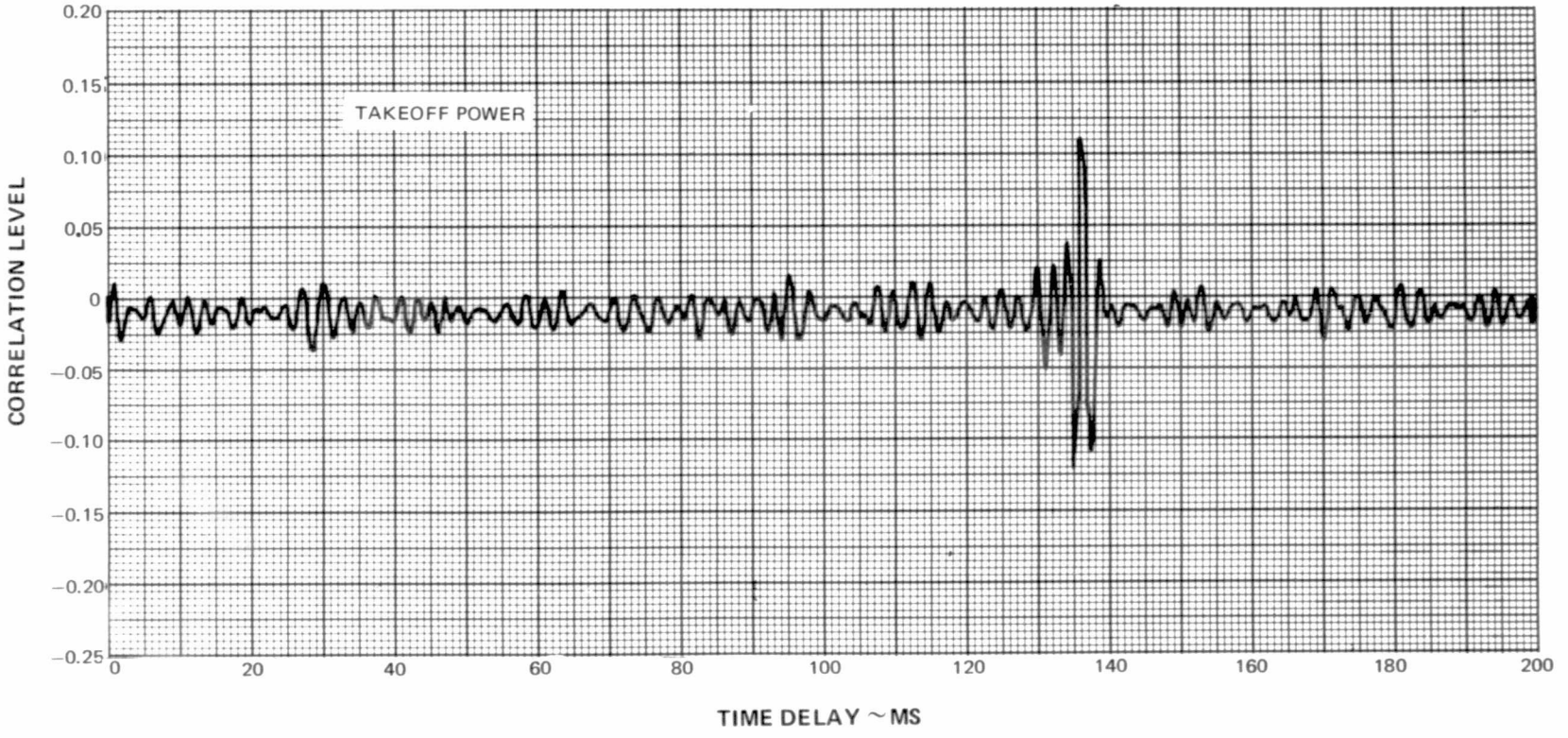

Figure D-98 Cross Correlation of Tailpipe Kulite with Far Field Microphone (120°) ~ Takeoff Power

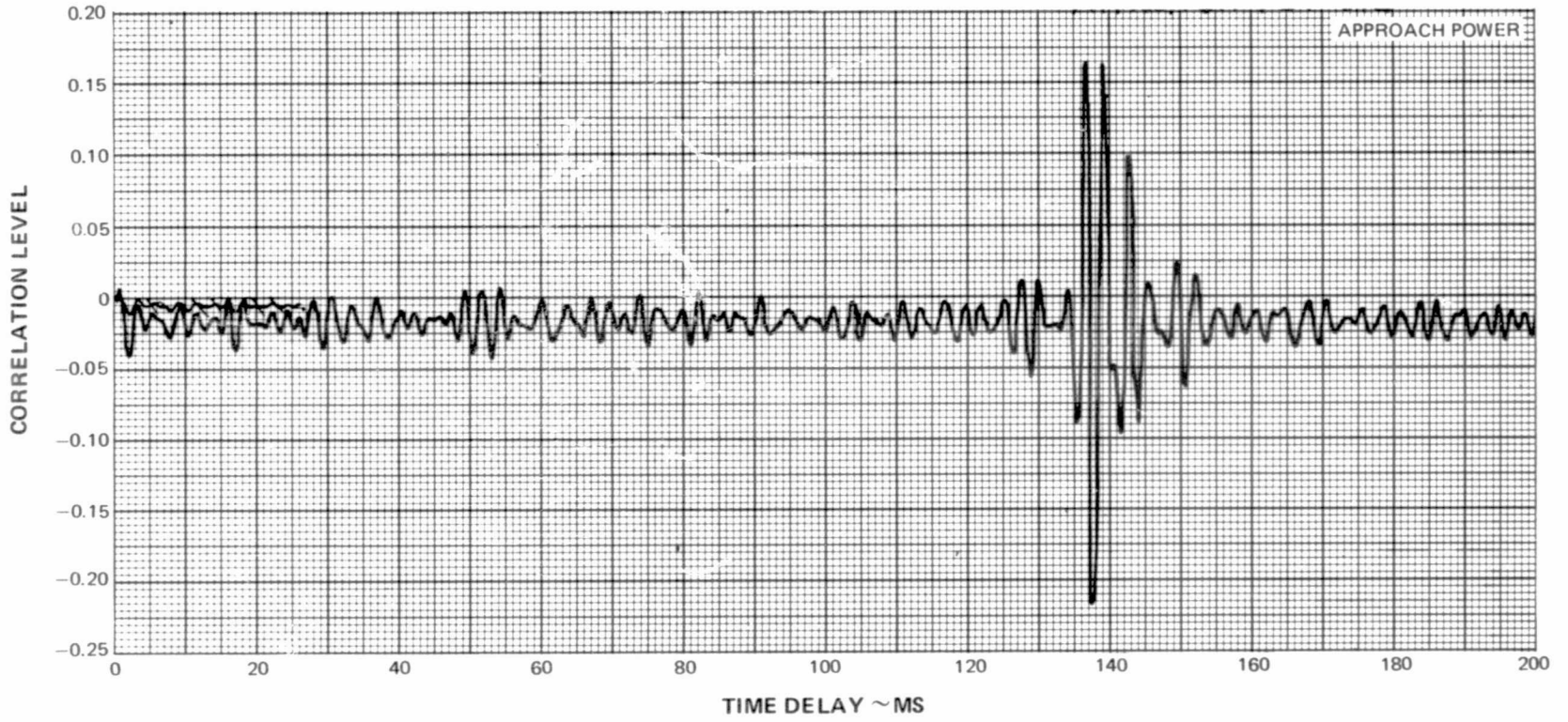

Figure D-99 Cross Correlation of Splitter Kulite with Far Field Microphone (120°) ~ Approach Power

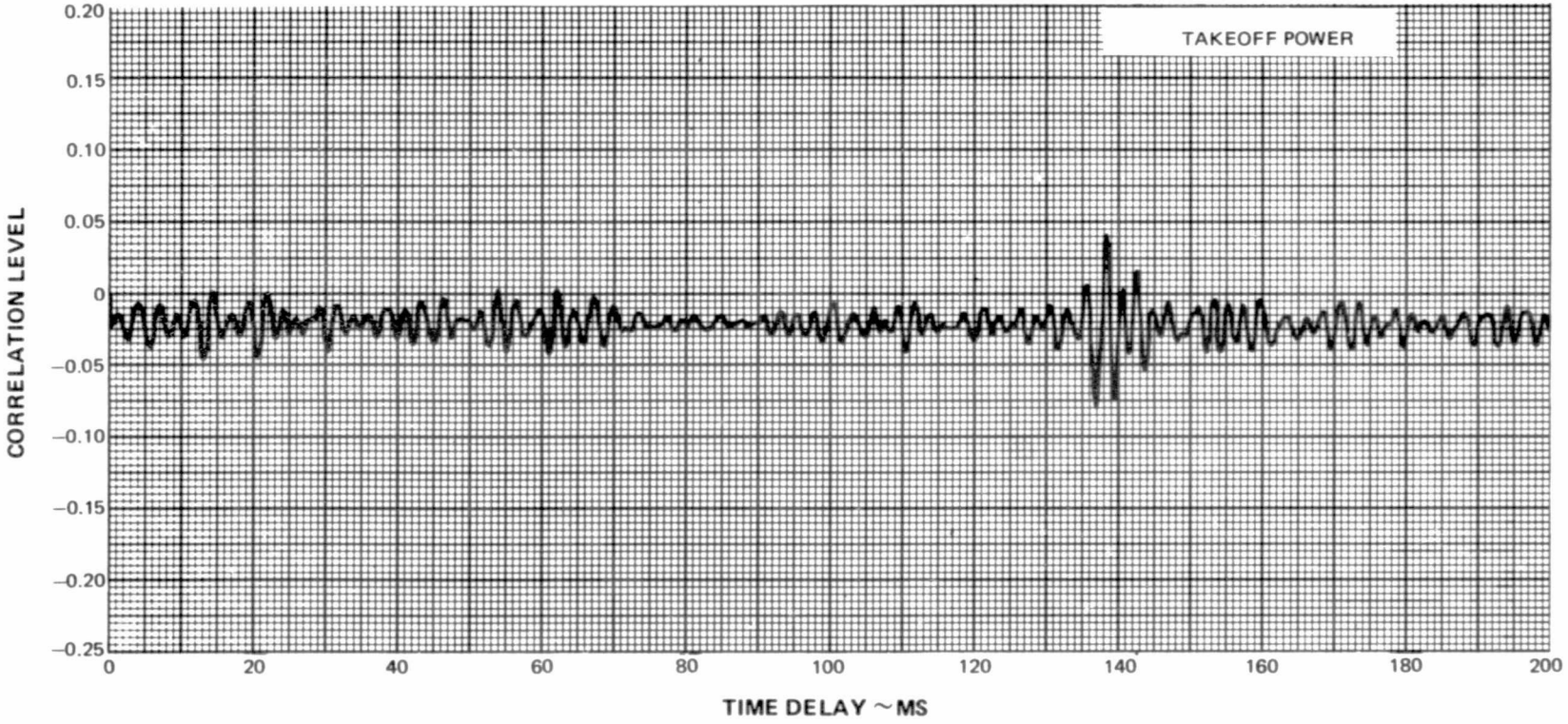

Figure D-100 Cross Correlation of Splitter Kulite with Far Field Microphone (120°) ~ Takeoff Power

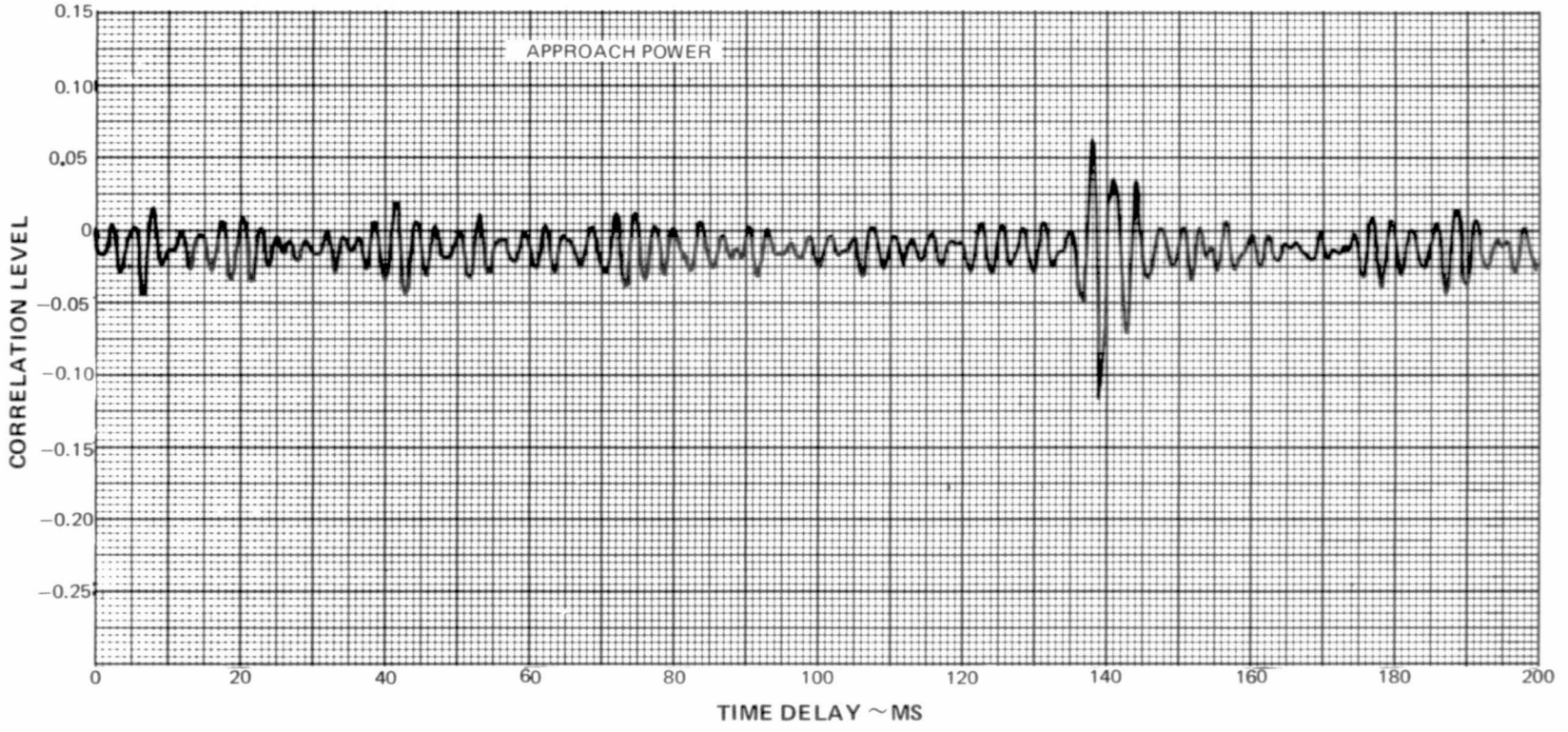

Figure D-101 Cross Correlation of Combustor Kulite with Far Field Microphone (120°) ~ Approach Power

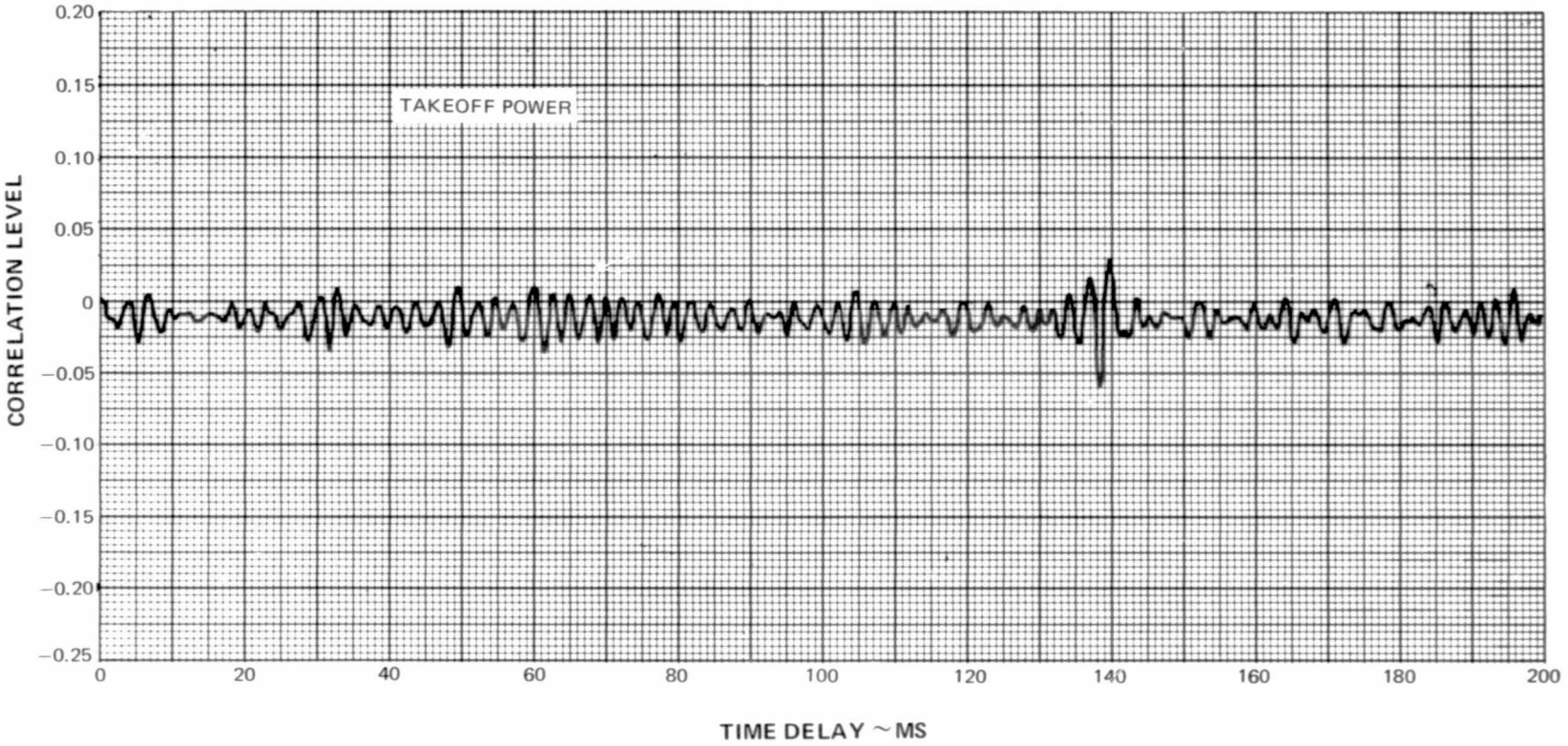

Figure D-102 Cross Correlation of Combustor Kulite with Far Field Microphone (120°) ~ Takeoff Power

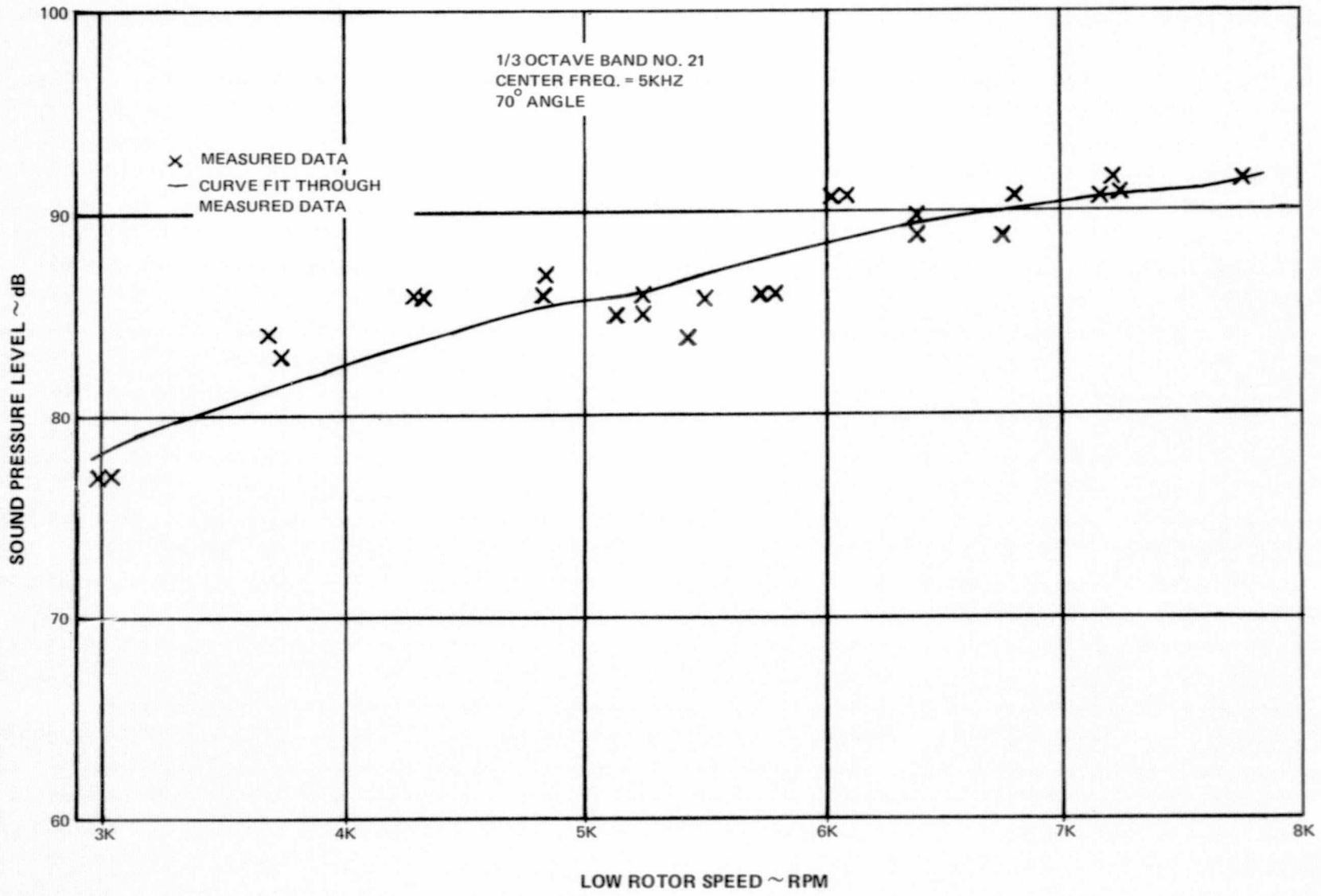

Figure D-103 Typical Least Squares Curve Fit Through Measured Inlet Fan Noise Data

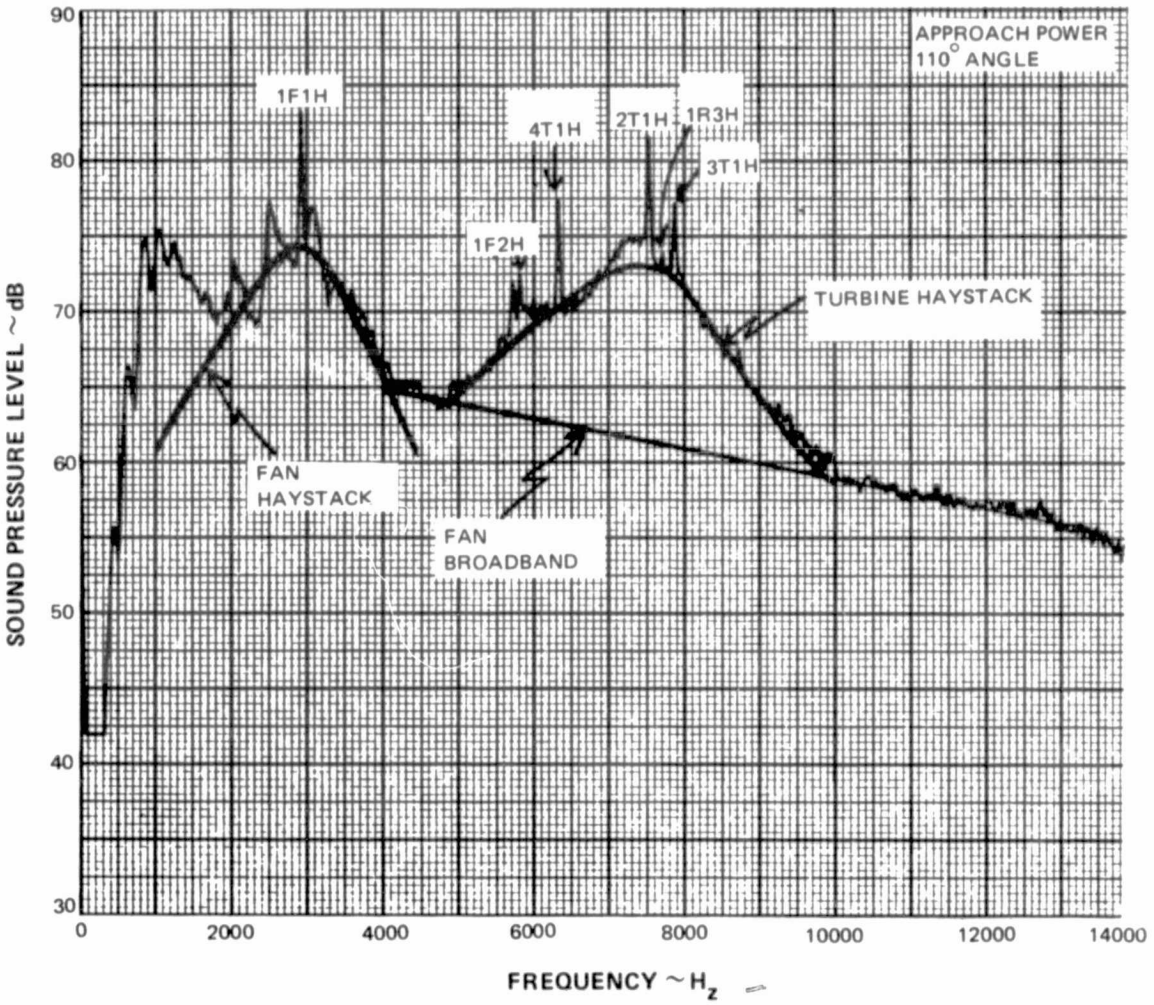

Figure D-104 Typical Approach Power Aft Quadrant Narrowband Spectra Showing Fan and Turbine Noise Components

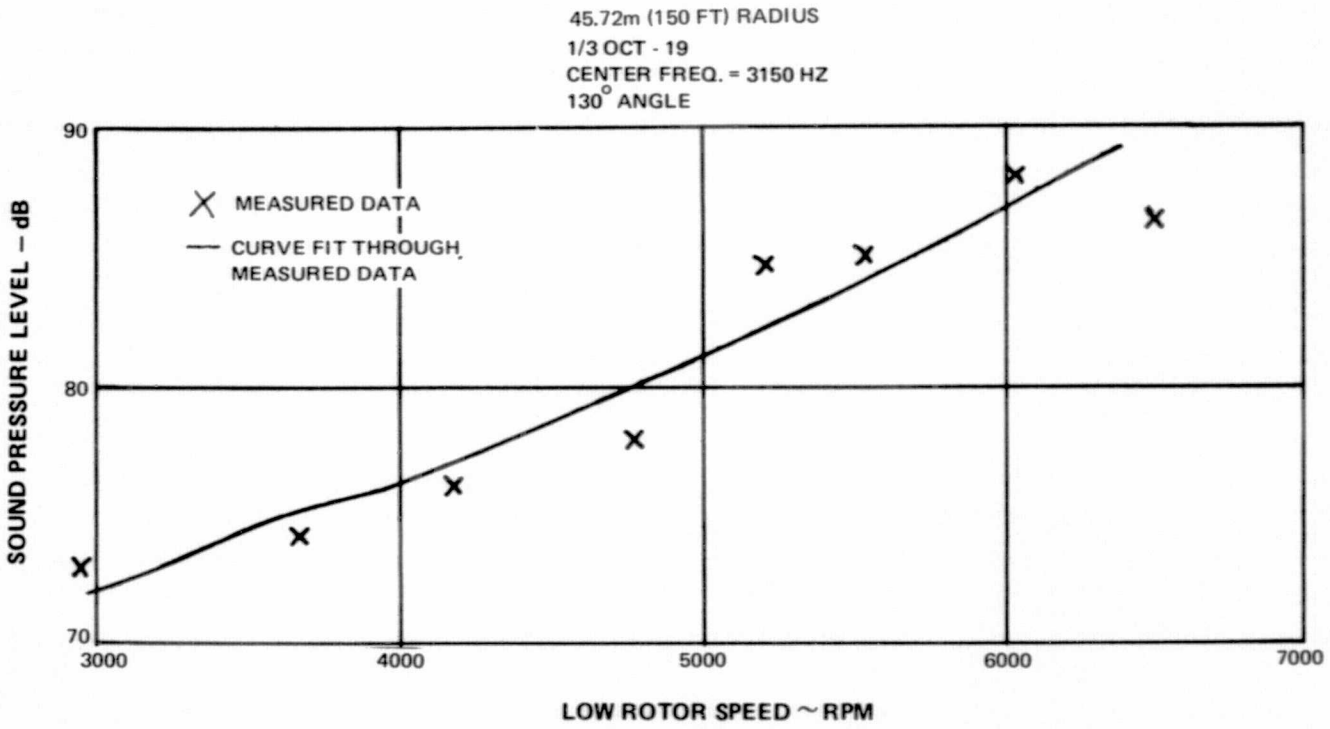

Figure D-105 Typical Least Squares Curve Fit Through Aft Fan Noise Data

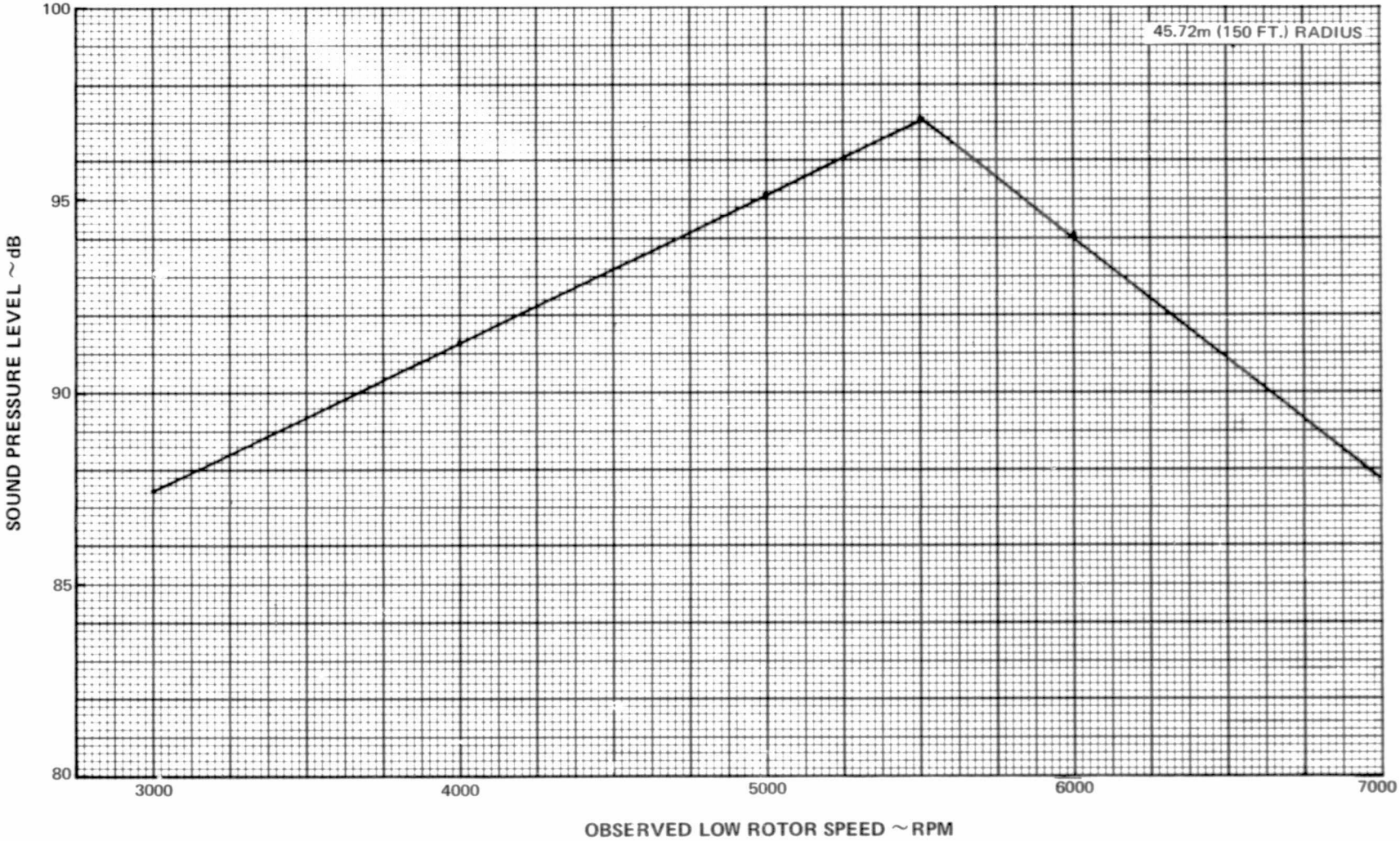

Figure D-106 Turbine Noise Component ~ Peak 1/3 Octave Band Level as a Function of Observed Rotor Speed

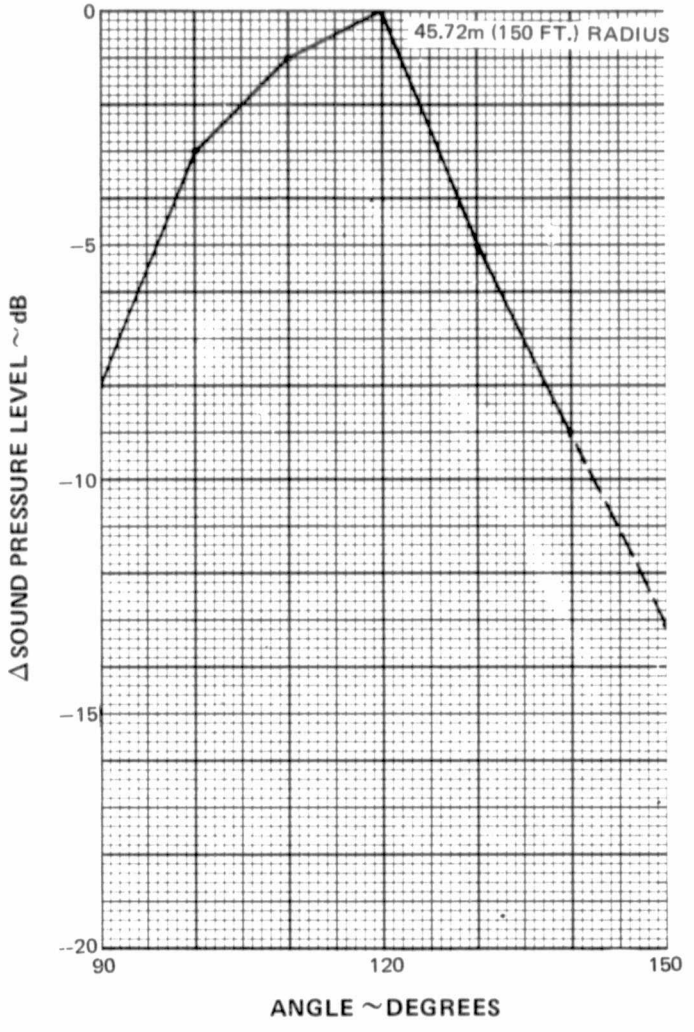

Figure D-107 Turbine Noise Component Directivity

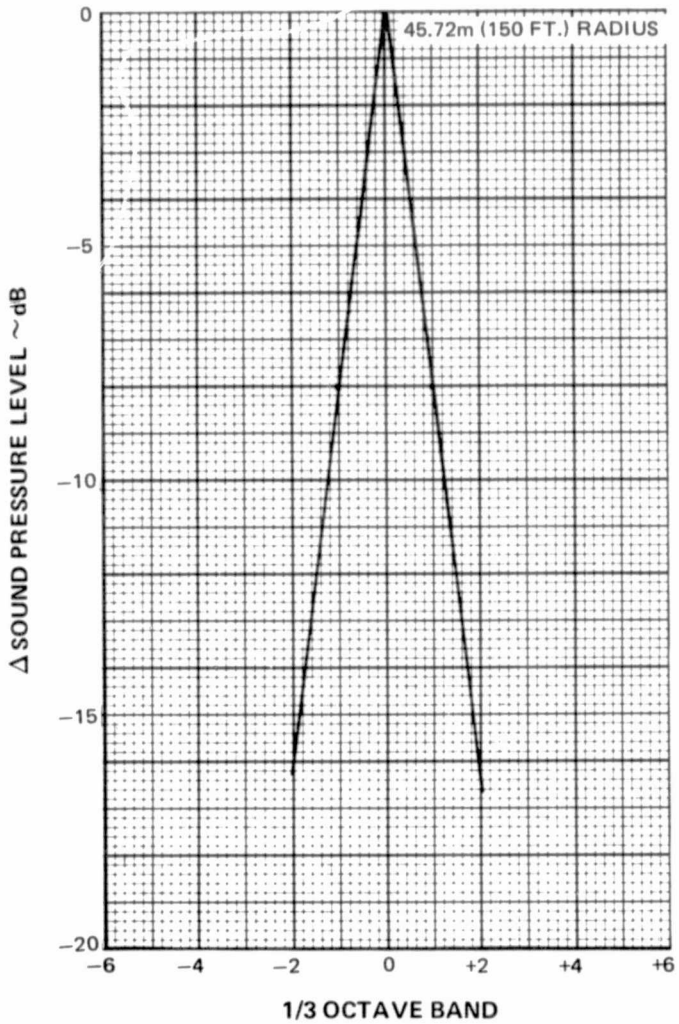

Figure D-108 Turbine Noise Component Spectrum

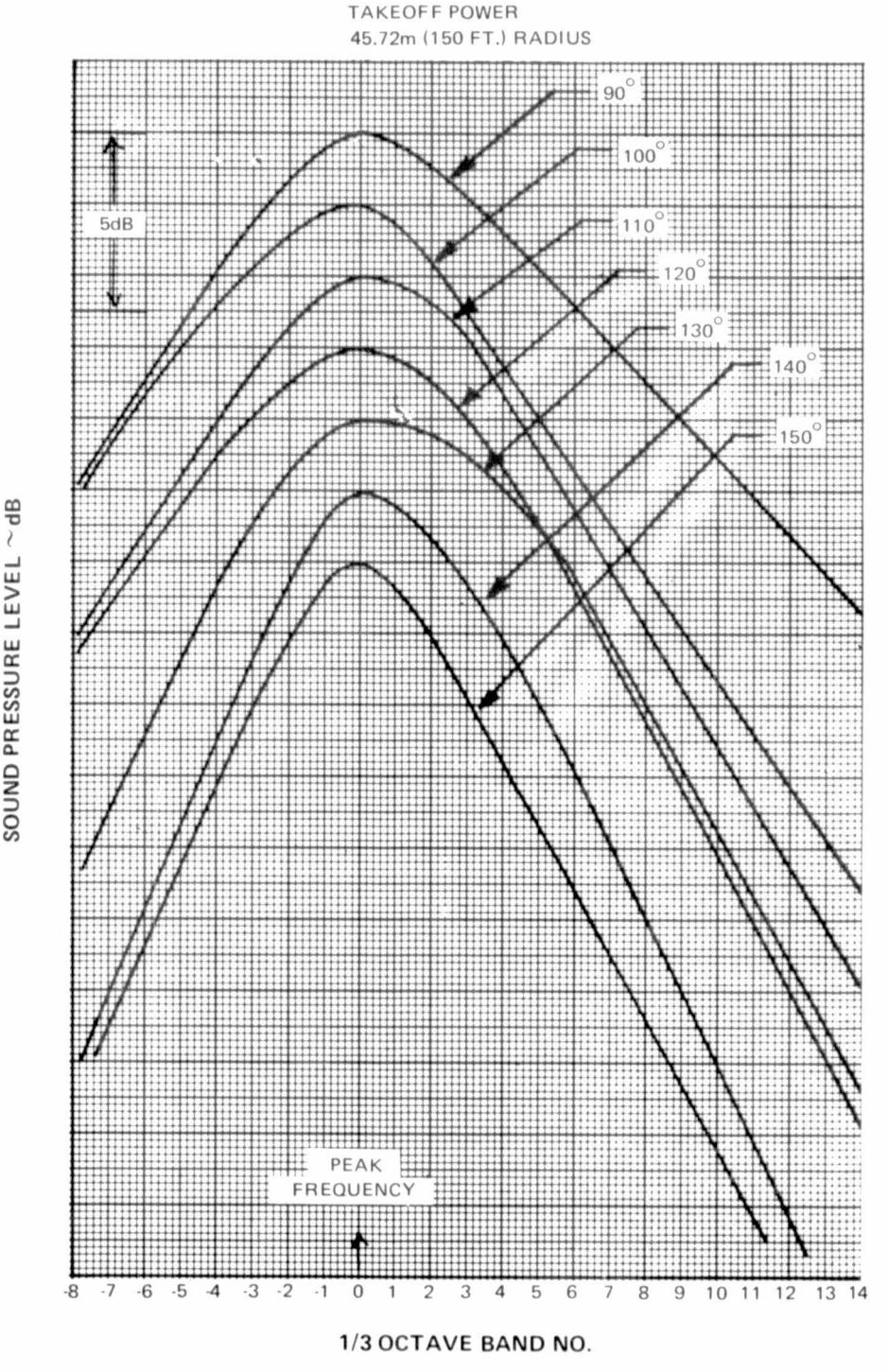

Figure D-109 Jet Noise Component Spectra

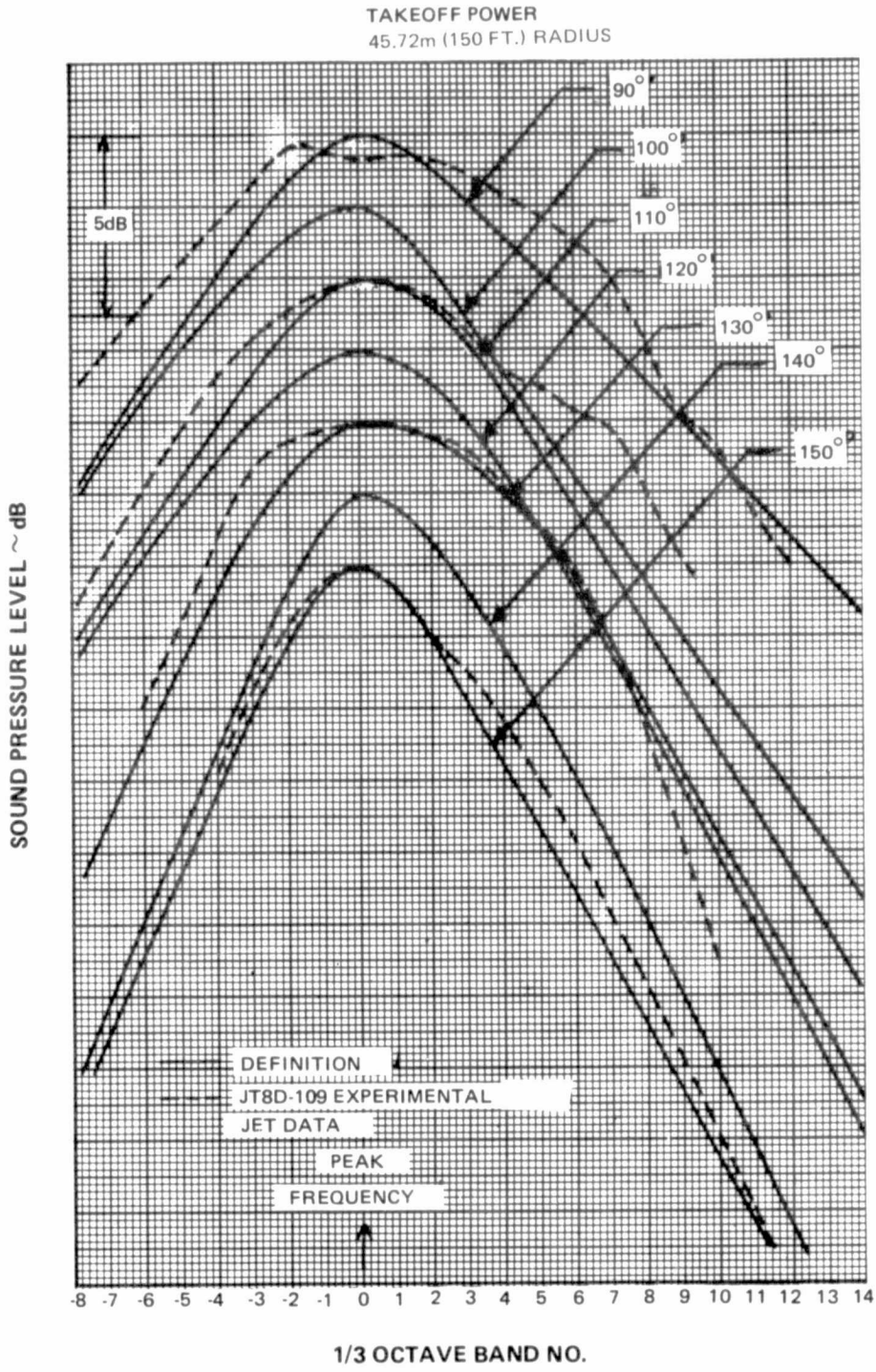

Figure D-110 Jet Noise Component Spectra Compared with Model Jet Data

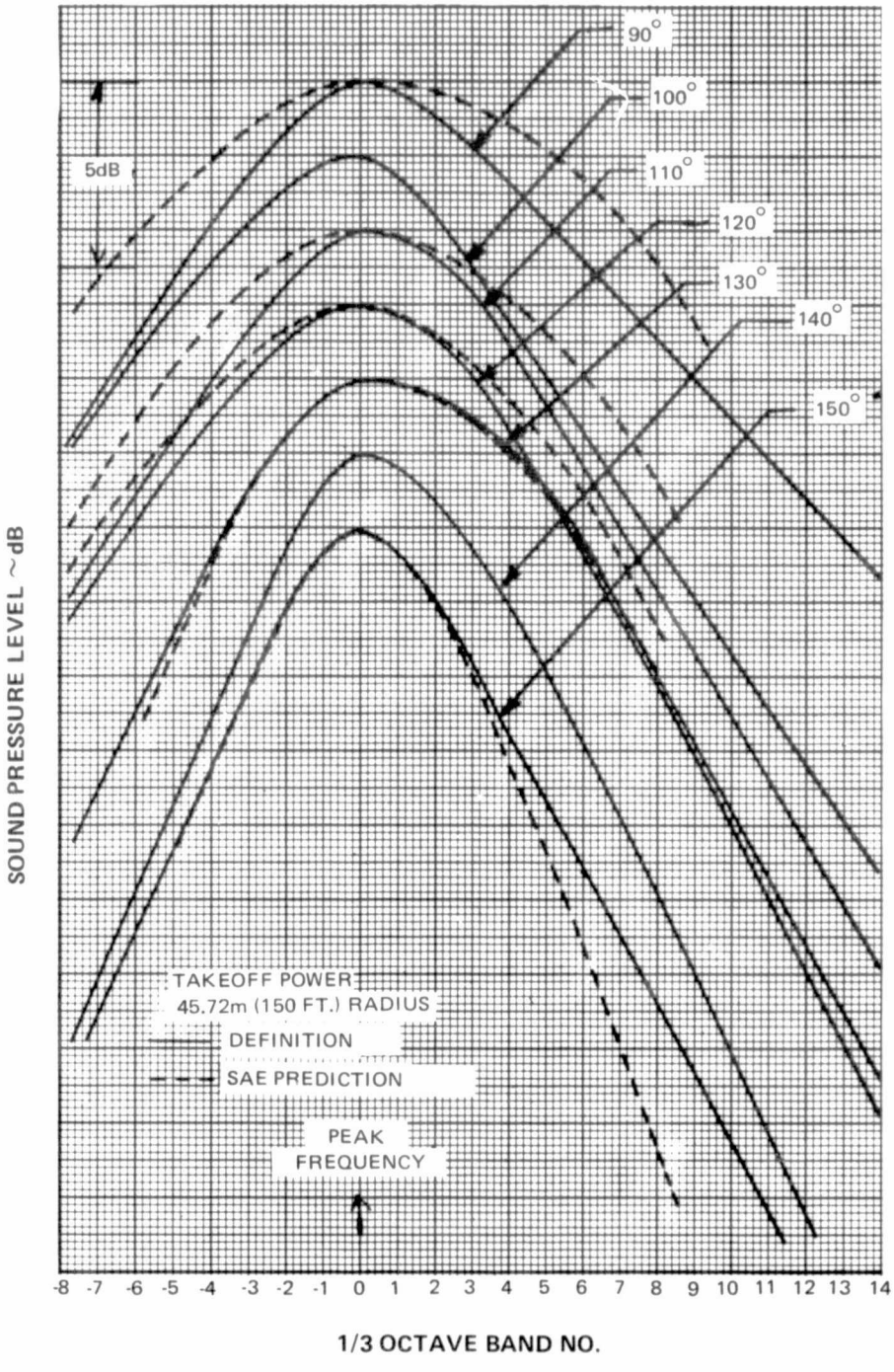

Figure D-111 Jet Noise Component Spectra Compared with SAE Prediction

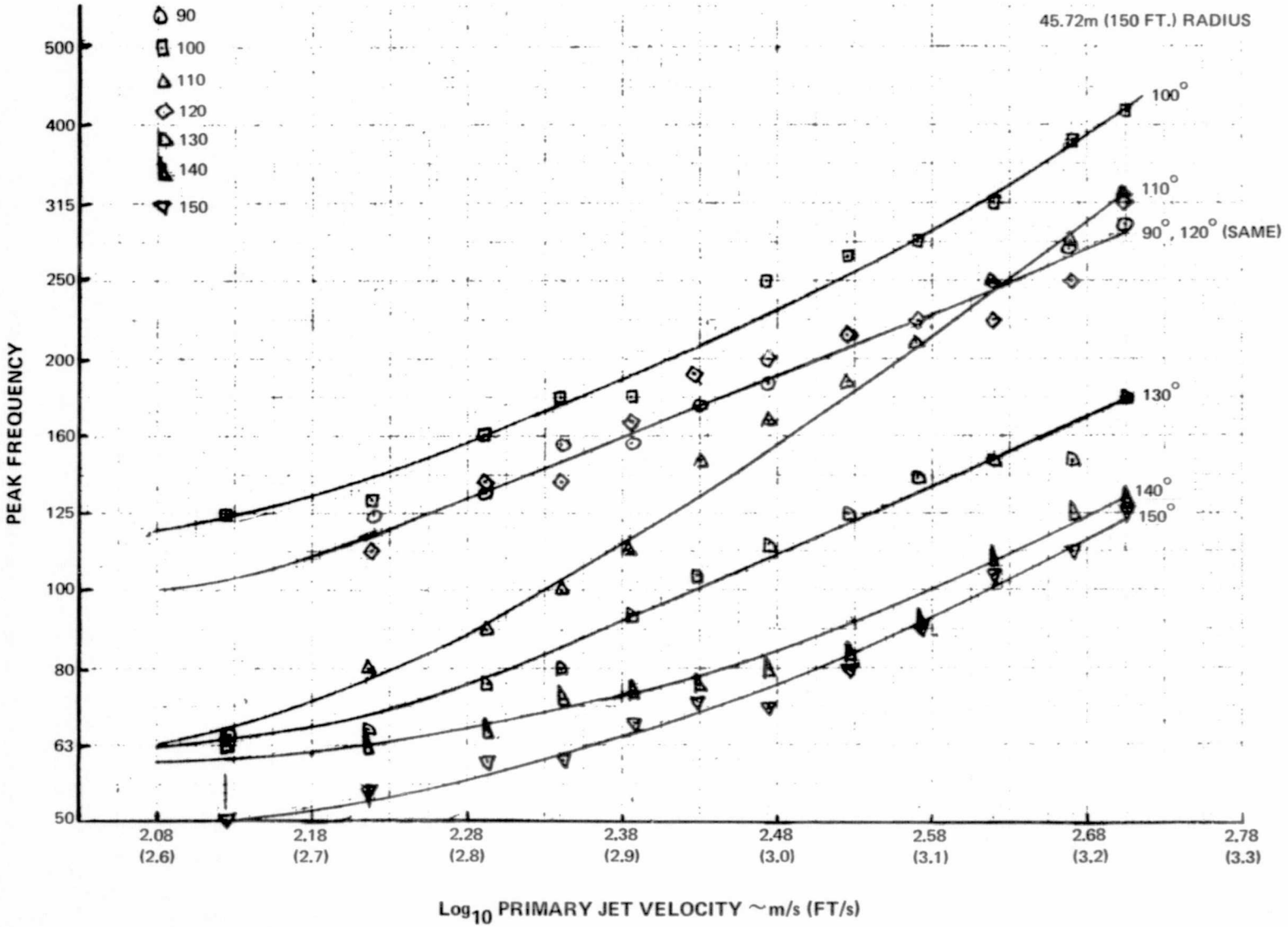

Figure D-112 Jet Noise Component Peak Frequency as a Function of Primary Jet Velocity

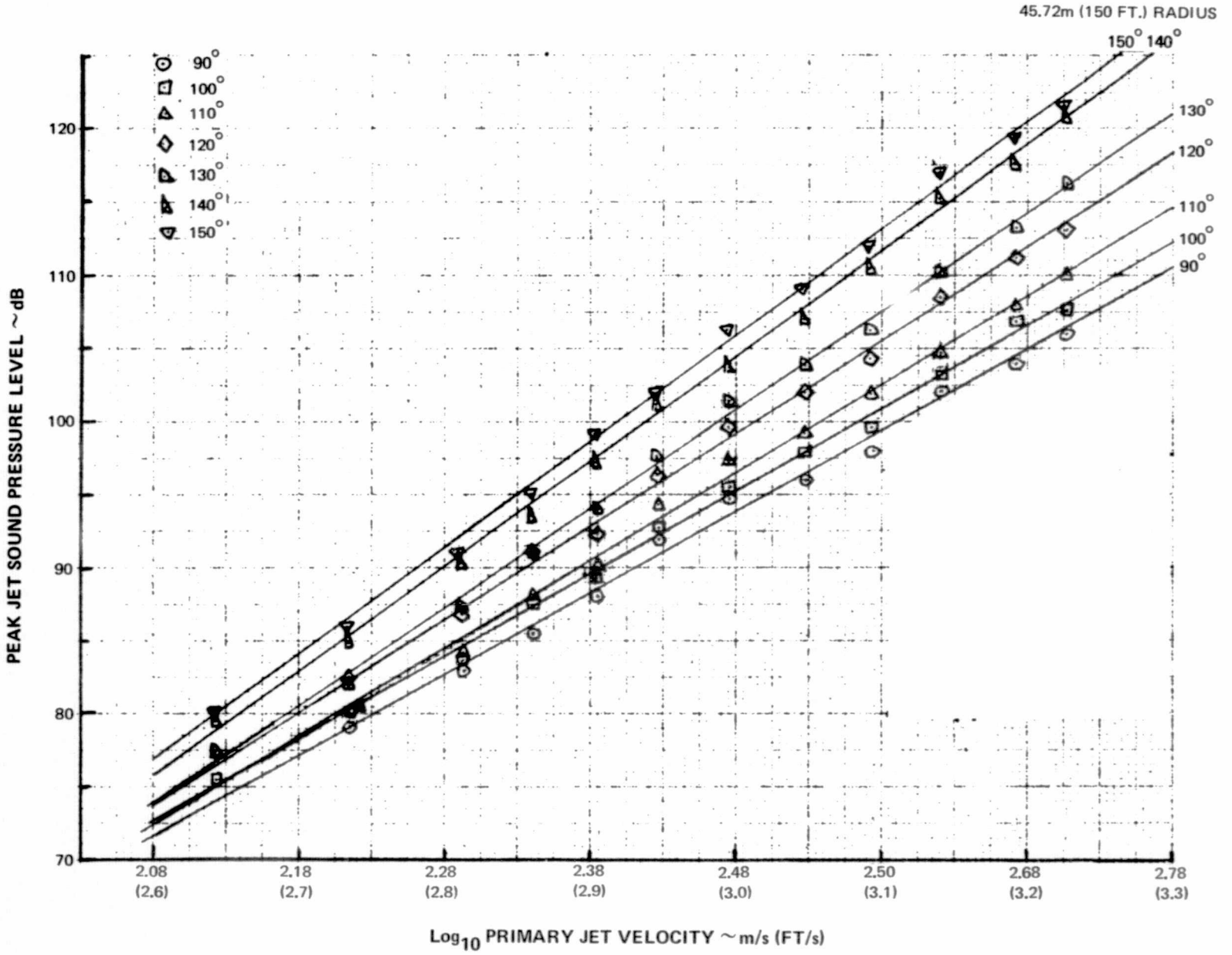

Figure D-113 Jet Noise Component Peak Level as a Function of Primary Jet Velocity

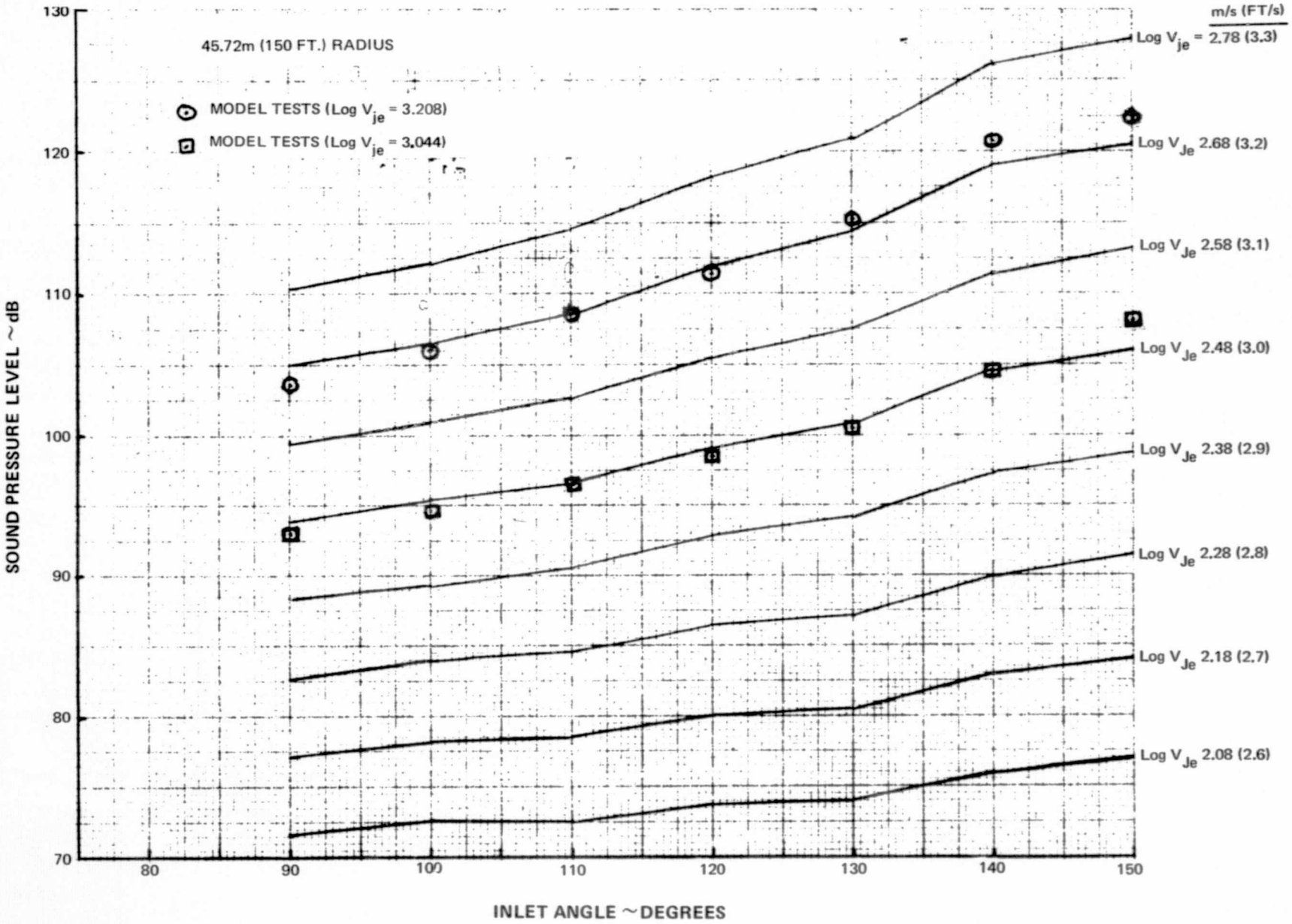

Figure D-114 Jet Noise Component Directivity Compared with Model Test Data

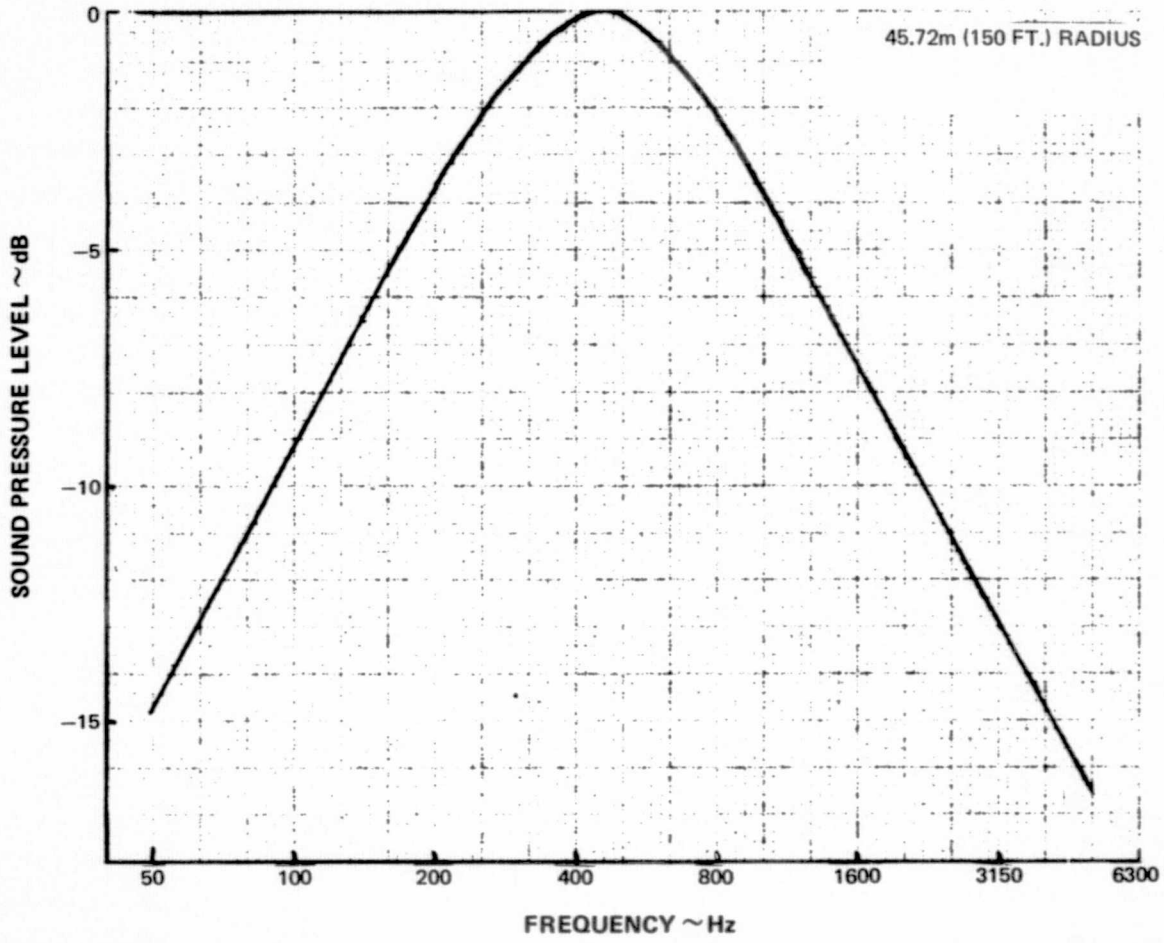

Figure D-115 **Core Engine Noise Component Spectra**

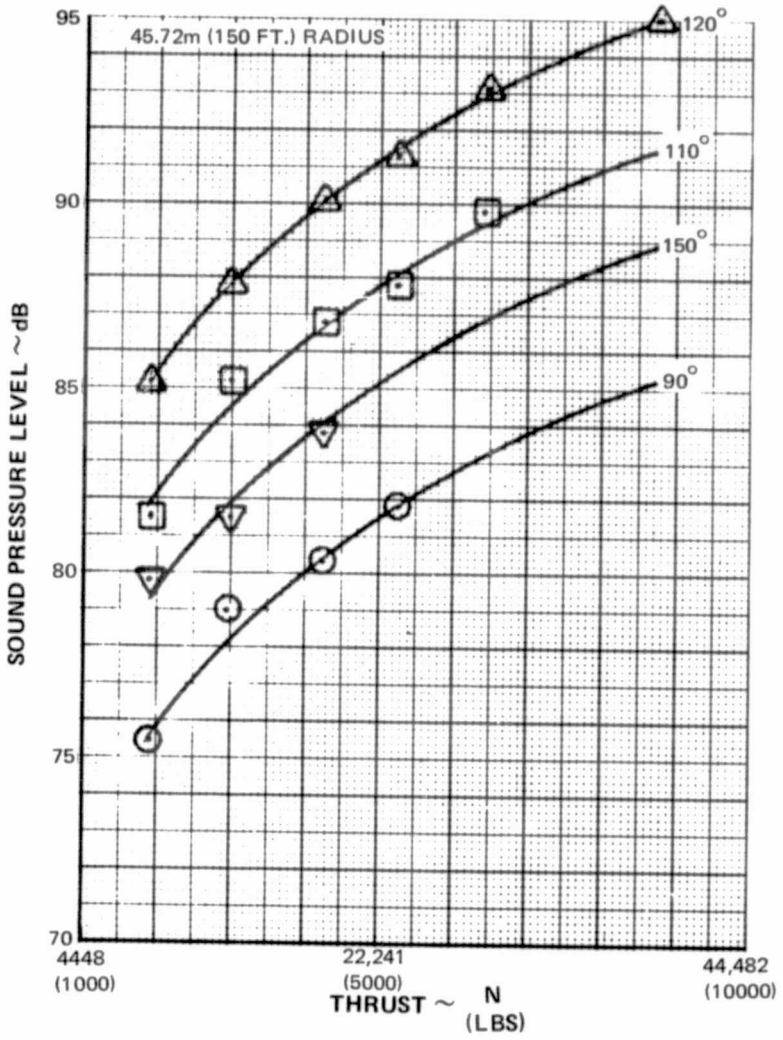

Figure D-116 Core Engine Noise Component Peak Level

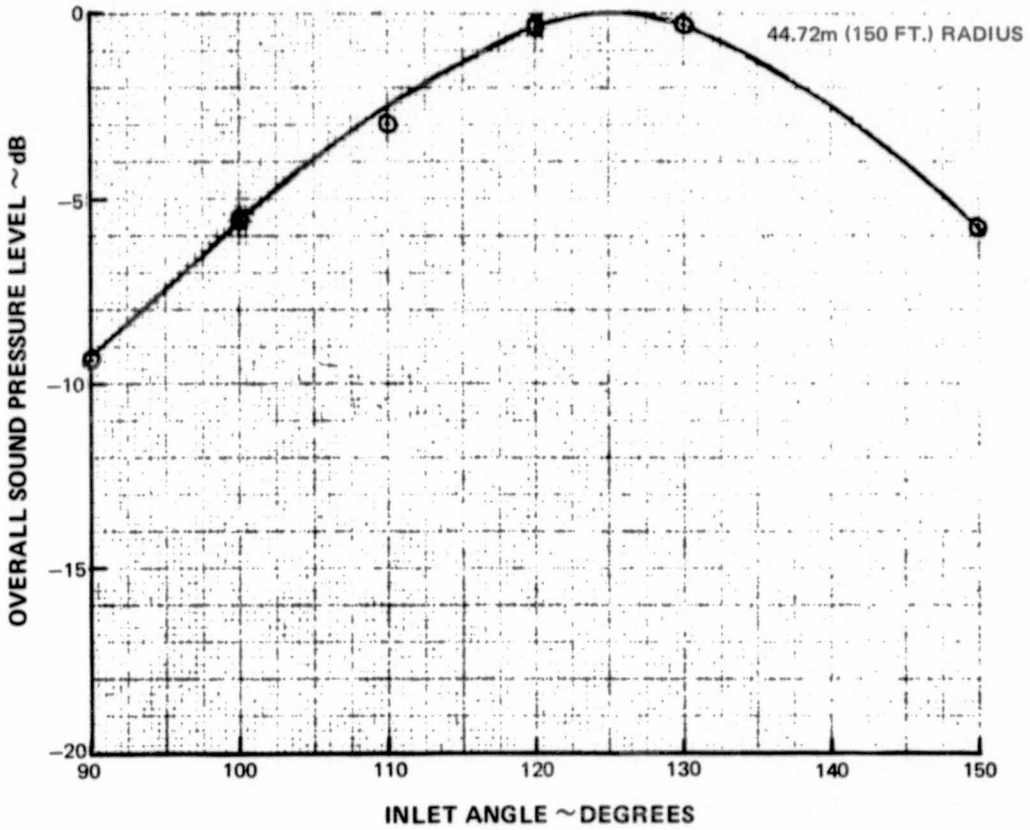

Figure D-117 Core Engine Noise Component Directivity

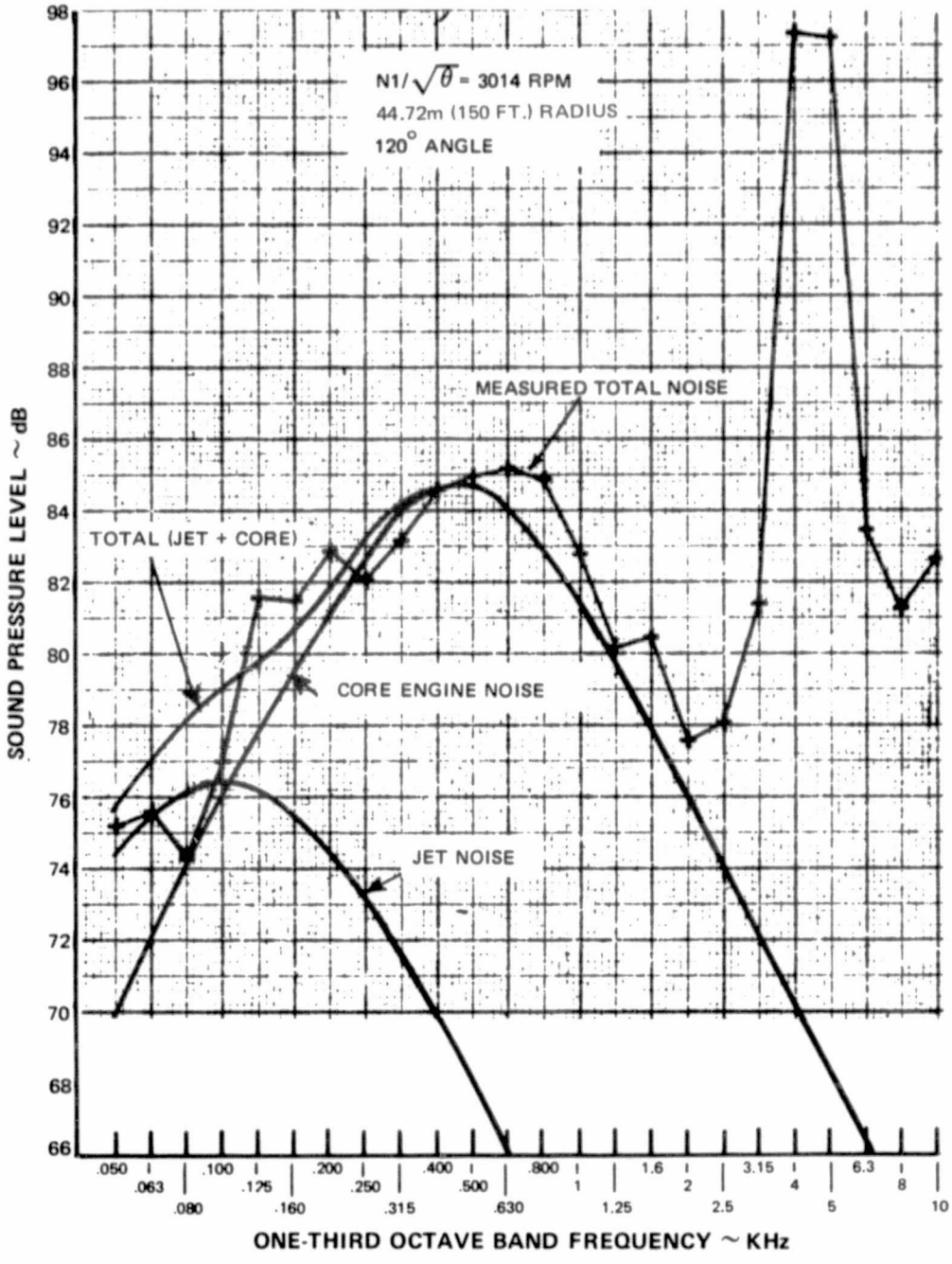

Figure D-118 Comparison of Component Noise Levels to Measured Data where Core Engine Noise is Dominant

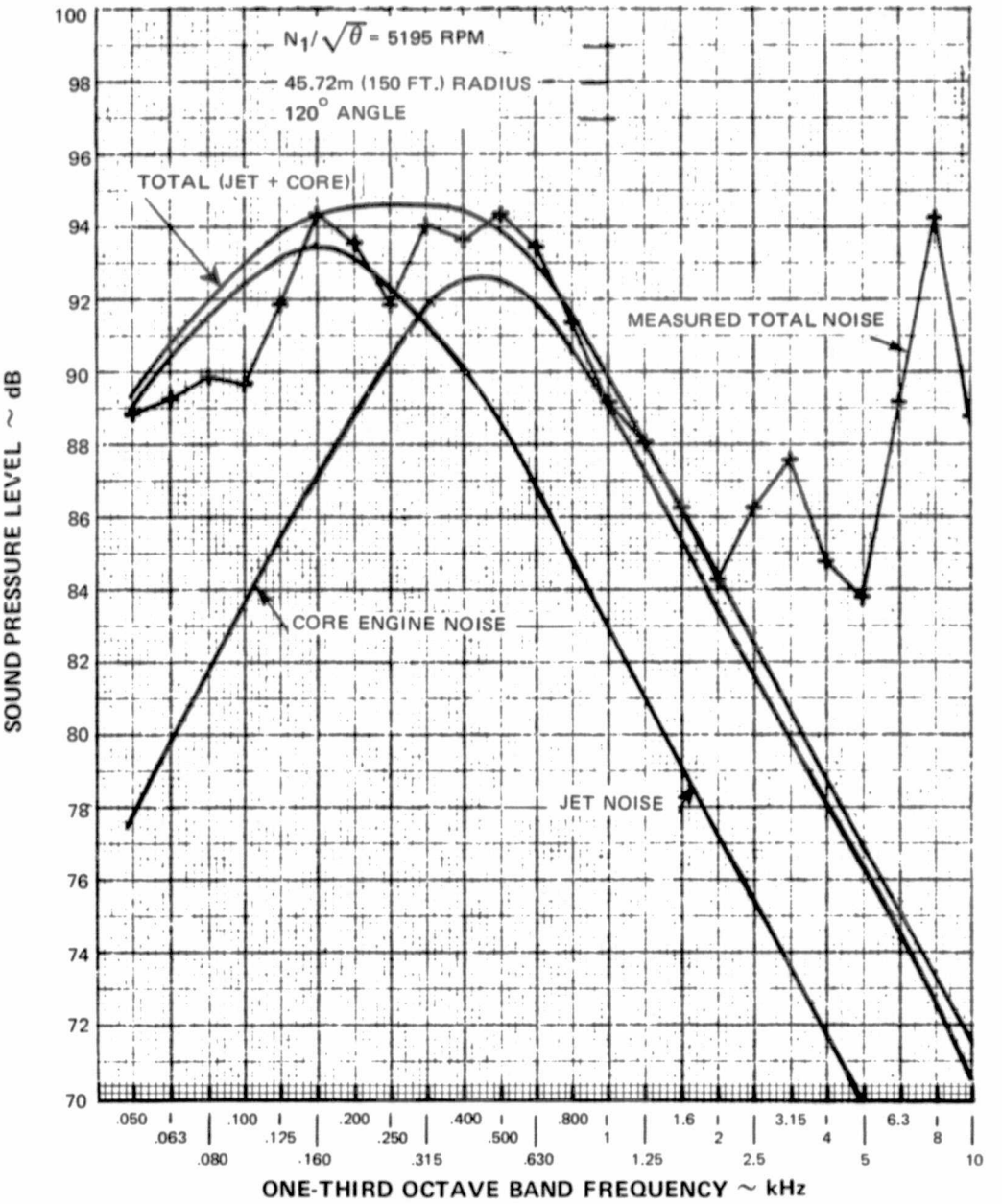

Figure D-119 Comparison of Component Noise Levels to Measured Data where Core and Jet Noise are Dominant

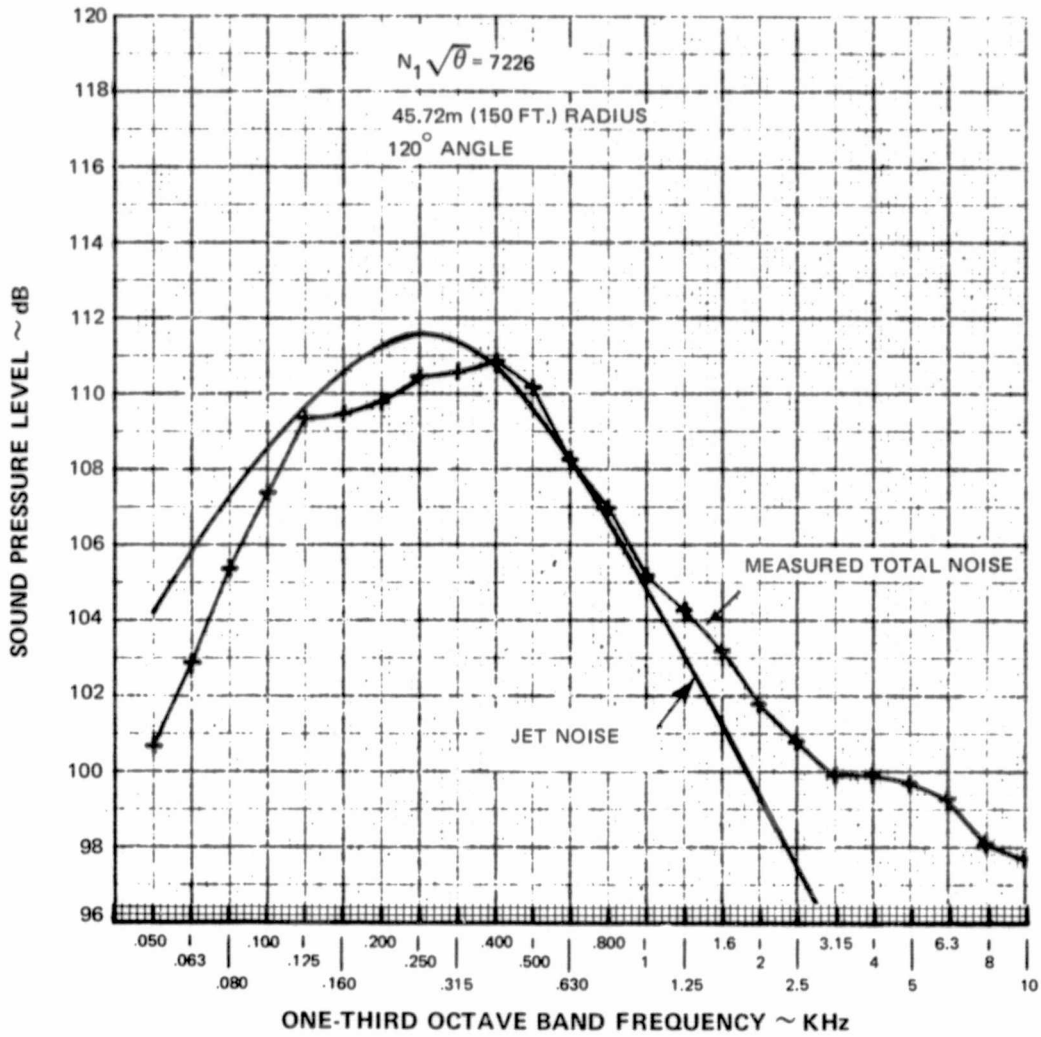

Figure D-120 Comparison of Component Noise Levels to Measured Data where Jet Noise is Dominant

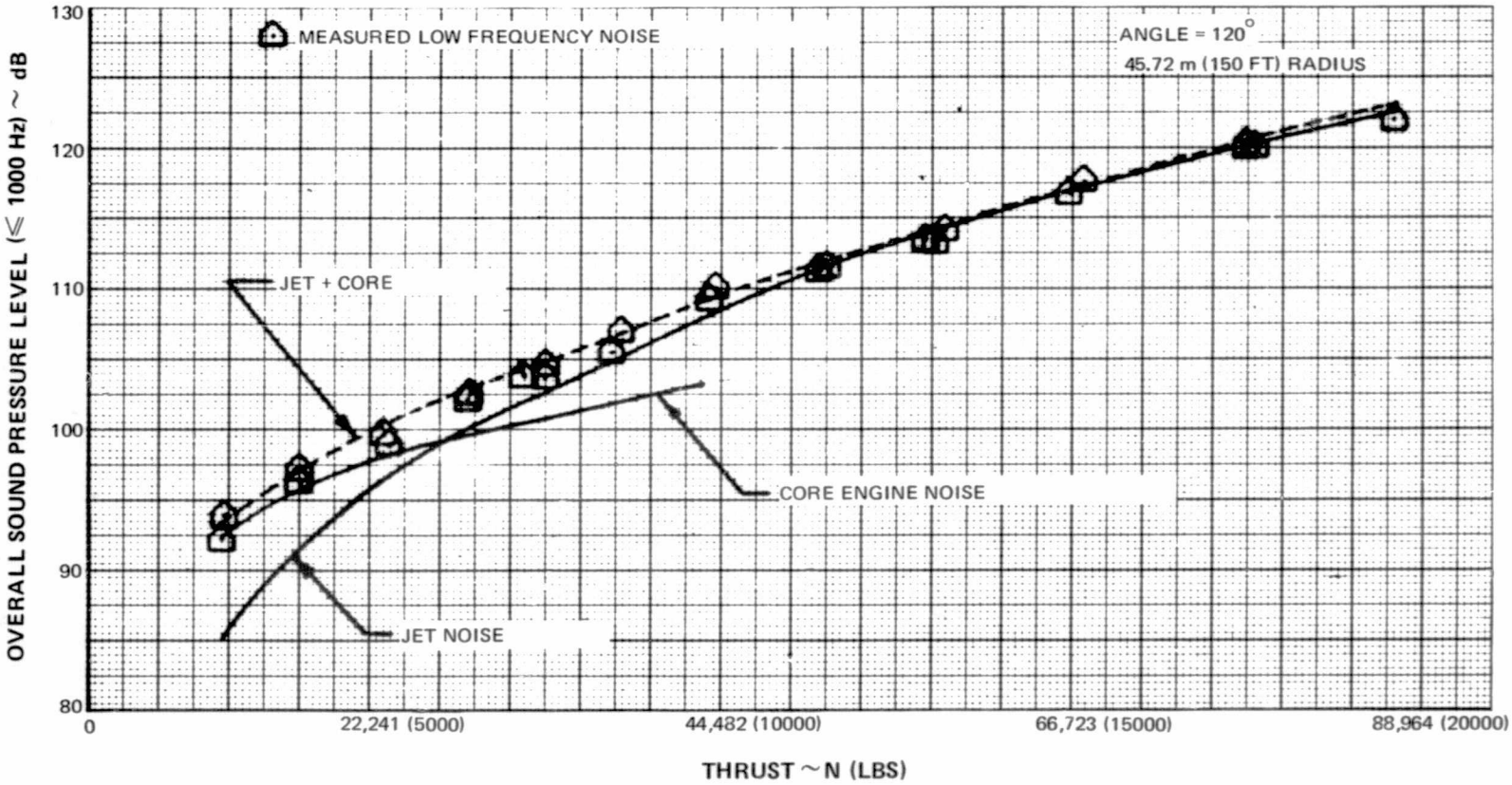

Figure D-121 Low Frequency Component Noise Levels Compared to Measured Data

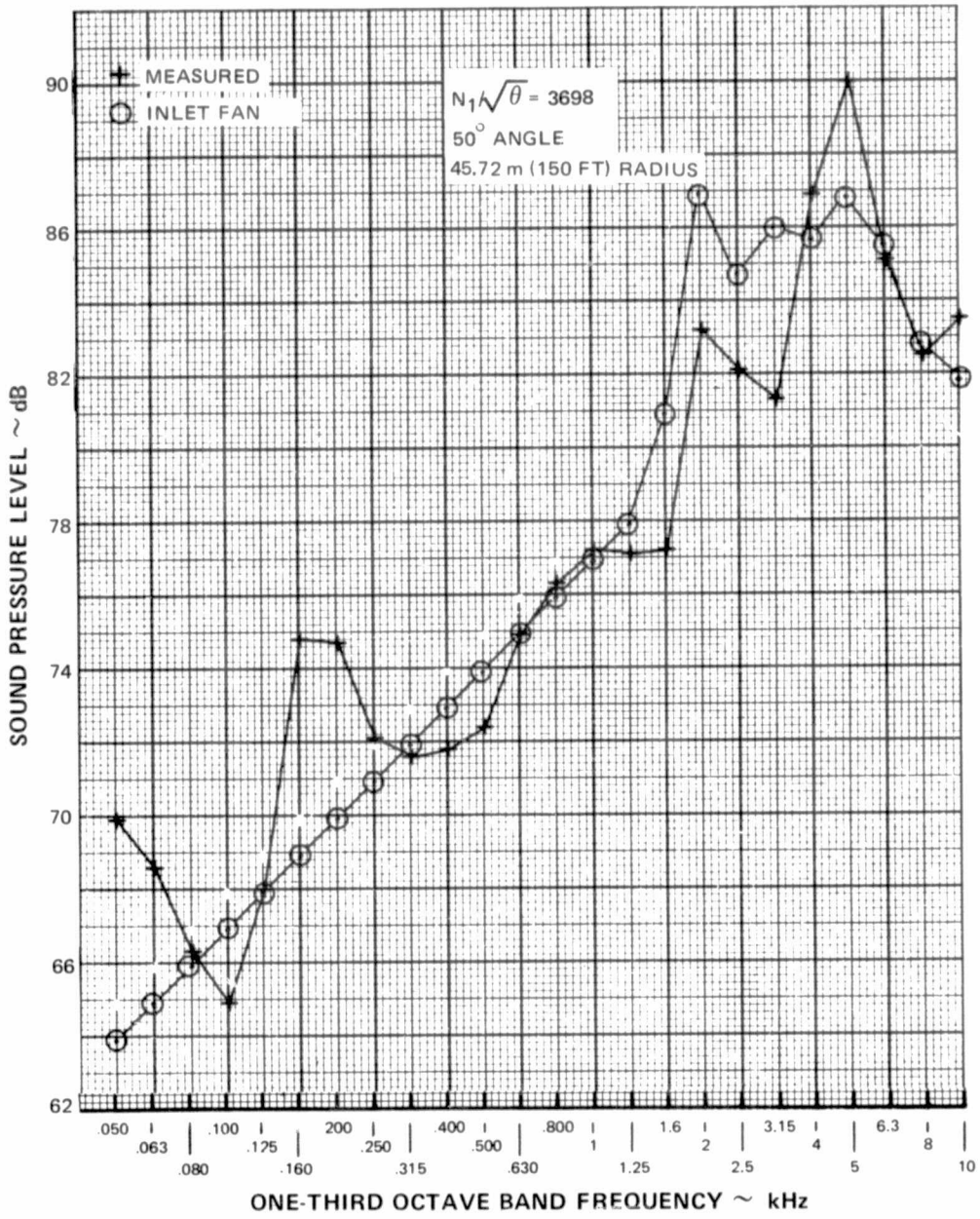

Figure D-122 Summation of Component Noise Levels Compared to Measured Data ~ 3698 N1, 50° Angle

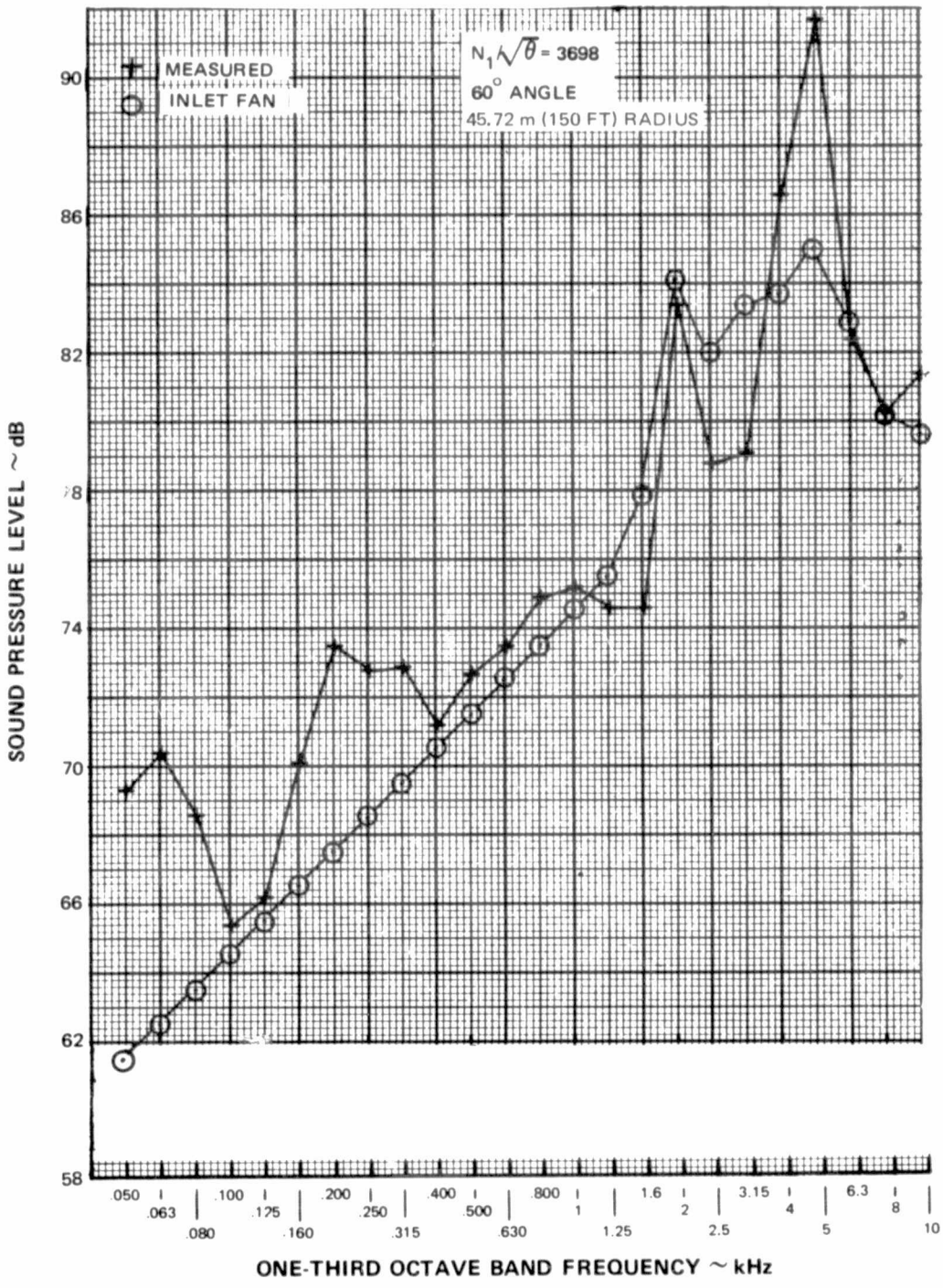

Figure D-123 Summation of Component Noise Levels Compared to Measured Data ~ 3698 N1, 60° Angle

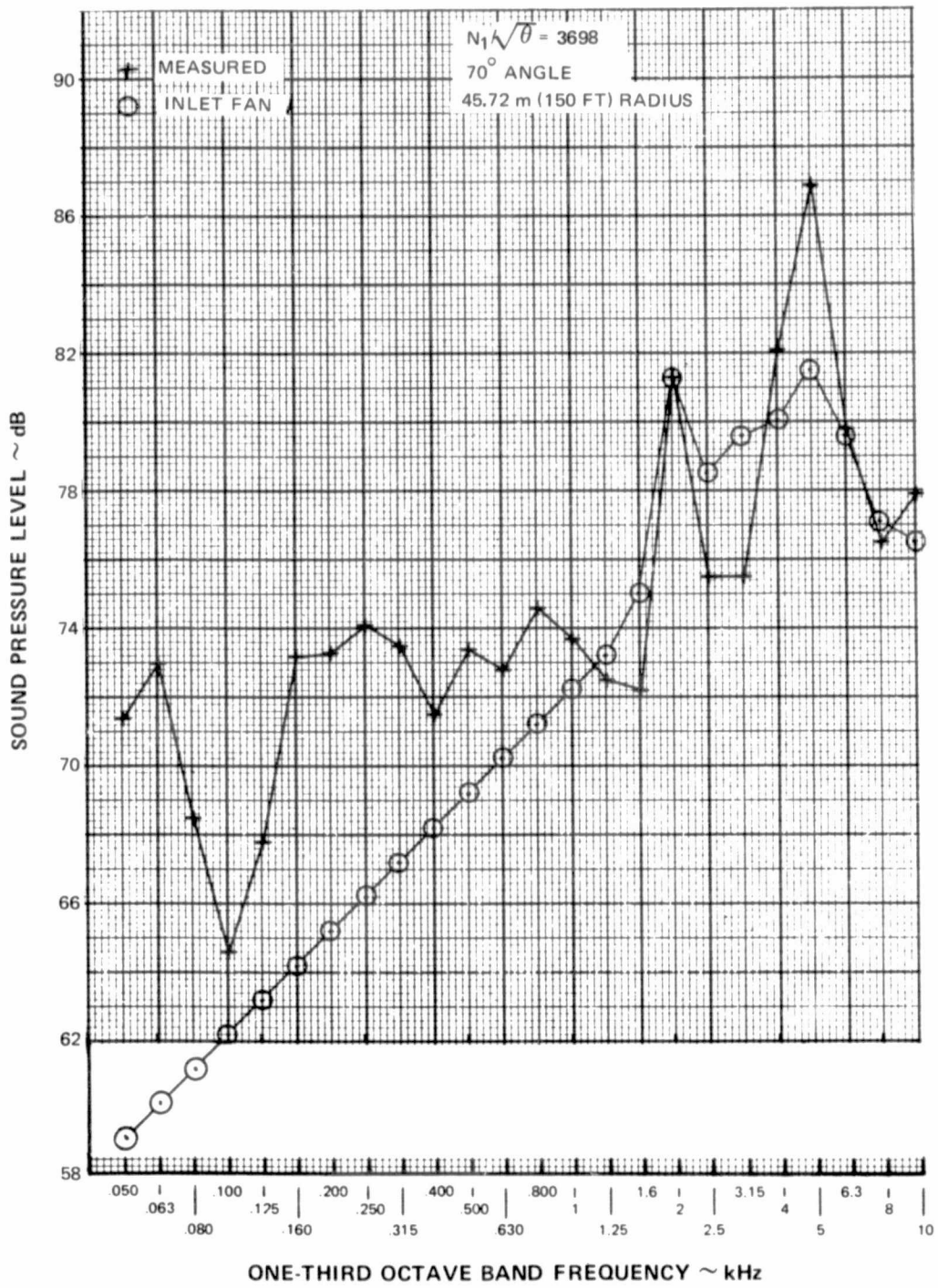

Figure D-124 Summation of Component Noise Levels Compared to Measured Data ~ 3698 N1, 70° Angle

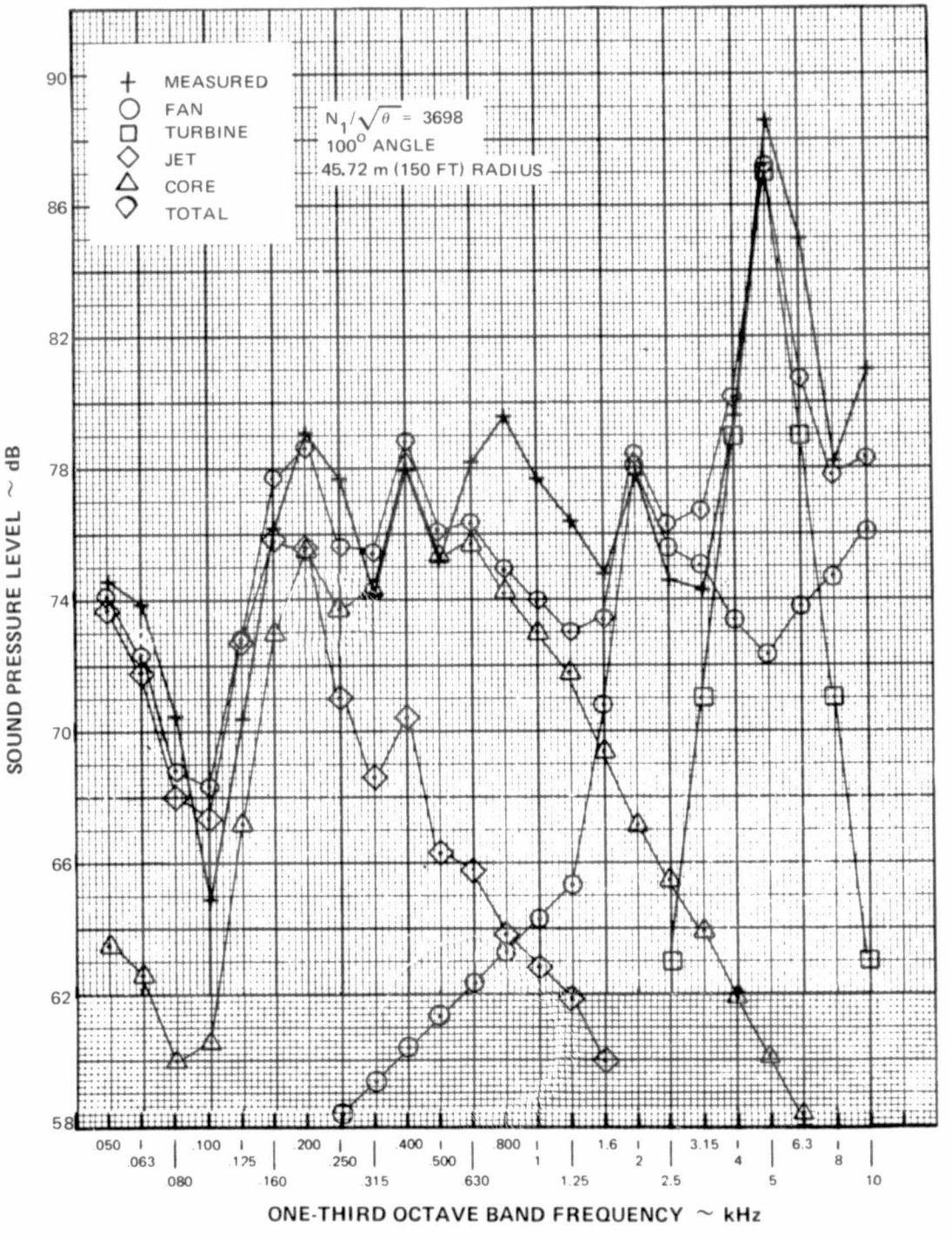

Figure D-125 Summation of Component Noise Levels Compared to Measured Data ~ 3698 N1, 100° Angle

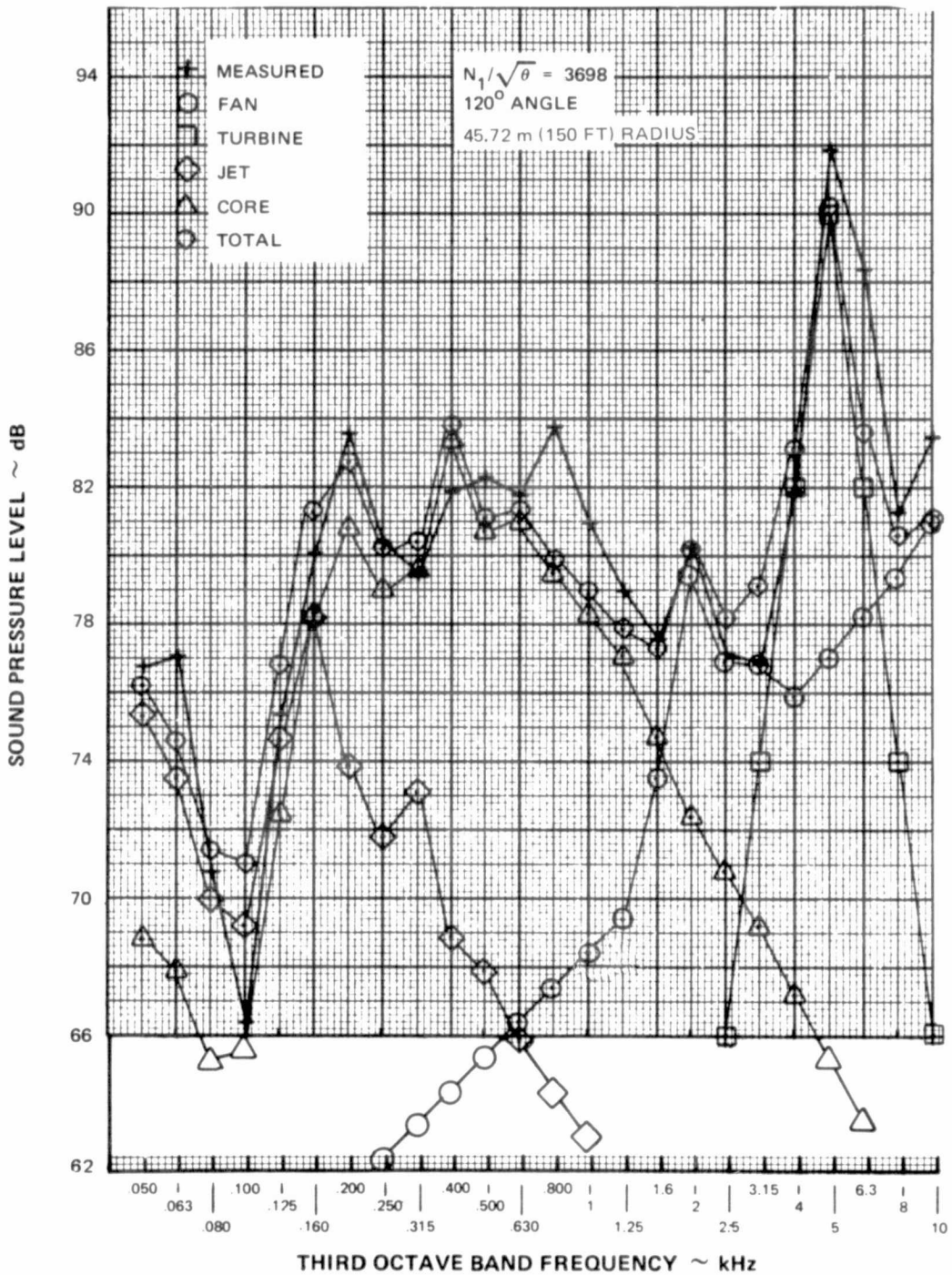

Figure D-126 Summation of Component Noise Levels Compared to Measured Data ~ 3698 N1, 120° Angle

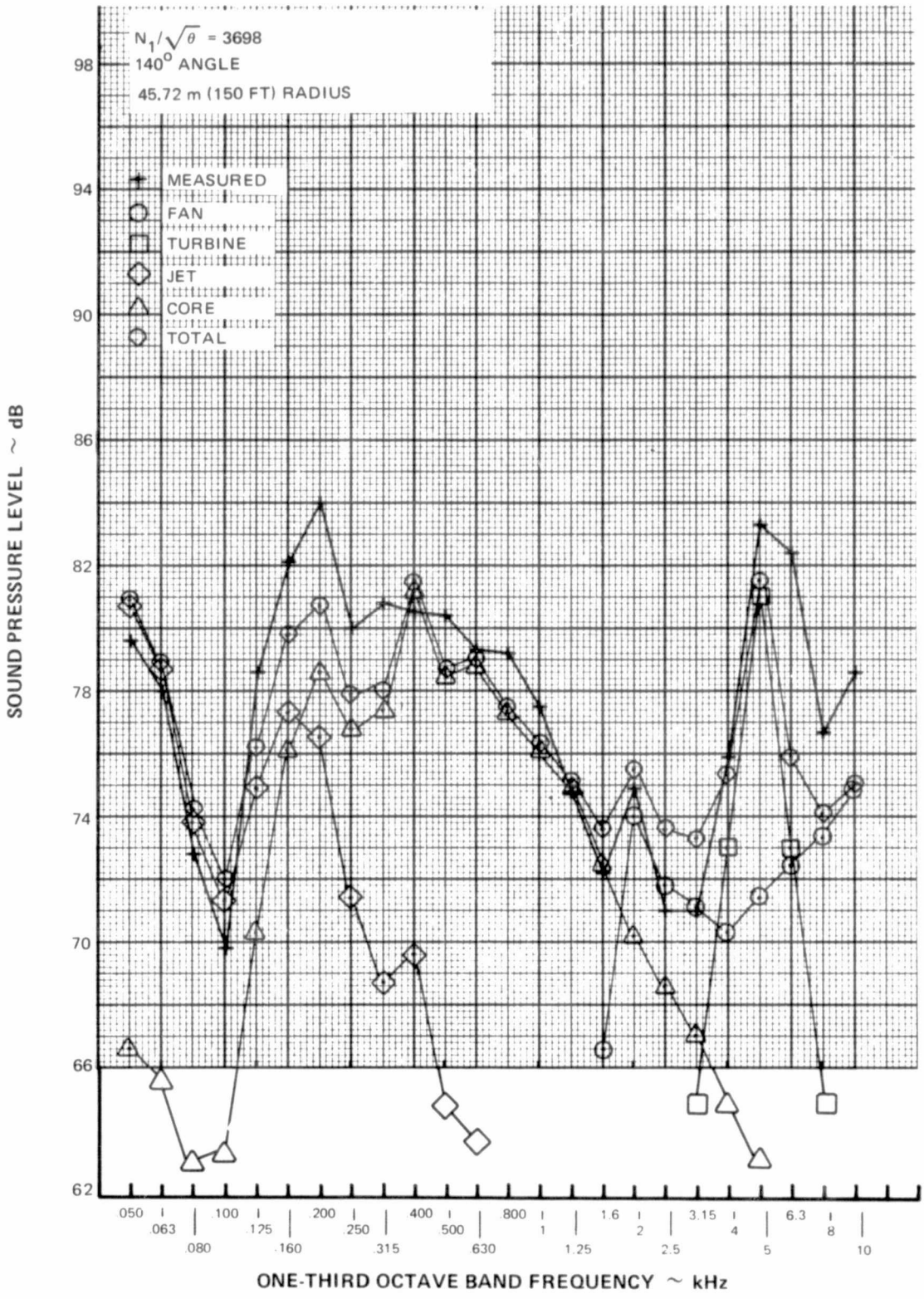

Figure D-127 Summation of Component Noise Levels Compared to Measured Data ~ 3698 N1, 140° Angle

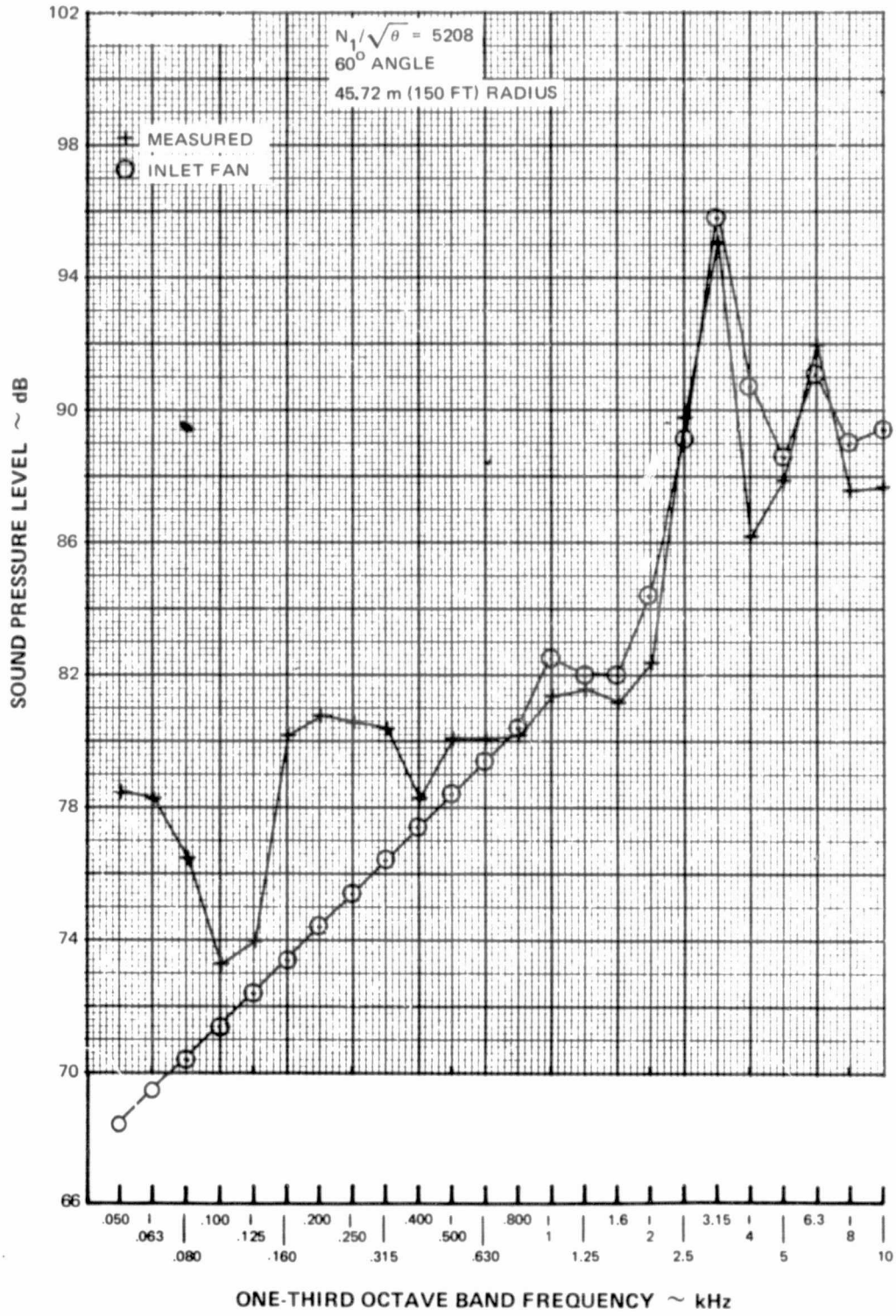

Figure D-128 Summation of Component Noise Levels Compared to Measured Data ~ 5208 N1, 60° Angle

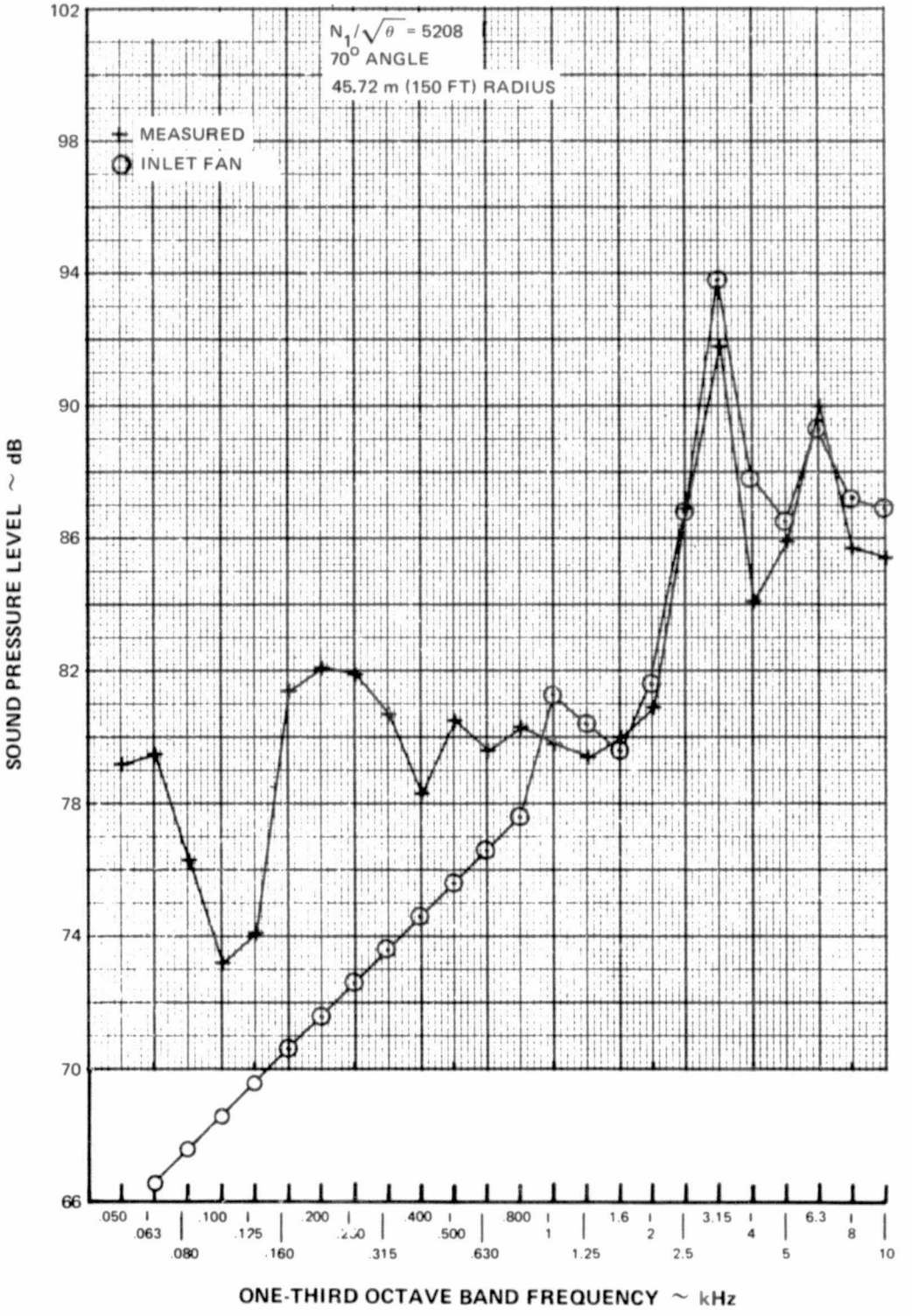

Figure D-129 Summation of Component Noise Levels Compared to Measured Data ~ 5208 N1, 70° Angle

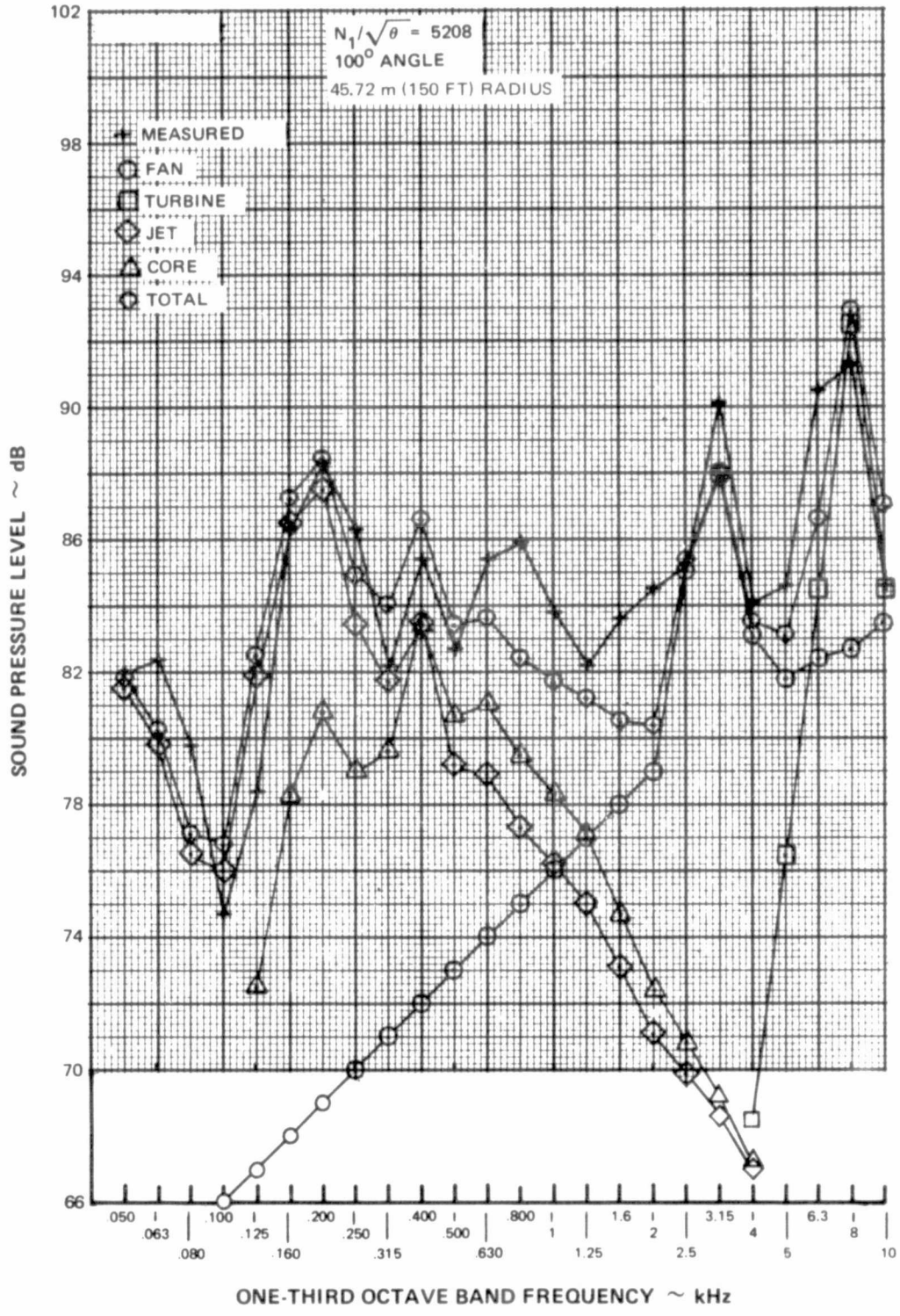

Figure D-130 Summation of Component Noise Levels Compared to Measured Data ~ 5208 N1, 100° Angle

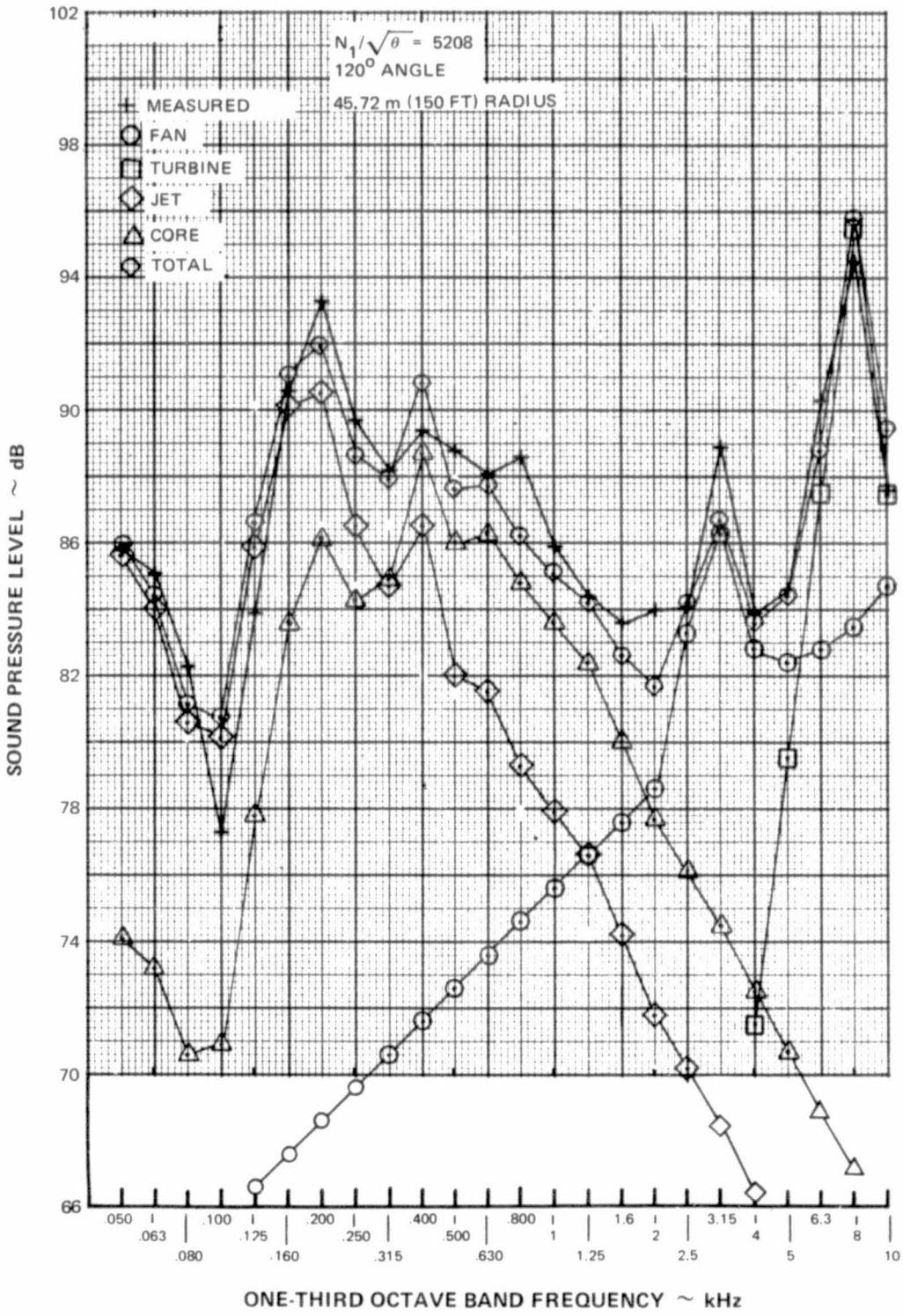

Figure D-131 Summation of Component Noise Levels Compared to Measured Data ~ 5208 N1, 120° Angle

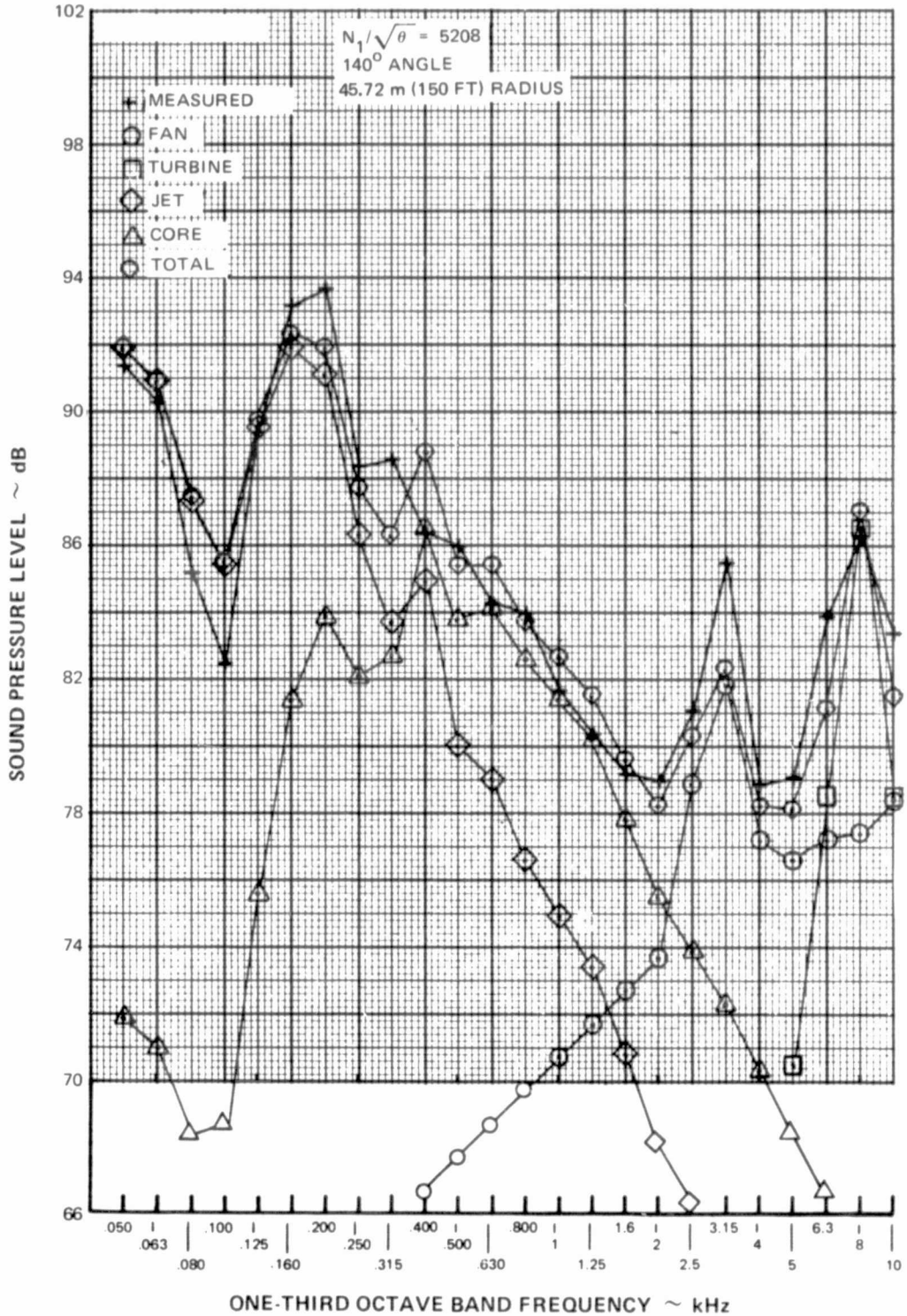

Figure D-132 Summation of Component Noise Levels Compared to Measured Data ~ 5208 N1, 140° Angle

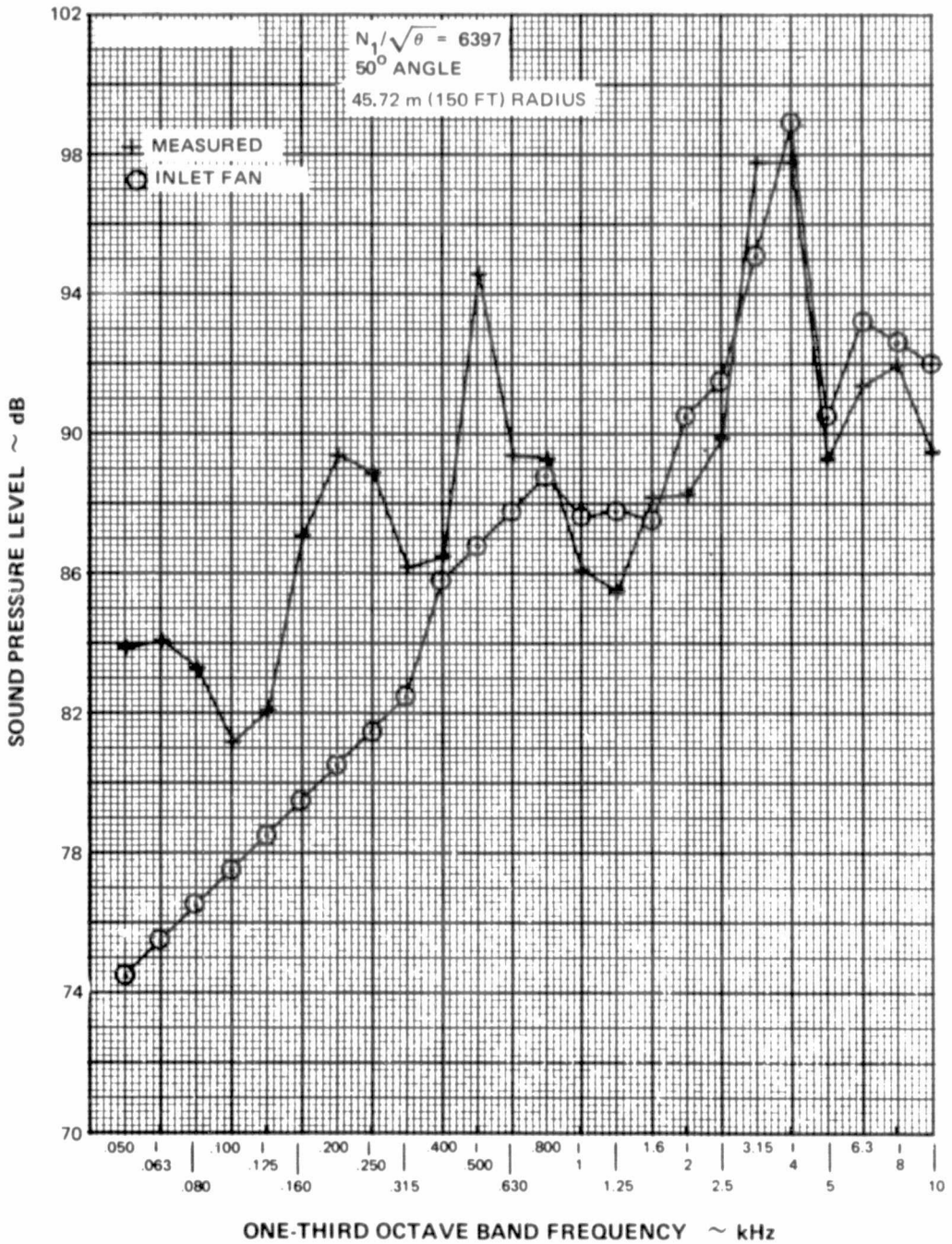

Figure D-133 Summation of Component Noise Levels Compared to Measured Data ~ 6397 N1, 50° Angle

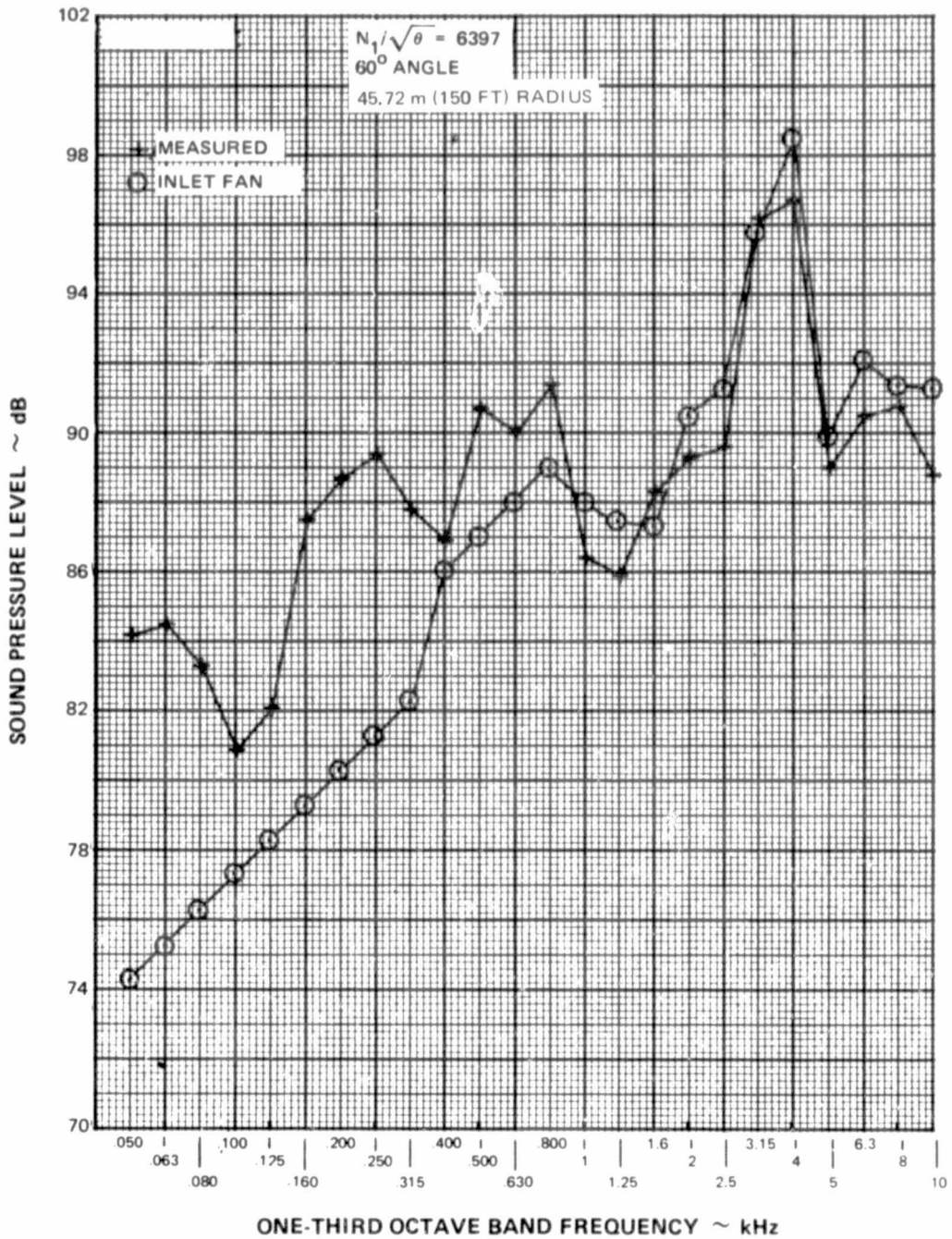

Figure D-134 Summation of Component Noise Levels Compared to Measured Data ~ 6397 N1, 60° Angle

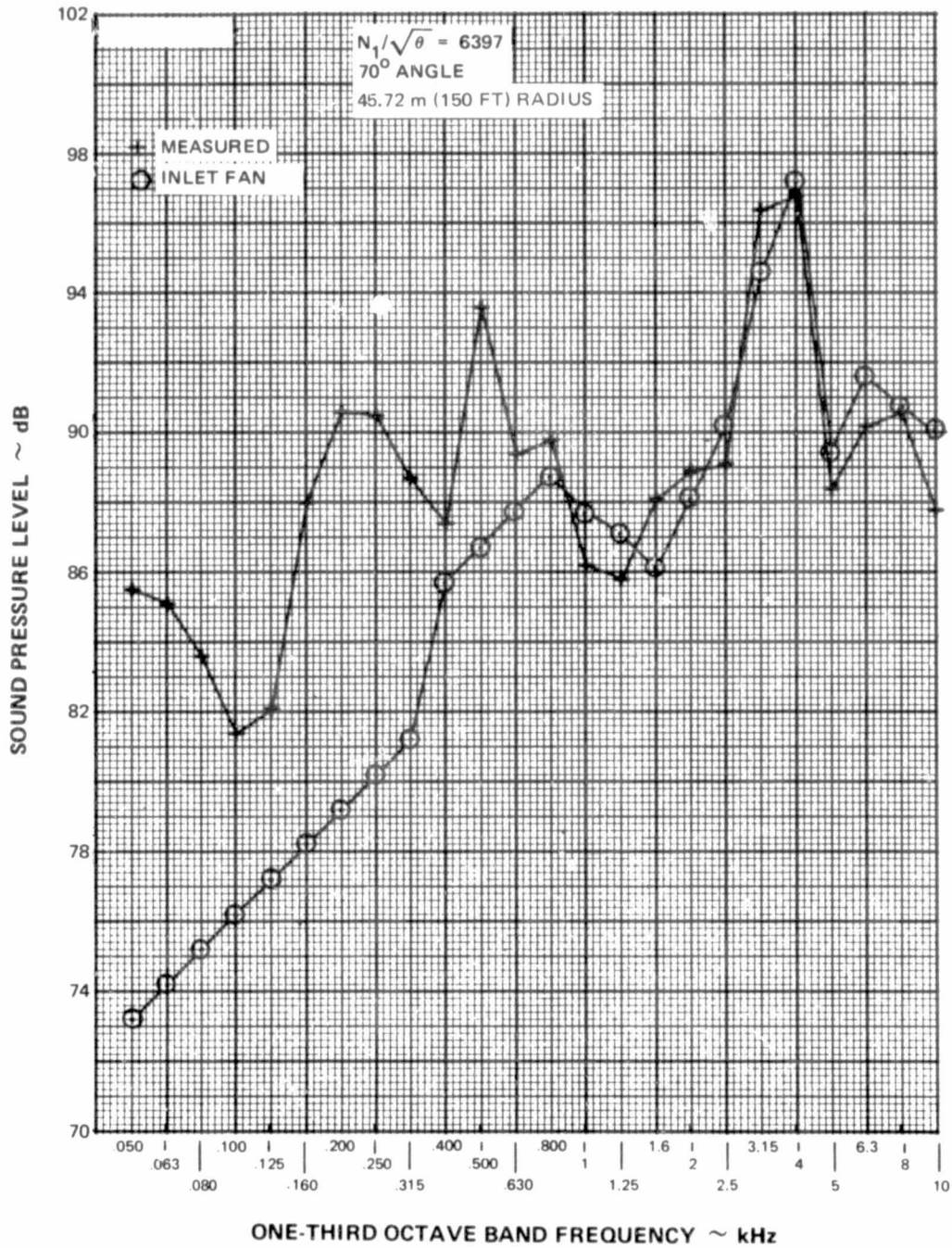

Figure D-135 Summation of Component Noise Levels Compared to Measured Data ~ 6397 N1, 70° Angle

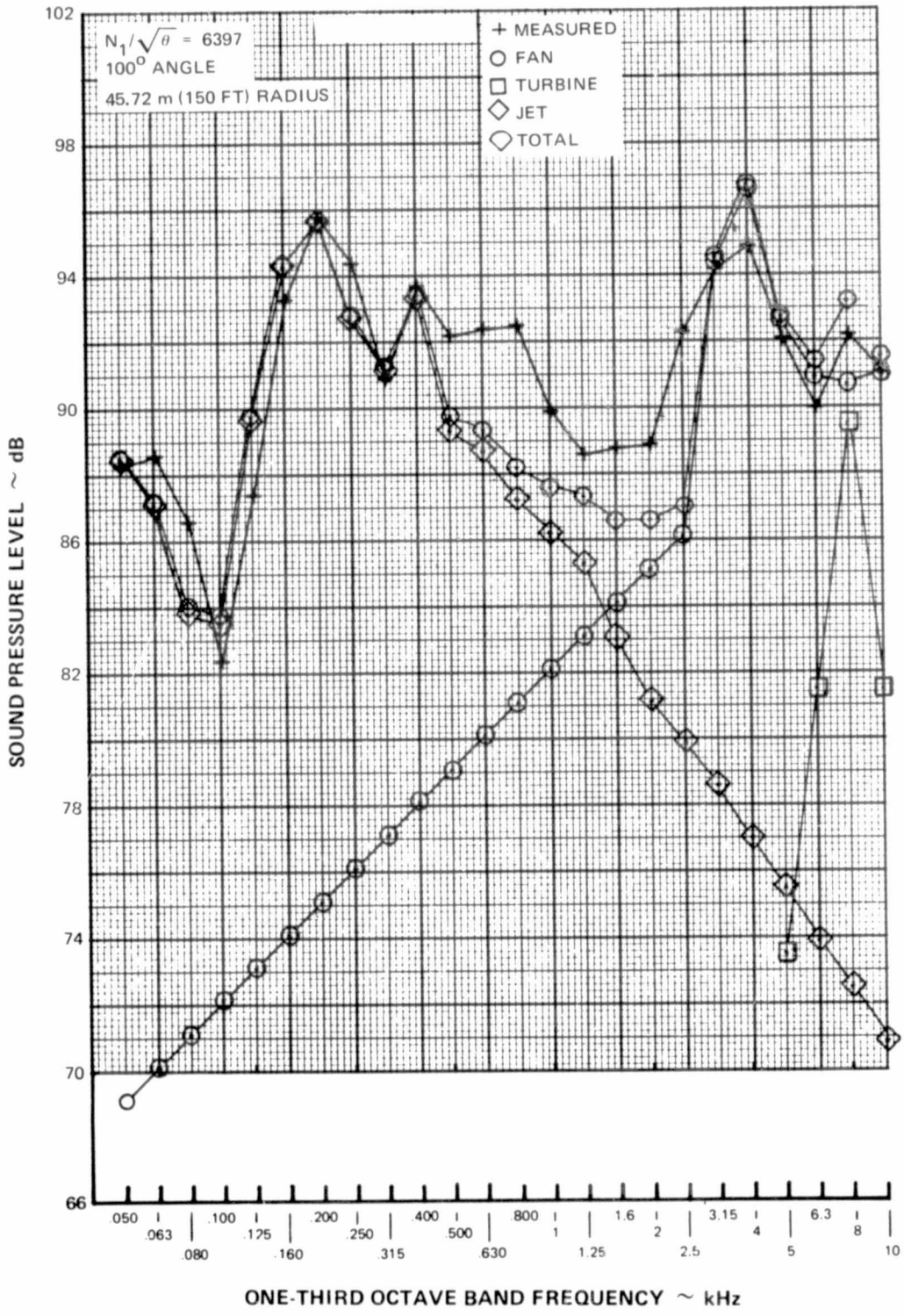

Figure D-136 Summation of Component Noise Levels Compared to Measured Data ~ 6397 N1, 100° Angle

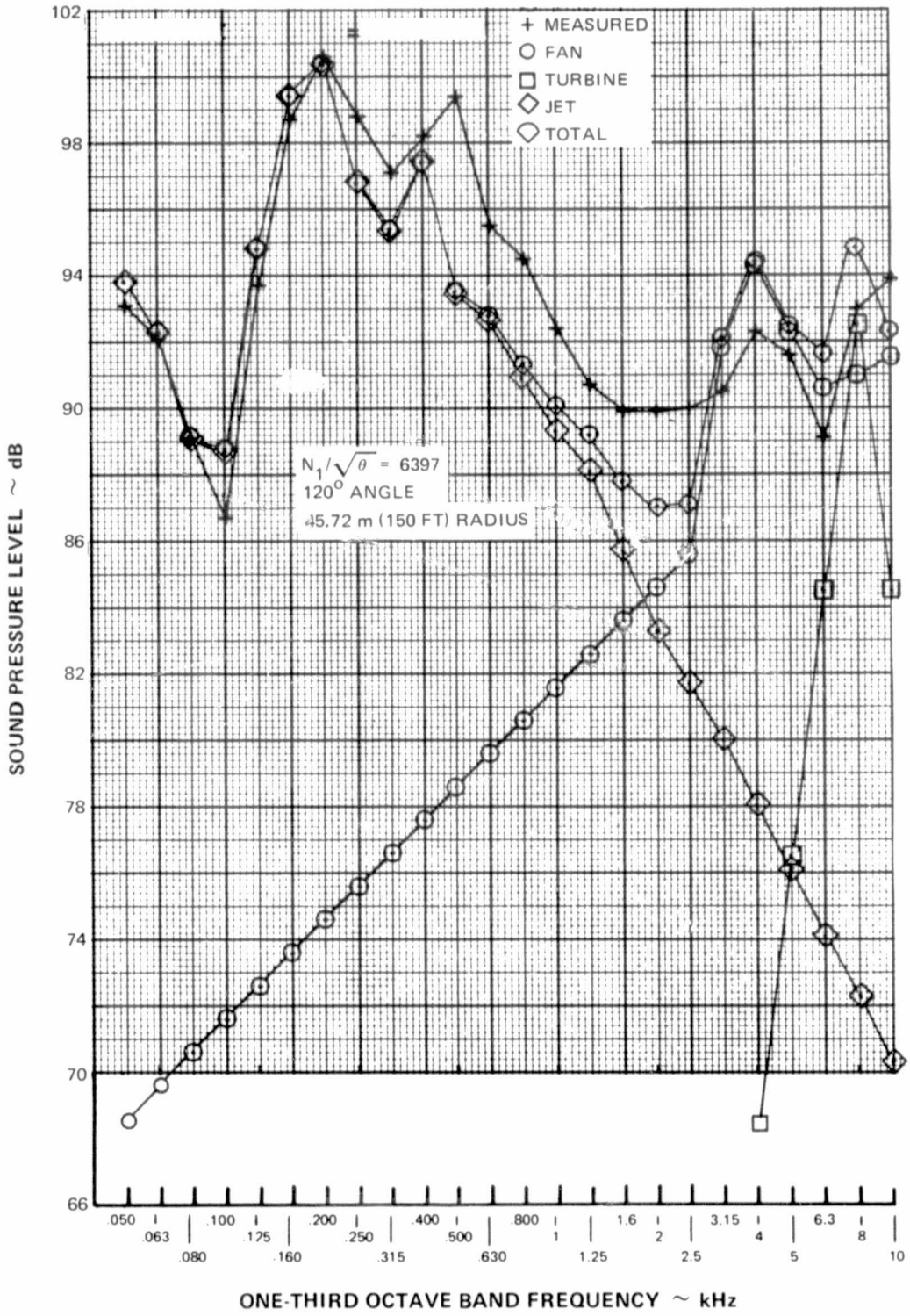

Figure D-137 Summation of Component Noise Levels Compared to Measured Data ~ 6397 N1, 120° Angle

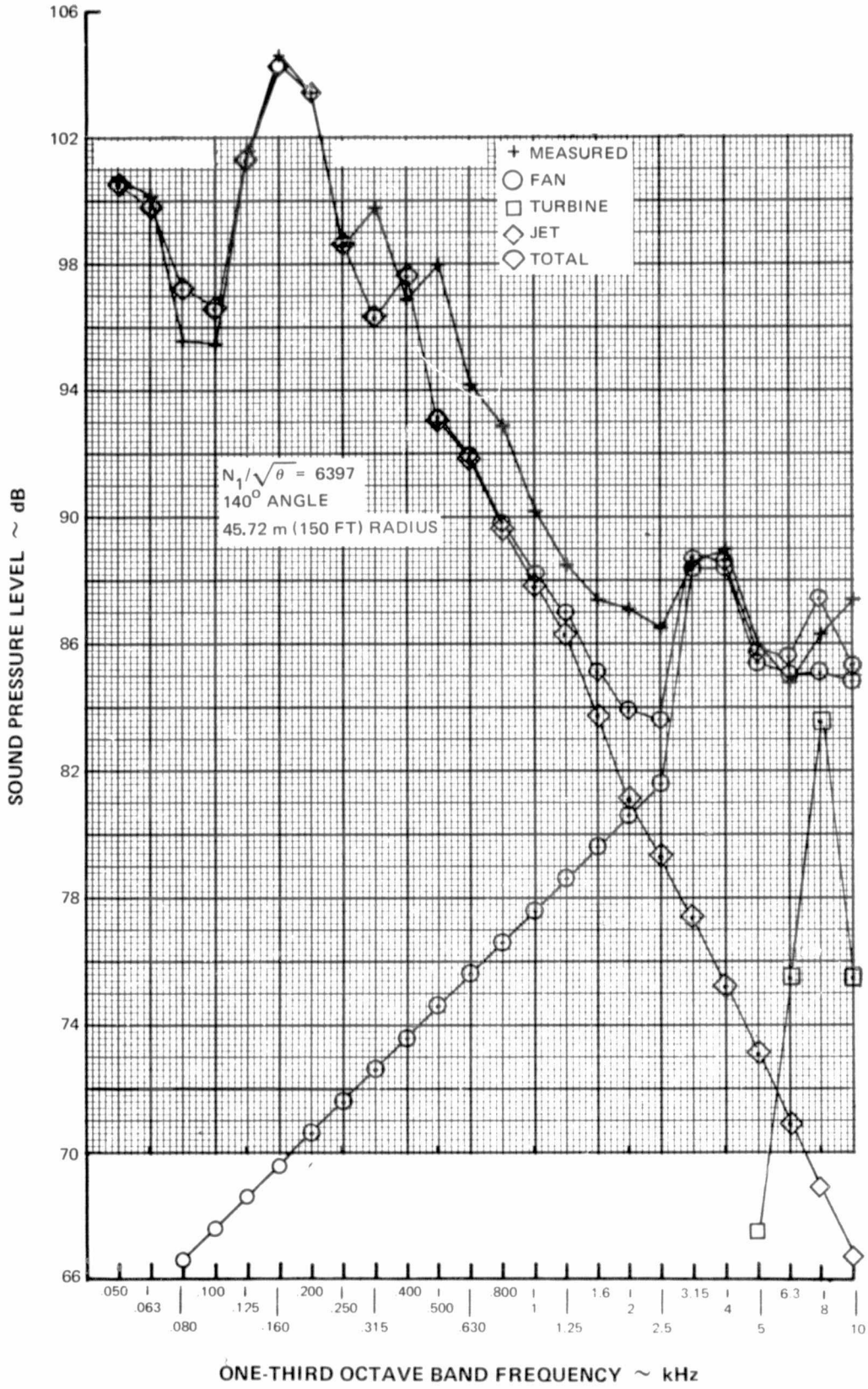

Figure D-138 Summation of Component Noise Levels Compared to Measured Data ~ 6397 N1, 140° Angle

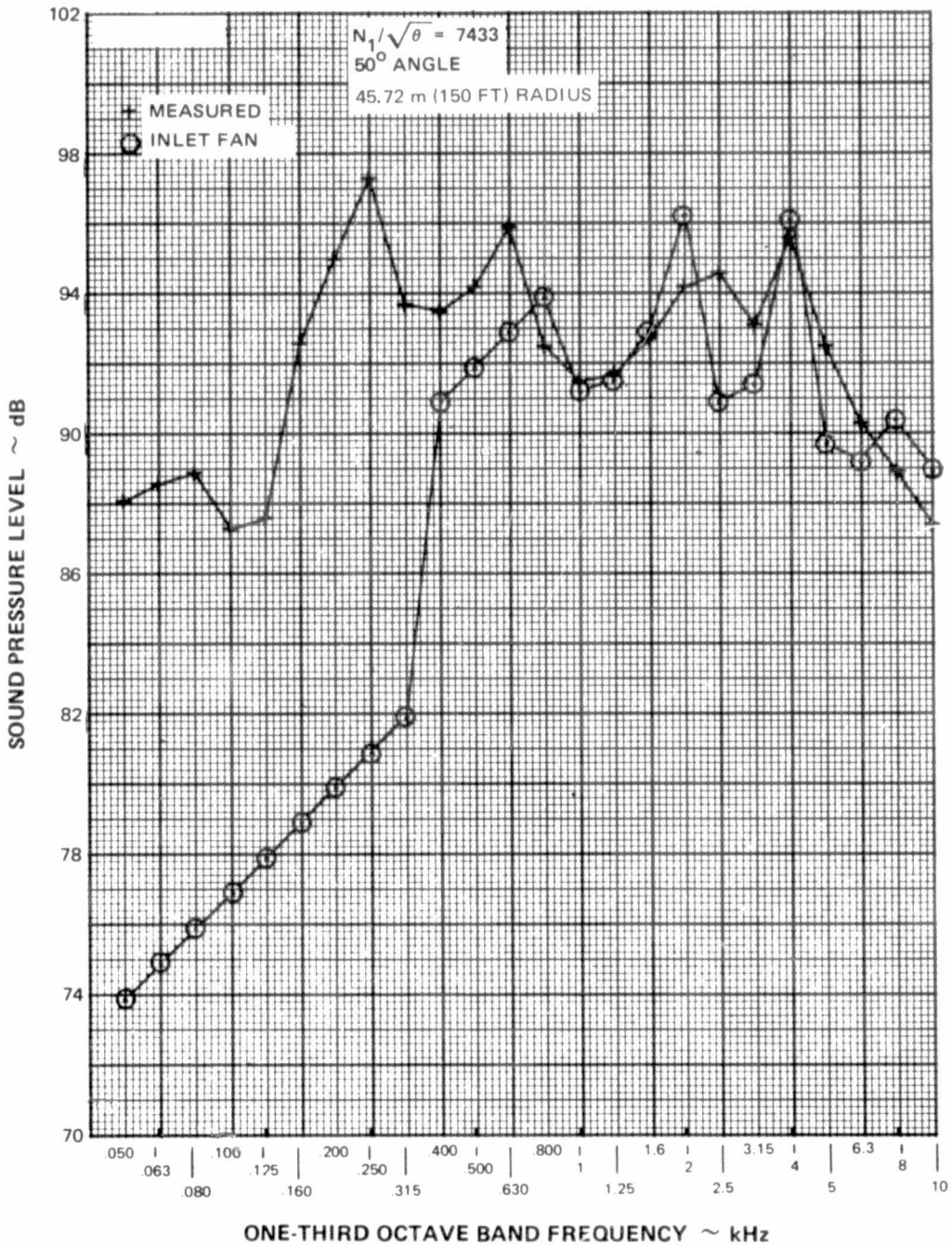

Figure D-139 Summation of Component Noise Levels Compared to Measured Data ~ 7433 N1, 50° Angle

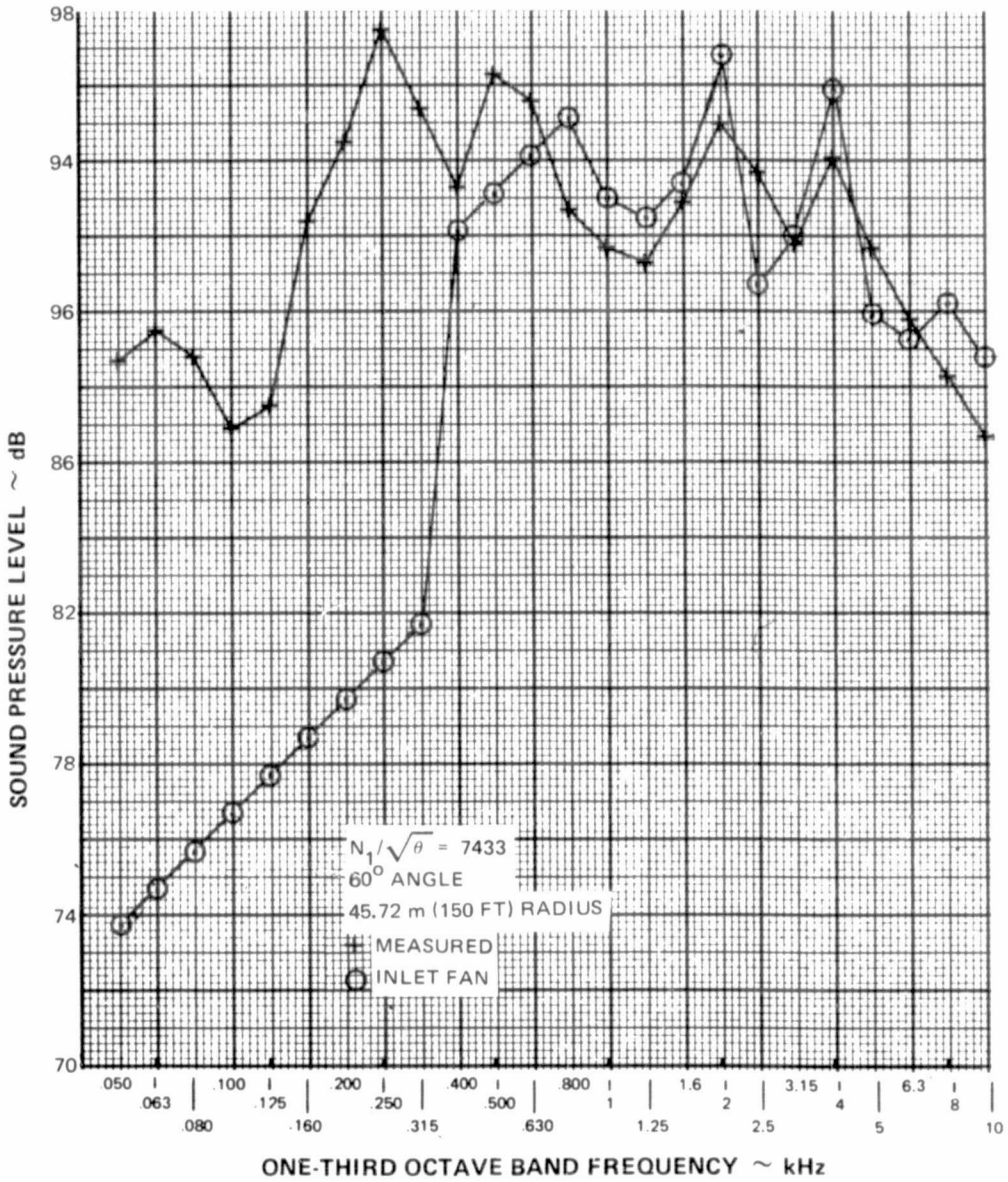

Figure D-140 Summation of Component Noise Levels Compared to Measured Data ~ 7433 N1, 60° Angle

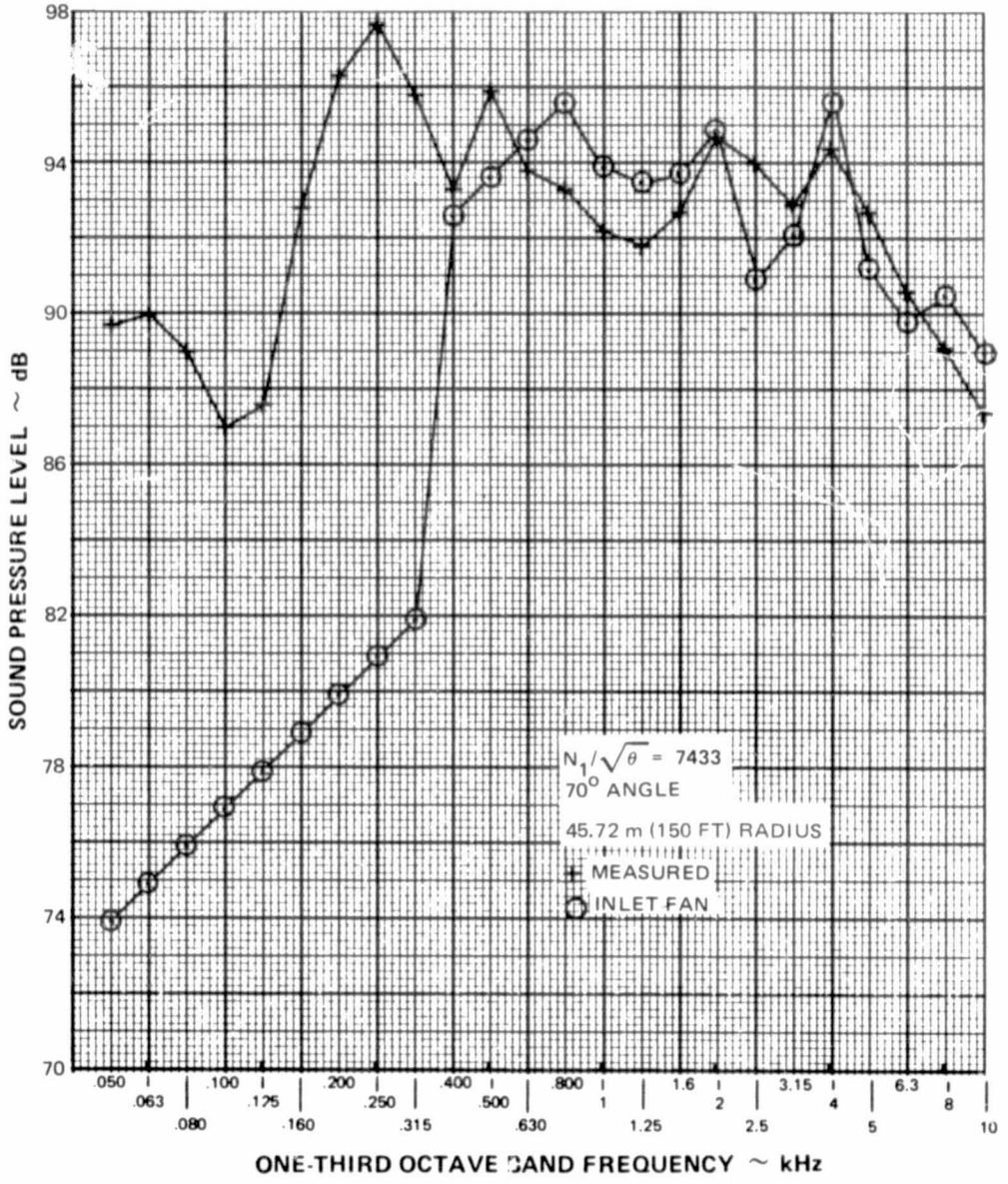

Figure D-141 Summation of Component Noise Levels Compared to Measured Data ~ 7433 N1, 70° Angle

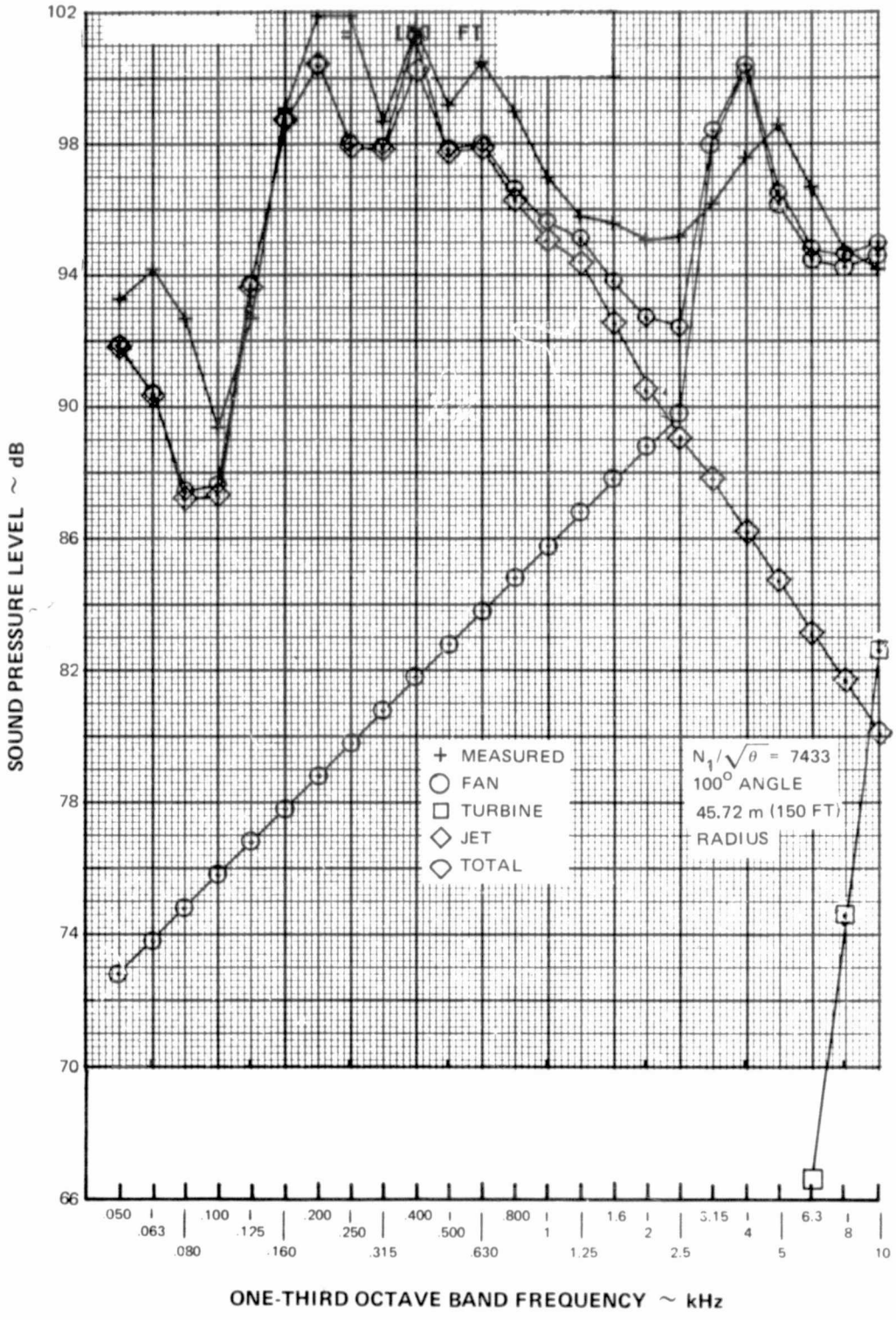

Figure D-142 Summation of Component Noise Levels Compared to Measured Data ~ 7433 N1, 100° Angle

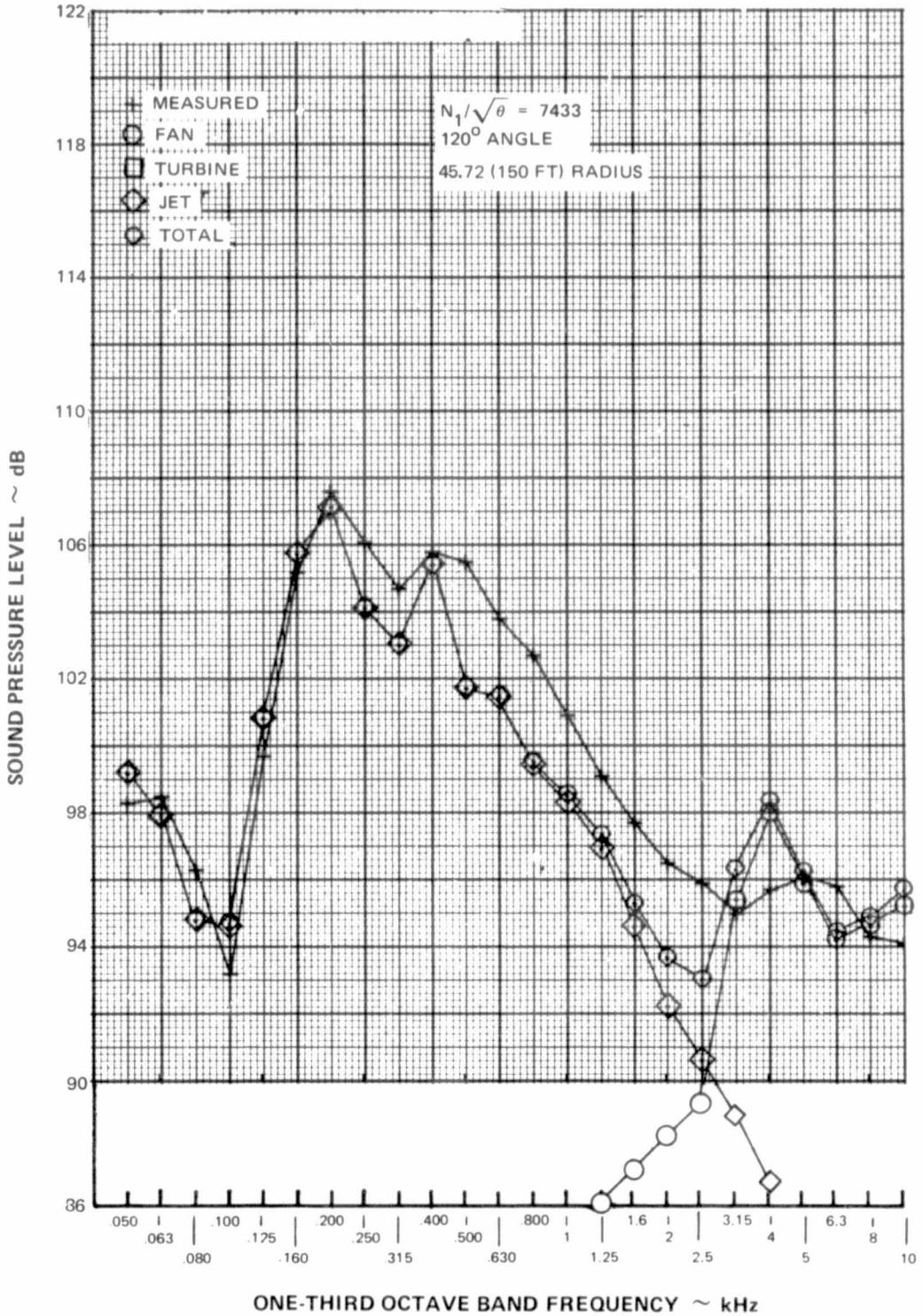

Figure D-143 Summation of Component Noise Levels Compared to Measured Data ~ 7433 N1, 120° Angle

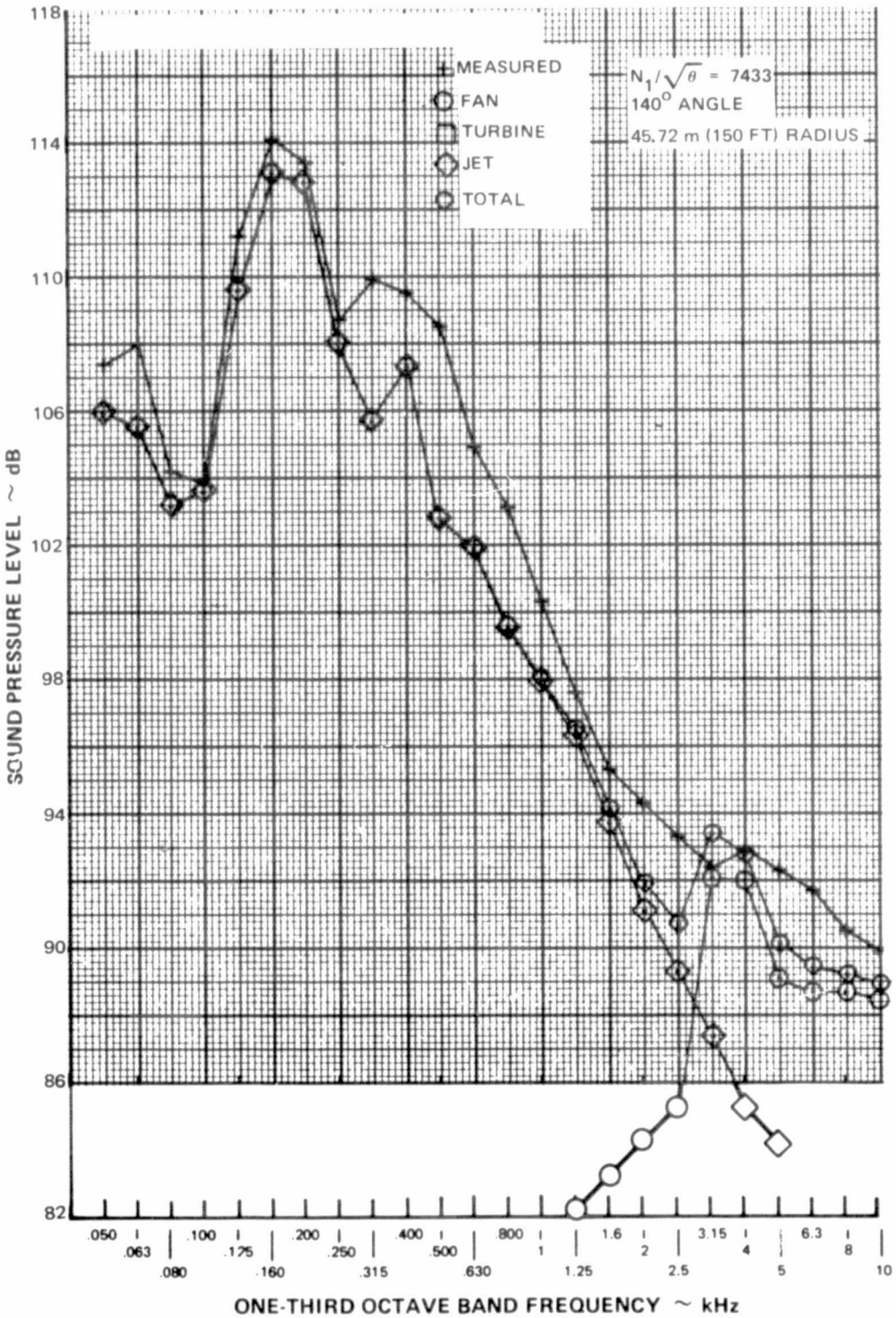

Figure D-144 Summation of Component Noise Levels Compared to Measured Data ~ 7433 N1, 140° Angle

IV. CONCLUDING REMARKS

The principal results of the JT8D-100 Refan program are summarized below:

Mechanical Design

- Subsystem and system development programs substantiated the structural integrity and overall acceptability of the engine design.

Performance Characteristics

- Sea level static testing of the JT8D-109 refan engine showed a thrust specific fuel consumption decrease of 12.76%, as compared to the base JT8D-9 configuration, which was within the design goal of 12.66%.

- The thrust specific fuel consumption at altitude average cruise power exceeded design goals by 0.5%.

- The thrust specific fuel consumption at altitude maximum cruise power exceeded design goals by 1.7 - 3.7% due primarily to higher than anticipated fan duct pressure losses and slightly lower than predicted exhaust nozzle performance.

Stability Characteristics

- The JT8D-109 ground starting characteristics were consistent with typical JT8D-9 base engine experience.

- Successful flight starts were demonstrated without starter assist within the current JT8D-powered aircraft flight start envelope.

- The transient stall margin in the off-idle region was equivalent to that of the JT8D-9 base engine.

- Stable engine operation was demonstrated with inlet distortion screens installed to simulate flight conditions.

- Stable engine operation was demonstrated during both cold and hot engine snap accelerations from both minimum and flight idle around the DC-9/727 flight envelope.

- Stable engine operation was demonstrated during deceleration transients during sea level and DC-9 flight testing. Testing conducted at the NASA LeRC altitude test facility indicated pressure fluctuations at altitudes above 4572m (15,000 feet), which may have been caused by low-pressure compressor stall and surge bleed valve cycling or may have been induced by the test facility.

PRECEDING PAGE BLANK NOT FILMED

- The JT8D-109 engine accelerated 2.9 seconds slower than the base JT8D-9 engine due primarily to a 40% increase in low-rotor inertia. A flight idle setting was required to provide acceptable aborted-landing go-around acceleration capability.

Acoustic Characteristics

- Jet noise levels of the JT8D-109 engine were approximately 6 PNdB below that of the JT8D-9 engine at rated sea level static thrust.

- Fan noise levels of the higher tip speed fan were equal to or lower than those of the JT8D-9 fan over the entire engine operating range.

- Aft quadrant noise levels with the treated fan duct were within 3 PNdB of predicted noise levels.

- Fan duct acoustic treatment was not as effective as original analytical predictions had indicated. It is speculated that the apparent lack of attenuation was due to contamination of rotor/turbulence interaction noise at blade passing frequency which occurs only during static testing.

- Tailpipe treatment effectively attenuated turbine blade passage frequency noise at low engine power settings.

- Inlet treatment significantly reduced fan blade passing frequency noise at approach power.

- Positive cross-correlation between internal transducers and far field microphones confirmed the presence of core engine noise in the far field engine noise signature at low thrust operating conditions.

REFERENCES

1. "Final Report, DC9 Flight Demonstration Program with Refanned JT8D Engines," NASA CR-134857.

2. "Phase II - Final Report, Program of Ground Test of Refanned Turbofan Engines and Nacelles for 727 Airplane," NASA CR-134797.

3. "Phase I - Final Report, JT8D-100 Turbofan Engine," NASA CR-134654, PWA-4790, June 1974.

4. "Summary and Analysis of Performance and Stability Characteristics of the Refan JT8D-109 Engine," NASA CR-134874, PWA-5284, September 1975.

5. E. A. Burdsall, F. P. Brochu, V. M. Scaramella, "Results of Acoustic Testing of the JT8D-109 Refan Engines," NASA CR-134875, PWA-5298, October 1975.

6. E. A. Burdsall, R. H. Urban, "Fan-Compressor Noise: Prediction, Research, and Reduction Studies," FAA-RD-71-73. February 1971.

7. M. P. McMahon, "Static Noise Measurements of Full Scale Jet Engines," Naval Air Propulsion Test Center Environmental Conference, Trenton, New Jersey, May 21-22, 1974.

8. D. C. Mathews, R. T. Nagel, " Inlet Geometry and Axial Mach Number Effects of Fan Noise Propagation," AIAA Paper No. 73-1022, Seattle, Washington, October 15-17, 1973.

9. G. F. Pickett, "Effects of Non-Uniform Inflow on Fan Noise," Acoustical Society of America Paper, New York City, April 23-26, 1974.

10. T. G. Sofrin, G. F. Pickett, "Multiple Pure Tone Noise Generated By Fans Operating at Supersonic Tip Speeds," International Symposium on Fluid Mechanics of Turbomachinery, Penn State, 1970.

11. G. F. Pickett, "The Prediction of the Spectral Content of Combination Tone Noise," AIAA Paper No. 71-730, Salt Lake City, Utah, June 14-18, 1971.

LIST OF SYMBOLS AND NOMENCLATURE

A	Cross section area
A/A*	Ratio of actual area to critical area (where local Mach No. is 1.0)
ADP	Aerodynamic design point
	Engine Area Ratio (Fan/Engine) at tailpipe mixing plane
AJD, Ajd	Duct jet area
AJE, Aje	Engine jet area
AMS	Aerospace Material Specification
Aj	Location along chord line of maximum camber(1)
BPF	Blade passing frequency
b	Airfoil span
C_1	Absolute inlet velocity
C_2	Absolute exit velocity
C. G.	Center of gravity
CV	Gross thrust coefficient
ΔCu	Tangential velocity change
c	Chord(1)
D, D-F	Diffusion factor:

$$\text{Rotor} = 1 - \frac{V'_2}{V'_1} + \frac{r_2 V_{\theta 2} - r_1 V_{\theta 1}}{(r_1 + r_2) V'_1 \sigma}$$

$$\text{Stator} = 1 - \frac{V_3}{V_2} + \frac{r_2 V_{\theta 2} - r_3 V_{\theta_3}}{(r_2 + r_3) V_2 \sigma}$$

DB, dB	Decibels

PRECEDING PAGE BLANK NOT FILMED

DN	(Ref. bearings) Diam (mm) x RPM
dBA	"A" weighted decibels
E	Shaft rotating frequency
EGT	Exhaust Gas Temperature (TT7)
F	Thrust
°F	Degrees Fahrenheit
FEGV	Fan Exit Guide Vane
FFT	Fast Fourier transfer
FOD	Foreign Object Damage
Fn	Net thrust
Fn/δt2	Corrected thrust
Fx(t)	Magnitude of signal at point x
f	Frequency
f/N	Frequency/nodal diameter
HOL	High Operating Line
HPC	High Pressure Compressor
HPT	High Pressure Turbine
HPX	Horsepower Extraction
HTS	High Tip Speed
Hz	Hertz
ΔH_{HPT}	Work extracted from high pressure turbine
ΔH_{LPT}	Work extracted from low pressure turbine
"haystack"	Broadband spectral peak
I.D.	Inner Diameter

IGV	Inlet Guide Vane
in.	Inch
Kc	TSFC correction factor
Kg	Kilograms
Kh	Specific humidity correction factor for WF and TSFC
ksi	1000 pounds per square inch
LB	Pounds
LER	Airfoil Leading Edge Radius(1)
LHV	Lower Heating Value
LPC	Low Pressure Compressor
LPT	Low Pressure Turbine
L/H	Length/height ratio
M, Mn	Mach No.
m	Meter
m/s	Meters/Second
MCA	Multiple Circular Arc
N	Newton
N	Rotational speed
N1,N_1	Low Rotor speed
N2	High Rotor speed
N1C2	Low rotor shaft speed corrected to engine station 2, $N1C2 = N1\sqrt{\theta T2}$
NOL	Nominal Operating Line
OASPL	Overall Sound Pressure Level
OBS	Octave Band Sound
O. D.	Outside Diameter
O/L	Operating Line

P	Static pressure
PAMB (Pamb)	Ambient Pressure
PLA	Power Lever Angle
PNLT	Tone corrected perceived noise level
PO	Standard Sea Level Pressure
PR	Pressure Ratio
PS3	Low pressure compressor discharge static pressure
PS4	High pressure compressor discharge static pressure
PSD	Power Spectral Density
PT	Total Pressure
PT2	Engine inlet total pressure
PT2.4	Low-pressure compressor inlet total pressure
PT3	Low pressure compressor inlet total pressure
PT4	Low pressure compressor discharge total pressure
PT7	High pressure compressor discharge total pressure
PT7F	Low pressure turbine discharge total pressure
PT8	Exhaust nozzle discharge total pressure
P&WA	Pratt & Whitney Aircraft
P/A	Pressure/Area
P_o	Total or stagnation pressure
$P_{t2, 2.4, etc.}$	Total pressure at station 2, 2.4, etc.
P_s/P_t	Static pressure/total pressure
$\Delta P/q$	Loading parameter = $(p_{exit} - p_{inlet})/ (\frac{1}{2} \rho V^2)$ inlet
p	Static pressure

PNdB	perceived noise
psi	Pounds per square inch
R-1.5, 2	Rotor 1.5 stage, 2 stage
RPM, rpm	Revolutions Per Minute
RMS (rms)	Root Mean Square
R_1	Radial load
R_{xy} (τ)	Cross correlation factor
SLS	Sea Level Static
SLTO	Sea Level Take-Off
SM	Surge Margin
SPL	Sound Pressure Level
SPR	Surge Pressure Ratio
SPRC	Surge Pressure Ratio Undistorted
SPRD	Surge Pressure Ratio Distorted
STD	Standard
STO	Overall Turbine (Efficiency)
S-1.5, 2	Stator 1.5 Stage, 2 stage
S/L	Surge Line
s	Second
T	Temperature
TEGV	Turbine Exit Guide Vanes
TER	Airfoil trailing edge radius(1)
TSFC	Thrust Specific Fuel Consumption
TT2	Engine inlet total temperature
TT5	High pressure turbine inlet total temperature

TT7	Low pressure turbine discharge total temperature
T_l	Tangential load
T_t	Total temperature
$T_{t2, 2.4, etc.}$	Total temperature at station 2, 2.4, etc.
Δ TSFC	Change in thrust specific fuel consumption
t	Blade maximum thickness(1)
t/p	Tailpipe
U	Rotor speed
U_{tip}, u_{tip}	Rotor tip speed
V	Air velocity
VFR	View from rear
Vmix	Mixed jet velocity
VJD, Vjd	Fan jet velocity
VJE, Vje	Primary jet velocity
W	Weight flow
WAE	Core Engine Airflow
WAT (Wat)	Total airflow
WATC2	Corrected Total Airflow
WOL	Wide Open Line
WF/PB (Wf/Pb)	Fuel Flow/Burner Pressure
ΔW	Change in weight
Wad, Wa duct	Duct airflow
Wae Wa eng, Wg	Engine airflow

$W_{eng'}$	Engine core airflow
Wjet fan	Fan airflow at station 7
Wjet prim	Engine airflow at station 7
x/b	Ratio of position on an airfoil to total airfoil length
Z_i	Total pressure loss coefficient:

$$\text{Rotors} = \frac{P'_1 - P'_2 (T'_1/T'_2)^{\frac{\gamma}{\gamma-1}}}{(\gamma/2)\, p_1 M'^2_1}$$

$$\text{Stators} = \frac{P_2 - P_3}{(\gamma/2)\, p_2 M_2^2}$$

1C1H	First compressor tone, first harmonic
1F1H	First fan tone, first harmonic
1F2H	First fan tone, second harmonic
1F3H	First fan tone, third harmonic
2C1H	Second compressor tone, first harmonic
2T1H	Second turbine tone, first harmonic
3T1H	Third turbine tone, first harmonic
4T1H	Fourth turbine tone, first harmonic

α	Angle, location denoted by subscript
α_{ch}	Angle between airfoil chord line and tangential plane
β	Absolute air angle $[\cot^{-1} (V_m/V_\theta)]$, degrees
β^*	Metal angle between tangent to mean camber line and through flow direction, degrees (1)
β_1	Inlet relative gas angle
β_2	Exit relative gas angle
δ	Ambient total pressure/standard atmospheric pressure
δ_{aero}	Aerodynamic damping factor
Δ	Change in value
η	Adiabatic efficiency
θ	Ambient total temperature/standard total temperature
θ^*	Airfoil metal turning angle, degrees(2)
ρ	Density
σ	Solidity(1)
σ	Stress (where used in relation to structural loading)
τ	time delay
τ/b	Gap/chord
ω	Total pressure loss coefficient:

$$\text{Rotors} = \frac{P'_1 \left(T'_2/T'_1\right)^{\frac{\gamma}{\gamma-1}} - P'_2}{P'_1 - p_1}$$

$$\text{Stators} = \frac{P_2 - P_3}{P_2 - P_2}$$

ϕ	Blade camber angle(1)

ϕ_E	Blade camber angle on plane of "unwrapped" conical surface
$>$	Greater than
$<$	Less than
$\measuredangle$	Angle of peak sound level
$\sqrt{fx^2}$	RMS value of signal at point x
$\sqrt{fy^2}$	RMS value of signal at point y
$\sqrt{\theta_{t2}}/\delta_{t2}$	Correction factor
Δ hlt/θt2	Corrected low turbine work

Subscripts

a	Air
am (b)	Ambient
duct	Fan duct
eng	Engine
g	Gas
m	Meridional (velocity)
mix	Mixed flow
prim	Primary
ss	Suction surface
t	total
θ	Tangential (velocity)
1	Station into rotor
2	Station out of rotor or into stator
3	Station out of stator

Superscripts

'	Relative to rotor
*	Blade metal (angle)

Subscripts relative to engine station location

2.0	Engine inlet case entry
2.4	Fan rotor exit
2.5	Fan exit guide vane exit
3.0	Low-pressure compressor exit
4.0	High-pressure compressor exit
5.0	High-pressure turbine entry
6.0	Low-pressure turbine entry
7.0	Exhaust duct entry (primary or fan)

Pressure Correction Factor

ST2: Station 2 pressure correction factor DELTA-TT2

$$ST2 = \frac{PT2}{14.697}$$

PT2 = Absolute total pressure at station 2 in psia

Samb: Ambient pressure correction factor DELTA-Ambient

$$Samb = \frac{Pamb}{14.697}$$

Pamb = Absolute total ambient pressure in psia

NOTE: The factor 14.697 is the absolute total ambient pressure in PSIA at sea level standard day

Temperature Correction Factors

$\theta T2, \sqrt{\theta T2}$: Station 2 temperature correction factor THETA/T2 and the square root of THETA/T2

$$\theta T2 = \frac{TT2}{518.7}$$

TT2 = Absolute total temperature of engine station 2 in °R

$\theta amb, \sqrt{\theta amb}$ Ambient temperature correction factor THETA - ambient and the square root of THETA -ambient

$$\theta amb = \frac{Tamb}{518.7}$$

Tamb = Absolute total ambient temperature in °R

NOTE: The factor 518.7 is the absolute total ambient temperature at sea level standard day in °R

Notes:

(1) Rotor 1 geometry is on flow surface. Geometry of other rotors is on manufacturing plane.

(2) In general, Greek letters are used to indicate angles. Those not followed by an asterisk refer to gas angles, whereas those followed by an asterisk refer to angles of metal surfaces.